Studies of particles associated with air showers of size around 3.10(5)particles

I. A. Ward

FRONTISPIECE

THE FLASH-TUBE CHAMBER AFTER MODIFICATION TO OPERATE IN CONJUNCTION WITH THE DURHAM AIR SHOWER ARRAY.

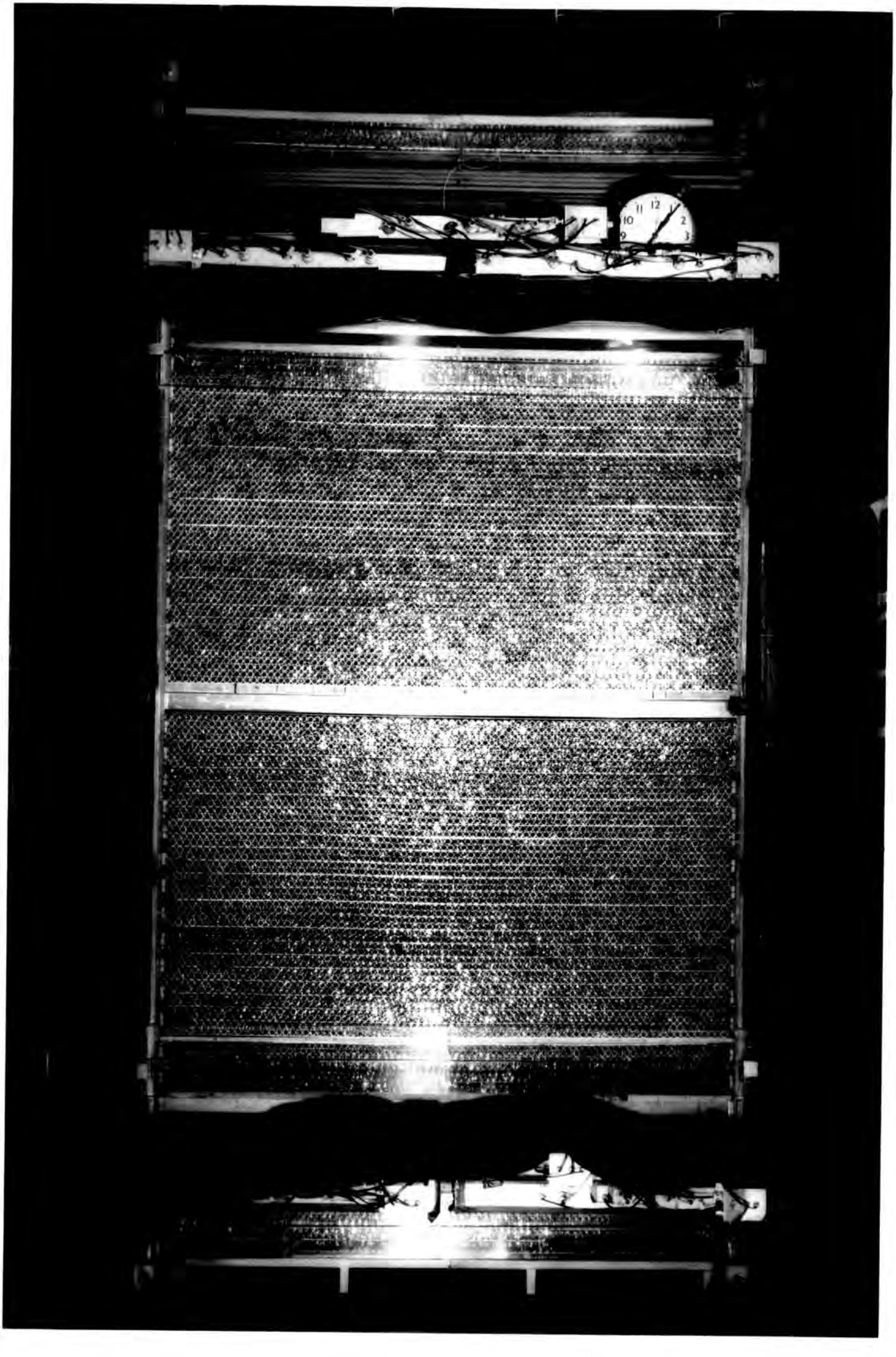

STUDIES OF PARTICLES ASSOCIATED WITH AIR SHOWERS OF SIZE AROUND 3.10^5 PARTICLES

by

I. A. WARD, B.Sc.

A thesis submitted to the
University of Durham
for the Degree of Doctor of Philosophy

October 1980

"For oft, when on my couch I lie
In vacant or in pensive mood,
They flash upon that inward eye
Which is the bliss of solitude;"

W. Wordsworth

in LAODAMIA (1815)

CONTENTS

A B S T R A C T

A study of particles associated with air-showers of median size 3.10^5 particles has been undertaken. Measurements on muons indicate that the apparatus is inadequate to cope with regions greater than 30 m. from the core.

However some interesting results have been produced within this limitation. There is strong evidence for non-random spacing of muons at densities greater than 1 m^{-2}. The lateral distribution of hadrons of energy greater than 50 GeV is slightly steeper than for hadrons of energy greater than 10 GeV. The ratio of neutral to charged hadrons is a lot lower than predicted by current production models.

A search for precursors to air-showers has also been carried out. The results imply that there are a statistically significant number of precursors in the range 20 to 100 μs before the arrival of an air-shower.

The early chapters concern themselves with measurements that can be made with the flash-tube chamber in isolation. A measurement of the incoherent hadron energy spectrum shows a smoothly falling spectrum between 7.10^2 GeV and 5.10^3 GeV of slope 2.7.

An upper limit of $2.3.10^{-8}$ cm^{-2} st^{-1} sec^{-1} has been placed on the sea-level flux of high Z particles.

PREFACE

This thesis describes the work of the author while a Ph.D. student at Durham University under the supervision of Dr. F. Ashton.

The work described includes investigations of unusual phenomena in flash-tube chamber studies of hadrons in air-showers, and a measurement of the energy spectrum of the incoherent hadron component.

A thorough review of theoretical and experimental work on tachyons is included prior to the description of an experiment to search for tachyons associated with air-showers.

The final chapters are concerned with measurements on muons and hadrons in air-showers of median size 3.10^5 particles.

The work described herein has been previously reported by Ashton et al (1975a), Ashton et al (1977*).

CHAPTER 1

INTRODUCTION

1.1 Historical introduction

The nineteenth century saw many advances in the fields of electricity and magnetism, and, in the closing decades, the discovery of ionising radiation and the existence of radioactive substances.

One of the principal instruments used in the investigations of electrical phenomena was the electroscope, first the gold leaf type then later (1909) the more quantitative Wulf type.

The principle of an electroscope is that two light highly conductive isolated metal plates or wires when charged repel each other. They were mainly used in the investigation of electrostatic phenomena however it was well known that the metal conductors would not retain their charges indefinitely. At first the cause was thought to be leakage through poor insulation to the casing of the electroscope. However, with the advent of the atomic theory of matter and the discovery in 1897 by J. J. Thomson of the electron, as well as improved insulation techniques, a better understanding of the spontaneous discharge of electroscopes came about, and with it, a new mystery of nature to be solved.

The discharge was explained as being caused by the presence of non-neutral air molecules inside the casing of the electroscope. These enabled a net flow of charge between the metal conductors and the casing without any current flow through the insulation between the two. The question then

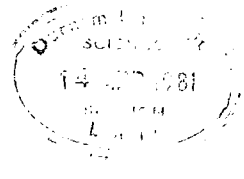

arose as to how these ionised molecules lost their neutrality. It was believed that some ionising agent (such as alpha or beta particles) which could penetrate the walls of the electroscope was the cause, and the source of these ionising particles was thought to be minute quantities of radioactive materials in the immediate vicinity of the electroscope.

The invention of a more quantitative type of electroscope by Wulf in 1909 enabled more systematic investigations of this phenomena to be undertaken and in particular the question as to the source of the ionising radiation could be answered.

In 1912 Hess undertook an historic series of balloon flights in which he carried Wulf type electroscopes to altitudes between 2,000 and 16,000 ft. Contrary to popular opinion he discovered that although the rate of spontaneous discharge did in fact decrease with altitude upto a height of 2,000 ft., beyond this the rate of discharge increased until at a height of 16,000 ft., the rate of discharge was found to be four times the rate at sea-level. Further balloon flights followed, some reaching altitudes of 28,000 ft., confirming the discovery that the ionising radiation did indeed come from above.

Various explanations were forthcoming, C. T. R. Wilson - the inventor of the cloud chamber - suggested that the ionised air molecules might be caused by thunderstorms. Others suggested the presence of traces of radioactive elements in the upper atmosphere. However, neither of these explanations could be reconciled with the observations that the rate of discharge, and hence the concentration of ionised air molecules, did not vary with weather conditions, climate or time of year.

However, the question as to whether the ionising radiation came from above was still unanswered in some physicists' minds. In particular, R. A. Millikan, the first man to measure the charge of an electron, decided to conduct a series of experiments at mountain altitudes and at various depths in lakes between 1923 and 1926. He concluded that the ionising radiation, which he named cosmic rays, did in fact come from above, and produced quantitative measurements of the intensity of cosmic rays as a function of altitude and depth below water. These measurements were extended and improved by Pegener and co-workers in the late 1920's and early 1930's with a series of unmanned balloon flights, and the first steps in the task of investigating the cosmic radiation had been undertaken producing measurements of the concentration of ion pairs as a function of altitude and as a function of depth in water.

Piecing together the clues as to the nature of these cosmic rays was undertaken by Millikan. Basing his hypothesis on the fact that γ-rays were the most penetrating of the three types of ionising radiation then known to occur naturally, and that the mean free path for Compton collisions (the method by which γ-rays were thought to be absorbed) increased with increasing photon energy, Millikan proposed that cosmic rays were high energy γ-rays. He also proposed a model by which they could be produced isotropically in interstellar space from the fusion of different numbers of protons to produce nitrogen, oxygen and silicon atoms. These particular atoms, if produced by the fusion of groups of fourteen, sixteen and twenty-eight protons respectively would release energy in the form of γ-rays of energies approximately equal to 26, 110 and 220 MeV respectively. A suitable combination of absorption curves for γ-photons of these energies

provided a fair approximation to the observed absorption curve for all cosmic rays.

However, the photon nature of cosmic rays could not explain the observed geomagnetic effects. The "East-West" effect, where more cosmic rays were observed to arrive from the East than the West, and the latitude effect, where the intensity of cosmic rays increased as you moved away from the equator, indicated that the paths of the cosmic rays were affected by the earth's magnetic field, and that they thus must be charged, and hence be particles.

Further evidence for the corpuscular nature of cosmic rays was provided by the invention in 1929 of the Geiger-Muller tube. This enabled individual charged particles to be detected by amplifying the ionisation caused by them using a high electric field.

Experiments by Bothe and Kohlhorster using such tubes placed one above the other indicated that the coincident signals observed were too frequent to be caused by the secondary electrons produced by Compton collisions of γ-rays. Placing a thick absorber between the two tubes also failed to decrease the rate of coincidences appreciably, and they concluded that the ionising radiation must consist of energetic charged particles which could directly trigger the tubes, and penetrate thick absorbers.

In the early 1930's two experiments using different types of detectors shed further light on the nature of cosmic rays by observing new interaction processes which they suffered in thick targets. Rossi performed experiments using triangular arrangements of Geiger-Muller tubes underneath lead and observed coincidences which could only be caused by the presence of more

than one ionising particle below the lead. These particles could not have been produced by ionisation processes, since the energies of secondary particles produced by ionisation are too low. Blackett and Occhialini in 1933 using a counter controlled cloud chamber observed multiple secondary particles produced by an interaction of a cosmic ray outside the confines of the chamber.

Extending his experiments to absorbers of different thicknesses Rossi produced shower curves which indicated that as the thickness of absorber was increased, so did the number of charged particles emerging until at some critical thickness the number of charged particles produced began to decrease if the thickness of the absorber was increased further. He also found that the rate at which showers were observed varied between absorbers of different materials but of the same thickness. The rate at which showers were produced under lead, iron and aluminium of the same thickness were found to be in the ratio of 4 : 2 : 1. Neither result was explicable by the Compton effect and ionisation processes alone.

At about the same time as these results were becoming available a more exact theory of the interactions of charged particles with matter was developed by Bethe and Heitler. Their calculations of the radiation losses by charged particles by bremsstrahlung as they traversed matter indicated these losses were much greater - for a given mass per unit area - in elements of high atomic number than in elements of low atomic number, and that radiation losses increase rapidly with energy, thus overtaking ionisation losses. They also conducted calculations on the pair production process by which γ-photons materialise in the electric field of a nucleus into an electron and a positron. These calculations produced the then

startling results that at energies greater than several MeV in lead the pair production process overtakes the Compton effect as the most important absorption process for γ-rays.

The currently held view of the nature of cosmic rays was that they were electrons, but the conclusions of Bethe and Heitler that the radiation losses were more important than ionisation losses, indicated that the electrons - being very light particles and hence easily affected by bremsstrahlung processes - must have absurdly high energies in order to traverse the large amounts of absorber they were observed to have.

However, a model of the shower process was developed along the lines indicated by Bethe and Heitler. The secondary shower particles observed under thick absorbers were assumed to come from a cascade process inside the absorber whereby an initiating electron or photon underwent either a bremsstrahlung or a pair production interaction producing two particles, an electron and a photon or an electron and a positron. These particles then travel on to undergo similar interactions (or an electron - positron annihilation process in the case of the positron) each interaction producing two particles where only one existed. The ensuing cascade process produced many particles, the number increased as the thickness of target increased. However the cascade process also caused an energy degradation until the energy per particle became too low for these high energy processes and any further interactions would be by Compton scattering and ionisation collisions, reducing the number of secondary particles of sufficient energy to leave the absorber.

This shower or cascade model was shown to explain the different shower curves observed, and the primary electron or photon initiating the cascade

was thought to come from a similar cascade produced in the atmosphere.

This explanation went a long way to explaining the nature of cosmic rays as observed, but could not explain the presence of penetrating particles which could traverse large amounts of matter without interacting. These particles were at first thought to be extremely high energy electrons only losing a small fraction of their energy by ionisation as they traversed matter. However as the theory of Bethe and Heitler (1934) became accepted, it became clear that these particles could not be electrons since radiation losses dominate ionisation losses for electrons at higher energies. According to the same theory, if these particles were only losing energy by ionisation, then they must be much heavier than electrons. The natural candidate was the proton, whose mass was known to be $\sim$1000 times the mass of an electron. However, experiments soon showed that these penetrating particles did not behave like protons.

Penetrating particles observed in multiplate cloud chambers, where their magnetic rigidity was also measured, did not ionise as strongly as protons of the same rigidity, implying that they had a mass less than the mass of a proton. Experiments by Street and Stevenson around 1937 on low energy penetrating particles determined the mass of such particles which came to rest inside the cloud chamber. They found them to have a mass 200 times the mass of an electron, and thus proved the existence of a new particle, the mu-meson.

The discovery of a second type of meson, the pi-meson in 1947, almost established a coherent view of cosmic rays and opened a new chapter in elementary particle physics, the spectrum of hadrons. The discovery of

the pi-meson by observation of its decay into the muon and the latter's subsequent decay into an electron in a nuclear emulsion, provided an explanation for the nuclear interactive particles observed to produce showers in multiplate cloud chambers and stars in nuclear emulsions, which effects could not be explained by mu-mesons or electrons. The last piece in the jigsaw puzzle of cosmic ray showers came with accelerators, the discovery of the neutral pi-meson which had a lifetime some 10^{-8} times less than a charged pi-meson, decaying almost instantaneously into two γ-photons.

By the early 1950's the picture of the cosmic ray shower process was complete. The primary cosmic rays were the long lived protons which interacted with air nuclei to produce a shower of charged and neutral pi-mesons. The neutral pi-mesons immediately decayed into γ-photons initiating an electron - photon shower. The high energy charged pi-mesons interacted with further air nuclei to produce further pion showers. This nuclear cascading process contributed to the electron - photon shower process and also served to degrade the energy carried by the pi-meson component. These pi-mesons of low energy eventually decayed to produce mu-mesons which provided the second most abundant component of sea-level cosmic radiation.

1.2 Outline of the following chapters

In the following chapters are described various measurements of important components of the cosmic radiation at sea-level using a flash-tube chamber.

Chapter 2 provides an introduction to the flash-tube chamber and the techniques by which these various components of the cosmic radiation can be investigated using the flash-tube chamber in isolation.

Chapter 3 describes, by way of an experiment conducted to investigate a phenomenon of relativistic electromagnetic effects, the ionisation process in depth. This latter is fundamental to the effectiveness of the flash-tube chamber as an investigative instrument. A thorough understanding of the process is essential to the correct interpretation of the flash-tube chamber's responses to the various components of cosmic radiation.

Chapter 4 is concerned with an experiment to measure the energy spectrum of hadrons in sea-level cosmic radiation. This is considered an important component in its own right since it is the only natural phenomenon of physics, at energies that are orders of magnitude higher than can presently be attained by artificial means, which is directly observable in the immediate environment.

Possible candidates as highly charged fundamental particles observed in the latter experiment are investigated in depth in Chapter 5. The problems of interpretation encountered in all investigations of natural phenomena, lead to interesting considerations on some basic formation processes involved in nuclear-electromagnetic cascade production.

The availability of an extensive air-shower array in the vicinity of the flash-tube chamber made it necessary to modify the chamber in order to use it in conjunction with the array. Chapter 6 describes these modifications, as well as a brief description of the array.

The array was designed to study air-showers whose primary particles' energies lie in the region of a distinct steepening of the primary cosmic radiation's energy spectrum. This region provides an interesting area of study because, although only at fairly mediocre energies compared with the majority of air-showers that have been investigated in the past, the energy region is just beyond the capabilities of existing particle accelerators. Such a position provides a hot debating ground as to whether the steepening of the spectrum is an astrophysical or a nuclear physical effect. Alternative causes of the steepening to the presently accepted astrophysical explanations would involve either the onset of new physical processes in high energy interactions, or the creation of new, and as yet undetected, classes of particles. Both the latter phenomena can be fruitfully investigated using the flash-tube chamber in conjunction with an air-shower array.

The following chapter describes how air-shower events are interpreted using the air-shower array, whereas Chapters 9 to 11 describe such investigations which have been carried out.

Chapter 8 is a survey of the available theoretical and experimental studies of faster than light particles, called tachyons. These, if they exist, and are produced at the energies in question, could, by their unusual energy attributes, provide a sink for the energy of higher energy particles, and thus cause a steepening of the observed primary spectrum.

There follows a description, Chapter 9, of a search for tachyons, whose results raise an intriguing, but incompletely persuasive, question mark as to the existence of such particles.

Chapters 10 and 11 are respectively concerned with the muonic and hadronic components of air-showers. The results are compared with comparative previous experiments and model-dependant predictions, as well as with laboratory measurements at energies just below the energies under investigation.

Summaries and Conclusions are provided at the end of each chapter and a qualitative summary of the knowledge acquired during these investigations is given in Chapter 12.

CHAPTER 2

THE FLASH - TUBE CHAMBER

2.1 Introduction

The flash-tube chamber is a large area visual detector of cosmic ray particles. It can be used:

a.) To identify particles with anomolously high or low ionising powers (see Chapters 3 and 5).

b.) To measure the energies and arrival directions of individual particles that interact in the chamber (see Chapters 4 and 11).

c.) To observe the individual tracks of penetrating particles (see Chapter 10).

The various triggering modes available to the flash-tube chamber allow either the properties of unaccompanied particles or particles associated with air-showers to be observed and measured.

2.2 The neon flash-tube

When an ionising particle passes through the gas of a neon filled flash-tube it produces positive ions, free electrons and excited gas atoms. In Lloyd's discussion of the problem he concludes that only the free electrons thus generated can cause a discharge if an electric field is applied across the tube after time t_d μs (Lloyd, 1960). Essentially

this is because in order to cause a discharge an avalanche of electrons needs to be created on the application of the electric field. The relatively massive ions move too slowly to cause such an avalanche, and the photons emitted from the decay to ground state of the excited gas atoms have too low a photoionisation coefficient.

In the time td, the free electrons can be removed from the gas by various means:

a.) Recombination with the positive ions. This process can be neglected because of the small number of electron - ion pairs created and the very low value of the recombination coefficient ($\sim 10^{-7}$ cm^3/sec)

b.) Attachment to electronegative impurities, this process can only be neglected if the tubes have been accurately evacuated and then filled with neon gas of sufficiently high purity

c.) Diffusion to the glass walls where the electrons stick and cannot come back into the gas

d.) Drifting to the glass wall under the action of any electric field that may be present. This process can only be neglected if sufficient time is allowed between ionisation events for the gas to recover.

Lloyd set up diffusion equations for the electrons produced and solved them to find the probability that a discharge would take place if an electric field were applied td μs after the passage of the ionising particle. He found that the probability of a discharge occurring (the internal efficiency) can be expressed as a function of $D.td/_{a^2}$ (where D is the diffusion coefficient of thermal electrons and a is the internal radius of the tube), with the parameter afq (where f is the probability

that a single electron produces an avalanche and q is the probability per unit track length of the primary particle producing an electron - ion pair). His results are displayed by the curves of Fig. 2.7.

2.3 The flash-tube chamber

2.3.1 Construction of the flash-tube chamber

Scale diagrams of the chamber are shown in front and side view in Figs. 2.1 and 2.2. The flash-tubes are 2 metres long of mean internal diameter 1.58 cms and mean external diameter 1.78 cms. They are made of soda glass filled with neon gas (98%) and helium gas (2%) to a pressure of 60 cm Hg. Alternate layers contain 84 and 85 tubes, the tube positions being staggered with respect to the layers immediately above and below. Each tube is covered with a black polythene sleeving to inhibit light transfer between neighbouring tubes. There are a total of 10,748 flash tubes used in the chamber.

Between every other layer of flash-tubes there is an aluminium electrode 0.122 cms thick, 3.3 cms apart. In the sections F2 and F3 (see Fig. 2.2) the electrodes cover an area of 2.94 m^2. In the sections F1a, F1b, F4a and F4b the electrodes are shorter in depth by 30 cms, and cover an area of 2.48 m^2.

The roof of the chamber is 15 cms of lead. This serves 2 functions:

a.) To filter out the soft component (low energy electrons and photons) of the cosmic radiation so that the flash-tube photographs clearly identify the more penetrating components (muons and hadrons).

FIG. 2·1

Front view of the flash-tube chamber

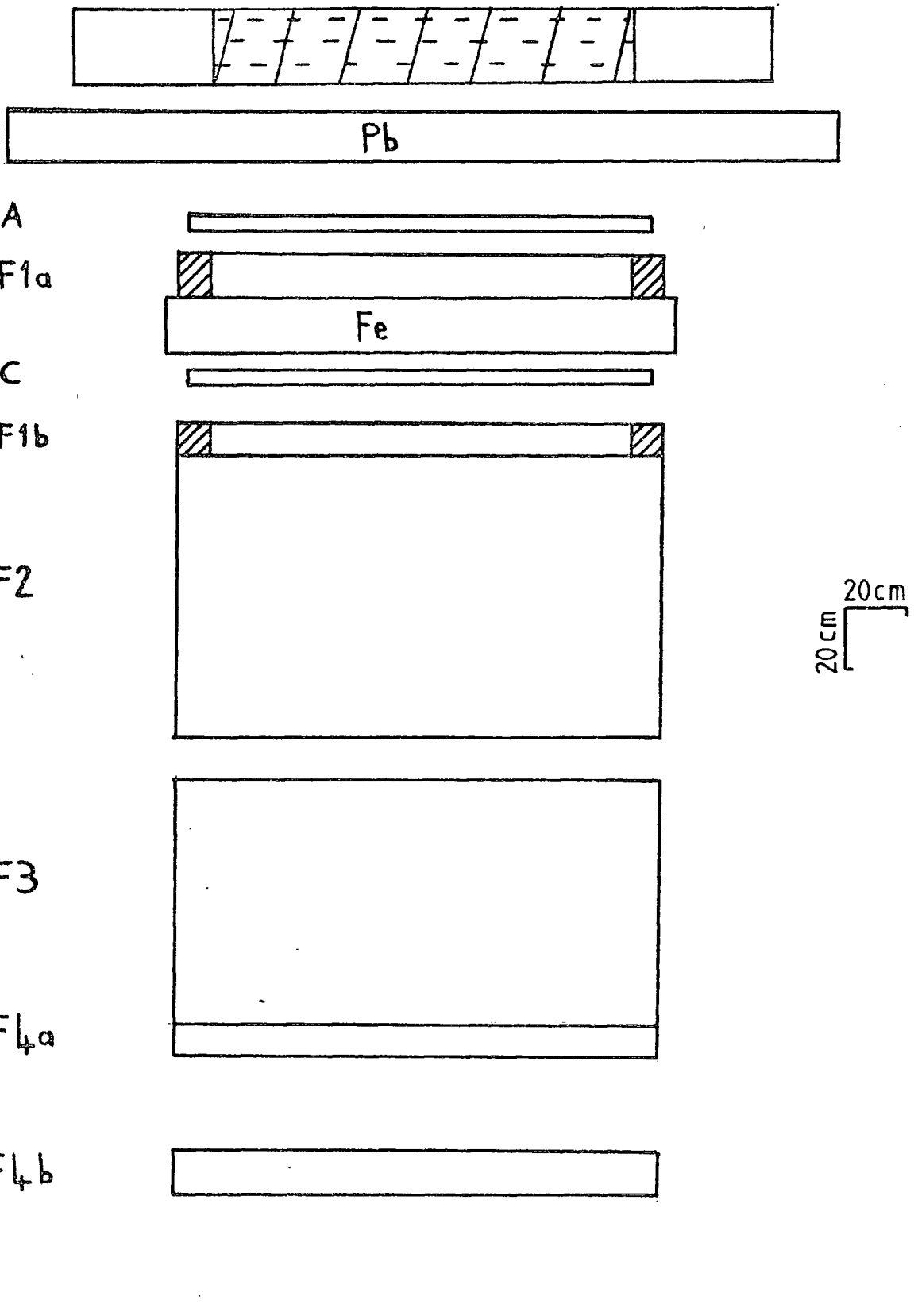

FIG. 2.2

Side view of the upper half of the flash-tube chamber

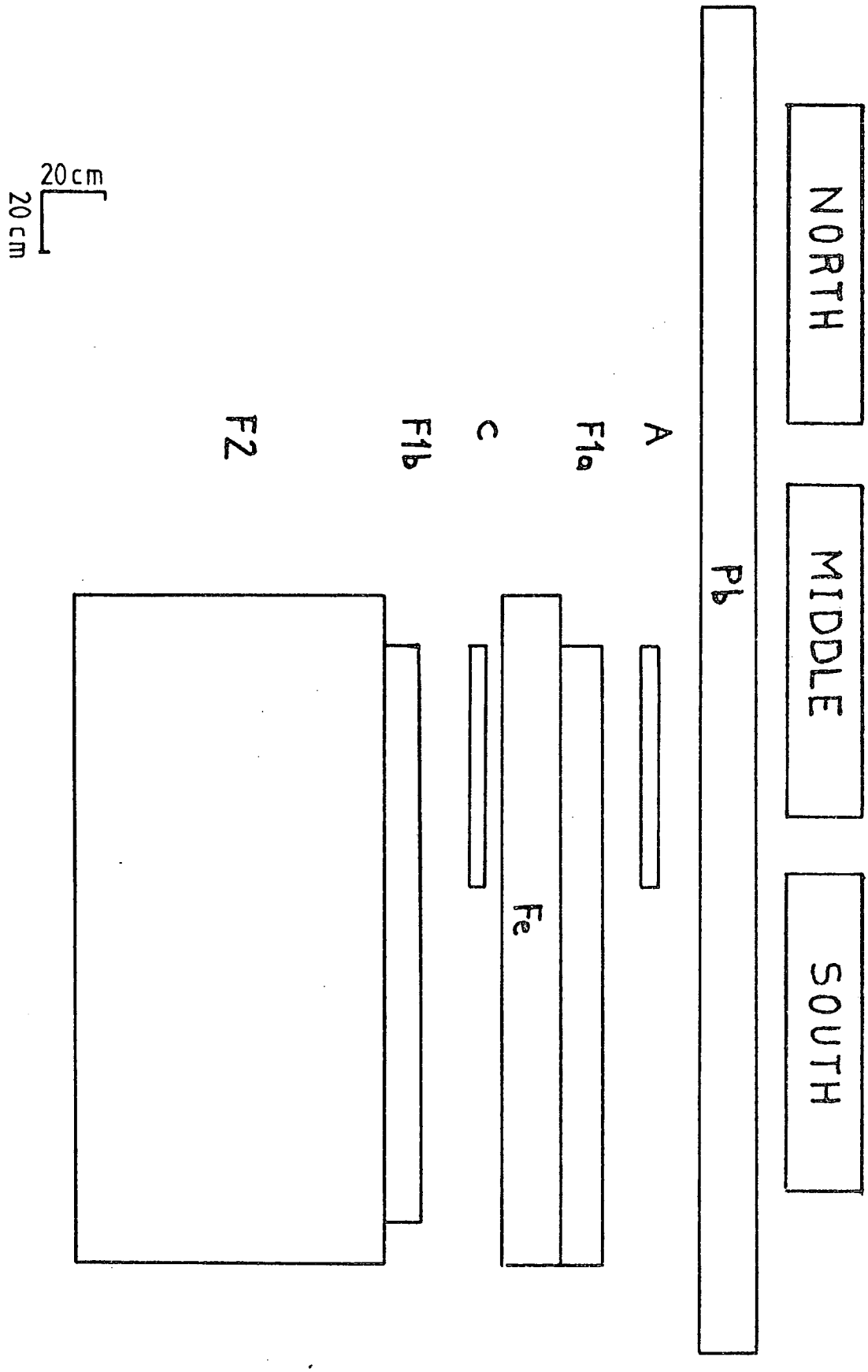

b.) To act as a target for nuclear interactions of hadrons.

Below the roof are the first defining layers of flash-tubes F1a. There are 8 layers of flash-tubes in F1a pushed back 15 cms with respect to the front of the main body of flash-tubes (F2 and F3). These act as:

a.) a visual identifier of nuclear interactions that occur in the lead.

b.) an identifier of the nature of the hadron (charged or neutral) that undergoes a nuclear interaction in the iron target.

c.) a defining layer for single particle tracks whose ionising power can be gauged from the main body of the chamber (F2 and F3) without the possibility of edge effects i.e. the reduced efficiency of a flash-tube a few cms beyond the edge of the electrode (Ashton et al 1971).

Below F1a there is a 15 cm iron target for nuclear interactions. There are a further 6 layers (F1b) of defining flash-tubes, then the main body of flash-tubes F2 (52 layers) and F3 (44 layers). Below these there are a further 2 defining sections, F4a (6 layers) and F4b (8 layers).

Directly below each target there is a plastic scintillator of area 1.05 m^2 and thickness 5 cms, each viewed by five 53 AVP photomultiplier tubes and one 56 AVP tube (see fig. 23). These scintillators measure the number of electrons produced in the electron photon shower caused by a nuclear interaction in either target. Above the lead are three large liquid scintillators used to measure any air-shower accompaniment. These scintillators are each of area 1.24 m^2, depth 15 cms and are each viewed by two EMI 9583B photomultiplier tubes (see fig. 2.4).

The sides of the chamber are protected from background cosmic radiation by 30 cm thick walls of barytes concrete. The whole chamber is kept in

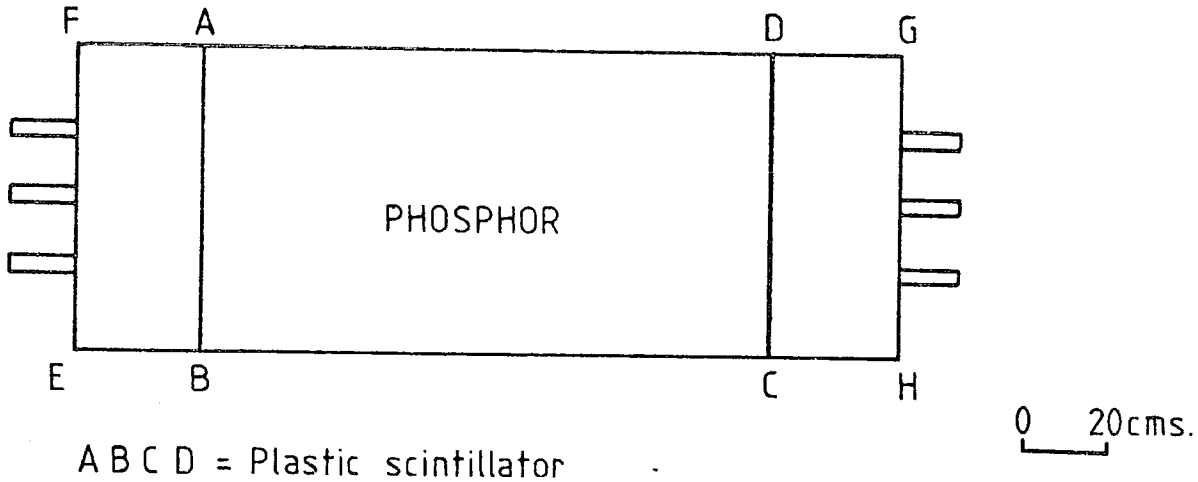

A B C D = Plastic scintillator

A B E F, C D G H= Perspex light guides

FIG. 2·3 The basic design of a plastic scintillation counter.

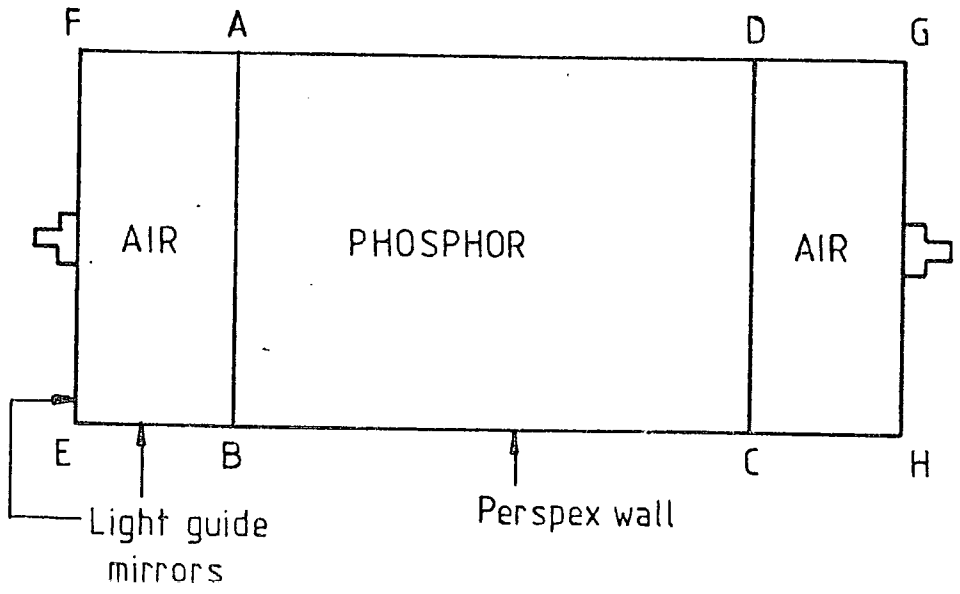

FIG. 2·4 The basic design of a liquid scintillation counter.

continuous darkness, enabling the use of a shutterless camera. This means that the camera is continuously sensitive, the film being wound on one frame automatically after each event.

2.3.2 The high voltage pulsing system

In order that a visible discharge occurs in a neon flash-tube after the passage of an ionising particle a high voltage pulse must be applied to the aluminium electrodes. This high voltage pulse is provided by the circuitry of Fig. 2.6, which is triggered by a 300 volt pulse provided by a thyristor.

The occurrence of a selected event provides a 5 volt trigger pulse to the thyristor. The +300 volt output pulse of the thyristor is fed into a high voltage pulse transformer (Fig. 2.5), the output of which provides the trigger pulse for the "Trigatron" spark gap.

A voltage of +16 kV is applied across the main spark gap, the trigger spark causes the gap to break down largely by the production of photo-electrons. The high voltage pulse applied to the electrodes is approximately rectangular in shape of height 8 kV and 10 μs duration, it is produced by the circuit of Fig. 2.6. When the main gap of the Trigatron breaks down, the lumped circuit transmission line discharges through its characteristic impedance producing a rectangular pulse for a time $2n\sqrt{LC}$ (for n identical L, C stages). The transmission line has four stages each of capacitance C = 0.1 μF and inductance L = 22 μH. The capacity of the flash-tube chamber which this unit supplies is 0.087 μF.

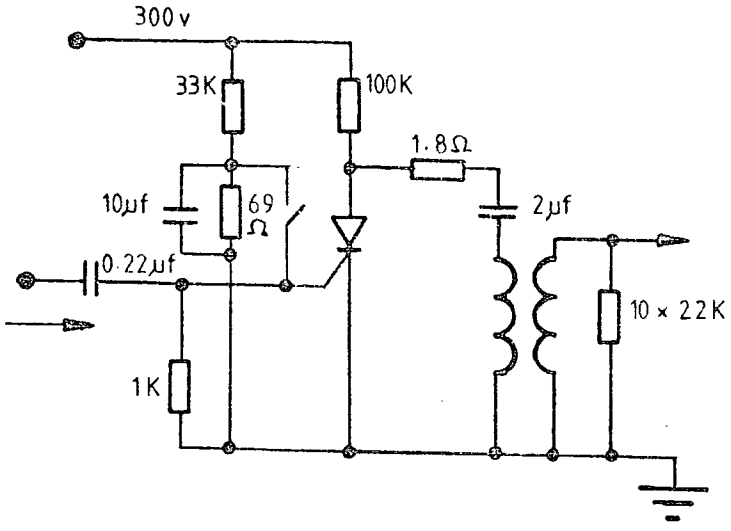

FIG. 2·5 High Voltage pulsing unit

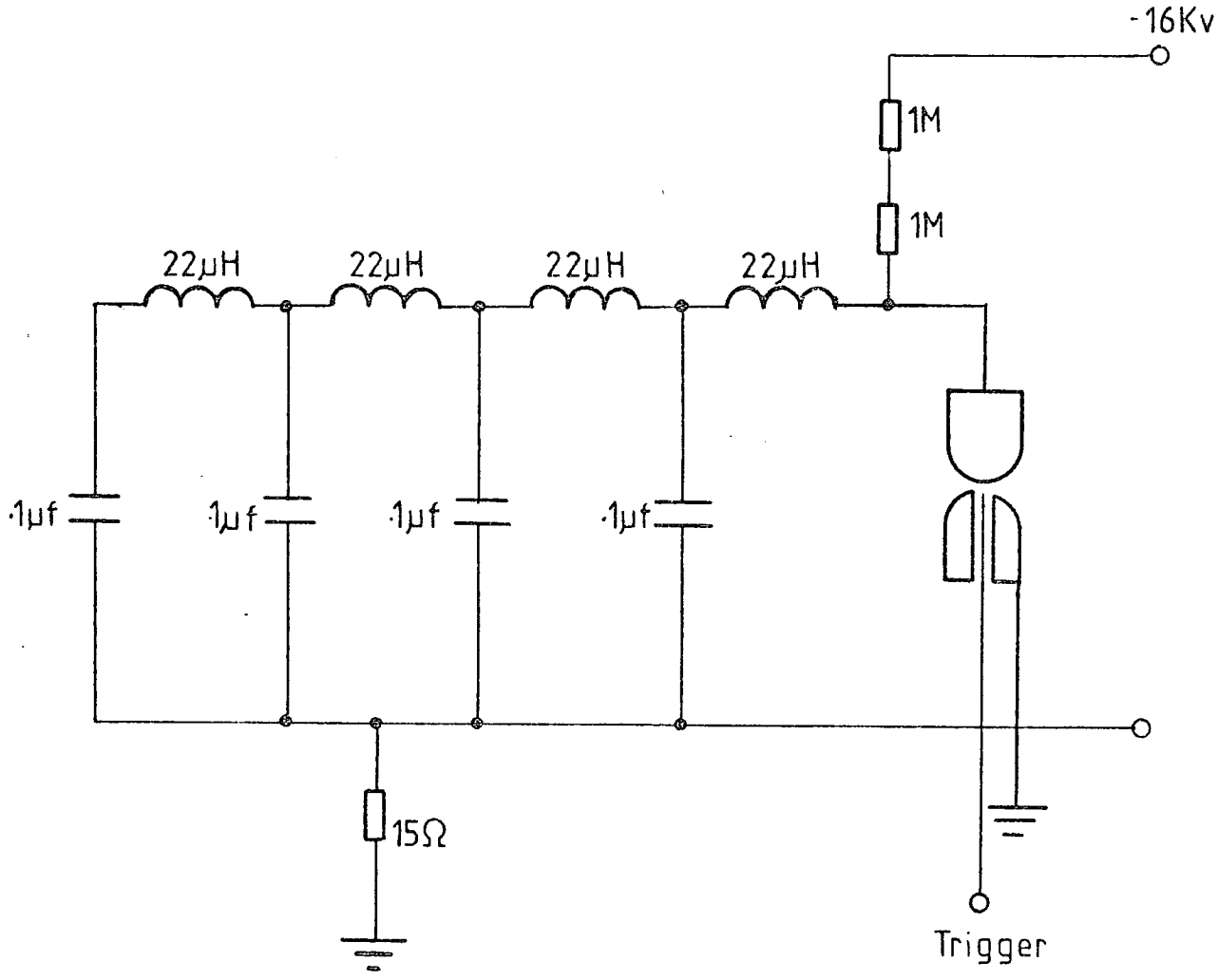

FIG. 2·6 Air Spark Gap and Delay Line

Fig. 2.7: Variation of the internal efficiency of a neon flash-tube with time delay t_d for particles of different charge Ze.

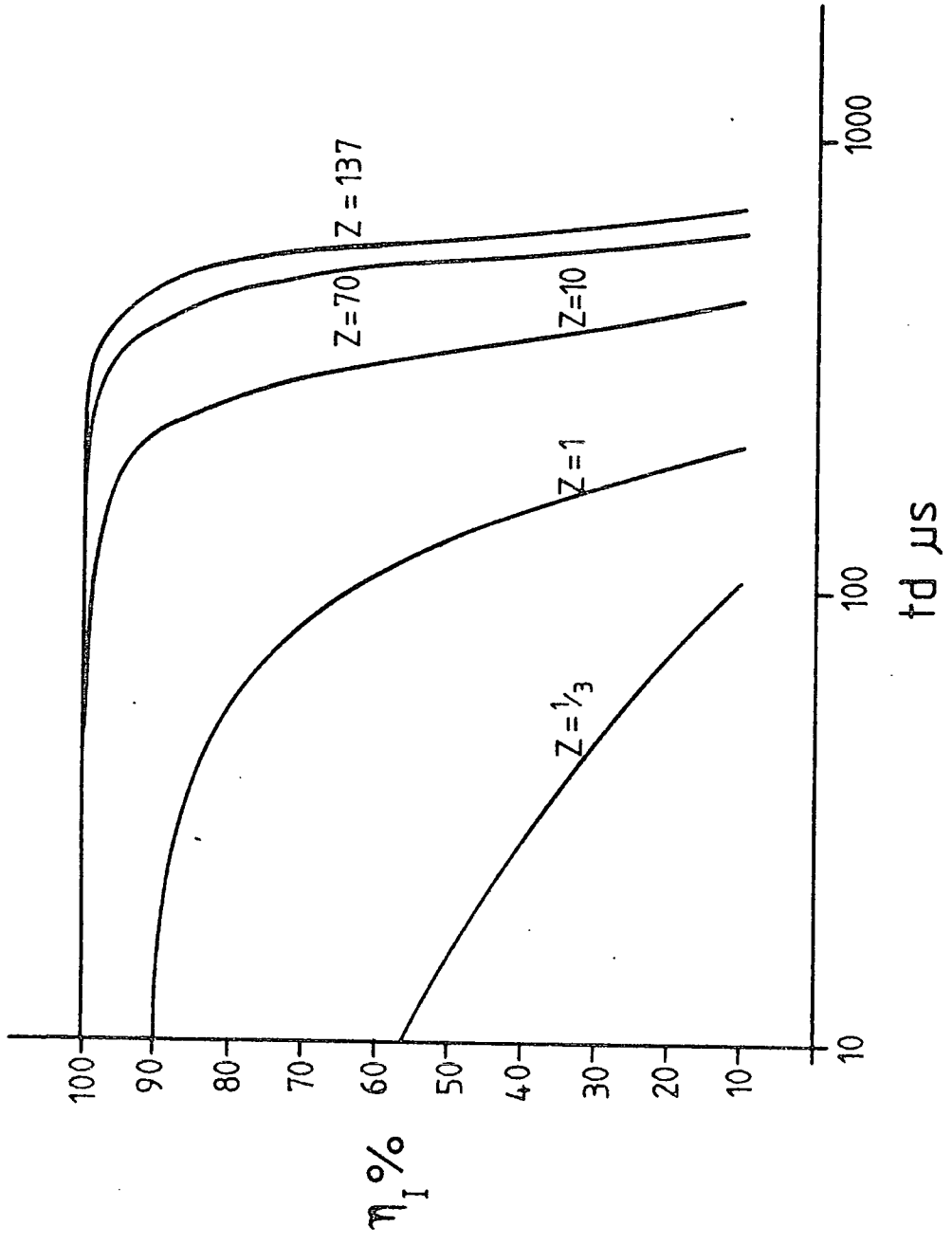

FIG 2.7

Figures 2.8a): The expected response of the flash-tube chamber at time delay of 20μs to particles of different charge Ze.

FIG. 2:8 a)

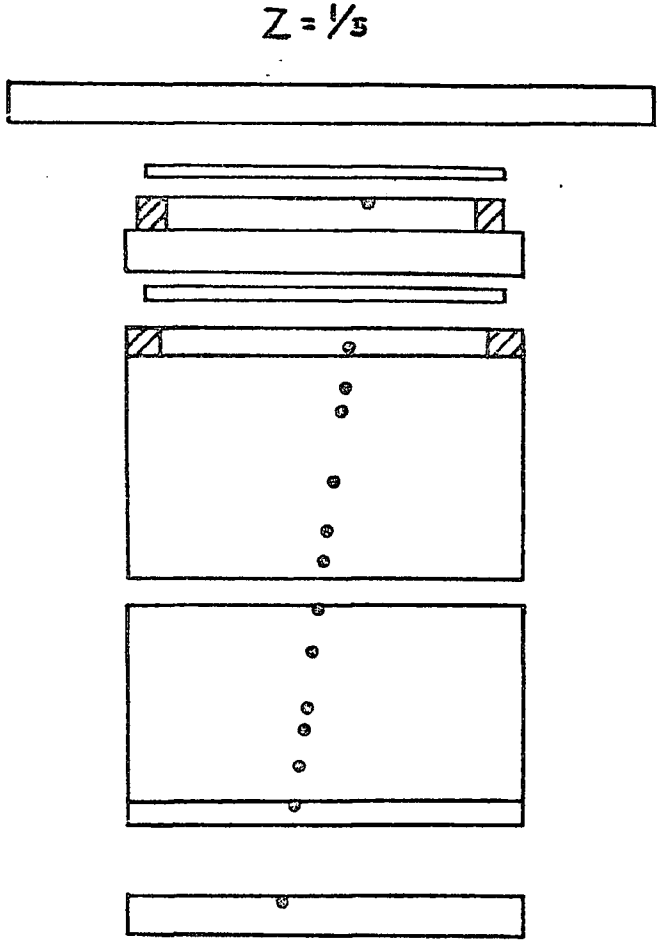

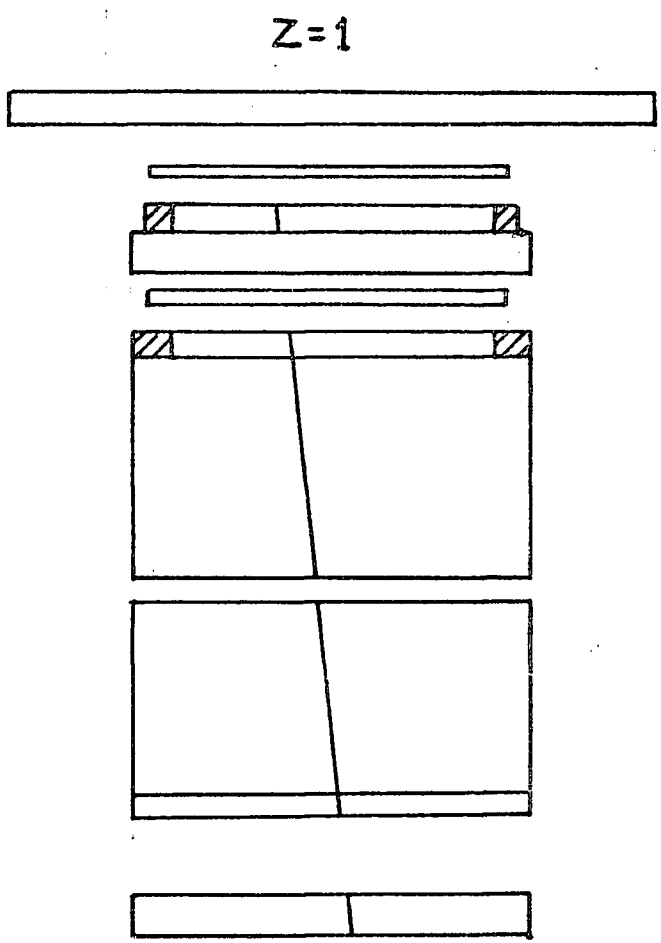

FIG. 2-8 a)

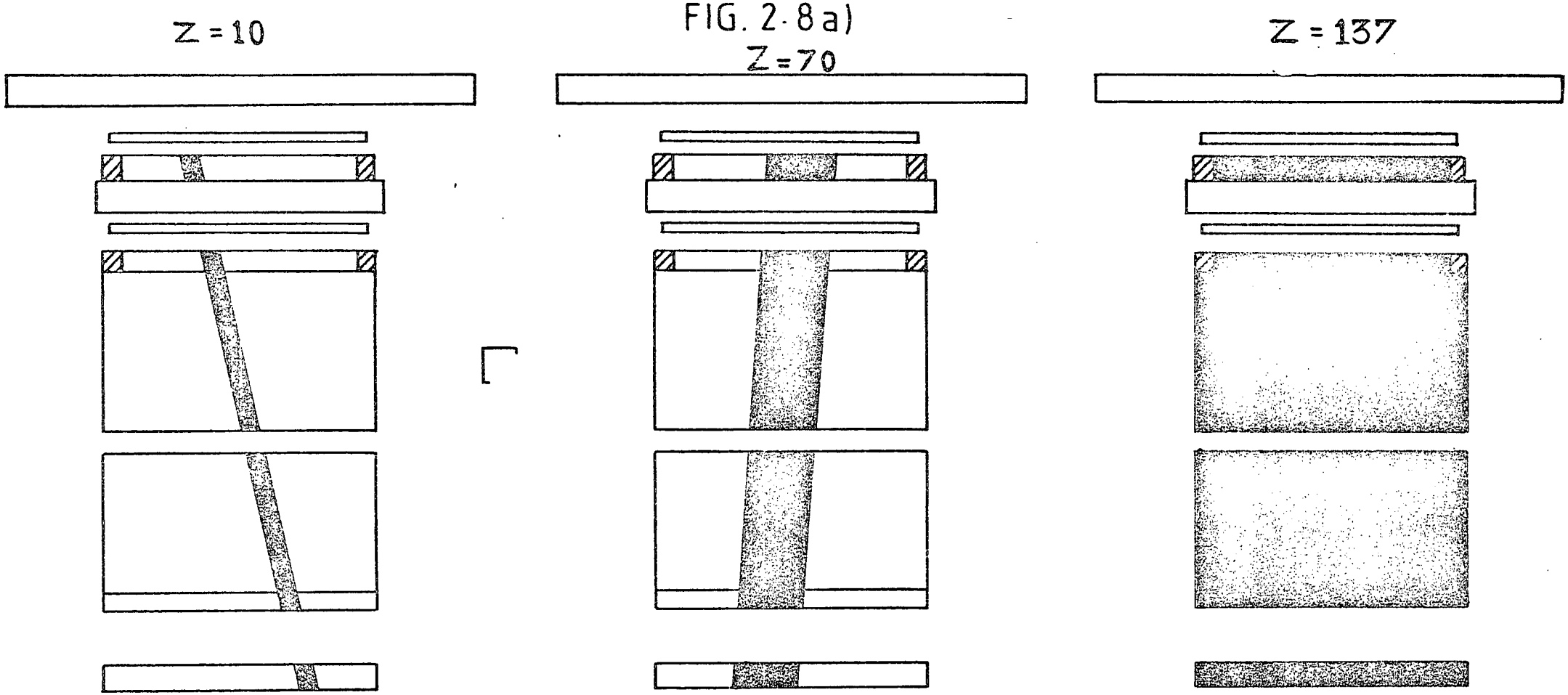

Figure 2.8b): The expected response of the flash-tube chamber at time delay of 330μs to particles of different charge Ze.

FIG. 2·8b)

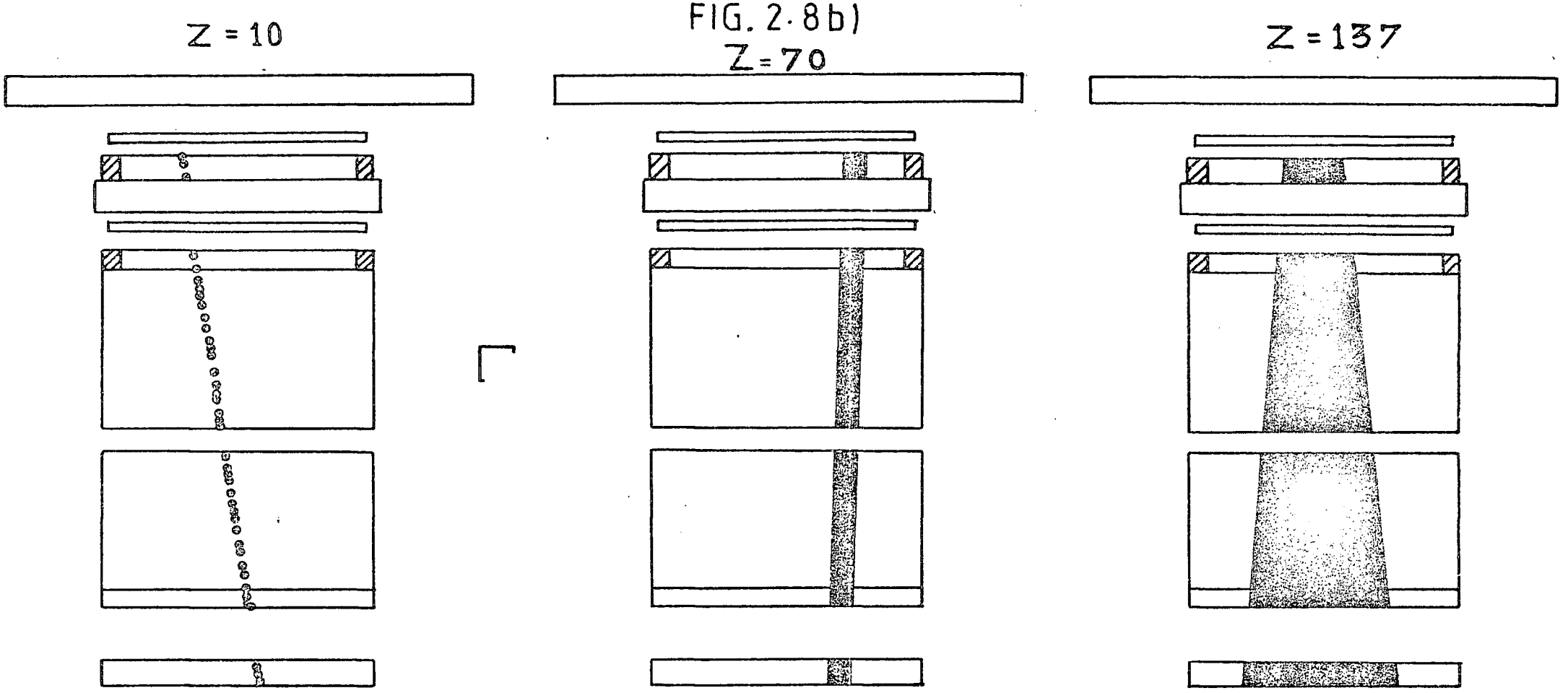

FIG. 2·8 c)

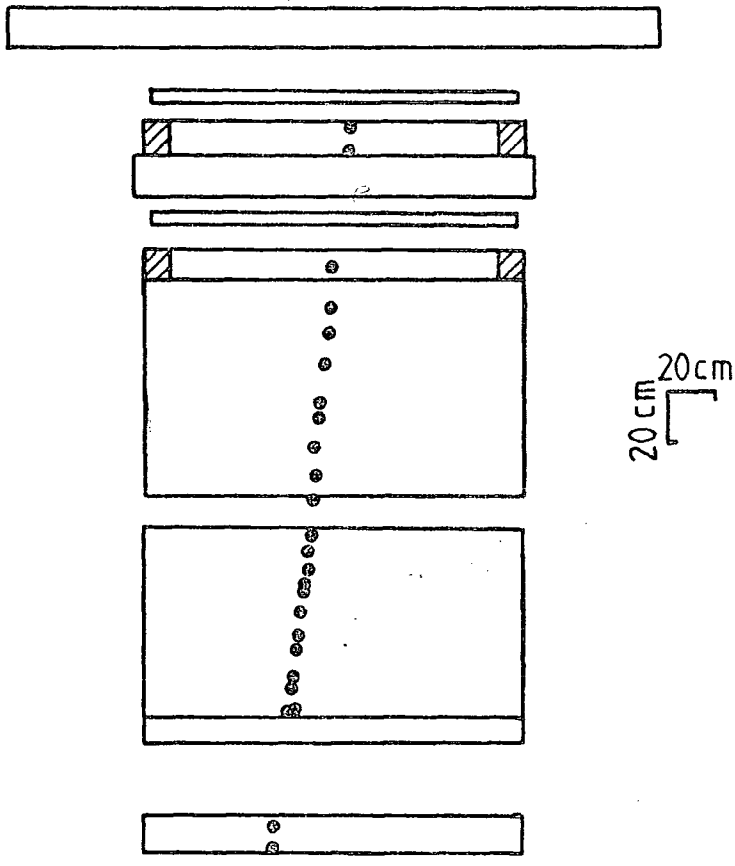

The expected response of the flash-tube chamber at time delay of 600ns to a particle of charge Ze where Z=137

2.4 Use of the flash-tube chamber in measuring the charge of individual particles

It is clear from the work of Lloyd (1960) (see Section 2.2) that the efficiency of a neon flash-tube response to a charged particle depends on the charge of the particle and the time delay between the passage of the particle and the application of the high-voltage pulse.

By observing the response of the flash-tube chamber at various time-delays to the passage of a singly charged particle previous authors (Cooper [1974], Parvaresh [1975], Saleh [1975], see also Chapter 3) have determined the "ionisation parameter" afQ for the flash-tubes used in the chamber to be 9 for $Z = 1$ particles. Hence, since Q (the probability per unit track length of particle producing a free electron) is the only component of this parameter dependent on the charge of the ionising particle, $Q \propto Z^2$ (a = internal diameter of the flash-tube, f = probability that a single electron produces an avalanche), it is a simple matter to infer the response of the flash-tube chamber to particles with unusually high or low values of Z, the electric charge of the particle.

Fig. 2.7 shows the expected internal efficiency of the flash-tube chamber for particles of $Z = \frac{1}{3}$ (quarks), $Z = 1$, $Z = 10$ (Yock-particles, Yock [1973]), $Z = 68.5$ (Dirac monopole) and $Z = 137$ (Schwinger monopole), as a function of time-delay. Figs. 2.8a) and 2.8b) show the expected response of the flash-tube chamber to these particles for a typically short (20 μs) time-delay and a typically long (330 μs) time-delay. The exceptionally broad tracks produced by the highly-charged particles are due to the large number of knock-on electrons produced by these particles. Fig. 2.8c) shows the response of the chamber to $Z = 137$ particle at $td = 600$ μs.

In order to measure the internal efficiency corresponding to these tracks the number of layers flashed in F2 and F3 is counted. Only those tracks which show a track in the defining layers F1a, b and F4a, b are considered since this avoids introducing spurious low efficiency tracks due to "edge-effects". (See Chapter 3.) This number divided by the total number (96) of layers in F2 and F3 gives the layer efficiency η_L. To convert this to the internal efficiency η_I it has to be multiplied by the ratio of the total area covered by the flash-tubes to the sensitive area, i.e.

$$\eta_I = \frac{1.81}{1.58} \eta_L = 1.145 \eta_L$$

2.5 Use of the flash-tube chamber in measuring the energies of interacting particles

2.5.1 Nuclear-electromagnetic cascades

When a hadron travels through a dense medium of depth greater than or of the order of its interaction length in that medium there is a high probability that it will suffer a strong interaction. This probability follows an exponential distribution with the amount of medium travelled through. The result is the production of a number of secondary hadrons (predominantly pions). If the incident hadron is a pion then all of its energy will be taken up by the secondary particles, whilst a nucleon only loses a fraction of its energy and travels on to interact again.

The pions produced either travel deeper to suffer further interactions (as in the case for $\pi^{\pm}$) or immediately decay into two photons (π^0). The probability of a fast charged pion decaying in a dense medium is small compared with the probability of interaction.

The photons produced either materialise or undergo a Compton collision. The electrons and positrons thus produced will lose energy predominantly by radiation, and the photons produced will give rise to further electrons and positrons.

Since the secondary particles have the same order of magnitude energies as the primaries, energy degradation is slow compared with the increase in the number of electrons and photons.

This allows a significant increase in the total number of particles as the cascade develops with depth. Eventually the point is reached where the mean energy of the electrons falls below the critical energy and collision losses become more important than bremsstrahlung. The total number of particles in the cascade now begins to decrease and the energy input is dissipated in excitation and ionization of the atoms of the medium.

If the target is of finite thickness then showers of electrons and photons will emerge at various stages of development and from the number of electrons appearing below the target some measure of the energy of the initiating hadron can be ascertained.

The emerging shower of electrons will be broadened due to multiple scattering of the electrons and the angular separation of the electrons produced by pair-production. Less important, because of the higher energies involved, broadening effects also arise from the transverse momenta of the pions, multiple scattering of the pions, and the angular separation of the photons from Π decay.

The flash-tube chamber can be used to measure the energies of the incident hadrons by either:

a.) Measurements of the number of particles produced in such a process under the lead or iron and calculation of the relationship between these measurements and the primary energy input into the cascade. This technique is used for the hadron energy measurements of Chapter 4.

or

b.) Measurement of the width of the burst produced below either the lead or the iron target and either calculation of the relationship between the width of the cascade and the primary energy inputs, or by measuring the relationship between the width of the burst and the burst-size and calibrating the burst width - primary energy relationship using a.). The former technique has been shown to be insensitive (Coats [1967]), Cooper [1974]) at short time-delay because of the multiple scattering of low energy electrons. Hence the latter technique has been used for the hadron energy measurements of Chapter 11.

2.5.2 Measurement of burst size with the flash-tube chamber

The plastic scintillators A (under the iron) and C (under the lead) facilitate the measurement of the number of particles emerging from either target consequent to a nuclear interaction taking place. The scintillators are positioned directly below each target and with their fronts lined up with the front of the defining layers, F1a, F1b (see Fig. 2.2). This ensures that the whole of the burst measured by the scintillator passes through the defining layers. The scintillators were calibrated by measuring

FIG 2.9

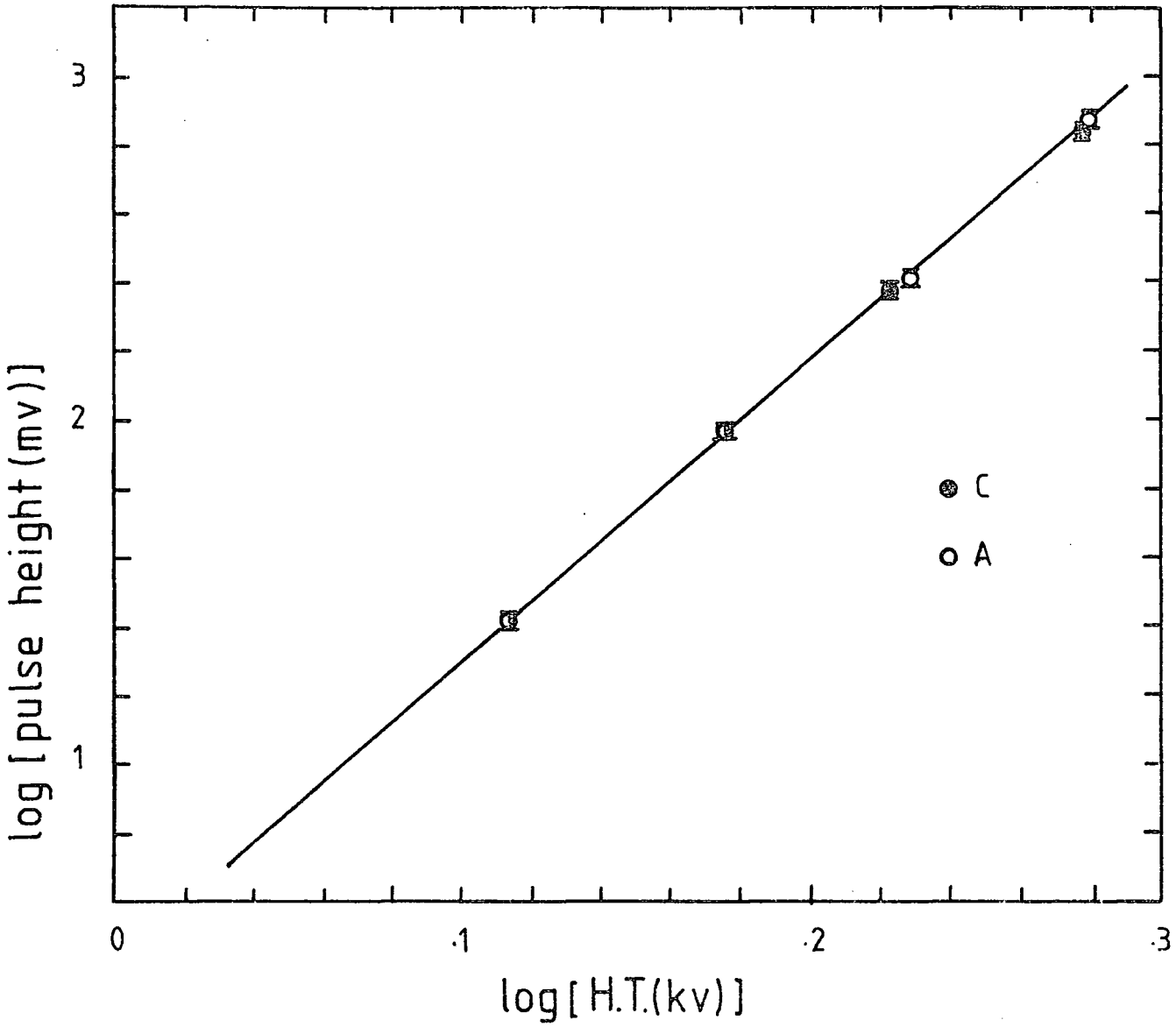

Variation of the output pulse height with the applied H.T. voltage from the plastic scintillators A and C. (after Cooper(1974))
The pulse height is given at the output of the photomultipliers for a single penetrating particle traversing the centre of the scintillator at vertical incidence.

their response to vertical penetrating particles passing through the centre of each scintillator for different values of the high voltage applied to the photomultipliers.

The calibrations were carried out and thoroughly described by previous authors (Cooper [1974], Saleh [1975]). The calibration curves for both scintillators are shown in Fig. 2.9.

2.5.3 The burst-size energy relationships

These have been calculated by previous authors (Cooper [1974], Parvaresh [1975], Saleh [1975], Nasri [1977]) and a description of their methods is presented in Appendix VII. The results of their calculations are presented in Figs. 2.10 and 2.11. It can be seen that a burst-size of N particles below 15 cm of lead or iron corresponds approximately to an average a hadron with primary energy N GeV.

2.5.4 The measurement of burst-width with the flash-tube chamber

The width of a burst can be measured by projecting the photograph of the event onto a 1 : 20 scale drawing of the front-view of the chamber. For short time-delay the whole of the burst width is measured, but this method is impractical for events >1000 particles as the burst width fills the chamber. For the higher energy events a long time-delay (330 μs) is used and the resulting photograph gives an image of the core of the shower. The burst-width on long time-delay is then defined as the number of flashes

FIG 2.10

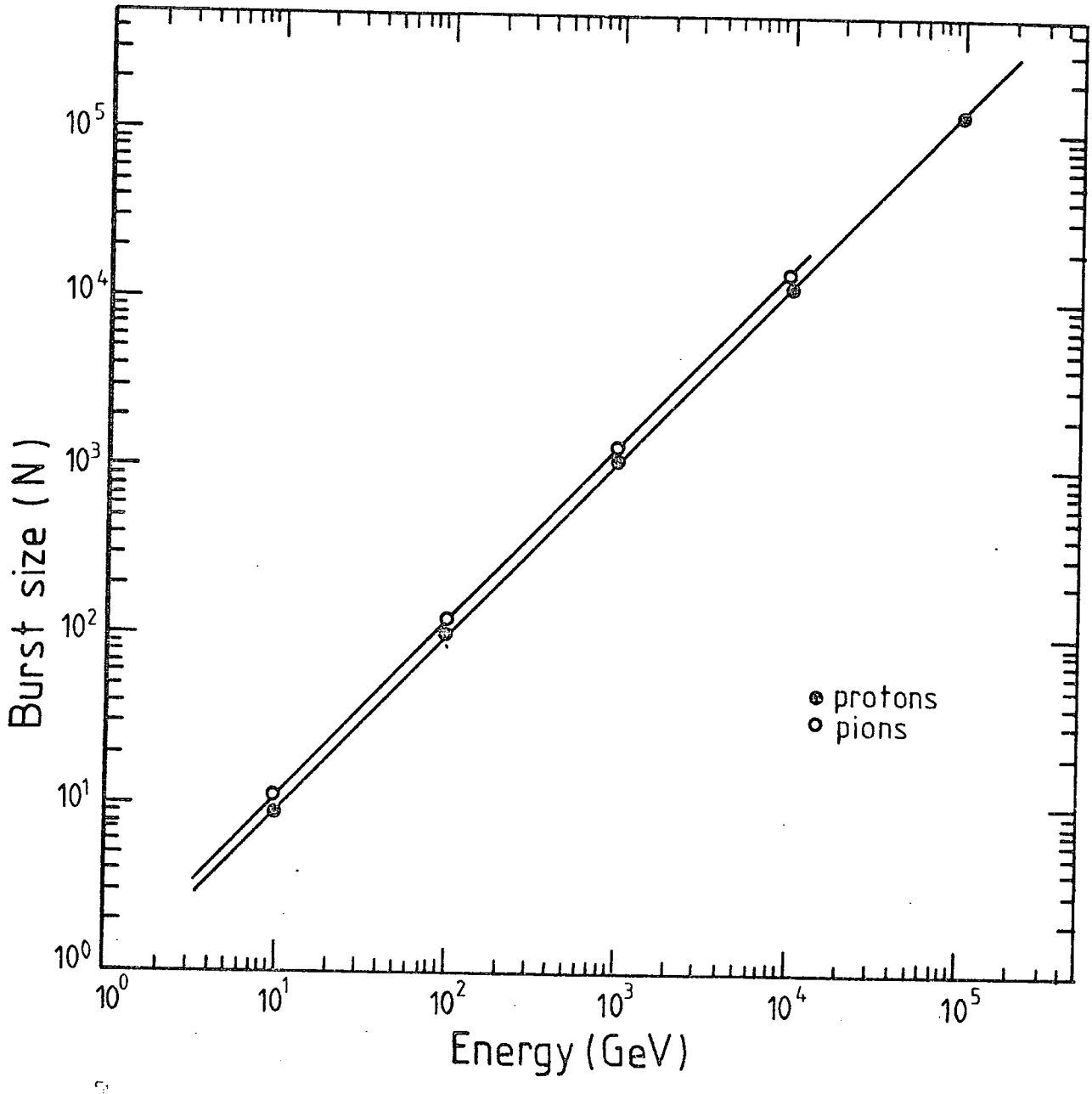

The average burst size(N) produced by a proton or pion of energy E GeV incident on 15cms. of lead. (After Saleh(1975))

FIG 2.11

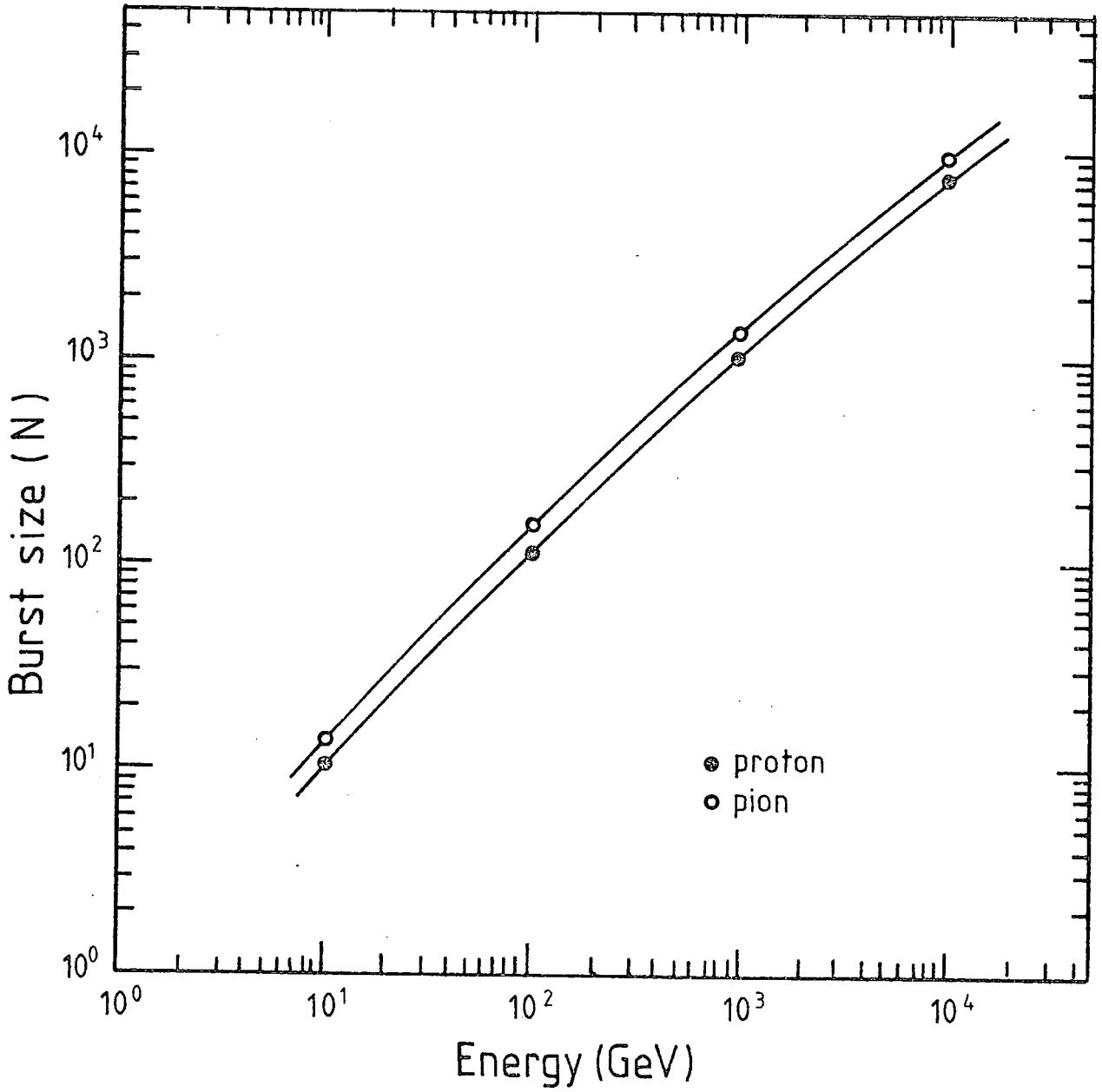

The average burst size(N) produced by a proton or pion of energy E GeV incident on 15cms. of iron. (After Saleh(1975))

within $\pm \frac{1}{2}$ cm, on the scanning sheet, of the centre of the burst.

In both cases the burst width measurement is made either in F1a (for bursts that are produced in the lead) or F1b (for bursts that are produced in the iron).

2.5.5 The burst-width - burst-size relationship

In Chapter 5 (Fig. 5.9) are shown the results of calculations of the burst-widths for different ages of shower. Figs. 5.12b), 5.13b), 5.14b) show how the predictions from theory adequately describe the measured burst-widths on long time-delay. However Fig. 2.12 shows the comparison between the theory and experiment for short-time delay. The experimental results are from two experiments performed by Coats (1967) in which the burst spectra produced in 25 cms of iron from horizontal muons (electromagnetic) and vertical particles (mainly nuclear - electromagnetic) were measured on short time-delay.

The predicted relationship between burst size and burst width can be seen to fall much lower than either of the measured relationships. This is thought to be due to the high scattering of the low energy electrons which have an almost isotropic angular distribution (Messel and Crawford [1970]).

In order, then, to measure the energies of the primary particles from the width of the bursts they produce at short time-delays it is necessary to measure the burst width - burst size relationship and then use the curves of 2.10 and 2.11 for the final burst-width to energy conversion.

Such measurements have been made by Cooper (1974) and Saleh (1975) and the results of their measurements are summarised in Figs. 2.13 and 2.14.

FIG 2.12

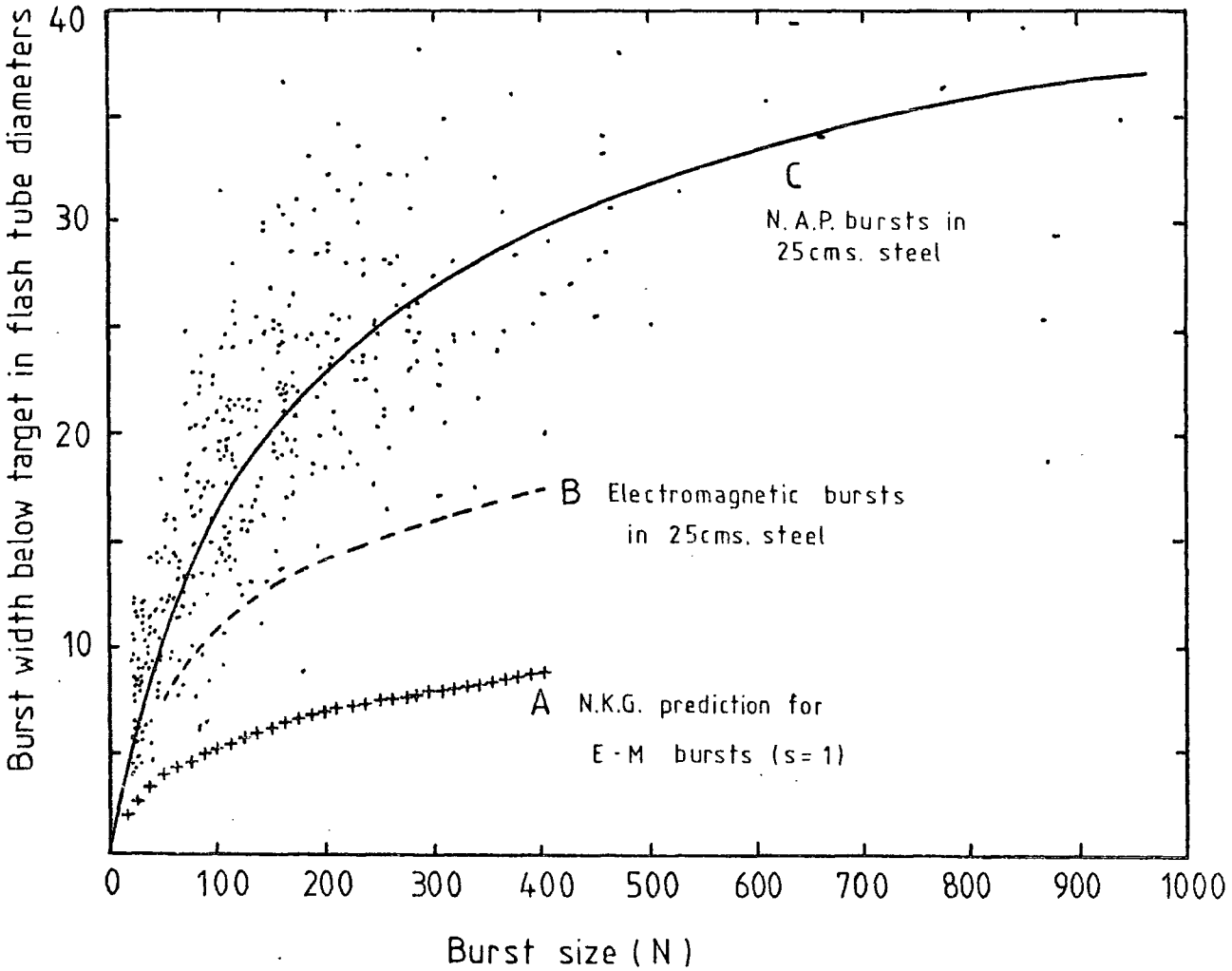

Correlation between the width of a burst emerging from a thick steel target and the number of particles in the cascade

Curve A - Nishimura-Kamata-Greisen (N.K.G.) prediction for a pure electron-photon cascade .(Greisen(1956)).

Curve B - measured relationship for electromagnetic bursts from muons.

Curve C - as B but for nuclear-electromagnetic bursts.

(After Coats(1967))

FIG. 2·13

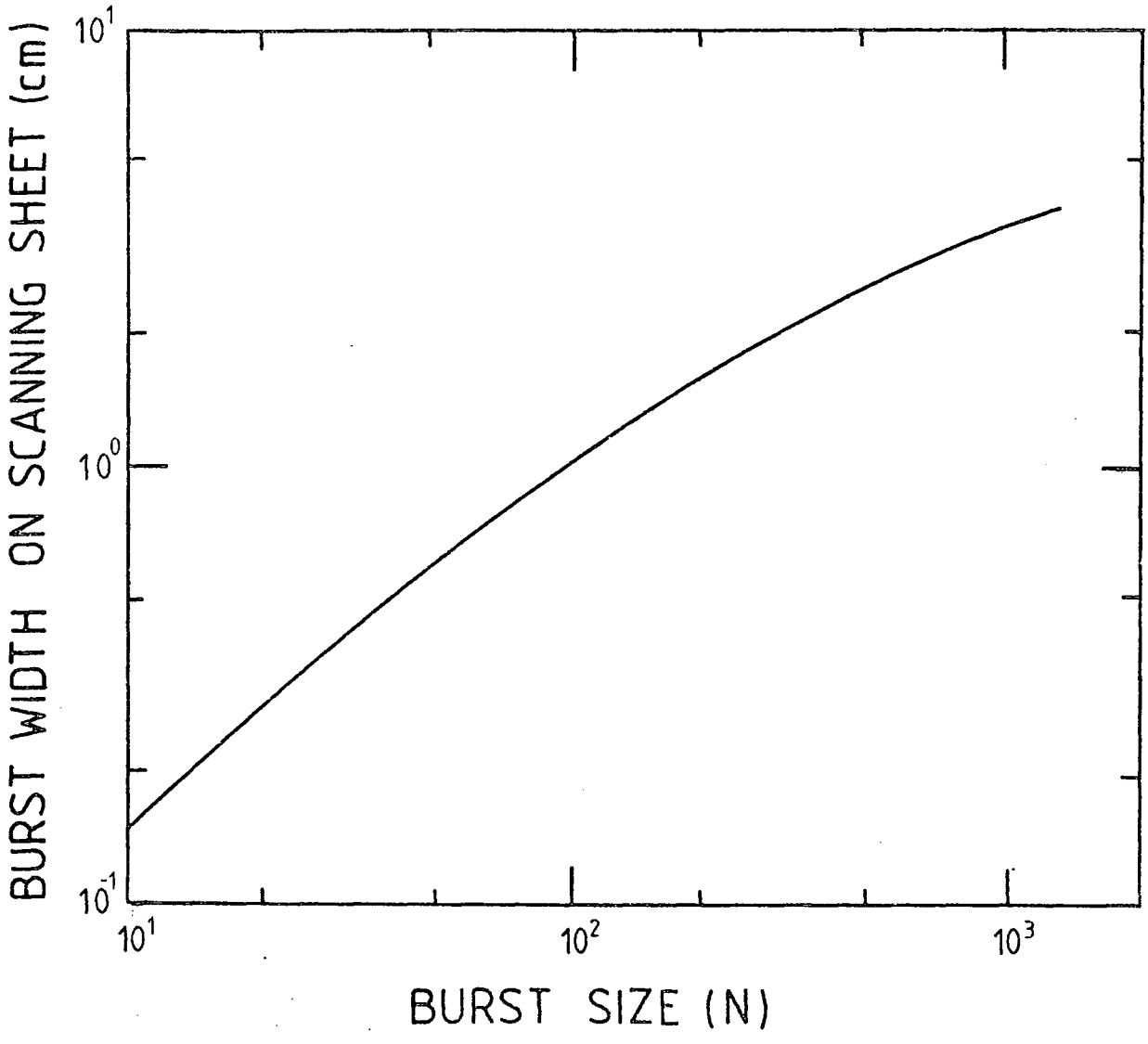

Mean burst width (as measured on scanning-sheet) variation with burst size for bursts produced in the lead; 1 cm. on scanning-sheet corresponds to 20cms. in real space.

(After Cooper(1974), Saleh(1975))

FIG. 2·14

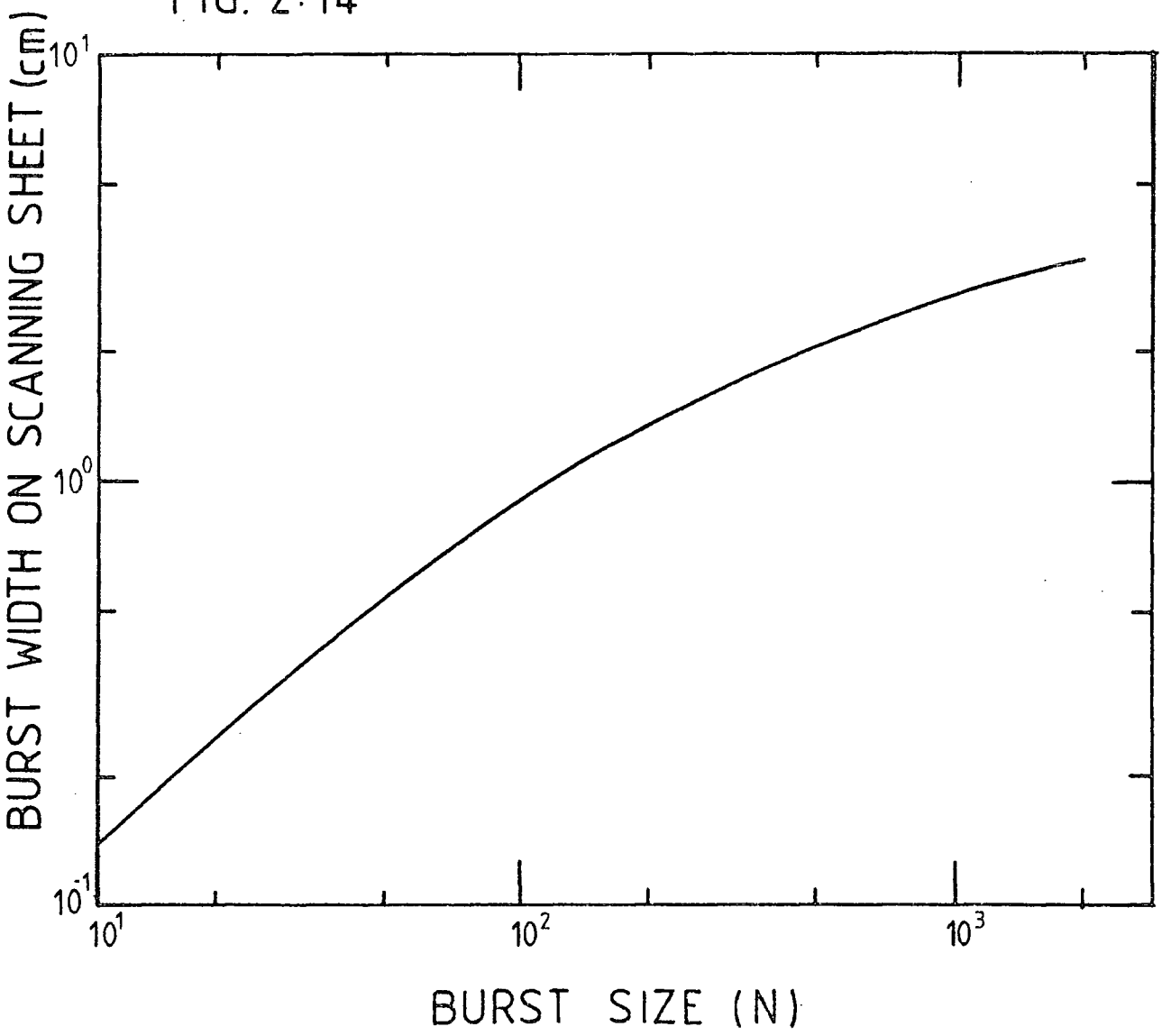

Mean burst width (as measured on scanning-sheet) variation with burst size for bursts produced in the iron; 1 cm. on scanning-sheet corresponds to 20cms. in real space.

(After Cooper(1974), Saleh(1975))

Figs. 2.15 and 2.16 show the resulting burst-width energy relationships derived from Figs. 2.10, 2.11, 2.13, 2.14.

2.6 The various triggering modes available to the flash-tube chamber

Since the high-voltage pulsing system is triggered by a 5 volt pulse the flash-tube chamber can be triggered by events detected by the scintillators A and C (internal triggering) or by an external device such as the three liquid scintillators situated above the lead (external triggering).

2.6.1 Internal triggering

Internal triggering can be classified into two regions:

a.) Single or few particle triggers

b.) Many particle or burst triggers.

Penetrating particles i.e. muons have a high probability of passing through the chamber without interacting in either the lead or iron targets or the glass and aluminium of the flash-tube array. By determining the mean single particle pulse height as a function of the voltage applied to the photo-multiplier tubes of scintillators A and C (Fig. 2.9) the trigger pulse can be set to respond to the passage of 1 or 2 or n single particles through the chamber. This technique has been used in searches for fractionally charged particles (Cooper [1974], Parvaresh [1975], Saleh [1975]) since the track of the muon has a markedly greater number of flashes than that of a charge $\frac{e}{3}$ particle (a quark) (see Figs. 2.7 and 2.8a)).

FIG. 2·15

The average burst width as measured on scanning-sheet produced by a proton incident on 15cms. of lead as a function of proton energy; 1 cm. on scanning-sheet corresponds to 20 cms. in real space.

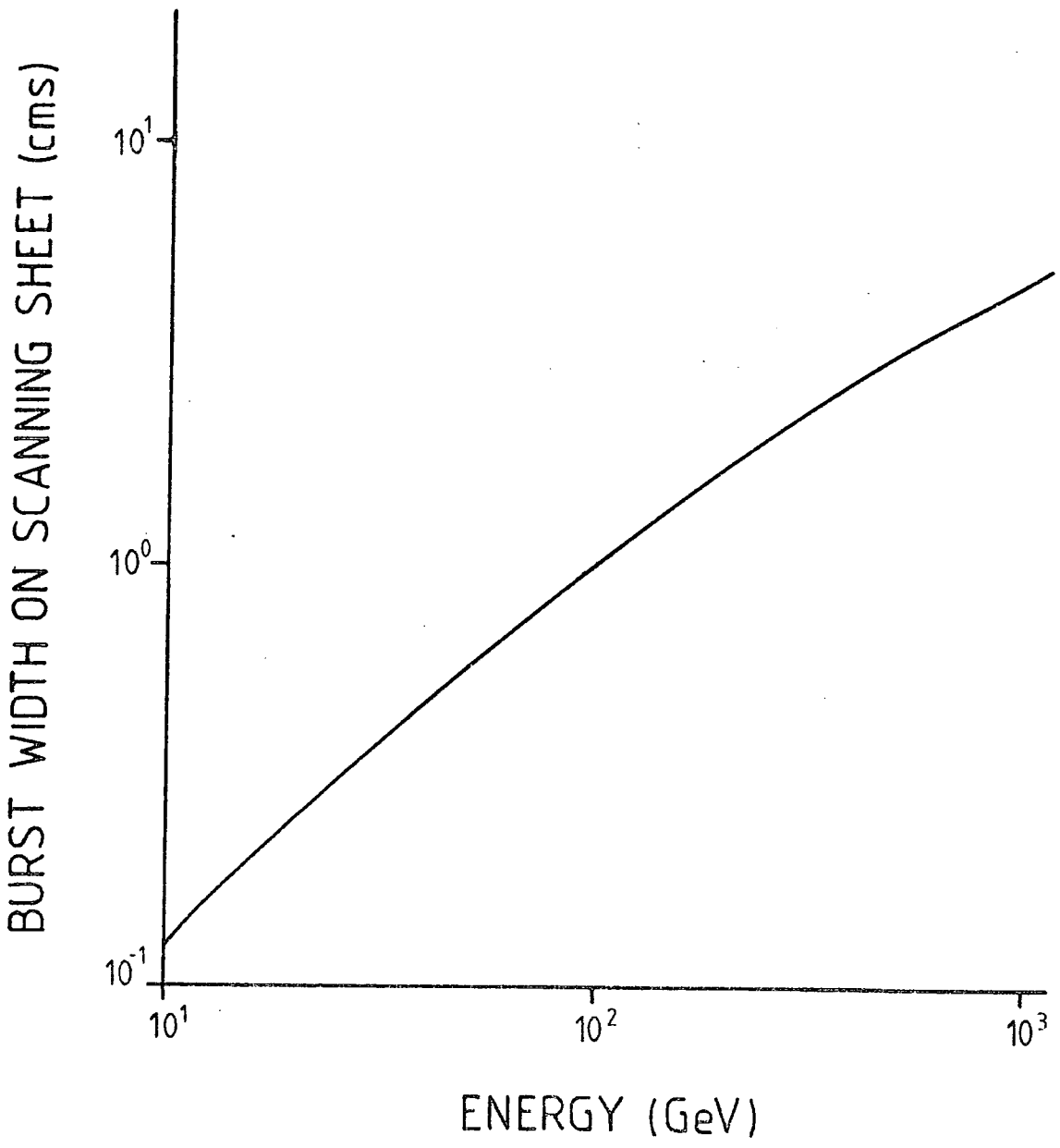

FIG 2.16

The average burst width as measured on scanning-sheet produced by a proton incident on 15cms. of iron as a function of proton energy; 1 cm. on scanning-sheet corresponds to 20cms. in real space.

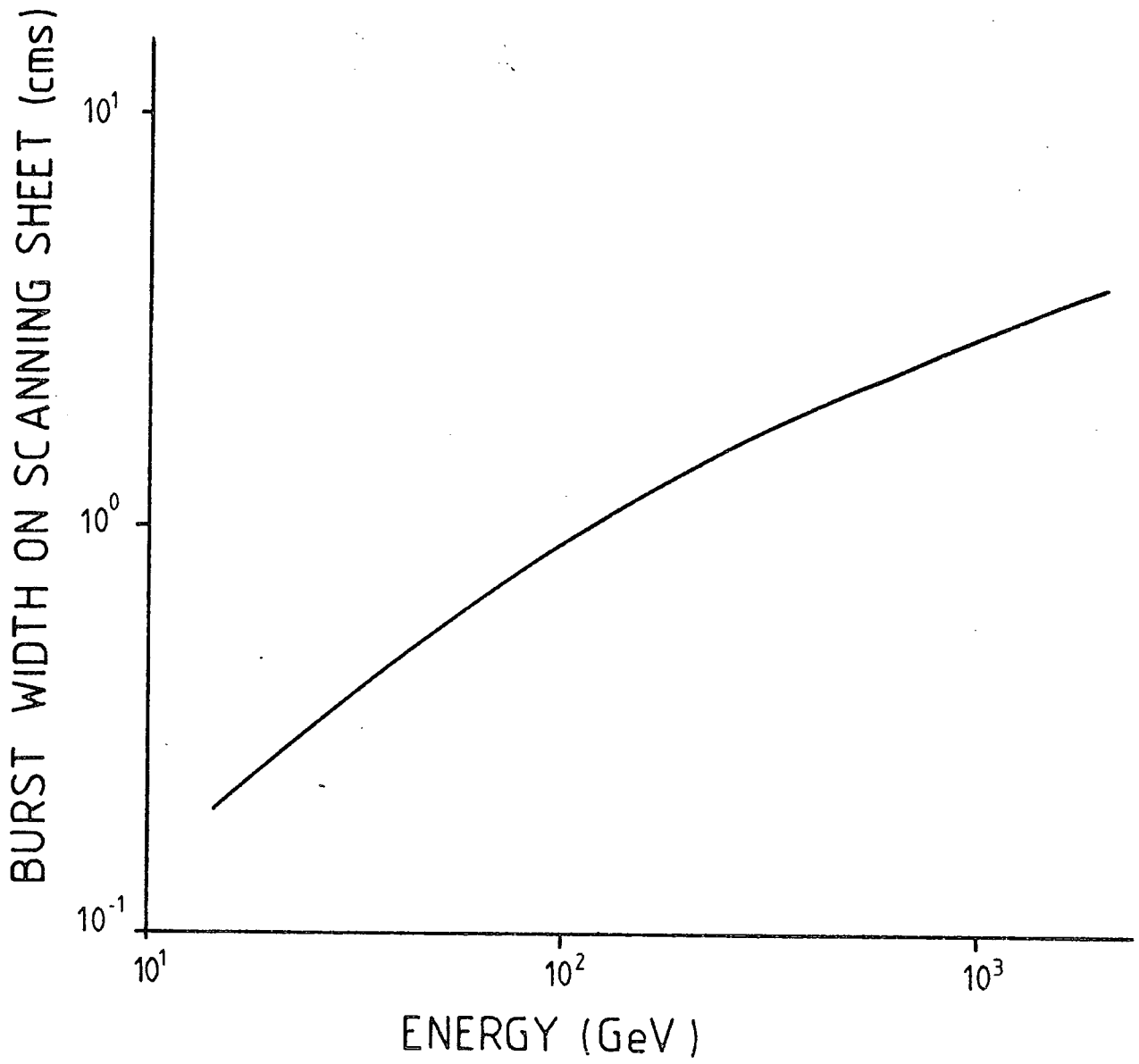

If we assume that the pulse height from a scintillator produced by a relativistic electron is no different to the height of a pulse produced by a relativistic muon, the trigger pulse can be set to respond to the production of a large number of electrons beneath either the lead or the iron targets. In this way measurements of the energy spectrum of hadrons at sea-level can be made over a wide-range of energies (see Chapter 4). Also, the characteristics of nuclear - electromagnetic cascades at different energies can be studied (see Chapter 5).

A block diagram of the electronics involved in internal triggering is presented in Fig. 2.17.

2.6.2 External triggering

The characteristics of muons and hadrons accompanied by extensive air showers can also be studied using either

a.) a local density trigger from the liquid scintillators above the lead or

b.) a multicoincidence trigger from scintillators situated at various distances from the flash-tube chamber. (A thorough discussion of this technique is presented in Chapters 6 and 7.)

Using a geiger-telescope, the mean single particle pulse height as a function of the voltage applied to the photomultipliers of the liquid scintillators above the lead can be determined (Fig. 2.18). The trigger pulse can hence be set to respond to the detection of various electron densities above the chamber. Figs. 2.19 and 2.20 show the expected

BLOCK DIAGRAM OF ELECTRONICS FOR INTERNAL TRIGGERING FROM PLASTIC SCINTILLATORS A OR C

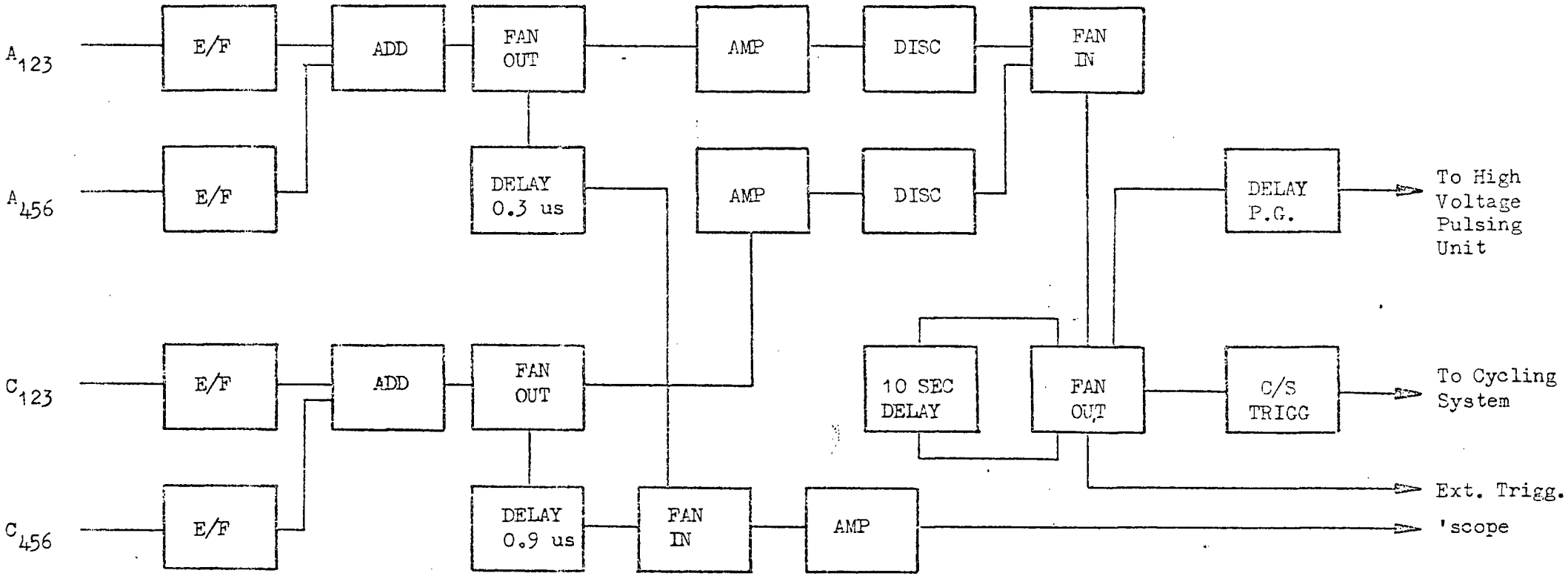

FIG. 2-17

distribution in shower-sizes and core-positions for different local electron densities. These have been calculated assuming the Nishimura - Kamata - Greisen (1960) expression for the lateral distribution of electrons in an extensive air shower

$$\text{i.e.} \quad f(N_e,r) = \frac{0.4\,Ne}{r_1^2}\left(\frac{r}{r_1}\right)^{0.75}\left(\frac{r_1}{r+r_1}\right)^{3.25}\left(1+\frac{r}{11.4r_1}\right)^{m^{-2}}$$

The integral number spectrum according to Hillas (1970) has been used

$$\text{i.e.} \quad R(>N) = 52.0\,N^{-1.5}\ m^{-2}\ s^{-1}\ st^{-1} \text{ for } N < 5.10^5$$

$$R(>N) = 36{,}920.0\,N^{-2.0}\ m^{-2}\ s^{-1}\ st^{-1} \text{ for } 5.10^5 < N < 3.10^7$$

$$R(>N) = 6.76\,N^{-1.5}\ m^{-2}\ s^{-1}\ st^{-1} \text{ for } N > 3.10^7$$

A block diagram of the electronics involved in external triggering is presented in Fig. 2.21.

2.7 Summary

The flash-tube chamber is a versatile visual detector which can be used to study the ionisation properties of fast particles as well as in conjunction with suitably situated scintillators, the energies of high energy hadrons in the cosmic radiation

The various triggering modes available allow different regions of the sea-level cosmic radiation to be examined enabling comprehensive searches for exotic particles to be carried out.

FIG 2.18

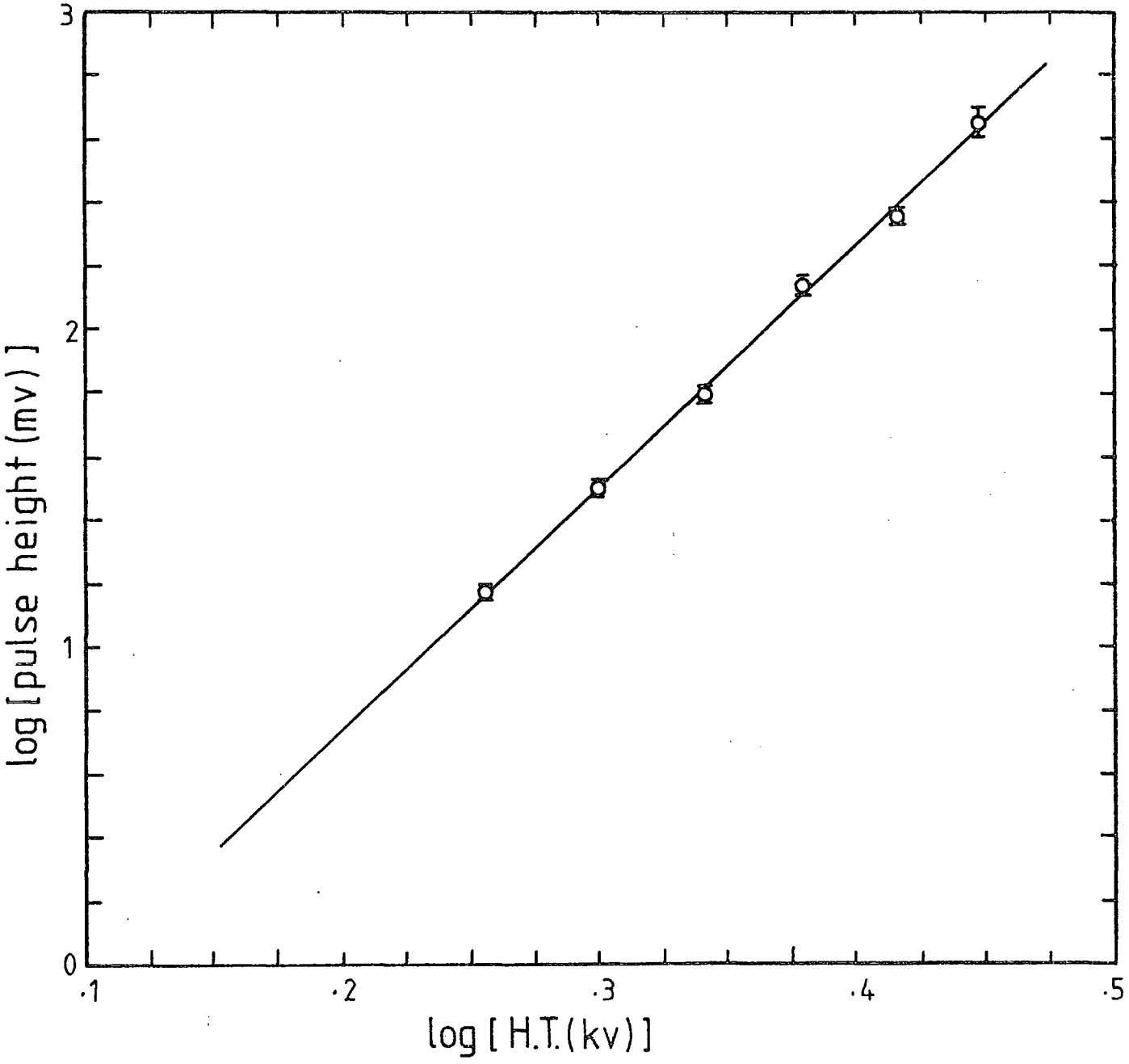

Variation of output pulse height with the applied H.T.voltage from the liquid scintillator M.
The pulse height is given at the output of the photomultipliers for a single penetrating particle traversing the centre of the scintillator at vertical incidence. (After Saleh(1975))

Fig. 2.19: Predicted distribution of shower sizes that give electron densities greater than $20m^{-2}$ and $40m^{-2}$ at detector.

Median shower size for densities $> 20m^{-2} = 10^5$,
Median shower size for densities $> 40m^{-2} = 2.10^5$.

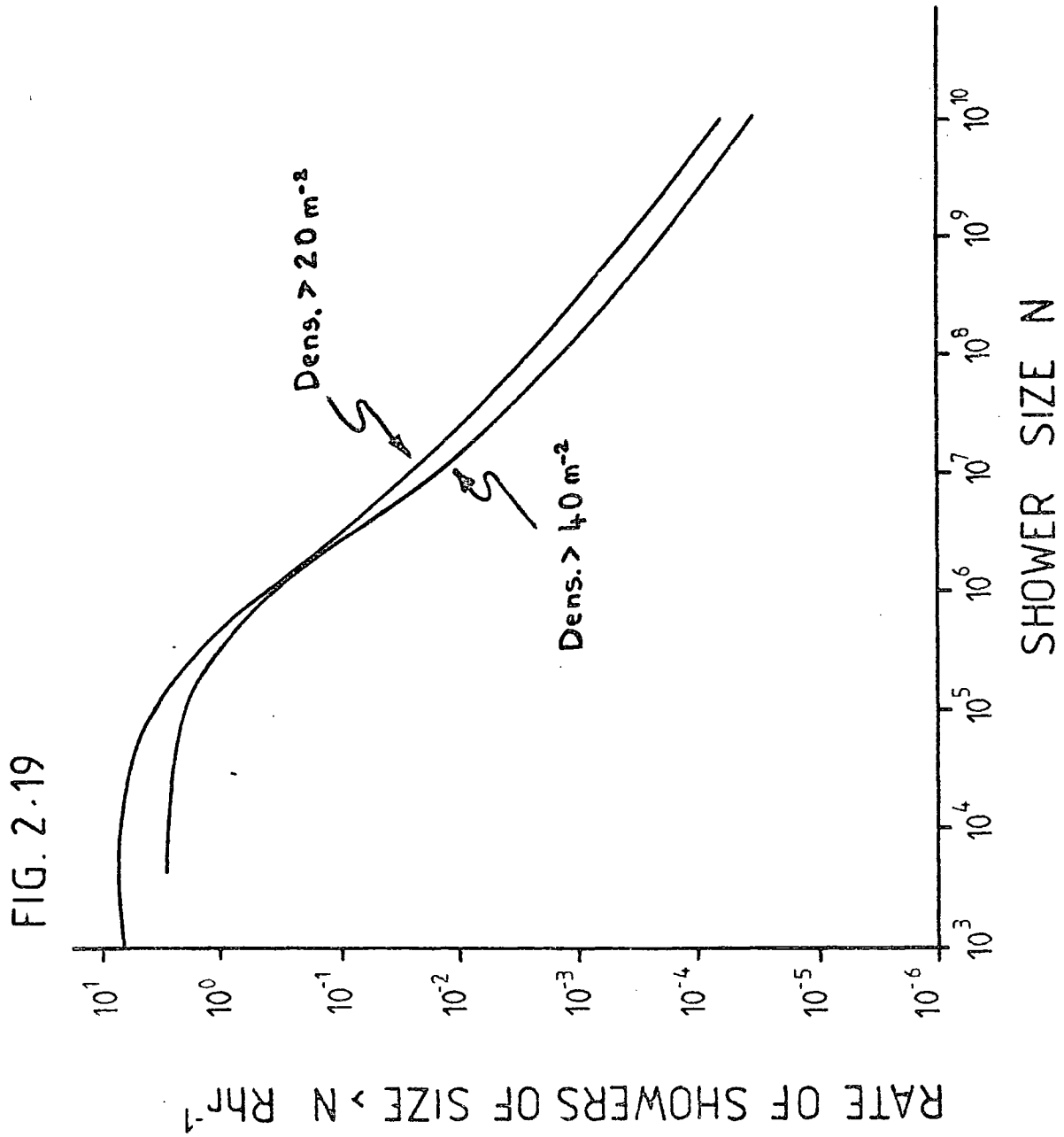

FIG. 2.19

Fig. 2.20: Predicted distribution of core distances that give electron densities greater than $20m^{-2}$ and $40m^{-2}$ at detector.

Median core distance for densities $20m^{-2}$ = 11 m.
Median core distance for densities $40m^{-2}$ = 10 m.

FIG. 2·20

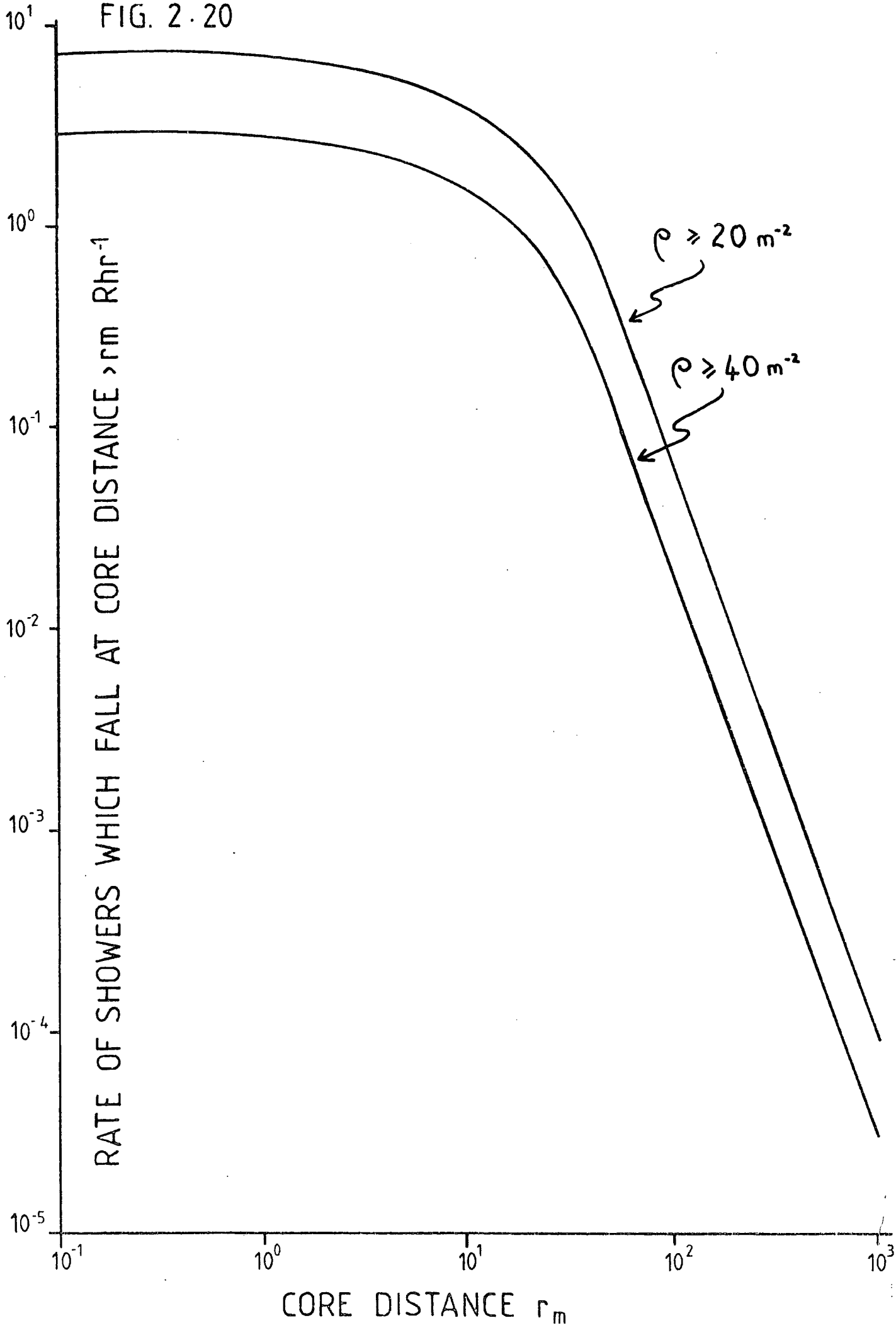
10^{1}
10^{0}
10^{-1}
10^{-2}
10^{-3}
10^{-4}
10^{-5}
RATE OF SHOWERS WHICH FALL AT CORE DISTANCE > rm Rhr^{-1}
$\rho \geq 20$ m^{-2}
$\rho \geq 40$ m^{-2}
10^{-1}
10^{0}
10^{1}
10^{2}
10^{3}
CORE DISTANCE r_m

BLOCK DIAGRAM OF ELECTRONICS FOR EXTERNAL TRIGGERING FROM LIQUID SCINTILLATOR M

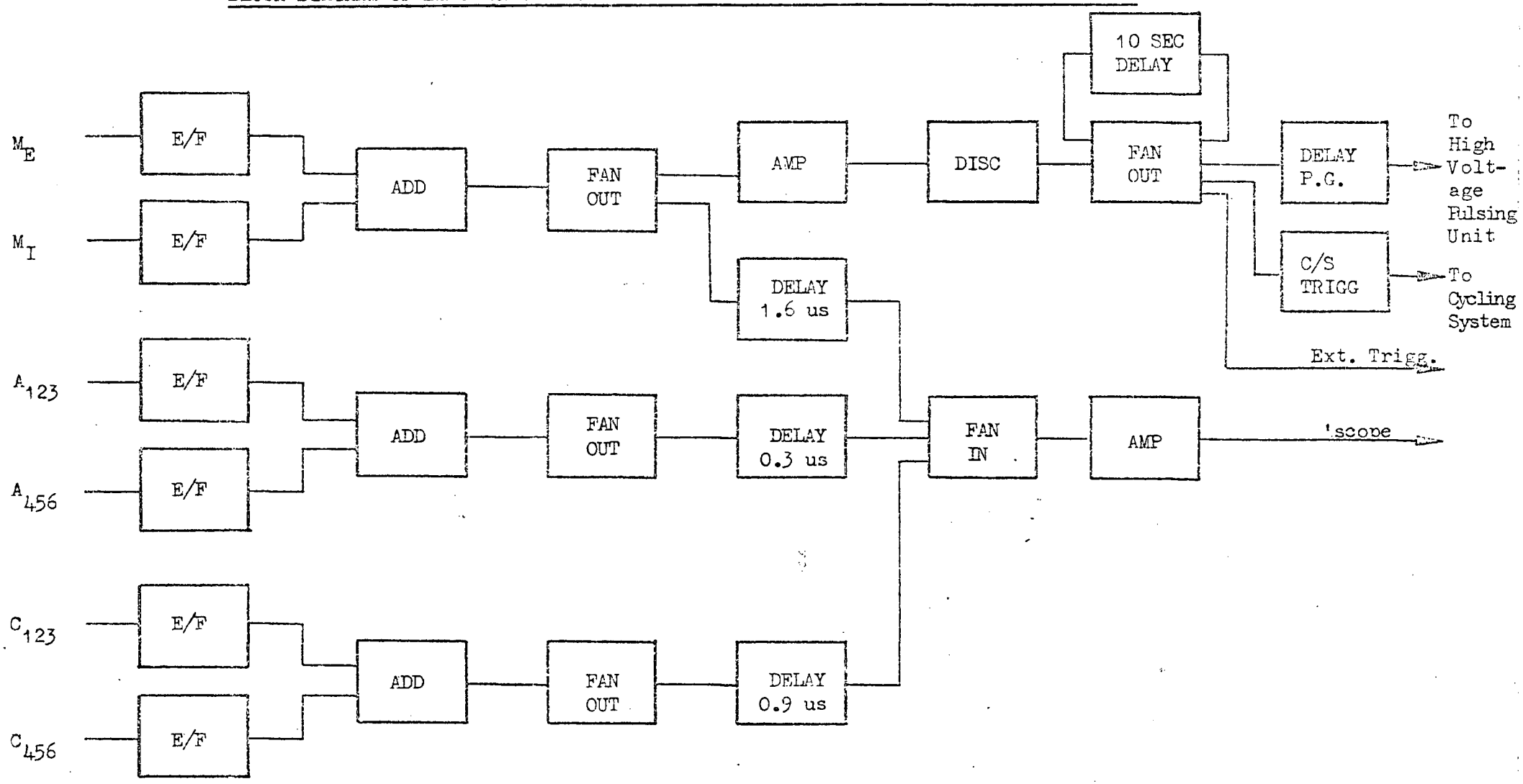

FIG. 2.21

CHAPTER 3

THE GARIBYAN EFFECT

3.1 The ionisation loss of charged particles

When a fast charged particle is incident on matter it makes collisions with both the atomic electrons and the atomic nuclei which have different consequences. The collisions of heavy charged particles with the atomic electrons impart appreciable amounts of energy to the latter without causing significant deflections to the direction of motion of the incident particle. Collisions with the more massive nuclei on the other hand impart very little energy but because of the greater charge of the nuclei the incident particle suffers scattering. The main energy loss mechanism is thus by collisions with atomic electrons which is the process termed ionisation loss.

The thecretical expression for dE/dx most commonly used is the Bethe - Bloch formula (Bethe [1930], Bloch [1933]) modified to take account of the density effect (see below and Fermi [1940]).

$$(3.1) \qquad -\frac{dE}{dx} = \frac{2\pi n z^2 e^4}{mv^2} \left[\ln\left(\frac{2mv^2 W_{max}}{I^2(1-\beta^2)}\right) - 2\beta^2 - \delta - U \right]$$

where n = no. of electrons/cc in stopping material

m = electron mass

$\beta = \frac{v}{c}$, v = velocity of incident particle

z = charge of incident particle

I = mean excitation potential of atoms of stopping material

δ = correction for density effect (see below)

U = term due to non-participation of electrons in the inner shells (K, L . . .) for low incident velocities

Wmax = maximum energy transfer (corresponding to head-on collisions)

$$= \frac{2mv^2}{1 - \beta^2}$$

for energies $E \ll \left(\frac{mi^2}{2m}\right) c^2$

where m_i = mass of incident particle

For velocities greater than the mean velocity of an atomic electron in orbit the expression can be divided into 3 distinct regions of

$\frac{p}{mc} = \beta\gamma = \beta(1 - \beta^2)^{-\frac{1}{2}}$, p is the momentum of the incident particle.

i.) $\frac{p}{mc} < 4$; the non-relativistic region where the energy loss goes as β^{-2} corresponding to the decreasing amount of time spent by the incident particle in the vicinity of the atom.

ii.) $\frac{p}{mc} > 4$; the "relativistic rise" region where the energy loss slowly increases logarithmically, corresponding to the increase in the transverse component of the electric field of a relativistic charged particle. The decrease in the longitudinal component has no effect since the net momentum transfer to the

atomic electron from the longitudinal component is zero for incident velocities large compared with the orbital velocity of the atomic electrons.

iii.) $\frac{P}{mc} \gtrsim 1000$; the "Fermi plateau" region where the energy loss flattens off and - if we ignore the relatively rare large energy transfers (which are usually undetected by thin detectors) - becomes constant. This corresponds to screening of the transverse component of the electric field by polarisation of the atoms close to the path of the incident particle, thus confining the energy loss to close collisions only.

A comprehensive review of the various theoretical methods of deriving expressions for both the relativistic rise and the density effect was published in 1970 by Crispin and Fowler (Crispin and Fowler [1970]), which also contains a review of the status of experimental determinations up to 1970. More approximate but simpler derivations can be found in Jackson [1970]. In a series of papers between 1952 and 1956 Sternheimer (Sternheimer 1952, 1953, 1954, 1956) parameterised the Bethe - Block formula and gives for the most probable energy loss εp of Landau theory (see below),

$$(3.2) \qquad \varepsilon p = \frac{Lx}{\beta^2} \left(\beta + 1.06 + 2 \ln \frac{p}{mc} + \ln \left(\frac{Lx}{\beta^2} \right) - \beta^2 - \delta \right) ;$$

his expression for the density effect δ being

$$(3.3) \qquad \delta = 4.606 y + C + a (y_1 - y)^b \qquad \text{for } y_0 < y < y_1$$

$$\delta = 4.606 y + C \qquad \text{for } y > y_1$$

where $y = \log_{10} \frac{p}{mc}$, $L = \frac{2\pi ne^4}{mc^2\rho} = 0.1536 \frac{z}{A_0}$ MeV $g^{-1}cm^2$; $\beta = \ln\left[\frac{mc^2 10^6 eV}{I^2}\right]$

Simultaneous with this parameterisation he calculated from both theoretical arguments and experimental measurements - values for the parameters L, B, y_0, y_1, a, b, C for many different stopping materials of interest. A convenient summary of his results can be found in Hayakawa [1969].

3.2 Fluctuations in the ionisation loss

Comparisons of theory with experiment are particularly fraught with difficulties in the case of ionisation loss. The first major modification - pointed out by Bohr (1913, 1915), Williams (1929) and Landau (1944) - is that since the energy lost by a particle passing through matter is the result of a large number of independent events, the process is a statistical phenomenon i.e. no unique value for the energy loss is obtained. The resultant distribution is negatively skewed with a high energy-loss tail due to events where there is a large energy transfer in a single collision.

Parameterisation in terms of the two parameters β and K

$$(3.4) \quad K = \frac{1}{W_{max}} \left(\frac{2\pi e^4 z^2 N x}{mv^2}\right) \frac{z}{A_0} \approx \frac{Ax}{\beta^2 W_{max}} \quad \text{for } z = 1$$

provides three regions of interest (Vavilov [1957])

a.) $K \gtrsim 1$, the number of collisions in any energy loss interval is large and the effect of fluctuations negligible, the distribution is Gaussian with variance σ^2 (Bohr [1915], [1948])

where $\sigma^2 = 4\pi e^4 z^2 NxZ$

This distribution is applicable in, for example, the case of low energy protons.

b.) $K \lesssim 0.01$, the number of collisions in any energy loss interval is small, the resulting distribution (first calculated by Landau (ib id) has a broad peak and is asymmetric with a long high-energy tail. Most experiments find general agreement with Landau theory, which is inapplicable however in the case of thin absorbers (Maccabee et al [1968]) and should be broadened (Blunck and Leisegang [1950]) if the collision spectrum is not directly proportional to the inverse square of the energy loss.

c.) $0.01 < K < 1.0$. The intermediate region which has been the subject of rigorous calculations by Vavilov (1957), whose calculations and results can be applied over the whole range of K (Maccabee et al [ib id]).

These 3 regions can be roughly associated with the non-relativistic region $\frac{p}{mc} \ll 4$, the "relativistic rise" region $\frac{p}{mc} > 4$, and the region of $-\left(\frac{dE}{dx}\right)_{min}, \frac{p}{mc} \simeq 4$ respectively.

In most conventional detectors, the high energy tail has a cut off to take into account the fact that the high energy losses due to close collisions usually escape detection e.g. knock on electrons from scintillators and flash-tubes. Most experimenters thus find it more convenient to measure the most probable energy loss (i.e. the peak of the response distribution) for comparison with theory, rather than the average

energy loss. However in most detectors what is actually measured is the number of ion pairs created, and the energy loss per ion pair (of the order of 30 eV for all gases) is assumed constant independent of energy and type of particle acting as ionising agent. Since most experimental determinations of energy loss per ion pair are made with low energy alpha particles (Crispin and Fowler [ib id]) which results do not necessarily accurately reflect the conditions of an actual ionisation loss investigation, a normalisation procedure is usually invoked in order to compare theory with experiment. With this in mind, the distinction between average or most probable energy loss in comparisons with theory does not appear so crucial, especially when W_{max} detectable is constant. Essentially if we assume that the average restricted energy loss is proportional to the most probable energy loss - which it most certainly is in the Fermi plateau region (since both are constant) - then measurement of the former combined with a normalisation at a well known value of p/mc will suffice for comparison with theory.

3.3 Radiative corrections to the ionisation loss

The Bethe - Bloch formula (3.1) includes the contribution to the energy-loss process by Cerenkov radiation from the relaxing polarised region of the medium in the "relativistic rise" region. The Cerenkov loss is given by the formula of Frank and Tamm (1937)

$$(3.5) \quad -\left(\frac{dE}{dx}\right)_c = \frac{4\pi^2 e^2}{c^2} \int_{\beta n > 1} \left(1 - \frac{1}{\beta^2 n(\nu)^2}\right) \nu \, d\nu$$

where the integral is over all frequencies for which $\beta n(\nu)>1$ and $n(\nu)$ is the refractive index of the medium for radiation of frequency ν. The magnitude of this correction to the Bethe - Bloch formula is, however, only small in realistic dielectric media. This is because there are large regions of absorption in both the discrete and continuous excitation regions of the K, L, M . . . shells, severely limiting the region over which $n(\nu)> 1$. Sternheimer (op cit) has shown that the only region of importance is below the first absorption limit i.e. the optical and near-ultraviolet region.

For condensed materials Sternheimer (ib id) calculates that $\left(\frac{1}{\rho}\frac{dE}{dx}_c\right)$, where ρ is the density of the medium, is of the order of 10^{-3} MeV/gcm^{-2} (c.f. total ionisation loss >1 Mev/gcm^{-2}). Even in the light gases (where there are still regions of absorption in the continum $-\left(\frac{dE}{dx}\right)_c$ is only of the order of 0.1 MeV/gcm^{-2} for H and He (15% of the relativistic rise at most) falling to 0.01 MeV/gcm^{-2} for gases with medium and large z. The correction in the case of neon (z = 10) is hence only of the order of 3% of the plateau-level.

Tsytovich (1962) has argued that in the energy regions beyond the onset of the Fermi plateau radiative corrections are important. His arguments are based on the fact that the mass of a highly relativistic charged particle in a medium differs from its mass in a vacuum due to the emission and absorption of virtual photons which will propagate in the medium. An atom in the medium excited by such virtual photons has a reduced cross-section for energy loss by other means, e.g. ionisation, Cerenkov radiation, and Tsytovich's calculations (ib id) predict a 5 to 10% decrease in the plateau-level for energy-loss predicted by the Bethe - Bloch formula. Crispin and Fowler (op cit), however, argue that

in the presence of strong absorption, the equations used by Tsytovich to find the energy loss are inapplicable over important ranges of frequency, and his consequential radiative corrections are thus inapplicable to real dielectric media.

When considering energy losses in gaseous detectors contained by walls of finite thickness, Garibyan (1972) has suggested that the theory of transition radiation implies a serious radiative correction that should reduce the level of the Fermi-plateau in thin absorbers (of the order of 1 - 10 cms) by an amount which can vary from 25% to 100%, depending on how thin the detector is.

His arguments are based on the fact that the field of a highly relativistic charged particle in a medium is confined by the polarisation of the atoms of the medium. The extent of the confinement region is clearly dependent on the density of the medium, and in passing from a dense to a rarified medium there is a region near to the entry wall where the field behaves as if still in the dense medium. This zone (the distance from the boundary which the particle has to travel before its field has expanded to be confined only by the polarised rarified medium) is called the formation zone in transition radiation theory (Garibyan [1958])

$$(3.6) \qquad Z_m(\gamma, w, \theta) = \frac{\frac{c}{\omega}}{1 - B\sqrt{\varepsilon - \sin^2\theta}}$$

where $\varepsilon(\omega)$ is the dielectric constant of the medium and θ is the emission angle, which is approximately zero at extremely relativistic energies. The expansion (or contraction in the reverse case of passing from a rarified to a dense medium) of the particle's field in this formation

zone gives rise to the emission of transition radiation (typically in the X-ray region).

Taking $\gamma \gg 1$ and putting $\varepsilon(\omega) = 1 + \chi(\omega)$ in equn (3.6) yields

$$(3.6)a \qquad Zm(\gamma, W) = \frac{4.10^{-5}}{\hbar\omega(eV)\left[\frac{1}{\gamma^2} - \chi(\omega)\right]} \quad (cm)$$

which, for those frequencies responsible for the ionisation of the gas atoms, can be of the order of cms. ($\varepsilon \approx 1 - \frac{w_o^2}{w}$ where w_o is the plasma frequency $(4\pi Ne^2/m)^{\frac{1}{2}}$, [$w_o \sim 6.10^{15}$ rad/sec, $\lambda_o \simeq 3.3.10^{-5}$ cm], N = number of electrons/cc, m = mass of electron.)

Using pions and electrons of the same momenta (374 MeV/c), Ramana Murthy (1968) has found the ratio of the ionisation losses in the Fermi plateau region to be 1.45 instead of 1.78 (the value according to Sternheimer). The above arguments would indicate a value of 1.5 for this ratio, an interesting agreement.

This effect, if physically valid, has disturbing implications for measurements based on ionization loss in the flash-tube chamber. The walls consist of aluminium electrodes and glass of total thickness ~ 0.9 gcm^{-2} per transition boundary, enclosing ~ 0.0016 gcm^{-2} of neon (plus argon) per flash-tube. Equn (3.6) indicates that at $\gamma = 1000$ (corresponding to a cosmic ray proton of energy of the order of 1 TeV) $Zm \simeq 4$ cm., which would imply that the efficiency of the flash-tube chamber should be significantly reduced when detecting very high energy particles (see Fig. 3.2).

Attempts to detect, in particular, low efficiency tracks due to either fractionally charged particles (quarks) or "previous particles" (tachyons)

could be severely hampered by the "Garibyan effect". A data analysis has thus been carried out to determine whether or not the effect can be distinguished in the flash-tube chamber at the energies at which it operates most effectively in sea-level cosmic ray measurements (10 - 10,000 GeV). The data on which the analysis was carried out were collected by various colleagues and the basic details are tabulated in Table 3.1.

3.4 Experimental details

Efficiency measurements were carried out on stack F1a (eight layers of flash tubes) by counting the number of flashes along the track corresponding to the extrapolated core of either a burst produced in 15 cms. of iron and appearing in the main body of the chamber (F1b, F2 , F3, see Fig. 2.1 and Figs. 3.1,.2,.3 for typical events), or a single track which travelled through the whole of the main body of the chamber, see below). For clarity I shall quickly recap the relevant features of the flash-tube chamber which were employed in this experiment.

The flash-tubes (containing 98% neon, 2% methane, at a pressure of 60 cm. Hg.) are 1.58 cm. internal diameter, 1.78 cm. external diameter, 196 cm. long, clothed in a black polythene sheath - to prevent light from one tube affecting an adjacent tube - thus increasing the distance between adjacent tube-centres to 1.81 cm. The tubes are stacked regularly in a "close-packing" configuration the line joining the centres being at 30° to the vertical. The high-voltage pulse is applied across pairs of layers by aluminium electrodes 0.122 cm. thick, the time-delay between the passage of a charged particle and the application of a high-voltage pulse being 20 μs.

Beneath the eight layers of F1a is 15 cm. of iron, a plastic scintillator, and a further 96 layers of neon flash-tubes. Above F1a is another plastic scintillator and above this a further 15 cm. of lead, to remove the soft component of the cosmic radiation.

Events were selected in a variety of ways.

i.) E-Series: From this data (see below) came the measurement for $\gamma = 3$ ($min^{m.}$ ionization pt.). These events were selected by a two fold coincidence between the plastic scintillator below the iron (dimensions 146 x 80 x 5 cm^3) and a plastic scintillator directly beneath F4a (see Fig. 2.1). Particles which pass through both the lead and the iron as well as all the lower layers of tubes were presumed to be muons. Low energy muons show a curved track due to multiple scattering in these lower 116 layers. From the curvature and length of this track the energy of the muon can be calculated (Ashton et al [197]). (See equation (3.7.)

ii.) C-Series: From this data came the measurements for $\gamma = 20$ (relativistic rise region) and most of the events for $\gamma = 130$. These events were selected primarily by an air-shower trigger of ≥ 40 particles m^{-2} striking a liquid scintillator (dimensions 132 x 96 x 15 cm^3) placed on top of the lead (see Fig. 2). The $\gamma = 20$ pt. is from measurements on single particle tracks that traverse the whole chamber as above but with no bending. From considerations on the spectrum of core distances the shower-sizes thus collected, and a knowledge of the energy spectrum and lateral distribution of muons contained therein, an estimate can be made of the mean energy of these muons (see D. Cooper [1974]). Zenith angle measurements were as for the H-Series.

FIG. 3·1

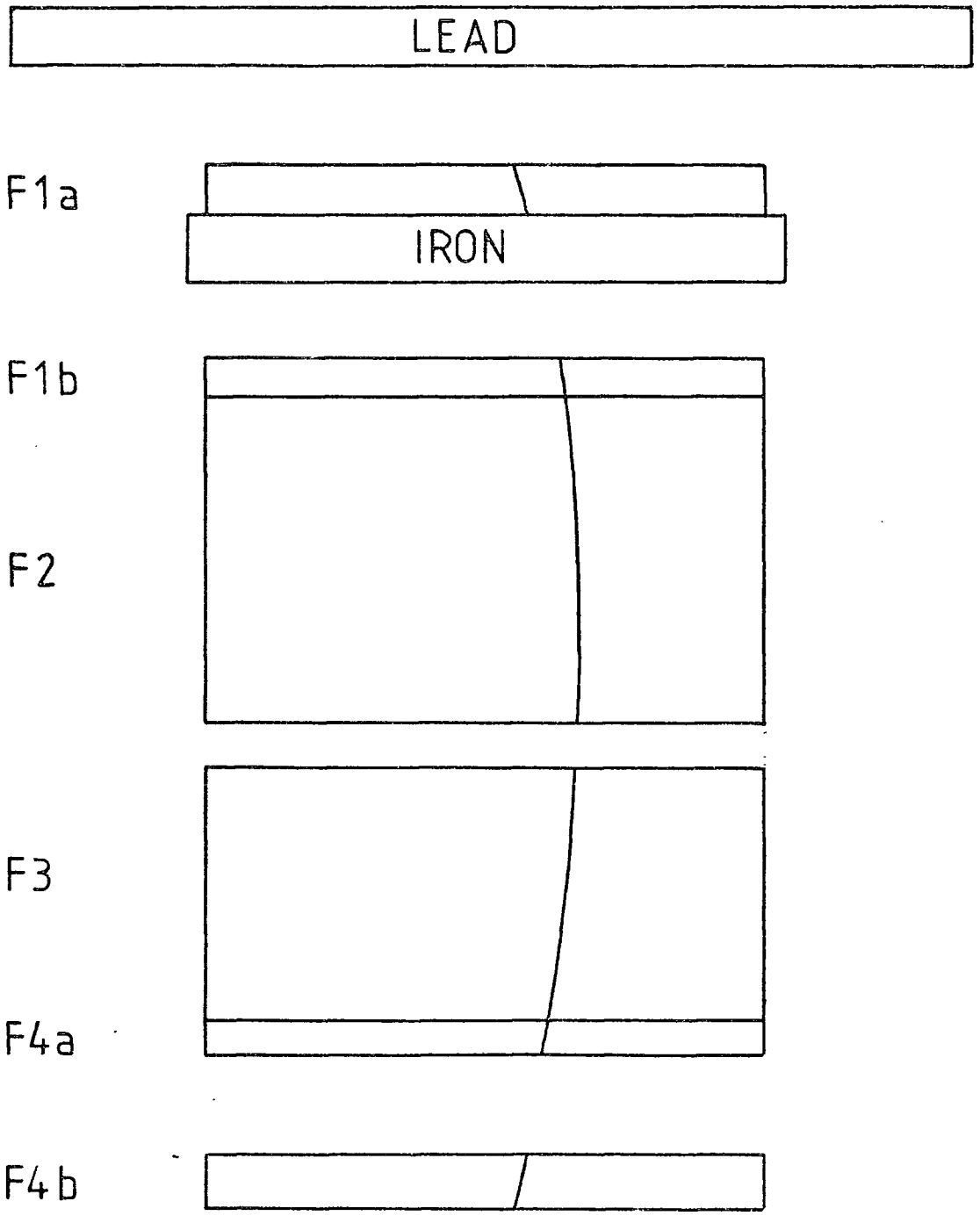

Figure 3.1 A slow muon showing a curved track due to multiple scattering in the flash-tube chamber.
This is a typical event of those used from the E-series data.

FIG. 3·2

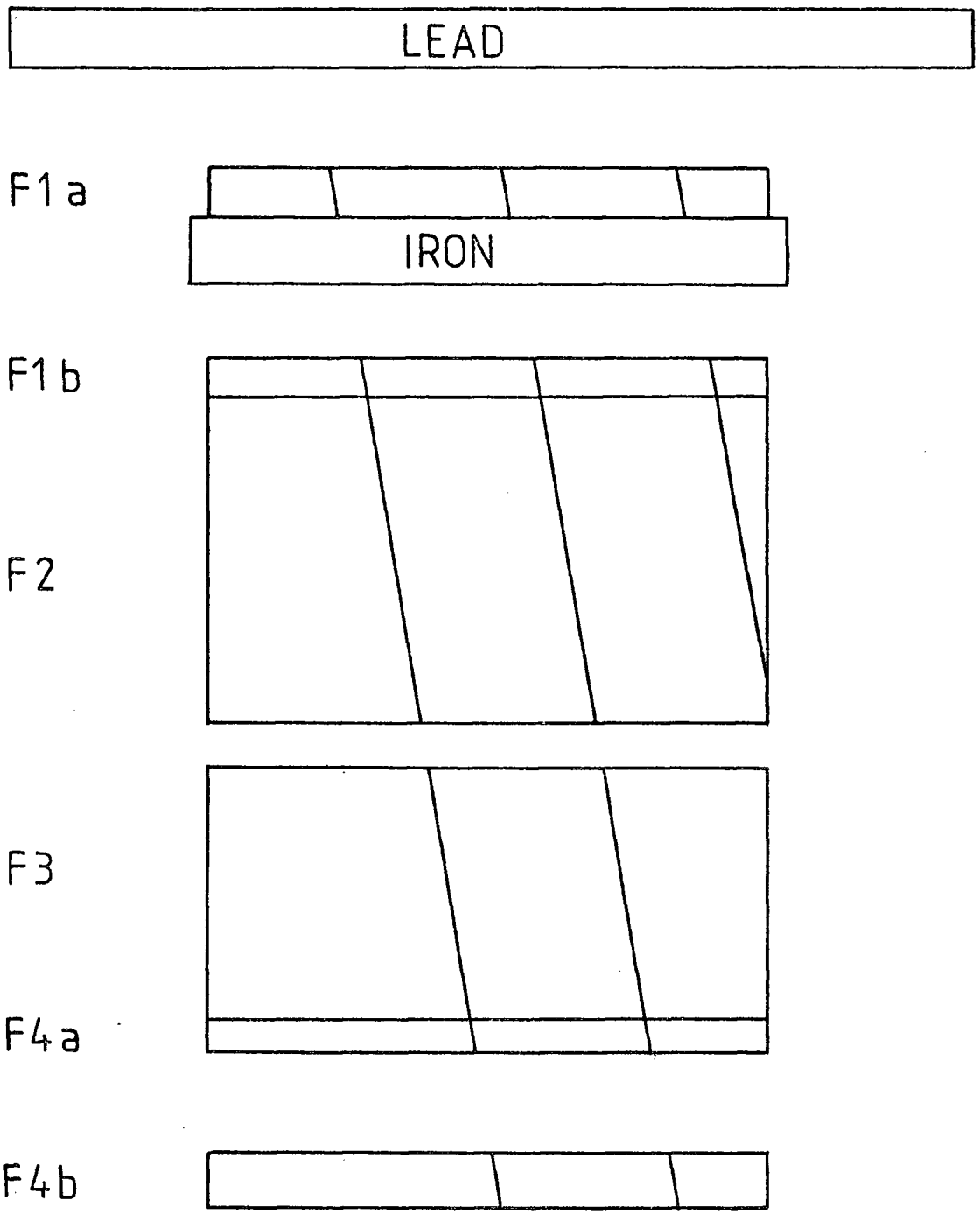

Figure 3.2 Unscattered fast muons in an air-shower.
Typical event seen in C-series.

FIG. 3.3

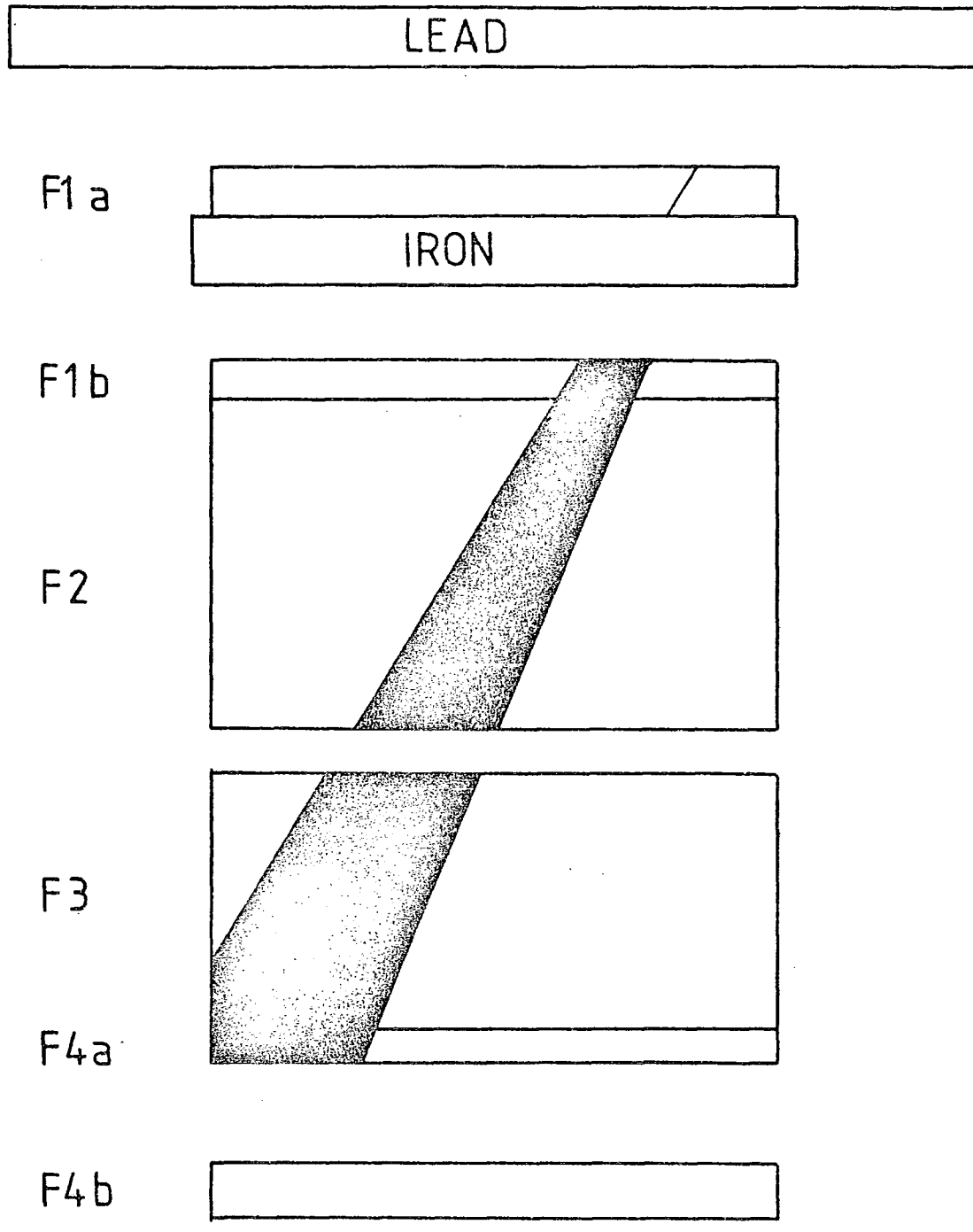

Figure 3.3 Hadron interaction in iron, energy of hadron = 80 GeV.
A typical event seen in H-series.

iii.) H-Series: From this data came the measurements for $\gamma > 100$ (the "Fermi plateau" region). These events were selected by a burst size trigger of $\geq n$ particles (values of n = 40, 100, 200, 400 were used) in either the plastic scintillator under the lead or the scintillator under the iron. Only those events which gave no measurable signal in the scintillator under the lead were used. The energy of the charged particle was derived from the burst-size (as measured by the lower plastic scintillator) produced in the iron (see Ch. 2). For $\gamma > 10$ the conversion from burst size to γ was done assuming the incident charged particles were pions (Ashton and Saleh [1975] and M. Whalley [private comm.]) The zenith angle of the event was measured from the best line through the core of the burst, as viewed in the lower 96 layers, and the single track produced in the first eight layers.

In the efficiency measurements on F1a, only those tracks with ≥ 2 in the geometry layers flashed were considered to avoid including neutral particle events (neutrons, kaons).

Variations in the mode of triggering and structure of the flash-tube chamber cause experimental corrections to be made before all three sets of data can be combined. These various corrections are discussed in the next section.

(3.7)

$$p\beta c = \frac{y}{\Delta} 1.86\ t^{\frac{1}{2}}$$

where y = distance travelled in cm.

Δ = max. displacement from a straight track

t = thickness of material traversed in $g.cm^{-2}$

p = momentum of particle

β = vel. par.

c = vel. of light

E-Series - Energy determination

TABLE 3.1 Summary of sources of data for investigation of Garibyan effect.

Film Series	Purpose of Experiment	Author	Lorentz Factor Range
C-Series	Search for Quarks in Air-Showers	D. Cooper (1974)	10 - 100
E-Series	Search for Quarks in Incoherent Component	A. Parveresh (1975) A. Saleh (1975)	1 - 10
H-Series	Measurement of Incoherent Sea-Level Hadron Spectrum	A. Saleh (1975) I. Ward (present work)	$\gtrsim$100

3.5 Data and corrections

Only those events which flashed the first layer of F1a were used. This avoids the inclusion of tracks which have not passed through all eight layers. It does, of course, introduce a slight bias up in the effeciency measurements but this is roughly only of the order of $(1-\eta_i) \times \frac{1}{8} \times \frac{n_<}{n}$ (where η_i = layer efficiency, $n_<$ = no. of events which are observed to flash <8 layers, n = total no. of events) at most, i.e. less than 1%.

The problem (edge-effect) of particles travelling in regions of the flash-tube beyond the edge of the electrodes and producing a reduced efficiency has been discussed previously (Ashton et al [1971]). The method used to avoid such events is to use shorter electrodes in the defining layers F1a, F1b, F4a, F4b than in the main body of the chamber (F2., F3 see Fig. 2.1), the difference in length being determined by the distance away from the edge of an electrode its fringing field becomes ineffective (a distance $\simeq 3$ cm. for a reduction of field to 1% field well inside the plates) between parallel plates at a distance of 2 cms. apart (Ashton et al [ib id]). These sort of events are thus excluded in the burst selected events of the H-Series where the electrodes in F1a, F1b had been shortened if we require the burst to be visible in F1b and below, and we have the electrodes of F1a and F1b shortened. However, no such electrode-shortening had been introduced for the C and E-Series events, but a correction based on the expected fraction of events which would be in the edge-effect region ($\simeq 7\%$) and their expected reduced efficiency (average $\simeq 0.5\eta_i$) in the fringing field can be easily applied.

The production of knock-on electrons with sufficient energy to enter and flash the next layer tends to increase the measured efficiency. A

FIG. 3·4

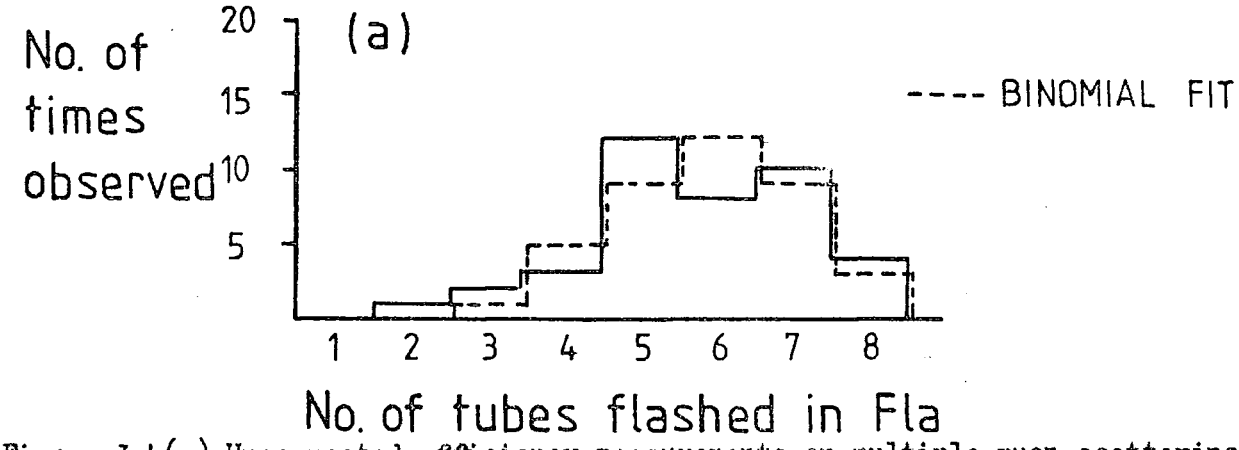

Figure 3.4(a) Uncorrected efficiency measurements on multiple muon-scattering tracks observed on 20 μs. time-delay during film-series E39 - E69.

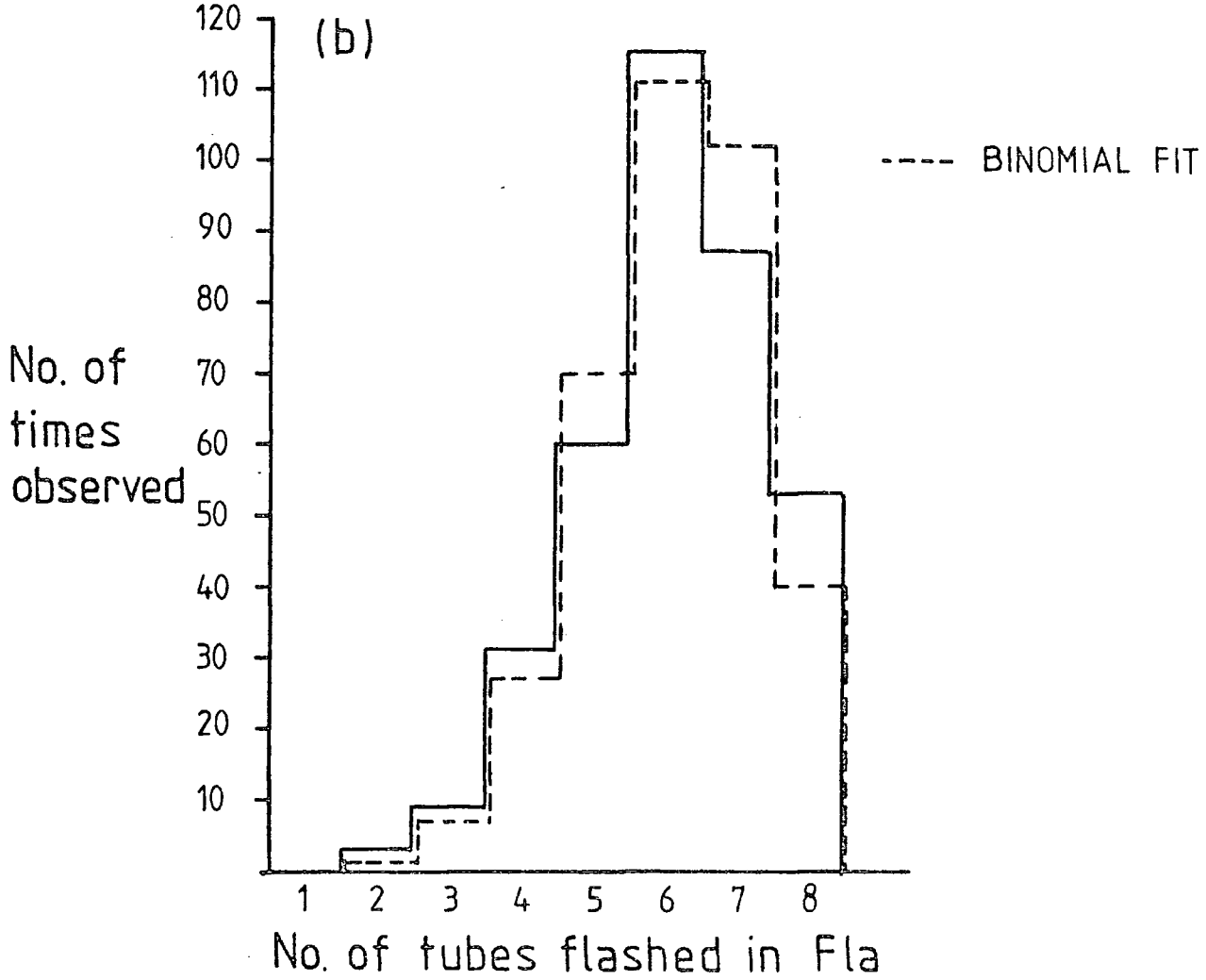

Figure 3.4(b) Uncorrected efficiency measurements on unscattered muon tracks observed on 20 μs. time-delay during film-series $C_{1a}C_{1b}C_{1c}C_{1d}$.

FIG. 3·4 (c)

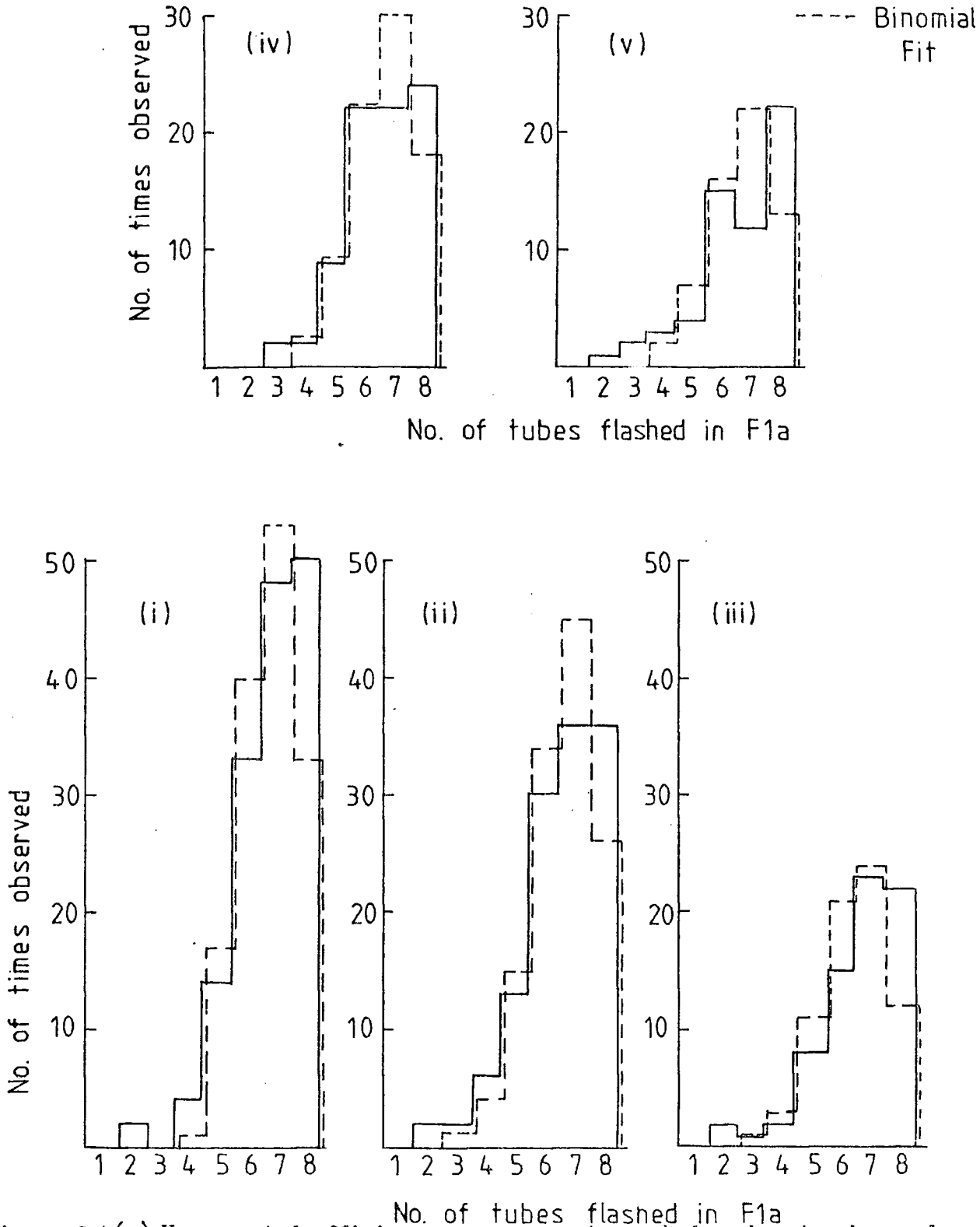

Figyre 3.4(c) Uncorrected efficiency measure ments on hadron bursts observed on 20 μs. time-delay during H and E -film series'.
Burst-size ranges are:-
(i)0- 100 (ii)100 - 300 (iii)300 - 500 (iv)500 - 800
(v)800 -1500 particles.

correction (to all data) can be applied here too, and the correction used assumed that 100% of the knock-ons produced with sufficient energy to enter the next layer would enter a tube which would be counted as in the primary particle track (essentially that all knock-ons will travel forward).

The correction is a bootstrap technique, which assumes that the correction to be applied is only small. The data were first histogrammed into bins of 8, 7, 6 etc. layers flashed in different burst-size/γ ranges (Fig. 3.4). A mean number of layers flashed in each burst size range was found and a binominal distribution calculated. The binomi al distribution was deemed more appropriate than the theoretical distributions discussed above because of the small number of layers used (8), and the ensuing poor resolution. From this distribution can be found the relative probability $\alpha : \beta$ of n layers flashing to (n-1) layers flashing. This gives a measure of the relative probability that a given number of layers would have flashed without the presence of a knock-on electron from an adjacent tube.

From the calculations of Bhabha (1938) on the differential collision probability for particles of spin $\frac{1}{2}$, the probability $P(E>E^1)$ of a knock-on electron having energy $E>E^1$ can be shown to be (Parvaresh 1975)

$$P(E>E^1) \simeq \frac{2c^1 m_e c^2}{B^2} \cdot \frac{1}{E^1} \Big/ \text{g.cm}^{-2}$$

where $c^1 = 0.15 \frac{Z}{A}$, and we take $\frac{Z}{A} \simeq 0.5$ over all material in F1a

$m_e c^2$ = mass of electron in eV

β = velocity parameter of incident particle (heavier than an electron)

Now the energy required to traverse one flash-tube (i.e. enter one tube from an adjacent tube) is 1.8 MeV. Hence the number of electrons that can be produced with sufficient energy to enter the next layer of flash-tubes can easily be calculated to be 0.316 per single particle crossing 8 layers.

Hence we can correct the number x of events in a bin corresponding to flashes by using the equn.

$$x_{\text{corrected}} = x - 0.316.x.\frac{\beta}{\alpha+\beta} + 0.316y.\frac{\alpha}{\alpha+\gamma}$$

where x = uncorrected no. of events in the $n^{th.}$ bin

y = uncorrected no. of events in the $(n+1)^{th.}$ bin

$\frac{\gamma}{\alpha}$ = relative probability of $(n+1)$ layers flashing to n layers flashing

$\frac{\alpha}{\beta}$ = relative probability of n layers flashing to $(n-1)$ layers flashing

and α, β, γ are integers.

The resulting corrected distributions are shown in Fig. 3.5 and a table indicating the goodness of fit of a binominal to both the uncorrected and corrected data is given as Table 3.2.

Only events for which the zenith angle $\theta \leq 30^{o}$ were used because of the possibility of a charged particle passing through more than one tube in a layer for large zenith angles.

Data from the air-shower triggered run (C-Series) corresponding to the relativistic rise region will be contaminated by the large amount of background flashes in F1a due to the air-shower accompaniement. This

FIG. 3·5

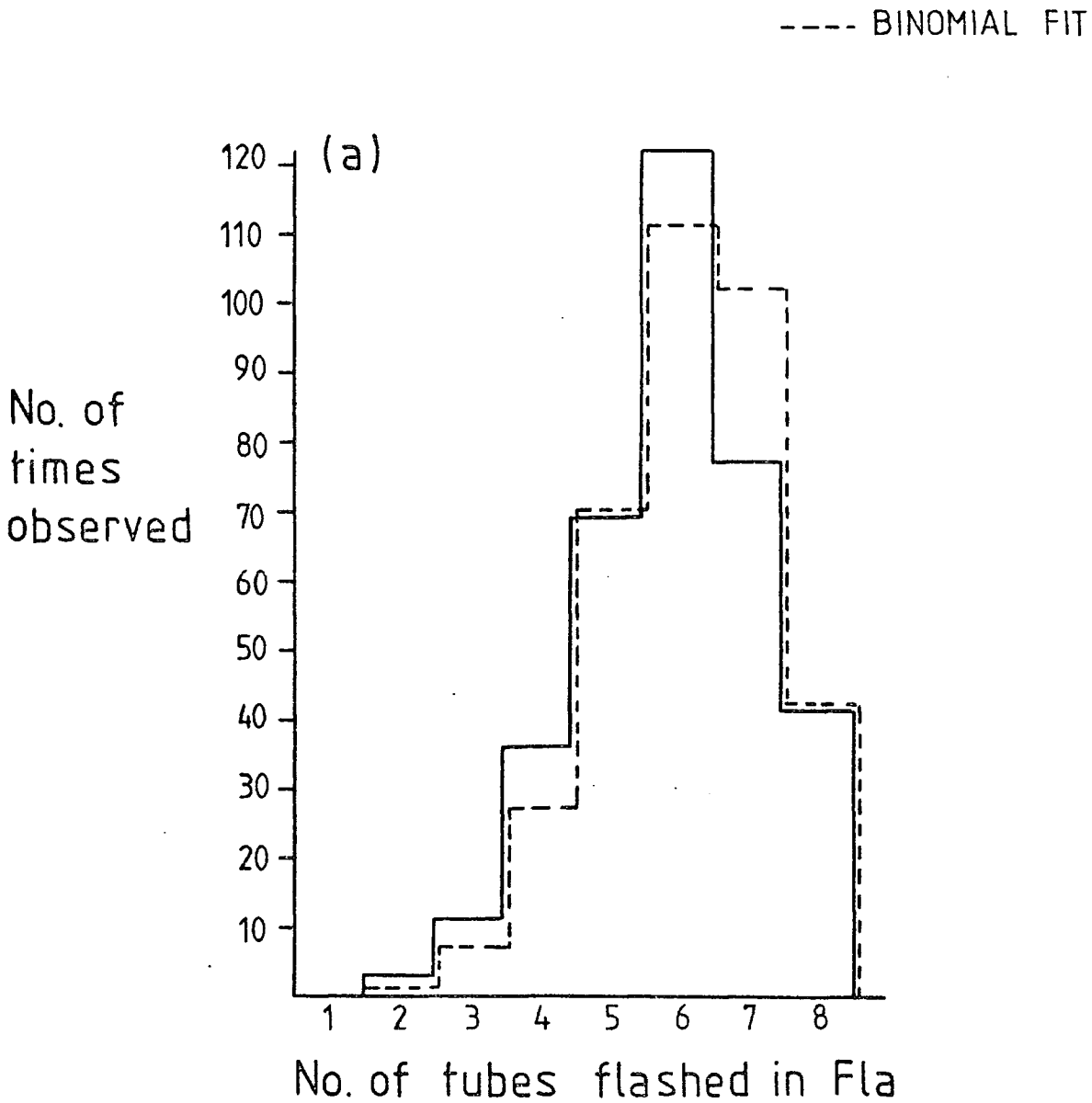

Figure 3.5(a) As for figure 3.4(b) but corrected for knock-on electrons.

FIG. 3·5 (b)

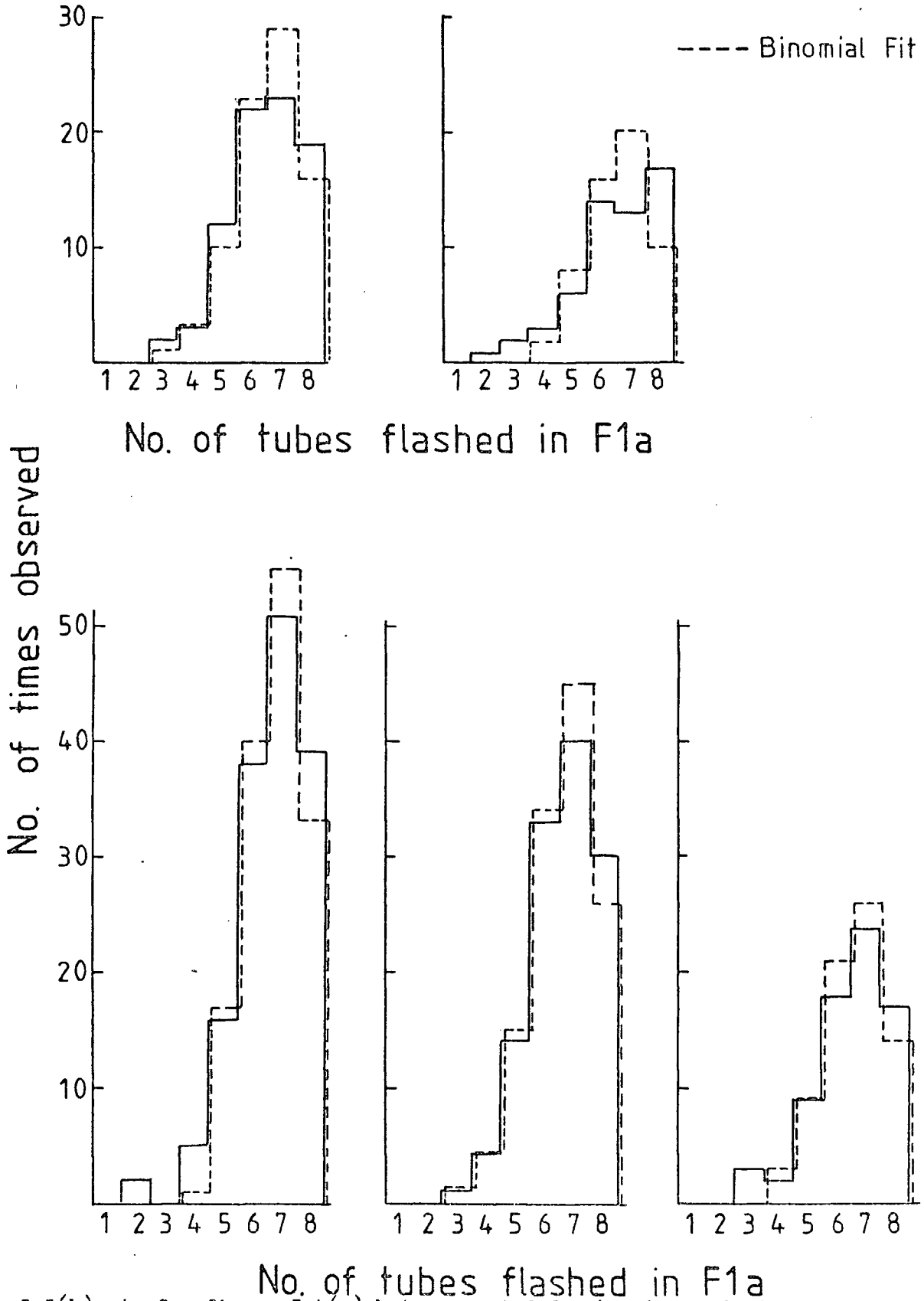

Figure 3.5(b): As for figure 3.4(c) but corrected for knock-on electrons.

TABLE 3.2 **Comparison of uncorrected and corrected data**

Burst size Range	Y	Uncorrected Layer Efficiency	Corrected Layer Efficiency
	3.7	.712 ± 0.024	No correction applied
	20	.761 ± .009	.762 ± .008
0 - 100	103	.864 ± .015	.829 ± .011
100 - 300	980	.825 ± .012	.824 ± .015
300 - 500	2,050	.825 ± .017	.811 ± .017
500 - 800	3,550	.826 ± .015	.812 ± .018
800 - 1500	5,950	.828 ± .018	.807 ± .021

Burst size Range	Y	Chi square of fit to Uncorrected data of a Binomial	Chi square of fit to Corrected date of a Binomial
	3.7	3.444	No correction applied
	.20	10.596	12.52
0 - 100	103	11.096	2.871
100 - 300	980	11.185	1.267
300 - 500	2,050	11.159	2.595
500 - 800	3,550	3.886	2.454
800 - 1500	5,950	10.950	8.25
		7 BINS	

will tend to increase the measured efficiency of the hadrons in showers ($\bar{\gamma} \simeq 130$) because all such hadrons will be close to the core and hence in regions of dense accompaniement.

The finally corrected average layer efficiencies can now be converted to internal efficiencies by multiplying by the ratio of the area covered by a layer to the actual area covered by gas in that layer i.e. $\eta_I = \eta_L \frac{1.81}{1.58}$

where η_I = internal efficiency

η_L = layer efficiency.

3.6 Results

The corrected average efficiencies of Fig. 3.5 are plotted as a function of Lorentz-factor γ in Fig 3.7. The theoretical curves are based on Sternheimer's parameterisation (op cit) using the tabulated values as quoted by Hayakawa (op cit). The curve with the highest plateau efficiency corresponds to energy loss in neon, the next curve down corresponds to a 50% reduction in this energy loss, the lowest curve is the energy loss curve for neon without the density effect in neon, but reduced by the same factor as the energy loss in aluminium is reduced by the density effect, this is approximately the result that would be expected if the Garibyan effect is applicable.

The two points at small values of γ are low possibly for the reasons already outlined, and a correction based on previously quoted figures would bring both these points up to the theoretically predicted values. The rather high value at $\gamma = 130$ has already been discussed and is probably due to background flashes increasing the number of flashes falling along the track.

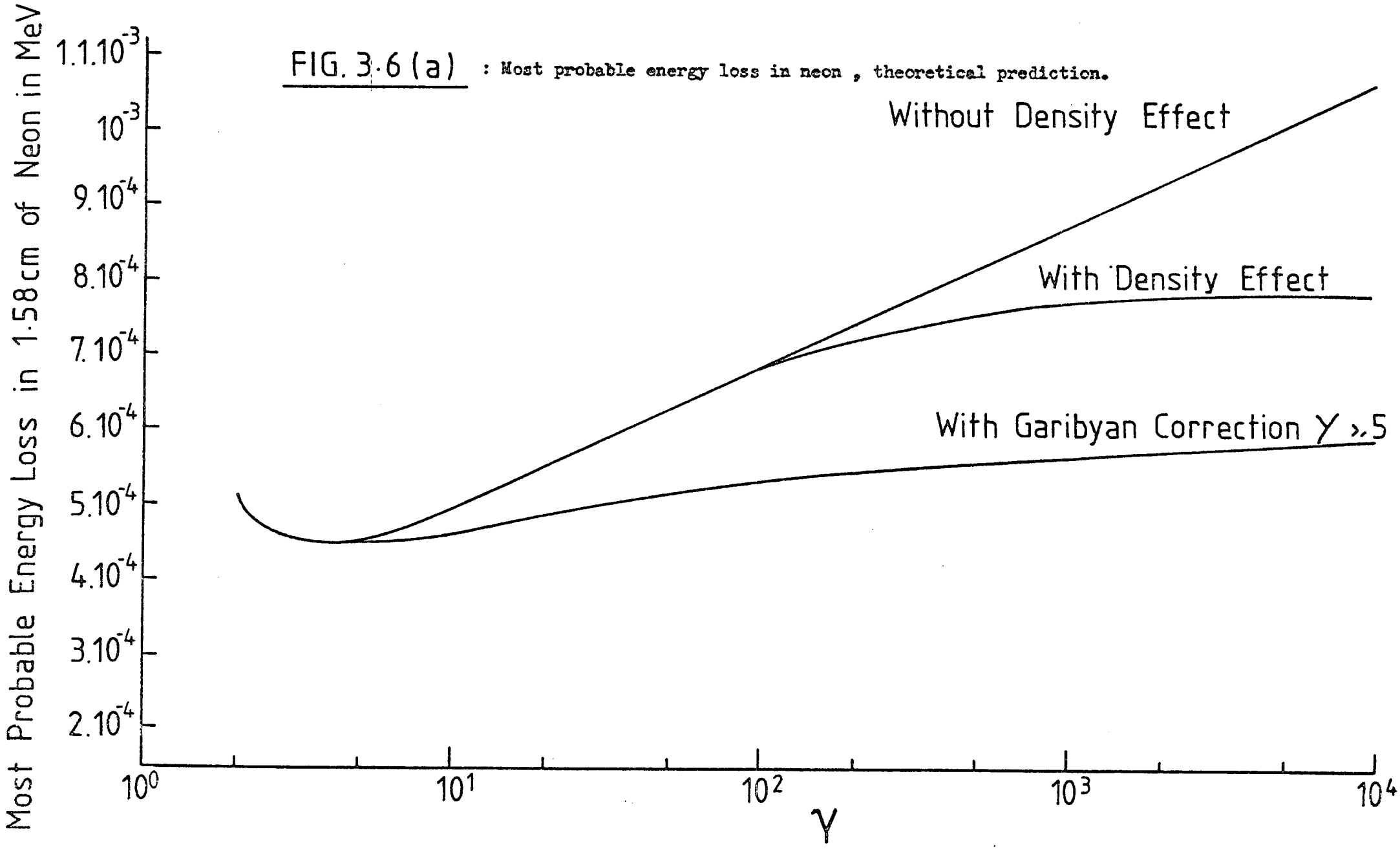

FIG. 3·6 (a) : Most probable energy loss in neon , theoretical prediction.

FIG. 3·6 (b) : Most probable energy loss in aluminium , theoretical prediction.

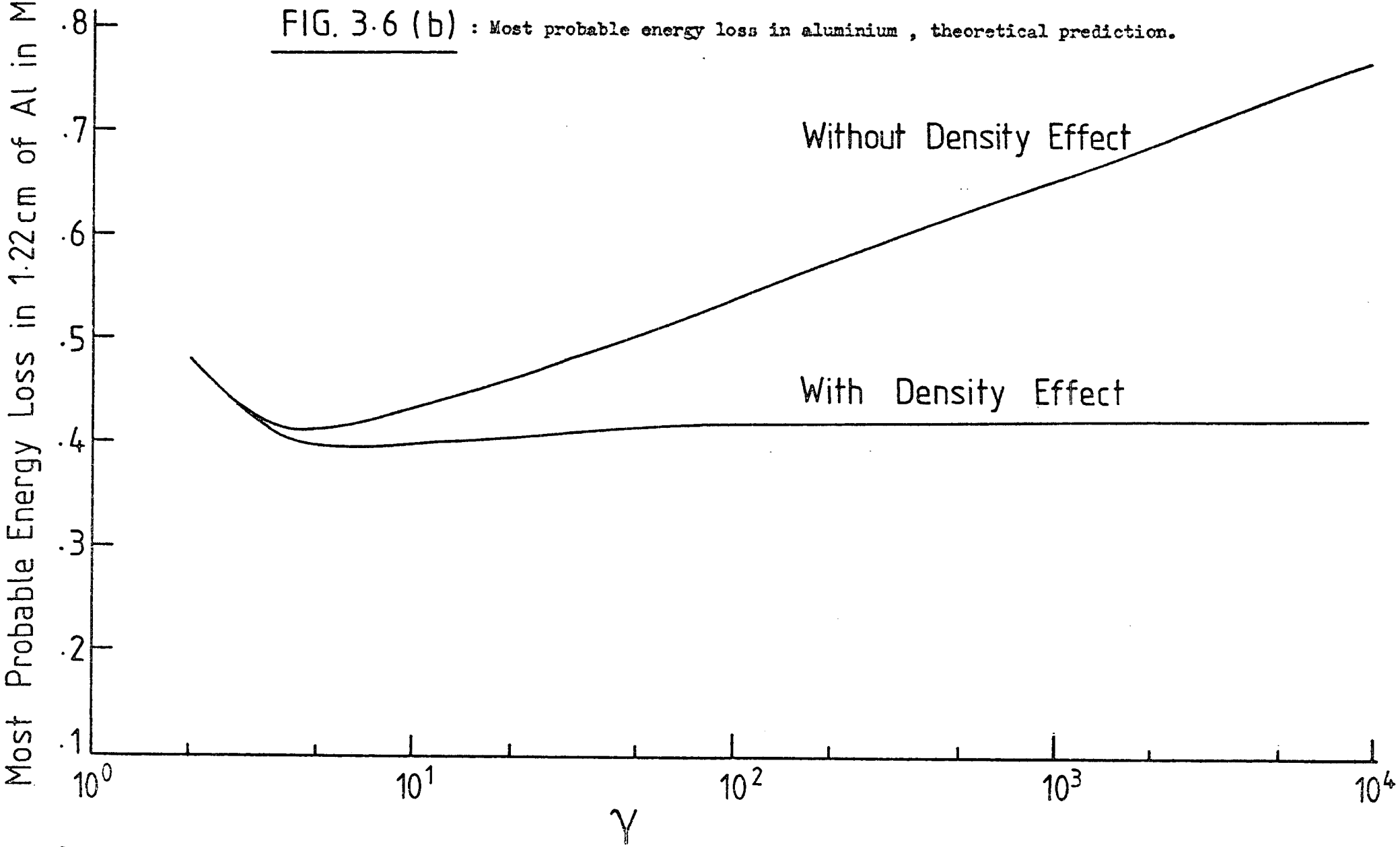

FIG. 3.7 : Variation of internal efficiency of neon flash-tubes with Lorentz-factor γ

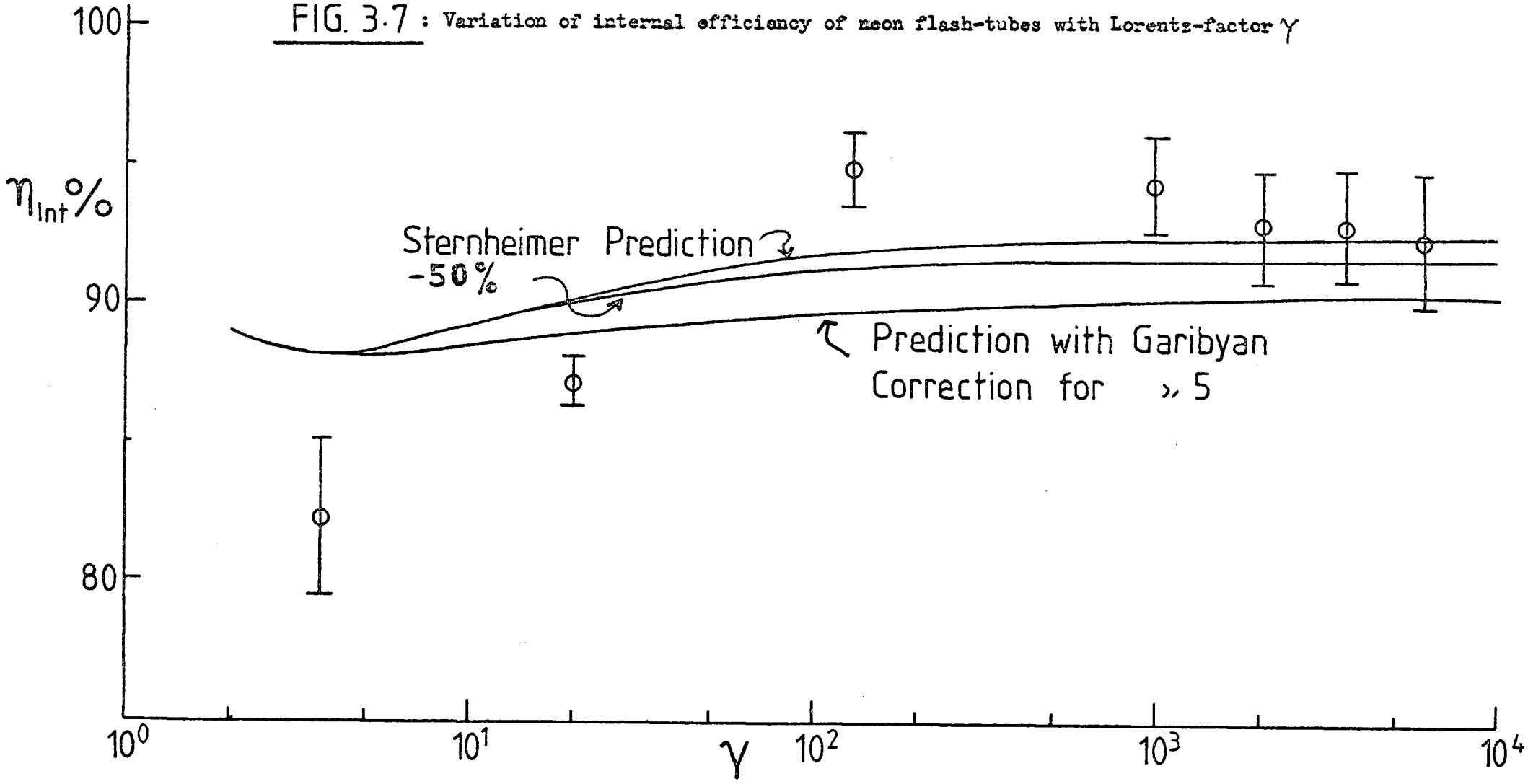

If the systematic bias upward introduced by only considering tracks which flash the first layer is as much as 1%, then the results will fall between the two curves and the size of the error bars make any further quantitative conclusions impossible. A slight decrease from $\gamma = 10^3$ to $\gamma = 2.10^3$ might be taken as indicative, but taking an average value for the plateau efficiency (see Figs. 3.8, 3.9) forces the conclusion that no discernible deviation from Sternheimer's predictions can be seen (see Table 3.3).

Fig. 3.6(a) gives the most probable energy loss in 1.58 cm. of neon (in MeV) as a function of Lorentz-factor γ for the 3 cases no density effect, density effect according to Sternheimer, density effect according to Sternheimer with Garibyan correction. To obtain the predicted efficiencies from the predicted energy loss normalisation at $\gamma = 20$ has been used. The normalisation is based on extensive studies on the 96 flash-tubes at $\gamma = 20$ (Cooper 1974) for different time-delays (i.e. the time between the passage of a charged particle through the chamber and the application of the H.T. pulse across the tubes). The result was that at a time-delay of 20 μs the flash-tubes had a value $afQ = 9$ for $\gamma = 20$ where a = internal radius

f = probability of the tube flashing on the passage of a charged particle

Q = number of ions/cm. created during this passage.

Hence, by assuming $afQ \propto$ energy loss and using the predicted internal efficiency as a function of afQ at 20 μs (Lloyd [1960]) the theoretical curves of Fig 3.7 can be calculated.

Fig. 3.6(b) gives the most probable energy loss in 0.122 cm. of aluminium with and without the density effect (Sternheimer [op cit]).

FIG. 3.8

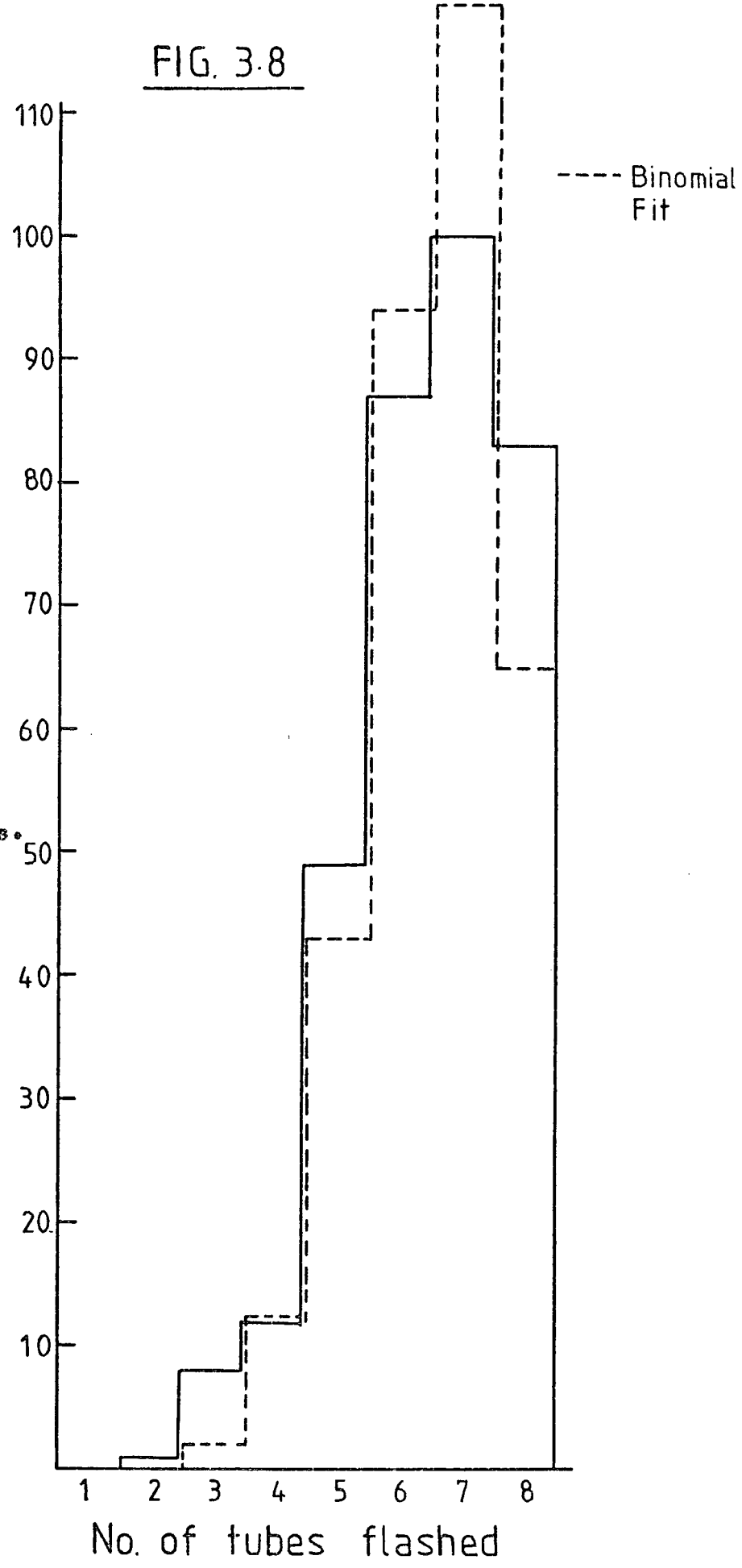

Figure 3.8:
Total data for burst-size greater than 100 particles.
(The corrected data for the calculated plateau-region.)

Figure 3.9: Variation of internal efficiency of neon flash-tubes with Lorentz-factor γ

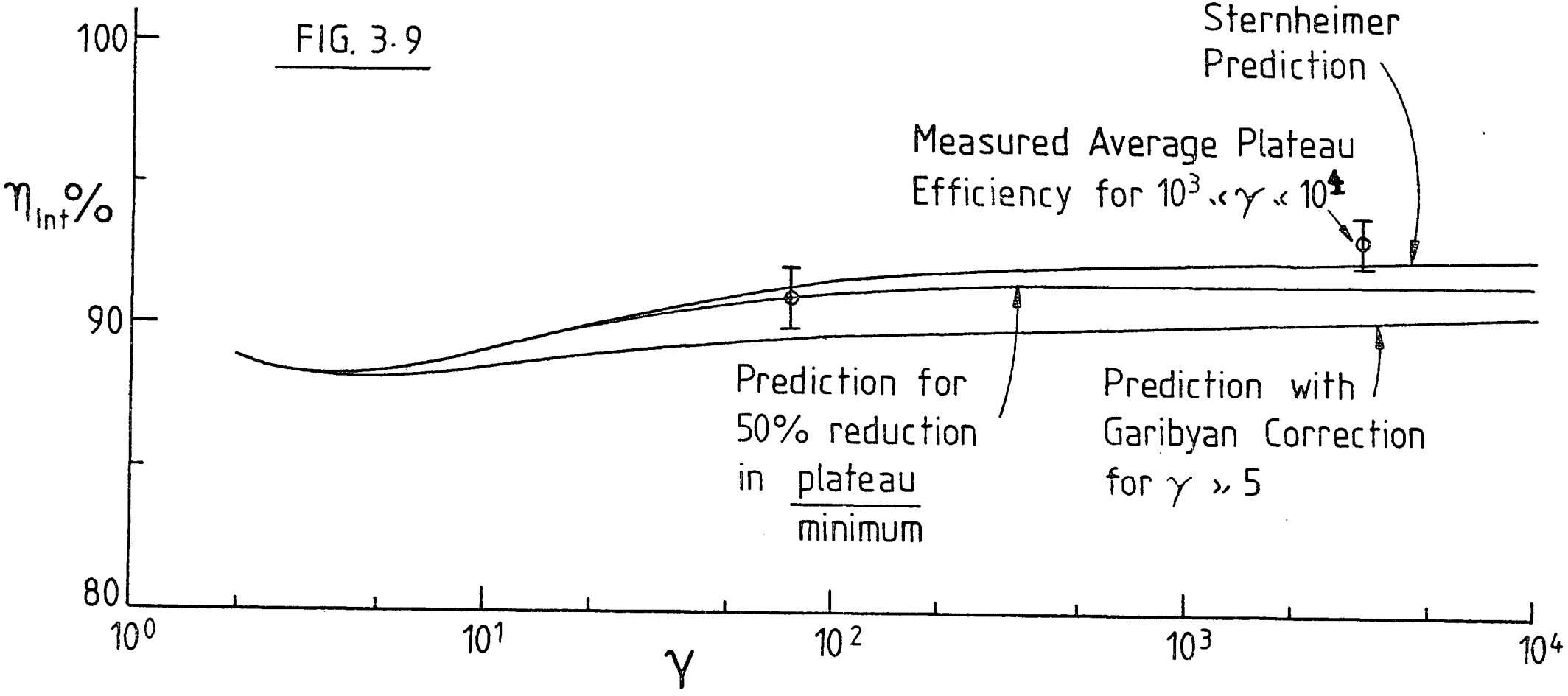

TABLE 3.3

Comparison of Result with Predictions

Mean Measured Plateau Efficiency	93.2 ± 0.9%
Predicted Plateau Efficiency from Sternheimer	92.5%
Predicted Plateau Efficiency for 50% Reduction in Plateau/Minimum Ionization	91.7%
Predicted Plateau Efficiency from Calculated Garibyan Correction	90.5%

N.B. The mean measured plateau efficiency is for all events with burst-size >100 particles and is plotted at the mean γ of $3.15.10^3$.

3.7 Comparison with other work

Energy loss measurements in the relativistic region on similar neon - methane mixtures to the one used in the flash-tube chamber have been made by Eyeions et al (1955) and Jones et al (1963), no serious disagreement with Sternheimer's predictions were discovered except for a slight decrease in the rate of increase noted by Eyeions. These results together with the results of the present measurements are shown in Fig. 3.10.

More serious discrepancies in argon have been noted by Ramana Murthy (1968), Harris (1973), Jeanne (1973), Aderholz (1974), Dimcorski (1971). However an experiment specifically designed to investigate the Garibyan effect in argon by using various windows through which the charged particle passed before entering the gas yielded no significant difference in energy loss between various windows (Smith and Mathieson[1975]).

The above quoted results, however, have been explained by recent recalculations of theoretical predictions based on a Monte Carlo method rather than a continuous integral over the spectrum of single collision processes. Because of the small number of ionising collisions in a gas this method more accurately reflects physical reality, and predicts a lower rate of increase and plateau level - in agreement with the above mentioned authors - than conventional Sternheimer predictions (Cobb, Allison and Bunch [1976]).

3.8 Conclusions

A decrease in the Fermi plateau level of ionisation by the amount predicted by Garibyan was not observed. A smaller decrease, as predicted

Figyre 3.10: Comparison with previous results on neon , normalised to 1 cm. of neonat 60 cm. Hg pressure.

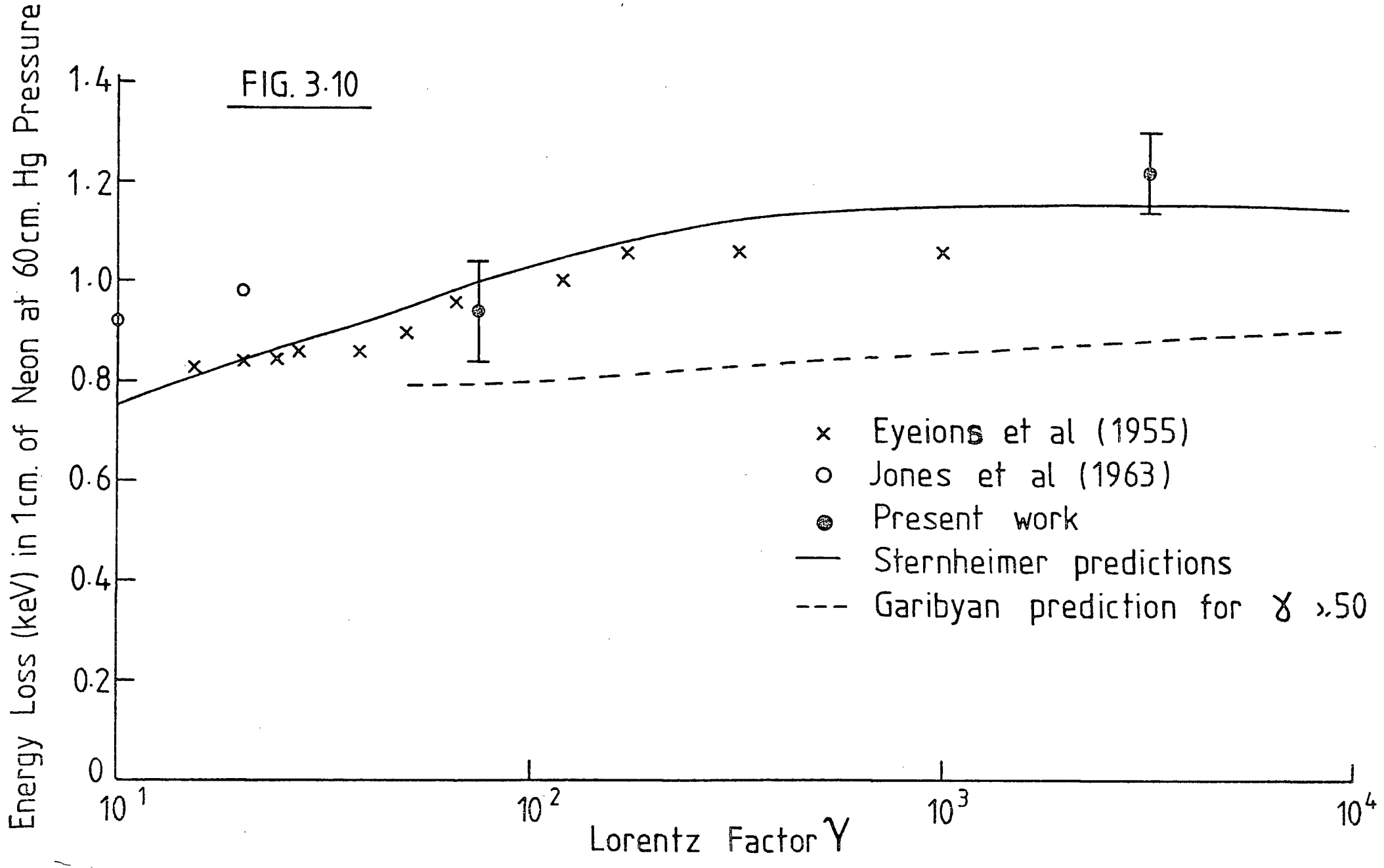

from the calculations of Cobb et al (op cit) cannot be ruled out, however the physical basis for such a reduction should not seriously affect searches for fractionally charged or previous particles based on efficiency measurements.

However, there are possible experimental effects that might mask the Garibyan effect in this experiment:-

a.) Low energy electrons that are produced by ionisation in the glass could enter the gas and cause an increase in apparent internal efficiency. Low energy electrons are able to cross the solid-gas boundary if they are incident at slanting angles to the interface, since the interface is circular (tubular) all possible angles of incidence are available:

b.) For γ in the "high" range ($\sim 10^2 - 10^3$) the strongly collimated transverse electric field might be causing electrons from the inner shells to become ionized. This effect would be better investigated with relativistic particles of a well-defined momentum, since it should show up as a step up in the measured plateau value at some high value of Lorentz-factor γ .

CHAPTER 4

THE INCOHERENT HADRON SPECTRUM

4.1 Introduction

The incoherent hadron spectrum consists of all hadrons (nucleons, pions, kaons account for most sea-level hadrons) which arrive at sea-level unaccompanied by any electron - photon shower. It is customary to include all shower accompanied hadrons in the spectrum as the ratio of unaccompanied to shower accompanied hadrons detected by a hadron-trigger is of the order of 5.5:1 (see Table 4.1). These hadrons consist mainly of secondary (including third, fourth etc. generation) nucleons and pions from interactions of primary cosmic-ray particles high up in the atmosphere, whose subsequent electron - photon showers have reached maximum high up in the atmosphere and have died out. There is a possible small contribution from (a) secondary particles with large transverse momentum from younger showers whose core falls far from the detector; (b) primary particles from low elasticity events in which only a small fraction of the primary cosmic-ray's energy is converted to a nuclear - electromagnetic cascade; (c) secondary (and primary) particles from primary interactions very deep in the atmosphere whose cascade component has not sufficient matter in which to develop before reaching sea-level; (d) finally there are the very rare cases of primary cosmic-rays which have traversed the whole atmosphere without interacting.

Any departures from a smoothly decreasing spectrum would arouse great interest as it would indicate an increase in the contribution from (a), (b), (c) or (d) (c.f. for example the interest generated by the kink in the spectrum reported by Baruch et al [1973] but later found to be due to faulty electronics).

The increase in complexity of Monte Carlo calculations of cosmic-ray and air-shower development in the atmosphere have made the comparison of broad measurements such as the incoherent hadron spectrum, especially if it can be subsequently divided into its pionic, neutronic and protonic components (Ashton and Saleh [1975]), with prediction a valuable test of interaction models and/or primary spectrum models (e.g. M. Whalley [1975]).

Finally, the assumption of a smooth spectrum can be used to test the performance of a hadron detector designed to investigate more intimate details of the sea-level cosmic radiation such as hadron spectra in air-showers, lateral distribution of hadrons in air-showers, searches for exotic particles.

4.2 Apparatus

The flash-tube chamber as described in Chapter 2 was used to detect hadrons at sea-level. The liquid scintillator M (see Fig. 2.1) detected and measured any air-shower accompaniment close to the path of the hadron. Plastic scintillators C and A under the lead and iron (see Fig. 2.1) respectively provided the trigger as well as recording the size of the electron - photon shower produced by a hadron which interacted in either target. The high voltage pulse was applied to the electrodes 330 μs, after the trigger signal was received because the trigger-level was set at 500 particles (to detect only the higher energy hadrons), and such large bursts would completely fill the flash-tube chamber at short time-delays. The long time-delay enabled the direction of the hadron to be measured from the direction of the residual core of the electron - photon shower produced. It also enabled a study of the characteristics of such

bursts to be carried out at high-energies so that highly charged particles could be identified (see Chapter 5). Bursts were considered as being initiated in the lead or the iron from the recording of the pulse heights from scintillators C and A as photographed on a C.R.O. The pulse heights from each scintillator M, C, A were delayed by 1.6, 0.9, 0.3 μs respectively using delay-line before being displayed, and the oscilloscope time base was triggered with no delay by the same pulse which triggered the H.T. pulse to the flash-tube chamber. The events as recorded on film from the flash-tube chamber and the oscilloscope were co-ordinated by photographing a synchronised clock and watch respectively. A more detailed account of the apparatus is given in Chapter 2.

4.3 Data-measurement technique

The record of the flash-tube chamber events was projected onto a 1:20 scale drawing of the front view of the flash-tube chamber (see Fig. 2.1) and the direction of the event measured. The number of flashes within $\pm$0.5 cm in F1a and F1b was counted and note taken of events which occured in the walls, or at large angles so that they would have missed one of the scintillators (these events were then dismissed).

The flash-tubes of F1a and F1b are pushed back (see Fig. 2.2) so that we can be sure that if a burst is seen in the flash-tubes, the whole of it must have passed through the scintillator above. Hence acceptable bursts are only those where all the flash-tube layers in F1a (for bursts in lead) or F1b (for bursts in F1b) are flashed, thus avoiding any bursts near the edge of the chamber at the front.

Figure 4.1: A rare event in which two hadrons arrived simultaneously. The burst to the right of the chamber is due to a hadron of primary energy 850 GeV interacting in the lead, the subsequent electron-photon shower has clearly continued to develop in the iron.This would be considered as a burst in the lead, and within the acceptance geometry, hence its energy was derived from the burst-size as measured by scintillator C (under the lead).
The burst in the centre of the chamber appears to have occurred in the iron, but no flashes associated with such a burst can be observed in the defining layers F1b. This burst could have originated in the lead and missed the defining layers F1a, or at the front of the iron target and missed the scintallator A under the iron. Either way it would not be considered as a candidate for further analysis since it did not fall within the acceptance geometry.

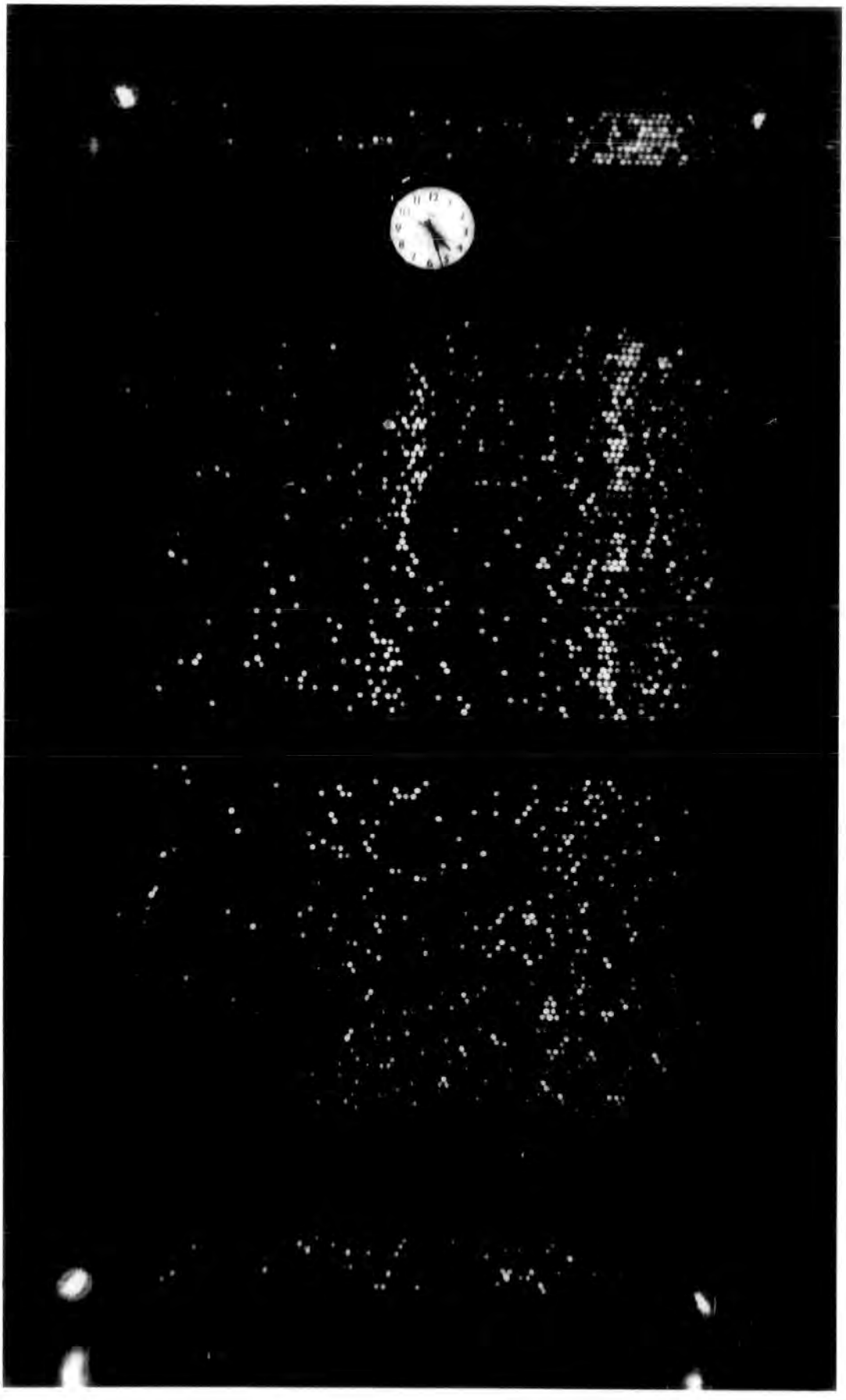

The record of the oscilloscope events was projected onto a scale which measured the pulse height directly in terms of the number of particles producing the pulse (see Chapter 2, Section 2.6.1). Due note was taken of the scintillator which triggered the recording equipment and the event duly assigned as occurring either in the lead (a pulse from C with or without a pulse from A) or in the iron (a pulse from A with no pulse from C). However, this method of assigning events as occurring in either the lead or the iron gave rise to two problems:

i.) Events were observed to produce a faint burst under the lead followed by a well defined burst under the iron, but no measurable pulse was observed from the scintillator C under the lead.

ii.) From considerations of the probabilities of a hadron interacting in each target, more bursts are expected to occur in the lead than in the iron (see Appendix VI and Table 4.5). However this method of assigning bursts indicated that more bursts were apparently being produced in the iron than in the lead (see Table 4.5).

The events were thus scanned again and bursts which appeared in the flash-tube chamber photograph to begin under the lead were called bursts produced in lead whether or not they produced a measurable pulse in the scintillator C under the lead. The burst size of those events which were thus re-assigned was assumed to be the burst-size as detected by scintillator A under the iron. These events were due to two effects:

i.) Bursts which begin at the very bottom of the lead do not have sufficient depth of lead in which to develop into a measurable shower, however the energy per particle is very high and so the equivalent energy of the burst size as observed after the shower has developed

TABLE 4.1

SUMMARY OF DATA COLLECTED TO DETERMINE SEA-LEVEL INCOHERENT HADRON SPECTRUM (FILMS H78 - H94)

Trigger Level (≥N particles)	Time-Delay of High Voltage Pulse	Running Time	Number of Triggers	Total number of bursts within acceptance geometry		No. of bursts within $\pm 30^{\circ}$ to vertical within acceptance geometry	
				Pb	Fe	Pb	Fe
500	330 μs	1422 hrs.	346	131	194	121	102
	Total number of bursts where scintillator M showed shower accompaniment.			27	32	23	27

Figure 4.2a) Frequency of bursts in lead of different sizes that arrived within $\pm$ 30° to the vertical.

Figure 4.2b) Frequency of bursts in iron of different sizes that arrived within $\pm$ 30° to the vertical.

FIG. 4.2

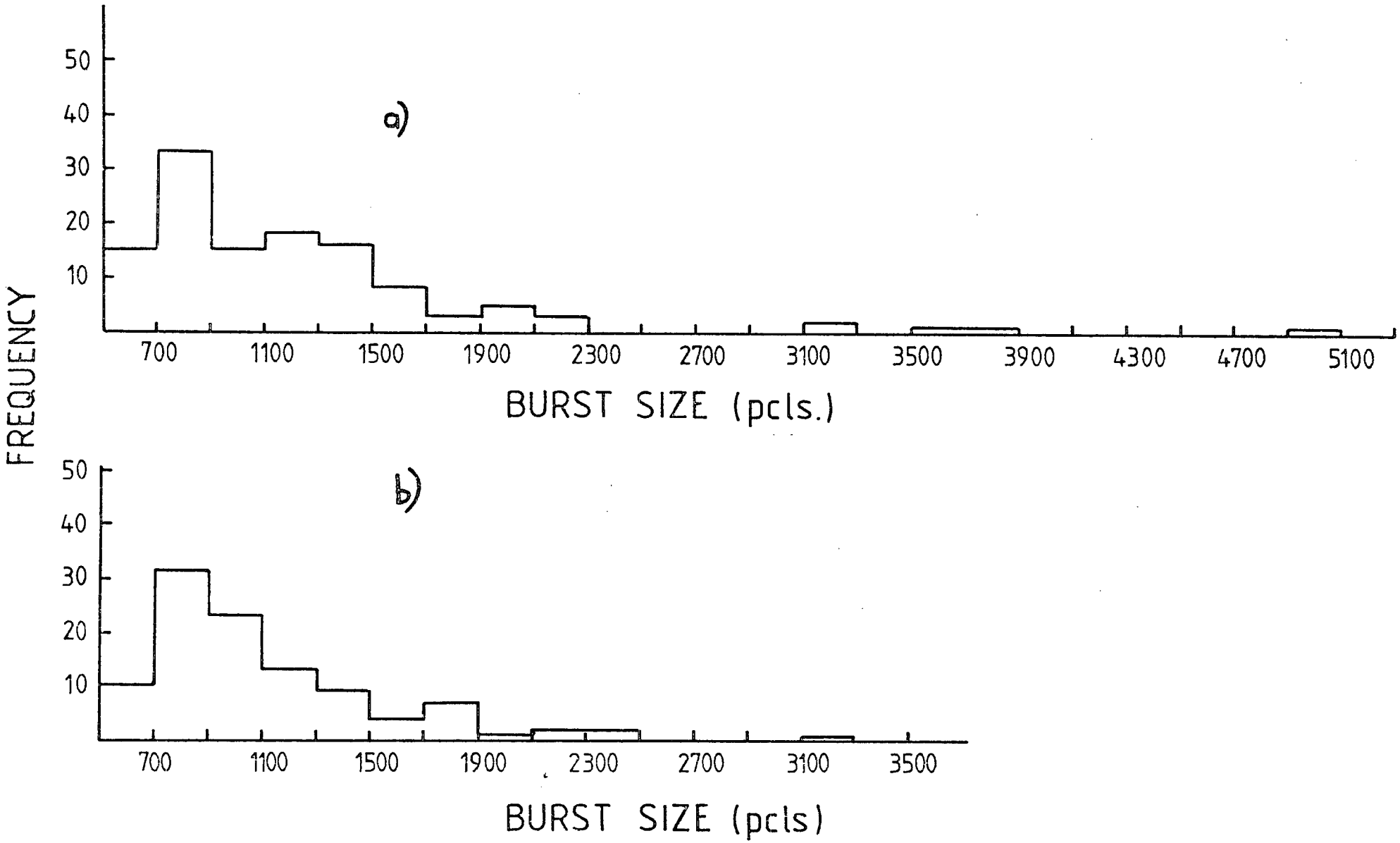
a)
50
40
30
20
10
FREQUENCY
700
1100
1500
1900
2300
2700
3100
3500
3900
4300
4700
5100
BURST SIZE (pcls.)
b)
50
40
30
20
10
700
1100
1500
1900
2300
2700
3100
3500
BURST SIZE (pcls)

Figure 4.3a) Frequency of bursts in lead of different sizes that arrived within $\pm 60^{\circ}$ to the vertical.

Figure 4.3b) Frequency of bursts in iron of different sizes that arrived within $\pm 60^{\circ}$ to the vertical.

FIG. 4.3

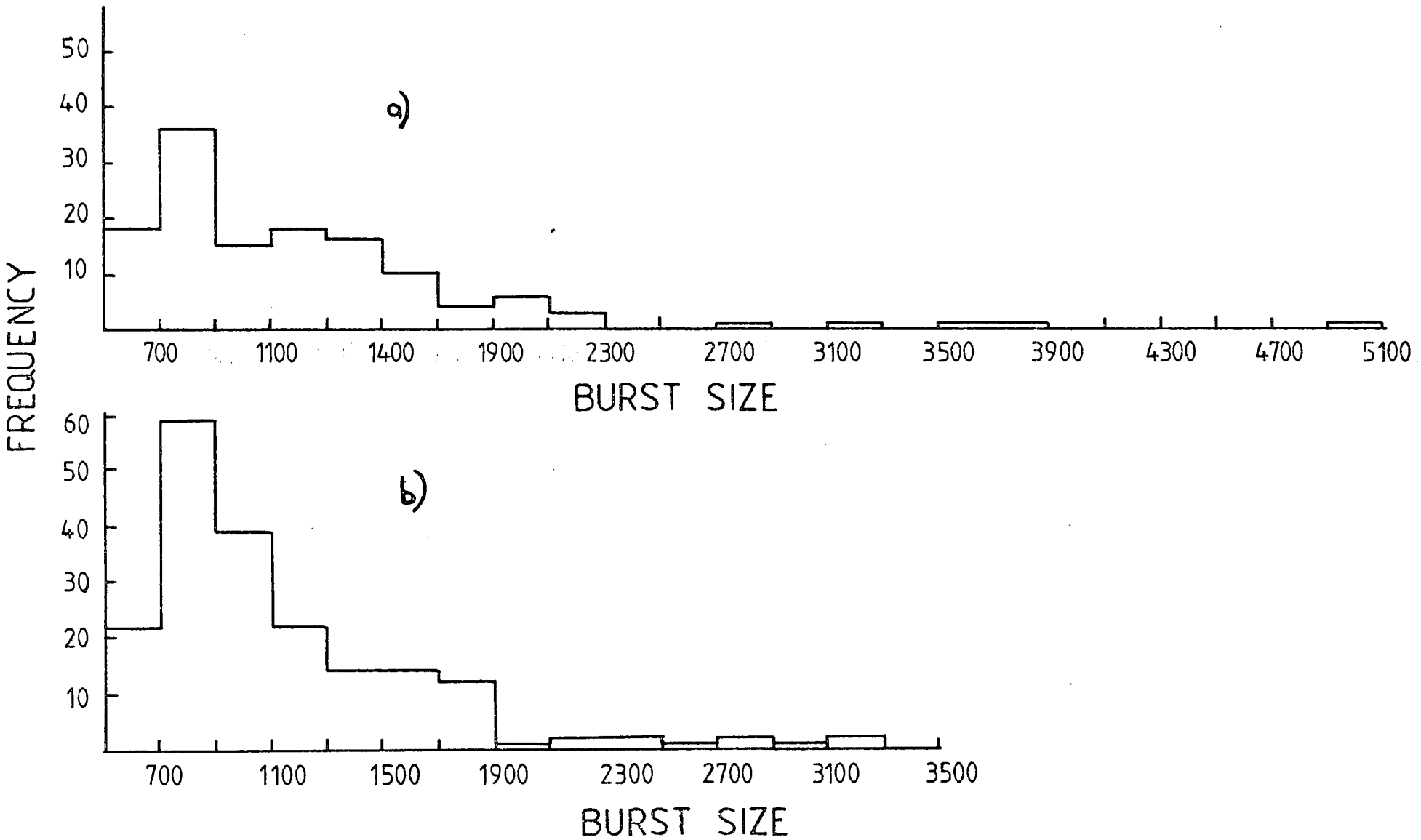
a)
FREQUENCY
50
40
30
20
10
700
1100
1400
1900
2300
2700
3100
3500
3900
4300
4700
5100
BURST SIZE
b)
60
50
40
30
20
10
700
1100
1500
1900
2300
2700
3100
3500
BURST SIZE

in the iron can be assumed to be the energy of the hadron which interacted in the lead.

ii.) Since the lead roof extends beyond the scintillator C both forwards and backwards (see Fig. 4.7b)), bursts can be produced in the lead, miss scintillator C, but trigger the chamber by passing through scintillator A, and hence be mistaken for bursts produced in the iron.

A summary of the data recorded on films H78 to H94 for which both a measurable pulse height and arrival direction were available is presented in Table 4.1. Figs. 4.1, 5.1, 5.2, 5.3 show some typical events. Figs. 4.3a) and 4.3b) show the frequency of bursts of increasing size that arrived from all angles upto 60°.

4.4 Summary of data

Figs. 4.4a) and 4.4b) show the frequency of bursts of all sizes that arrived as a function of arrival direction. Fig. 4.4c) is the calculated arrival direction distribution for hadrons at sea-level assuming

(4.1)
$$I(\theta) = I(0) \cos^{8}\theta$$

Clearly the steep θ dependence for large θ is due to the high power of the cos θ index, but the histograms of Fig. 4.4 do not reflect this. This is thought to be due to muon contamination which is negligible in the vertical direction (Saleh [1975]) but will increase with increasing θ because of the much weaker θ dependence of the muon spectrum.

To minimise the muon contamination a cut has been made at 30° and the derived hadron spectrum and hadron interaction length in air are based on all events which arrive within $\pm 30^{\circ}$ of the vertical. The resulting data is presented in figures 4.2a) and 4.2b).

Figure 4.4a) Histogram of arrival direction distribution of all the bursts that occurred in the lead.

Figure 4.4b) Histogram of arrival direction distribution of all the bursts that occurred in the iron.

FIG. 4.4 a)

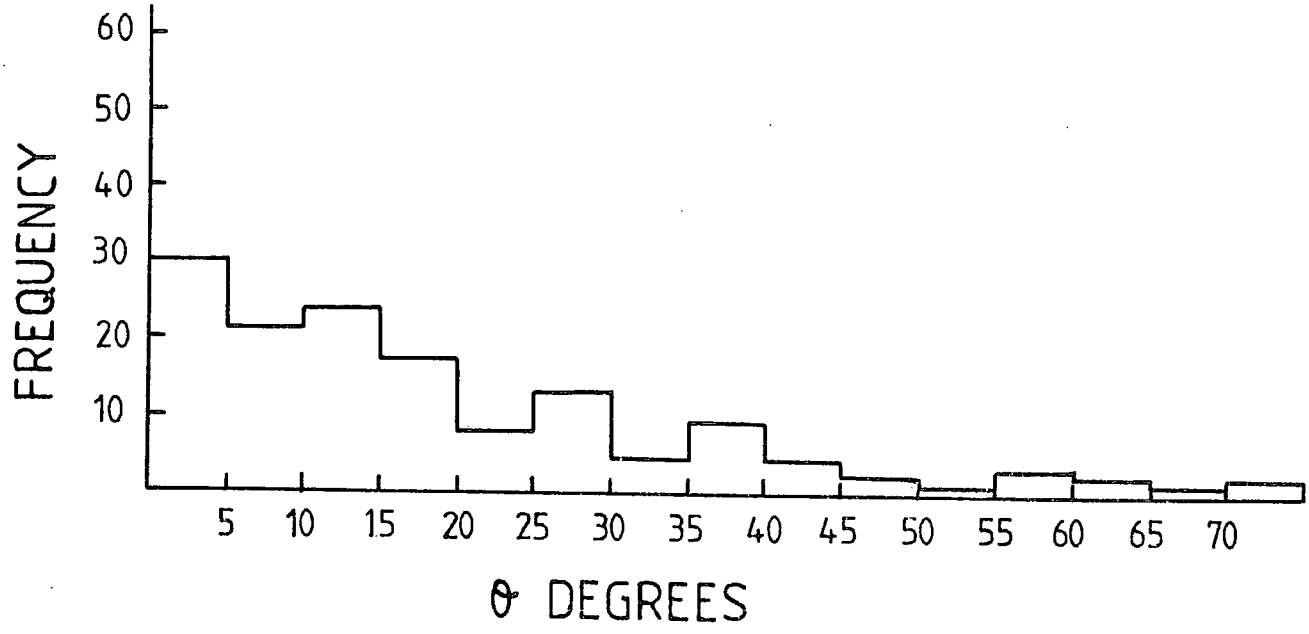

FIG. 4.4 b)

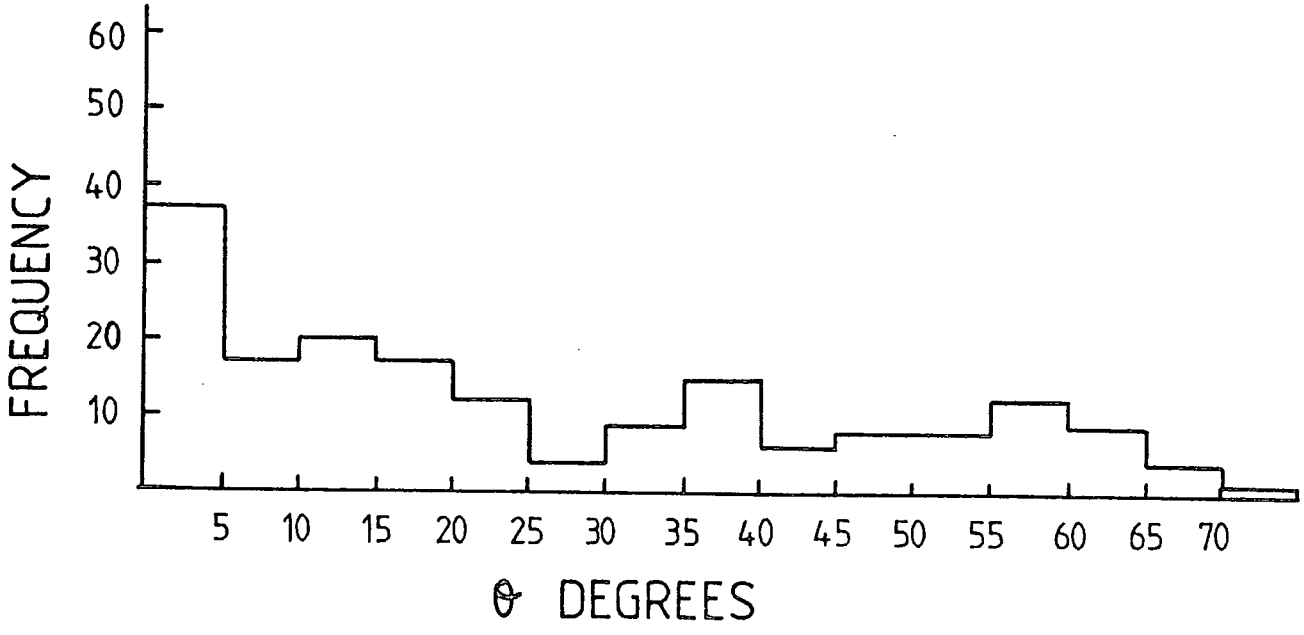

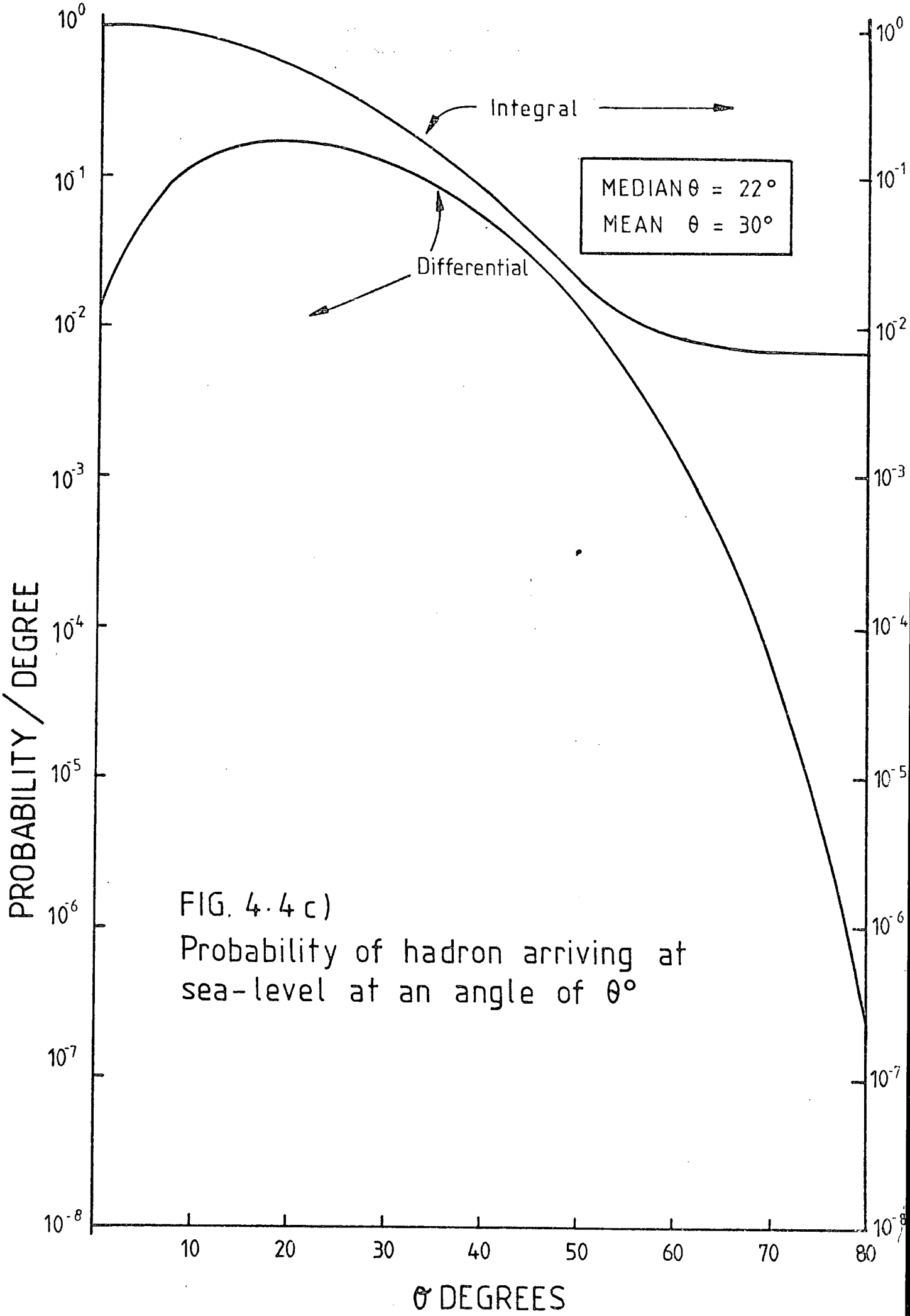

FIG. 4.4 c)
Probability of hadron arriving at sea-level at an angle of θ°

4.5 The hadron spectrum

Figs. 4.5 and 4.6 show the integral burst spectra before correction to an absolute rate.

The solid angle available for detection of hadrons is simply calculated if we assume the intensity of hadrons at θ to the vertical $I(\theta) = I(0)\cos^8\theta$ and we define the acceptance area of detector as A cm^2.

(4.2)

$$\text{Then I TOTAL} = \int_0^{\pi/2} I(o)\cos^8\theta \; 2\pi \sin\theta \, d\theta \, A\cos\theta$$

$$= I(o)\,\frac{2\pi}{10}\,A$$

If the total number of events >500 particles is n in a total sensitive time t sec. Then:-

(4.3a)

$$\text{The Vertical Intensity >500 particles} = \frac{n}{t}\,\frac{10}{2\pi A}\ cm^{-2}\ s^{-1}\ st^{-1}$$

The acceptance area A is defined by demanding that the whole of the burst be visible, hence events within 0.5 cm (on the scanning sheet) of the edge of the chamber are inadmissible. The acceptance geometry for bursts occuring in the lead and iron respectively are shown in Figs. 4.7a), b) and 4.8a), b).

Clearly the acceptance geometry for bursts occuring in the lead or the iron is not a simple detector of area A cm^2. The acceptance geometry has 3 peculiar features:-

i.) It consists of two planes separated by a distance z, measured from the top of the scintillator below the target to the bottom of the

defining layers (F1a for bursts produced in the lead, F1b for bursts produced in the iron).

ii.) Since we only measure the projected zenith angle, the simple integral of equation 4.2 has to be replaced by more complicated expressions. This point is discussed further in section 4.6 and Appendix V, the differential apertures thus derived are shown in fig. 4.12.

iii.) Since a cut at projected zenith angle 30° has been made, the aperture is further reduced, and can be calculated by integrating under the required curve of fig. 4.12 between 0° and 30°.

Assuming n = 8, the aperture for bursts produced in either the lead or the iron within the acceptance geometry has thus been calculated to be 0.496 m^2 st. Figs. 4.5 and 4.6 have been derived from the equation:

$$\text{The Vertical Intensity} > N \text{ particles} = \frac{n}{t} \frac{1}{0.496} \quad m^{-2}\ st^{-1}\ sec^{-1}$$

where t = total sensitive time; n = number of events >N particles.

In order to convert to the required spectrum of hadrons incident on the chamber requires two further steps

i.) Using the burst size-energy relationships (whose derivation is described in Chapter 2) of figs. 4.9a) and 4.9b) , we can convert the burst-size measurements to energy measurements

ii.) Dividing the number of bursts produced in an absorber by the probability of a hadron producing a burst in that absorber gives the number of hadrons incident on the chamber. For bursts produced in the lead this probability is simply the probability of a hadron interacting in 15 cms

Figure 4.5 Integral burst size spectrum before correction to an absolute rate of bursts that occurred in the lead.

FIG. 4.5

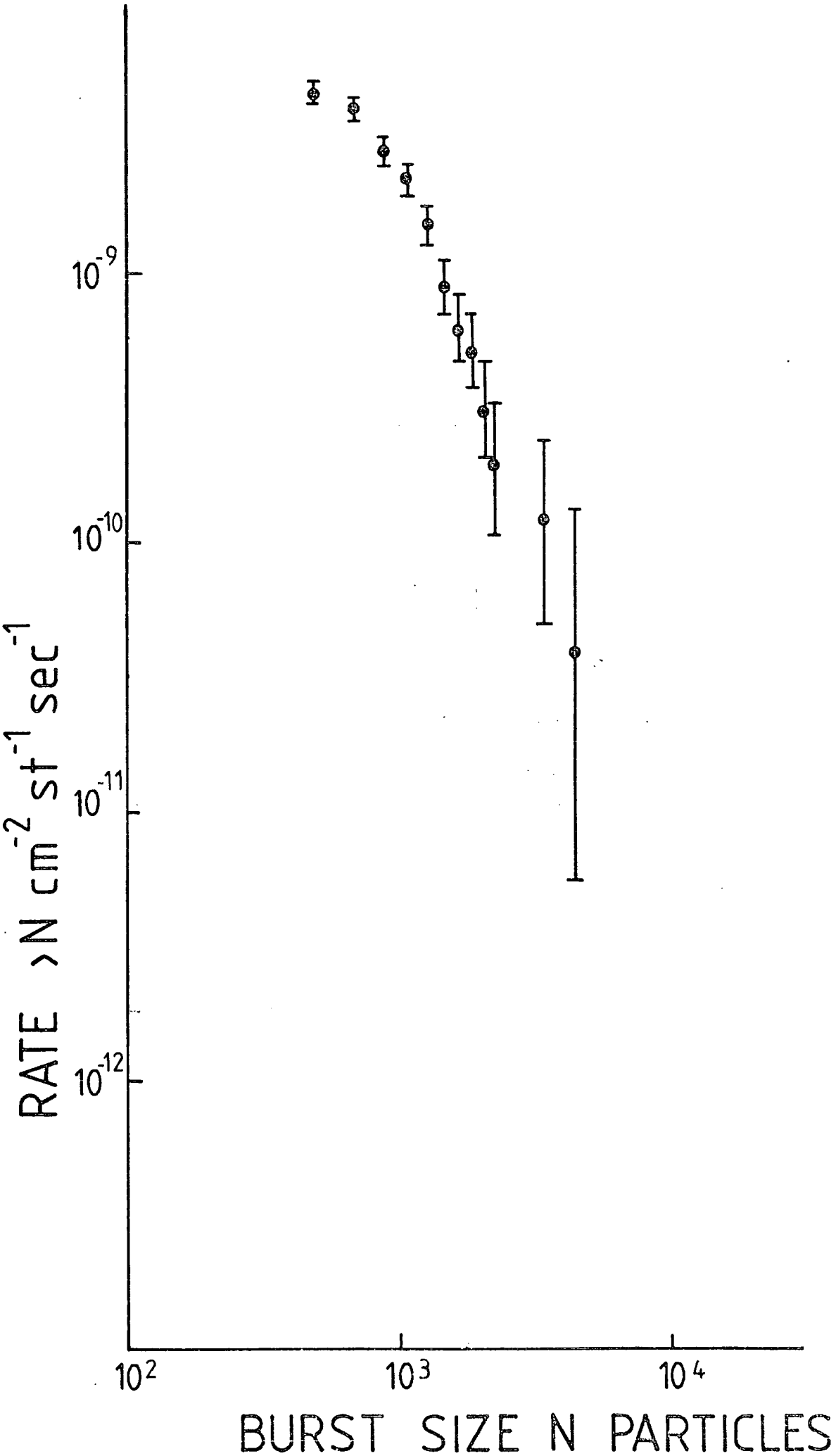
10^{-9}
10^{-10}
10^{-11}
10^{-12}
RATE $>N$ cm^{-2} st^{-1} sec^{-1}
10^2
10^3
10^4
BURST SIZE N PARTICLES

Figure 4.6 Integral burst size spectrum before correction to an absolute rate of bursts that occurred in the iron.

FIG. 4·6

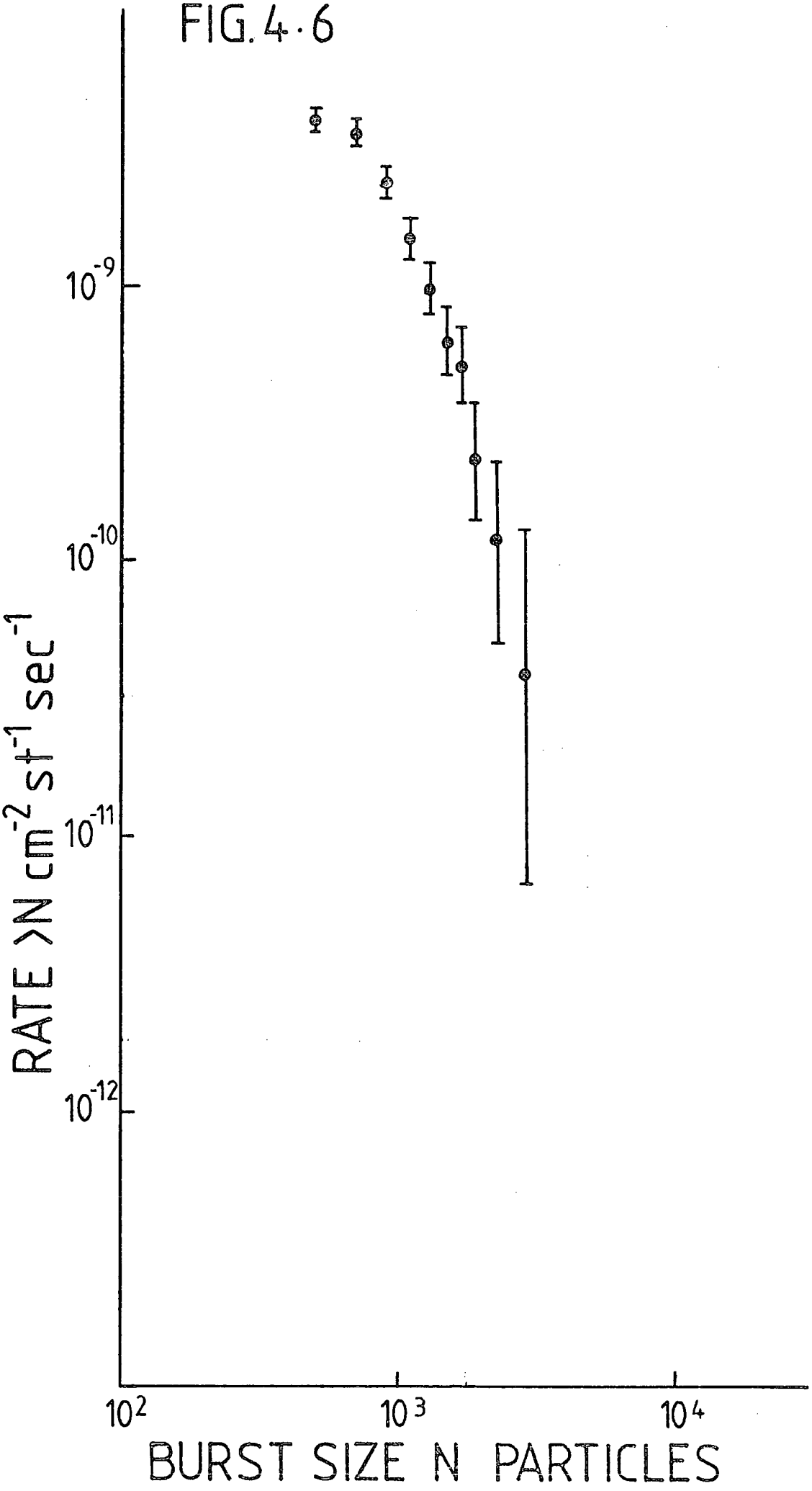
10^{-9}
10^{-10}
10^{-11}
10^{-12}
RATE >N cm^{-2} st^{-1} sec^{-1}
10^2
10^3
10^4
BURST SIZE N PARTICLES

of lead, however for bursts produced in the iron this probability is the product of the probability of a hadron interacting in 15 cms of iron and the probability of a hadron not interacting in the lead. This point is discussed further in Section 4.8 and Appendix VI.

Figs. 4.10a) and 4.10b) are thus the absolute differential energy spectra of hadrons incident on the chamber as measured from their interactions in 15 cms of lead and 15 cms of iron respectively, assuming 100% nucleons incident.

The lowest burst-size point in each figure lies well below the expected level. This is a triggering effect, the fluctuations of the lowest energy initiated bursts to small burst-sizes will not trigger the system.

Both sets of data have been combined to produce the final vertical differential energy spectrum of sea-level hadrons depicted in fig. 4.10c). The spectrum has a smooth $E^{-\gamma}$ dependence in the range 700 - 5000 GeV with a best estimate value for $\gamma = 2.7$.

Table 4.2 lists the work of various authors who have measured the differential hadron energy spectrum and all agree that the spectrum is smoothly decreasing in intensity. However there is a large spread in the measured values of the differential slope with a mean value ~3.0 between 10 GeV and 10 TeV.

4.6 The zenith angle dependence

In the present experiment we can only measure the projected zenith angle of each event. In order to relate the measured distribution to the actual zenith angle distribution a method first described by Lovati (1954) and

FIG. 4.7 a)

Acceptance function parameters for bursts that occurred in the lead.

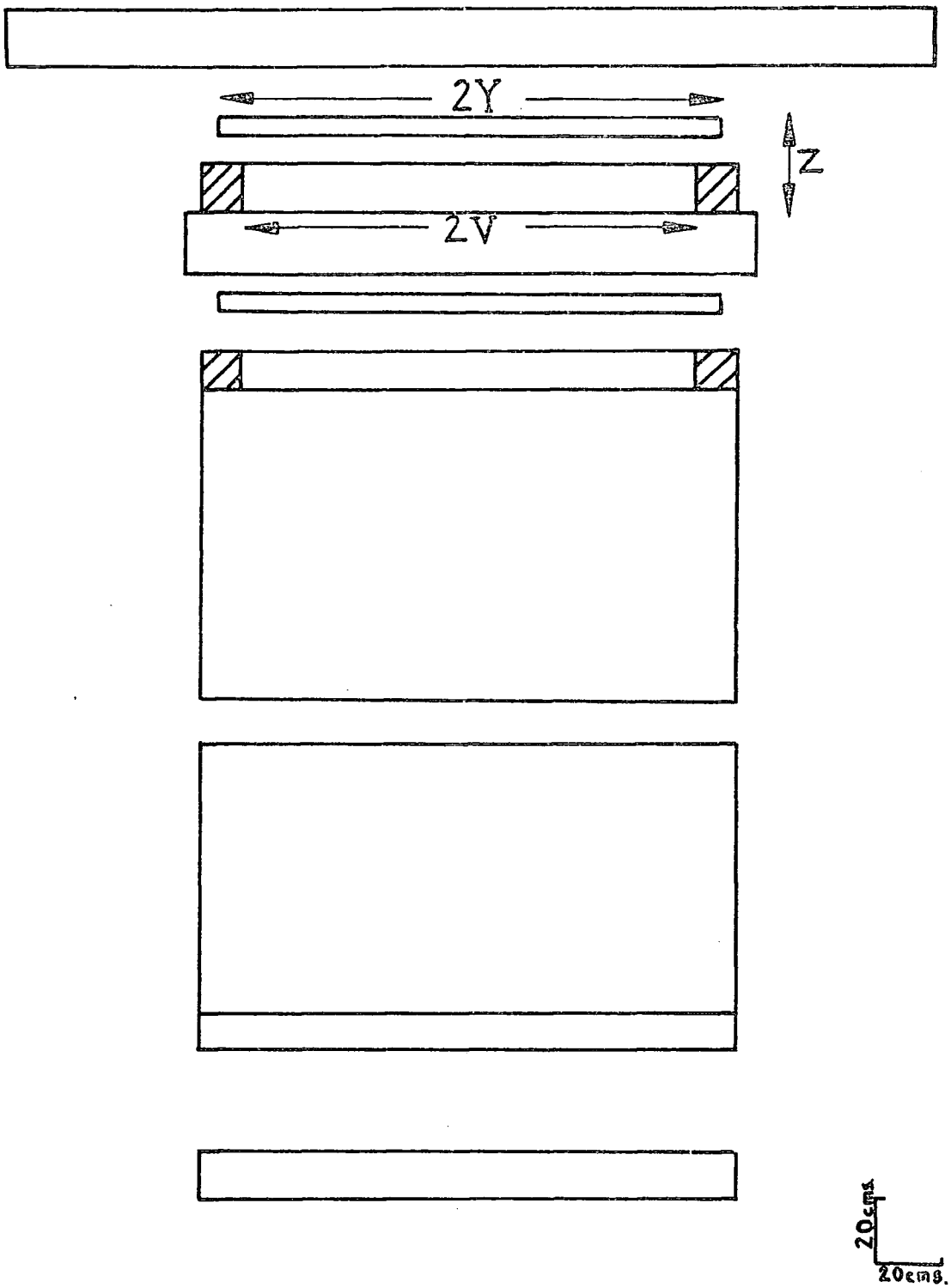

Acceptance function parameters for bursts that occurred in the iron.

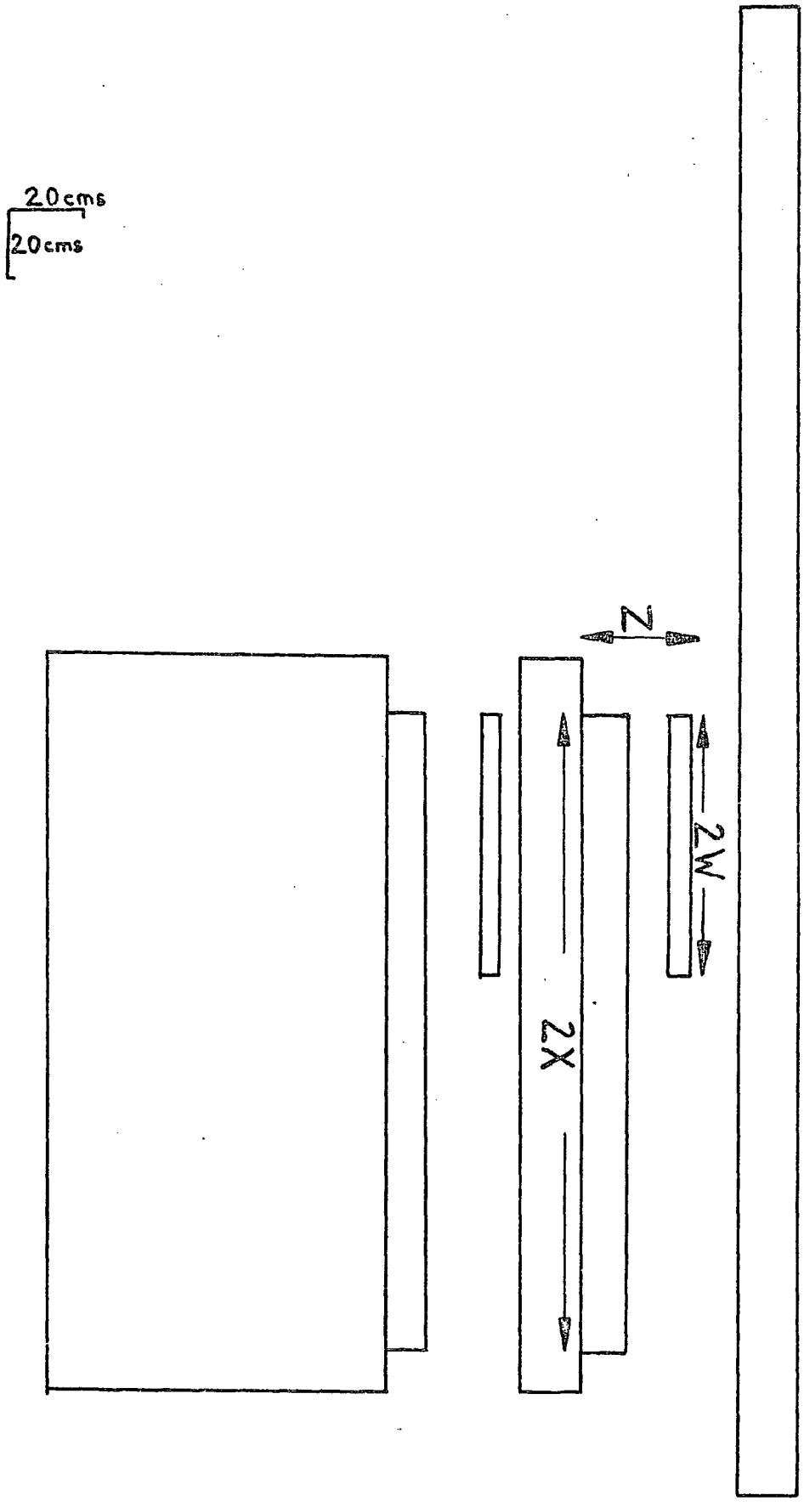

FIG. 4.7b)

FIG. 4·8 a)

Acceptance function parameters for bursts that occurred in the iron.

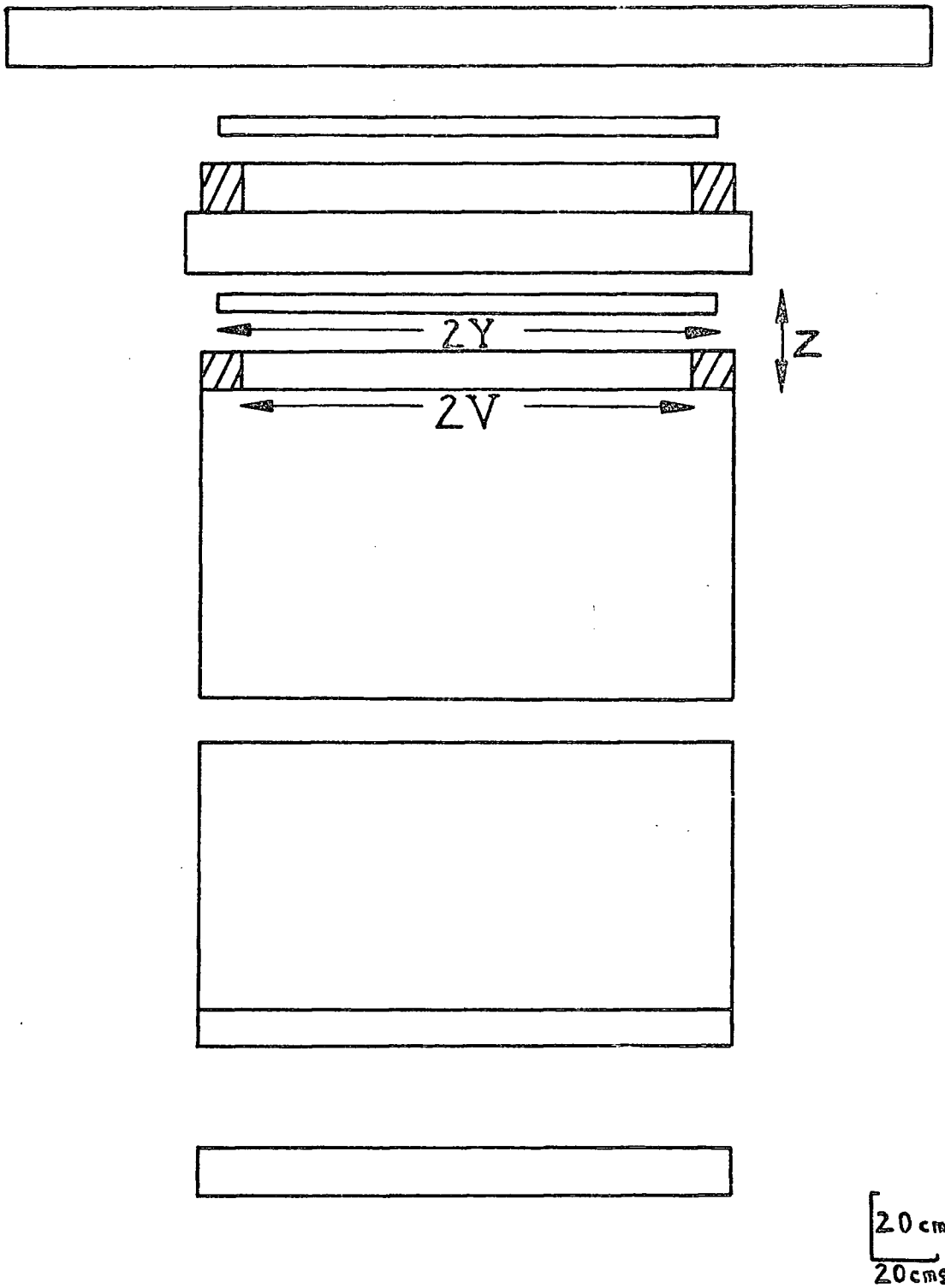

Acceptance function parameters for bursts that occurred in the iron.

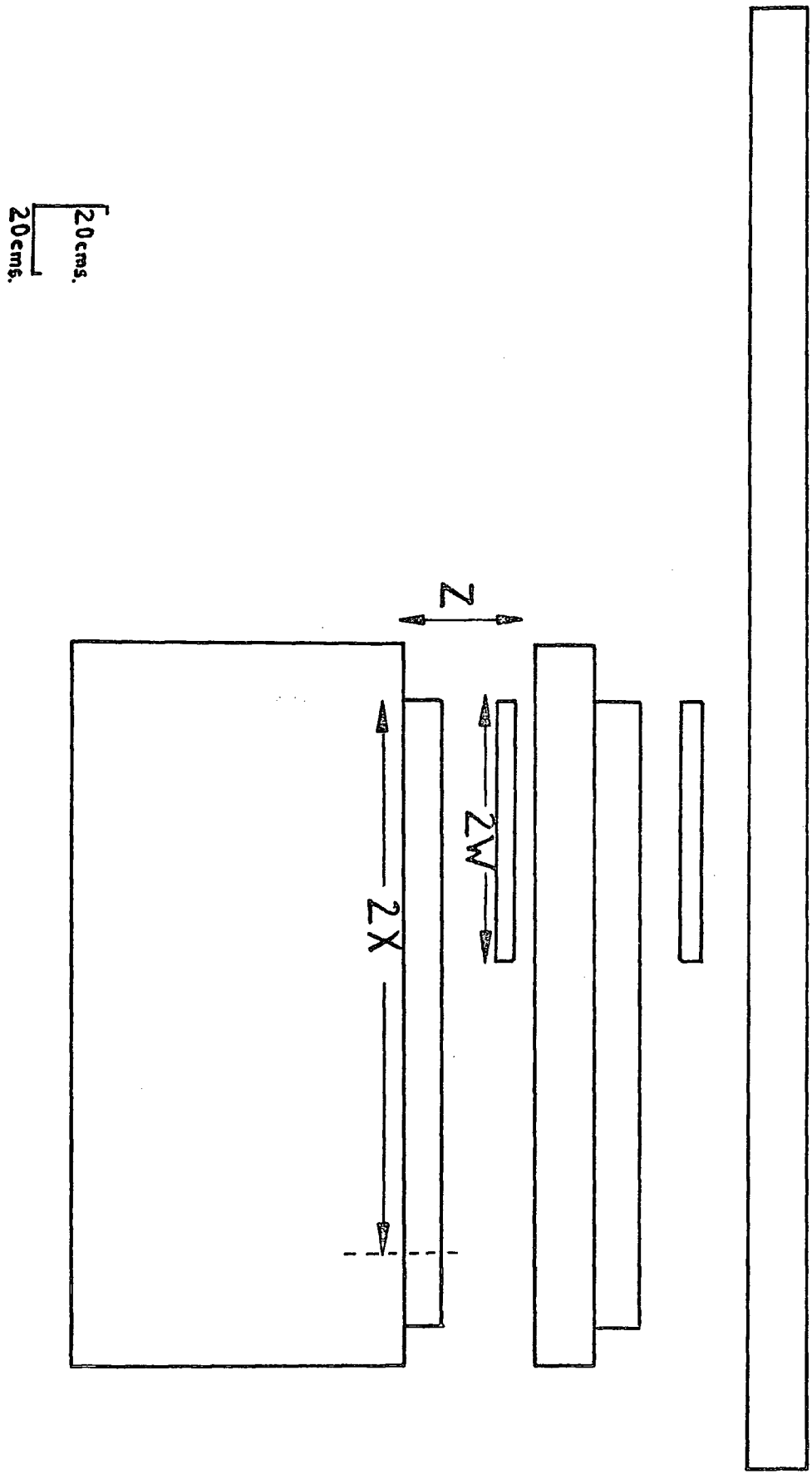

FIG. 4.8b)

later generalised by Pattison (1965) is used. These previous authors have considered the case of a telescope with two symmetrically arranged planes. However, the present experiment involves a telescope (the scintillator under the target and the bottom layer of the defining block of flash-tubes i.e. F1a for the lead target and F1b for the iron target) with two asymmetrically aligned planes (see Figs. 4.7a), b) and 4.8a), b)). In Appendix V is presented an explicit derivation of the "Lovati" formulae for the projected angular distribution in a telescope of cosmic rays incident with an angular distribution $I(\phi) = I(0)\cos^{n}\phi$, where ϕ is the angle between the incident cosmic ray and the zenith and n is an integer greater than or equal to zero. The necessary modifications to the derivation and subsequent formulae necessary for the particular geometry used in this experiment are shown. Table 4.3 is a summary of the formulae thus derived in both cases, the parameters are defined in Figs. 4.7, 4.8. Fig. 4.12 shows the differential apertures thus derived for a telescope consisting of two symmetrically aligned planes. Fig. 4.13 is a comparison of the two cases for n = 0 and n = 8 where $I(\phi) = I(0)\cos^{n}\phi$. By fitting these curves to the data of Figs. 4.3a) and 4.3b) and running a minimum chi-square fit a best value for the exponent n has been found.

The results of these tests are shown in Figs. 4.14 and 4.15 and Table 4.4.

The fits were made by considering only those events which arrived within $\pm 30^{\circ}$ to the vertical in the projected plane. As mentioned previously, although the curves are more sensitive at larger angles, only bursts near the vertical are used to avoid any excessive contamination from muon induced bursts.

FIG.4.9a)

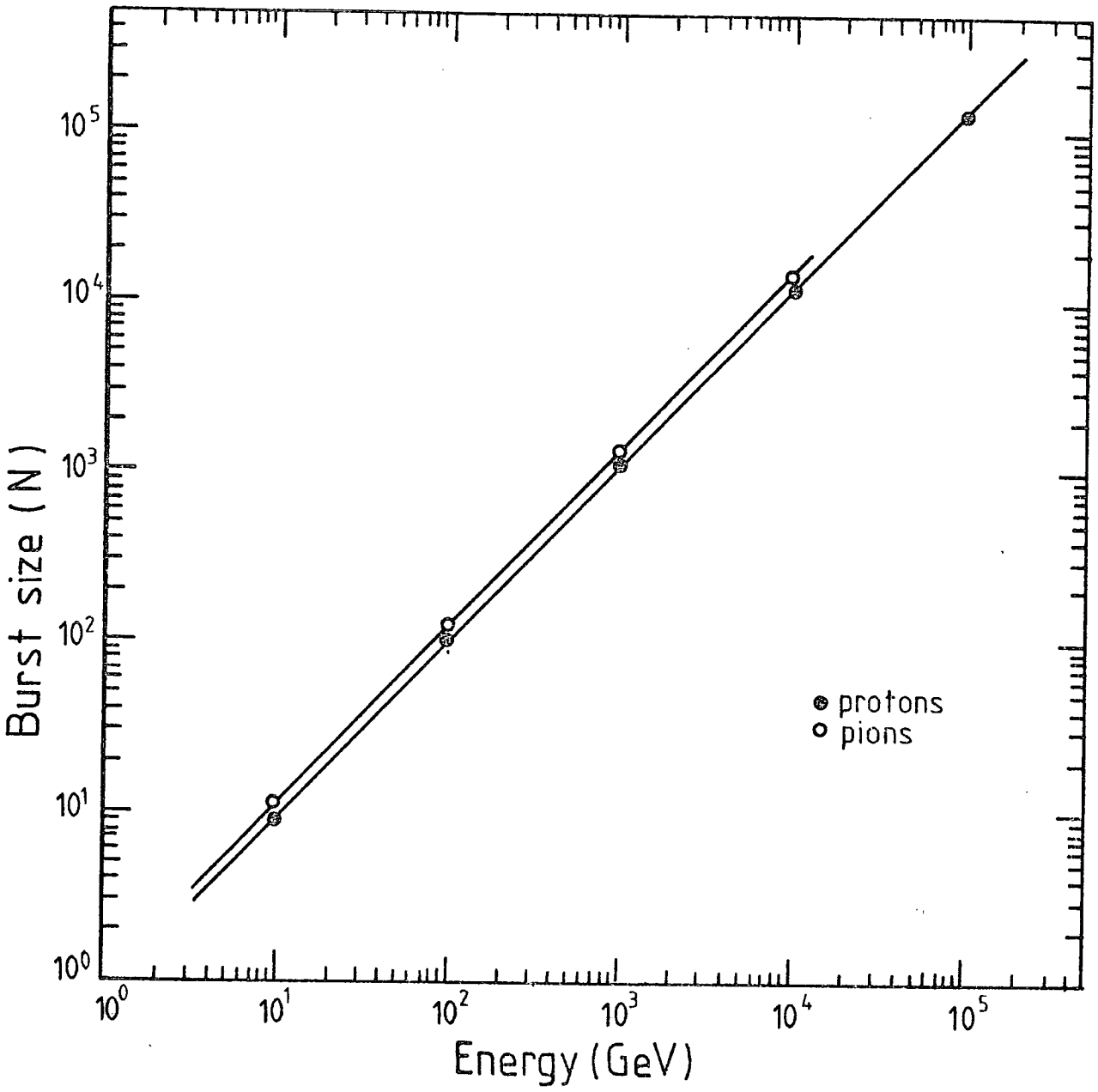

The average burst size(N) produced by a proton or pion of energy E GeV incident on 15cms. of lead. (After Saleh(1975))

FIG. 4.9 b)

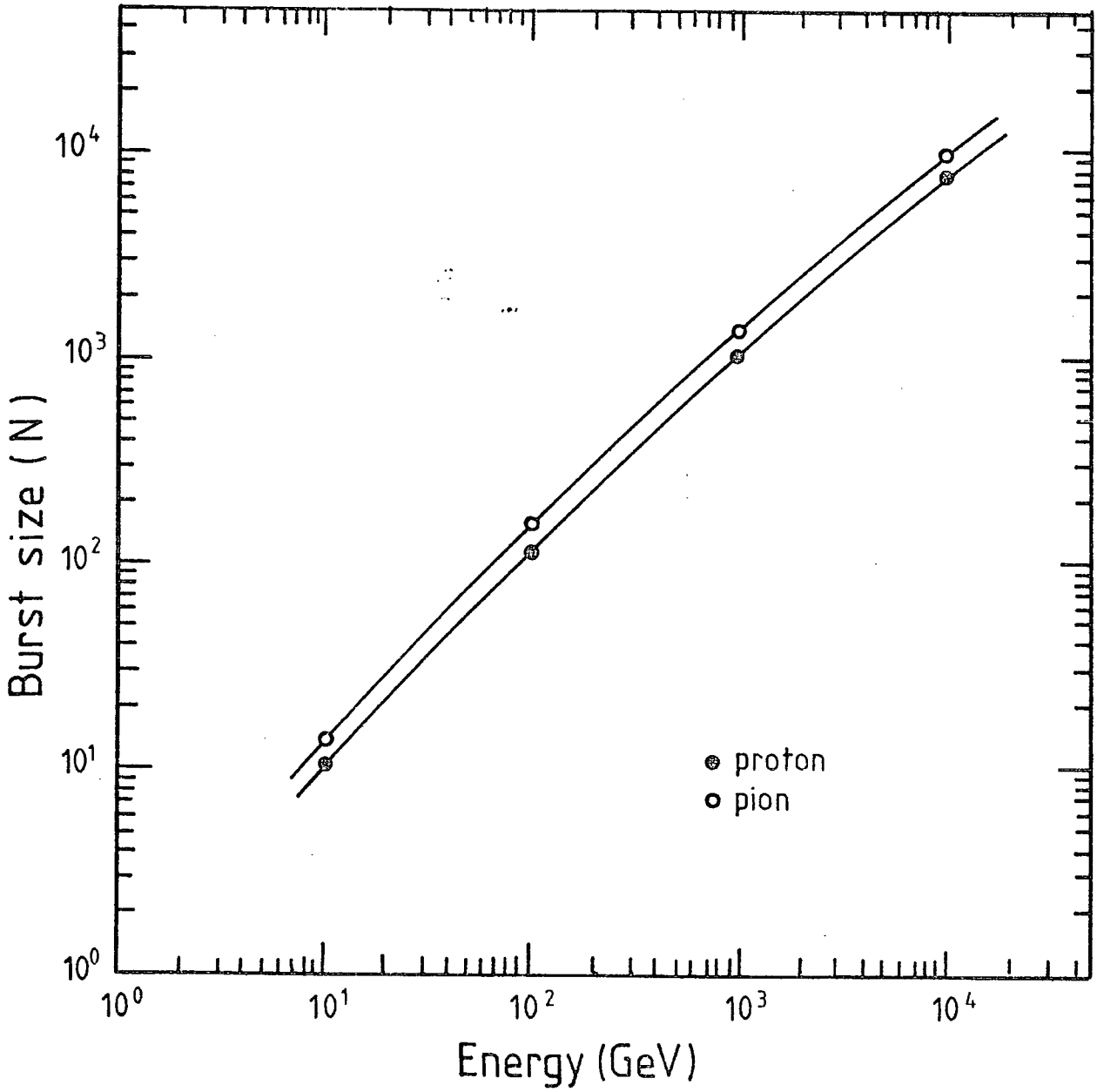

The average burst size(N) produced by a proton or pion of energy E GeV incident on 15cms. of iron. (After Saleh(1975))

Figure 4.10a) The absolute differential energy spectrum of hadrons incident on the flash tube chamber as measured from their interactions in 15cms. of lead, assuming 100% nucleons incident.

FIG. 4·10 a)

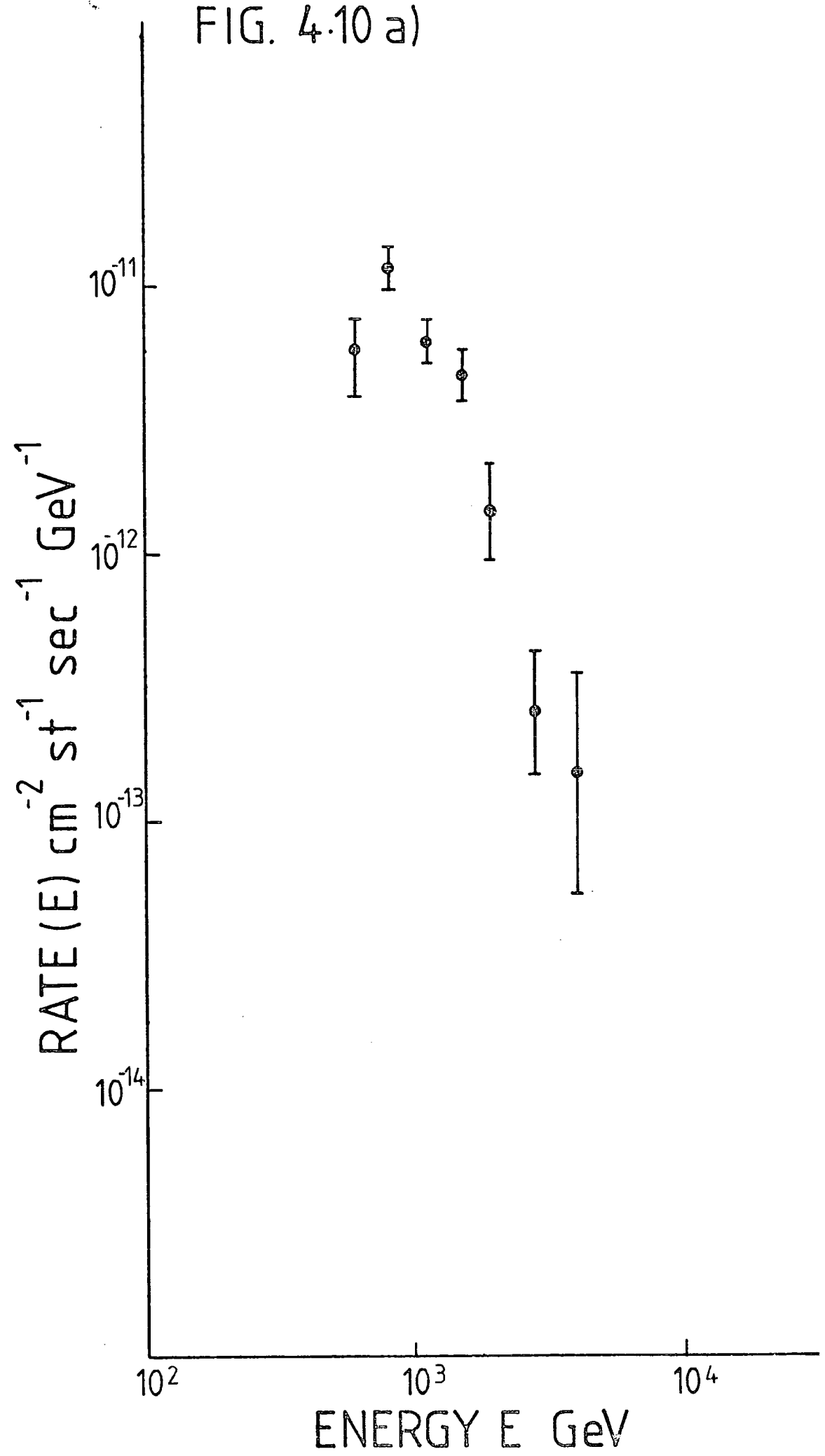
RATE (E) cm^{-2} st^{-1} sec^{-1} GeV^{-1}
10^{-11}
10^{-12}
10^{-13}
10^{-14}
10^{2}
10^{3}
10^{4}
ENERGY E GeV

Figure 4.10b) The absolute differential energy spectrum of hadrons incident on the flash tube chamber as measured from their interactions in 15cms. of iron, assuming 100% nucleons incident.

FIG. 4·10 b)

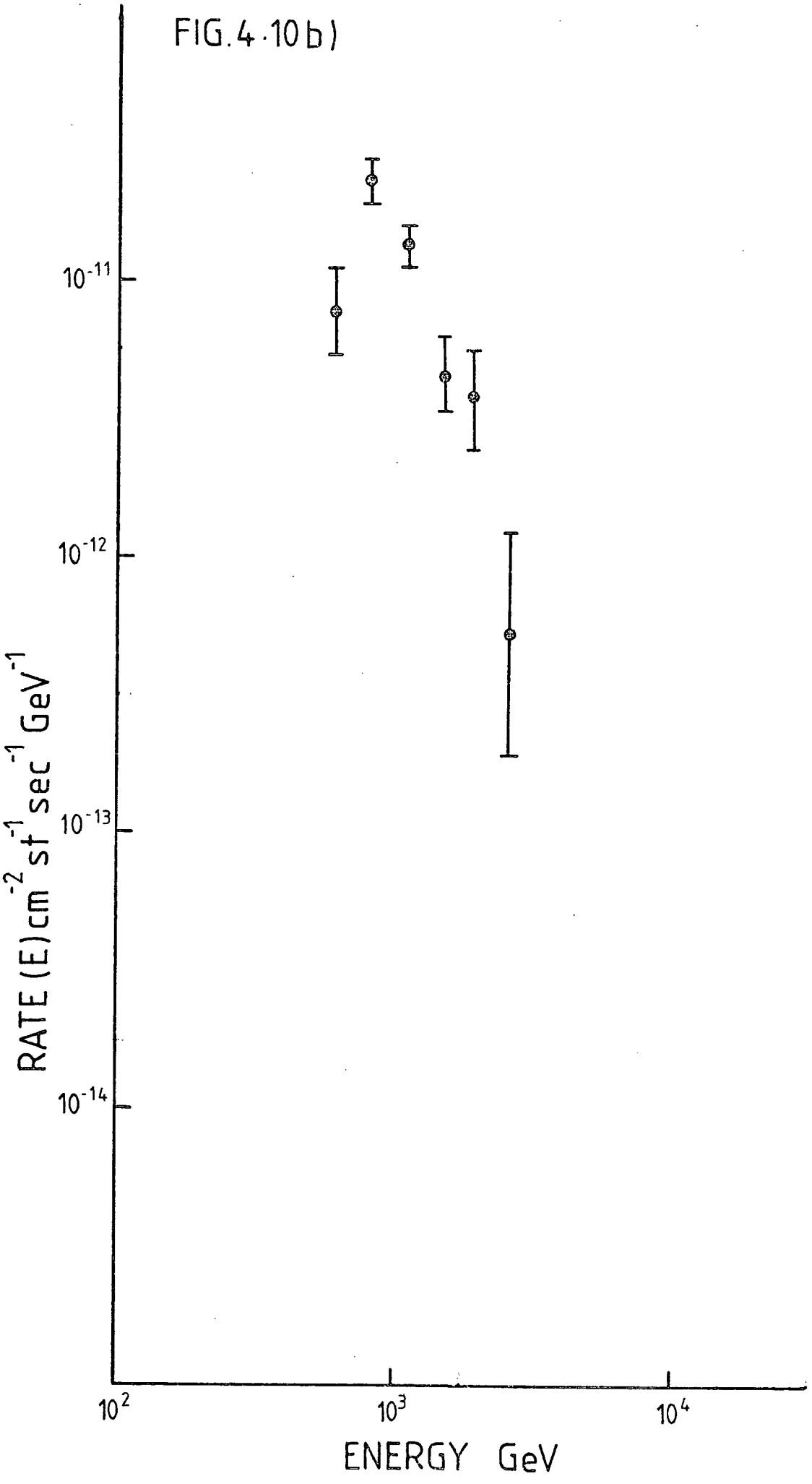
10^{-11}
10^{-12}
10^{-13}
10^{-14}
RATE (E) $cm^{-2} st^{-1} sec^{-1} GeV^{-1}$
10^{2}
10^{3}
10^{4}
ENERGY GeV

Figure 4.10c) The vertical differential energy spectrum of hadrons at sea-level as measured with the flash tube chamber. Rate of hadrons of energy E GeV per sq.cm. per steradian per second per GeV between 700 and 5000 GeV is proportional to $E^{-\gamma}$, where $\gamma_{\text{best estimate}} = 2.7$.

FIG. 4·10c)

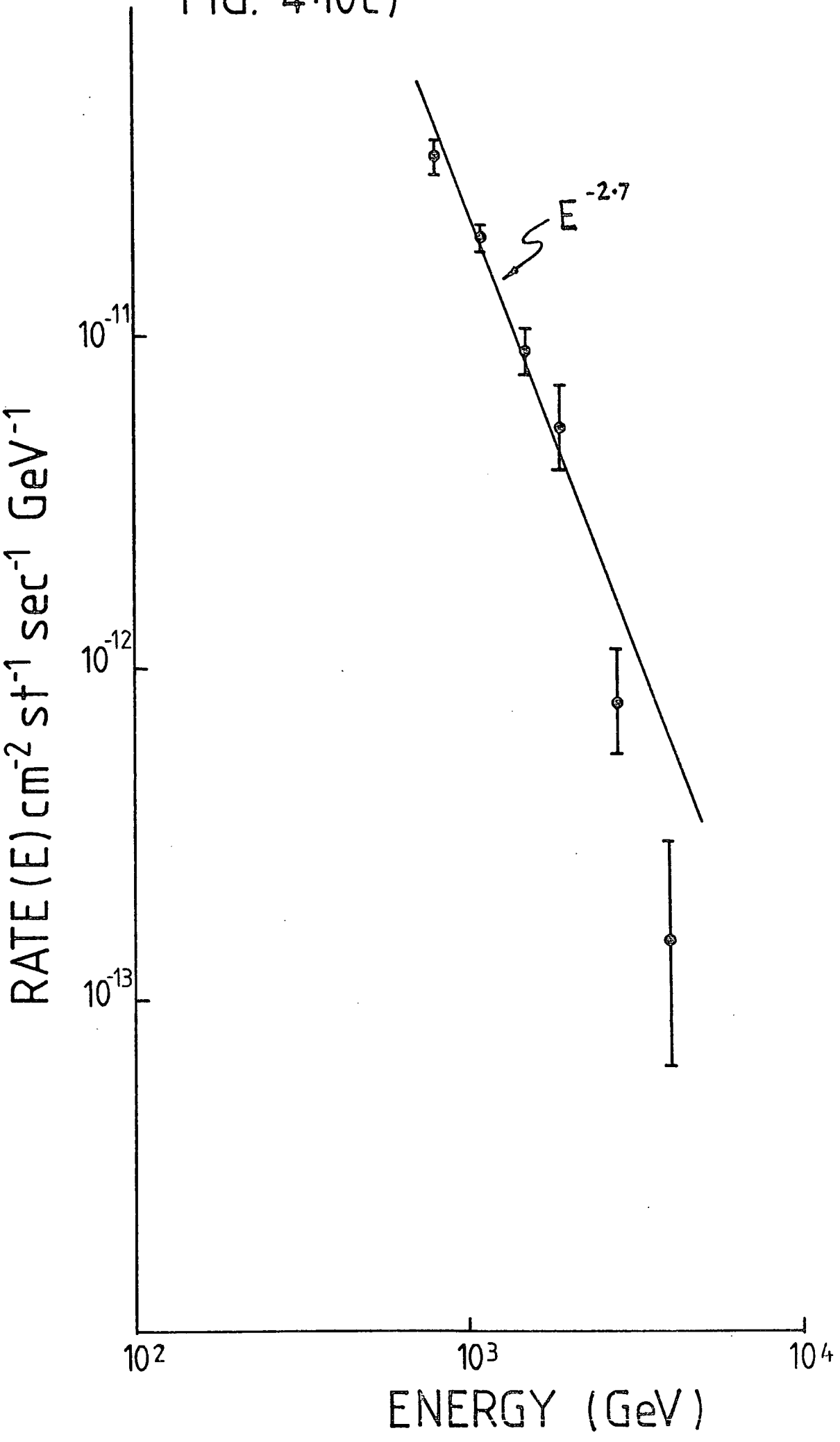
$E^{-2.7}$
10^{-11}
10^{-12}
10^{-13}
RATE (E) cm^{-2} st^{-1} sec^{-1} GeV^{-1}
10^2
10^3
10^4
ENERGY (GeV)

TABLE 4.2

SUMMARY OF PREVIOUS MEASUREMENTS OF THE SLOPE OF THE DIFFERENTIAL ENERGY SPECTRUM OF HADRONS

Author	Year	Depth gm. cm^{-2}	Nature of Hadrons	Energy Range GeV	γ
Dmitriev	1960	700	All	500 - 3000	2.0
Babecki	1961	1,030	All	10^3 - 10^4	2.9 $\pm$0.05
Brooke et. al.	1964	1,030	Protons	0.6 - 150	2.75
Grigorov	1965	700	All	500 - 3000	4.5
Jones et. al.	1970	700	All	70 - 1000	3
Kaneko	1971	550	All	3.10^3 - 3.10^4	3.7
Cowan et. al.	1971	1,030	All Charged	100 - 1000	3.1
Ashton et. al.	1973	1,030	Neutrons	0.4 - 1.2	2.95 $\pm$0.10
Siohan	1973	730	All	100 - 1200	3.2
Diggory	1974	1,030	Protons	1 - 150	2.75
Ashton et. al.	1975	1,030	Pions	40 - 7.10^3	2.55 $\pm$0.10
Yodh	1975	730	All	400 - 6.10^3	3.5 $\pm$0.1
Baruch et. al.	1975	1,030	All	10^3 - 2.10^4	2.7
Present Work	1979	1,030	All	900 - 4000	2.7

4.7 The interaction length in air of the hadrons producing the bursts

If the intensity of primary nucleons at the top of the atmosphere is Ip, then the intensity at some depth y at zenith angle ϕ is

$$I(\phi) = Ip \exp\left(\frac{-y}{\cos\phi} \cdot \frac{1}{\lambda_a}\right)$$

where λ_a = attenuation length of the nucleons in air.

Thus $I(0) = Ip \exp\left(\frac{-y}{\lambda_a}\right)$

and $I(\phi) = I(0)\exp -\left(\frac{y}{\lambda_a}\left[\frac{1}{\cos\phi} - 1\right]\right)$

The term in the square brackets can be expanded to give

$I(\phi)\ \ I(0)\exp -\left(\frac{y\phi^2}{2\lambda_a}\right)$, ignoring higher order terms and expansion of the exponential ignoring higher order terms gives $I(\phi) \simeq I(0)\cos^n\phi$

where $n = \frac{y}{\lambda_a}$

At sea-level y = 1,030 $g.cm^{-2}$

So $\lambda_a = \frac{1,030}{n}$ $g.cm^{-2}$

The measured value of n = 9.5 ±2.7 for the bursts produced in the iron, gives $\lambda_a = 108\ ^{+43}_{-24}$ $g.cm^{-2}$

whereas λ_a for nucleons = 127 ±15 $g.cm^{-2}$ (Ashton [1970])

and λ_a for pions = 158 ±19 $g.cm^{-2}$ (Ashton [private comm.])

The small value for λ_a measured indicates that the bursts in the iron are mainly produced by nucleons, however the large margin of error does not

preclude a substantial contribution from pions. However this is not strictly true since the argument presented above does not apply to pions.

If we assume that $n(E,x)dx$ is the number of pions of energy E found at depth $(x,x+dx)$ in the atmosphere then

$$n(E,x)dx = F(E)dE\ e^{-x/\lambda_\pi}\ \frac{x}{\lambda_p}\left[\frac{1}{1+\beta/E} - \frac{x/\lambda'}{2+\beta/E}\right]$$

where $\frac{1}{\lambda'} = \frac{1}{\lambda_p} - \frac{1}{\lambda_\pi}$ (Brooke et al [1964])

where $F(E)dE$ = primary differential nucleon spectrum

λ_p = attenuation length of nucleons in air

λ_π = attenuation length of pions in air

β = inelasticity for nucleon - nucleon interactions

Then the number of pions with energy E at depth y in the atmosphere at angle ϕ to the zenith is $N(\phi)$

where $N(\phi) \simeq \frac{y}{\cos\phi\,\lambda_p} \exp - \left[\frac{y}{\cos\phi\,\lambda_\pi}\right]$ to first order

and $N(0) = \frac{y}{\lambda_p} \exp - \frac{y}{\lambda_\pi}$

now following a similar pattern to the previous derivation

gives $I(\phi) = I(0)\cos^{n-1}\theta$ for pions

where $n = \frac{y}{\lambda_\pi}$

Hence assuming $\lambda_\pi = 158$ g.cm^{-2} we expect $I(\phi) = I(0)\cos^{5.5}\theta$ at sea-level.

The value of $n = 4.5 \pm 1.2$ found for the bursts produced in the lead might at first sight indicate that the bursts produced in the lead are

mainly due to pions whereas the bursts produced in the iron are mainly produced by nucleons.

However Table 4.5 shows the probabilities of interactions taking place in the iron and the lead for the case of pions incident and protons incident in the two extreme cases

a.) When only vertical hadrons are considered

b.) When hadrons at all angles up $\pi/2$ to the zenith are considered. (See Appendix VI.)

Since the data collected referred to projected angle upto 30° to the zenith the relevant probabilities lie somewhere between these two extremes. However it is quite clear that there is little difference between the probability of a pion interacting in the lead and the probability of a proton interacting in the lead. This seems to rule out the possibility of the bursts in the lead being mainly due to pions if we accept that the bursts in iron are mainly due to nucleons.

A more likely explanation for the flatter projected zenith angle distribution of bursts observed under the lead is that because there are only eight layers of flash-tubes between the lead and iron, it is difficult to accurately ascertain the direction of a burst which is initiated in the lead but does not continue under the iron. The bursts produced in the iron can be seen in the main body of the flash-tube chamber (96 layers) and hence the measurement of projected zenith-angle can be made with much greater accuracy.

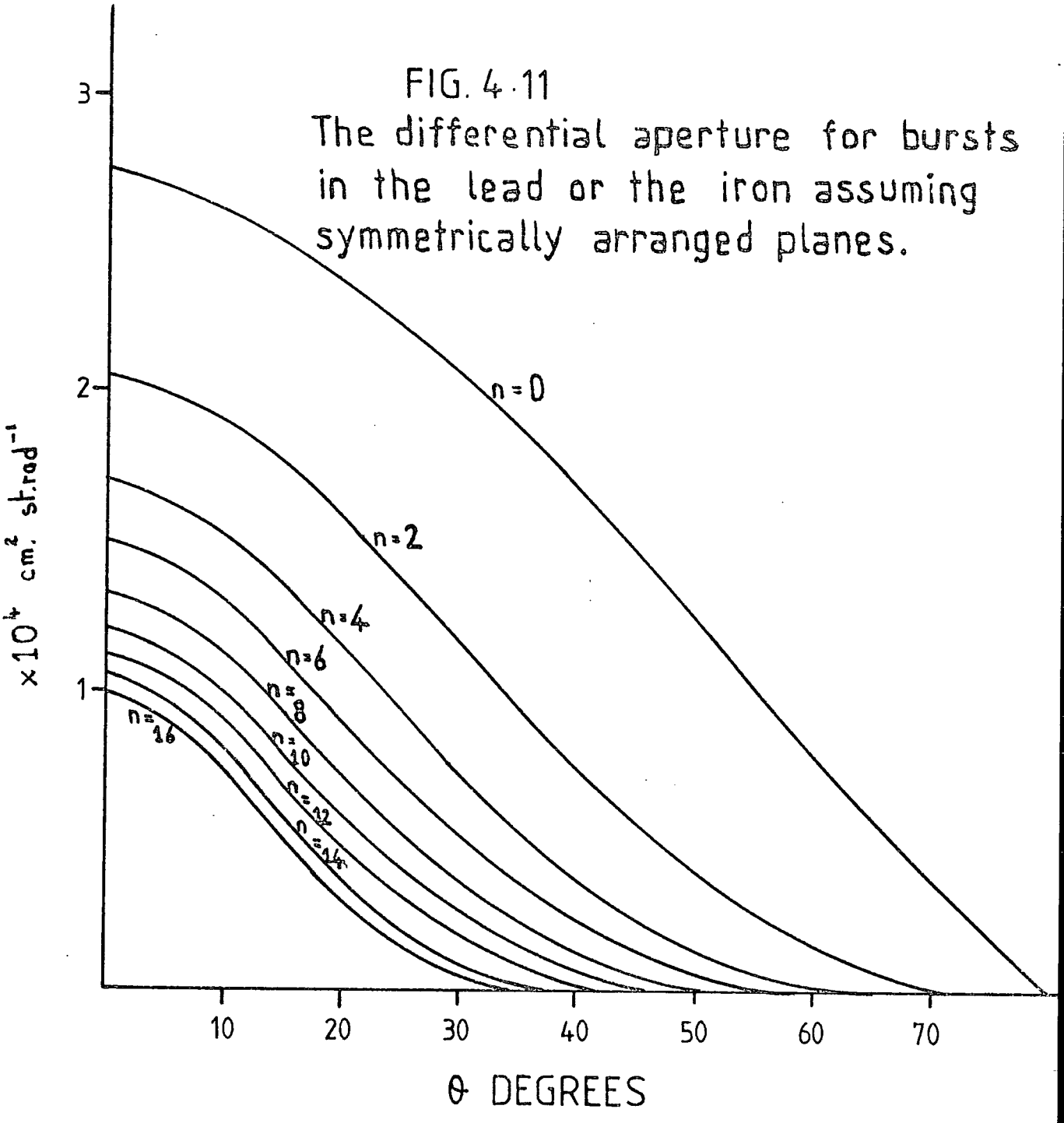
FIG. 4·11
The differential aperture for bursts in the lead or the iron assuming symmetrically arranged planes.
3
2
1
×10⁴ cm.² st.rad⁻¹
n=0
n=2
n=4
n=6
n=8
n=10
n=12
n=14
n=16
10
20
30
40
50
60
70
θ DEGREES

FIG. 4·12

The differential aperture for bursts in the lead or the iron assuming asymmetrically arranged planes.

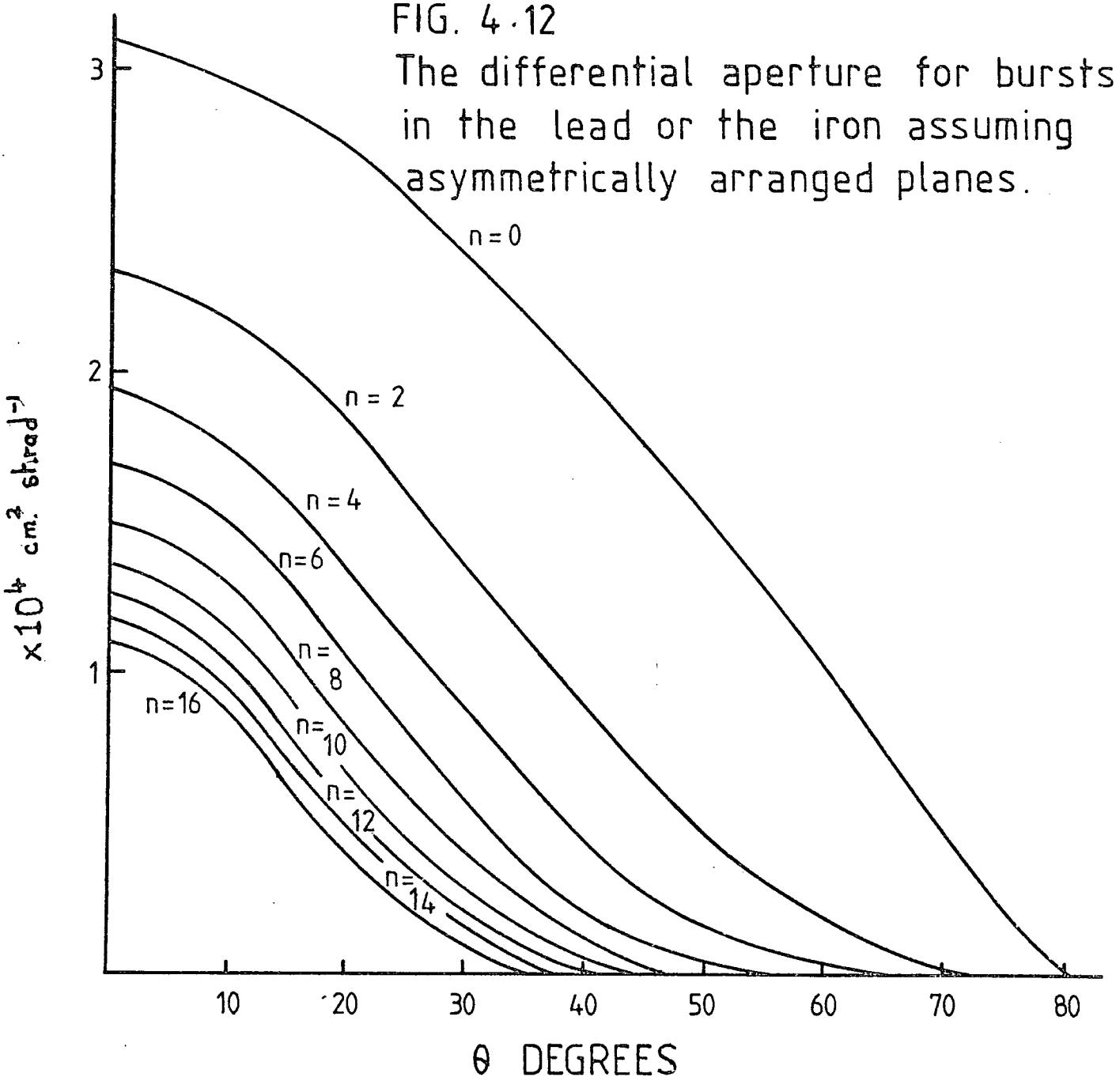

FIG. 4.13 Comparison of the Lovati curves for.

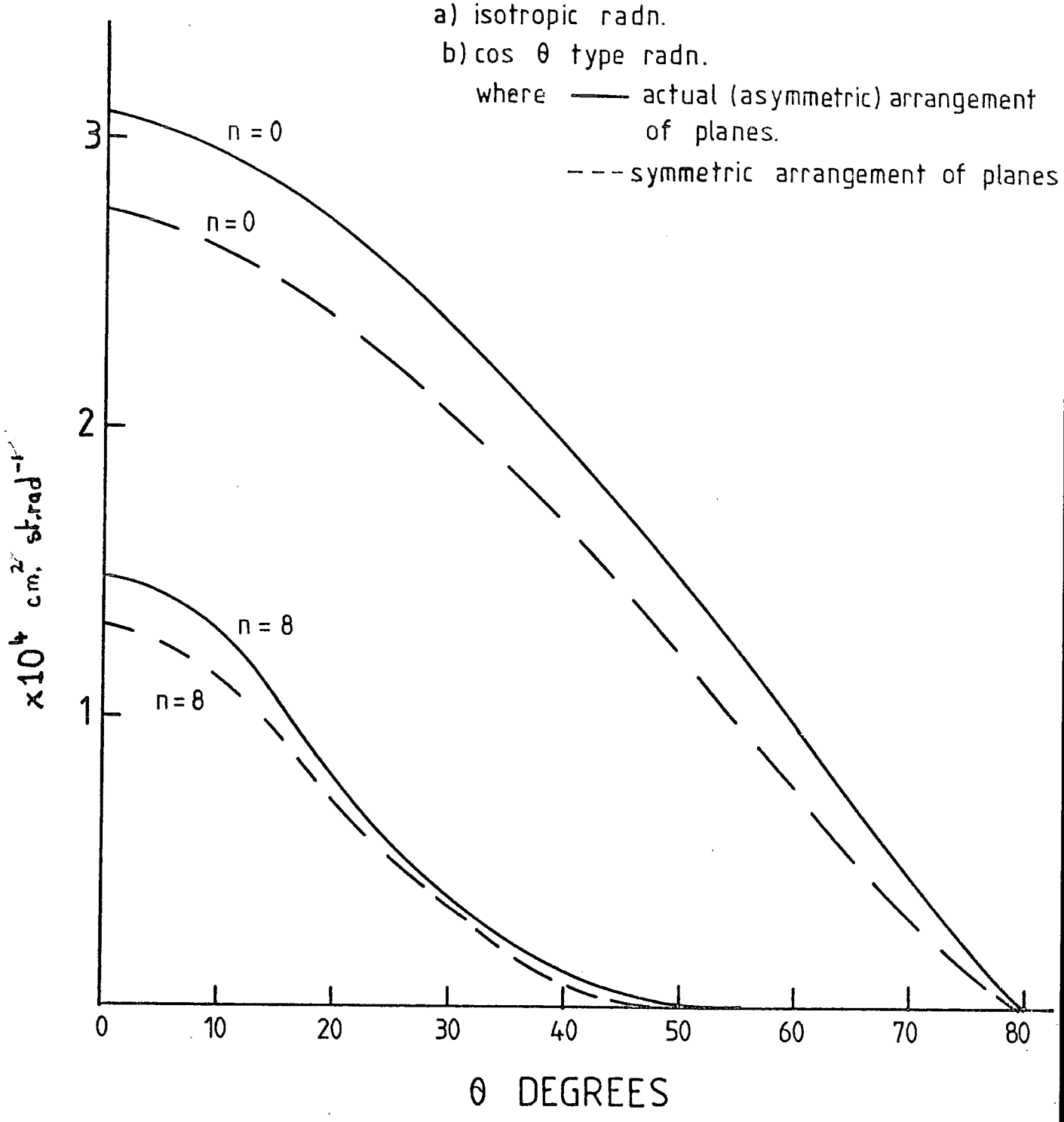

TABLE 4.3

A SUMMARY OF THE "LOVATI FORMULAE" FOR THE PROJECTED ANGULAR DISTRIBUTION $N_n(\theta)$ OF RADIATION INCIDENT WITH ZENITH ANGLE DISTRIBUTION $\cos^n(\phi)$ ON TWO HORIZONTAL PLANES SEPARATED BY VERTICAL DISTANCE Z; (symmetrically and asymmetrically aligned).

n=0

Symmetrical:- $N_0(\theta) = \frac{1}{2}K.\cos(\theta).((X-W).\tan^{-1}((W-X).\cos\theta/Z) + (X+W).\tan^{-1}((W+X).\cos\theta/Z)$

Asymmetrical:- $N_0(\theta) = \frac{1}{4}K.\cos(\theta).((2W+\delta).\tan^{-1}((2W+\delta).\cos\theta/Z) - (2W+\delta-2X).\tan^{-1}((2W+\delta-2X).\cos\theta/Z) - (2X-\delta).\tan^{-1}((2X-\delta).\cos\theta/Z) - \delta.\tan^{-1}(\delta.\cos\theta/Z)$

n=1

Symmetrical:- $N_1(\theta) = \frac{1}{3}K.\cos\theta.\left(\frac{Z^2 + 2(W+X)^2.\cos^2\theta}{A_+^{\frac{5}{2}}}\right) - \left(\frac{Z^2 + 2(W-X)^2.\cos^2\theta}{A_-^{\frac{5}{2}}}\right)$

Asymmetrical:- $N_1(\theta) = \frac{2}{6}K.\cos\theta.\left(\frac{B_1}{(Z^2+B_1)^{\frac{5}{2}}} + \frac{B_4}{(Z^2+B_4)^{\frac{5}{2}}} - \frac{B_2}{(Z^2+B_2)^{\frac{5}{2}}} - \frac{B_3}{(Z^2+B_3)^{\frac{5}{2}}}\right)$

n=2

Symmetrical:- $N_2(\theta) = \frac{K.\cos^2\theta.Z^3}{8}(\ln A_- - \ln A_+) + \frac{3}{4}N_0(\theta).\cos^2\theta$

Asymmetrical:- $N_2(\theta) = \frac{K.\cos^2\theta.Z^3}{6}(\ln A_1 + \ln A_4 - \ln A_2 - \ln A_3) + \frac{3}{4}N_0(\theta).\cos^2(\theta)$

n>2

Symmetrical:- $N_n(\theta) = \frac{K.\cos^n\theta.Z^{n+1}}{n(n+2)}(A_-^{-n/2} - A_+^{-n/2}) + \frac{n+1}{n+2}.N_{n-2}(\theta).\cos^2\theta$

Asymmetrical:- $N_n(\theta) = \frac{K.\cos^n\theta.Z^{n+}}{n(n+2)}(A_1^{-n/2} + A_4^{-n/2} - A_2^{-n/2} - A_3^{-n/2}) + \frac{n+1}{n+2}.N_{n-2}(\theta).\cos^2\theta$

where:

$K = 4I_0(Y+V-Z.\tan\theta)$; $A_\pm = Z^2+(W\pm X)^2.\cos^2\theta$; $A_1 = Z^2+(2W+\delta-2X)^2.\cos^2\theta$

$A_2 = Z^2+(2W+\delta)^2.\cos^2\theta$; $A_3 = Z^2+(2X-\delta)^2.\cos^2\theta$; $A_4 = Z^2+\delta^2.\cos^2\theta$;

$B_1 = 2A_1-Z^2$; $B_2 = 2A_2-Z^2$; $B_3 = 2A_3-Z^2$; $B_4 = 2A_4-Z^2$.

χ^2 Fits for parameter n

FIG. 4·14

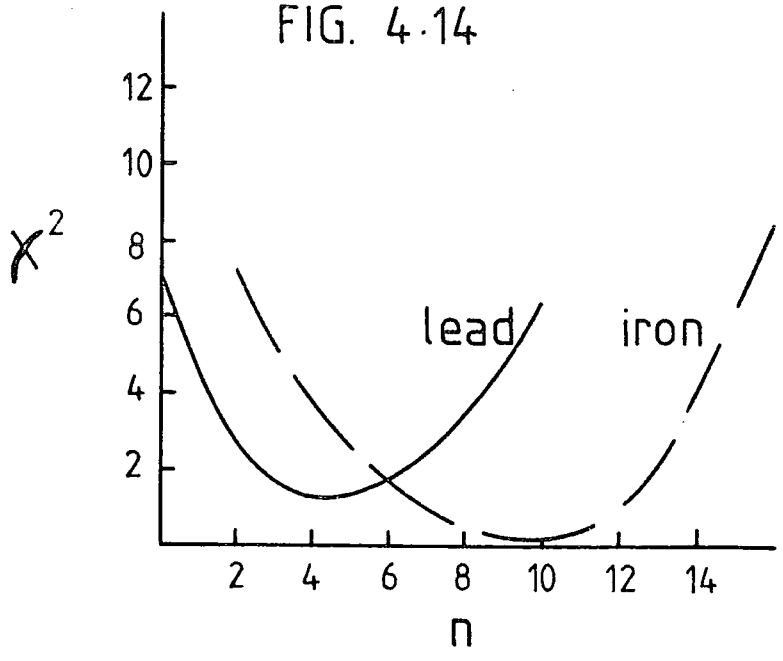

FIG 4·15

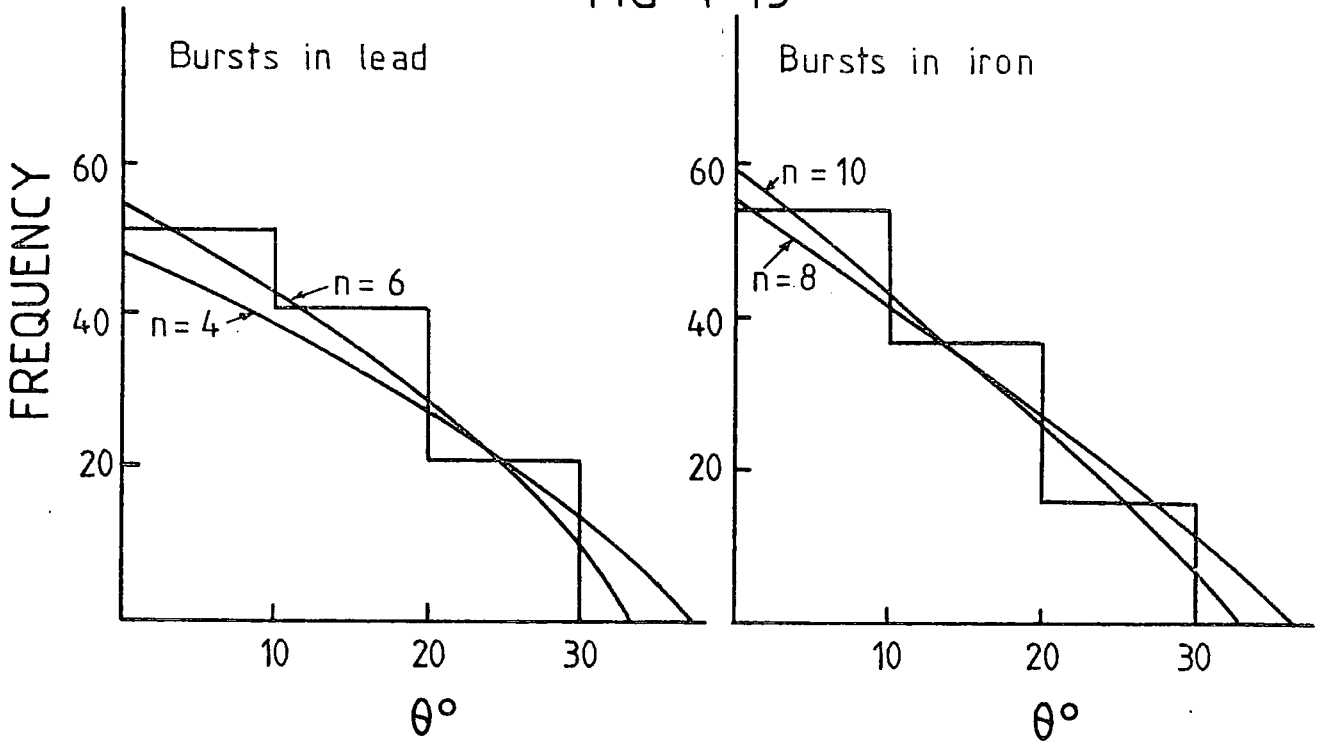

TABLE 4·4

	n	sig level
LEAD	4·5 ± 1·2	50%
IRON	9·5 ± 2·7	50%

4.8 The ratio of the number of bursts in lead to the number of bursts in iron

Table 4.5 also includes the prediction that the number of bursts in the lead should be twice the number of bursts in iron. This is physically quite simple to understand, since both targets are approximately the same depth in interaction lengths (see Table 4.4) in order for a hadron to interact in the iron it has first to survive passing through the lead without interacting i.e.

Probability of a hadron interacting in the iron	=	Probability of a hadron interacting in 15 cm.Fe	x	Probability of hadron NOT interacting in 15 cm.Pb

However the final column of Table 4.4 shows that this ratio is significantly smaller than the prediction for either pions or protons incident.

The reason for this is probably linked with the reason why the projected zenith-angle distribution is flatter for bursts produced in the lead than for bursts produced in the iron.

The data summarised in Table 4.1 excludes all events for which no measurement of the arrival direction could be made. Such events produced a pulse in either scintillator A or C but no coherent burst can be seen in the flash-tube chamber. These are probably mature showers that have begun near the top of the absorber and the electrons have become highly scattered so that insufficient numbers of electrons are passing through the same flash-tube to provide the high degree of ionisation required to fire the flash-tube at long time-delay.

TABLE 4.5 COMPARISONS OF THE PROBABILITIES OF PIONS AND PROTONS INTERACTING IN THE LEAD OR THE IRON

	P	π
Probability of interaction in Pb for normal incidence	0.53	0.53
Probability of interaction in Pb for 0 - $\pi/2$ incidence	0.57	0.46
Probability of interaction in Fe for normal incidence	0.26	0.24
Probability of interaction in Fe for 0 - $\pi/2$ incidence	0.25	0.25
Expected No. of bursts in Pb/No. of bursts in Fe for normal incidence	2.03	2.21
Expected No. of bursts in Pb/No. of bursts in Fe for 0 - $\pi/2$ incidence	2.28	1.84
Measured No. of bursts in Pb/No. of bursts in Fe	1.18	$\pm$0.16
Number of interaction lengths in 15 cm. of Pb	0.79	0.76
Number of interaction lengths in 15 cm. of Fe	0.81	0.70

We should expect more difficulty in ascertaining the direction of such bursts produced in the lead than in the iron because of the relatively few layers of flash-tubes available under the lead compared with under the iron. Hence more events produced in the lead would be excluded because of lack of an arrival-direction measurement than in the iron. It is of interest to note that substantially more events at large zenith-angle are observed in the iron than in the lead. These would be just such events since at large zenith angle the burst has greater thickness of absorber in which to develop.

4.9 Summary and conclusions

A measurement of the differential hadron energy spectrum at sea-level has been made using plastic scintillators and lead/iron targets to measure the energy of the incident hadrons, and a flash-tube chamber to measure their arrival direction in projection. The results show a smooth $E^{-\gamma}$ dependence between 7.10^2 GeV and 5.10^3 GeV with a best estimate value of $\gamma = 2.7$.

An analysis of the arrival directions based on zenith angles up to 30° in the projected plane apparently indicate that the bursts in lead are due mainly to pions whereas the bursts in iron are due to protons. However, further considerations on the probabilities of pions and protons producing bursts in the targets and on the limitations of the zenith-angle measurements of bursts which are produced in the lead but fail to continue below the iron indicate that this is a spurious effect.

Based on the more accurate zenith angle measurements of the bursts produced in the iron the interaction length in air of the hadrons producing the bursts was found to be $\lambda_a = 108 \pm^{43}_{24}$ g.cm^{-2}.

This would indicate that the majority of hadrons incident at sea-level between 7.10^2 GeV and 5.10^3 GeV are nucleons, however the large margin of error involved in this measurement does not preclude a substantial contribution from pions.

CHAPTER 5

HIGHLY IONISING PARTICLES

5.1.1 Introduction

Ever since the earliest theories (Rutherford [1911] , Bohr [1915]) and experimental investigations (Rutherford [1911], Millikan [1910]) of the subatomic nature of matter, all fundamental particles have been found to have the same magnitude of charge as the electron $e = 1.6021917 \times 10^{-19}$ coul., or zero charge. The only particles ever found to have $z>1$ have been nuclei- collections of singly and neutrally charged baryons held together by a force (the "strong" nuclear force) $\sim 10^2$ times stronger than the electromagnetic repulsive force between the charged nucleons (protons) - stripped electromagnetically of their neutralising shells of electrons.

Highly charged nuclei are definitely present in the primary cosmic radiation incident on the earth's atmosphere and have been found deep in the atmosphere on balloon flights. However at sea-level, no surviving nucleons have been found with $z>3$, in fact the measured rate of arrival at sea-level of particles with mass $>m_p$ in measurements on the incoherent hadronic component at sea-level is $10^{-10} cm^{-2} s^{-1} st^{-1}$ (Ashton et al [1968]). This is because the large amount of atmosphere (~12 nucleon interaction lengths) and the increased interaction cross section ($\sigma_{int} \propto A^{2/3}$) for highly charged nuclei combine to reduce the probability of a nucleus surviving the journey to sea-level without interacting to $\sim e^{-12A^{\frac{2}{3}}}$. From emulsion stack studies of the interactions of high energy nuclei (see for example O'Dell [1962]), the probability of a heavy nucleus interaction resulting in fragmentation of the nucleus is about 20%. The above considerations of the very short interaction length (~14 $g.cm^2$ in air for $z>20$ Hayakawa [1969]) combined with fragmentation lead us to believe that all heavy nuclei are broken up into nucleons within a short thickness of the atmosphere.

Hence, searches for highly charged, exotic particles (e.g. monopoles, Yock particles, tachyons, see below) in the highly relativistic (>1 GeV) component of sea-level cosmic radiation can set severe limits on the probabilities of producing such particles in conventional regions of space and time.

5.1.2 Magnetic monopoles

Maxwell's theory of electromagnetism based on the experiments of amongst others Faraday, Ampere, Biot-Savart included the asymmetric pair of source field equations:-

(5.1) $\nabla.\underset{\sim}{D} = 4\pi\rho$

(5.2) $\nabla.\underset{\sim}{B} = 0$

where D = electric displacement (field in a medium)

B = magnetic field

which were based on experiments carried out at the macroscopic level and indicate that although free electric charge can be found, magnetic charge only occurs in a free state in regions of space and time much smaller than those accessible to the electromagnetic detectors at that time.

With the advent of detectors capable of distinguishing down to atomic, sub-atomic and even sub-nuclear regions, and an accompanying fundamental change in the currently held theories as to the nature of matter, this apparent asymmetry became an anathema to the theoretical architects of quantum theory. Symmetry became an operator on rather than a property of physical systems, and systems which were asymmetric under symmetric operations always yielded a more fundamental structure than had at first been apparent.

If Maxwell's laws of electromagnetism are truly fundamental, argued Dirac [1931]), then at some level of detection free magnetic monopoles must exist. His arguments, based on further analogy with the quantum electrodynamics of the electron, yielded a value for this charge of $\frac{1}{2} e/\alpha$

where α = fine structure constant = $\frac{e^2}{\hbar c} = \frac{1}{137}$

with an ionising capability some 10^4 times as strong as that due to an electron (ionising power $\propto Z^2$ where Z = charge). If the fundamental charge is $e/3$ then Dirac's monopole would have charge $3/2\ e/\alpha$ and a subsequent 9 fold increase in ionising power.

Schwinger's (1966, 1968) arguments for the existence of a magnetic monopole of charge ne/α are rooted in a more physical interpretation of the fundamentality of the electromagnetic force, that it is the force which binds a nucleon together through the cross-talk between elementary monopole - antimonopole pairs inside the nucleon, dyons. (See Table 5.1 for salient properties of both types of monopole.)

The only detractors from the "High Z" school of thought are those authors (Recami and Mignani [1976], Parker [1969]) whose arguments are based on extensions to Special Relativity theory rather than quantum electrodynamical theory, brought about again by considerations of symmetry. In extended relativity (extended to include the possibility of particles travelling faster than light - see Chapter 8) magnetic monopoles are in fact electric monopoles travelling faster than light, tachyon monopoles. Hence the value of the magnetic monopole's charge becomes the magnitude of the source of the superluminally Lorentz transformed field of the electric charge. Parker (1969) estimates a value for this source terminating at $\frac{e}{\sqrt{2}}$ at some finite

TABLE 5.1

EXPECTED PROPERTIES OF MAGNETIC MONOPOLES CORRESPONDING TO FUNDAMENTAL ELECTRIC CHARGES e AND e/3.

AFTER ASHTON, (1973).

Author	Fundamental electric charge	Fundamental monopole strength, g.	$\frac{dE}{dx}$ GeV gm^{-1} cm^{-2}	Z of nucleus with same $\frac{dE}{dx}$	Ionisation loss in penetrating the atmosphere to sea level
Dirac	e	$\frac{\hbar c}{2e}$	9.4	68.5	$9.4\ 10^{12}$ eV
Dirac	$e/3$	$\frac{3\hbar c}{2e}$	84.6	205.5	$8.5\ 10^{13}$ eV
Schwinger	e	$\frac{\hbar c}{e}$	36.6	137	$3.8\ 10^{13}$ eV
Schwinger	$e/3$	$\frac{3\hbar c}{e}$	329.4	411	$3.4\ 10^{14}$ eV

superluminal velocity. Recami and Mignani choose a more conventional value of the order of e/α , but this is more based on speculation as to the ioni-ing power of a superluminal electric charge rather than deductive reasoning.

In fact a quantum mechanical approach to the electromagnetic interactions of superluminal charged particles with ordinary matter (Lemke [1975] [1976], see Chapter 8) indicates that the reduced cross section for electromagnetic interactions of a superluminal electric field would make the energy loss by ionisation of a tachyon monopole less than the minimum for a subluminal relativistic charged particle (Lemke [1975]).

5.1.3 Yock particles

An errant disciple of Schwinger's, Yock has formulated a theory of the structure of the proton based on the existence of highly charged ($Z \geq 10$) fundamental particles whose electromagnetic attractions are responsible for the "strong" nature of the hadronic force (Yock [1969], [1970]).

As with Schwinger, Yock feels that the known electromagnetic force should be investigated thoroughly as a possible candidate for the force which binds the proton together, before proceeding to invoke more exotic gluon and parton exchange mechanisms (Weinberg [1974], Rev. Mod.Phys. 46, 255). In order to account for the great strength of the force, Schwinger hypothesises magnetic monopoles whereas Yock hypothesises highly electrically charged particles. Neither model, however, has yet dimmed the dazzle of attention which has surrounded the fractionally charged quark model of Gell-Mann

[1964] and Zweig [1965] , particularly since the discovery of the J and Psi charmed muons, whose discovery, incidentally, in no way diminishes the arguments for the electromagnetic nature of the sub-nucleon binding force.

5.1.4 Tachyons

A more thorough discussion of various theories of tachyons (faster than light particles) is presented in Chapter 8. However, it proves convenient to mention two aspects of the electromagnetic interactions of tachyons with sub-luminal matter - both of which are still the subject of much debate - which could produce signatures which might simulate a highly charged particle.

a.) The electric field of a tachyon

As can be seen from Chapter 8, 8.1.2 , transforming to a superluminal reference frame involves similar transformation equations to those for sub-luminal relativistic particles, except that the equation for the Lorentz factor $\gamma_{sub} = (1 - \beta^2)^{-\frac{1}{2}}$ becomes (5.3)

$$\gamma_{sup} = -i(1 - \beta^2)^{-\frac{1}{2}} \qquad (5.4)$$

and the rest mass m of a sub-luminal particle becomes the mass parameter $i\mu_o$ (where $\mu_o = m$) for a superluminal particle.

Hence, if we consider simplified expressions for the Lorentz transformed electric field of a relativistic particle viz.

(5.5) $E_{//}$ = Field parallel to line of flight = $\frac{e}{X^2}(1 - \beta^2)$

(5.6) $E_{\perp}$ = Field normal to line of flight = $\frac{e}{r^2}(1 - \beta^2)^{-\frac{1}{2}}$

at a point (x, y, z) where $r^2 = y^2 + z^2$, for a sub-luminal relativistic particle of charge e. As $\beta \rightarrow 1$ this provides the well established behaviour of the field normal to the line of flight increasing drastically (the "relativistic rise" region of the energy loss by ionization curve) whereas the field parallel to the line of flight diminishes. A spherical electric field (due to a point charge) at small velocities becomes pancaked normal to the line of flight at sub-luminal relativistic velocities.

However, if we assume that electromagnetic radiation from a super-luminal particle still travels at the velocity of light (see Chapter 8) then the transformation equation becomes:-

$$(5.7) \quad E_{/\!/} = \frac{e}{X^2} (\beta^2 - 1) \approx \frac{e}{X^2} . \beta^2$$

$$(5.8) \quad E_{\perp} = \frac{e}{r^2} (\beta^2 - 1)^{-\frac{1}{2}} \approx \frac{e}{r^2} \cdot \frac{1}{\beta}$$

The behaviour can be visualised as the electric field streaming out behind the particle along its track with an angular spread $\frac{1}{\beta^3}$. This is the reverse of the sub-luminal behaviour inasmuch as the field is now strongest parallel to the line of flight (but is now only in one direction, -X) and becomes weaker normal to the line of flight. Hence, one might expect this strong β^2 dependence of the electric field to show up in a dense (e.g. solid) ioni ation detector. The candidates for ionisation can only lie very close to the path of the particle (c.f. the close collisions dominance at sub-relativistic velocities), but there will be no accompanying levelling off due to polarisation of the medium (the density effect) since the particle goes past every ioni ation candidate.

It should, however, be remembered (see above, "Monopoles") that Lemke (1975) has argued, from more rigorous quantum mechanical calculations,

that the small angular spread of the electric field is the dominating effect, reducing the effective cross section to such a level that at even moderate values of β (~10) the energy loss by ionisation should be less than that at minimum for a sub-luminal relativistic particle. The problems of creating a quantum mechanics of tachyons have been pointed out by Feinberg (1967), and the calculations of Lemke should be viewed with a critical eye.

b.) Cerenkov radiation from a tachyon

The discussion of Cerenkov radiation from a tachyon given in Appendix I is particularly concerned with photon emission from a vacuum. However, in the absence of rigorous calculations for emission and absorption of Cerenkov radiation in matter it is not impossible that large fluxes of photons could be produced and detected either directly (as in the case of a photomultiplier tube viewing a scintillator) or by photoionization and subsequent multiplicative knock-on processes (as in the case of a neon flash-tube). This could simulate a highly ionising particle particularly in the flash-tube chamber.

5.2 Previous searches

Searches for a highly ionising component of the sea level cosmic radiation have been mainly concerned with the magnetic monopole. Production of monopoles in the atmosphere is expected to be similar to electron - positron pair production (Ashton [1973]).

(5.9) $\gamma + p \longrightarrow p + g + \bar{g}$

(5.10) $p + p \longrightarrow p + p + g + \bar{g}$

where g and $\bar{g}$ are the magnetic monopole and antimonopole respectively.

Carrithers, Stefanski and Adair (1966) using a solenoid to collect monopoles travelling along the geomagnetic field lines put an upper limit on the flux of such monopoles of 10^{-6} cm^{-2} $year^{-1}$.

Ashton et al (1969) measured a flux limit less than $1.3.10^{-10}$ cm^{-2} s^{-1} st^{-1} for particles ionizing greater than 4000 times the rate of single particle muons. Fleischer et al (1971), using an 18 m^2 area lexan polycarbonate array found no event ionizing greater than $(137)^2$ times the rate of a singly charged particle and give an upper limit to the flux of monopoles at sea-level of $1.5.10^{-13}$ cm^{-2} s^{-1} st^{-1}.

Yock (1975) found no events ionising > 49 times the rate of a singly charged particle and gives an upper limit to the flux of particles with $Z > \pm 7e$ at sea-level as 7.10^{-10} cm^{-2} sec^{-1} st^{-1} - under 600 $g.cm^{-2}$ of concrete - at the 90% confidence limit.

Searches for magnetic monopoles produced at accelerator energies have yielded zero events. Amaldi (1963), Purcell (1963) using a 30 GeV proton accelerator conclude that the rest mass of a monopole is in excess of 2.8 GeV/c^2.

Gurevich et al (1972) at 70 GeV finds an upper limit to the cross section for producing a monopole of mass 4.9 GeV/c^2 of $1.4.10^{-43}$ cm^2.

More recently, Giacomelli (1975) using the increased laboratory energy available from the two colliding 30 GeV proton beams at Cern-ISR has found an upper limit to the production cross section of a monopole of mass 30 GeV of 2.10^{-36} cm^2 at the 90% confidence limit.

The only search which has shown a positive result has been at high altitude in the balloon-borne experiment of Price et al (1975). They reported the passage of a slow moving highly ionising particle through a stack of

Cerenkov detector films, emulsions and lexan sheets. The latter indicated that the track was due either to a high Z nucleus ($Z \simeq 80$) or a monopole with magnetic charge 137e. The absence of any Cerenkov signal combined with the emulsion track indicated that the monopole was moving downward with velocity $\sim 0.5c$. However Fowler (1975) and others have argued that the resulting track is not dissimilar from a high Z nucleus which suffers partially fragmenting collisions as it passes through the stack, and since the presence of high Z nuclei in the primary radiation is a well established fact, searches for monopoles at low flux levels are better performed at sea level than high altitude.

5.3 Experiment

The experiment consists of a more thorough analysis of part of the data collected for the measurement of the incoherent sea level hadron spectrum (see Chapter 4). The essential features of the data are that the triggering level was a signal equivalent to 500 particles from the scintillator either under the lead or under the iron (see Chapter 2 for a description of the apparatus and Fig.2.2); the time delay between the detection of the triggering signal and the application of the high voltage pulse was 330 μs; the data relevant to this chapter was collected between 19. 7. 74 and 10. 4. 75 providing total sensitive time of 4,500 hours. Table 5.2 gives a summary of the basic data collection details.

5.4 Data

This can be sub-divided into 3 groups:

a.) Those bursts which begin in the lead but are absorbed in the iron;

TABLE 5.2 **Basic data collection details.**

Number of bursts in Pb	299
Number of bursts in Pb which continue under Fe	115
Number of bursts in Fe	523
Sensitive time	4,531.25 hrs.
Aperture for bursts in Pb	5,000 cm^2 st.
Aperture for bursts in Fe	4,500 cm^2 st.

Figure 5.1: A burst in the lead that does not develop, but is absorbed, in the iron.

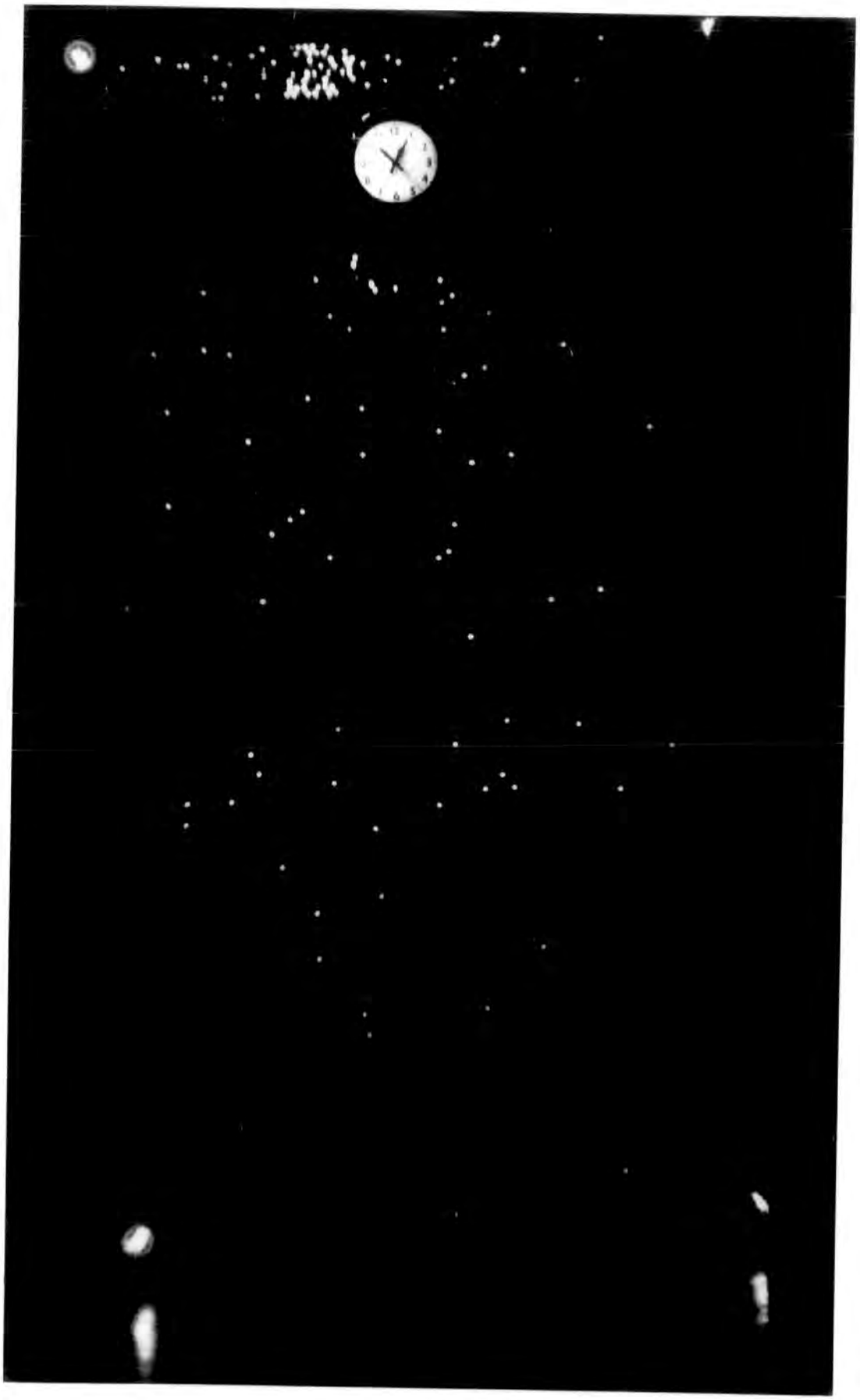

Figure 5.2: A burst in the lead that continues to develop in the iron.

Figure 5.3: Aburst in the iron that shows no track in Fig a of the initiating particle. This is because of the long time-delay (330 μs) between the passage of the particle and the application of the high voltage pulse.

b.) Those bursts which begin in the lead and develop in the iron producing a burst below both lead and iron;

c.) Those bursts which begin in the iron.

Typical examples from each group are shown in Figs. 5.1, 2, 3, the relative frequencies can be seen from Table 5.2.

The search for highly ionising particles concentrates on bursts of group c.) which are initiated in the iron. At a time delay of 330 μs between the passage of a relativistic charge e particle and and the application of a high voltage pulse to the flash-tubes, nearly all the ionised electrons have diffused to the walls. Calculations show (Lloyd [1960], Holroyd [1971]) that the efficiency of a stack of flash-tubes as used in the chamber (commercial grade neon at a pressure 60 torr) in detecting such a track should be only ~6% (see Fig. 5.4).

Consequently, the region co-linear with the core of the burst for events of group c.) in the stack of 8 layers in F1a has been scanned for the presence of 0, 1, 2, 3 etc. co-linear flashes. A minimum chi-square fit of a binomial distribution to the measured distribution of efficiences yielded a most probable efficiency of 5.5% at 50% sig. level, excluding all events of group c.) which could be due to high Z particles, i.e. 4 or more co-linear flashes corresponding to efficiencies greater than $5.5\% + 7\sigma$.

Fig. 5.5 shows the predicted and measured distributions from a sample of 200 events from group c.). Also shown in the figure is the possible high Z contamination contained in this sample. Figs. 5 .6,.7 are examples of these high Z candidates, which should be compared with Fig. 5.3 which is a typical burst in Fe with no flashes in F1a.

Figure 5.4 The variation of internal efficiency of a neon flash tube η with the parameter afq for a time delay of 330 μs, where afq = internal radius of tube x probability of an ionising collision in tube x number of ionising created per cm.
afq = 9 for a relativistic charge e particle.

FIG. 5.4

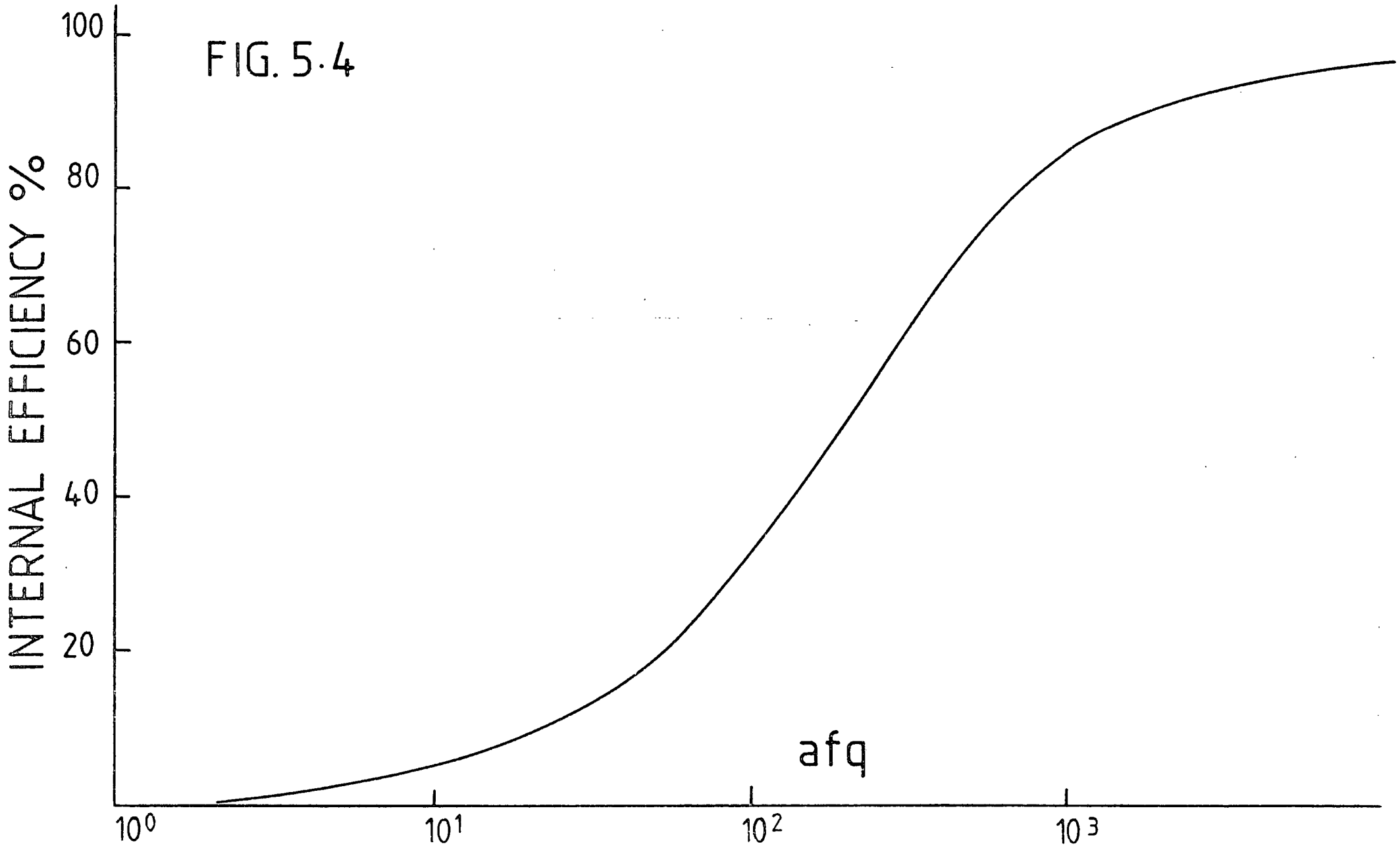

Figure 5.5 Frequency distribution for n out of 8 layers flashing on the passage of a single charge e particle. The observed distribution is from the sample of 200 bursts in the iron observed between 19. 7. 74 and 10. 4. 75 . The predicted distribution is from a minimum chi-squared fitted binomial distribution to the data excluding those events in which more than 4 layers were flashed co-linearly.

FIG. 5·5

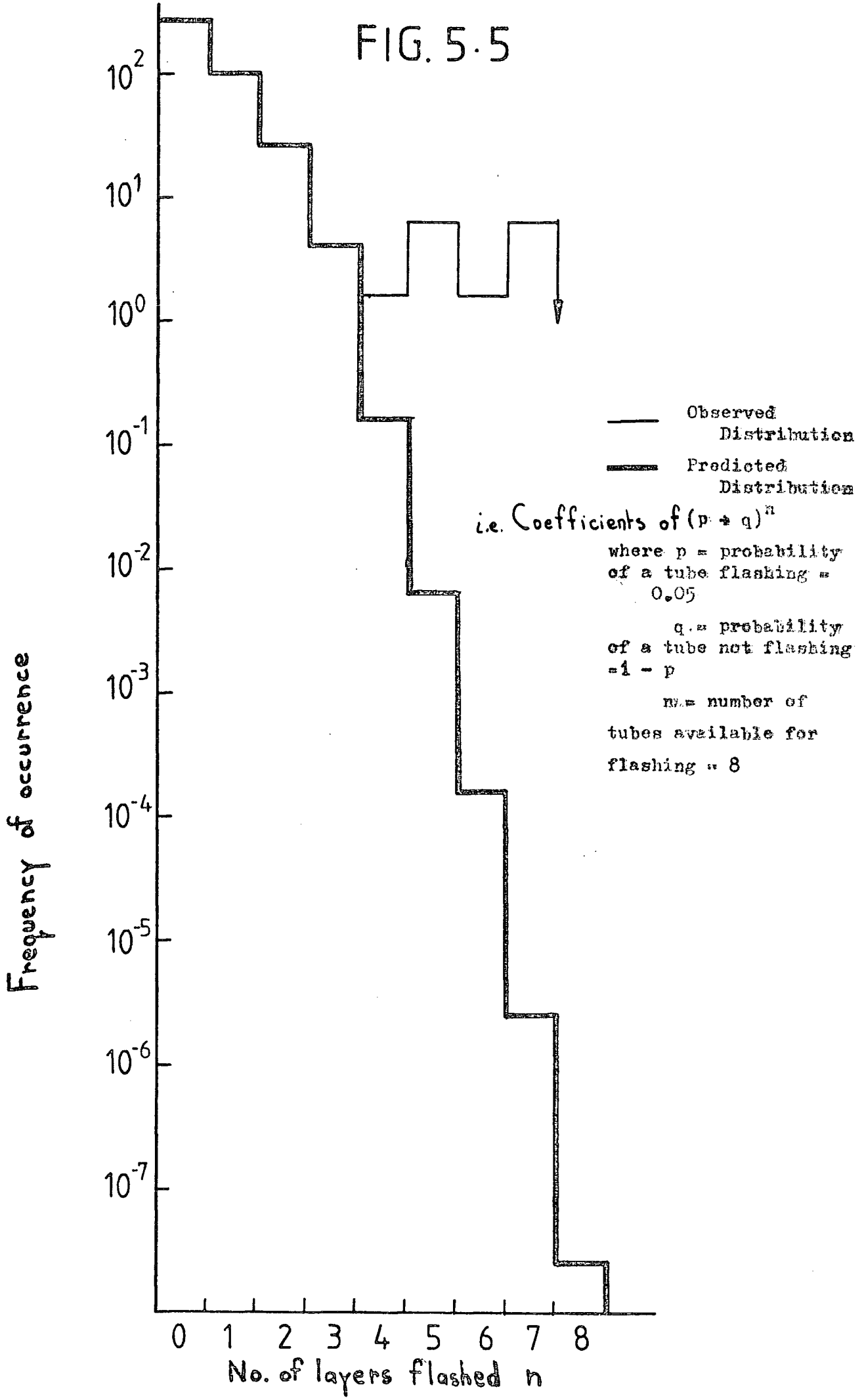
Frequency of occurrence
10^{2}
10^{1}
10^{0}
10^{-1}
10^{-2}
10^{-3}
10^{-4}
10^{-5}
10^{-6}
10^{-7}
0 1 2 3 4 5 6 7 8
No. of layers flashed n
Observed Distribution
Predicted Distribution
i.e. Coefficients of $(p + q)^n$
where p = probability of a tube flashing = 0.05
q = probability of a tube not flashing = 1 - p
n = number of tubes available for flashing = 8

Figure 5.6: High Z candidate, event no. 62 on film H36.

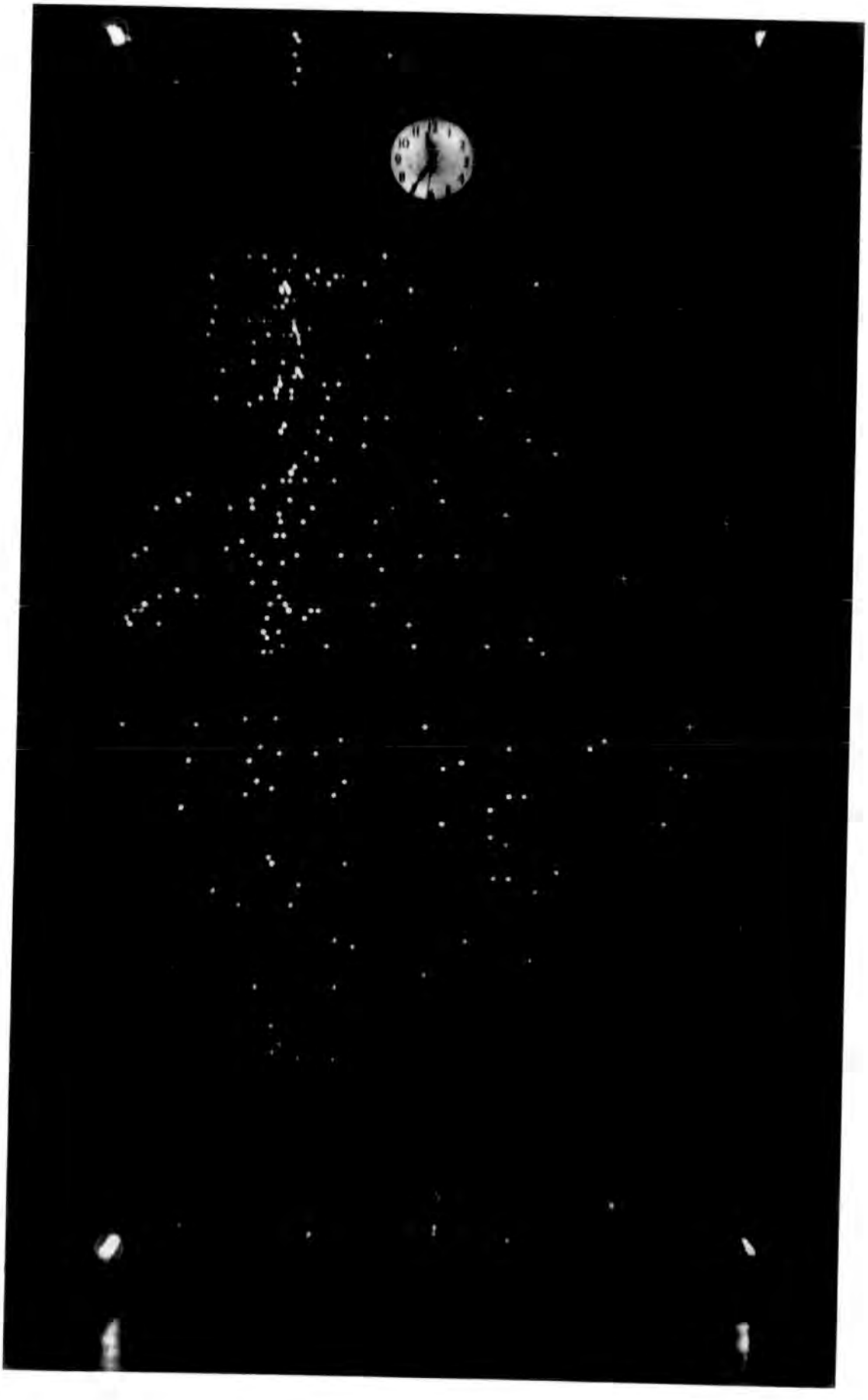

Figure 5.7: High Z candidate, event no. 11 on film H90(ii).

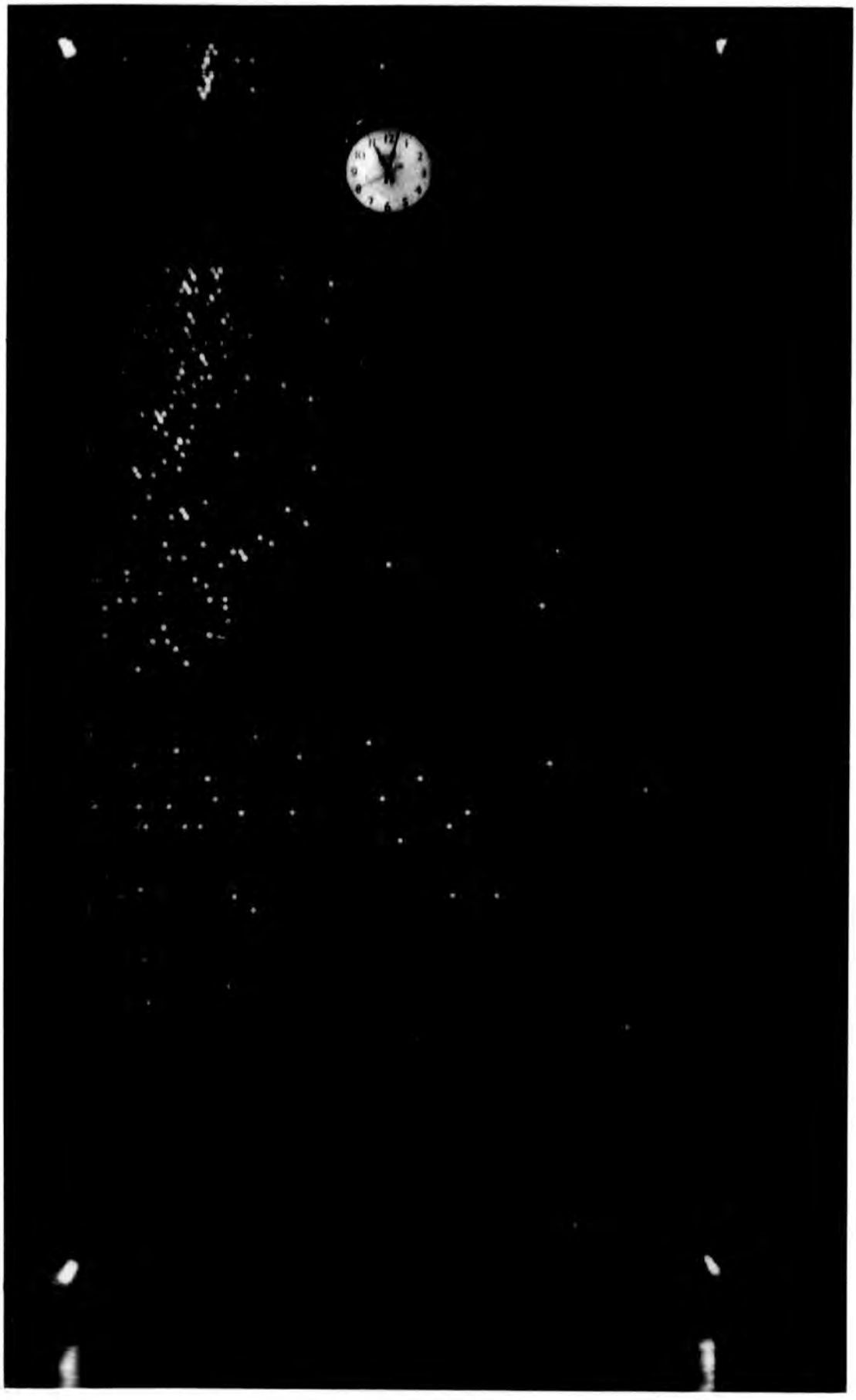

TABLE 5.3 **Summary of the measured parameters of the high Z candidates.**

Film No.	Event No.	Equivalent No. of particles passing through scintillator under Pb	Equivalent No. of particles passing through scintillator under F_E	Equivalent No. of particles passing within 3 tube-widths through 8 layers of flash-tubes under Pb	R = ratio of no of tubes flashed o/s 3 tube-widths to no. of tubes flashed 3 tube-widths	Equivalent Z from scint. under Pb	No. of tubes out of 8 flashed in a line below Pb	Equivalent Z from flash-tubes below Pb
H36	52	510	590	408	0.25	23e	6	16e
H33	62	350	700	190	0.17	19e	5	13e
H43	39	650	1225	211	0.125	25e	4	10e
H83	11	420	850	240	0.125	20e	5	13e
H83	14	1140	4000	333	0.33	34e	6	16e
H89 (iii)	2	275	670	286	0.14	17e	6	16e
H90 (ii)	11	500	525	620	0.36	22e	7	22e
H90 (iii)	2	420	740	663	0.25	20e	7	22e

Figure 5.8 a) Sketches of the high z candidates :-

(i) is event no. 39 on film H43

(ii) is event no. 52 on film H36

(iii) is event no. 62 on film H36

Fig. 5.8 a)

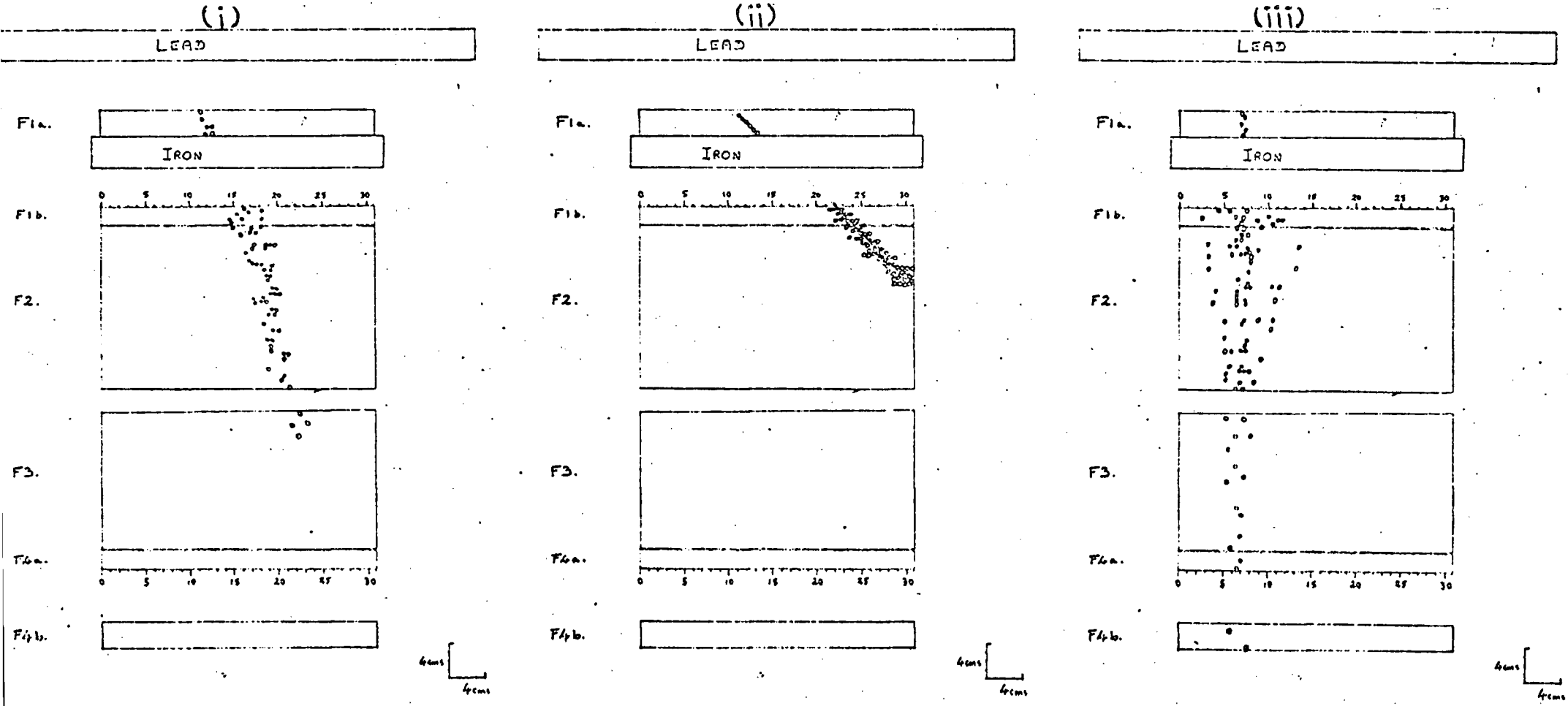
(i)
LEAD
IRON
F1a.
F1b.
F2.
F3.
F4a.
F4b.
0 5 10 15 20 25 30
4cms
4cms
(ii)
LEAD
IRON
F1a.
F1b.
F2.
F3.
F4a.
F4b.
0 5 10 15 20 25 30
4cms
4cms
(iii)
LEAD
IRON
F1a.
F1b.
F2.
F3.
F4a.
F4b.
0 5 10 15 20 25 30
4cms
4cms

Figure 5.8 b) Sketches of the high Z candidates :-

(i) is event no. 11 on film H83

(ii) is event no. 14 on film H83

(iii) is event no. 2 on film H89 (iii)

Fig. 5.8 b)

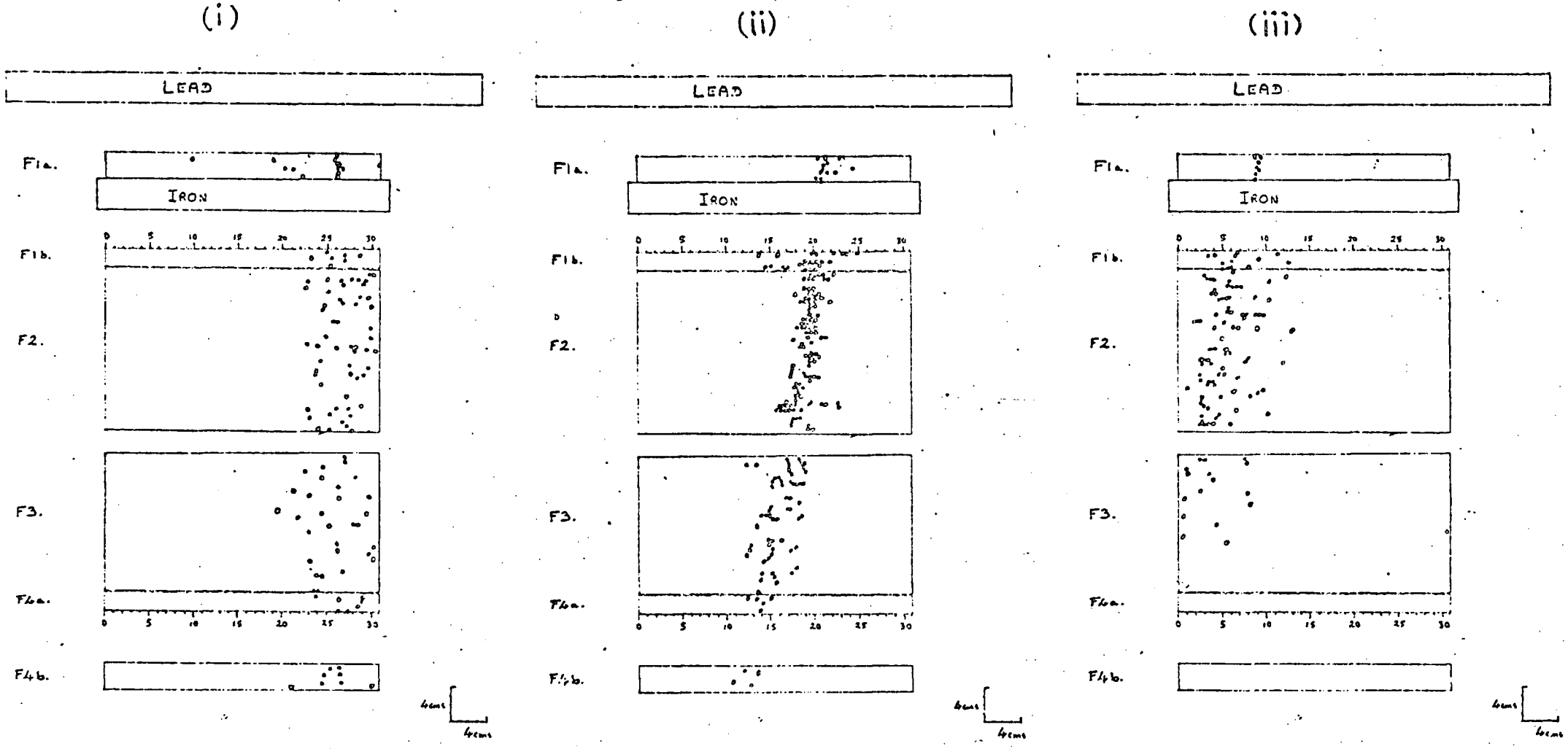
(i)
(ii)
(iii)
LEAD
LEAD
LEAD
F1a.
IRON
F1a.
IRON
F1a.
IRON
F1b.
F2.
F3.
F4a.
F4b.
F1b.
F2.
F3.
F4a.
F4b.
F1b.
F2.
F3.
F4a.
F4b.
0 5 10 15 20 25 30
4cms
4cms

Figure 5.8 c) Sketches of the high Z candidates :-

(i) is event no. 11 on film H90(iii)

(ii) is event no. 2 on film H90(iii)

Fig. 5.8c)

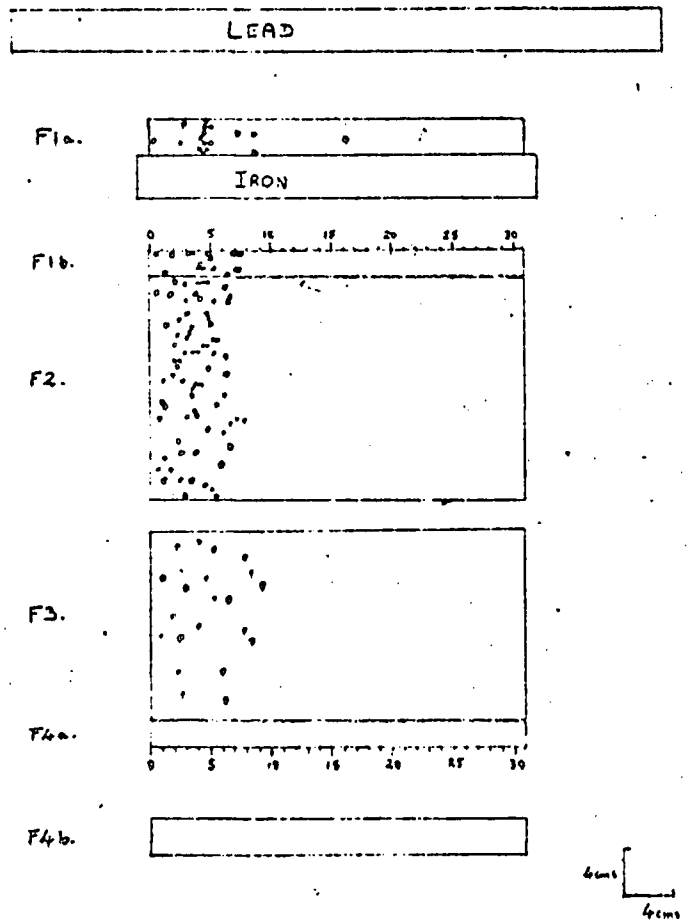
LEAD
F1a.
IRON
F1b.
F2.
F3.
F4a.
F4b.
4cms
4cms

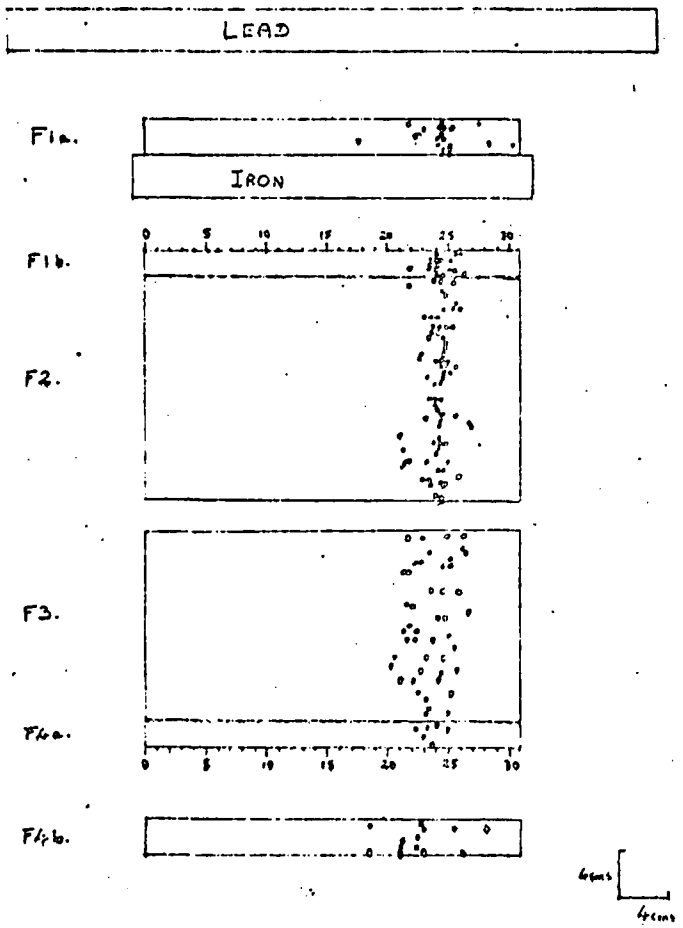
LEAD
F1a.
IRON
F1b.
F2.
F3.
F4a.
F4b.
4cms
4cms

All the possible high Z candidates are sketched in Figs. 5.8a), b), c) and Table 5.3 lists their measured parameters. Essentially Table 5.3 indicates that

a.) None of the events produced a measurable signal, equivalent to 3 or more particles, in the liquid scintillator above the lead. This implies that these anomolous events have their origin in some interaction which takes place either in the lead or the plastic scintillator under the lead.

b.) The majority of these events occur in the region of the triggering threshold (equivalent to 500 particles either under the lead or under the iron). Since a burst size of n particles under the lead or the iron corresponds to a laboratory energy of the initiating hadron $\simeq$ 500 GeV (see Chapter 2), unless such events are due to an exotic component of the cosmic radiation, they should be observed in accelerator experiments.

c.) If these events are due to high Z particles which have either missed the liquid scintillator (unlikely) or have been produced in the lead, then taking an average over all the observed efficiencies yields a mean Z of $(15 \pm 5)e$. It should be pointed out too that the close agreement between the signal produced in the scintillator under the lead and the signal produced in the flash-tube indicates that we are probably seeing in the flash-tubes the whole component of the event responsible for the signal produced in the scintillator (see below).

5.5 Possible alternative explanations

If we reject the hypothesis that these anomolous events are due to high Z particles, the alternative explanations that present themselves can be classified into two types:-

i.) Spurious effects of a normal i.e. charge e particle. Such possibilities are a slow proton back scattered from the iron, a residue of slow highly ioni ing knock-on electrons from the initiating hadron, a background muon which arrives within 100 μs prior to the application of the high voltage pulse etc.

ii.) A burst of type b.) which actually begins in the lead and develops further in the iron. The burst must be collimated strongly to produce an image which simulates a high Z particle. Such an event could be due to a very young shower, initiated at the bottom of the lead; or an older shower where the e - γ shower produced electrons have become widely dispersed and we are seeing the effects of a fluctuation to large multiplicity of the pionisation component; or a fireball type of interaction where the fireball is produced with high forward γ in the centre of mass frame thus collimating the subsequent electron - photon shower.

Causes of type i.) can be assessed according to whether or not they could produce the sort of efficiencies observed and the probability that such an event could take place. The latter figure has been assessed according to both observation - as in the case of a back scattered proton where no events with a high efficiency track coincident but not parallel with the burst was seen - and the probability of fluctuations (according to a random distribution about the typical efficiency). The different possibilities and their respective probabilities are listed in Table 5.4.

Causes of type ii.) require further analysis of the details of bursts of group b.) i.e. those which originate in the lead and develop under the iron.

TABLE 5.4 **Possible causes due to single charge e particles, their ionising efficiencies, and likliehood of occurrence.**

Possible cause	Typical efficiency	Probability of causing one anom. event of efficiency ~70%
The singly charged hadron which initiated the burst in the iron	5.5%	10^{-4}
An unrelated background singly charged particle (e.g. a muon) which has passed through the chamber in the 100 μs immediately preceding the application of the high voltage pulse	84%	5.10^{-5}
A slow moving highly ionizing proton back-scattered from a collision at the top of the iron	23%	6.10^{-4}
Slow moving highly ionizing knock on electrons produced by the hadron which initiated the burst in the iron	70%	6.10^{-20}
	Required efficiency	Required level of occurrence
Actually observed events	70%	2.10^{-2} (i.e. considered as bursts in Fe.)

5.6 The width of nuclear-electromagnetic bursts

The production of a shower of electrons (and protons) below either the lead or the iron indicates that a nuclear interaction has taken place between an incoming hadron and a target nucleus:

(5.11) either $p + p \rightarrow p + n_1 \pi^+ + n_2 \pi^- + n_3 \pi^o + p$

(5.12) or $\pi + p \rightarrow p + n^1_1 \pi^+ + n^1_2 \pi^- + n^1_3 \pi^o$

One other possibility is the bremsstrahlung of a muon in the electric field of a target nucleus i.e.

(5.13) $\mu + z \rightarrow \mu + z + \gamma$

At high energies bremsstrahlung dominates direct pair production and knock on electron prediction. If we only concern ourselves with bursts >500 particles (corresponding to a primary energy ~500 GeV) then the percentage of bursts that are due to muon interactions is ~10% (Saleh [1975], Fig. 6.15). Hence, we need only consider the hadron induced cascades. The charged pions produced may go on to interact again (as in equation 5.12) or leave the target without interacting. The neutral pions, however, decay immediately ($\tau_o \simeq 10^{-16}$ sec., hence distance travelled before decay for a 500 GeV $\pi^o \simeq 30$ nm) via an electromagnetic decay:-

(5.14) $\pi^o \rightarrow \gamma + \gamma$

and the shower then proceeds to develop via the processes

(5.15) $\gamma \rightarrow e^+ + e^-$; (pair production)

(5.16) $\gamma + e^- \rightarrow \gamma + e^-$; (Compton scattering)

(5.17) $e^- + \gamma \rightarrow e^- + \gamma$; (inverse Compton scattering)

(5.18) $e^+ + e^- \longrightarrow \gamma + \gamma$; (electron positron annihilation)

The calculations which give the average number of electrons leaving the target for a given primary hadron energy are more thoroughly discussed in Chapter 2.

Clearly, the stage of development of the shower when it leaves the target depends on where in the target the burst originated. For a pure e - γ shower (initiated by either an electron or a photon) the age of the shower s is given by (Nishimura & Kamata [1958]).

$$(5.19) \qquad s = \frac{3t}{t + 2\ln\left(\frac{E_o}{\epsilon_o}\right) + 2\ln r}$$

where t is the depth in radn. lengths through which the shower has developed and E_o is the energy of the primary electron/photon. Similarly the width of the shower can be calculated from the lateral distribution of electrons in the shower (Nishimura & Kamata [ibid]) (and Greisen [1956]).

$$(5.20) \quad \triangle\left(\frac{r}{r_1}\right) = c(s)\left(\frac{r}{r_1}\right)^{s-2}\left(1 + \frac{r}{r_1}\right)^{s-4.5}$$

where r is measured in Moliere units (r_1).

By integrating along strips corresponding to the width of a flash-tube we can calculate the percentage of electrons which should fall within 1, 2, 3 etc. tube widths of the centre of the shower, i.e.

$$(5.21) \qquad F(R) = \int_0^\infty 2\pi r\triangle(r)\,dr - 4\int_R^\infty r\triangle(r)\sin^{-1}\left(\frac{R}{r}\right)dr;$$

where F(R) = fraction which fall outside a strip width 2R

Fig. 5.9 shows the results of such a calculation for various values of s. Knowing the efficiency of the flash-tube at 330 μs it is a simple step to

Figure 5.9 The fraction of an electromagnetic shower which falls outside a strip of width 2R Moliere units for different values of the age-parameter s of the shower.
Curve m is for m x 0.25 = s.
Alternative values of 2R in tube-widths are indicated along the top of the figure.
Calculated according to equation 5.21.

FIG. 5.9

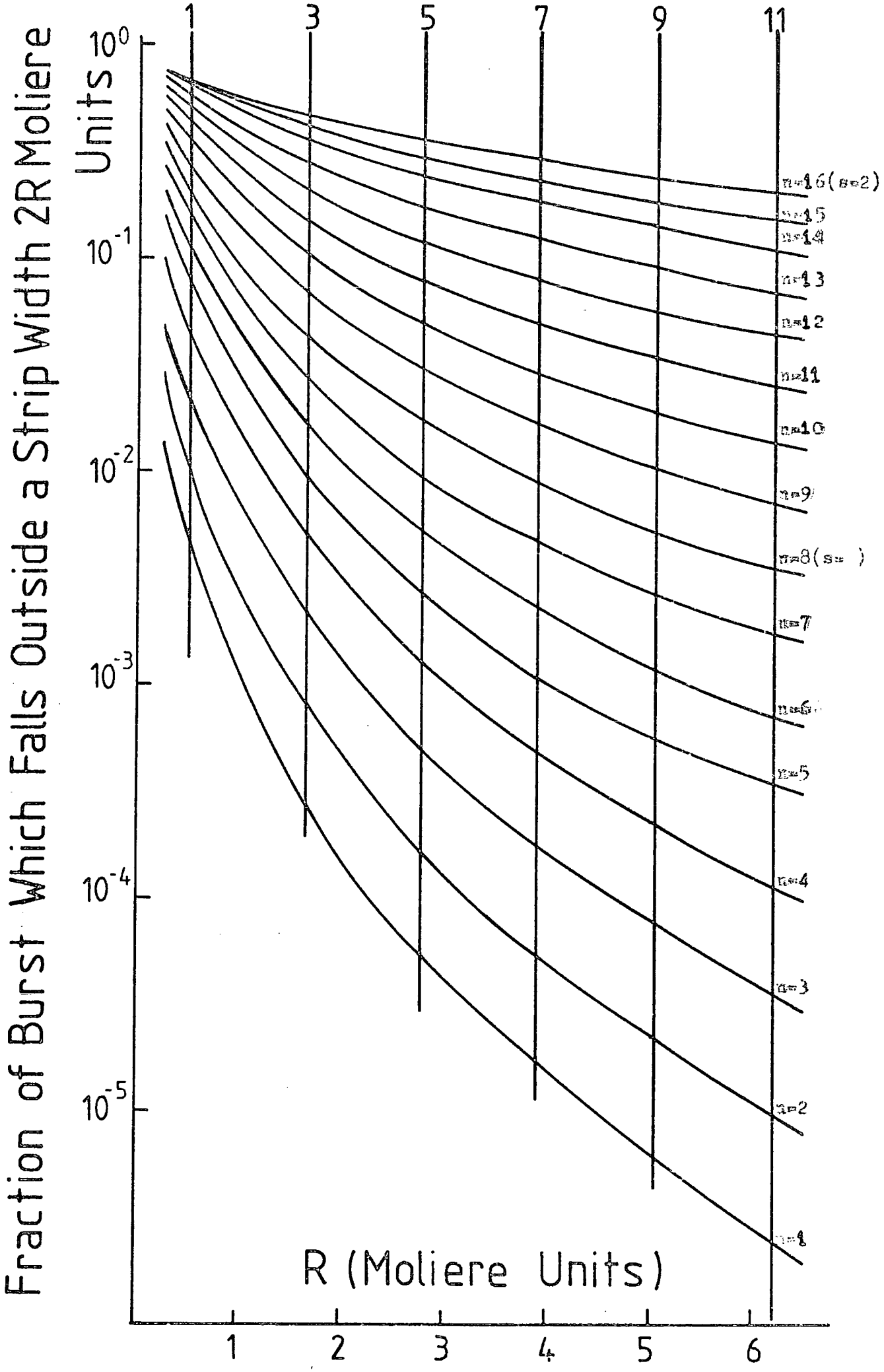
Fraction of Burst Which Falls Outside a Strip Width 2R Moliere Units
10^0
10^{-1}
10^{-2}
10^{-3}
10^{-4}
10^{-5}
1
3
5
7
9
11
n=16(s=2)
n=15
n=14
n=13
n=12
n=11
n=10
n=9
n=8(s=
n=7
n=6
n=5
n=4
n=3
n=2
n=1
R (Moliere Units)
1
2
3
4
5
6

Figures 5.10 and 5.11

The number of tubes out of eight layers within $\pm n/2$ tubewidths of the core of an electromagnetic shower that would flash at 330 μs time delay as a function of burst size and age parameter s of the shower.

S	n tube-widths	Fraction of shower which falls outside n tube-widths	Number of tubes flashed out of eight within $\pm n/2$ tube widths of core								
			250	500	750	1000	2000	3000	4000	5000	Burst Size
0.125	1	$4.8\ 10^{-3}$	6	7	8	8	8	8	8	8	
	3	$2.8\ 10^{-4}$	0	0	0	0	0	1+0	1+0	1+0	
	5	$5.4\ 10^{-5}$	0	0	0	0	0	0	0	0	
	7	$1.7\ 10^{-5}$	0	0	0	0	0	0	0	0	
	9	$6.2\ 10^{-6}$	0	0	0	0	0	0	0	0	
	11	$2.4\ 10^{-6}$	0	0	0	0	0	0	0	0	
0.25	1	$1.1\ 10^{-2}$	6	7	8	8	8	8	8	8	
	3	$8.5\ 10^{-4}$	0	0	0	0	1+0	1+1	1+2	1+2	
	5	$1.7\ 10^{-4}$	0	0	0	0	0	0	0	0	
	7	$5.6\ 10^{-5}$	0	0	0	0	0	0	0	0	
	9	$2.3\ 10^{-5}$	0	0	0	0	0	0	0	0	
	11	$9.5\ 10^{-6}$	0	0	0	0	0	0	0	0	
0.375	1	$2.3\ 10^{-2}$	6	7	8	8	8	8	8	8	
	3	$2.2\ 10^{-3}$	0	0	0	1+0	1+1	2+1	2+2	3+3	
	5	$5\ 10^{-4}$	0	0	0	0	0	0	0	0	
	7	$1.8\ 10^{-4}$	0	0	0	0	0	0	0	0	
	9	$7.7\ 10^{-5}$	0	0	0	0	0	0	0	0	
	11	$3.2\ 10^{-5}$	0	0	0	0	0	0	0	0	
0.5	1	$4.6\ 10^{-2}$	6	7	8	8	8	8	8	8	
	3	$6\ 10^{-3}$	0	1+0	1+1	1+2	2+2	3+3	4+3	4+4	
	5	$1.3\ 10^{-3}$	0	0	0	0	0	0	1+0	1+1	
	7	$4.9\ 10^{-4}$	0	0	0	0	0	0	0	0	
	9	$2.3\ 10^{-4}$	0	0	0	0	0	0	0	0	
	11	$1.1\ 10^{-4}$	0	0	0	0	0	0	0	0	

FIGS 5.10, 5.11

S	n tube-widths	Fraction of shower which falls outside n tube-widths	Number of tubes flashed out of eight within ± n/2 tube widths of core								
			250	500	750	1000	2000	3000	4000	5000	Burst Size
0.625	1	$7.5\ 10^{-2}$	6	7	7	8	8	8	8	8	
	3	$9.6\ 10^{-3}$	1+0	1+1	1+2	2+2	3+3	4+4	5+5	5+6	
	5	$2.65\ 10^{-3}$	0	0	0	0	0	1+0	1+0	1+1	
	7	$1.12\ 10^{-3}$	0	0	0	0	0	0	0	0	
	9	$5.8\ 10^{-4}$	0	0	0	0	0	0	0	0	
	11	$3.8\ 10^{-4}$	0	0	0	0	0	0	0	0	
0.75	1	$1.1\ 10^{-1}$	6	7	7	8	8	8	8	8	
	3	$1.7\ 10^{-2}$	1+0	1+2	2+2	2+3	4+4	5+5	6+6	6+7	
	5	$5.2\ 10^{-3}$	0	0	0	0	1+0	1+1	1+1	1+2	
	7	$2.4\ 10^{-3}$	0	0	0	0	0	0	0	0	
	9	$1.27\ 10^{-3}$	0	0	0	0	0	0	0	0	
	11	$7.6\ 10^{-4}$	0	0	0	0	0	0	0	0	
0.875	1	$1.6\ 10^{-1}$	6	7	7	8	8	8	8	8	
	3	$2.8\ 10^{-2}$	1+1	1+2	2+2	2+4	5+5	6+6	6+7	7+7	
	5	$9.5\ 10^{-3}$	0	0	0	0	1+1	1+2	1+3	2+3	
	7	$4.8\ 10^{-3}$	0	0	0	0	0	0	0	1+0	
	9	$2.7\ 10^{-3}$	0	0	0	0	0	0	0	0	
	11	$1.7\ 10^{-3}$	0	0	0	0	0	0	0	0	
1	1	$2.1\ 10^{-1}$	6	7	7	8	8	8	8	8	
	3	$4.4\ 10^{-2}$	1+1	2+2	2+4	3+4	5+6	6+7	7+7	7+7	
	5	$1.7\ 10^{-2}$	0	0	0	1+0	1+2	1+3	3+2	2+4	
	7	$9\ 10^{-3}$	0	0	0	0	0	1+0	1+1	1+1	
	9	$4.2\ 10^{-3}$	0	0	0	0	0	0	0	0	
	11	$3.6\ 10^{-3}$	0	0	0	0	0	0	0	0	

FIGS 5.10, 5.11

S	n tube-widths	Fraction of shower which falls outside n tube-widths	Number of tubes flashed out of eight within $\pm n/2$ tube widths of core								
			250	500	750	1000	2000	3000	4000	5000	Burst Size
1.125	1	$2.8\ 10^{-1}$	5	7	7	7	8	8	8	8	
	3	$7\ 10^{-2}$	1+2	2+3	3+5	4+5	5+7	7+7	7+7	7+8	
	5	$3\ 10^{-2}$	0	1+0	1+1	1+1	2+2	3+3	3+4	4+4	
	7	$1.7\ 10^{-2}$	0	0	0	0	1+0	1+1	1+2	1+2	
	9	$1.08\ 10^{-2}$	0	0	0	0	0	0	1+0	1+1	
	11	$7.4\ 10^{-3}$	0	0	0	0	0	0	0	0	
1.25	1	$3.6\ 10^{-1}$	5	6	7	7	8	8	8	8	
	3	$1.1\ 10^{-1}$	1+2	2+4	3+5	4+5	6+7	7+7	7+8	7+8	
	5	$6\ 10^{-2}$	0	1+0	1+1	1+2	2+3	3+4	4+4	4+5	
	7	$3\ 10^{-2}$	0	0	1+0	1+1	1+2	1+3	2+3	2+4	
	9	$2\ 10^{-2}$	0	0	0	0	1+0	1+1	1+1	1+2	
	11	$1.36\ 10^{-2}$	0	0	0	0	0	1+0	1+0	1+1	
1.375	1	$4.5\ 10^{-1}$	5	6	7	7	8	8	8	8	
	3	$1.53\ 10^{-1}$	2+2	3+4	4+5	4+6	6+7	7+7	7+8	8+8	
	5	$8\ 10^{-2}$	0	1+1	1+2	1+3	3+4	5+5	5+5	5+6	
	7	$5.2\ 10^{-2}$	0	0	1+0	1+0	1+2	1+3	2+3	3+4	
	9	$3.5\ 10^{-2}$	0	0	0	0	1+1	1+2	2+2	2+2	
	11	$2.6\ 10^{-2}$	0	0	0	0	0	1+0	1+1	1+1	
1.5	1	$5.2\ 10^{-1}$	4	6	7	7	8	8	8	8	
	3	$2.1\ 10^{-1}$	2+2	3+4	4+5	5+6	7+7	8+7	8+7	8+8	
	5	$1.2\ 10^{-1}$	1+0	1+1	2+2	2+3	4+4	4+6	5+6	5+7	
	7	$8.2\ 10^{-2}$	0	0	1+0	1+1	1+3	3+3	3+4	4+4	
	9	$6\ 10^{-2}$	0	0	0	1+0	1+1	1+2	2+2	3+3	
	11	$4.4\ 10^{-2}$	0	0	0	1+0	1+1	1+3	2+3	3+3	

FIGS 5.10, 5.11

S	n tube-widths	Fraction of shower which falls outside n tube-widths	Number of tubes flashed out of eight within $\pm n/2$ tube widths of core								
			250	500	750	1000	2000	3000	4000	5000	Bur Siz
1.75	1	$6.6\ 10^{-1}$	3	5	6	7	7	8	8	8	
	3	$3.7\ 10^{-1}$	2+2	3+4	4+5	5+5	6+7	7+7	7+8	8+8	
	5	$2.5\ 10^{-1}$	1+1	1+2	2+3	2+4	4+5	5+6	5+7	6+7	
	7	$1.9\ 10^{-1}$	0	1+1	1+1	1+2	2+4	4+4	4+5	5+5	
	9	$1.53\ 10^{-1}$	0	0	1+0	1+1	2+2	3+3	3+4	4+4	
	11	$1.1\ 10^{-1}$	0	0	1+1	1+1	2+2	3+3	4+4	4+5	

FIGS 5.10, 5.11

convert these figures into the number of flash-tubes flashed in a stack of of 8 layers (F1a) within 1, 2, 3 etc. tube widths from the centre of the burst for various burst sizes. Such burst profile calculations are summarised in Figs. 5.10 and 5.11 but a first glance at Fig. 5.9 indicates that the region where 90% of the electrons are found is within $\pm_1$ Moliere units of the centre of the shower.

Consequently each burst has been scanned (on a scale 1:20 to real space) and the number of flashes within ± 0.5 cm (on the scanning table) corresponding to ± 6.25 Moliere units in real space counted. Figs. 5.12a), 5.13a) 5.14a) show the resulting scatter plots for bursts of type a, b, c respectively. Figs. 5.12b), 5.13b) 5.14b) are average values derived from the scatter diagrams with the predictions from Nishimura - Kamata theory plotted for comparison.

Fig. 5.12b) indicates that the data best fit an average age parameter $s \simeq 1.1$ to 1.25 (i.e. slightly greater than one).

Fig. 5.13b) indicates that those bursts which originate in the lead but continue under the iron are best fitted with a younger age parameter $s \simeq 1.0$ to 1.1. This would be expected since this section of the data must select those showers which are youngest in order that they will continue through the iron without being absorbed.

Fig. 5.14b) indicates that those bursts which originate in the iron are best fitted with an age parameter $s \simeq 0.8$ to 1 for bursts < 2000 particles, but the larger bursts seem to have a much larger age parameter ~ 1.5.

It is interesting to compare the results with the work of previous authors at smaller time delays (e.g. Coats [1967], Cooper [1974]). In these cases the measured burst widths were considerably wider than the predictions of

Figure 5.12a) Scatter plot of the burst size-no. of flashes within $\pm$ 0.5 cms. on scanning-sheet relationship for bursts that originate in the lead but do not continue beneath the iron.

FIG. 5·12 a)

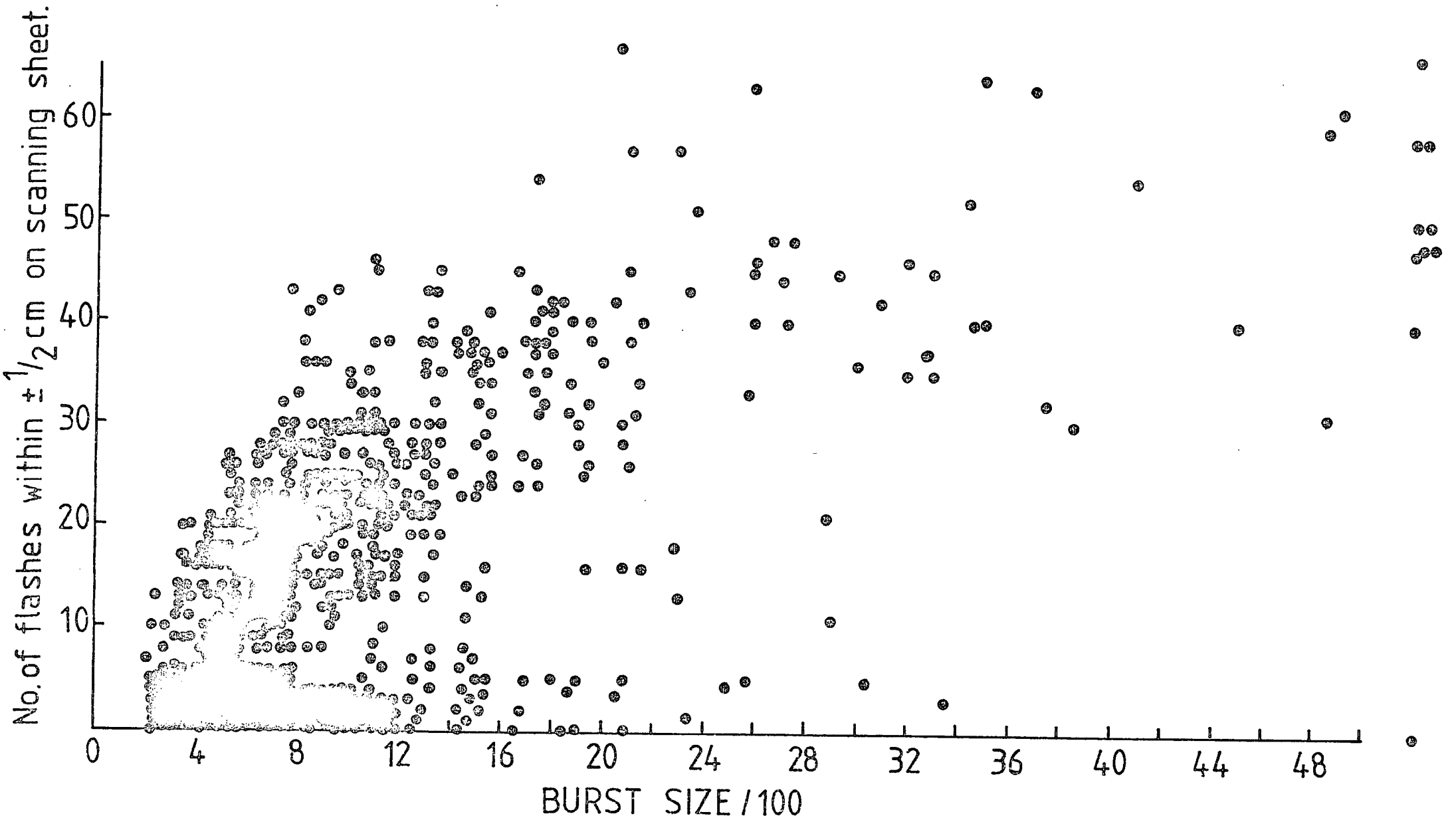
No. of flashes within ± 1/2 cm on scanning sheet.
60
50
40
30
20
10
0
4
8
12
16
20
24
28
32
36
40
44
48
BURST SIZE / 100

Figure 5.12b) Averaged values of the burst size - no. of flashes within $\pm$ 0.5 cms. of shower-core (on scanning-sheet) relationship compared with the predictions of Nishimura - Kamata theory for different values of the age-parameter s of the showers for bursts that originate in the lead but do not continue beneath the iron.

FIG. 5·12 b)

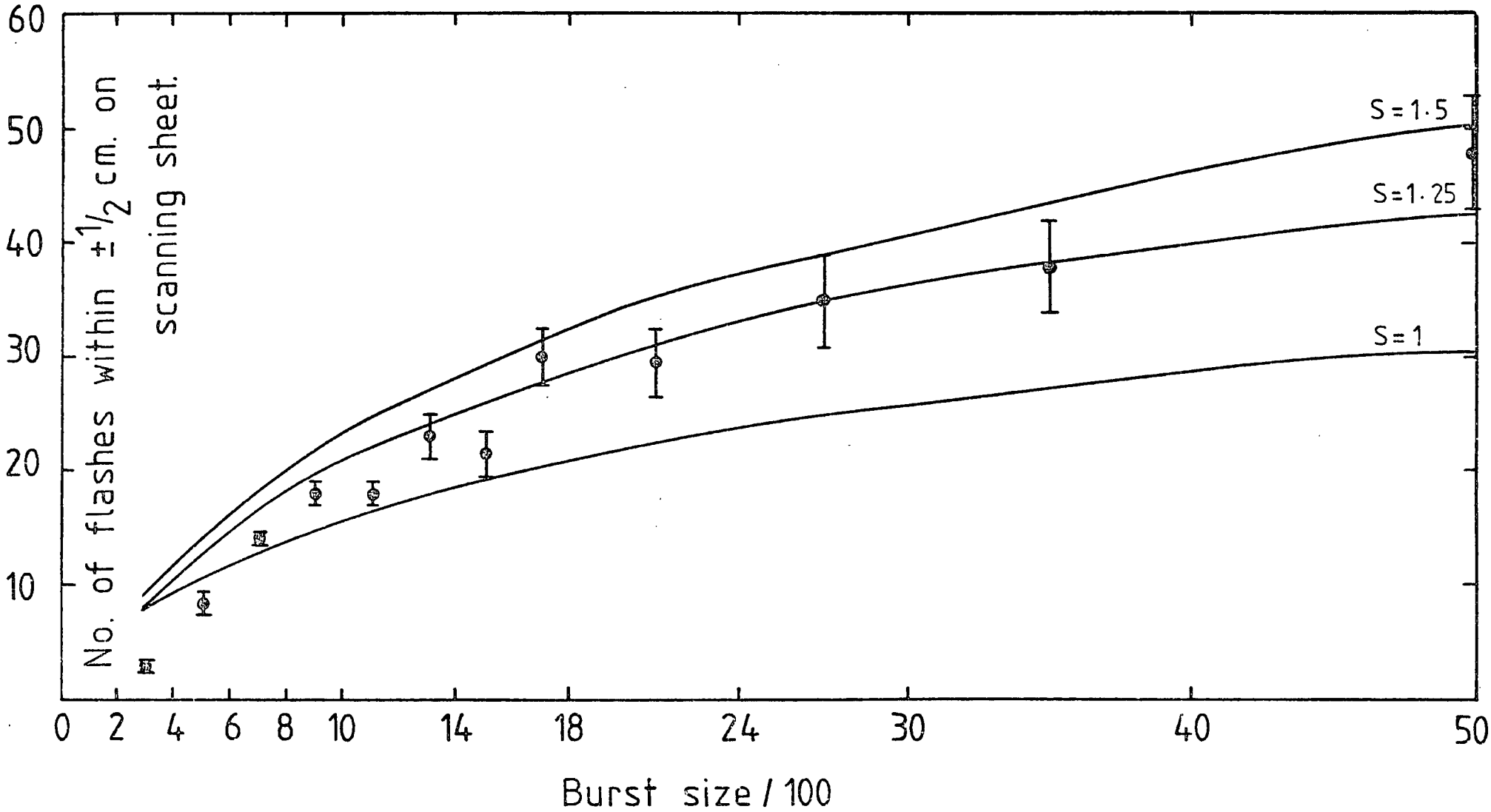
60
50
40
30
20
10
No. of flashes within ±1/2 cm. on scanning sheet.
S = 1·5
S = 1·25
S = 1
0
2
4
6
8
10
14
18
24
30
40
50
Burst size / 100

Figure 5.13a) Scatter plot of the burst size - no. of flashes within $\pm$ 0.5 cms. on scanning-sheet relationship for bursts that originate in the lead but continue beneath the iron.

The dots are the data from the film-series H78 to H94 used in figure 5.5.

FIG 5·13 a)

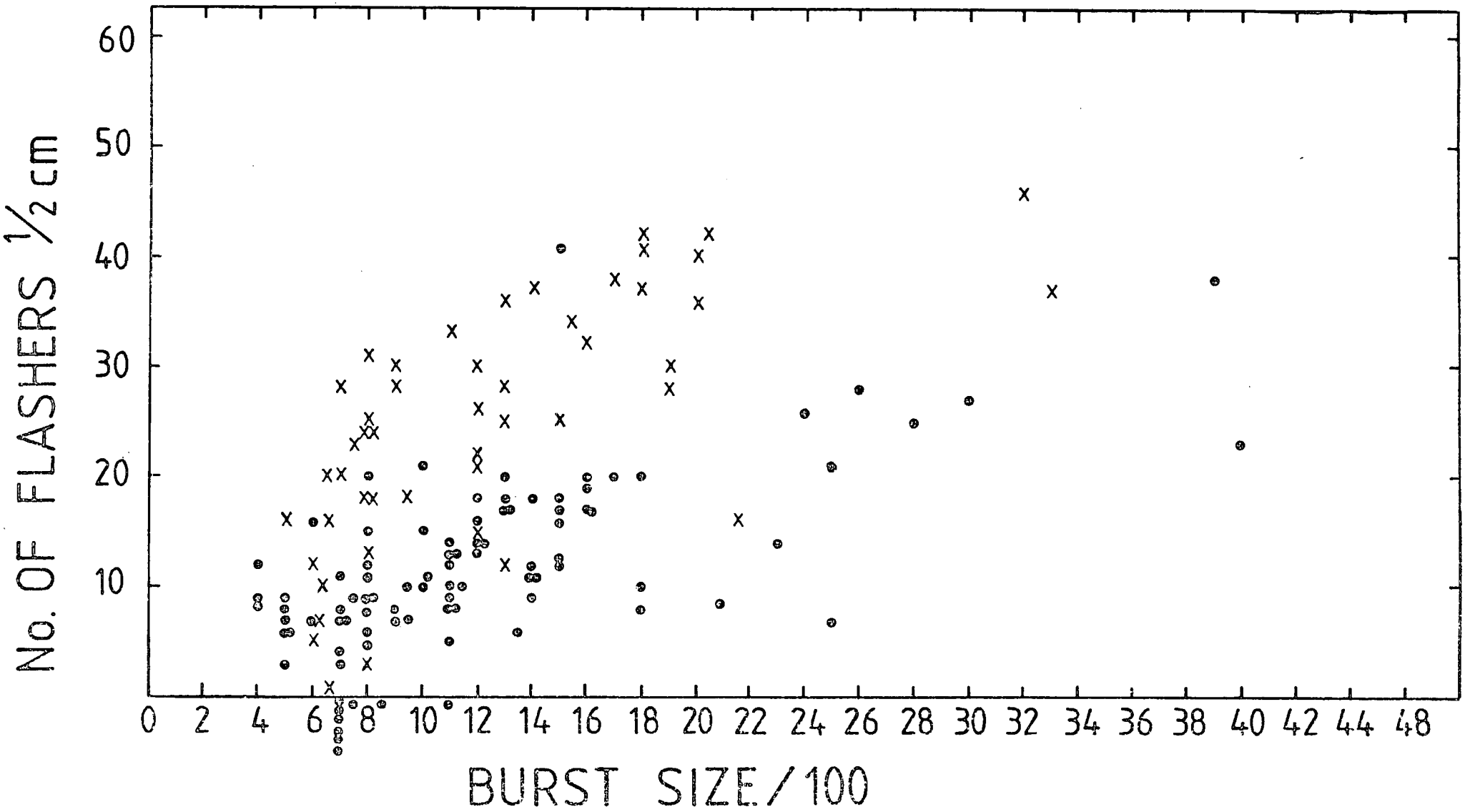
No. OF FLASHERS ½ cm
60
50
40
30
20
10
0 2 4 6 8 10 12 14 16 18 20 22 24 26 28 30 32 34 36 38 40 42 44 48
BURST SIZE / 100

Figure 5.13b) Averaged values of the burst size - no. of flashes within $\pm$ 0.5 cms of shower-core (on scanning-sheet) relationship compared with the predictions of Nishimura - Kamata theory for different values of the age-parameter s of the shower; for bursts that originate in the lead but continue beneath the iron.

FIG. 5·13 b)

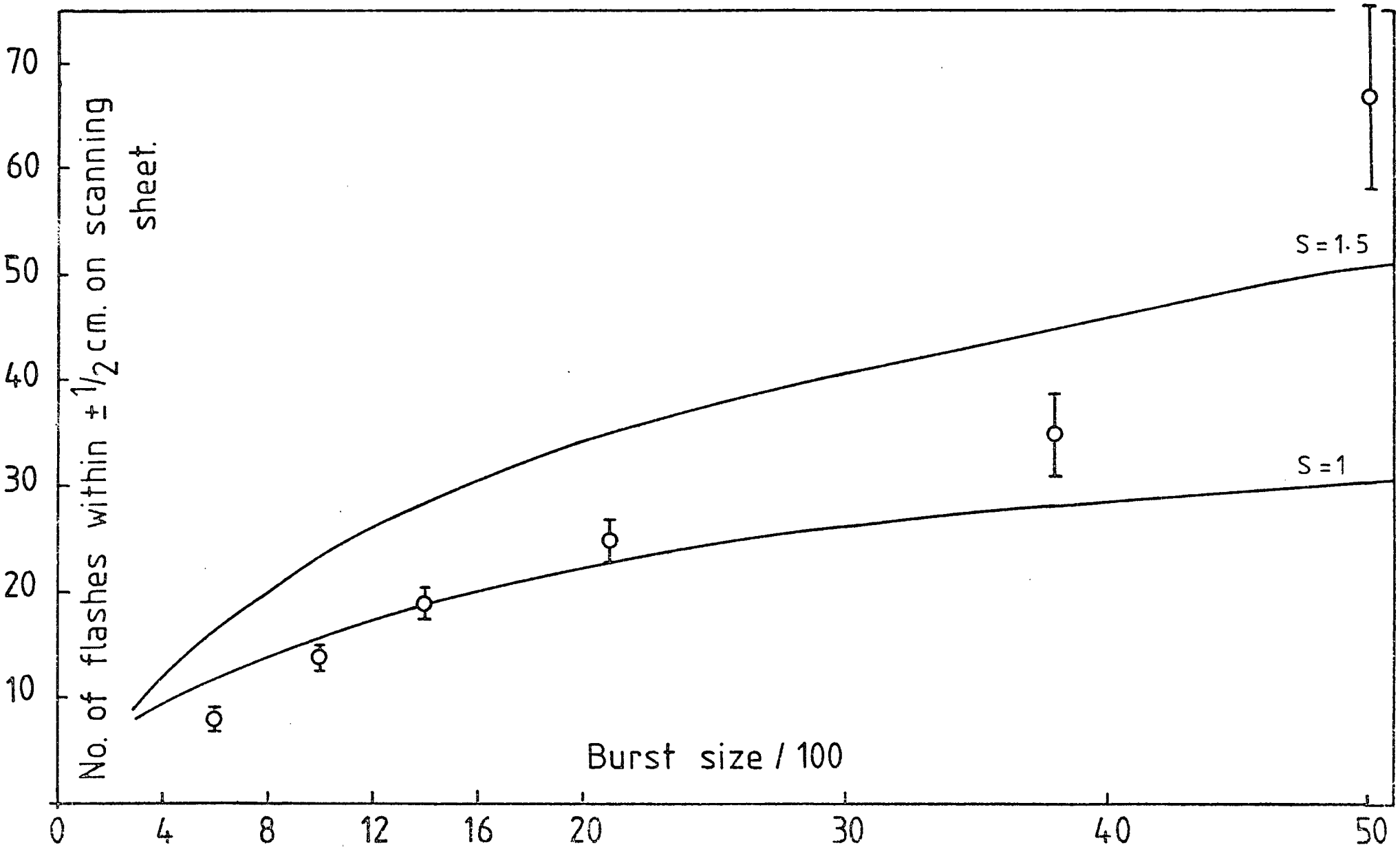
70
60
50
40
30
20
10
No. of flashes within ± 1/2 cm. on scanning sheet.
S = 1·5
S = 1
Burst size / 100
0
4
8
12
16
20
30
40
50

Figure 5.14a) As for Fig. 5.12a) but for bursts that originate in the iron.

FIG. 5·14a)

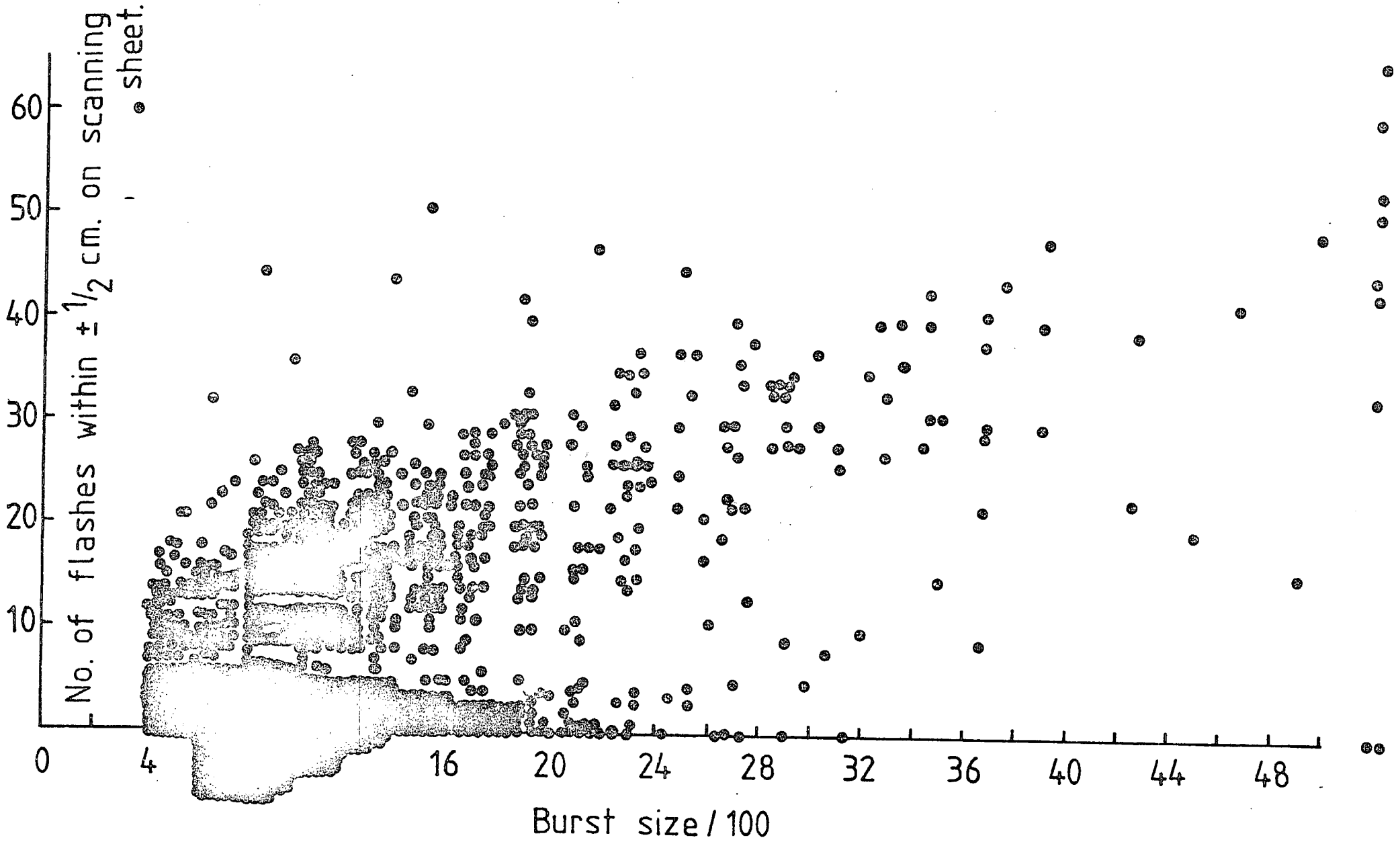
No. of flashes within ± 1/2 cm. on scanning sheet.
60
50
40
30
20
10
0
4
16
20
24
28
32
36
40
44
48
Burst size / 100

Figure 5.14b) As for Fig. 5.12b) but for bursts that originate in the iron.

FIG. 5·14 b)

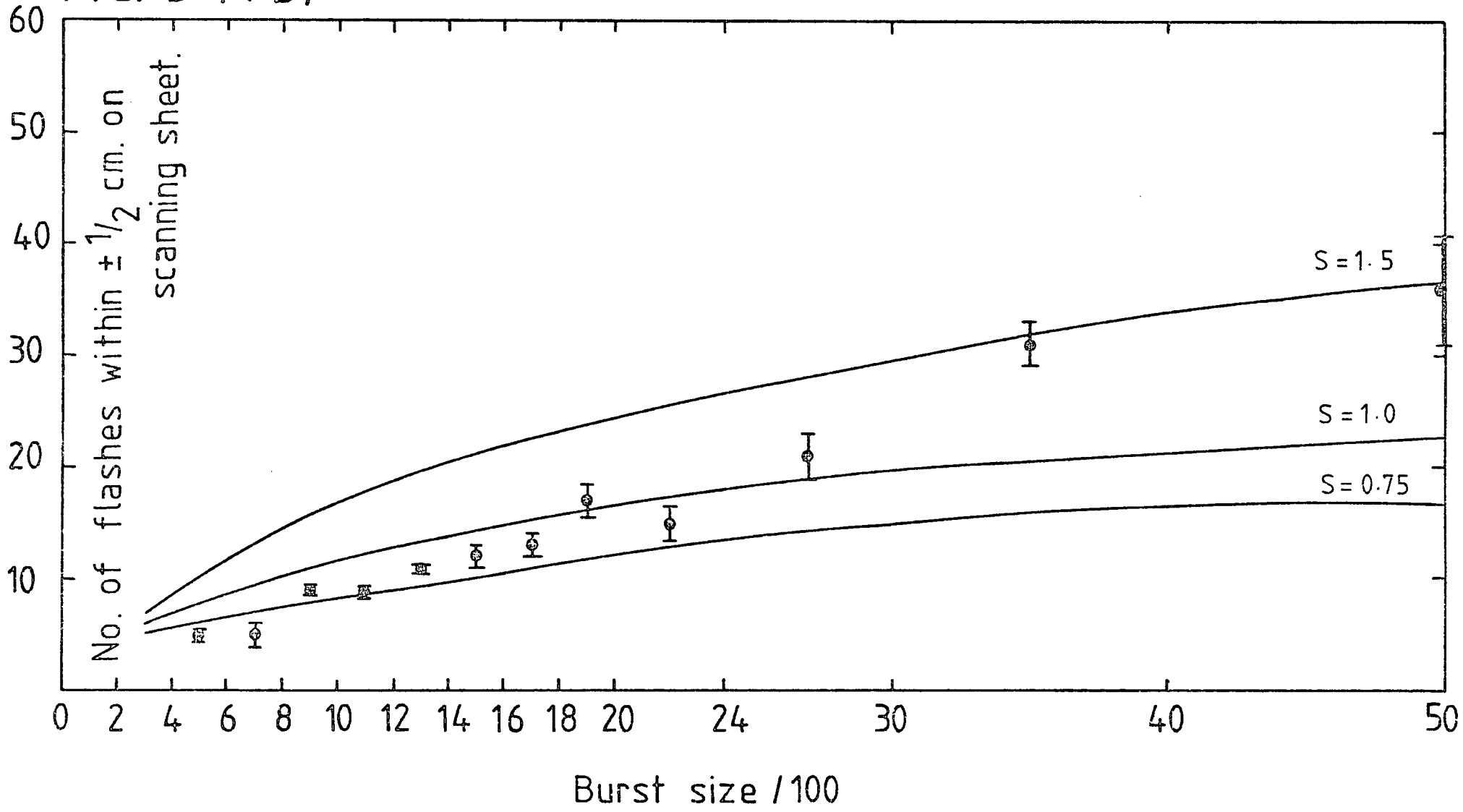
60
50
40
30
20
10
No. of flashes within ± 1/2 cm. on scanning sheet.
S = 1·5
S = 1·0
S = 0·75
0
2
4
6
8
10
12
14
16
18
20
24
30
40
50
Burst size / 100

theory, and the reason supposed to be the presence of large angle scattered electrons (Nishimura - Kamata theory is based on the small angle of scattering approximation, $\tan\theta \simeq \theta$). The present work goes some way to justify this explanation since at long time delay the few singly (and therefore wide angled) scattered electrons should be undetectable, and hence Nishimura - Kamata theory should be applicable. It is interesting to observe that although the actual bursts are nuclear-electromagnetic, pure electromagnetic shower theory is sufficient to describe the burst width data. Hence any broadening due to the nuclear interactions must be swamped by electromagnetic broadening of the subsequent electron - photon shower. It is not clear, however, whether any narrowing due to the nuclear interactions would be likewise swamped, so in order to investigate further the origins of these anomolous "High Z" events the broadening due to the nuclear interaction must be considered.

In Appendix III it is argued that, if we assume that pions are emitted isotropically in the centre of mass system, the ratio

$$R = \frac{\text{number of flashes beyond } \pm 1.5 \text{ tube widths from core}}{\text{number of flashes within } \pm 1.5 \text{ tube widths from core}}$$

roughly represents the ratio of the number of neutral pions emitted in the backward cone to the number of neutral pions emitted in the forward cone for young showers ($s \sim 1$). I assume that this distribution should be fitted by a suitably binned binominal distribution of the form $(p + q)^n$ where p = probability of a π^0 residing in forward cone = $\frac{1}{2}$; q = probability of a π^0 residing in backward cone = $\frac{1}{2}$; n = number of π^0's available ($n = A^{0.13}(2.9 \log E + 0.03E^{\frac{1}{2}})$). (Feinberg [1972]). Figs. 5.15a) and 5.15b) are the experimentally determined distributions for showers which begin in the lead and either continue under or are absorbed in the iron respectively.

Figure 5.15a) Comparison of measured ——— and predicted - - - distribution of R where

$$R = \frac{\text{Total number of flashes outside central 3 tubewidths}}{\text{Total number of flashes within central 3 tubewidths}}$$

for bursts which begin in the lead and continue beneath the iron.

The diagram indicates how these regions correspond to the forward and backward regions of the nuclear-electromagnetic bursts.

The measured distribution is for all bursts in the size-range 500 to 1000 particles under the lead.

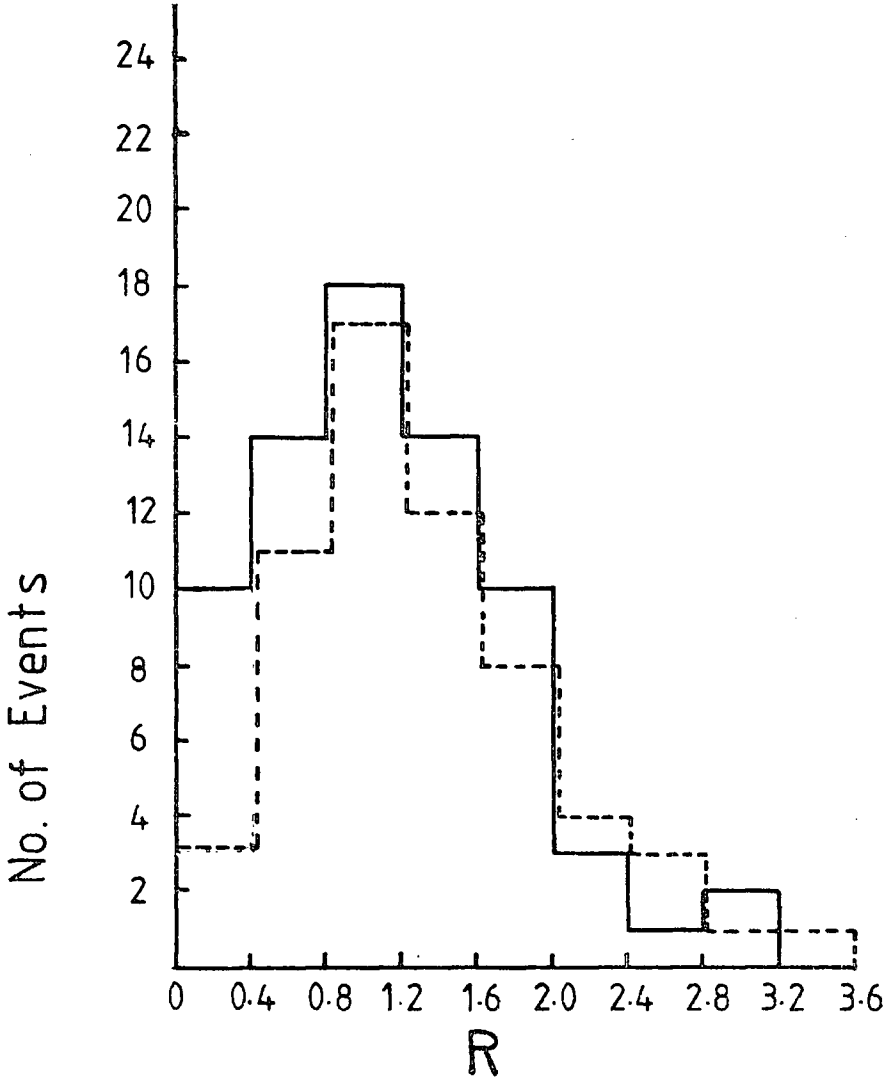
No. of Events
24
22
20
18
16
14
12
10
8
6
4
2
0
0.4
0.8
1.2
1.6
2.0
2.4
2.8
3.2
3.6
R

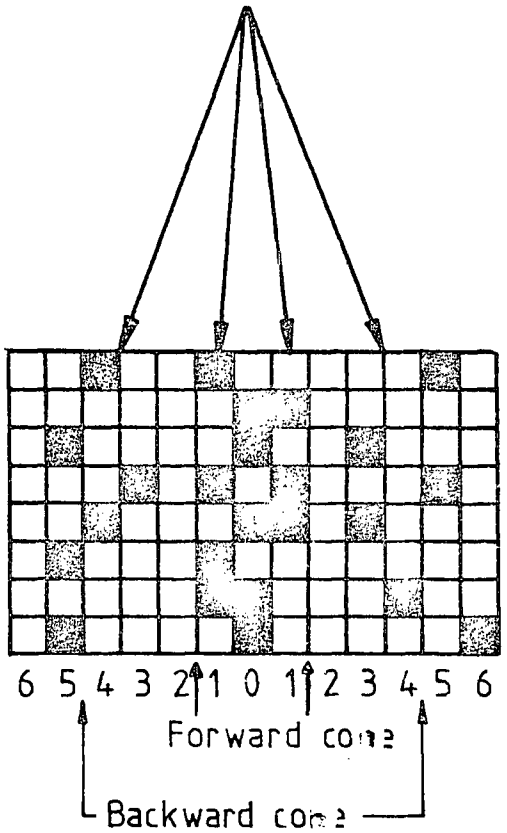
6 5 4 3 2 1 0 1 2 3 4 5 6
Forward cone
Backward cone

FIG. 5·15 a)

Figure 5.15b) As for Fig. 5.15a) but for bursts that begin in the lead but do not continue under the iron.

FIG. 5·15 b)

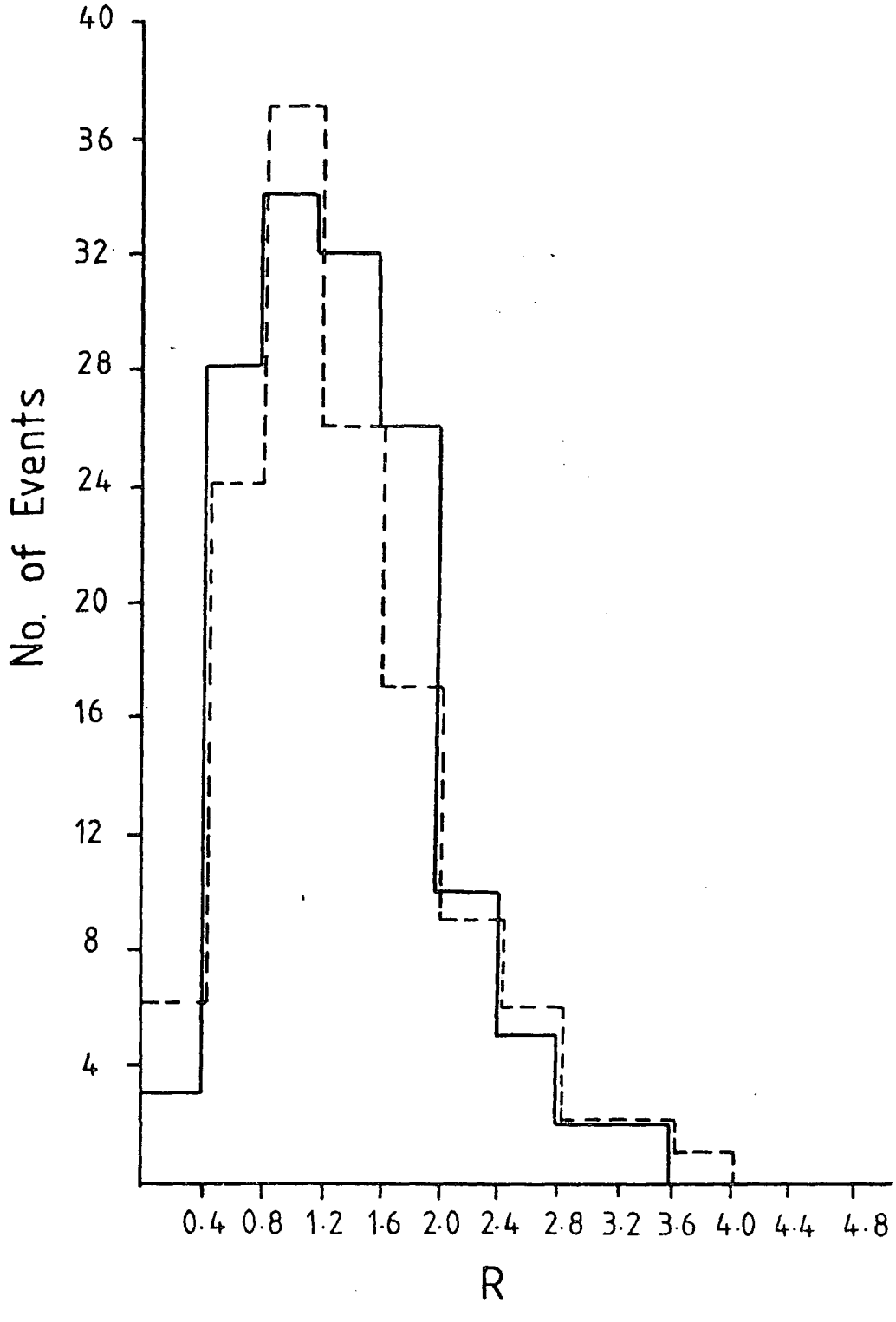
40
36
32
28
24
20
16
12
8
4
No. of Events
0·4 0·8 1·2 1·6 2·0 2·4 2·8 3·2 3·6 4·0 4·4 4·8
R

Included in 5.15a) are the anomolous events (high Z candidates) and they clearly show a significant departure from smooth behaviour.

Clearly, these events, if they are bursts, are not the result of an extreme fluctuation from normal behaviour, e.g. very young showers which have begun at the bottom of the lead and are produced by a fluctuation to a large value of n_3 (or n_3^1) in equation 5.11 (5.12), since all experimental measurements of distributions in multiplicity, charged to neutral ratios etc. in accelerator work show smooth behaviour (see for example J. Whitmore [1974]).

One possible explanation is that we are seeing not one distribution but two (possibly three), the majority of events appear to be due to isotropic emission from a centre at rest in the centre of mass system, but very narrow bursts could be part of a distribution due to emission from a centre moving forward in the centre of mass system, a fireball. One would expect there to be a distribution due to emission from a backward moving fireball as well, but this would only show up as a broadening effect - producing slightly larger than unity value for the peak of the distribution in Fig. 5.15a). In a review of observations of cosmic ray produced interactions, E. L. Feinberg (1972) points out that in this energy range (500 - 1000 GeV) 50% of the events can be attributed to emission from a single fireball with Lorentz factor $\gamma \sim 1.2$ in the centre of mass frame.

In Appendix IV there is a derivation of the value of $\gamma_{c.m.}$ required to simulate a high Z particle (i.e. that all the pions are emitted with an angular spread less than the width of one tube, assuming there is no significant broadening, because of the high energies involved, due to scattering of the subsequent electron - photon shower). The conclusion is that these events could be due to emission from a fast forward moving fireball

with $\gamma \geq 3$ in the centre of mass frame. According to Jabs (1975), a fireball produced at such a high velocity is probably due to the fragmentation or leading isobar component rather than the pionisation component. This is puzzling because the leading isobar is generally regarded as an excited nucleon which emits pions as it decays back to the ground state. However, the pionisation component is the one responsible for the subsequent electron - photon shower, since this is where the high multiplicity of pions originates, so we would not expect to see any narrowing effects on the shower due to the isobar fireball.

5.7 Conclusions

The lack of response from the liquid scintillator above the lead would indicate that the special events originate in some interaction with the lead. No evidence for the observation of a highly ionising component of the cosmic radiation at sea-level was observed. Assuming an isotropic distribution this means that the upper limit on the flux of high Z particles at sea-level at the 90% confidence limit is $2.3.10^{-8}$ $cm^{-2}st^{-1}sec^{-1}$.

A possible high Z particle that might be produced in lead would be the new class of hadrons predicted by Yock, but these should have been detected in accelerator experiments (there might be similar problems of identification however) since the production threshold is only ~ 500 GeV.

If the anomolous events are fast fireballs, then current ideas of fireball models must be modified to accommodate pionisation fireballs with $\gamma_{c.m.} \geq 3$.

One possible modification that would enable the question as to whether or not these events could be high Z particles would be to construct a calorimeter type of apparatus, where the target is interspersed at distances ~1 r.l. with flash-tubes so that shower development can be identified.

CHAPTER 6

THE AIR-SHOWER ARRAY AND FLASH-TUBE CHAMBER

6.1 The Durham Extensive Air Shower Array (D.A.S.A.)

6.1.1 Introduction

D.A.S.A. was built in the period 1973 - 1976 on the Durham University Science Site by members of the M.A.R.S. research group under the supervision of Dr. M. G. Thompson.

The array (see Fig. 6.1) is based on two triangular networks for efficient triggering, with various intervening detectors for improved density sampling. The situation is as closely as possible symmetric about the two previously independent cosmic ray detecting instruments already in existence, the neon flash-tube chamber and a muon spectrograph (M.A.R.S.) (the latter has now been dismantled).

The dimensions of the array make it most sensitive to air showers in the range 10^5 to 10^7 particles, showers which come from primaries which are in the "kink" region of the energy-spectrum.

All of the array detectors are plastic scintillators, fourteen in all. Each detector is viewed by several photomultiplier tubes to record the particle density, and, on seven of the detectors is a photomultiplier tube that is used for fast timing measurements. Four sizes of scintillator are used. The $2m^2$ scintillators are based at the apexes of the triangular

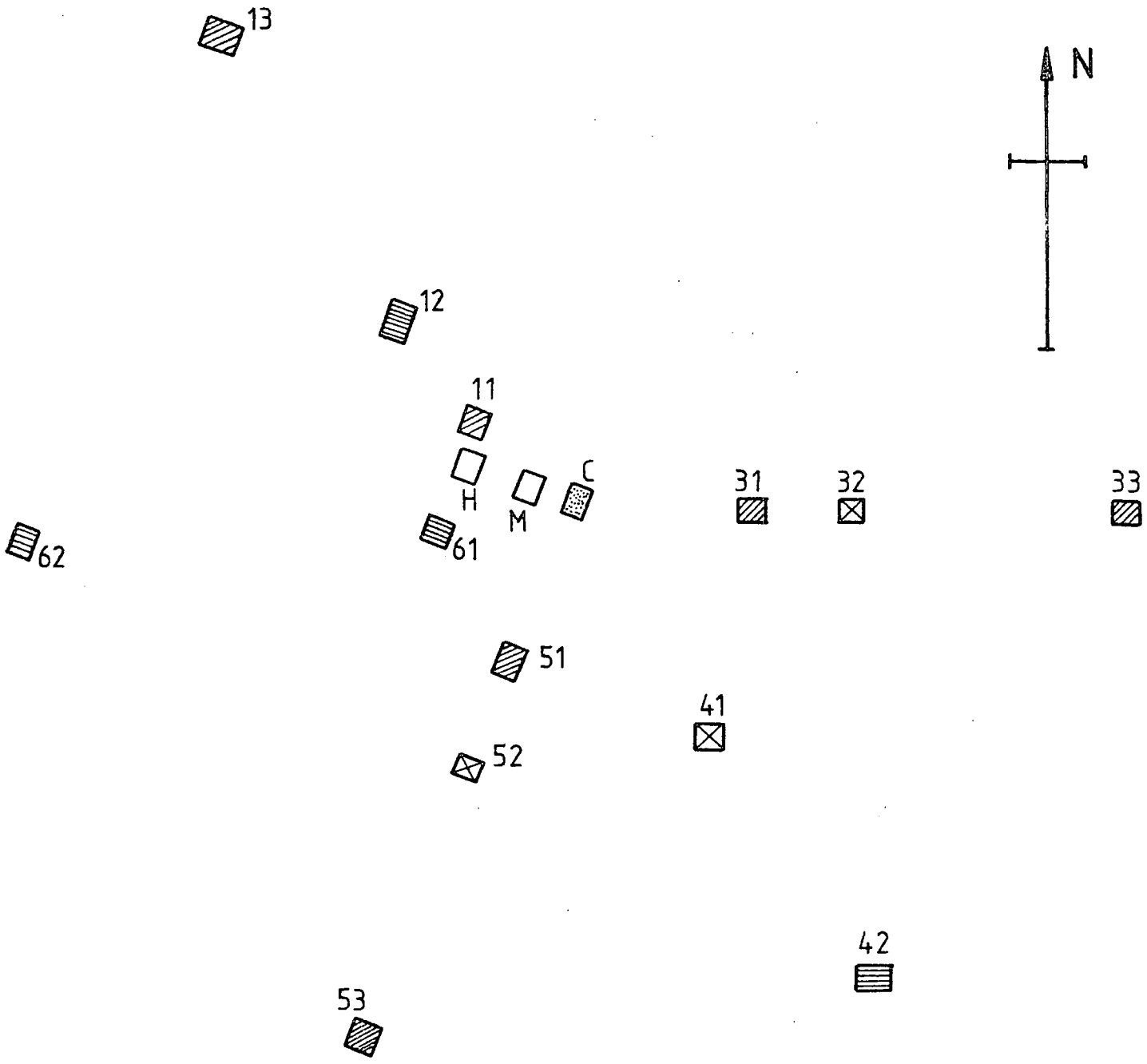

Key	Description
	0.75 m^2 — Density and fast timing
	2.0 m^2 — Density and fast timing
	1.6 m^2 — Density
	1.0 m^2 — Density
M	Muon Spectrograph
H	Hadron Chamber

0 — 25 m

Scale

FIG 6.1

The Durham Extensive Air Shower Automated Research Array.

networks, and provide (with the 0.75 m^2 central detector C) triggering, fast timing and density pulses.

6.1.2 The central detector C

This detector is situated on the roof of the laboratory containing the flash-tube chamber at the centre of the air-shower array. It has geometrical area 0.75 m^2 made up of two identical 5 cm thick slabs of NE102A plastic scintillator each viewed by two Philips 53AVP photomultipliers via perspex light guides. Attached to one of the light guides on each half is a Philips 56AVP photomultiplier which supplies the timing pulse to which all of the other timing pulses are referred (see Fig. 6.2a)).

6.1.3 The 2.0 m^2 detectors

There are six 2.0 m^2 detectors forming the backbone of the air-shower array, they are used in coincidence with the central detector to establish an event. They each consist of a 2 m x 1 m x 2.5 cm slab of NE110 plastic scintillator viewed by four 5" diameter E.M.I. 9579B photomultiplier tubes for particle density measurements and one 2" diameter Philips 56AVP photomultiplier tube for fast timing. The configuration of the photomultiplier tubes is shown in Fig. 6.2b).

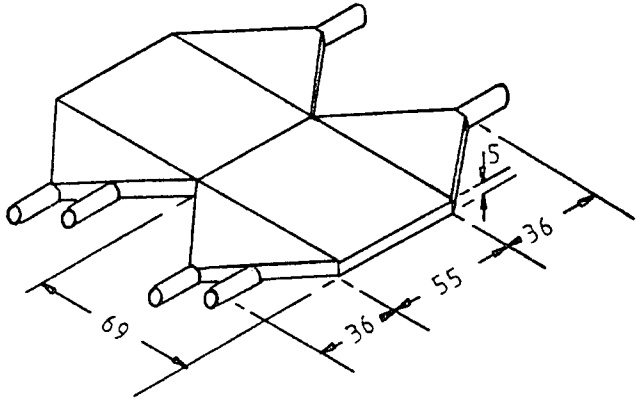

(a) The central detector (NE102A)

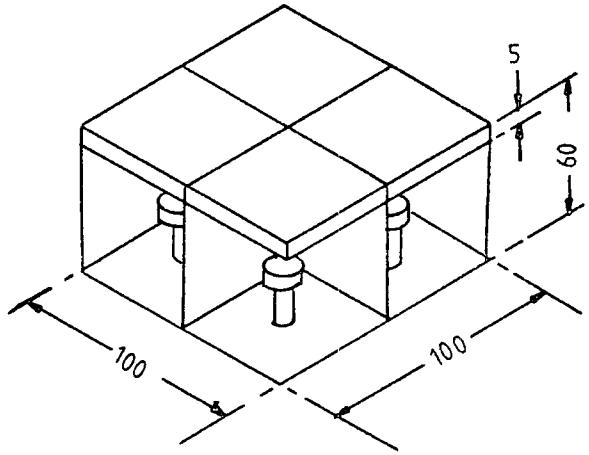

(d) A 1·0m^2 detector (composition unknown)

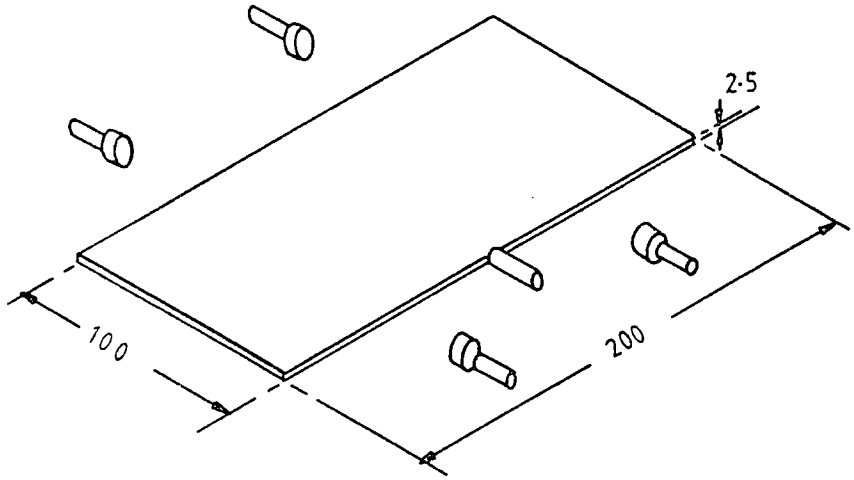

(b) A 2·0m^2 detector (NE110)

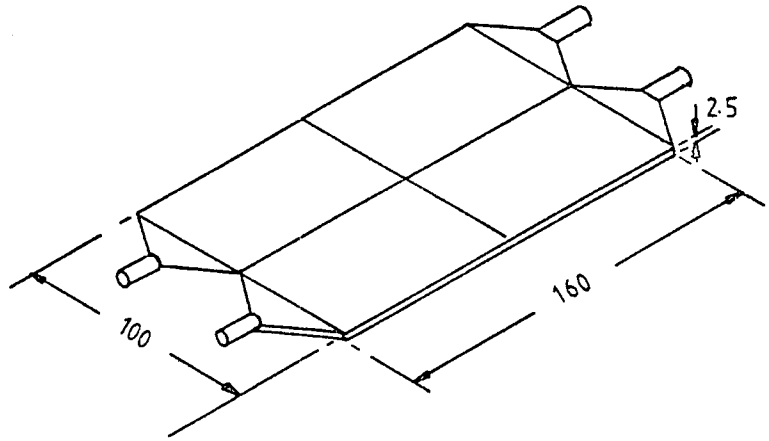

(c) A 1·6m^2 detector (NE102A)

FIG.6·2 The Array Scintillators.

6.1.4 The 1.6 m^2 detectors

There are four of these detectors, each consisting of four individually light-proofed quarters of 2.5 cm thick slab of NE102A plastic scintillator. Each quarter is viewed by a Philips 53AVP photomultiplier tube through a perspex light guide (see Fig. 6.2c)).

6.1.5 The 1.0 m^2 detectors

There are three of these detectors in the array, each situated approximately 25 m from the central detector. They each consist of four identical individually light-proofed slabs of 5 cm thick scintillator. The scintillator plastic is not of the highest quality necessitating viewing each slab broad-face on with a photomultiplier tube. This does have the advantage of increasing the detector's response to almost unity over all its area. The arrangement of photomultipliers is depicted in Fig. 6.2d).

6.2 Air-shower detection and measurement

The arrival of an air shower is detected by coincidence between a pulse from scintillator C and either the three inner 2.0 m^2 scintillators, or the three outer scintillators. The former mode has a smaller collecting area but can be used to study small air-showers ($\sim 5.10^4 - 10^5$ particles) or to examine in detail the core-structure of larger air-showers. The latter mode makes full use of the available collecting area and is used either as a bare air-shower trigger, with no electron component information recorded, or to examine the shower size spectrum up to 10^7 particles.

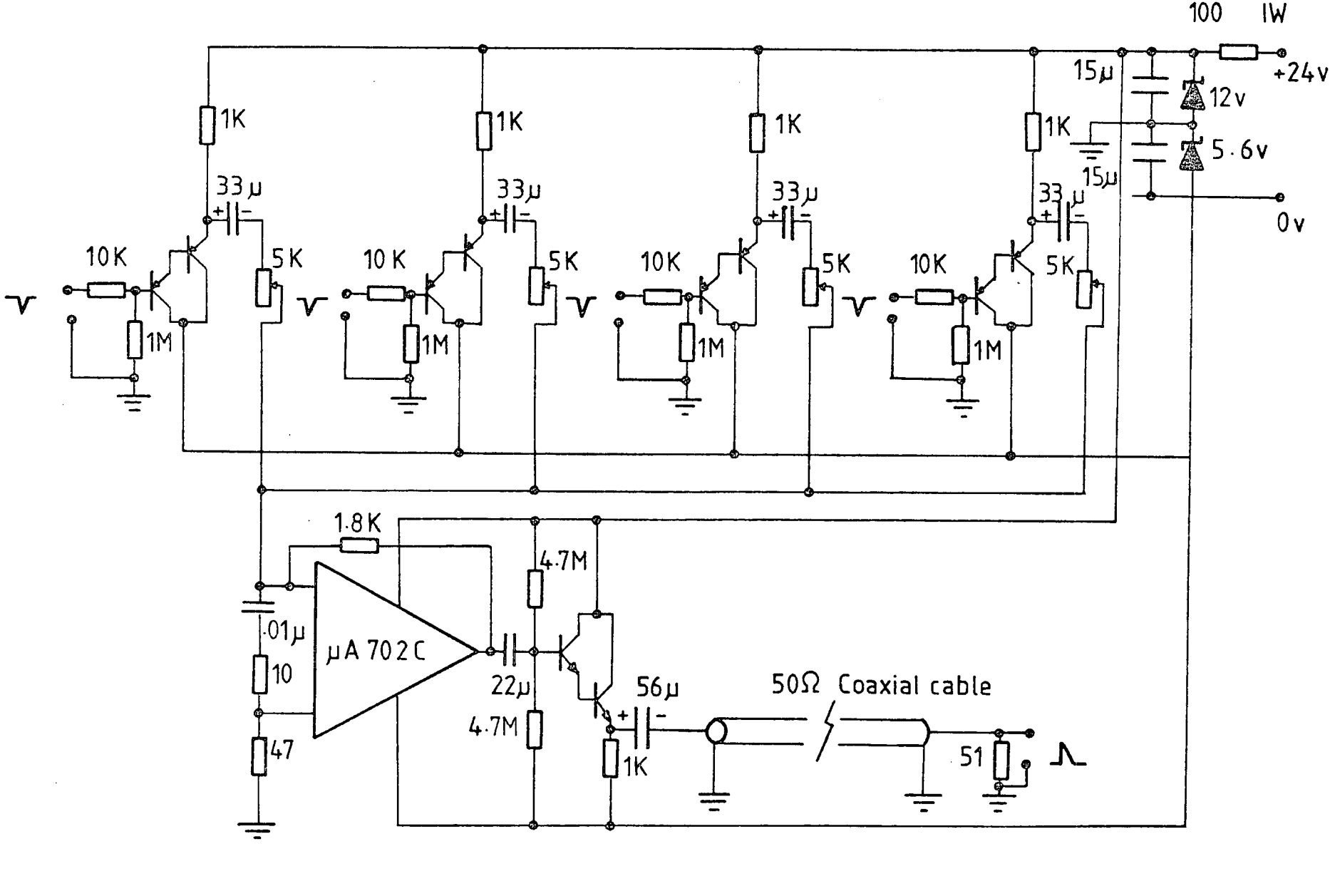

FIG. 6·3 Four input gain five mixer-amplifier (Transistors: PNP ZTX501, NPN ZTX301)

The density pulses used for air shower size and core location are provided by the "slow" photomultiplier tubes and have an exponential delay time constant of 20 μs. The pulses used for fast timing measurements, to determine the direction of arrival of the shower or investigate shower-front structure, are provided by the "fast" photomultiplier tubes, and are of ~5nS f.w.h.m.

The pulses from each photomultiplier viewing a single scintillator are summed in a mixer amplifier at the detector which also inverts the signal (see Fig. 6.3). The consequent positive pulses are then sent via an emitter-follower down RG58 c/u 50Ω coaxial cable to the data storage units in the laboratory. This cable has no significant effect on the shape of either the density or fast timing pulses, however, pulse information propagates down such a line with 0.9dB per 100 m loss, which has to be compensated for by increasing the photomultiplier E.H.T.

The outputs of the mixer-amplifiers are calibrated such that the pulse height corresponds to the number of particles per square metre (i.e. density) detected by the whole scintillator which that mixer-amplifier serves.

The progress of the pulses after leaving the cables is depicted in Fig. 6.4. All pulses are first amplified and split to provide information on the pulses as well as a driving pulse for a discriminator to provide event triggers and a monitor of the rate of detection of individual detectors.

The timing pulses are converted to pulse height measurements via time-to-amplitude conversion monitors (T.A.C.). These 'start' on the arrival of a timing pulse from detector C, and 'stop' on the arrival of a timing pulse from a scintillator. An analogue pulse corresponding in height directly to the delay time between the arrival of a pulse from detector C and a timing scintillator is then available for digitisation and storing.

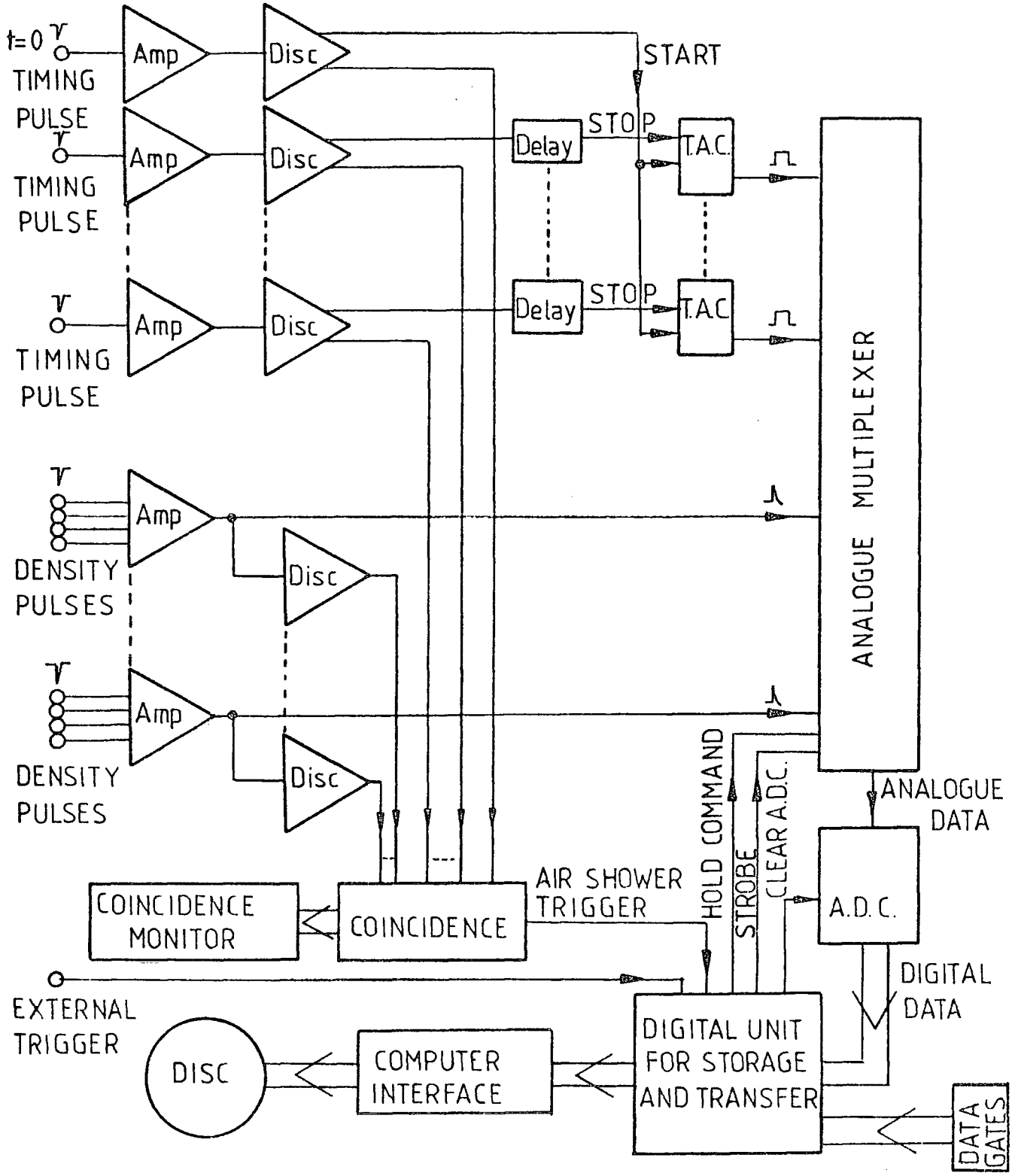

FIG.6·4. The Event Handling Circuitry.

All such timing pulses and the density pulses are held in an Analogue Multiplexer and sequentially released to an Analogue to Digital Converter (A.D.C.) for subsequent digitisation.

The digitised pulse heights are read into a unit for storage and transfer to an I.B.M. 1130 computer where they are stored on magnetic tape or disc for subsequent analysis on a larger computer.

6.3 Expected range of the air-shower array

If we assume that a relativistic electron produces a pulse with a unique size then it is a simple matter to calculate the expected shower size range and range of core distances that can be expected for a given discriminator level on the coincidence unit fed by the triggering scintillators.

Such calculations are only a first-order approximation since a relativistic particle produces a spectrum of pulse heights in a scintillator. Since the spectrum produced can be described by a Lorentzian type of curve (see, for example, Chapter 3, Section 3) it has a long tail. Hence the mode of such a spectrum can be more accurately determined than the mean, and for daily calibration testing it proves a more convenient parameter. However, if more accurate determination of the shower size range and range of core distances detectable by the array are required, these fluctuations must be folded into the calculations. This essentially has the effect of increasing the collecting areas for all shower sizes, and especially reduces the minimum shower size that can be detected. This effect, though, is somewhat compensated for by the difficulties of analysing small shower sizes, because of the relatively large errors present on small particle density determinations.

FIG. 6.5

Collecting areas for showers of size $n.10^5$ particles producing ≥ 2 particles $m.^{-2}$ in detectors C,13,33,53 simultaneously. (NORMAL MODE).

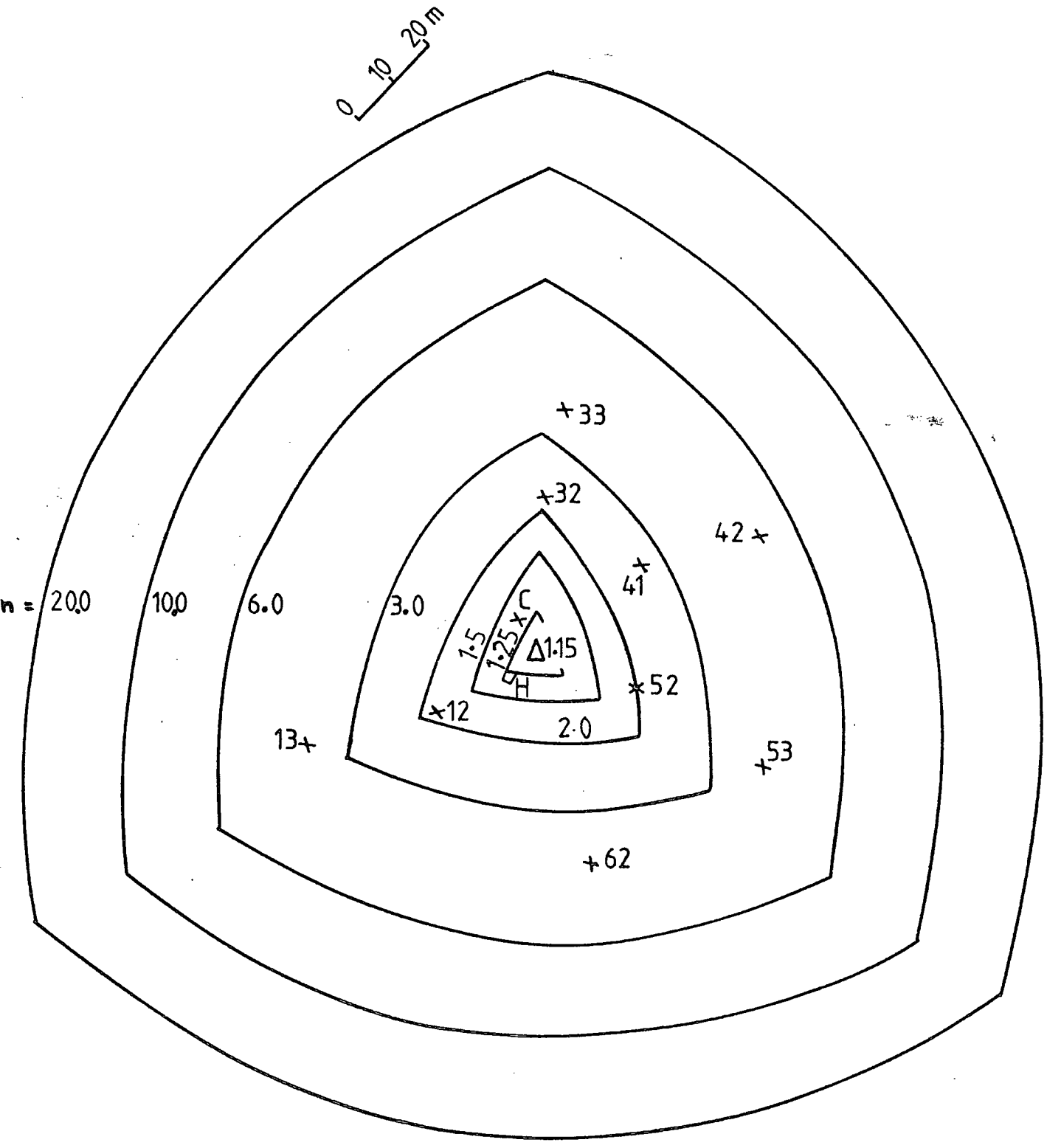

Fig. 6.5 shows the expected collecting areas (assuming every relativistic electron produces a pulse at the mode of the distribution) for different shower sizes based on ≥ 2 particle m^{-2} being detected in each of the scintillators C, 13, 33 and 53 in coincidence. Figs. 6.6a) and 6.6b) show the resulting range of shower-sizes and core-distances detectable under these triggering requirements.

It can be seen that for a triggering requirement of 2 pt m^{-2} in each of the outer 2 m^2 scintillators and 2 pt m^{-2} in the central detector, from Figs. 6.6a) and 6.6b), the median shower size detectable is 6.5 10^5 pt and the median core-distance is 36 m.

6.4 Triggering modes with external devices

The Flash-Tube Chamber can be used in conjunction with the array in a variety of ways. Either an event in the chamber can be used to trigger the array, or vice-versa, or a coincidence between the air-shower coincidence unit and the flash-tube chamber, or the two apparatuses can be triggered independently and correlated by a visual scaler, corresponding to the book keeping scaler incorporated in the air-shower data storage unit, being photographed accompanying the flash-tube chamber events.

6.5 The modified flash-tube chamber

6.5.1 Reasons for modifying the flash-tube chamber

The flash-tube chamber was originally built to search for fractionally charged particles (quarks) that may be present in the sea-level cosmic

FIG. 6.6a) Range of Shower Sizes Detectable.
(NORMAL MODE).

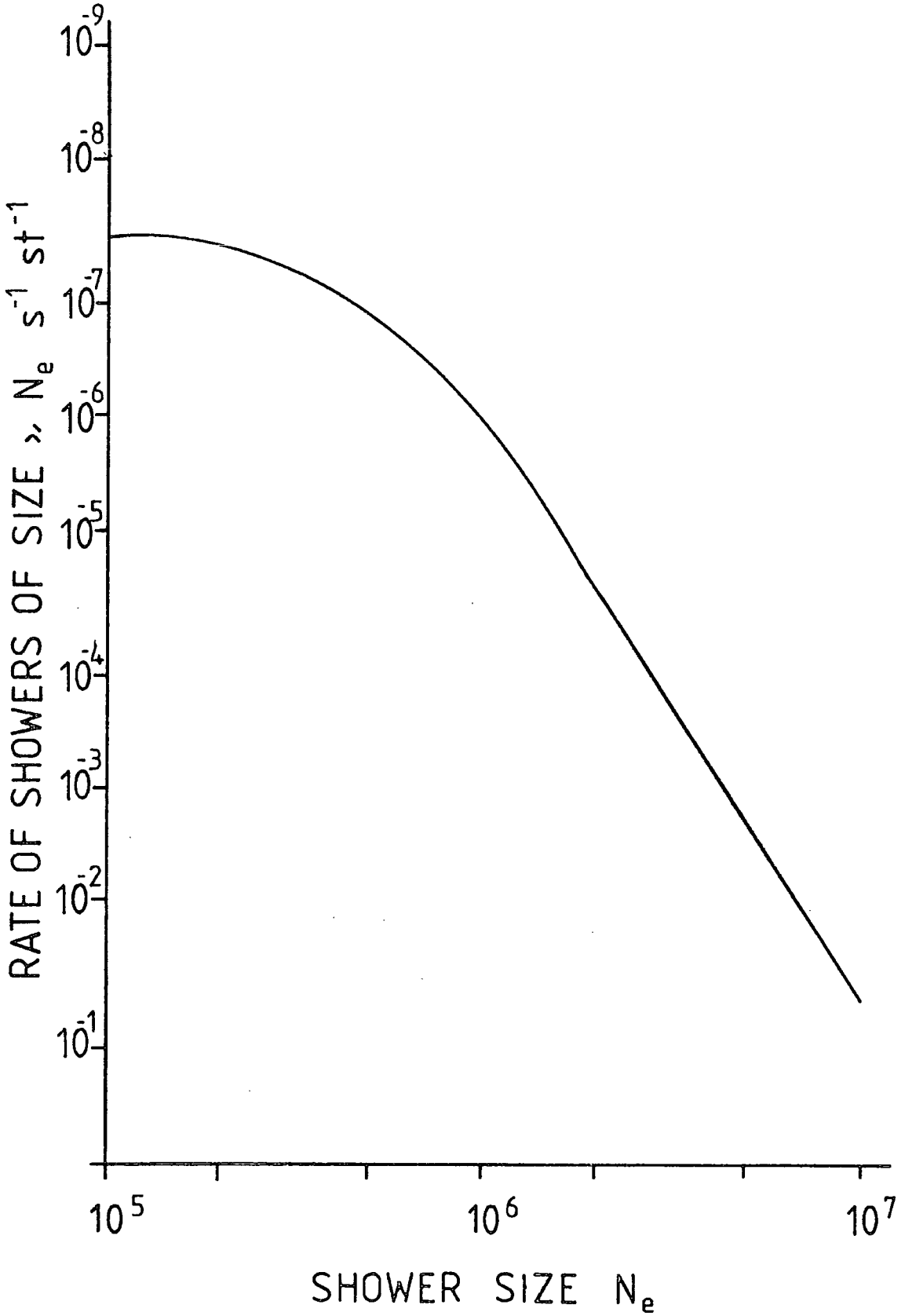

FIG 6.6b) Rate of showers which fall at a distance greater than r metres from the flash-tube chamber that can be detected when the air-shower array is operated in NORMAL MODE.

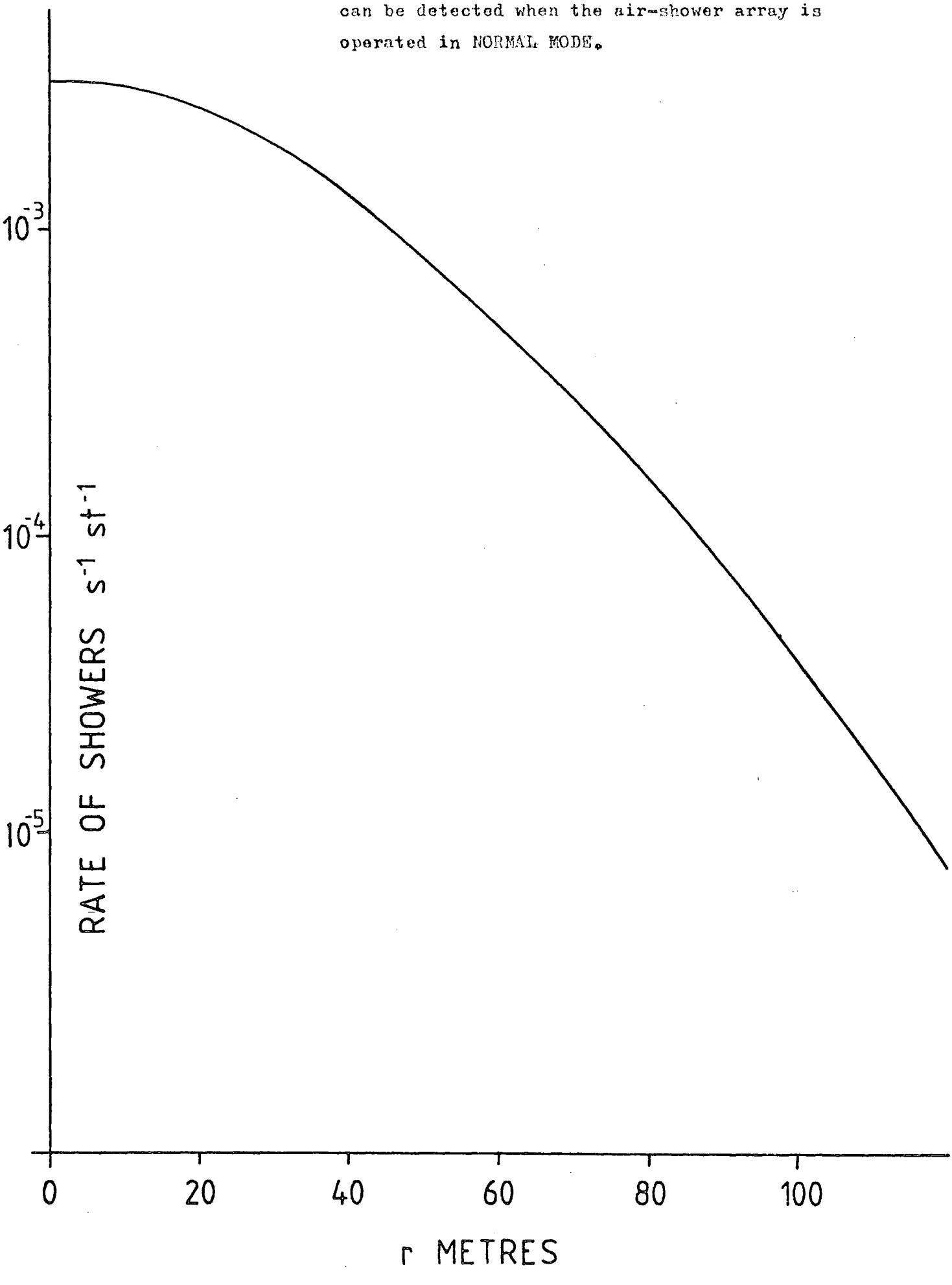

radiation. It was found in a number of quark searches (D. Cooper [1974], A. Parvaresh [1975]) that a fractionally charged particle could be simulated by a background muon if the latter had travelled through the chamber ~100 μs before the application of the H.T. pulse (see Fig.2.7 in Chapter 2). To eliminate these background effects a previous particle indicator is required that is sensitive to particles which travel through any region of the flash-tube chamber where they might simulate a fractionally charged particle, and which arrive in the time-interval 50 μs to 150 μs prior to the application of the H.T. pulse.

Such a previous particle indicator could be provided by the modifications required to incorporate into the flash-tube chamber a system for detecting tachyons associated with extensive air showers. Since the shower front travels at approximately the speed of light, any faster than light particle produced at some interaction in the development of the shower should arrive at some time 0 μs to 120 μs prior to the arrival of the air-shower (the precise time depending on the height of production of the tachyon, the speed with which it propagates, and the zenith angle of the shower's direction of travel). If the flash-tube chamber has incorporated into it a, preferably large area, detector that can indicate the time of arrival of particles in the 240 μs prior to the arrival of an air-shower, a comparison of the arrival times and frequency of events between the 0 - 120 μs and the 120 μs to 240 μs prior to the arrival of an air-shower should indicate whether or not there are previous particles associated with air showers.

If the previous particle indicator includes an increased area of scintillator under the iron target this will increase the number of high energy hadron interactions in the iron that can be detected, thus improving the statistics on these comparatively rare events.

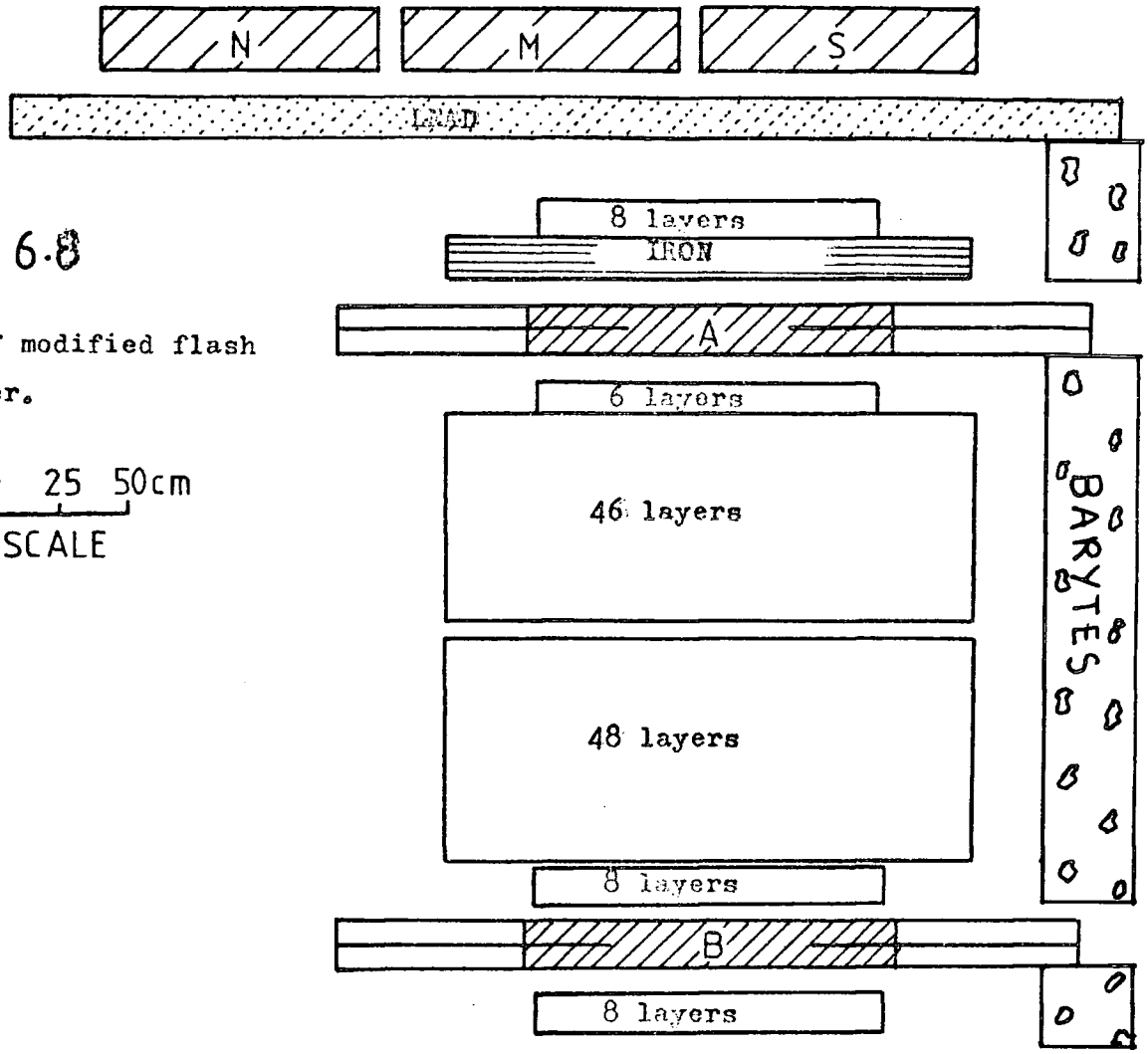

FIG. 6.8

Side view of modified flash-tube chamber.

0 25 50cm
SCALE

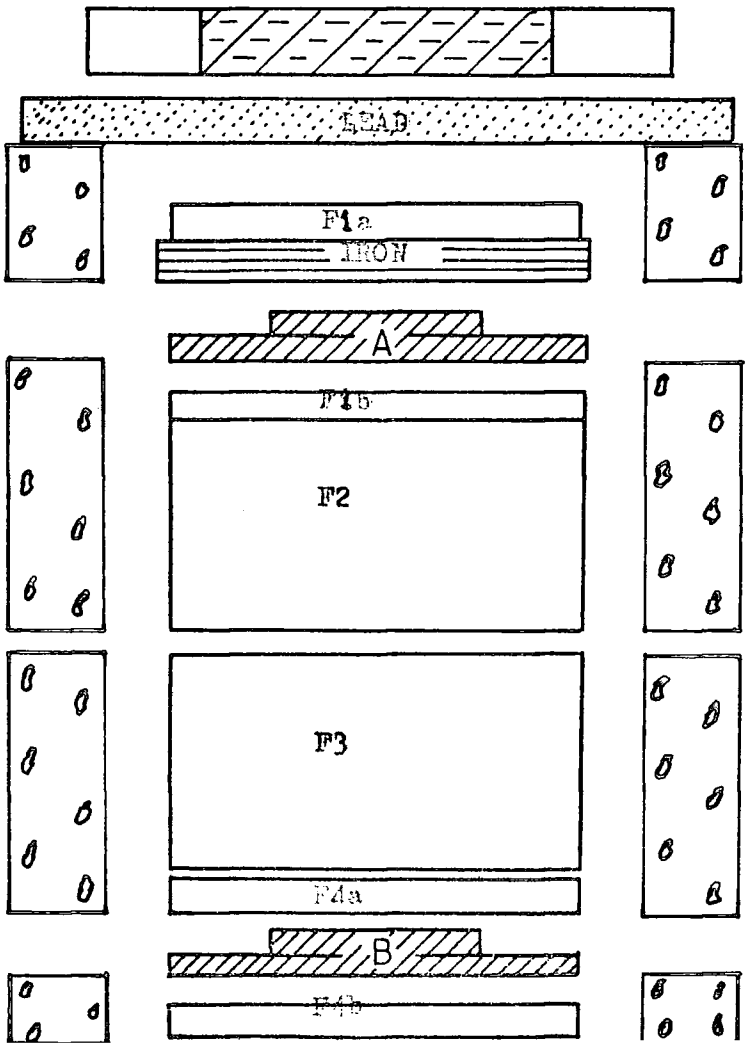

FIG. 6.7

Front view of modified flash-tube chamber.

6.5.2 The previous-particle indicator

To accommodate the facilities outlined above the plastic scintillators under the lead and iron were removed, and three plastic scintillators of identical construction were placed under the iron so as to completely cover the sensitive area of the stack of flash-tubes. Since these scintillators had to be positioned normal to the direction in which the previous scintillators had been removed, the electrodes in the defining layers F1a and F1b had to be shortened further to avoid edge-effects (see Chapter 2, Section 2.3.1). Three more scintillators were similarly positioned below the main body of the chamber between the defining layers F4a and F4b, where again the electrodes had to be shortened.

Diagrams of the modified flash-tube chamber in front and side view are shown in Figs. 6.7 and 6.8.

The six plastic scintillators used were identical in construction and are described in Chapter 2 (see Fig. 2.3).

The H.T. supply to the photomultipliers (6 photomultipliers per scintillator, 36 photomultipliers in all) was a 0 - 3.5 kV Oltronix LS 329R. The optimum operating voltage for each tube having been previously determined (F. Ashton [private communication]), the different voltages were obtained by interposing various resistor chains in the supply line to each tube. The outputs of the three tubes viewing one edge of a scintillator were connected together through 3 parallel identical capacitors C (0.1 uF). This provides a voltage pulse equal to Q/C, where Q is the average charge generated by the 3 photomultipliers. The outputs from each end of a scintillator were added and then the outputs from each scintillator in the same stack (either the upper or lower) were all added before being sent down the delay line.

By storing the pulses in n μs of delay line before displaying them on an oscilloscope, if the time-base of the oscilloscope is triggered by the arrival of an air-shower, the particles that have travelled through the scintillator stacks in the previous n μs can be detected.

The delay line used was copper wire wound on a ferrite core with a delay of 1 μs per foot (Hackethal H.H. 1600). Since the pulses provided by the scintillators were fast (150 ns f.w.h.m.) the delay line caused severe attenuation. This was compensated for by dividing the line into 3 equal sections (each providing 80 μs delay) and interposing an amplifier between each section and between the output of the final section and the oscilloscope. To reduce the attenuation further, a stretcher was inserted between the second adder and the first section of delay line which provided pulses 5 μs wide for input rectangular pulses 0.2 μs wide.

In Chapter 9 is presented a more detailed discussion of the previous particle indicator with the accompanying circuit diagrams (Figs. 9.2a), 9.4) and calibration curves (Figs. 9.1, 9.2b), 9.3a), 9.3b)).

6.5.3 The single particle pulse height distributions of the scintillators

The single particle pulse height (s.p.p.h.) distributions for individual photomultipliers, scintillators and combinations of scintillators are shown in Figs. 6.9a, b, c, d, e and 6.10a, b, c, d, e.

The distributions were obtained using a Laben model 100 pulse height analyser (p.h.a.). The channels of the p.h.a. were calibrated using 100 ns and 200 ns rectangular pulses (Fig. 6.11).

Figure 6.9: Single Particle Pulse Height (S.P.P.H.) distributions for different combinations of photomultipliers viewing the scintillators of scintillator-stack B, (the lower stack).
The position of the photomultiplier(s) producing the different S.P.P.H. distributions is marked with X on an inset plan view of the scintillator-stack on each figure.

Figure 6.9a): S.P.P.H. distribution from one photomultiplier.

Figure 6.9b): S.P.P.H. distribution from three photomultipliers.

Figure 6.9c): S.P.P.H. distribution from six photomultipliers, a single scintillator.

Figure 6.9d): S.P.P.H. distribution from twelve photomultipliers, the two coplanar scintillators.

Figure 6.9e): S.P.P.H. distribution from eighteen photomultipliers, the whole of stack B.

FIG. 6·9 a)

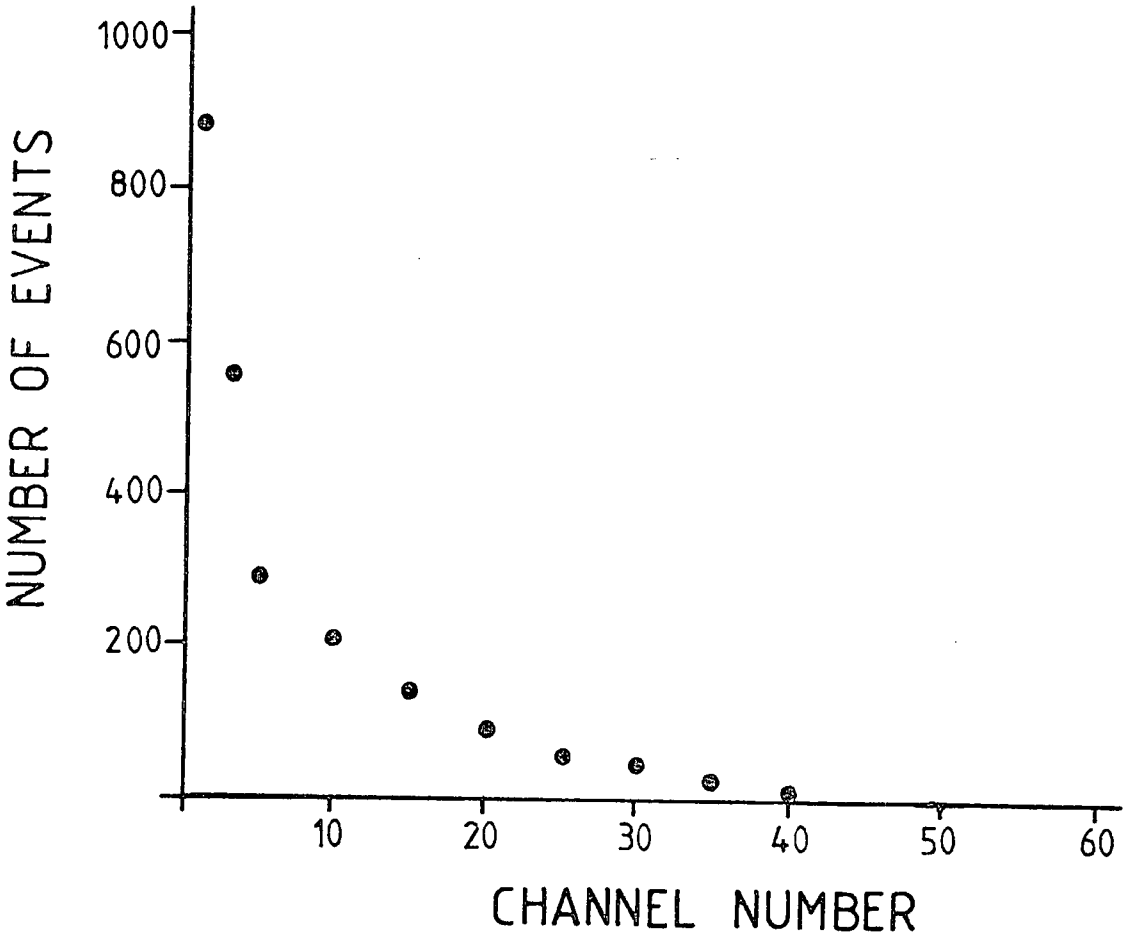
NUMBER OF EVENTS
1000
800
600
400
200
10
20
30
40
50
60
CHANNEL NUMBER

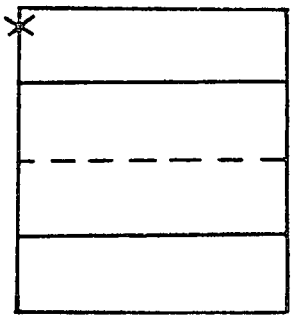

FIG. 6·9 b)

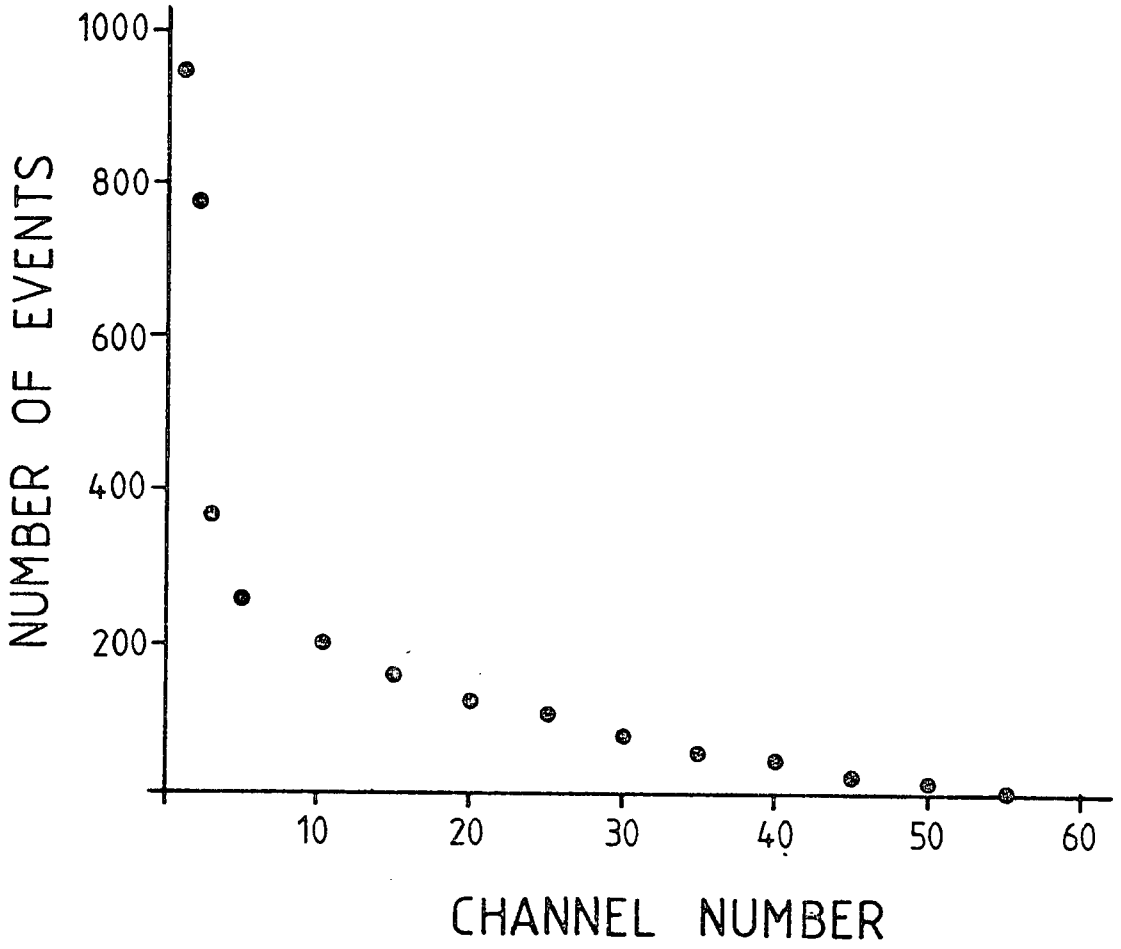
NUMBER OF EVENTS
1000
800
600
400
200
10
20
30
40
50
60
CHANNEL NUMBER

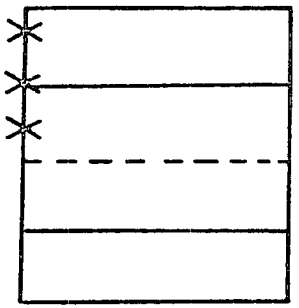

FIG. 6·9c)

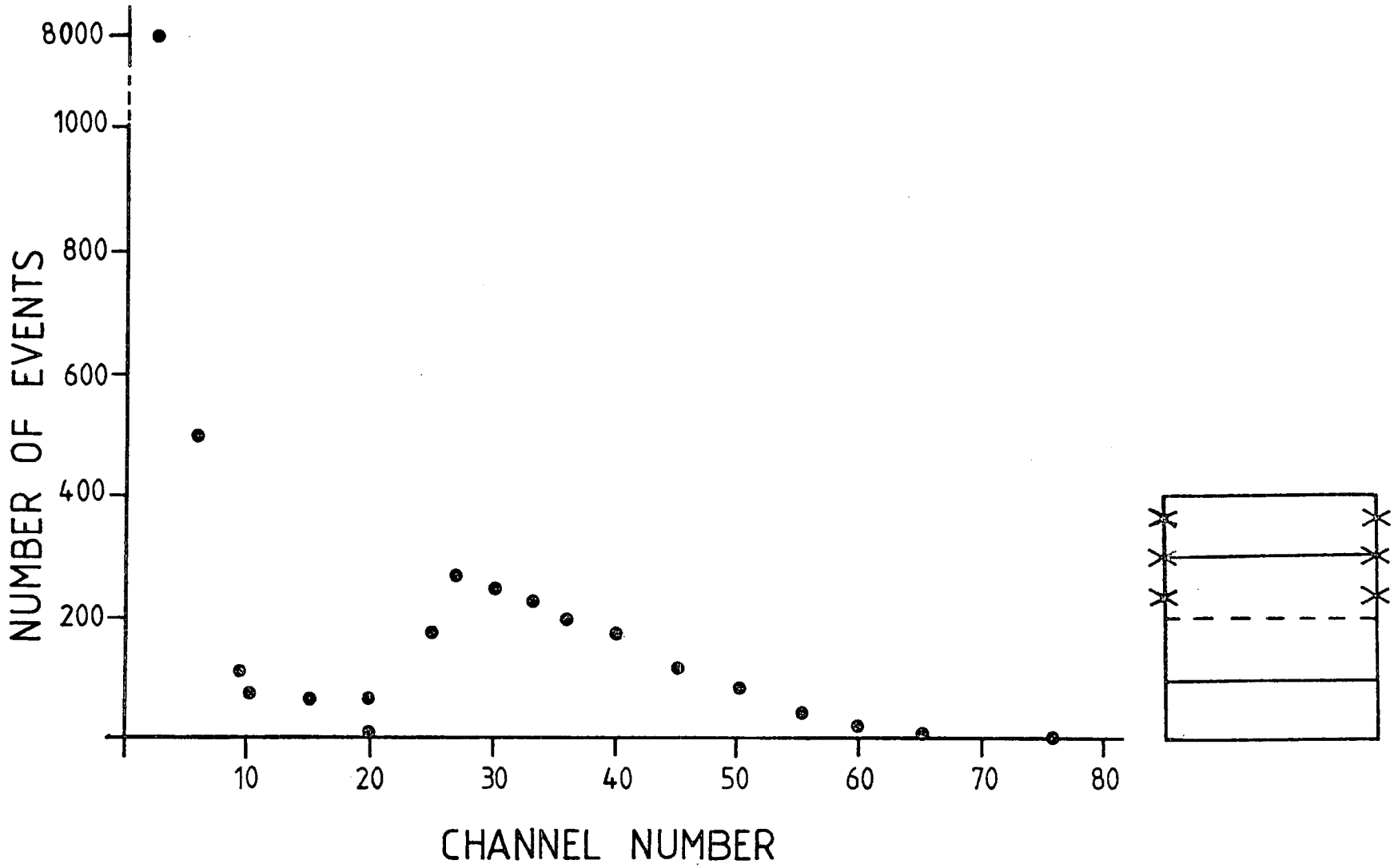
8000
1000
800
600
400
200
NUMBER OF EVENTS
10
20
30
40
50
60
70
80
CHANNEL NUMBER

FIG. 6.9 d)

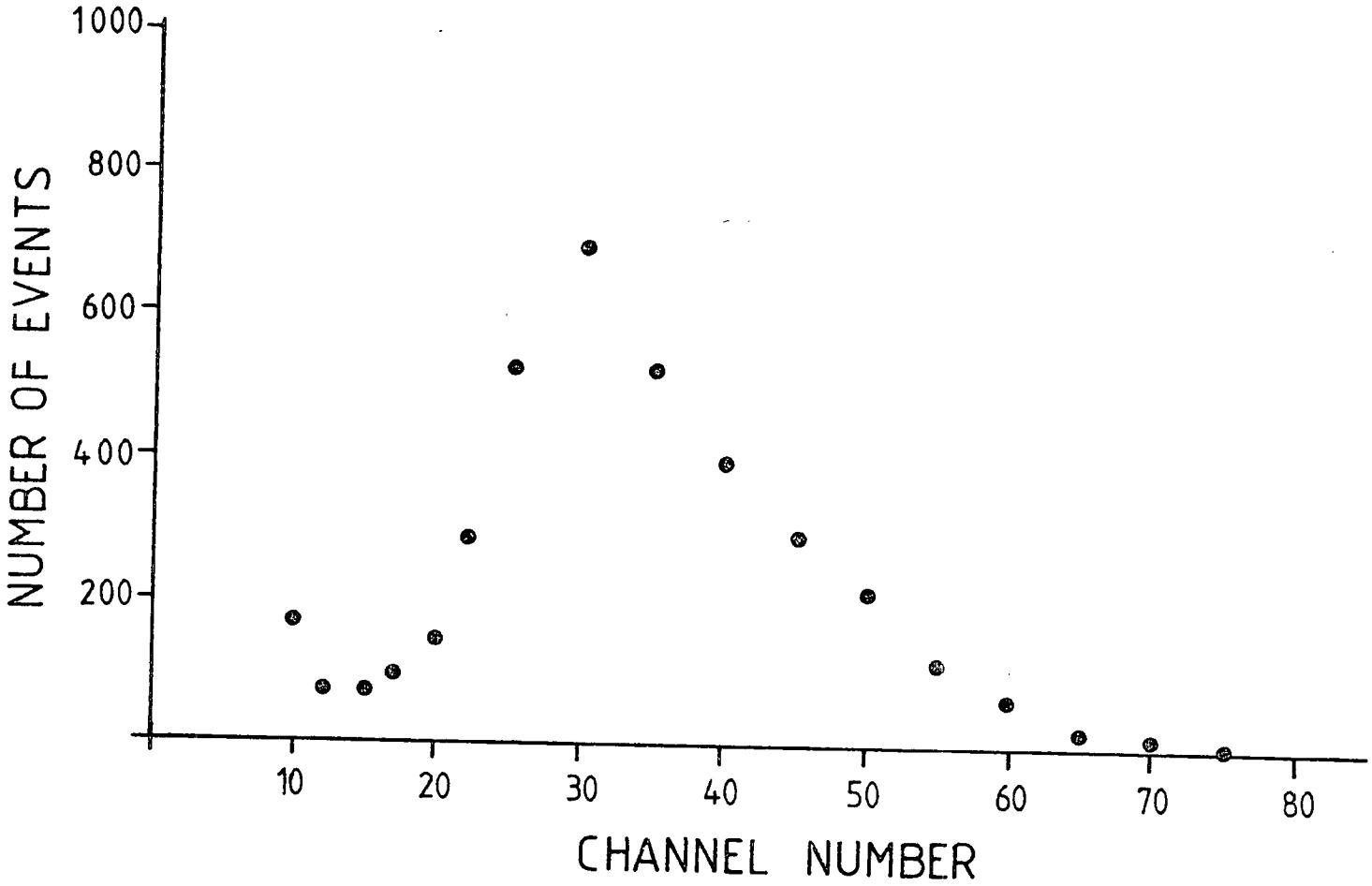
1000
800
600
400
200
NUMBER OF EVENTS
10
20
30
40
50
60
70
80
CHANNEL NUMBER

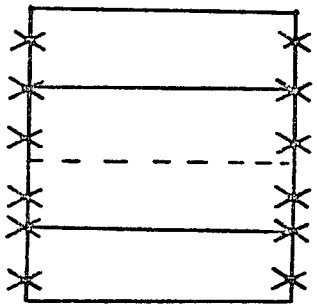

FIG. 6.9e)

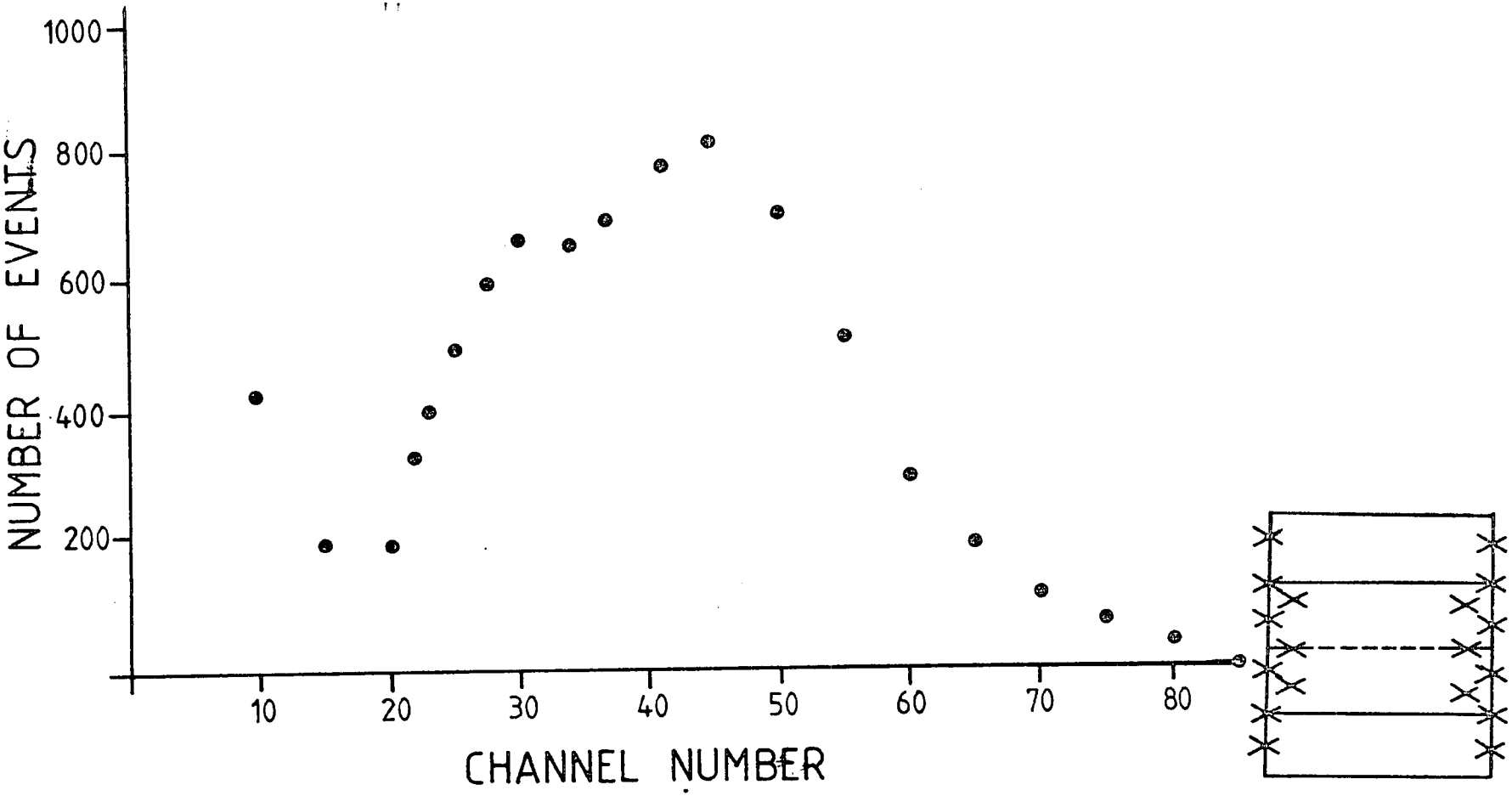
1000
800
600
400
200
NUMBER OF EVENTS
10
20
30
40
50
60
70
80
CHANNEL NUMBER

Figure 6.10: Single Particle Pulse Height(S.P.P.H.) distributions for different combinations of photomultipliers viewing the scintillators of scintillator-stack A, (the upper stack).

Figure 6.10a): S.P.P.H. distribution from one photomultiplier.

Figure 6.10b): S.P.P.H. distribution from the three photomultipliers viewing one end of the top scintillator of the stack.

Figure 6.10c): S.P.P.H. distribution from the six photomultipliers viewing the whole of the top scintillater.

Figure 6.10d): S.P.P.H. distribution from the twelve photomultipliers viewing the two bottom co-planar scintillators of the stack.

Figure 6.10e): S.P.P.H. distribution from the eighteen photomultipliers viewing the whole of the upper stack A.

FIG. 6·10 a)

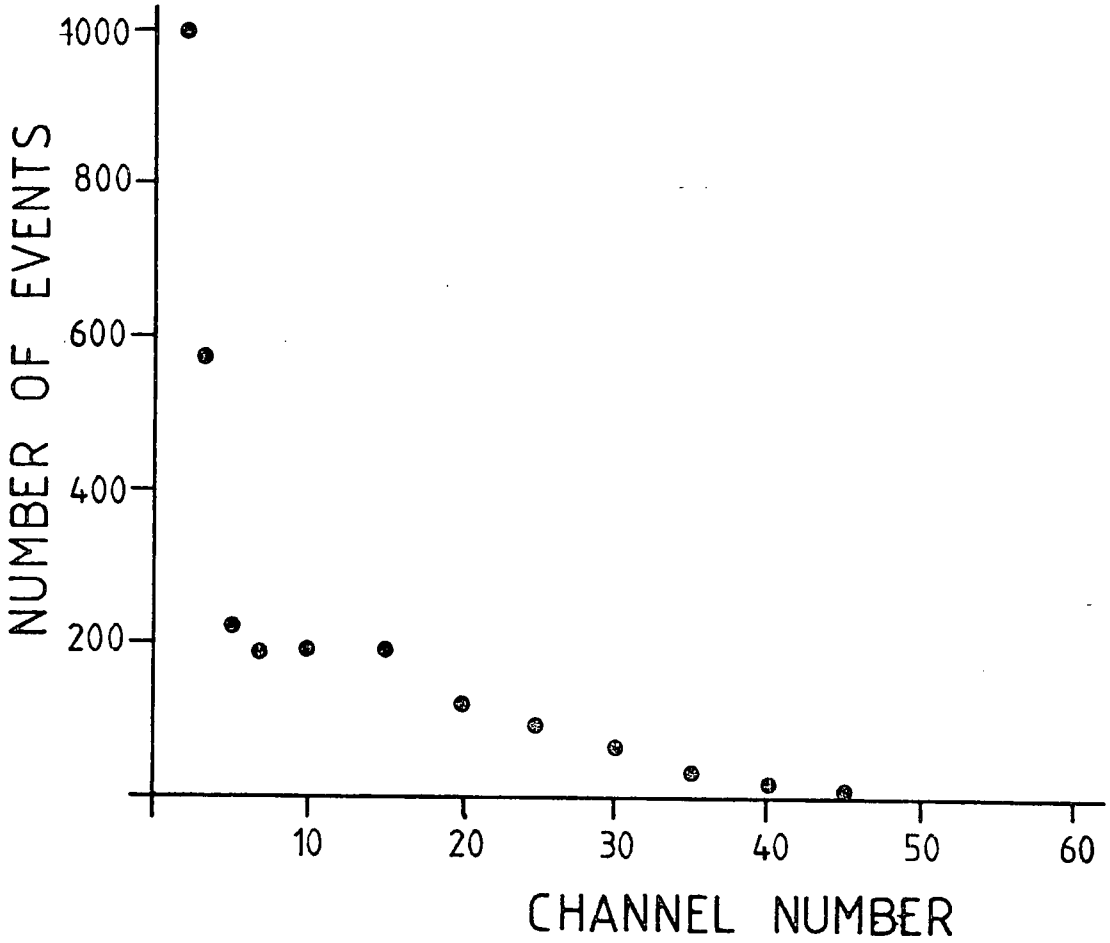
NUMBER OF EVENTS
1000
800
600
400
200
10
20
30
40
50
60
CHANNEL NUMBER

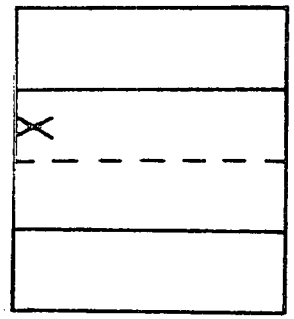

FIG. 6·10 b)

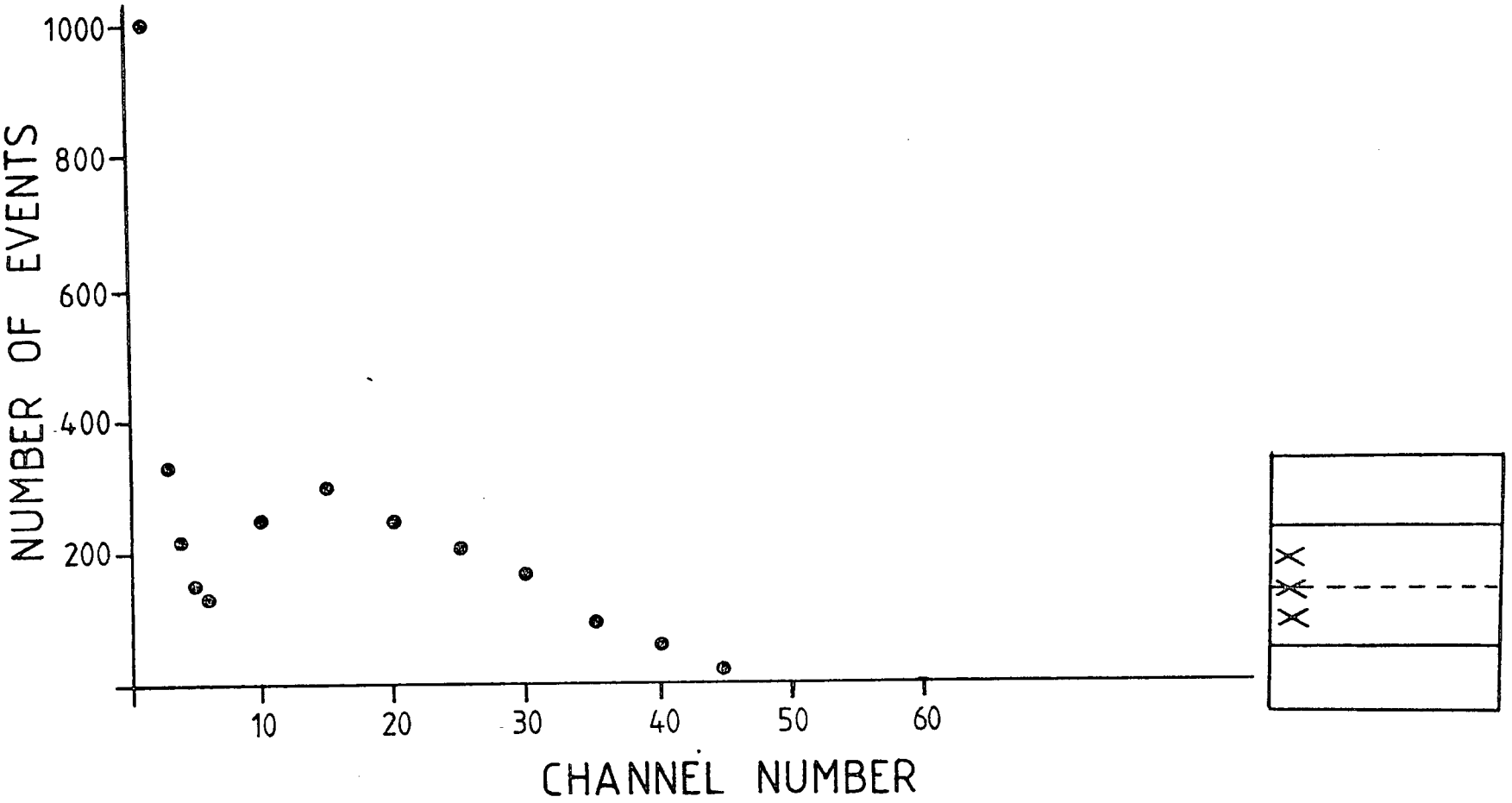
1000
800
600
400
200
NUMBER OF EVENTS
10
20
30
40
50
60
CHANNEL NUMBER

FIG 6.10c)

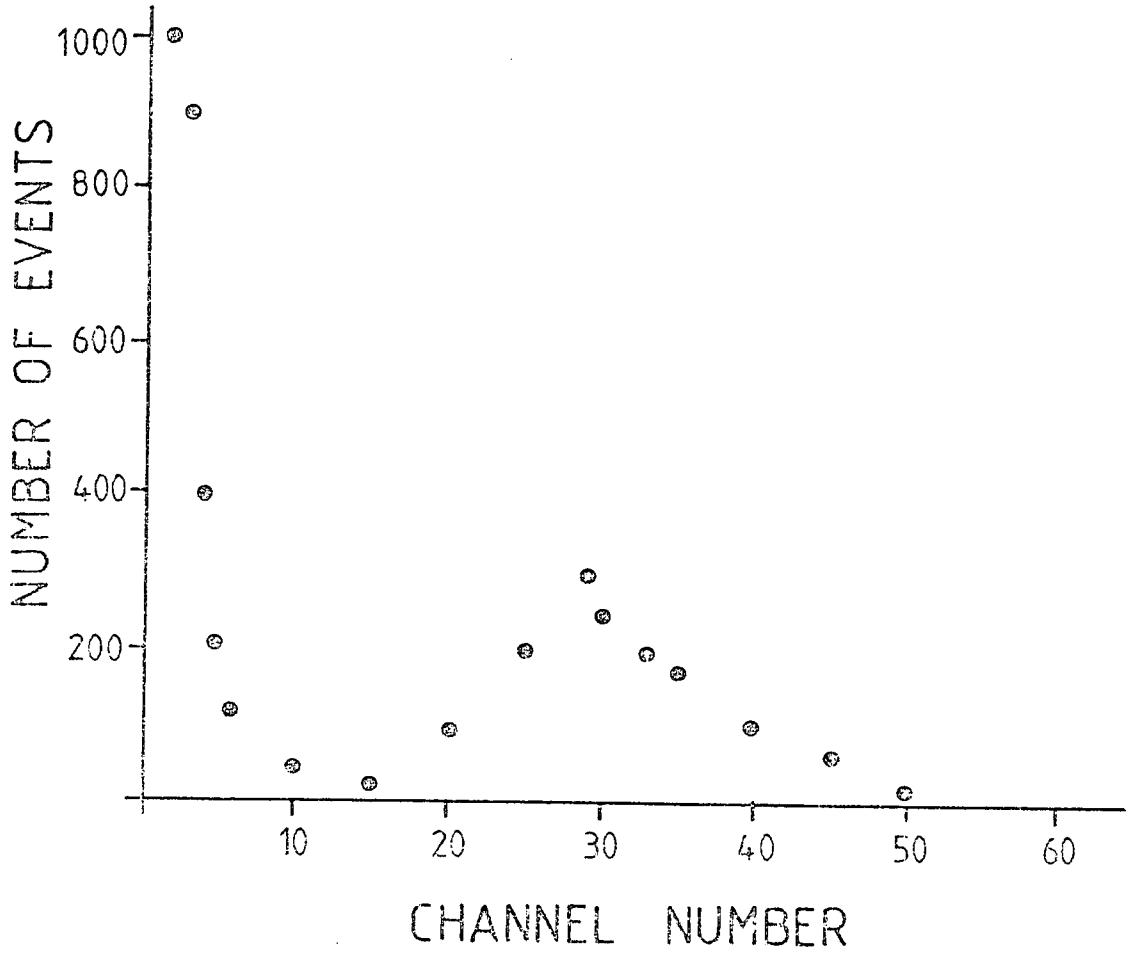
NUMBER OF EVENTS
1000
800
600
400
200
10
20
30
40
50
60
CHANNEL NUMBER

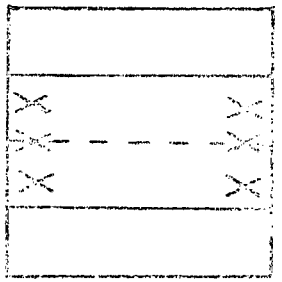

FIG. 6·10 d)

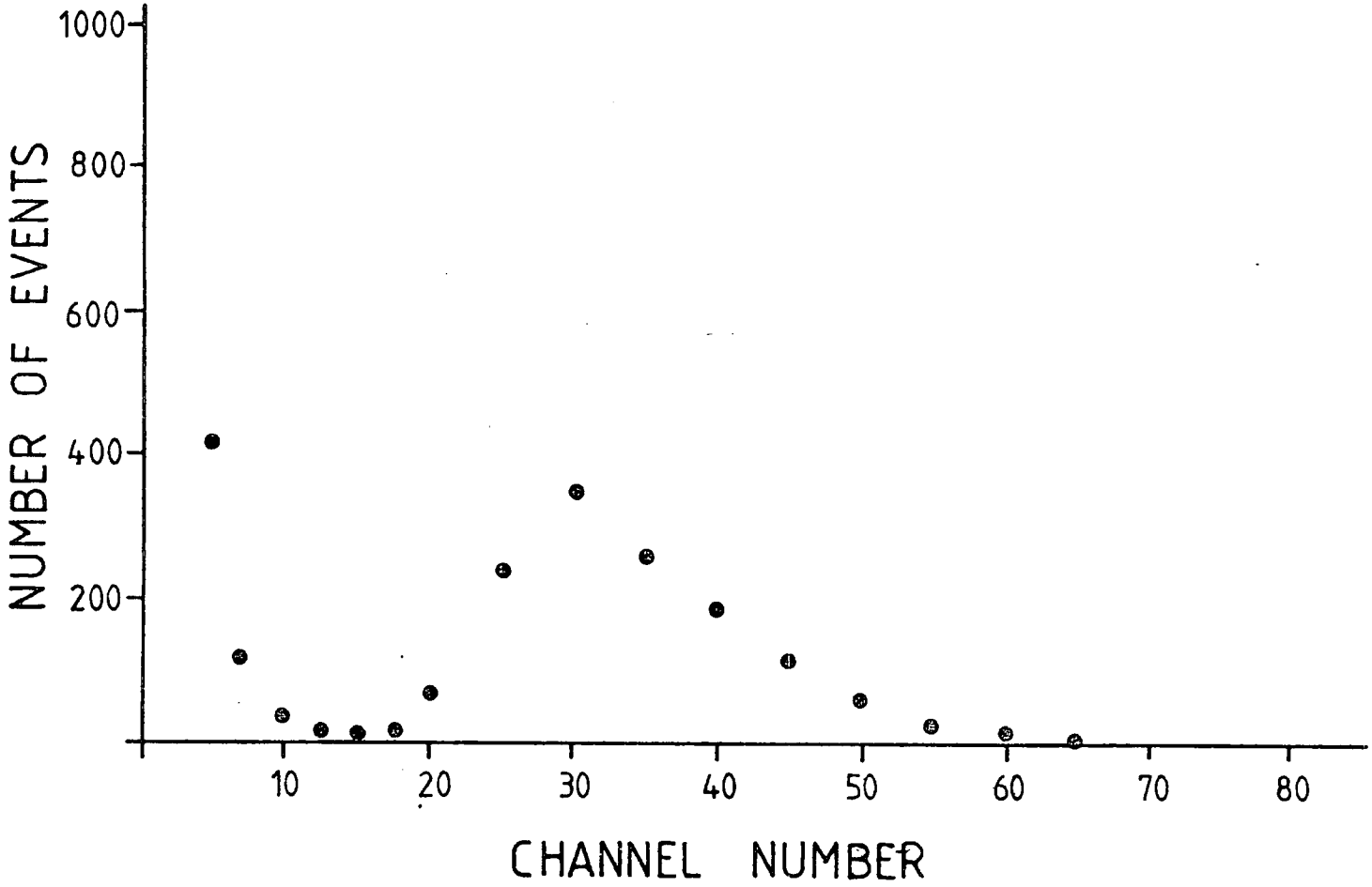
1000
800
600
400
200
NUMBER OF EVENTS
10
20
30
40
50
60
70
80
CHANNEL NUMBER

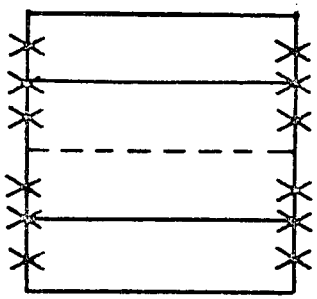

FIG. 6·10 e)

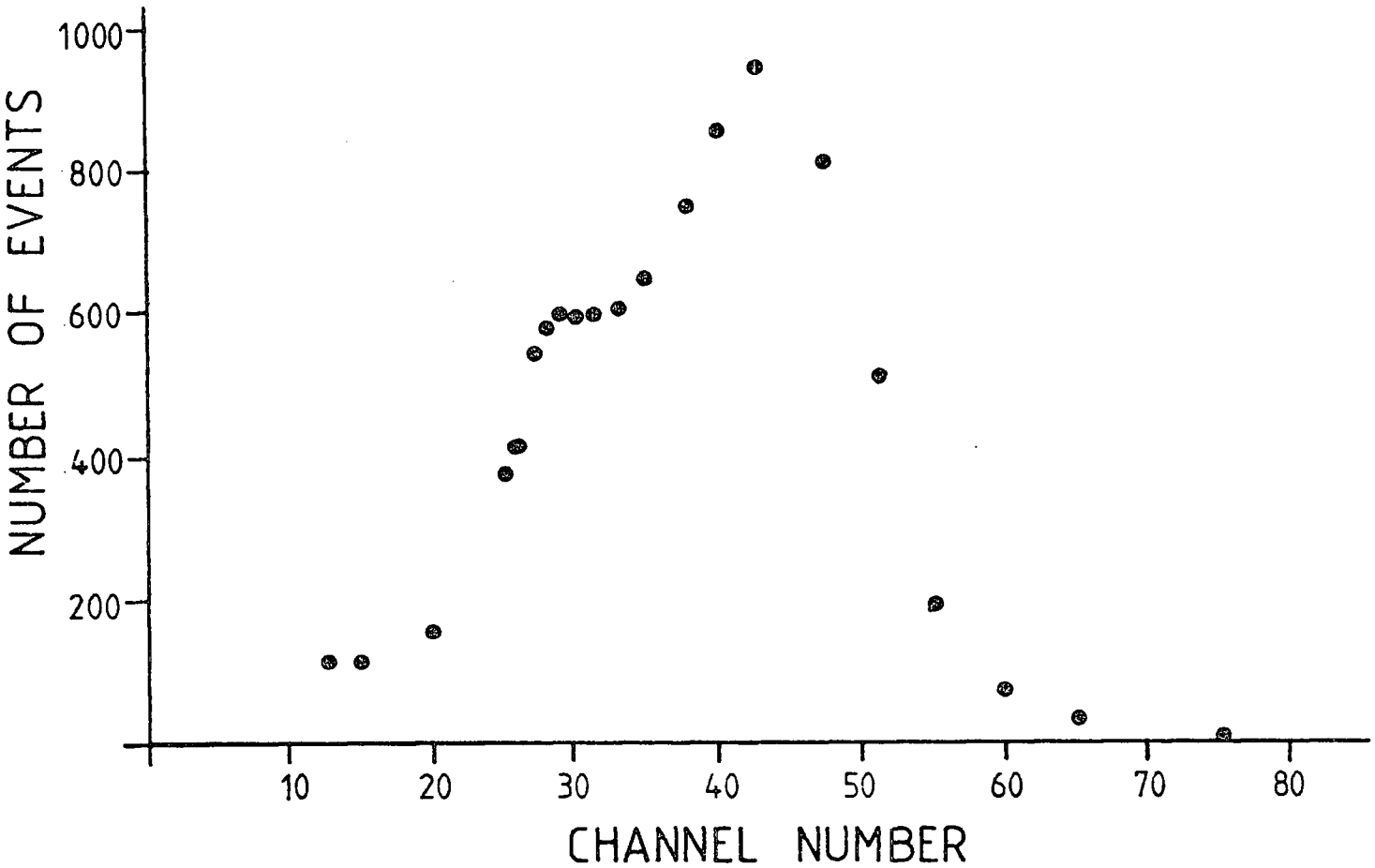
NUMBER OF EVENTS
1000
800
600
400
200
10
20
30
40
50
60
70
80
CHANNEL NUMBER

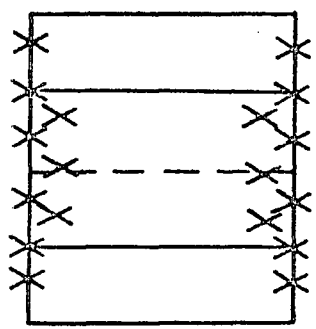

The scintillators (photomultipliers, scintillator combinations) were calibrated in situ to avoid any soft component contamination. The p.h.a. was triggered by each pulse which it was ready to digitise and measure. Hence there was a dead-time associated with every event, the average dead-time was 20% for the upper stack, and 12% for the lower stack. This reflects the presence of secondary particles, from interactions of the muons which trigger the p.h.a. - in the iron target, in the upper scintillator stack.

It is clear that the resolution of the peak of the s.p.p.h. improves with the number of photomultipliers used. However, the poor resolution for 1, 3 photomultipliers (e.g. Figs. 6.12a, b) makes a more quantitative evaluation of the relationship difficult.

The twin peaks of the final s.p.p.h.'s of each stack are due to the presence of pulses corresponding to the addition of pulses corresponding to the same particle passing through two scintillators. The relative heights of the twin peaks reflect the acceptance geometry available for such events. The relative height of the peaks is reduced as we go lower in the flash-tube tray. This is due to the increased amount of matter that muons have to pass through to reach the lower scintillators, which involves the barytes-brick walls for particles travelling at some non-zero zenith angle.

Figure 6.11 : Calibration curves for the Pulse Height Analyser (P.H.A.) using 100 and 200 ns square pulses.

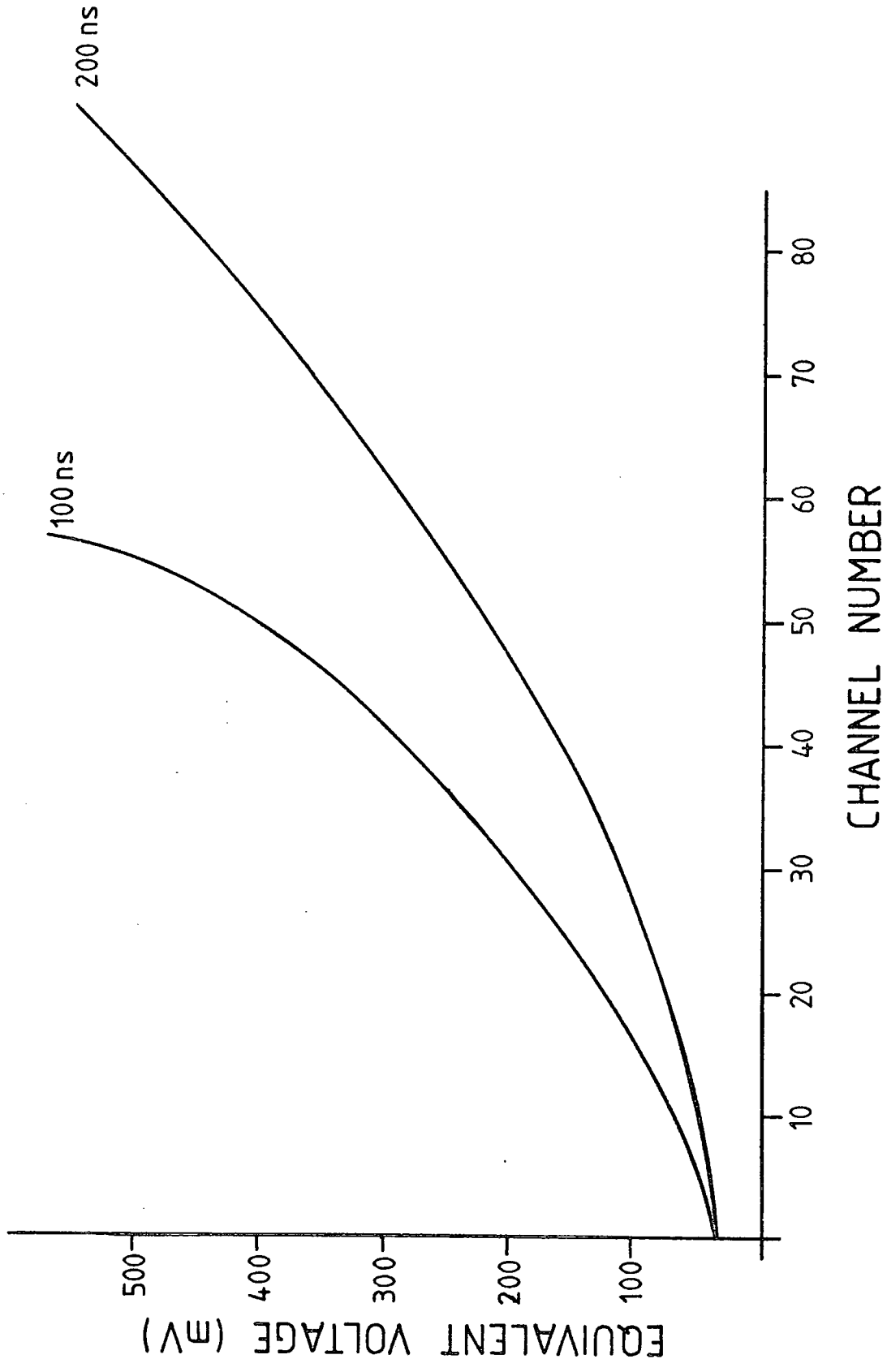

FIG. 6.11

6.5.4 Calibration of the electronics

Each individual element (see block diagram Fig. 9.4) of the previous particle indicator was calibrated using the relevant width of square pulse from a pulse generator. Although designed to produce 5 μs pulses, the stretchers could only stretch the 150 ns. "exponential" pulses to 2 μs pulses. Hence the attenuation of the delay line (Fig. 9.1) was determined using 2 μs square pulses.

Once the gains of the amplifiers had been set for a run (the settings were determined by the need to be able to distinguish a prompt air shower pulse whilst minimising the height of the noise pick-up pulse from the flash-tube chamber's H.T. pulse) the whole system was calibrated to produce the final input/output curves of Figs. 9.3a) and 9.3b).

6.5.5 Summary

A small air-shower array has been built to detect air-showers of size around 3.10^5 particles. The flash-tube chamber has been modified to improve the searches for fractionally charged particles, search for tachyons associated with air-showers detected by the array, and increase the collecting area for hadron detection in such air-showers.

CHAPTER 7

THE DETERMINATION OF AIR-SHOWER PARAMETERS

7.1 The method of intersecting loci

The two basic parameters of an air-shower which need to be determined are the shower size N and the position of the axis of the air-shower, the core position.

A method first suggested by Williams (1948) of constructing loci of possible core positions from the information given by several pairs of detectors has been found useful in the analysis of showers when only a few (4) air-shower detectors are used (Nasri [1977]). This method has been further investigated in the present work, and used in the analysis of a certain class of air-showers (see Chapter 11).

The method depends on assuming that the lateral distribution of electrons in an air-shower can be expressed as an explicit function of shower size N and distance from the core of the shower r. If we let the electron density at detector 1 be Δ_1, and the electron density at detector 2 be Δ_2, then

$$(7.1) \quad \frac{\Delta_1}{\Delta_2} = \frac{f_1(N).\ f_2(r_1)}{f_1(N).\ f_2(r_2)} = \frac{f_2(r_2)}{f_2(r_1)}$$

Hence, for any pair of detectors, a series of loci of possible core positions corresponding to different electron density ratios between the two detectors can be constructed. Examples of such series' for the arrangement of detectors in the Durham Air-Shower Array are presented in Figs. 7.1a), b).

Figure 7.1 : Examples of intersecting loci curves for different pairs of detectors according to the Nishimura-Kamata-Greisen (N.K.G.) equation for the lateral distribution of electrons in an air-shower.

Figure 7.1 a): Curves for detectors C and 53

$$\frac{\Delta A}{\Delta B} = \frac{\text{Electron density indetector C}}{\text{Electron density in detector 53}}$$

Figure 7.1 b): Curves for detectors C and 62

$$\frac{\Delta A}{\Delta B} = \frac{\text{Electron density in detector C}}{\text{Electron density in detector 62}}$$

Figure 7.1 c): Curves for detectors 4 and 42

$$\frac{\Delta A}{\Delta B} = \frac{\text{Electron density in detector 41}}{\text{Electron density in detector 42}}$$

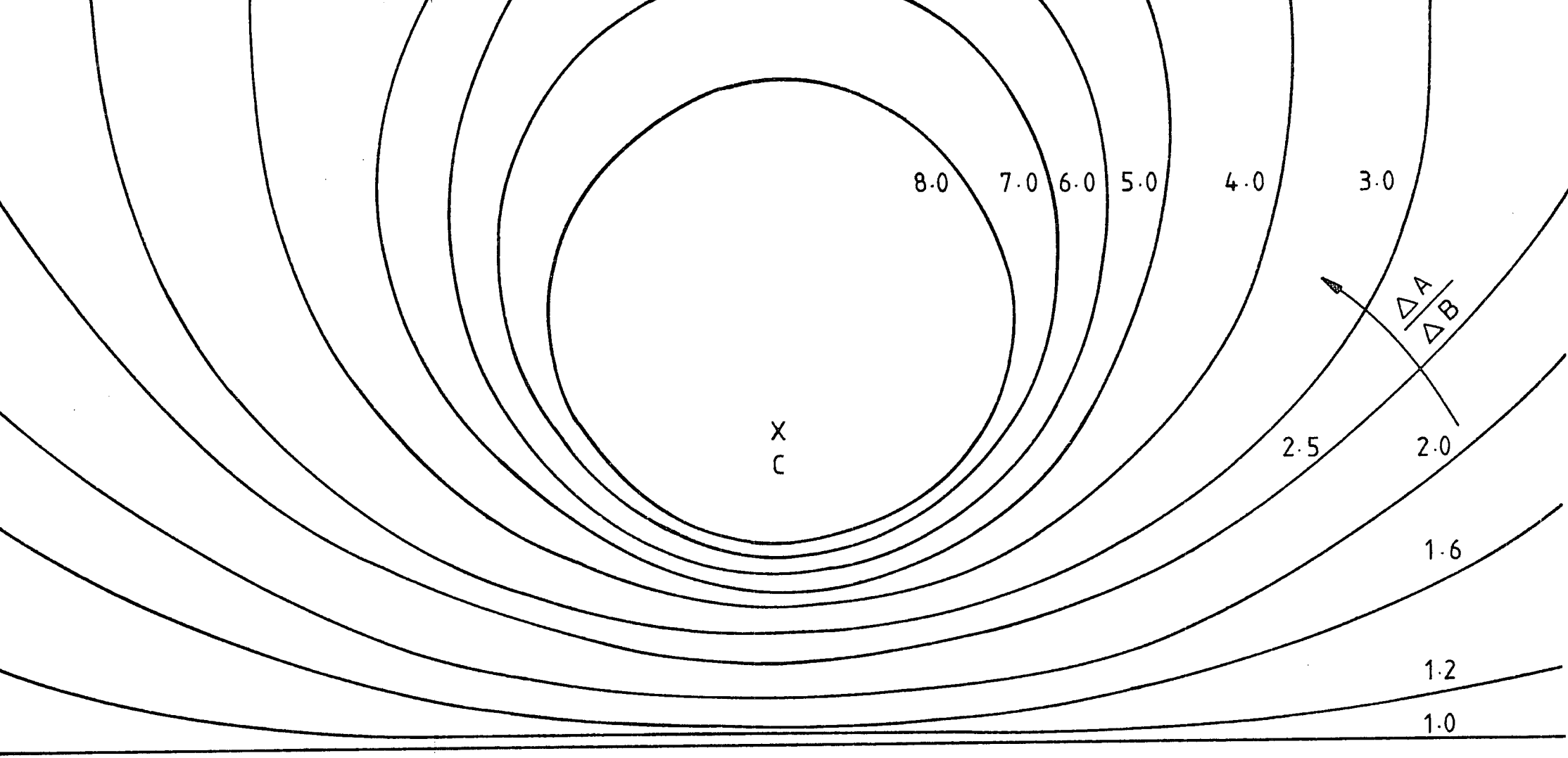

FIG. 7·1a)

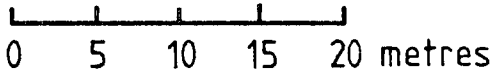

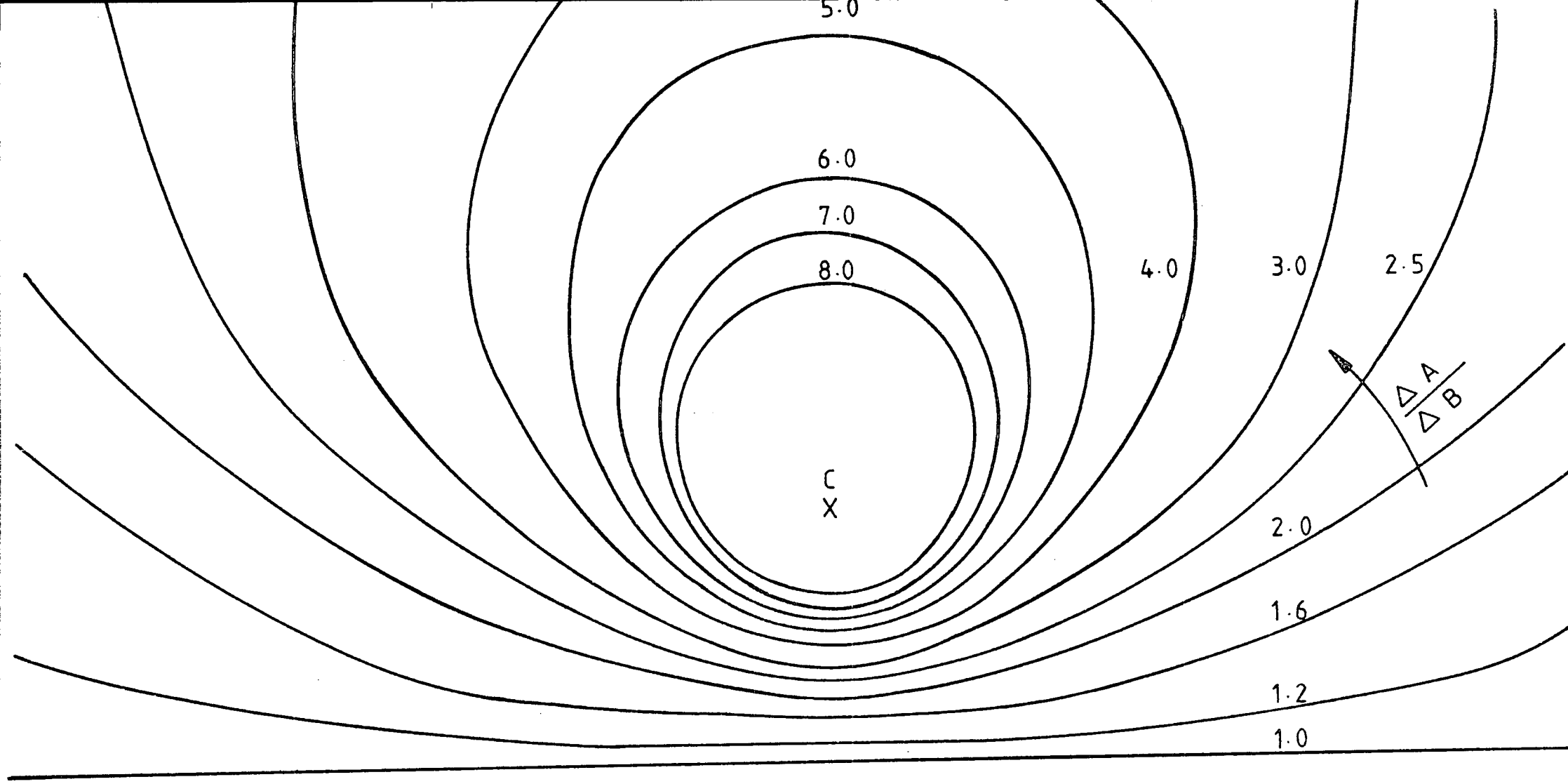

FIG. 7·1b)

0 5 10 15 metres

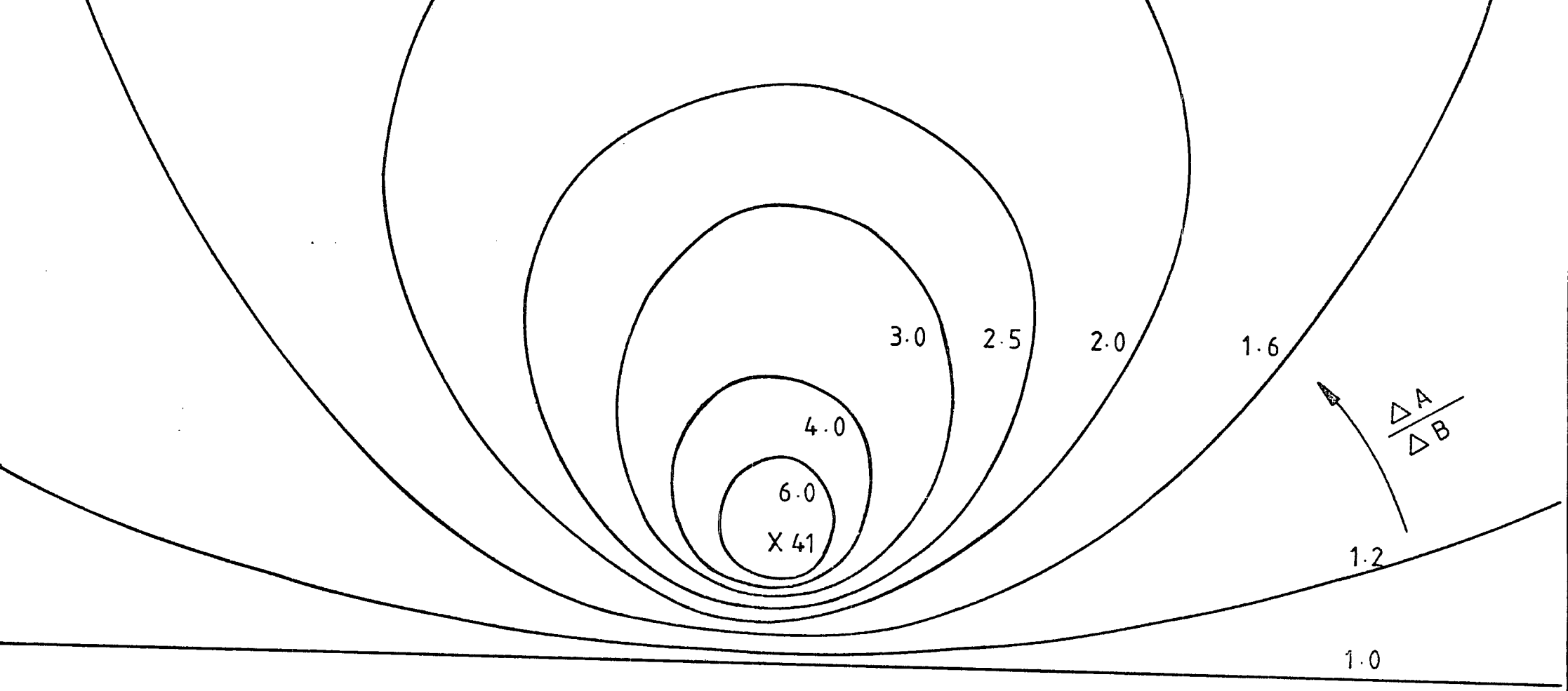

FIG. 7·1c)

X 42

0 5 10 15 20 metres

Three detectors thus give two independent ratios and the corresponding loci will intersect at two places. To decide which of the two positions is the true core position a fourth detector is required, the third loci constructed from the ratio of the electron density in this detector to the electron density in any one of the other three detectors will define the core position uniquely. Once the core position has been determined it is a simple matter to find the shower size N by substituting for r_i in the equation

$$\triangle_i = f_1(N)\ f_2(r_i)$$

The electron lateral distribution function used to construct the loci of Figs. 7.1 is usually referred to as the Nishimura - Kamata - Greisen (N.K.G.) curve (Greisen [1960]) and has the form

$$(7.2) \qquad \triangle_e(N,r) = \frac{0.4N}{r_1^2} \left(\frac{r_1}{r}\right)^{0.75} \left(\frac{r_1}{r + r_1}\right)^{3.25} \left(1 + \frac{r}{11.4\ r_1}\right)$$

where $r_1 = 79$ m.

The curve is presented in Fig. 7.2 for a shower size of 3.10^5 particles. It has been noted (A. C. Smith [private communication]) that the core position determination is insensitive to the particular lateral distribution function assumed, however the resulting shower size does depend strongly on the distribution function.

Since, with the Durham Air-Shower Array, electron density information from 10 detectors was available, a choice of detectors to be used in the core location has to be made. Two particular choices of detectors have been investigated:

FIG. 7·2

Lateral distribution of electrons in an air-shower of size 3.10^5 particles according to the Nishimura-Kamata-Greisen formulation.

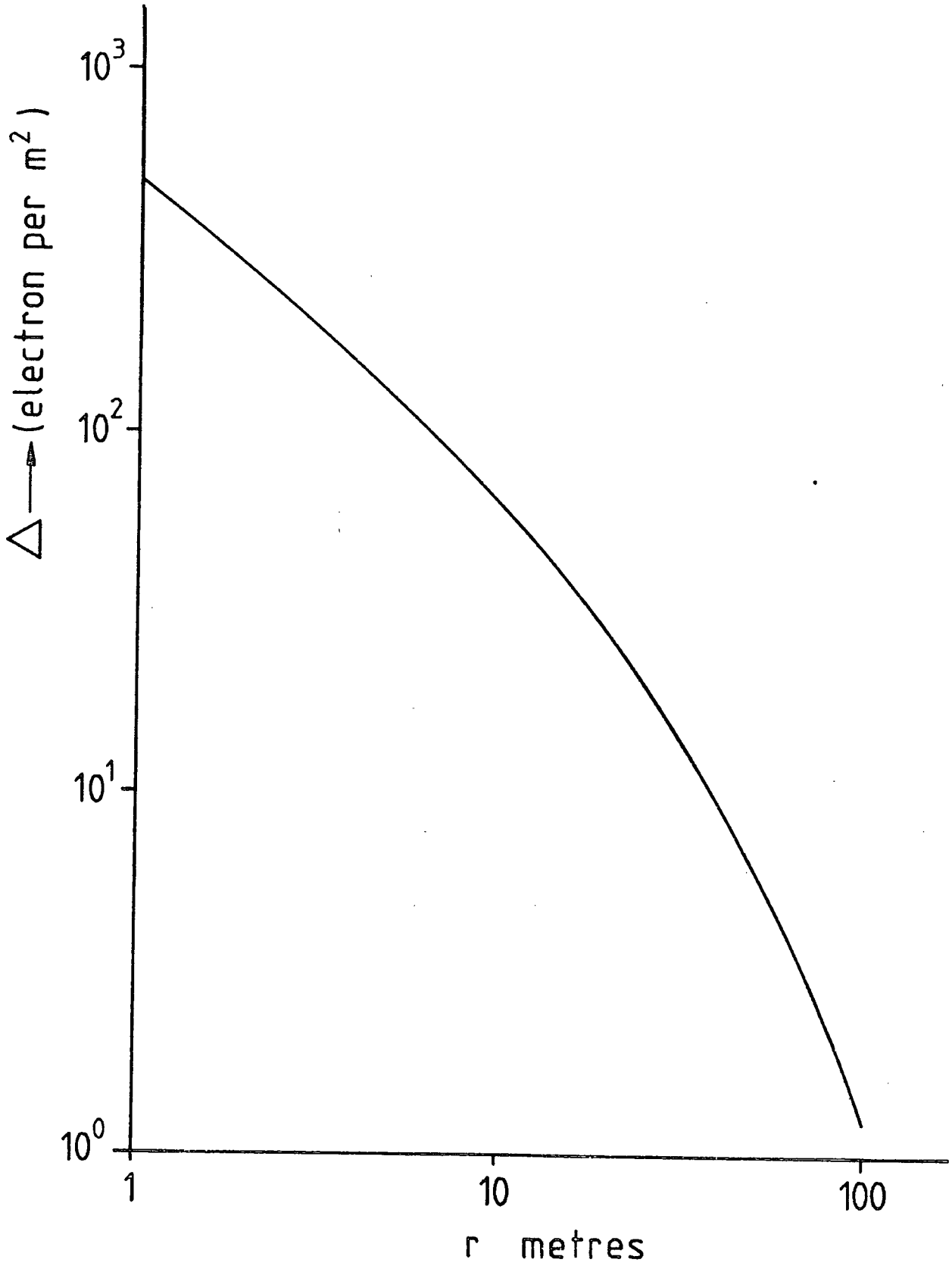

Method 1 : Since every air-shower detected requires there to be a signal greater than 2 pcles m^{-2} in the central detector C, one choice of detector combinations that might prove useful is to take the three detectors with the largest signals in combination with the central detector C. This method does have the disadvantage of relying very heavily on detector C even if there are only a few particles detected in C.

Method 2 : A more refined choice is to take the four detectors with the largest signals and take the detector with the largest signal in combination with each of the other three detectors.

7.2 Statistical fluctuations in detector response

Air-showers at sea-level are usually past maximum, and the particles can thus be considered as independent. Hence fluctuations in the particle numbers from the average (as predicted by the electron lateral distribution function) can be considered as purely random, and be described by a Poisson distribution. However, in practice, the observed fluctuations are usually broader than purely Poissonian, due mainly to the fluctuations in detector response (i.e. the superposition of n single particle pulse height distributions when n particles pass through the detector). In order to characterise the broader distributions that are observed, they can be considered as roughly Poissonian in shape but with a broader f.w.h.m., and the width can be described by some factor $k>1$ times the standard deviation σ_s ($= n^{\frac{1}{2}}$) of a normal Poissonian distribution.

There are two methods of obtaining k, by experiment and by theory.

To determine k experimentally, a sample of showers needs to be analysed and the core positions and shower sizes determined. The intersecting loci method provides a convenient method of determining these parameters for this purpose since it only requires the use of four detectors, hence, in the case of the Durham Air-Shower Array, the measured and expected particle numbers in the other six detectors can be compared to determine the size of the observed fluctuations.

This technique has been used to analyse 100 showers (J. Fatemi [private communication]), and over the whole range of shower sizes measured (7.4×10^4 to 2.7×10^6 particles), the average width of the fluctuations was found to be $1.2n^{\frac{1}{2}}$ (i.e. $k = 1.2$). This means that in a plot of measured particle number against predicted particle number, 68% of the points fell within $\pm\ 1.2n^{\frac{1}{2}}$ of the mean. Incidentally, the slope of the mean being equal to unity lends some support to the assumed electron lateral distribution function.

The second method of determining k involves assuming that the actual fluctuations are Poissonian, and by calculating the width due to the detector response, the finally observed fluctuations can be determined.

The effects of fluctuations in detector response have been calculated by a Monte Carlo technique (A. C. Smith [1976]) to be representable by a Poisson type curve of standard deviation $0.66\ n^{\frac{1}{2}}$ (i.e. 0.66σ poisson). Hence, if we characterise the finally observed fluctuations by a standard deviation σ_{TOT},

$$\sigma_{TOT}^2 = \sigma^2_{poiss} + (0.66\ \sigma^2_{poiss})$$

$$= n\ (1 + 0.66^2)$$

$$\therefore\ \sigma_{TOT} \simeq 1.2n^{\frac{1}{2}} \quad \text{(i.e. } k = 1.2\text{)}$$

Since both methods of obtaining k agree, we can proceed to simulate real showers in order to investigate the accuracy of the parameter determination by assuming that the fluctuations can be characterised by a slightly broadened Poisson distribution of standard deviation 1.2 times the standard deviation of a normal Poisson distribution.

7.3 Simulated air-showers

A sample of data was analysed to provide a provisional shower size spectrum and core distance distribution. A sample of simulated air showers was then constructed according to these results, the simulated air shower size spectrum and core distance distribution are shown in figs. 7.3a) and 7.3b). The core distances are measured from the central detector C.

Core positions were randomly generated in a 75 m x 75 m matrix using tables of random numbers in pairs, and the showers assigned their core positions according to fig. 7.3b).

Fluctuations from $\pm 0.25\sigma_T$, to $\pm 4.25\sigma_T$ were randomly selected according to a normal (gaussian) distribution and randomly assigned to the detector signals of each event.

$(\sigma_T = 1.2\sigma_{poisson})$.

The expected signal from each detector for each event was then calculated, including fluctuations, providing 30 simulated air shower events which were then analysed according to methods 1 and 2 (see Section 7.1 and below).

FIG. 7.3 a) Shower size distribution used in simulated air-showers.

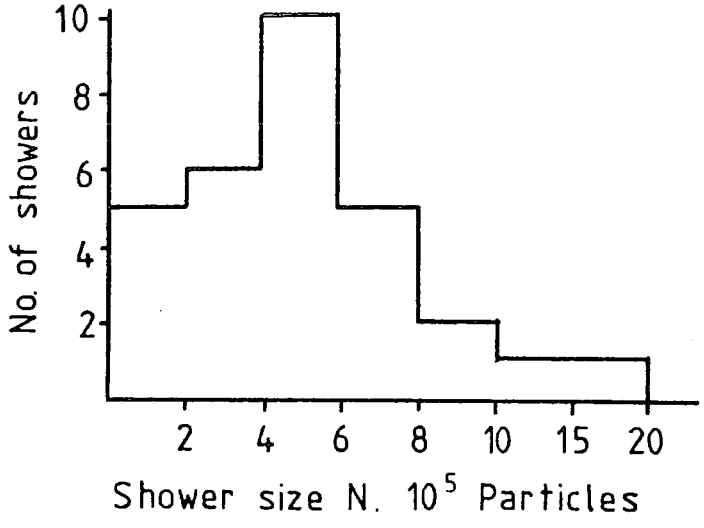

FIG. 7.3 b) Core distance distribution used in simulated air-showers.

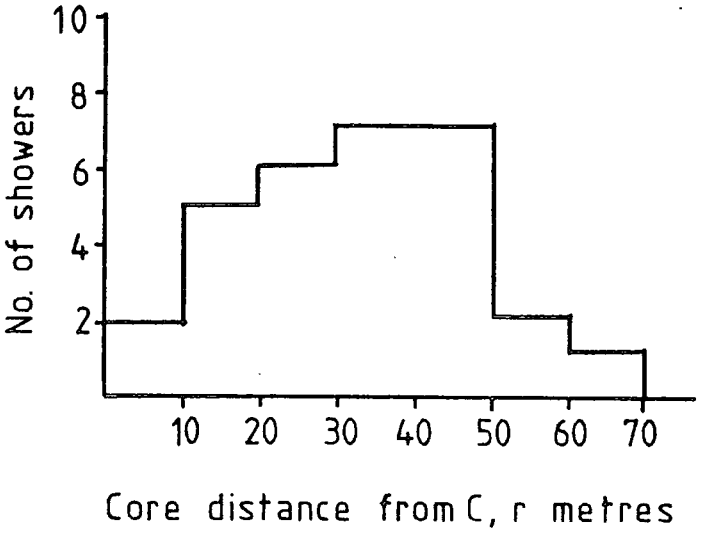

7.4 Method 1 of analysing air-showers

Having generated simulated air-showers, their cores were located by considering the detectors with the 3 largest signals in pairs with detector C, with the following provisos:-

a.) In the case of a signal >85 particles m^{-2}, the detector was assumed saturated and thus only defining an area (rather than a locus) in which the core must fall.

b.) In the case of no core being located with the three curves, error curves were calculated at the $1.2\,b_{poiss}$ level according to the following:-

if detector area A has a pcles m^{-2}
and detector area B has b pcles m^{-2}
} errors added in quadrature

giving: $$\text{error in } \frac{a}{b} = \frac{1.2a}{b}\left[\frac{1}{aA} + \frac{1}{bB}\right]^{\frac{1}{2}}$$

The resulting triangle, either common or limited, was taken as the area in which the core must fall and the centre of the inscribed circle taken as the position (the intersection of the bisectors of the angles) since this point is equidistant from all 3 sides of the triangle.

The shower size N was calculated from the density in the detector nearest the located core position, unless saturated.

Some examples of core locations using Method 1 are presented in figs. 7.4a), b), and c). Fig. 7.5 summarises the results on core locations using Method 1. The bases of the arrows represent the input core position, and the tips of the arrows show the core position that has been determined using Method 1.

Figures 7.4a),b),c) : Examples of core-locations using Method 1.

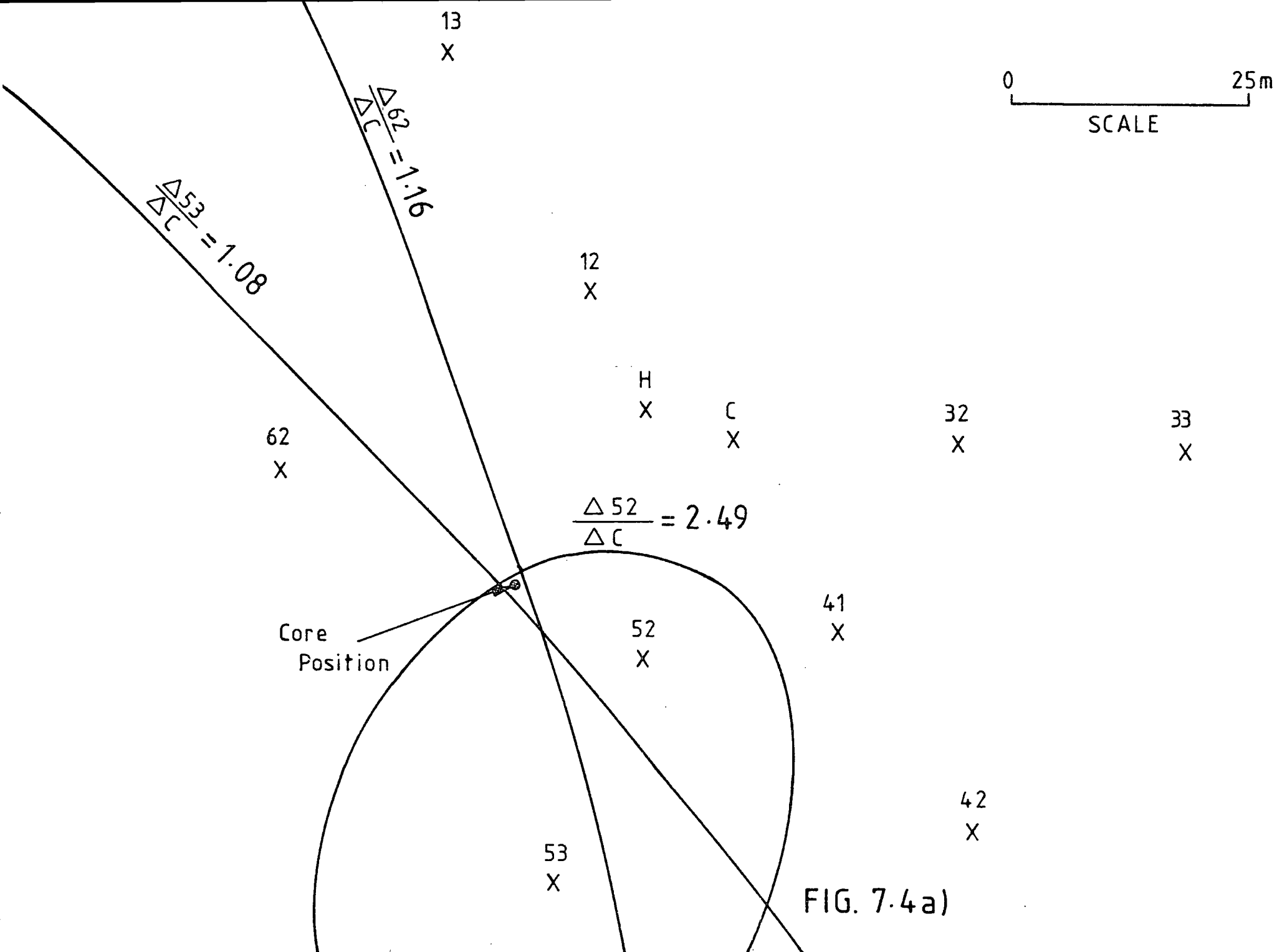
13
X
0
25m
SCALE
$\frac{\Delta 62}{\Delta C} = 1.16$
$\frac{\Delta 53}{\Delta C} = 1.08$
12
X
H
X
C
X
32
X
33
X
62
X
$\frac{\Delta 52}{\Delta C} = 2.49$
41
X
Core
Position
52
X
42
X
53
X

FIG. 7.4a)

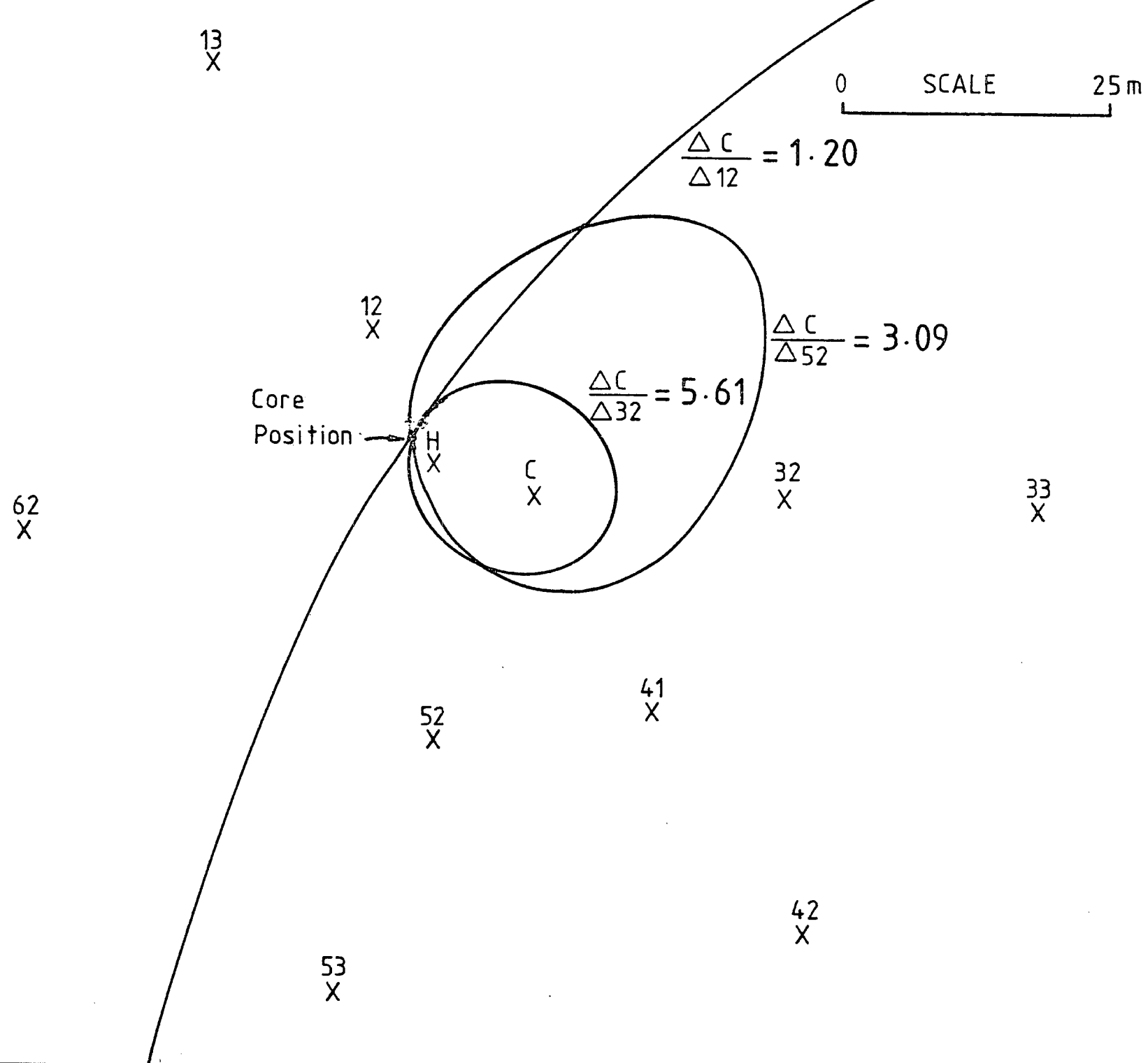
13
0 SCALE 25 m
ΔC/Δ12 = 1·20
12
ΔC/Δ52 = 3·09
ΔC/Δ32 = 5·61
Core
Position
H
C
62
32
33
41
52
42
53

FIG. 7·4 b)

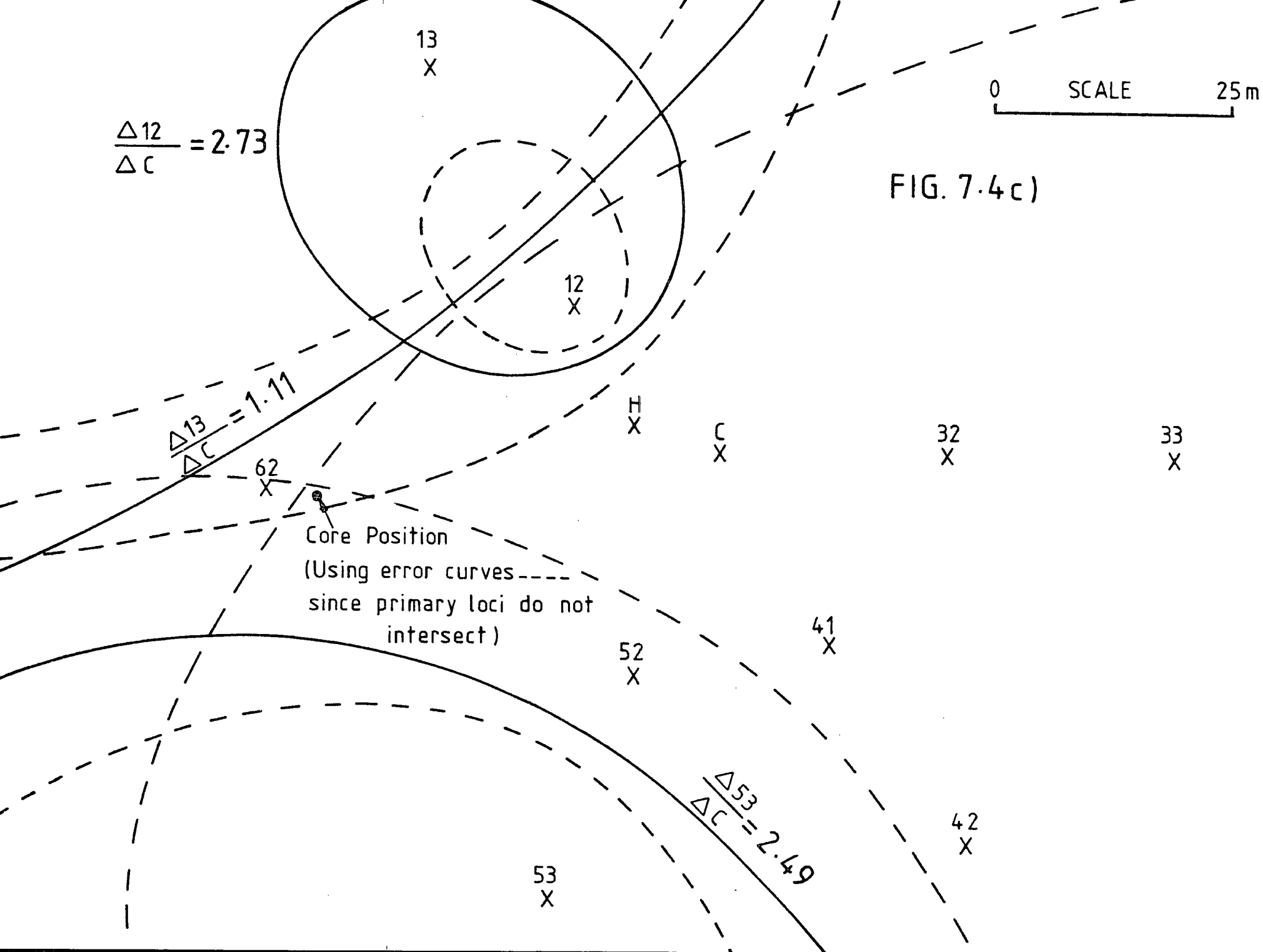
13
12
H
C
32
33
62
41
52
42
53
$\frac{\Delta 12}{\Delta C} = 2.73$
$\frac{\Delta 13}{\Delta C} = 1.11$
$\frac{\Delta 53}{\Delta C} = 2.49$
Core Position
(Using error curves---- since primary loci do not intersect)
0 SCALE 25 m

FIG. 7.4c)

Figure 7.5: A Summary of the results on core-location using Method 1.

Base of arrow = Actual core-position of simulated air-shower.

Tip of arrow = Core-position determined using Method 1.

FIG. 7·5

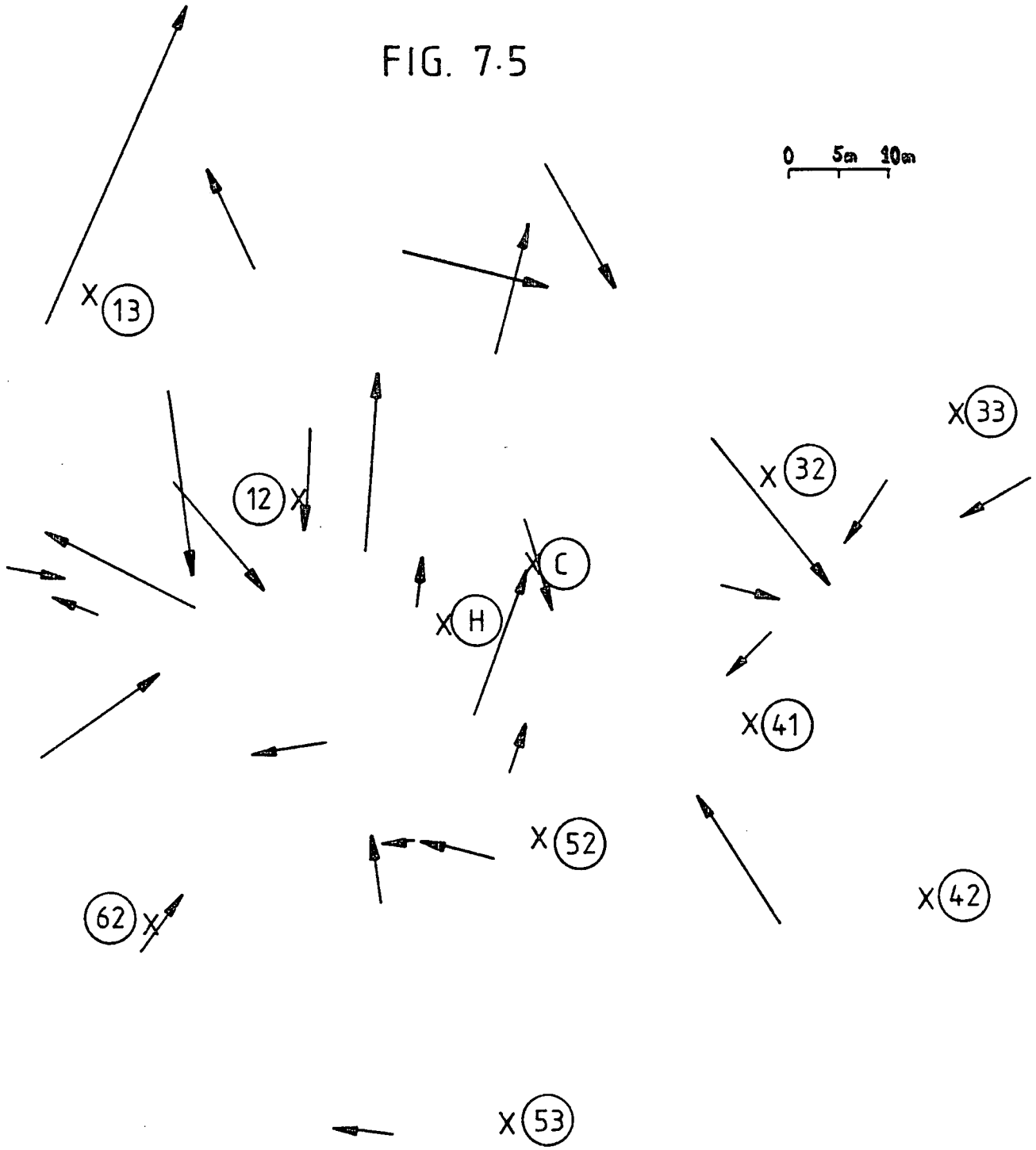

Figures 7.6a),b): Examples of core-locations using Method 2.

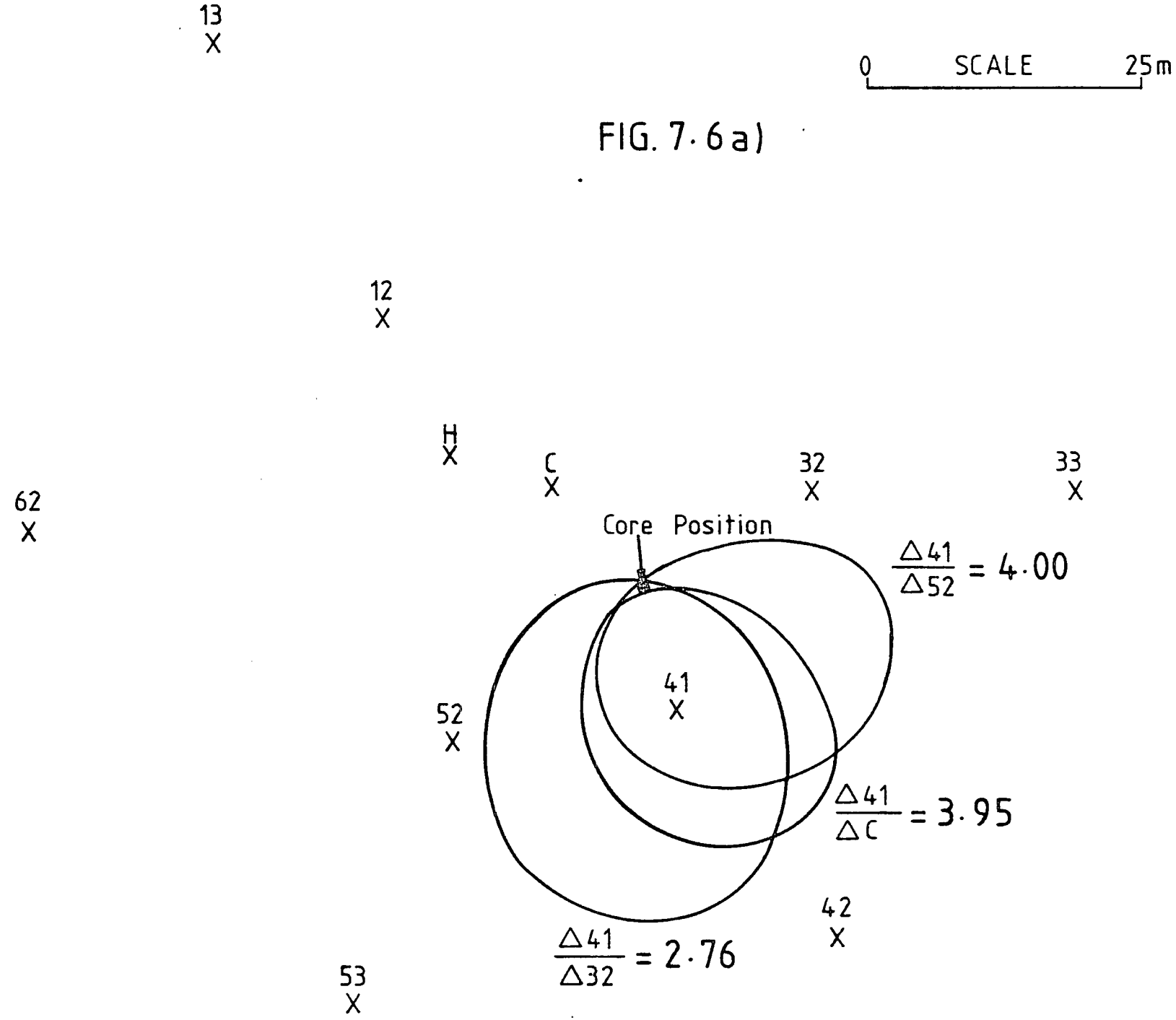
13
12
H
C
32
33
62
Core Position
$\frac{\Delta 41}{\Delta 52} = 4.00$
41
52
$\frac{\Delta 41}{\Delta C} = 3.95$
42
$\frac{\Delta 41}{\Delta 32} = 2.76$
53
0 SCALE 25m

FIG. 7·6 a)

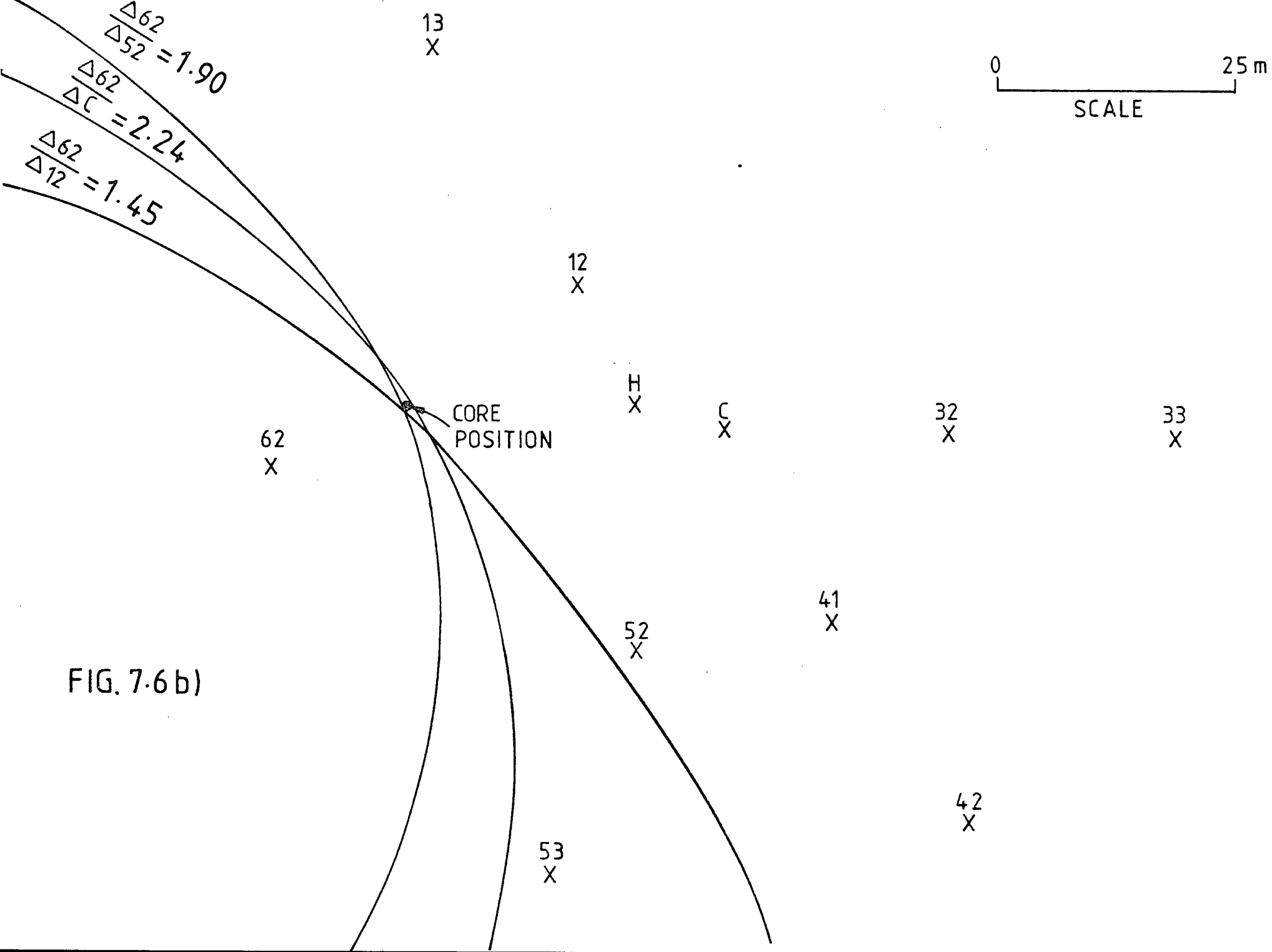
$\frac{\Delta 62}{\Delta 52} = 1.90$
$\frac{\Delta 62}{\Delta C} = 2.24$
$\frac{\Delta 62}{\Delta 12} = 1.45$
13
12
H
C
32
33
62
CORE
POSITION
41
52
53
42
0
25 m
SCALE

FIG. 7·6 b)

Figure 7.7: A Summary of the results on core-location using Method 2.

Base of arrow = Actual core-position of simulated air-shower.

Tip of arrow = Core-position determined using Method 2.

FIG. 7·7

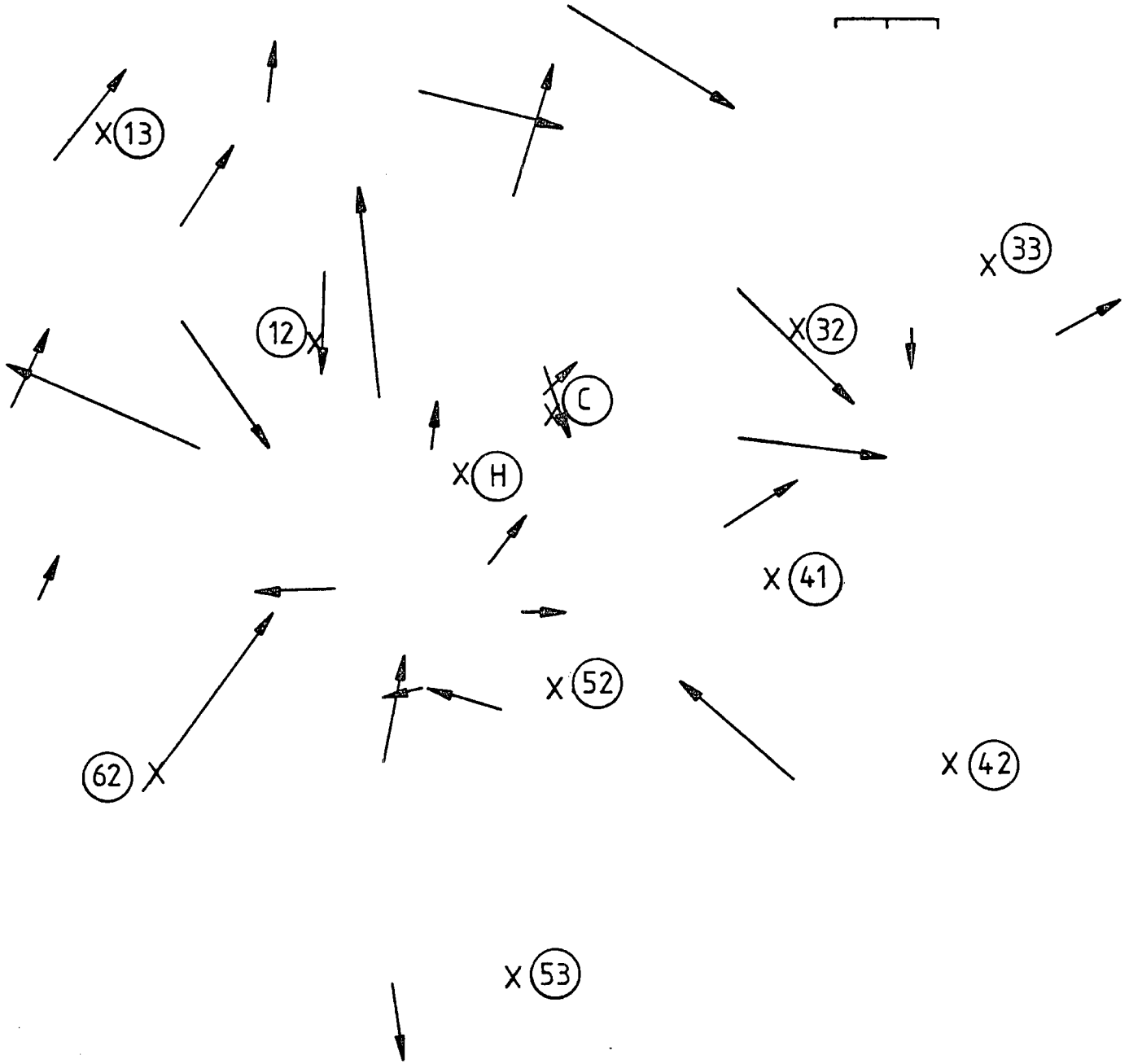

7.5 Method 2 of analysing air-showers

Method 2 differs only in that the role of detector C in Method 1 was allotted to the detector with the highest particle density - unless this was a saturated detector in which case saturation criteria as in a) of Section 7.4 were adopted, and the second highest density was used as the highest.

One further refinement of Method 2 is that the shower size was determined from the mean of the shower sizes determined from each of the 4 detectors used in the core location.

Examples of core locations using Method 2 are presented in figs. 7.6a) and b). Fig. 7.7 summarises the results on core location using Method 2 according to the format of fig. 7.5.

7.6 Results on core locations

Figs. 7.8a) and b) represent the comparative accuracy of the two methods by comparing the input core distance from H (the flash-tube chamber) r_1 with the determined core distance from H, r_2. There is no apparent difference between the accuracies of the two methods in core locating.

In order to assess the accuracy of either method a histogram of $|r_1 - r_2|$ is necessary. Figs. 7.9a) and b) are such histograms for each method. Clearly no greater accuracy than ± 10 m can be claimed with either method. Figs. 7.5 and 7.7 indicate that this accuracy is not core distance dependent.

Fig. 7.10 compares the input distribution of core distances from H with the determined distributions as determined by Methods 1 and 2. There is clearly no systematic error in core location.

Figure 7.8a): Histogram of the difference between the actual core-distance of the simulated air-showers from the flash-tube chamber (r_1) and the determined core-distance (r_2) using Method 1.

Figure 7.8b): As for Fig. 7.8a) but for Method 2.

FIG. 7·8 a)

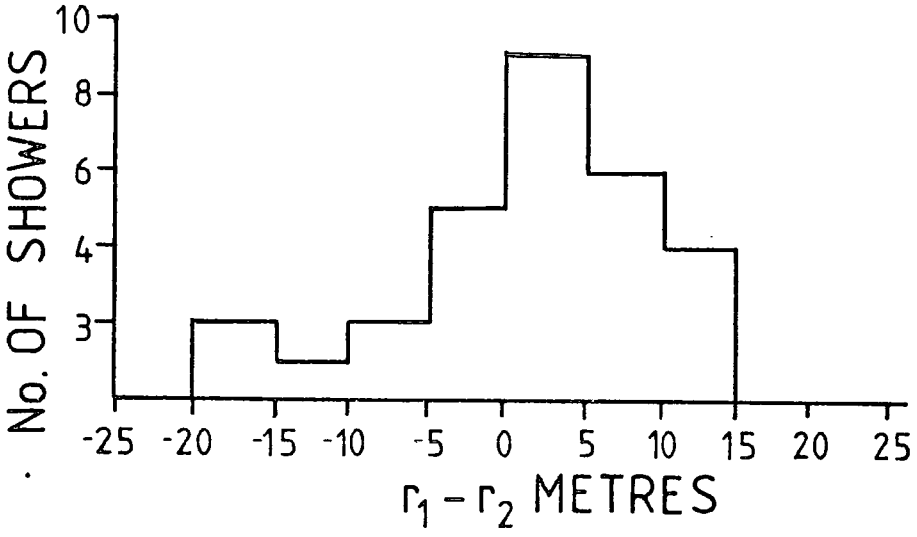

FIG. 7·8 b)

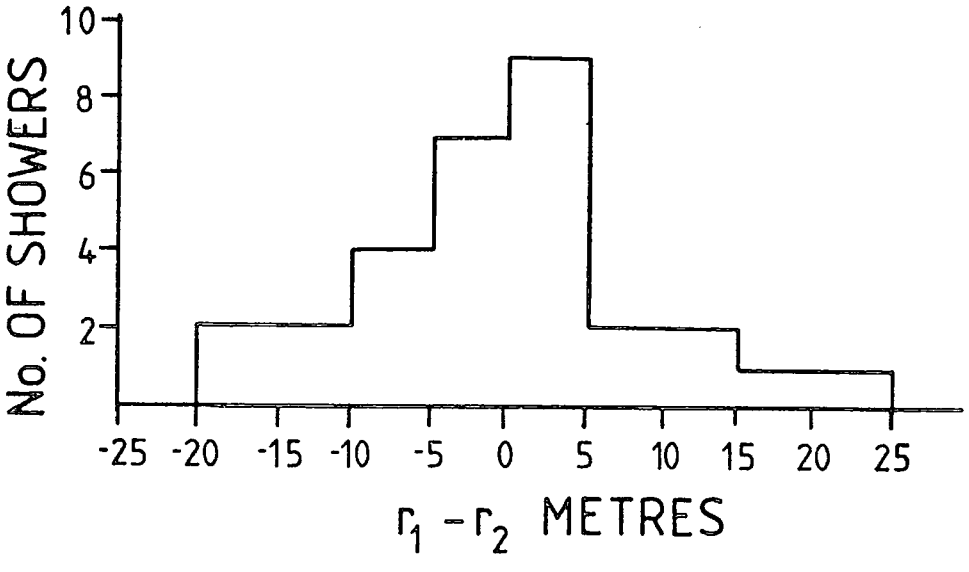

Figure 7.9a): Histogram of $|r_1 - r_2|$ for the results of using Method 1.

Figure 7.9b): Histogram of $|r_1 - r_2|$ for the results of using Method 2.

FIG. 7·9

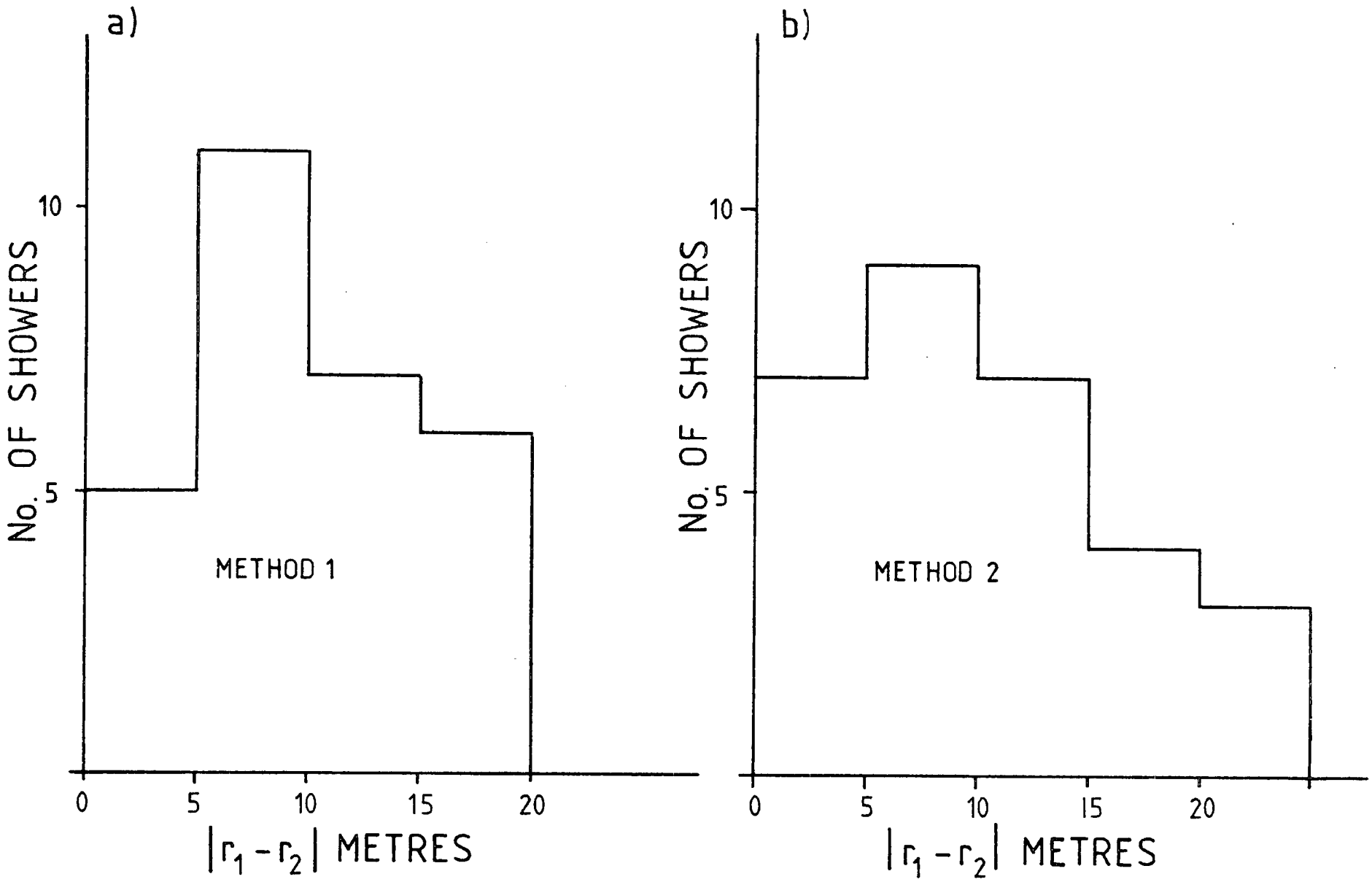
a)
No. OF SHOWERS
10
5
METHOD 1
0
5
10
15
20
$|r_1 - r_2|$ METRES
b)
No. OF SHOWERS
10
5
METHOD 2
0
5
10
15
20
$|r_1 - r_2|$ METRES

FIG. 7·10

Comparison of actual and determined core-distance distributions of simulated air-showers.

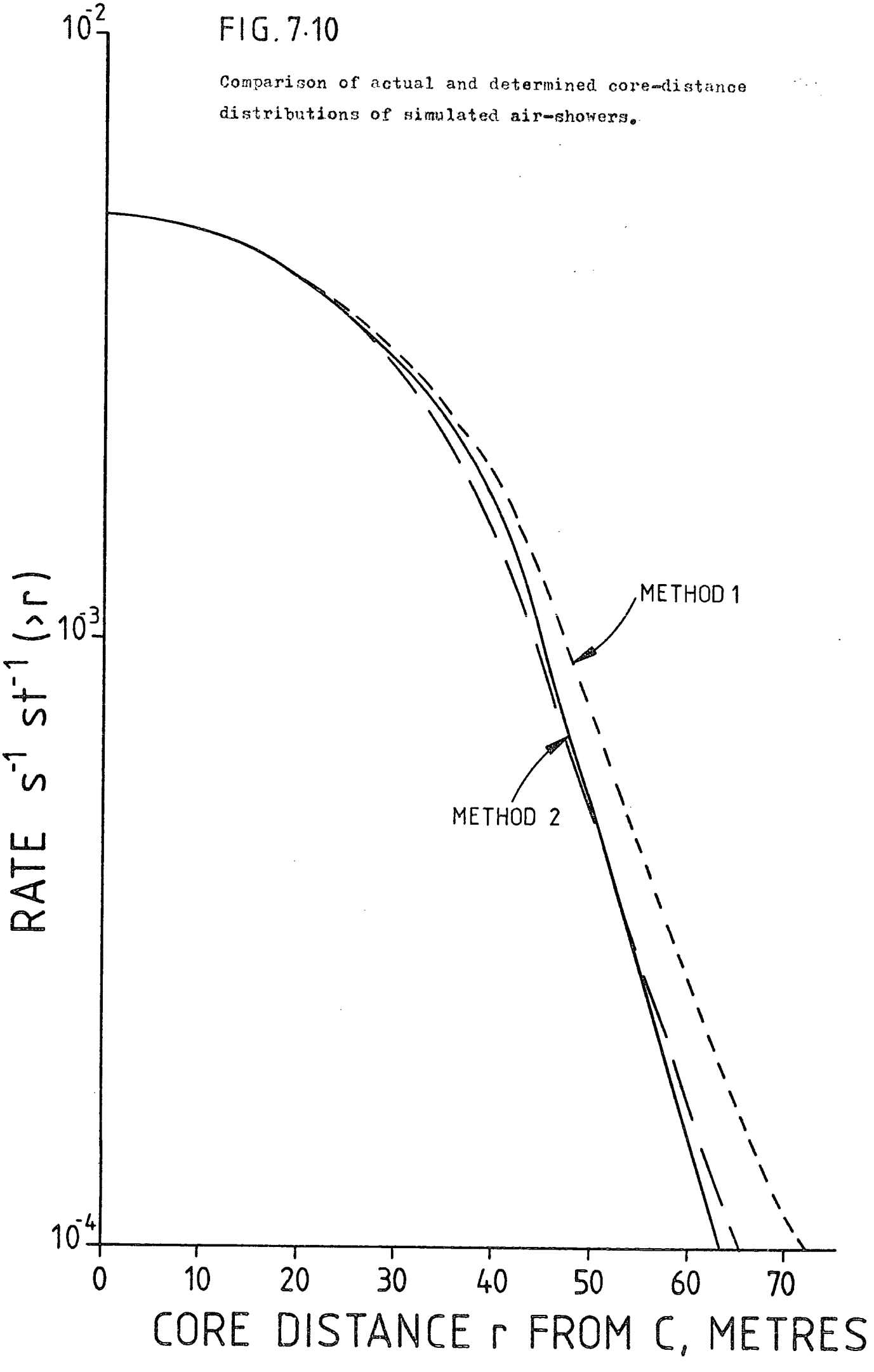

7.7 Results on shower size determination

Fig. 7.11 compares the input integral shower size spectrum with the determined shower size spectra of Methods 1 and 2. Clearly both methods overestimate the shower size, but Method 1 (using only the detector with the largest signal) gives a slightly less divergent result for the larger shower sizes. In order to correct for this overestimation of shower size a "calibration curve" can be constructed. Fig. 7.12 shows just such a curve constructed from a linear regression fit of logarithms to the scatter-plot of the results of Method 1.

Hence if the shower size is determined from the detector with the largest density this can be corrected to give a better estimate of the shower size according to the equation

$$(7.3)\quad \left(\frac{N_{\text{corrected}}}{10^5}\right) = \left(\frac{1}{1.56} \times \frac{N_{\text{measured}}}{10^5}\right)^{4/3}$$

7.8 Limitations of the intersecting loci method

The intersecting loci method has been demonstrated to be a viable method of obtaining air shower parameters, however some limitations of the method have also been made apparent.

Clearly the technique can only handle small quantities of data, if more than, say, 500 events need analysing, then this technique would prove too laborious.

FIG. 7·11

Comparison of actual and determined shower-size distributions of simulated air-showers.

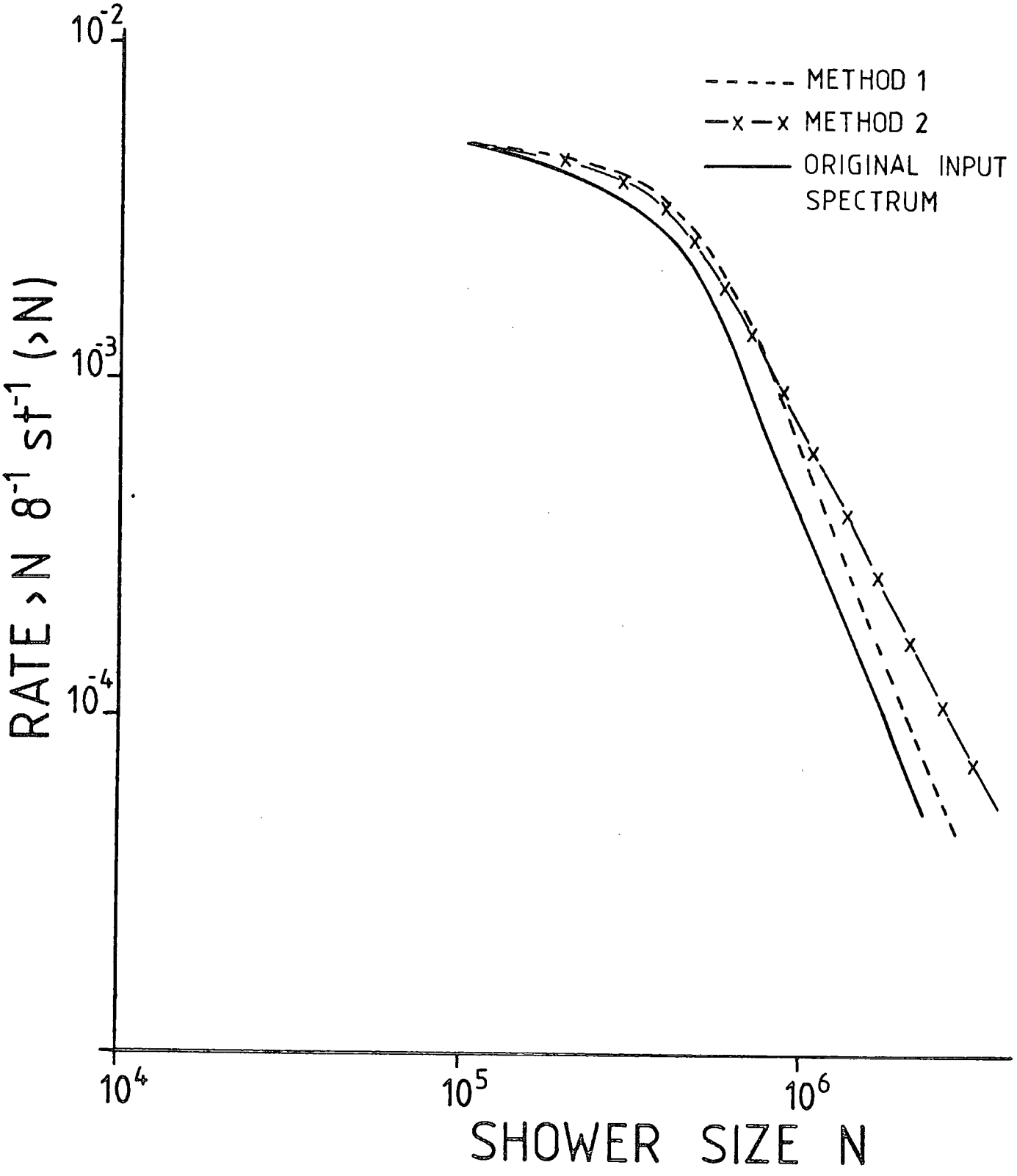

The accuracy in core location could be improved by using all the available data instead of just a sample (i.e. the information from 4 detectors only). It would be difficult to accommodate more information in the intersecting loci method since the different assessments of the location of the shower-axis would need to be weighted in their probability of accuracy occuring to the confidence which could be claimed for each detector signal.

All showers are assumed vertical, to take account of inclination of the shower-axis to the vertical a larger number of intersecting loci curves would have to be constructed corresponding to various angles of inclination of the shower-axis to the vertical.

The technique does not allow for the testing of various lateral distribution functions, and especially does not allow for the construction of a phenomenological distribution function that might be peculiar to the Durham array and the types and distribution of detectors used therein.

7.9 The "Minuit" method

A more comprehensive analysis technique has been devised (A. C. Smith [1976]) based on the minimisation package of computer programmes called "Minuit". This enables the three parameters shower angle, shower size and core location to be determined by simultaneously minimising fits to all three parameters.

Although expensive in computer time, the technique is designed to handle large quantities of data and use all the information available. The technique can also be modified to allow the construction of different lateral distribution functions.

FIG. 7·12

Correction curve for shower size measurements based on the electron density and distance from the air-shower core of the detector with the largest unsaturated signal (Method 1).

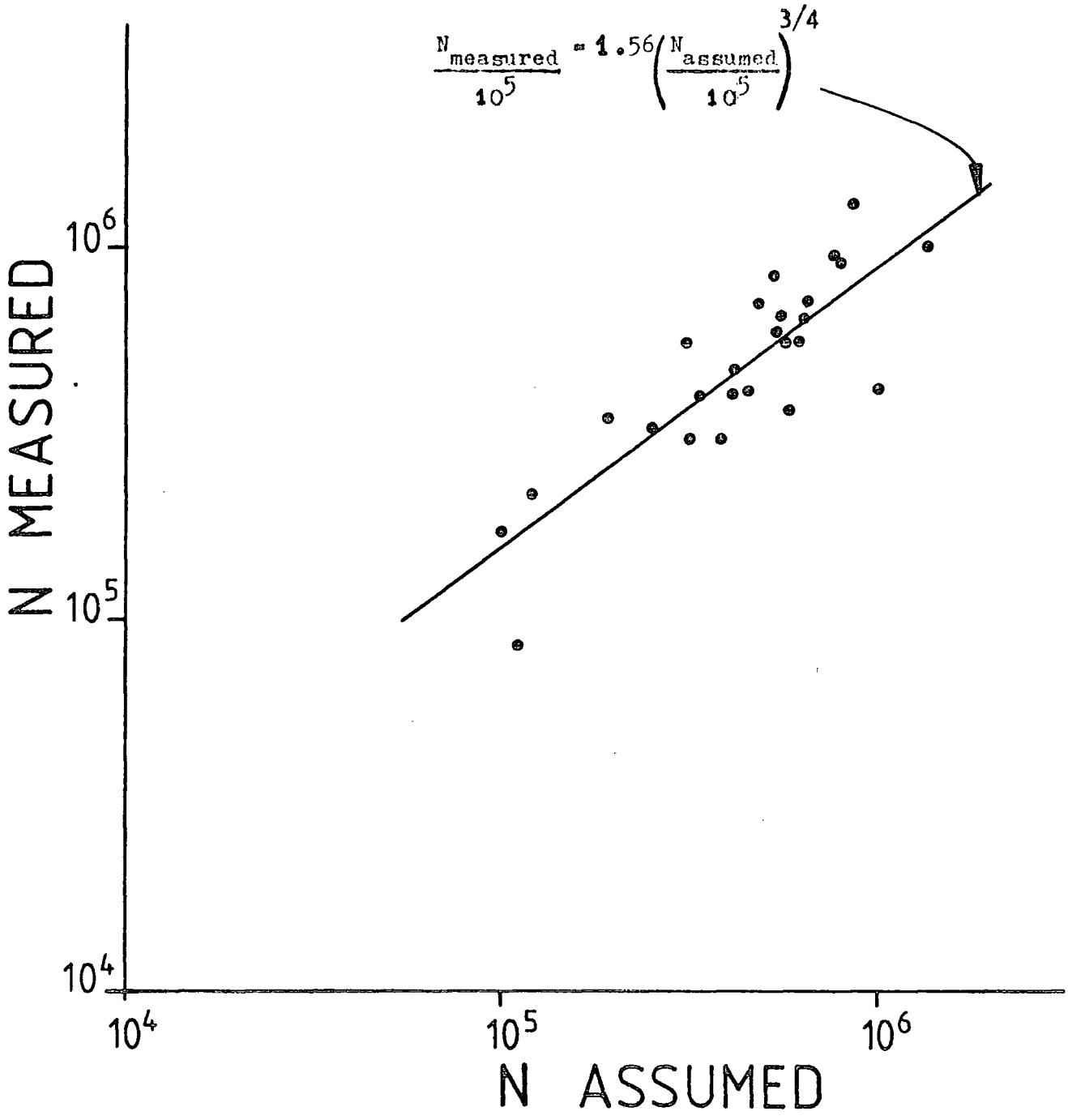

The "Minuit" technique is more thoroughly described by Smith (1976). Simulations described therein lead to the conclusion that core location accuracy is improved to ± 6 m, however the shower sizes are still overestimated and a correction curve similar to equation (7.3) is still necessary, i.e.

$$(7.4)\quad \left(\frac{N_{\text{measured}}}{10^6}\right) = (1.58 \pm 0.07)\left(\frac{N_{\text{corrected}}}{10^6}\right)^{0.91 \pm 0.02}$$

7.10 Summary

A method of determining air-shower parameters has been devised based on the intersecting loci method of Williams (1952). This has been shown, using simulated air-showers, to give core location accuracy of ±10 m and an overestimate of the shower size which can be corrected for.

The technique, however, cannot handle large quantities of data for which case a computer based numerical minimisation technique has been devised (Smith [1976]). This latter technique gives improved core location accuracy (±6 m) but does suffer similar overestimation of the shower size, which too can be corrected for.

The latter technique is most useful in handling large quantities of data and is most suitable for measurements on muons in showers (see Chapter 10).

The former technique is useful when only a few selected events need to be analysed, where avoidance of the time consumptive needs of the computerised technique (i.e. where not all the available data need be analysed) would be measurements on hadrons in showers (see Chapter 11).

CHAPTER 8

TACHYON THEORY AND PREVIOUS SEARCHES

8.1 Tachyon Theory

8.1.1 Subluminal relativity

The location of an event is uniquely defined by the four-vector (x, y, z, ct). However, implicit in this statement is the fact that the event is being observed, and the frame of reference from which the event is being observed defines the values of the parameters x, y, z, ct. The values of these parameters are different if measured in different frames of reference.

However, if the two frames of reference have the same origin, but one is moving with a low velocity parameter β (where $\beta \equiv \frac{v}{c} \ll 1$) then at the instant the two frames have a common origin the event as measured in both frames of reference appears to have the same values for the parameters x, y, z and ct. This is because the time taken for light signals to reach an observer in each reference frame is the same in each reference frame.

However, if we introduce the experimentally verified postulate that the velocity of light is the same in all reference frames, then as β approaches unity, clearly the time taken for light signals to reach an observer in a reference frame moving towards the event will be less than the time taken to reach the same observer in the reference frame in which the event is stationary. The values of the parameters x, y, z, ct will thus be different if measured from the same origin but in the two different reference frames. The only parameter which can now be uniquely defined in all reference frames

is the magnitude of the four-vector i.e. $(x^2 + y^2 + z^2 - c^2t^2)^{\frac{1}{2}}$ if the various reference frames have a common origin.

If the reference frame A is moving with uniform velocity parameter β in the x-direction with respect to a reference frame B:

(8.1) Then $$x^1 = \frac{1}{(1 - \beta^2)^{\frac{1}{2}}} (x - \beta ct); \quad y^1 = y; \quad z^1 = z;$$

and $$t^1 = \frac{1}{(1 - \beta^2)^{\frac{1}{2}}} (t - \beta x/c)$$

where (x^1, y^1, z^1, t^1) is the four-vector of an event as measured in A, and (x, y, z, t) is the four-vector of the same event measured from the same origin in B. These relationships can be visually summarised in one space dimension by a Minkowski space - time diagram.

The x, t axes of reference frame A are rotated into the positive quadrant of reference frame B by θ degrees where $\theta = \tan^{-1}(\beta)$.

Minkowski space - time diagram (subluminal)

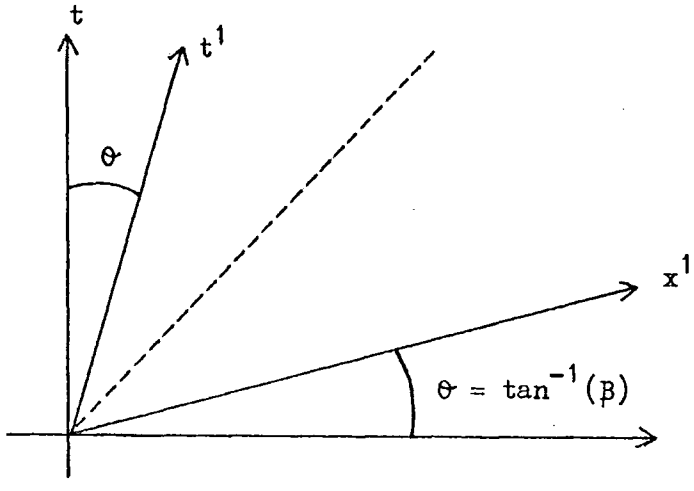

If the co-ordinates of two events in reference frame A are (x_1', t_1') and (x_2', t_2'), and all quantities in reference frame B are similarly

represented by unprimed parameters, then the following relationships can be simply derived from the above diagram:-

$$(8.2) \quad t_2 - t_1 = \frac{t_2' - t_1'}{(1 - \beta^2)^{\frac{1}{2}}}$$

$$(8.3) \quad x_2 - x_1 = \frac{x_2' - x_1'}{(1 - \beta^2)^{\frac{1}{2}}}$$

Equation (8.2) implies that time intervals in a moving reference frame are always smaller than a stationary reference frame (provided $\beta<1$). This phenomenon is called time dilation.

Equation (8.3) implies that spatial extent in the direction in which a moving reference frame is moving is always smaller in the moving reference frame than in a stationary reference frame. This phenomenon is Lorentz - Fitzgerald contraction.

Equations (8.2) and (8.3) also imply that no reference frame can be travelling at the speed of light ($\theta = 45^{\circ}$ in the Minkowski diagram) and that temporal and spatial separations have the same sense in all reference frames moving at velocities less than the velocity of light.

The four-vectors of position-time space can be replaced by the four vector (p_x, p_y, p_z, E) in momentum - energy space, or (Ax, Ay, Az, V) in magneto - electric potential space.

The above transformation equations have the same form in momentum - energy space except for the introduction of the velocity - transformation equations. These imply that the expressions for momentum p and energy E in a stationary reference frame of an object moving with velocity parameter β in the direction in which the momentum is being measured are:

$$(8.4)\quad p = \frac{M_0 \beta c}{(1 - \beta^2)^{\frac{1}{2}}} \; ; \quad E = \frac{M_0 c^2}{(1 - \beta^2)}$$

where M_0 is the rest - mass of an object, i.e. the mass as determined in the reference frame in which the object is stationary.

The above synopsis of subluminal special relativity rests on two postulates, the principle of relativity and the principle of the constancy of the velocity of light. These two postulates were first introducted by Einstein (1905).

"1. The laws by which the states of physical systems undergo change are not affected, whether these changes of state be referred to the one or the other of two systems of co-ordinates in uniform translatory motion.

2. Any ray of light moves in the 'stationary' system of co-ordinates with the determined velocity c, whether the ray be emitted by a stationary or by a moving body."

It is not necessary to introduce the third postulate that bodies cannot travel faster than light in order to derive all the transformation relationships of subluminal special relativity, but more importantly the absence of a third postulate in no way contradicts those relativistic arguements that are used to explain the physical phenomena that arise out of relativistic effects e.g. the equivalence of mass and energy, the stability of unstable particles travelling at high velocities.

8.1.2 Superluminal relativity

A frame of reference travelling with a velocity parameter $\beta > 1$ corresponds on the Minkowski space - time diagram to $\theta > 45^{\circ}$.

Minkowski space - time diagram (superluminal)

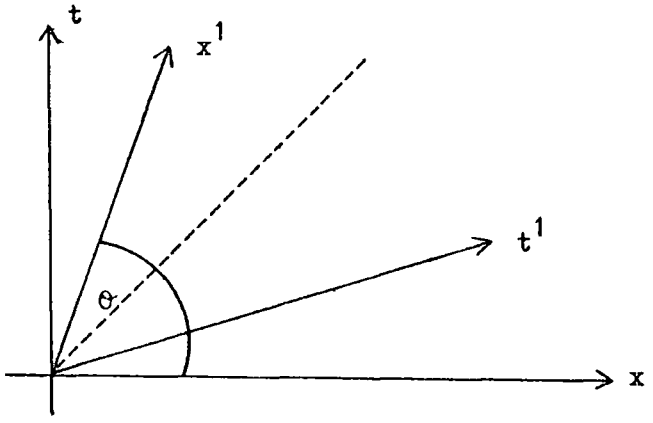

The first problem that has to be faced with superluminal frames of reference is that since the factor $(1 - \beta^2)$ is negative for $\beta > 1$, all expressions which contain the term $(1 - \beta^2)^{\frac{1}{2}}$ become imaginary. This problem has been dealt with in a variety of ways by various authors whose work will be described in more detail in the next section. One example of this problem arises when we consider the mass of a particle travelling faster than light:-

$M = \frac{M_o}{(1 - \beta^2)^{\frac{1}{2}}}$, where Mo is now the rest mass of the particle. If $\beta > 1$ then M becomes imaginary unless the rest mass of a particle travelling faster than light is imaginary.

(8.5) If we let $Mo = i\mu_o$

then $M = \frac{\mu_o}{(1 - \beta^2)^{\frac{1}{2}}}$ becomes real.

The significance of this introduction of the mass parameter μ_o is that since the rest mass of a faster than light particle is defined as imaginary, then

it must be an unobservable in all reference frames i.e. if a particle is travelling faster than light in any reference frame then it must travel faster than light in all reference frames. This means that particles that travel faster than light are a new class of particles (in the same way that photons are a different class of particles to particles that always travel slower than light). These particles are called TACHYONS (Feinberg [1967]) and have some unusual properties, and their existence gives rise to some apparent paradoxes.

8.1.3 The energy of a tachyon

Substituting identity (8.5) into equations (8.4) and considering the case $\beta > 1$ gives the expressions:

$$(8.6) \qquad p = \frac{\mu_o \beta c}{(\beta^2 - 1)^{\frac{1}{2}}} \; ; \qquad E = \frac{\mu_o c^2}{(\beta^2 - 1)^{\frac{1}{2}}}$$

for the momentum and energy of a tachyon. The behaviour of the energy and momentum of particles slower and faster than light as the particles' velocities are increased can be seen in the following diagram:-

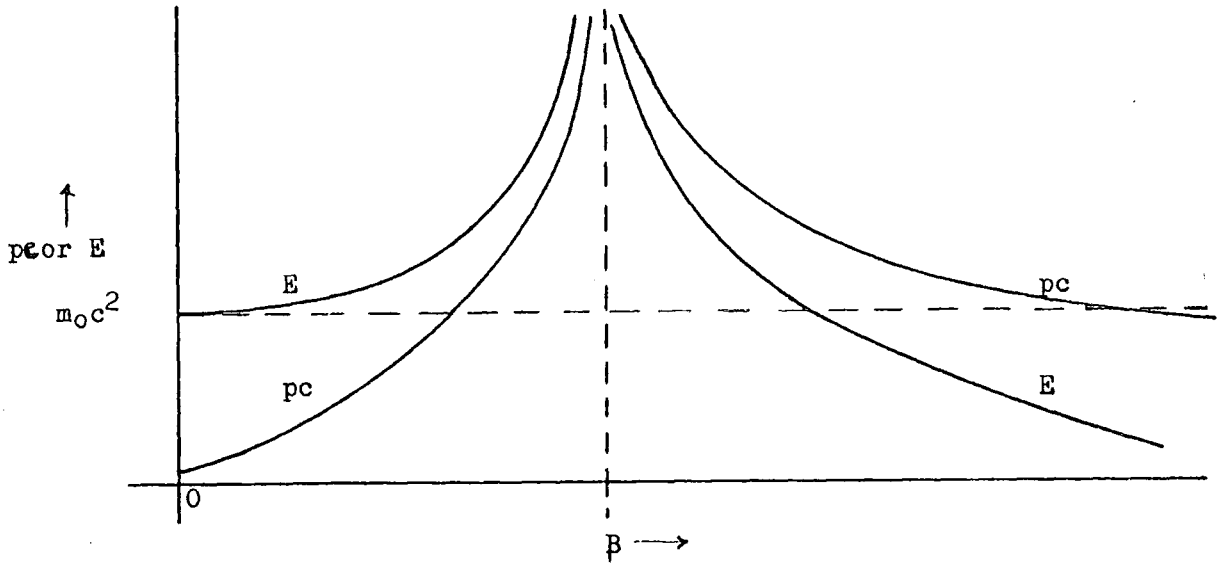

The diagram clearly illustrates the following points:

i.) Since the $E - \beta$ and $p - \beta$ relationships are asymptotic in the region $\beta = 1$, a particle travelling slower than light can never travel faster than light, and a particle travelling faster than light can never travel slower than light. (This emphasises the point made earlier that tachyons are a new class of particles.)

ii.) As the velocity of a tachyon increases so its energy and momentum decreases. Any processes which involve an energy loss from the tachyon serve to increase the velocity of a tachyon. So we expect most tachyons to be travelling at very high velocities (i.e. $\beta \to \infty$), if they have travelled through regions containing matter with which they could interact.

It is also more likely that on production tachyons are travelling with very high velocities, since the production of "fast" tachyons requires less energy than the production of "slow" tachyons.

If we consider the transformation equations (8.1) in momentum - energy space these have the form

$$(8.5) \quad p_x' = \frac{1}{(|1 - \beta_1^2|)^{\frac{1}{2}}} \left(p_x - \frac{\beta_1 E}{c}\right); \quad p'y = py; \quad p'z = pz$$

$$E = \frac{1}{(|1 - \beta_1^2|)^{\frac{1}{2}}} (E - \beta_1 p_x c)$$

where the primed quantities refer to measurements made in a reference frame moving with velocity parameter β_1 in the x-direction, and E and p are the energy and momentum of a tachyon in its rest frame.

Since the velocity parameter $\beta = \frac{pc}{E}$ of the tachyon is greater than unity we can choose a value for β_1 such that the energy of the tachyon is negative. This implies the existence of reference frames in which tachyons would be copiously produced, since the system could not be stable against their spontaneous emission.

However, the same apparent problem arises if we consider the transformation equations in spatio-temporal space:-

$$(8.6)\quad \Delta x' = \frac{1}{(|1 - \beta_1^2|)^{\frac{1}{2}}} (\Delta x - \beta_1 c \Delta t); \quad \Delta y' = \Delta y; \quad \Delta z' = \Delta z;$$

$$\Delta t' = \frac{1}{(|1 - \beta_1^2|)^{\frac{1}{2}}} \left(\Delta t - \frac{\beta_1 \Delta x}{c}\right) = \frac{\Delta t}{(|1 - \beta_1^2|)^{\frac{1}{2}}} (1 - \beta_1 \beta)$$

where the primed quantities refer to quantities measured in a reference frame moving with velocity parameter β_1 in the x-direction, and $\beta = \frac{\Delta x}{c \Delta t}$ is the velocity parameter of a tachyon.

We can now choose a value for β_1 such that $\Delta t'$ is negative when Δt is positive. This implies that we can find reference frames in which the time ordering of events is reversed, which contradicts intuitive notions of causality.

Both problems arise from the same condition viz

$$(8.7)\quad \frac{E'}{E} = \frac{t'}{t} = \frac{1}{(|1 - \beta_1^2|)^{\frac{1}{2}}} (1 - \beta\beta_1)$$

and when $\beta_1 > \frac{1}{\beta}$, E' and $\Delta t'$ are negative for positive values of E and Δt. These apparent paradoxes led scientists for over half a century to dismiss the possibility of tachyons' existence, and not until the introduction of a third postulate (Sudarshan, Bilaniuk and Deshpande [1962]) were these

paradoxes resolved and further serious theoretical and experimental investigations of faster than light particles resumed.

8.1.4 Previous theoretical investigations of tachyons

8.1.4.1 Sudarshan, Bilaniuk and Deshpande (1962)

These authors postulate two criteria which a consistent relativistic theory should satisfy viz.:

"(a) In any frame of reference the energy of a particle must be positive."

"(b) Laws of particle dynamics must be independent of frame of reference."

Criterion (b) is identical to postulate 1. of Einstein's original theory, however the constancy of the velocity of light, or rather the fact that the value of the velocity of light in free space is 3.10^8 ms^{-1}, is now considered to be a physical law, and hence independent of frame of reference. Criterion (a), on the other hand, defines a criterion by which we can test whether a physical state has real significance, i.e. it is a definition of existence in the physical universe. Take for example the transmission of energy from a source to a sink. To an observer stationary with respect to both source and sink the time ordering of events is that first the observer sees the source suffer a decrease in positive energy followed by the sink suffering an increase in positive energy. However, consider a second observer travelling with a velocity greater than light such that the time-ordering of events is reversed. First he sees the sink suffer an increase of energy, followed by the source suffering a decrease in energy. However, according to equation 8.7, this same observer also observes changes in positive energy as changes in negative energy. Hence, the observer sees first the sink suffer an increase of negative energy, followed by the source suffering a decrease in negative energy. Thus the

second observer sees first the sink as a source, suffering a decrease in positive energy, followed by the source - which he calls the sink - suffering an increase in positive energy. Although the two observers disagree about the time ordering of events, in neither frame of reference does the series of events appear to conflict with causality.

An example of such an event is the elastic collision of a tachyon with a particle moving slower than light. To an observer in whose frame the two particles appreach each other with 4-momenta (p_1, E_1) and (p_2, E_2), after the collision there will appear to be two particles receeding from each other with 4-momenta (p_1^1, E_1^1) and (p_2^1, E_2^1). However to an observer moving such that the tachyon appears to have negative energy, since to this observer the tachyon appears to be travelling backwards in time, he will describe the event as the fusion of two tachyons with 4-momenta (p_1, E_1) and (p_1^1, E_1^1) with a third, slower than light, particle with 4-momentum (p_2, E_2) to produce a fourth, slower than light, particle with 4-momentum (p_2^1, E_2^1). The introduction of postulate (a) is now indirectly referred to by other authors as the introduction of the reinterpretation principle or R.I.P., and will be referred to simply as such in what follows.

8.1.4.2 Feinberg (1967)

One of the main objections to the possibility of particles travelling faster than light has been the fact that since the energy of a particle of non-zero mass appreaches infinity as its velocity approaches the velocity of light, it would require an infinite energy source to accelerate such a particle through the "light barrier". However, Feinberg points out that since the advent of relativistic quantum field theory, it is no longer necessary to accelerate a particle through the "light barrier" in order to obtain a tachyon. Particles travelling faster than light can be created in pairs without contradicting special relativity, and Feinberg directs his attention to the description of a quantum field theory of non-interacting tachyons.

As a first step in finding a wave function to describe a tachyon Feinberg points out that solutions to the Klein- Gordon equation with an imaginary mass have to be found:-

$$(8.8) \quad (\Box^2 + \mu^2)\phi \equiv \left(\nabla^2 - \frac{\partial^2}{\partial t^2} + \mu^2\right)\phi = 0$$

where the mass m of a tachyon is given by $m = i\mu$.

The set of elementary solutions:-

$$(8.9) \quad \phi_+, k = \frac{1}{(2\pi)^{3/2}} \exp i\,(kx - wt)$$

$$\phi_-, k = \frac{1}{(2\pi)^{3/2}} \exp -i\,(kx - wt)$$ in one space dimension have the restriction $|k| \geq \mu$ always where $w \equiv +(k^2 - \mu^2)^{\frac{1}{2}}$, in order that a superposition of such solutions give the wave function of a particle with real energy.

This restriction implies that, since a superposition of solutions of the form $\Psi(x) = \int \phi_+, k\,(x)\, f(k)\, d^3k \quad (|k| \geq \mu)$ cannot be made into $\delta^3(x)$, tachyons cannot be localised in space. This problem in turn creates difficulties in describing the propagation of a tachyon, and the term "velocity" becomes a loosely defined parameter.

The classical field theoretical treatment above leads to a quantum field theory of spinless tachyons by considering the field ϕ to be an operator i.e. we expand ϕ by

$$(8.10) \quad \phi(x,t) = \int \frac{d^3k}{(2w_R)^{\frac{1}{2}}} \frac{1}{(2\pi)^{3/2}} e^{i(kx - wt)} a(k) + \int \frac{d^3k}{(2w_R)^{\frac{1}{2}}} \frac{1}{(2\pi)^{3/2}} e^{-i(kx - wt)} a^\dagger(k)$$ (in one space dimension)

where again $|k| \geq \mu$, and $a(k)$, $a^{\dagger}(k)$ are operators. The same non-localisability in space is implied by this restriction, but another restriction on the commutation relations of $a(k)$, $a^{\dagger}(k)$ arises from the required Lorentz-invariance of the theory.

This requires the existence of unitary operations $L(1, a)$ associated with a Lorentz-transformation $x' = 1x + a$ satisfying

$$(8.11) \qquad L(1, a)\, \phi(x)\, L^{-1}(1, a) = \phi(1x + a)$$

This implies that:-

$$La(k)L^{-1} = \left(\frac{k_o'}{k_o}\right)^{\frac{1}{2}} a(k') \quad \text{if} \quad \frac{k_o'}{k_o} > 0 \quad \text{and} \quad k_o', k_o \neq 0$$

$$La(k)L^{-1} = \left(\frac{k_o'}{k_o}\right)^{\frac{1}{2}} a^{\dagger}(-k') \quad \text{if} \quad \frac{k_o'}{k_o} < 0 \quad \text{and} \quad k_o', k_o \neq 0$$

(8.12)

where $k_\mu' = 1_{\mu\nu} k_\nu$

Thus the canonical commutation relations

$$(8.13) \qquad \left[a(k), a^{\dagger}(k')\right] = \delta^3(k - k')$$

$$\left[a(k), a(k')\right] = 0$$

are not satisfied, since a Lorentz-transform changing $a(k)$ into $a^{\dagger}(k)$ will change the sign of the left hand side without changing the sign of the right hand side of equation (8.13).

Quantizing with anticommutators, on the other hand, gives no such trouble So a, $a^{\dagger}$ can be taken to satisfy:-

(8.14) $a(k)\, a^{\dagger}(k') + a^{\dagger}(k')\, a(k) = \delta^3(k - k')$

$a(k)\, a(k') + a(k')\, a(k) = 0$

Therefore the tachyons are fermions, even though they have spin-zero.

By further considering the differential equations

(8.15) $\partial_\mu \phi(x) = -i\,[P_\mu, \phi(x)]$

where P_μ are the 4-vector momentum operators, Feinberg concludes that the $a^{\dagger}(k)$ can be interpreted as a creation operator, and $a(k)$ an annihilation operator, of particles of momentum k. This is a more formal approach to the negative energy solutions of equation (8.8), but with the same conclusions, as the more qualitative approach of Sudarshan et al described in Section 8.1.4.1. Furthermore the transformation of a into $a^{\dagger}$ by a Lorentz-transformation which changes the sign of k_o describes the interchanging roles of absorption and emission implied by R.I.P.

The field theory has one further unusual implication in the existence of a conserved current μ given by

(8.16) $\mathcal{J}_\mu = \phi\, \partial_\mu \phi - \partial_\mu \phi\, \phi$

since the field equation (8.8) implies

(8.17) $\partial_\mu \mathcal{J}_\mu = \phi \Box^2 \phi - \Box^2 \phi\, \phi = 0$

The conserved charge associated with u can be written

(8.18) $\phi = -\int \mathcal{J}_4 \, d^3x = \int d^3k\; a^{\dagger}(k)\; a(k)$ + infinite constant; so that ϕ defines the tachyon number present in a given reference frame. This quantity, however, is not Lorentz invariant, which formally justifies the

reinterpretation of events described in the example of elastic collisions cited in Section 8.1.4.1.

To clarify this point consider the particle interpretation of field theory. This assumes the existance of a no-particle or vacuum state defined by

$$(8.19) \qquad a(k)\left|0\right\rangle = 0$$

out of which particle states are created by creation operators i.e. a state containing n particles of momenta $k_1, k_2, \ldots . k_n$ is

$$(8.20) \qquad \left|k_1, k_2, \ldots . k_n\right\rangle = a^\dagger(k_1)\, a^\dagger(k_2) \ldots . a^\dagger(k_n)\left|0\right\rangle$$

(Notice that since tachyons are fermions, all the momenta $k_1, k_2, \ldots . k_n$ must be different.)

Consider the state

$$(8.21) \qquad \left|k\right\rangle = a^\dagger(k)\left|0\right\rangle$$

Now, from (8.12) there exists a Lorentz transformation L that changes $a^\dagger(k)$ into an annihilation operator $a(\bar{k})$.

Let us further denote the transform of the vacuum corresponding to the Lorentz transformation L by

$$(8.22) \qquad \left|\Omega_L\right\rangle \equiv L\left|0\right\rangle$$

If k is a momentum such that $\bar{k}_o$ is positive when k_o is positive, then

$$(8.23) \qquad a(k)\left|\Omega_L\right\rangle = a(k)L\left|0\right\rangle = \left(\left|\frac{\bar{k}_o}{k_o}\right|\right)^{\frac{1}{2}} L\, a(\bar{k})\left|0\right\rangle$$

$$= 0$$

Hence these momenta are not present in $|\Omega\rangle$. If, however, k is a momentum such that $\bar{k}_o$ is negative when k_o is positive, then

$$(8.24) \qquad a^\dagger(k)|\Omega\rangle = a^\dagger(k)\llcorner|0\rangle = \left(\left|\frac{\bar{k}_o}{k_o}\right|\right)^{\frac{1}{2}} \llcorner a\,(-\bar{k})\,|\,0\rangle$$

$$= \left(\left|\frac{\bar{k}_o}{k_o}\right|\right)^{\frac{1}{2}} \llcorner|-\bar{k}$$

Hence, $|\Omega\rangle$ contains one particle with each momentum whose energy changes sign under the inverse Lorentz transformation. One interesting consequence of the non-invariance of the tachyon vacuum state under a Lorentz transformation is in the analysis of the causal anomolies apparently producible with tachyons.

Consider two observers 1 and 2. By agreement, observer 1 emits a tachyon and on detection of this by observer 2, he emits a tachyon which is in turn detected by observer 1. For simplicity assume that each observer, in his rest system, emits a tachyon with infinite velocity, then if observer 2 is travelling with velocity parameter β_1 in the direction in which observer 1 emits a tachyon, clearly $\beta_1 > \frac{1}{\beta}$ where β is the velocity parameter of the tachyon emitted by observer 1. So, according to equation (8.7) we have the situation that observer 1 will receive the tachyon from observer 2 before he has emitted the tachyon that causes observer 2 to emit a tachyon.

Applying the re-interpretation principle (R.I.P.), the tachyon observed by observer 2 will appear to have negative energy, so he will not observe it as having been emitted to him, but by him. Similarly, observer 1 will interpret the negative energy tachyon emitted by observer 2 to him as a positive energy tachyon emitted by him to observer 2. Since the agreement depended on the observation of a tachyon emitted from one observer to the other, neither observer will have observed this, and the sequence of events

will not have been deemed to trigger the agreement. This, however, does raise further questions as to the control each observer has over the emission of a tachyon from his reference frame which can best be investigated by considering a tachyon detection system in more detail.

If the tachyon detector is based upon the excitement of an atom from its ground state to either an excited state, or a state of motion, then by choosing the atom to be in its ground state, we rule out the possibility that it can emit a positive energy tachyon, as seen by the observer who is using it for a detector. Hence this type of detector cannot be used to detect a tachyon moving with a velocity such that its energy changes sign under the Lorentz transformation relating the two observers.

We must thus resort to a detector based upon the excitement of an atom which is already in an excited state, either translational or internal, so that it can emit a positive energy tachyon by changing to a lower energy state. In this case what each observer will see will be spontaneous emission of a tachyon from his detector, and he will not relate it to the detection of a tachyon emitted by the other observer. Hence what would at first sight appear to be a causal anomaly would only be interpreted as uncorrelated spontaneous emission.

This implies a method of detection of tachyons. If we observe the rate of spontaneous changes to lower energy states of a detection system not in the ground state, such as radioactive decay, or the lines produced by excited atoms, these should be increased by proximity to a tachyon source. Further discussion of such techniques will be presented in a later section where previous experimental searches for tachyons are described.

8.1.4.3 Aarons and Sudarshan (1968)

These authors point out, and in fact prove by a more rigorous treatment than Feinberg, that attempting to retain the standard positive energy particle interpretation by associating creation operators with the negative frequency part of the scalar field (see equation (8.10)) introduces non-invariance into the theory under superluminal Lorentz transformations. Feinberg's motivation behind this approach was to provide a formal representation of the reinterpretation principle.

However Aarons and Sudarshan write down the scalar field ϕ in terms of annihilation operators only i.e.

$$(8.10a)\quad \phi(x,t) = \int \frac{d^3k}{(2w_k)^{\frac{1}{2}}} \frac{1}{(2\pi)^{3/2}} e^{-i(kx - wt)} a(k)$$

and then $$\phi^{\dagger}(x,t) = \int \frac{d^3k}{(2w_k)^{\frac{1}{2}}} \frac{1}{(2\pi)^{3/2}} e^{+i(kx - wt)} a^{\dagger}(k)$$

where $|k| \geq \mu$

The unitary operators L (1, a) satisfying equation (8.11) will now transform the operator a(k) as

$$(8.12a)\quad L\, a(k) L^{-1} = e^{-ilk.a} a(k')$$

Since creation and annihilation operators are not now mixed, anticommutation rules (8.14) are not necessary for quantisation, and the conclusion that spin-zero tachyons are fermions is removed.

However, since the creation operators $a^{\dagger}(k)$ can create negative energy states, the authors are forced to introduce a physical postulate:-

"The only physically relevant quantities are the transition amplitudes. Any transition amplitude is to be interpreted as the amplitude for transition between positive energy particles where all negative energy particles (of momentum p) in the initial state are interpreted as outgoing positive energy particles (of momentum -p); similarly for negative energy particles in the final state."

Which is, in fact, the re-interpretation principle in a different form. The authors conclude their paper with a question:

"Is it possible that the notion of a physical state itself is not expressible in a relativistically invariant fashion, though the physical predictions like mass levels and transition probabilities are all relativistically invariant?"

The question of Lorentz invariance will be raised again (see for example Section 8.1.4.4), and the answer to the question posed by Aarons and Sudashan seems to be that, since tachyon physics has not yet been experimentally tested (because tachyons have not yet been observed) there is no reason to presume that Lorentz invariance should be applied to it.

8.1.4.4 Recami and Mignani (1974)

Recami and Mignani in 1974 published a comprehensive review of their own, and other authors' theoretical researches into the classical behaviour of tachyons. It is of interest to quote their version of the first two postulates of special relativity, since some of the conclusions of their theory can be directly traced to these postulates:-

"1. Space-time is homogenous and space is isotropic.

2. Physical laws of mechanics and electromagnetism are required to be covariant when passing from an inertial frame to another frame in rectilinear, uniform relative motion (principle of relativity). We complete this postulate by adding the requirement that the vacuum is covariant when changing inertial frame."

From these two postulates all the usual laws and relationships (including the existence of an invariant quantity c^2 with the dimensions of velocity squared) of special relativity can be deduced. In the case of a boost along the x-axis, the generalised Lorentz transformations in spatio-temporal space are for $-\infty<\beta<\infty$

$$(8.25) \qquad x' = \pm\left(\frac{x - \beta ct}{\sqrt{|1 - \beta^2|}}\right) \; ; \qquad t' = \pm\left(\frac{ct - \beta x}{\sqrt{|1 - \beta^2|}}\right) \; ;$$

$$y' = \pm y\sqrt{\frac{1 - \beta^2}{1 - \beta^2}} \; ; \qquad z' = \pm z\sqrt{\frac{1 - \beta^2}{1 - \beta^2}}$$

The double sign in equations (8.25) is required by the invertibility of generalised Lorentz transformations.

A third postulate (R.I.P.) is required when extending relativity to cover tachyons, and this is summarised by the observation that any Lorentz transformation which reverses the sign of the fourth component of any four vector describing a particle, will reverse the sign of the fourth component of all four vectors describing that particle.

The first important generalisation these authors deduce is a "duality principle" which briefly stated claims that the terms B (a bradyon, a slower than light particle), T (a tachyon, a faster than light particle),

s (a reference frame moving with uniform velocity less than the velocity of light), S (a reference frame moving with uniform velocity greater than the velocity of light), do not have an absolute meaning, but only a relative one. That is to say any bradyon B relative to a frame s will appear as a tachyon T to frame S, and vice-versa. The duality principle is completed by adding the assumption that "frames S are supposed to have at their disposal exactly the same physical objects as frames s have, and vice-versa".

Since any Lorentz transformation must preserve the magnitudes of the four vectors associated with the transformation this provides a ready interpretation of the two signs in the equation.

$$(8.26) \qquad \left((c^1t^1)^2 + (ix^1)^2\right)^{\frac{1}{2}} = \pm \left((ct)^2 + (ix)^2\right)^{\frac{1}{2}}$$

where we have suppressed two spatial dimensions for convenience of expression, and the four vector $(x_0, x_1, x_2, x_3) = (ct, ix, iy, iz)$. The positive sign refers to transformations from a s to a s, or from a S to a S, and the negative sign to transformations from a s to a S, or from a S to a s.

Although all observers in s or S will observe real quantities in their own reference frame, if an observer s wishes to look at space-time through the observations of an observer S, or vice-versa, then he will have to do his calculations by using the four vector (ict', x', y', z') without changing, however, the correspondence between norm sign and four vector type. According to this convention, then, there is no change of metric (the chosen metric being consistently (+ - - -)) when passing from subluminal to superluminal reference frames, or vice-versa.

The above described theory can already be seen to differ from the more conventional approach outlined in Sections 8.1.1, 8.1.2, and 8.1.4.2, namely:-

1. By choosing the metric (+ - - -) instead of the more conventional (- + + +), tachyons are no longer considered as a new class of particles (c.f. the duality principle).

2. By choosing the different metric, the problem of the imaginary rest mass of a tachyon does not arise. Since the four vector in momentum space has the form $(\frac{i}{c}E, ip_x, ip_y, ip_z)$, then in order to obey the above described convention, the proper expression for the mass of an object of rest mass m_o (real) travelling with velocity parameter β should be $m = \frac{m_o}{\sqrt{|1 - \beta^2|}}$. The rest mass m_o has a real meaning for a tachyon, since superluminal reference frames (in which the tachyon can be at rest) are deemed to exist.

3. The addition of the covariance of the vacuum to the principle of relativity is in direct conflict with Feinberg's deductions (Section 8.1.4.2) from a quantum field theory of tachyons. The duality principle implies that tachyons are not a new class of particles, but "frames S are supposed to have at their disposal exactly the same physical objects as frames s have, and vice-versa". These differences, however, are based mainly on a choice of convention, and can only be resolved by observations of nature. However, these authors highlight an intriguing implication of the re-interpretation principle which is valid under either convention.

If we introduce a charged particle into the examples cited above where R.I.P. is used to interpret negative energy particles travelling backwards in time, then the sign of the charge must be reversed. In fact if we use "charge" in its broadest sense, the particle will be re-interpreted as the antiparticle of the tachyon observed by a stationary observer. This is

essentially because R.I.P. interprets a change in sign of the fourth component of every four vector, and "charge" can be associated with the fourth component of some four vector e.g. electric charge has the same sign as the electric potential in the four vector (Ax, Ay, Az, V) in magneto-electric potential space.

If we consider R.I.P. as an operator and $\hat{\alpha}$ to be the operator which reverses the sign of the observable α, then

(8.27) $\quad R.I.P. = \hat{C}\,\hat{E}\,\hat{p}$

where E = energy; p = 3-momentum; C = change.

Now, if we remember that R.I.P. follows the Lorentz transformation to a frame of reference where t and x are reversed as well as E and p, this transformation can be represented by the equation

(8.28) $\quad \hat{P}\,\hat{p}\,\hat{T}\,\hat{E} = -1$

where P = parity; T = time

The whole process of reinterpreting such a Lorentz transformed event can be written as

(8.29) $\quad R.I.P.\ (\hat{P}\,\hat{p}\,\hat{T}\,\hat{E}) = \hat{C}\,\hat{E}\,\hat{p}\,(\hat{P}\,\hat{p}\,\hat{T}\,\hat{E}) = \hat{C}\,\hat{P}\,\hat{T} = -1$

where we are making observations in momentum space.

In order for an observer in s to look at space-time through the observations of an observer in S, the convention described above essentially requires that each component of the four vector be multiplied by a factor i. Since this is equivalent, on for example a Minkowski space-time diagram, to rotation through $\frac{\pi}{2}$, this implies that what an observer in s measures for a spatial co-ordinate in the direction in which the observer S is travelling, the observer in S will interpret as a temporal co-ordinate and vice-versa.

This requires unusual physical interpretation if postulate 1 is adhered to, but this point is glossed over by the authors.

However, this reciprocity between the two elements of the four vector is used when the authors proceed to discuss superluminal transformations of the electric and magnetic fields. Briefly they conclude that elements of the magnetic field of a tachyon are transformed into the electric field when observed in a reference frame s, and vice-versa. In particular the electric field due to an electric momopole travelling faster than light should give rise to the effects expected from a magnetic momopole when observed by an observer in s. A more detailed analysis of their arguements and conclusions is presented in Section 8.1.4.9. alongside the work of other authors who have discussed this problem. However, the reciprocity between space and time has caused other authors to formulate tachyon theories in which tachyons have a preferred direction in space. Such a theory will now be discussed.

8.1.4.5 Antippa (1972) and Antippa and Everett (1971, 1973)

These three papers discuss first a one-dimensional, then a three dimensional, tachyon theory. Although the metric chosen, and hence the derived transformation equations, are identical to those deduced by Recami and Mignani (8.25), postulates of the Antippa theory lead to a more definite physical interpretation of reciprocity. These postulates are:-

" i.) (a) Any co-ordinate system having a constant velocity of magnitude different than unity, relative to an inertial co-ordinate system is itself inertial.

(b) No two inertial co-ordinate system can have a relative velocity of unit magnitude.

ii.) The laws of physics have the same form in any inertial co-ordinate system.

iii.) A luxon (a "particle" travelling at the speed of light) travelling in vacuum has a velocity of unit magnitude relative to all inertial co-ordinate systems.

iv.) Space-time is homogeneous.

v.) Space and time are real in all inertial co-ordinate systems.

vi.) Among the three magnitudes of the relative velocities of three inertial co-ordinate systems, two or none are greater than unity.

vii.) The time axis is unidirectional with respect to bradyons but isotropic with respect to tachyons. The space direction is unidirectional with respect to tachyons but isotropic with respect to bradyons."

All the postulates upto vi.) are equivalent to or can be derived from the postulates of Recami and Mignani. However postulate vii.) removes Lorentz invariance since (in one dimension) it requires the existence of either only positive or negative momentum tachyons. Since the square of the amplitude of a four vector changes sign under a superluminal transformation, i.e.

$$(c^1 t^1)^2 - x^{1^2} - y^{1^2} - z^{1^2} = -c^2 t^2 + x^2 + y^2 + z^2 \qquad \text{c.f. equn. (8.26)}$$

Antippa and Everett interpret this as an exchange of the roles of space and time for tachyons as opposed to bradyons. The concepts of velocity β and rest system for bradyons can be replaced by the inverse velocity $\xi = \frac{1}{\beta}$

and "simultaneity" system. This restores a formal symmetry about the velocity of light under an interchange of x- and t-axis, together with an interchange of velocities and inverse velocities. The equations (8.25) of the generalised Lorentz transformation become (in one dimension):-

(8.30) $|\beta| < 1$ $\qquad$ $|\xi| < 1$

$$x = \frac{x' + \beta t'}{\sqrt{1 - \beta^2}} \qquad x = \frac{t' + \xi x'}{\sqrt{1 - \xi^2}}$$

$$t = \frac{t' + \beta x'}{\sqrt{1 - \beta^2}} \qquad t = \frac{x' + \xi t'}{\sqrt{1 - \xi^2}}$$

For superluminal transformations, then, the corresponding expressions can be obtained from the expressions for subluminal transformations by substitution according to the "reciprocity principle" viz. $(x, t, \beta) \rightarrow (t, x, \xi)$.

Generalizing to three dimensions, the authors suppose that for some preferred direction in space there is a class of co-ordinate systems, called preferred co-ordinate systems, whose relative velocities are along that direction (but may have magnitude greater or less than c) such that the co-ordinates of events as seen in two of these systems, say S and S', are connected by the extended Lorentz transformation equations (8.30). For direction normal to this preferred direction the usual transformation equations $y = y'$; $z = z'$; hold. The preferred direction is called the "tachyon corridor". Reference frames having velocity less than the velocity of light are called class I, reference frames having velocity greater than the velocity of light class II. The procedure for transforming between a general reference frame S, of class I to a general reference frame S_2 of class II is, first transform from S, to a preferred reference frame of class I, say S, then transform from S to a preferred reference frame of class II, say S^1, finally transform from S^1

to S_2. Each transformation is a Lorentz transformation, but since the extended Lorentz transformation between class I and class II must be along the tachyon corridor, this introduces a preferred direction in space and thus removes Lorentz invariance from the theory.

Since the procedure also introduces a preferred velocity, namely that of the preferred reference frames normal to the tachyon corridor, the result is not the same as using an extended Lorentz transformation along the direction of the relative velocity of S_1 and S_2. The authors claim that, since the group property is not obeyed using the latter procedure, one cannot construct a consistent theory using this latter procedure. It is this fact that forces the introduction of a tachyon corridor. Similar objections to the theory of Recami and Mignani have been raised by Yaccarini (1974).

However, in a reply (Recami and Mignani [1974]) the prescription for interpreting transformed events described in Section 8.1.4.3 is expanded (i.e. that multiplication by i is a necessary procedure if an observer in a subluminal frame wishes to look at space-time through the observations of an observer in a superluminal reference frame). The difficulties in physical interpretation of such a procedure are presumably what Antippa and Everett object to, and without such a procedure, of course, the theory becomes inconsistent.

Since the tachyon corridor now plays the same role for tachyons as the time axis does for bradyons, clearly this theory is free of any causal loops. That is to say since the component of the world line of a bradyon along the time axis is always increasing, the component of the world line of a tachyon is always increasing. Hence no combination of tachyons and bradyons can be used to send a signal around a path in space-time so that it returns to its

starting point at a time before it was sent. The authors are here ignoring the fact that apparent causal paradoxes can be adequately dealt with using R.I.P. and the implied reversal of roles of absorption and emission.

Before leaving this theory, three experimental consequences will be discussed:-

1. In a reference frame having a velocity u in a direction perpendicular to the tachyon corridor relative to a preferred reference frame the velocity vectors of tachyons are confined to a cone whose opening angle is of order $\tan^{-1}(1 - u^2)^{-\frac{1}{2}}$. Hence it is possible, depending of the velocity of the earth relative to the tachyon corridore, and on what is the orientation of the experimental apparatus relative to the preferred direction, that a particular experimental arrangement might be unable to detect tachyons.

2. The transformation equations (8.30) do not leave invariant the magnitude of the scalar product of two four-vectors when transforming to a superluminal reference frame. See for example equation (8.26).

   So for a light signal observed in a subluminal reference frame, whose four-vector is $(t, \bar{r})$ then $t^2 - r^2 = 0$. However, $t'^2 - \bar{r}'^2 = 0$ only if $\bar{r} = (x_1, 0, 0)$ i.e. if $\bar{r}$ is along the tachyon corridore. Thus a light signal in class I co-ordinate systems will only have speed c in class II co-ordinate systems if, as measured by a preferred observer it happens to be moving along the tachyon corridor. Hence electromagnetic fields associated with tachyons do not in general propagate with speed c in subluminal reference frames. Since such fields do not thus obey Maxwell's equations in subluminal reference frames, the theory implies nothing about the way charged tachyons' fields couple with ordinary matter, in particular their coupling to ordinary matter might be arbitrarily weak.

3. Since the theory contains a lack of invariance under rotations and under pure Lorentz transformations perpendicular to the tachyon corridor, if tachyons couple to ordinary matter, one will observe a lack of invariance even in processes involving only bradyons because of virtual tachyon effects. This would appear as, for example, a difference in the values obtained for the pp cross section in two measurements taken with the same beam 12 hours apart, when the earth's rotation will have caused the direction in space of the incident beam to reverse. The violation of rotational invariance will be discussed further below in Section 8.3.1.1. where an experimental search for tachyons based on such an effect is reviewed.

8.1.4.6 Goldoni (1972) (1973a) (1973b)

Prompted by the unsatisfactory interpretation scheme for the role of imaginary quantities proposed by Racami and Mignani, Goldoni points out that the four momentum of a subluminal particle is not invariant under superluminal transformations.

Hence since any two (or many) body interactions between a bradyon(s) and a tachyon(s) can only involve exchanges between those state vectors which are invariant under superluminal transformations, tachyons and bradyons can only interact by changes in internal quantum numbers e.g. strangeness.

Goldoni infers from similar considerations, i.e. demanding invariance under superluminal Lorentz transformations, that the introduction of tachyons can be justified only if we hypothesize suitable interactions between tachyons and bradyons which allow to interpret the breakdown of "slow" symmetries as

a process in which some quantum numbers are exchanged between slow and fast (i.e. bradyonic and tachyonic) world.

In fact, since it can be shown that a bradyonic field and a tachyonic field can only interact if the two fields are massless, Goldoni deduces the existence of two massless particles, the one slow, the other fast. He associates these particles on a Feynman graph of massless fields' interactions with a spurion and a tadpole respectively.

8.1.4.7 Pavlopoulus (1967)

An alternative solution to the problem of non-invariance under superluminal transformations is to propose that Lorentz invariance is an approximate invariance only valid in regions of space accessible to experiment. Pavlopoulus proposed that such regions can be characterised by a universal length of the order of the diameter of the proton, the distance of strong interactions, the "classical radius" of electrons. These examples are quoted from considerations of previous authors' proposals for a universal length e.g. Pauli's (1933) considerations on the infinite self-energy of electrons in the divergencies of quantum electrodynamics. The characteristic length $l_o \simeq 10^{-15}$ m and for regions of space less than this the hyperbolic wave equation $\Box\psi = 0$ is only an approximation to a higher order partial differential equation of the form .

$$(8.31) \qquad -l_o^2 \nabla^4 \psi + \Box\psi = 0$$

This, however, leads to the conclusion that for very short wave lengths the group velocity of an electromagnetic wave can exceed the velocity of light

viz.

$$(8.32) \quad v_{group} = c\,\frac{(1 + 2l_o^2k^2)}{(1 + l_o^2k^2)^{\frac{1}{2}}} \simeq c(1 + \tfrac{3}{2} l_o^2k^2)$$

for $1 \gg l_o^2k^2$ where k is the wave number. This poses the experimentally verifiable proposition that for γ-rays of short wave-length ($\sim 10^{-15}$ m) the group velocity is a function of wave-length.

The range of distances over which tachyons, according to this scheme, exist is $<10^{-15}$ m away from a bradyon, and they thus only take part in strong interactions between bradyons confined to such regions e.g. quark-quark interactions.

However, the physical model of an elastic medium in which a higher order partial differential equation describes the propagation of an elastic wave involves the association of a vector with every position, as well as a scalar position. This implies that, since these vectors constitute a preferred direction (or directions), the special principle of relativity is violated on a micro-scale. In particular, in this model one would not generally have invariance under reflection (c.f. Antippa and Everett, Section 8.1.4.6).

8.1.4.8 H. Lemke (1975a, 1975b, 1975c, 1976a, 1976b)

This author concerns himself primarily with deriving an electrodynamics of tachyons based on the real superluminal Lorentz transformations used by Antippa and Everett (Section 8.1.4.6). He proposes two criticisms of the electrodynamics of Recami and Mignani (Section 8.1.4.3) which is based on complex superluminal Lorentz transformations.

a.) The electromagnetic potential $\phi' \propto 1/(x'^2 + y'^2 + z'^2)^{\frac{1}{2}}$ of a tachyon in its rest frame transforms to $\phi^3 \propto 1/([x - vt]^2 - [v^2 - 1]\ [y^2 + z^2])^{\frac{1}{2}}$ (v = tachyon speed) in a subluminal reference frame by a complex transformation. Hence ϕ becomes infinite at the surface of a cone in space. Since the fields must also thus become infinite there, this implies that tachyons will produce Cerenkov radiation in media. However, based on more general arguements, Recami and Mignani predict that charged tachyons do not induce Cerenkov radiation in subluminal media. (Appendix I presents a further discussion of Cerenkov radiation from tachyons.)

b.) From the same expression a slightly accelerated, charged, pointlike tachyon produces infinite radiation energy and hence must immediately lose all its energy. On the other hand, the radiation energy is finite relative to the tachyon rest frame, so by a suitable superluminal Lorentz transformation, one can obtain finite values of the energy momentum vector relative to a subluminal frame. This cannot be achieved using the complex transformations.

In order not to have to invoke the existence of new particles, (c.f. Goldoni, Section 8.1.4.7) Lemke assumes that the law of light speed invariance is not valid in its most general form. In fact a law of the equality of the transverse co-ordinates of an event relative to all reference frames is assumed to be more fundamental than the law of light speed invariance.

Finally, since Lemke assumes space is isotropic, he does not interpret the fact that superluminal Lorentz transformations only form a group with ordinary Lorentz transformations in the same direction as implying the existence of a tachyon corridor (c.f. Antippa and Everett, Section 8.1.4.6). Instead he interprets the preferred direction as being the instantaneous direction of motion of the tachyon.

The derived transformation equations are identical to equations (8.30).

The transformation equations for the electromagnetic fields under superluminal transformations can have one of two forms:-

(8.33) $Ex = -Ex'$ $\qquad Hx = Hx'$

$Ey = \delta(E'y + vH'z)$ $\qquad Hy = \delta(H'y - vE'z)$

$Ez = \delta(E'z - vH'y)$ $\qquad Hz = \delta(H'z + vE'y)$

or $Ex = -Hx'$ $\qquad Hx = Ex'$

(8.34) $Ey = \delta(H'y - vE'z)$ $\qquad Hy = \delta(-E'y - vH'z)$

$Ez = \delta(H'z + vE'y)$ $\qquad Hz = \delta(-E'z + vE'y)$

where $\delta = 1/(v^2 - 1)^{\frac{1}{2}}$

Alternative (8.34) has been chosen by Recami and Mignani (1974) by requiring that, in analogy to the subluminal Lorentz transformations of the fields, Ey and Hz are transformed under a superluminal Lorentz transformation as the couple x and t. This implies that charged tachyons behave like magnetic monopoles to a subluminal observer. However, if we consider a superluminal reference frame to emit a charged tachyon relative to its rest frame, this will behave like a magnetic monopole relative to that frame. Transforming to a subluminal reference frame, E and H must be interchanged once more, and the tachyon will now appear as an electric charge relative to the subluminal reference frame. Lemke chooses equation (8.33) and thus obtains for the field of a uniformly moving charged tachyon the expression:-

(8.35) $\underset{\sim}{E} = (v^2 - 1)\, q\, \underset{\sim}{r}/R^3$

$\underset{\sim}{H} = [\underset{\sim}{v}, \underset{\sim}{E}]$

where $R = ([x - vt]^2 + [v^2/c^2 - 1]\,[y^2 + z^2])^{\frac{1}{2}}$

The electric field strength thus increases like v^2 with increasing v along the direction of flight of the tachyon, contrary to the behaviour of the electric field of a subluminal relativistic charged particle. Also the field strength normal to the direction of flight decreases like $\frac{1}{v}$, hence the electric field of a tachyon is confined to a tube along the direction of flight at high values of v.

The magnetic field lines are circles around the direction of flight. At high v, the magnetic field is independent of v and has the strength of the magnetic field of a charge moving with velocity $1/\sqrt{2}$. This independence, plus the decrease in the electric field normal to the line of flight, has led other authors e.g. Parker (1969) to suggest that charged tachyons might have properties similar to those of a magnetic monopole. This is a different approach to that of Recami and Mignani (op cit) but with a similar conclusion.

8.2 Indirect evidence for the existence of tachyons

8.2.1 The isotropy of the early universe

In the early stages of an expanding universe, distant regions of the universe are receding from each other at the velocity of light. Ordinary matter with $\beta \leq 1$ is bound by short particle horizons which prevent large scale communication in the early stages of a big-bang universe. Hence there is a problem in understanding why the universe has been so homogeneous and isotropic right from the very early stages.

Narlikar and Sudashan (1976) describe the life of a tachyon produced in the early stages of a big-bang universe. They conclude that the trajectory on

a space-time diagram reaches a limit at some co-ordinate (r_m, t_m) depending on the mass and initial energy of the tachyon. The trajectory then travels backwards in time until the point $(2r_m, t_o)$. This can be interpreted as the production of a tachyon and an antitachyon at $(0, t_o)$ and $(2r_m, t_o)$ respectively which meet and annihilate at (r_m, t_m). Such a tachyon - antitachyon pair provides an efficient way of establishing correlations over distant parts of the universe in the early stages.

8.2.2 Radio sources with superluminal velocities

In a review article by Cohen, Kellerman , Shaffer et al (1977) observations using very long baseline interferometery measurements of strong compact extragalactic radio sources are described. It is shown that nearly 50% of such sources appear to be expanding with velocities in the range 4 to 10 times the velocity of light.

Various attempts at explaining these phenomena without invoking the possibility of faster than light velocities have been proposed (see for example the review article by Blandford, McKee and Rees [1977]), but difficulties are encountered by all models since these sources seem to be primarily two components receding from each other along some preferred direction, rather than spherically symmetric expansions.

The combined phenomena of two bodies receding from each other at speeds greater than the speed of light along some preferred direction might indicate the presence of tachyons, but more comprehensive measurements are required before the more popular explanations can be dismissed.

8.3 Previous searches for tachyons

8.3.1 Laboratory searches

8.3.1.1 Alvager and Kreisler (1968)

This experiment hoped to detect the Cerenkov radiation emitted by a tachyon in a vacuum. Since tachyons only travel a short distance, if they do indeed emit Cerenkov radiation (see Appendix I), before losing all their energy, the tachyons were observed travelling through an evacuated electrostatic field of 3 kV/cm. The tachyons were hoped to be produced by pair production from γ-photons in a cylindrical lead shield surrounding a 5-mCi cesium-134 source (main γ-components: 797 keV (32%) and 605 keV (44%)).

The detector (a photomultiplier tube looking normal to the direction of the electrostatic field) would be sensitive to charged tachyons in the range 0.1e to 2e. No peak in the pulse height spectrum was observed and the authors estimate an upper limit on the cross-section for production of tachyons by 0.8 keV photons in lead of 3.10^{-30} cm^2.

The experiment does rest on 3 assumptions:

a.) that tachyons gain energy in an electric field in the same way as ordinary particles;

b.) that the emission of Cerenkov light in a vacuum is not suppressed by any selection rules;

c.) that tachyons do not have a large probability of being captured in matter.

The failure of any one of these assumptions would change the results of this experiment "quite drastically".

Although this experiment would be sensitive to the creation of tachyons of any "rest mass", it is possible that the production cross-section is very small below energies corresponding to the "rest mass" of the tachyon. Hence, the authors conclude that efforts to extend the measurements to higher photon energies would be justified.

8.3.1.2 Davis, Kreisler and Alvager (1969)

This experiment was basically the same as the previous one. The γ-source used (129 mCi C_o^{60}) gave photons with an average energy $\sim$1.2 MeV. The detection apparatus was two photomultipliers viewing two co-linear evacuated electric fields. The authors looked for coincident pulses from the two photomultipliers which would indicate the production of Cerenkov radiation by a tachyon travelling along the direction of the electric fields.

In 10^4 seconds, seven such co-incident pulses were observed when the γ-source was present, and seven pulses in 10^4 seconds without the source. The authors conclude that the cross-section for tachyon photo-production in lead by photons of 1.2 MeV is $\sigma < 1.67 . 10^{-33}$ cm^2. They point out that this limit is over eight orders of magnitude smaller than the cross-section for photo-production of electron-positron pairs at the same energy.

8.3.1.3 Baltay, Feinberg, Yeh and Linsker (1970)

These authors looked for neutral tachyons produced by capture of K^- and $\bar{p}$ at rest by protons in a hydrogen bubble chamber. The reactions envisaged

where:

(i) $K^- + p \longrightarrow \Lambda^o + t^o \longrightarrow p + \pi^- + t^o$

(ii) $K^- + p \longrightarrow \Lambda^o + t^o + \bar{t}^o \longrightarrow p + \pi^- + t^o + \bar{t}^o$

(iii) $\bar{p} + p \longrightarrow \pi^+ + \pi^- + t^o$

(iv) $\bar{p} + p \longrightarrow \pi^+ + \pi^- + t^o + \bar{t}^o$

where t^o and $\bar{t}^o$ and respectively a neutral tachyon and antitachyon. In reactions (i) and (iii) the missing mass technique was used. The four-momenta of the charged particles involved in these reactions are easily measured (using at rest kaons and antiprotons makes momentum measurements more accurate). Hence by plotting a histogram of the square of the missing mass required to balance the equations (i) and (iii) the presence of a tachyon should show up as a negative missing mass squared. (Since the "rest mass" of a tachyon is imaginary.)

From theoretical considerations (Feinberg op cit and see Section 8.1.4.2) pair production of tachyons seems more likely (i.e. reactions (ii) and (iv)). The negative missing mass squared method of searching for pairs of tachyons then only covers a small section of the spectrum available for this parameter when two neutral tachyons are produced.

Out of 2348 events where the products were produced from K^- and $\bar{p}$ at rest no events with a negative missing mass squared were found. The following limits for the ratio of the production of tachyons to the production of "ordinary" particles were thus deduced:-

$$(K^- + p \longrightarrow \Lambda^o + t^o) \Big/ (K^- + p \longrightarrow \Lambda^o + \pi^o) \leq 2.10^{-3}$$

$$(K^- + p \longrightarrow \Lambda^o + t^o + \bar{t}^o) \Big/ (K^- + p \longrightarrow \Lambda^o + \pi^o) \leq 2.5.10^{-3}$$

$$(\bar{p} + p \longrightarrow \pi^+ + \pi^- + t^o) \Big/ (\bar{p} + p \longrightarrow 3\pi) \leq 2.10^{-3}$$

$$(\bar{p} + p \longrightarrow \pi^+ + \pi^- + t^o + \bar{t}^o) \Big/ (\bar{p} + p \longrightarrow 4\pi) \leq 1.10^{-3}$$

Hence the authors conclude that the production of neutral tachyons in two typical hadron processes is at least three orders of magnitude smaller than the strong interactions. This method, though, does have the distinct advantage of assuming nothing about the interactions of tachyons with ordinary matter.

8.3.1.4 Danburg, Kalbfleisch, Borenstein, Strand and Vanderburg (1971)

These authors conducted a search for pairs of charged tachyons by measuring the momentum of the charged particles produced in the reaction $K^- p \longrightarrow \Lambda$ + two charged tracks, for 2.2 GeV/c K^- incident on a hydrogen bubble chamber. The velocities were measured from the curvature of the tracks in a magnetic field. The method rests on three assumptions:

a.) Charged tachyons of a given momentum follow curved paths in a magnetic field just as singly charged ordinary particles of the same momentum do.

b.) Tachyons leave ionised tracks in the bubble chamber with bubble densities comparable to that of ordinary particles.

c.) The Cerenkov radiation of charged tachyons is suppressed sufficiently to allow ionisation to be the dominant energy loss mechanism.

The analysis concentrates on reactions of the type

$$K^- p \longrightarrow \Lambda x^+ x^- (MM)$$

where x is assumed to be a pion and MM (the missing momentum required to balance the equation) corresponds to a negative missing energy. These events were then analysed to see whether they could be explained in terms of

ordinary particles and out of 179 events examined as possible examples of tachyon pair production via $K^- p \longrightarrow \Lambda t^+ t^-$, no event could be thus described.

The authors conclude with an upper limit on the cross-section for the production of tachyon pairs having "rest mass" between ~100 MeV and ~1 GeV of 0.2 μb.

8.3.1.5 Danburg and Kalbfleisch (1972)

Since a tachyon has negative energy these authors looked at bubble chamber photographs where a proton, with no incoming particle, recoiled, indicating the decay

$p \longrightarrow p + t^o$

or $p \longrightarrow p + t + \bar{t}$

These decays are energetically permissible and should be reinterpreted as the collision of a proton with an incoming (positive energy) tachyon. The accuracy of the scanning measurements allowed the authors to distinguish recoil protons down to a kinetic energy of 4 MeV. No such tracks were found and based on an upper limit of one spontaneous proton recoil event in 2×10^{27} protons veiwed for 27 seconds, the lifetime of free protons for elastic tachyonic decay via the above reactions was thus greater than 2×10^{21} yr.

8.3.1.6 Bartlett and Lahana (1972)

These authors used the same apparatus as Davis, Kreisler and Alvager (see Section 8.3.1.2) for the production and detection of tachyons. However,

instead of using an electrostatic field to provide the energy lost by Cerenkov radiation they used a magnetic field. This is based on the arguement (Recami and Mignani [1974] and see Sections 8.1.4.4 and 8.1.4.8) that an electrically charged tachyon should behave as a magnetic monopole.

They found that the cross-sections for the production of such particles by 1 MeV γ-rays in lead and water are less than 0.6×10^{-36} cm^2 and $2 \times 10^{-36} cm^2$ respectively.

8.3.2 Searches in the cosmic radiation

8.3.2.1 Ramana Murthy (1971)

Ramana Murthy was the first to search for tachyons in the cosmic radiation by making use of the fact that the particles (electrons and γ-photons) in the shower front of an extensive air-shower travel at or very near the speed of light. Hence if a tachyon is produced in, say, the first interaction of a primary cosmic ray high in the atmosphere - which subsequently produces an air-shower - then the tachyon should arrive t seconds before the air-shower. If d = distance from point of initiation of air-shower to detector; c = velocity of light, then $t = \frac{d}{c}$.

Ramana Murthy conducted his tachyon search at mountain altitude such that the average height of initiation of an air-shower above the apparatus is $\sim$2 km. His technique differed slightly from subsequent searches in that he used a tachyon detector as a gate and searched for a statistically significant number of air-showers associated with such a signal in the following 20 μs.

Two tachyon detectors were used for the gate. The first was a liquid scintillator (75 x 75 x 22 cm^3) which could detect either charged or neutral tachyons from the secondary electrons produced by a tachyon interacting with the material of the scintillator. The second detector was based on the same principle as that used by Alvager and Kreisler (1968) (see Section 8.3.1.1). Two photomultipliers viewed an air gap (800 millibars) normal to the direction of an electrostatic field of 2.1 kV/cm. At such a low pressure a distance of only 9.5 cm, the Cerenkov light produced by an ordinary charged particle, would be negligible. Hence any coincidence between pulses from both photomultipliers would be due to chance or to Cerenkov light produced by a charged tachyon in a (near) vacuum. The electric field supplied energy to the tachyon so that it could emit Cerenkov light without losing all of its energy in the first fraction of a centimeter (see Appendix I). The equilibrium energy of a singly charged tachyon emitting Cerenkov radiation in such an electric field was calculated to be 3.4 eV, the photomultipliers were sensitive to photons in the range 2.3 eV to 3.4 eV.

The air-shower detector consisted of 4 x 0.26 m^2 chronotron scintillators arranged in a square array of side 10 m symmetrically about the tachyon detectors.

In an operating time of 5079 hours using the liquid scintillator he observed 8271 coincidences between a particle depositing an energy ≥ 40 MeV in the scintillator and an air-shower arriving in the following 19 μs. (The 1 μs immediately following the production of a pulse was excluded to avoid recording coincident pulses due to the finite thickness of the shower front, ~500 ns.) The number of chance coincidences was calculated to be 8217 $\pm$91, hence no evidence for tachyons associated with air-showers was observed.

In an operating time of 1174 hours with the Cerenkov detector and the electric field polarised so as to detect positively charged tachyons, 52 coincidences were observed compared with an expected chance count of 46 ± 7.2.

In an operating time of 1423 with the Cerenkov detector and the electric field polarised so as to detect negatively charged tachyons, 44 coincidences were observed compared with an expected chance count of 41 ± 6.6.

A histogram of the delay time between the arrival of a trigger pulse and an air-shower showed no significant departure from a random distribution.

Observing air-showers of primary energy $\geq 3.10^{13}$ eV at the rate of 20 hr^{-1}, Ramana Murthy concludes that the frequencies of occurrence of tachyons in E.A.S. are less than 3.10^{-4} to 10^{-5}, relative to that of electrons. However failure to detect tachyons, as Ramana Murthy points out, implies either that they do not exist or that the production and interaction characteristics of tachyons are such that they could not have been detected in this experiment.

8.3.2.2 Ashton, Edwards and Kelly (1970)

In an experiment to determine the precision with which time of flight measurements can be made using two large (1 m^2) area scintillation counters separated by 5.30 m, these authors found no evidence for the presence of particles travelling with velocities > 1.6 c in cosmic rays at sea level. For a running time of 1.48 hr and an acceptance aperture of 19.5 cm^2 st, the limit at the 90% confidence limit was thus calculated to be $< 2.2.10^{-5}$ cm^{-2} s^{-1} st^{-1}. This limit refers to tachyons depositing > 2 MeV in each of three scintillators.

8.3.2.3 Clay and Crouch (1974)

These authors conducted a sea level search for tachyons associated with air-showers of energy $\geq 2.10^{15}$ eV. They used a plastic scintillator (1 m^2 x 5 cm) as a tachyon detector and fed the pulses recorded by this into a digital transient recorder which at any instant held a record of the previous 128 μs. On the arrival of an air-shower (determined by a square array of side 30 m - of five such scintillators with a fifth at the centre) the output of the recorder was fed (after digital to analogue conversion) was fed onto a chart recorder. In this mode the tachyon detector recorded the 114 μs previous to the arrival of an air-shower.

Comparison of the time of arrival of the largest pulse in the 97.5 μs previous to the arrival of 1,307 air-showers with a randomly generated set of arrival times gave a χ^2 probability of 10^{-4} that the test data and the E.A.S. data were from the same distribution.

Hence the authors conclude that they have found evidence for non-random events preceding the arrival of an air-shower, and that this is the result of a particle travelling with an apparent velocity greater than that of light.

However, Prescott (1975) points out two criticisms of the Clay and Crouch results which raise doubts as to their validity.

No excess of pulses appears in the interval 0 - 105 μs compared with the interval 105 - 210 μs, previous to the arrival of an air-shower. The main contribution to the χ^2-test comes from low counting rates in the first channel (earliest in time) of the interval scanned. If events in this channel were systematically low, then the overall results might no longer be significant.

In fact Prescott found such a systematic effect because of the method of analysis used by Clay and Crouch i.e. selecting the largest pulse in the 105 μs previous to the arrival of an air-shower.

The pulses received by the transient recorder were of a double differentiated form with a substantial overshoot (~30%). The arrival of a pulse immediately prior to the 105 us of tachyon sensitive time would reduce considerably the size of any pulse in the first, and to a lesser extent the second, bin (Clay and Crouch used 7.5 us wide bins for their χ^2-analysis). Thus if the largest pulse arrived in the earliest time interval this would not be observed to be the largest pulse, and the number of events in this channel would thus by systematically low.

By comparing the original Clay and Crouch data with a random distribution low (0.83) in the first channel, the two sets gave a χ^2 probability of 0.2 of being from the same distribution. (The figure 0.83 was arrived at by randomly triggering events and comparing the number of pulses in a channel in the first place with the average of the same channel in all other positions - thus isolating the effect of channel position from the neutral fluctuations between the channels.)

It is worth noting that the pulses observed by Clay and Crouch were ~10% the height of the pulse produced by a relativistic (subluminal) muon.

8.3.2.4 Crouch and Tanahashi (1974)

These authors used a 96 μs electromagnetic delay line to store the pulses from a 1 m^2 scintillator at the centre of a triangular array of similar

detectors A, B, C. On the arrival of an air-shower signified by a three fold coincidence of pulses corresponding to at least eight particles striking each detector A, B and C, four sets of data from the tachyon detector were recorded in sequence:-

(i) The signals stored in the 96 μs electromagnetic delay line together with signals from the 100 μsec following the air-shower.

(ii) A superimposed sweep with the input of the oscilloscope grounded about 0.6 sec later, providing a reference level of measuring signal amplitudes.

(iii) A "Random" sweep seven seconds after the air shower displaying the 196 μsec long train of signals from the delay line at that time.

(iv) A reference sweep with oscilloscope input grounded superimposed on the "Random" sweep.

(Sets of data (iii) and (iv) were recorded with the camera wound on one frame.)

The "Random" sweeps are used to measure the chance coincidence rate, they also enable comparison of the time and pulse height distributions between pulses prior to air-showers and random pulses which will be identically affected by spurious effects such as drift in detector sensitivity, electrical noise pickup, etc.

Analysis of the time distribution of signals preceding 1736 air-shower events with energy $E \geq 10^{15}$ eV gave no evidence of a tachyon component in the shower core. Using a scintillator with a threshold energy of 0.05 x the mean energy deposited by a relativistic muon, a tachyon/electron flux limit of 0.0006 was determined.

8.3.2.5 Prescott (1975) (1976)

Using a similar apparatus to Clay and Crouch (Section 8.3.2.3) Prescott conducted an independent search for tachyons. The refinements he introduced reduced the minimum detectable signal to 5.10^{-4} the signal produced by a relativistic muon, and the pulse overshoot was reduced to less than 0.5%.

Using a (50 x 50 x 10) cm^3 plastic scintillator located 17.5 m from the centre of the University of Adelaide air-shower array (Clay et al [1975]). Prescott compared the distribution in time of arrival of pulses preceding 4315 showers of size greater than 10^5 particles with the time of arrival of 5715 randomly triggered events. In both sets of events the time distribution of signals was found to be consistent with a uniform distribution. In addition, the frequency of events in which zero, one, two, etc. pulses were recorded was found to be consistent with a Poisson distribution, indicating no tendency for pulses to be associated in time.

He thus concludes that, at the 95% confidence limit, there are less than 30 tachyons per shower (which is comparable with the total number of hadrons of energies >100 GeV in showers of size 6.10^5 particles). Hence Prescott has observed, at the 95% confidence limit, an upper limit on the tachyon/electron flux of 0.00005.

8.3.2.6 Fegan, O'Brien, O'Brien and Porter (1975)

These authors conducted a search for tachyons, associated with air-showers, at sea-level using a 2.5 m^2 x 5 cm plastic scintillator as the tachyon

detector. This was placed at the centre of a triangular array of three 500 cm^2 x 0.5 cm plastic detectors which provided the air-shower trigger. Using a 200 bit static shift register clocked at 250 kHz to record the pulses in the tachyon detector, an 800 μs record of the time distribution of detected events in the tachyon detector could be obtained at any instant. A master pulse inhibited the register 380 μs after an air-shower event, and a record of the number of pulses in the 420 μs before to 380 μs after the air-shower arrival was obtained. No information on the pulse heights was recorded, however, using two photomultipliers viewing the tachyon detector in coincidence for 2649 showers, and a single photomultiplier for 1514 showers, the authors obtained two independent sets of data:-

Mode A - demanding coincidence between the two photomultipliers corresponds to demanding an energy deposit in the scintillator $\geq$1 MeV;

Mode B - demanding a signal from a single photomultiplier corresponds to demanding an energy deposit in the scintillator $\geq$0.5 MeV.

No statistical significant deviation from random expectation on the basis of a χ^2 test on the time distribution of events in the 408 μs to 12 μs before the air-shower arrival was observed in either Mode A or Mode B. The minimum shower size detectable was 2.10^{15} particles.

By comparing the observed number of pulses in the 108 μs to 12 μs before the air-shower arrival with the number expected in a random 96 μs time interval the authors produce an upper limit at the 3σ level of $2.06.10^{-2}$ tachyons m^{-2} per shower from Mode A, and $6.58.10^{-2}$ tachyons m^{-2} per shower from Mode B, at a mean shower energy of 2×10^{15} eV.

8.3.2.7 Hazen, Green, Hodson and Kass (1975) (1976)

These authors used a 1.44 m^2 x 3.8 cm^2 plastic scintillator and a transient recorder to record pulses between 0.03 and 0.1 times the height of a pulse due to a single muon that arrived in the 170 μs, previous to the arrival of an air-shower of size $\geq 10^5$ particles. In Run I they found no statistically significant difference between the number of largest pulses detected prior to the arrival of an air-shower and the number of largest pulses generated in the same time interval by a "Random" trigger. The "Random" trigger was essentially the arrival of a small air-shower as detected by two detectors 7 m away from the tachyon detector and separated by 7 m, triggering on a one particle m^{-2} threshold.

In Run II, two 1.44 m^2 plastic scintillators were placed one above the other and the time distribution of coincident pulses in the 160 μs prior to the arrival of an air-shower was plotted. A chi-squared test indicated that the results could be satisfactorily represented by a flat distribution.

Based on the 190 h observing time of Run II, where the minimum pulse observed was 0.02 times the pulse height due to a single muon, they calculated an upper limit on the flux of tachyons at sea-level associated with air-showers of size $\geq 10^5$ particles to be 10^{-8} cm^{-2} s^{-1} st^{-1}.

They do not include in their report (1976) an evaluation of the limit placed on the cross-section for tachyon production (assuming that the number of collisions per primary that are effective in producing a tachyon is 2) of 60 times the total production corss-section of a primary cosmic ray. Their statistical tests would only have been sensitive if 100 tachyons had been detected in 2366 showers, they thus conclude this method of searching for tachyons to be insensitive.

8.3.2.8 Emery, Fenton, Fenton, Greenhill and Humble (1975)

These authors conducted two searches for tachyons associated with air-showers. The first search demanded that a tachyon produce a pulse in one of 96 G-M tubes in four 1 m x 1 m trays evenly spaced around a circle of radius 21.2 m in the 108 μs before the arrival of an air-shower as detected by these trays of G-M tubes. They analysed 27,449 showers and observed 3,512 pulses which preceded these showers by up to 108 μs. They found a 0.9 probability that the time distribution of these pulses was no different to a flat distribution, based on a χ^2-test.

Because of the possibility (see also Chapter 9 Section 9.8) that a tachyon might not be detectable by a G-M tube they conducted a second search using a 75 cm diameter, 2.5 cm deep liquid scintillator at the centre of the air-shower detection array as a tachyon detector. This latter system registered pulses greater than 0.1 times the pulse height due to a single muon. In 9521 showers observed with this system they observed 3766 pulses from the liquid scintillator in the 108 us before each shower. They found a 0.15 probability that the time distribution of these pulses could be generated by random sampling.

They conclude that they found no positive evidence for tachyons in association with air-showers.

8.4 Summary and conclusions

8.4.1 Laboratory searches

All these searches assume that, since tachyons can exist with very low energies, there should be no energy threshold for their production. This

rather literal interpretation of the theory of tachyons demands that tachyons should be easily produced, and the only problem is in their detection.

The only conclusion that one can draw from such experiments is that tachyons are not easily produced, or that they interact with matter so weakly thay they cannot be detected.

The technique of searching for Cerenkov radiation in a vacuum, a unique signature, is more thoroughly discussed in Appendix I, where it is concluded that tachyons do not emit Cerenkov radiation in a vacuum.

8.4.2 Cosmic ray searches

Except for the mountain altitude search of Ramana Murthy, all authors used scintillation detector (or G-M tubes) techniques to search for tachyons. Some authors hoped for an interaction of the tachyon in the material of the detector, others hoped to detect a low ionisation loss by a tachyon but demanded a high rate of production.

All cosmic ray searches at sea-level have concentrated on looking for small pulses and thus they tend to count noise. Table 9.2 in Chapter 9 summarises the results of these searches and indicates the problems encountered in searching for small pulses in the noise region of the single particle pulse height spectrum (see figure caption).

8.4.3 Conclusions for a new search

From the arguements of Lemke (Section 8.1.4.8) any electromagnetic interaction between a tachyon and ordinary matter must take place in a narrow tube along the tachyon's trajectroy. Hence in order to observe a tachyon directly a dense (i.e. solid) ionisation detector is required. If tachyons cannot be detected directly, but only through the secondaries from their interactions with ordinary matter, a dense target is required e.g. lead or iron, in order that the chances of such an interaction are improved.

CHAPTER 9

A SEARCH FOR TACHYONS

9.1 Principle of experiment

The principle of experiments to search for tachyons in extensive air-showers was first suggested and used by Ramana Murthy et al (1971) at mountain altitude and then by Clay and Crouch (1974) and many other authors at sea-level (see Chapter 8).

The suggestion is that if tachyons are produced in high energy cosmic ray interactions, then they should be produced high in the atmosphere (20 km. to 30 km. above sea-level) in the first or subsequent early interactions of a primary cosmic ray proton for example with an atmospheric nucleus. The lack of any tachyon detection at laboratory energies (see Chapter 8) indicates that if they can be produced, there must be some energy threshold below which tachyons cannot be produced. At primary energies in the region of 10^6 GeV the secondaries have sufficient energy to initiate a nuclear - electromagnetic cascade through the atmosphere which results in an extensive air-shower of electrons and γ-photons arriving at sea-level in the size region of 10^6 particles. At such supra-relativistic energies the shower front velocity is approximately the speed of light, hence any particle produced with $v > c$ (i.e. $\beta > 1$ where $\beta = \frac{v}{c}$), will arrive before the air-shower. In fact, if we assume that $\beta_{tachyon} \longrightarrow \infty$ for any tachyon produced and that we can detect air-showers arriving with a zenith angle upto 60°, then for a tachyon-producing interaction occuring at 20 km. above sea-level, the tachyon should arrive some 60 μs to 120 μs before the air-shower.

The smaller times should occur most frequently due to the dominance of vertical showers i.e. $I(\theta) = I(0)\cos^{8}\theta$ = rate of arrival of showers at zenith angle θ. The assumption $\beta \rightarrow \infty$ is not unreasonable since at superluminal velocities the lowest energy states have the highest velocities, and any energy losing interaction in which a tachyon participates increases its velocity.

Hence a search for tachyons involves a statistical comparison between the number of particles that are detected in the 120 μs immediately previous to the arrival of an air-shower and the number of particles which are detected in a randomly selected 120 μs interval of time. Further, grouping of the times of arrival in the immediate 120 μs with a peak around 60 μs would be indicative, as would visual identification of unusual particle tracks associated with these tachyon candidates.

The same principle and conclusion can be applied to searches for astrophysically produced tachyons (assuming they have a similar interaction length to protons in air) since the first interaction could initiate an air-shower, and the arguments about the time difference between the arrival of the tachyon and the air-shower outlined above would then proceed identically.

9.2 The tachyon detector

The modified flash-tube chamber described in Chapter 6 was used as the tachyon detector. To detect the time separation between the passage of a particle through the chamber and the arrival of an air-shower, the

pulses from the scintillator stacks were fed into two separate 240 μs blocks of delay line. Hence at any instant a record of the previous 240 μs could be displayed by emptying the contents of the delay lines onto the 'y' channel of a C.R.O.

The use of delay lines instead of a digital memory does however present problems:-

a.) The delay line used was made of copper wire enclosed in a ferrite core with a fine copper wire wrapped around it enabling a delay of 1 μs per foot to be obtained. The capacitative load thus introduced causes severe attenuation, especially of fast pulses (see Fig. 9.1). Hence each 240 μs block had to be divided into 3 x 80 μs lengths and an amplifier inserted after each 80 μs length to boost the amplitude. The 150 ns wide pulses produced by the scintillator phototubes also had to be stretched to 5 μs by inserting a stretcher before the first 80 μs length (see Figs 9.2a), b)).

b.) At each junction of the delay line there is a sudden change in impedence which causes reflection of pulses. This can be corrected by making the delay line appear to be of infinite length, by terminating each section with its characteristic impedence (1.65 KΩ).

c.) Pick-up from high voltage sparks proved a severe problem with the delay lines. Thick copper braiding earths were used but the proximity of the scintillators to the flash-tube electrodes provided a pick-up pulse which could not be suppressed. Each amplifier in the delay line blocks also picked up a small pulse when the H.T. fired, hence the gain on each amplifier was limited so as not to swamp the trace

FIG. 9.1

The attenuation of a 2μs square pulse after transmission down 80μs of delay-line.

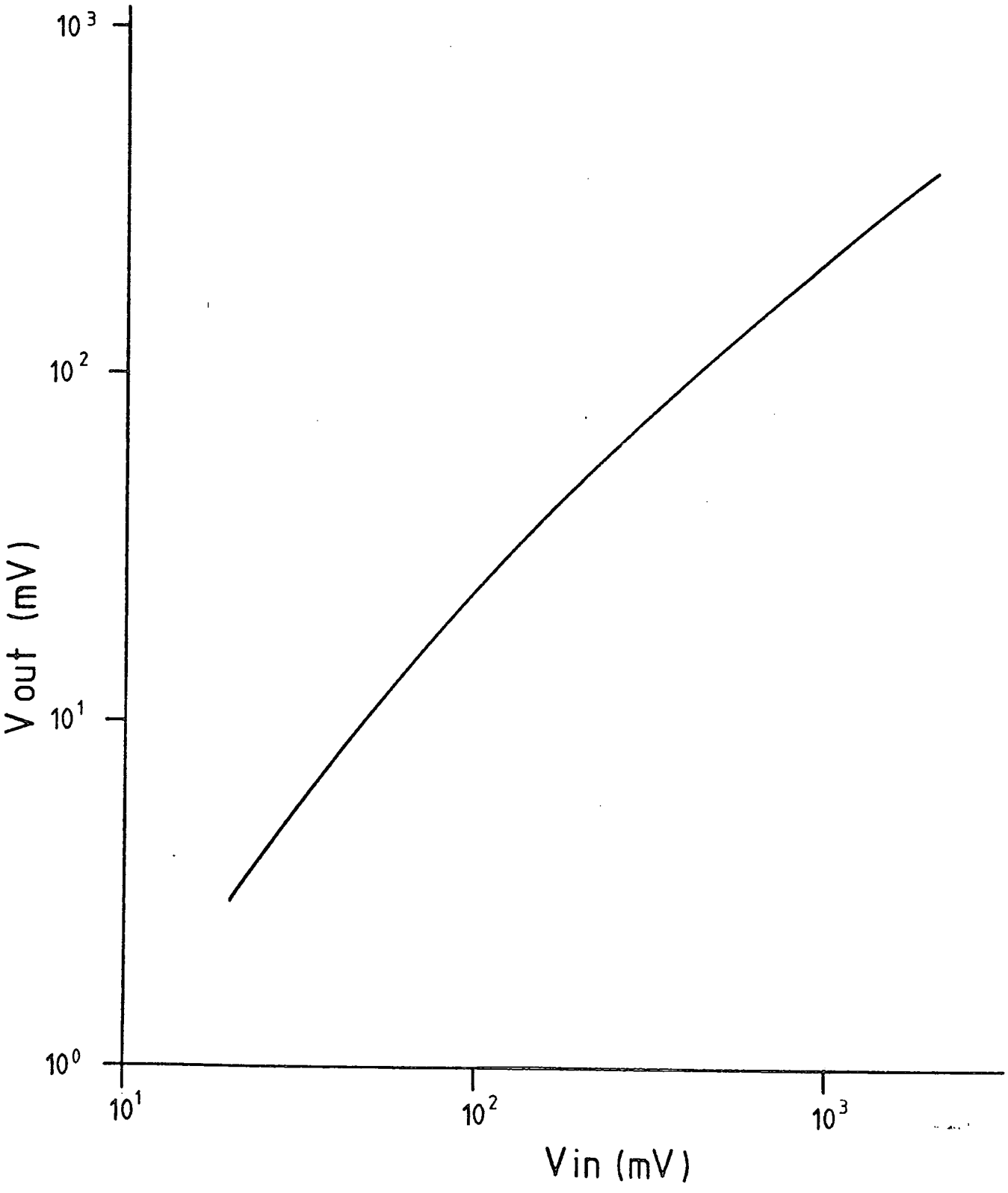

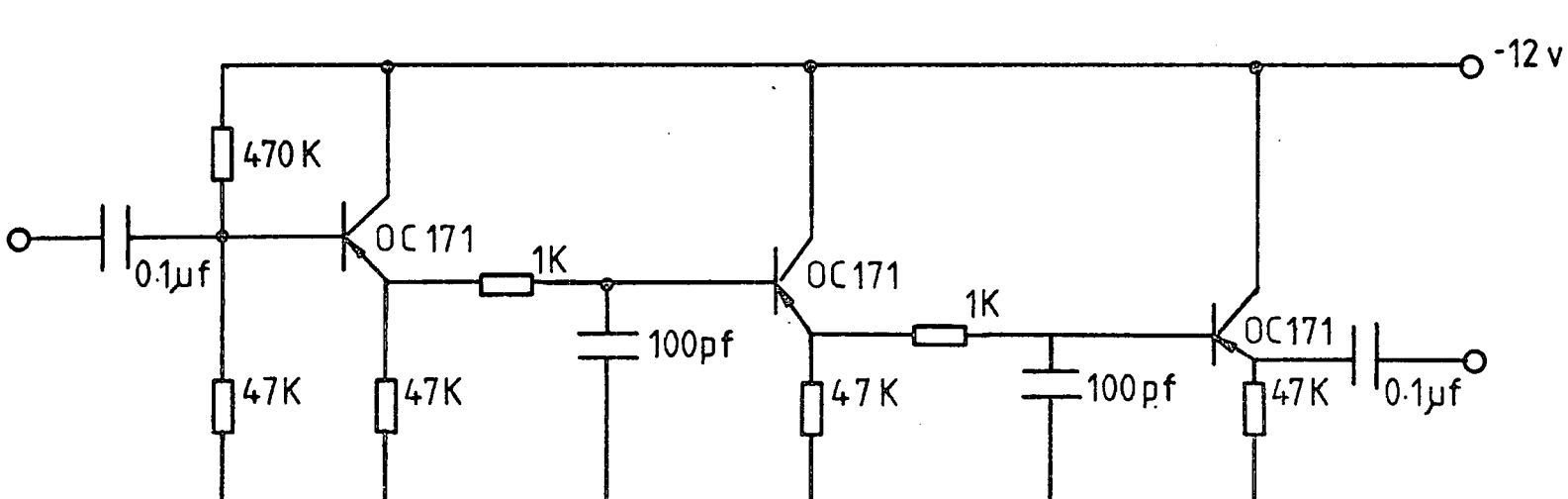

FIG. 9·2 a)

CIRCUIT DIAGRAM OF "STRETCHER"

USED IN TACHYON EXPERIMENT

FIG 9.2 b)

Input - Output characteristics of the stretchers
for 200ns square pulse input.

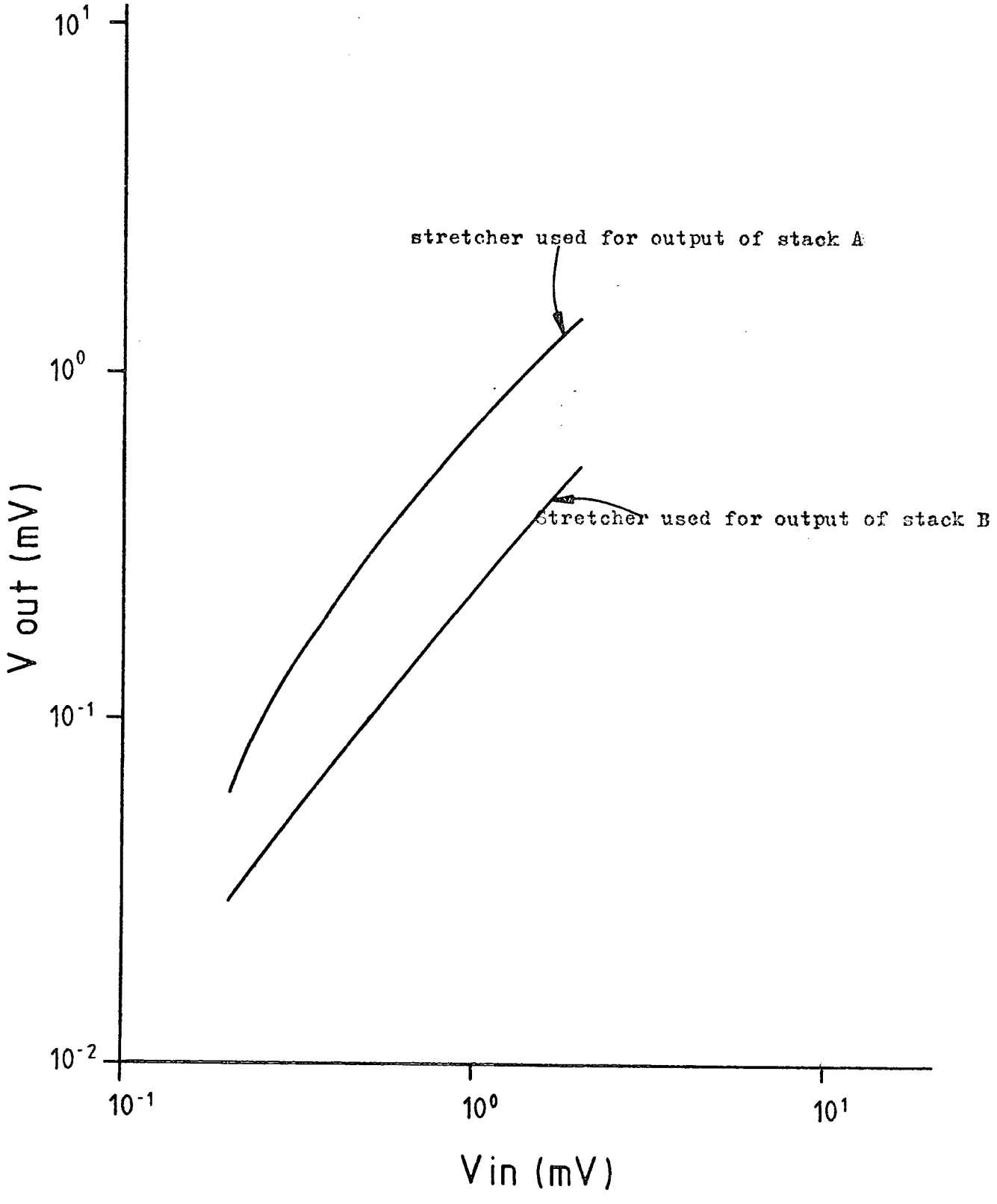

with "overswing" from these pick-up pulses. This did not prove a severe problem, as the experiment initially intended to search for large pulses well away from photomultiplier noise, in which region previous searches had already found no significant results (see Chapter 8).

The scintillator stacks' calibration procedure and results have been described previously (Chapter 6). The unusual shape of the final single particle pulse height distribution (Fig. 9.7) for a stack is due to the acceptance geometry for particles which go through one scintillator and particles which go through two scintillators. This point is discussed further below in the interpretation of the calibration data.

The final interpretation of the output pulse height displayed on a C.R.O. depends on calibration of the intervening electronics as well as experimentally determining an input - output pulse height curve from the output of the scintillator to the input of the oscilloscope using a pulse generator with identical pulses to those produced by the scintillator phototubes. These final curves (for the upper and lower stacks) determined for the amplifier settings used during the actual experiment are shown in Fig. 9.3, and a block diagram of the electronics used is shown in Fig 9.4. The calibration of the intervening electronics has already been described and the results presented in Chapter 6.

For part of the run, the contents of the delay lines were displayed on a dual beam oscilloscope, for the remainder 2 beams of a 4-beam oscilloscope were used. In both cases the trigger was provided by the Durham Extensive Air-Shower Array (see below and Chapter 6) and the displayed traces photographed. 20 μs after the reception of a trigger pulse the high voltage

Figure 9.3: Input - Output characteristic of circuit represented in fig. 9.4 for gain-settings used in run T27. Calibrated using 200 ns square pulses.

9.3a): Characteristic for circuit connected to upper scintillator stack (A).

9.3b): Characteristic for circuit connected to lower scintillator stack (B).

FIG 9.3 a)

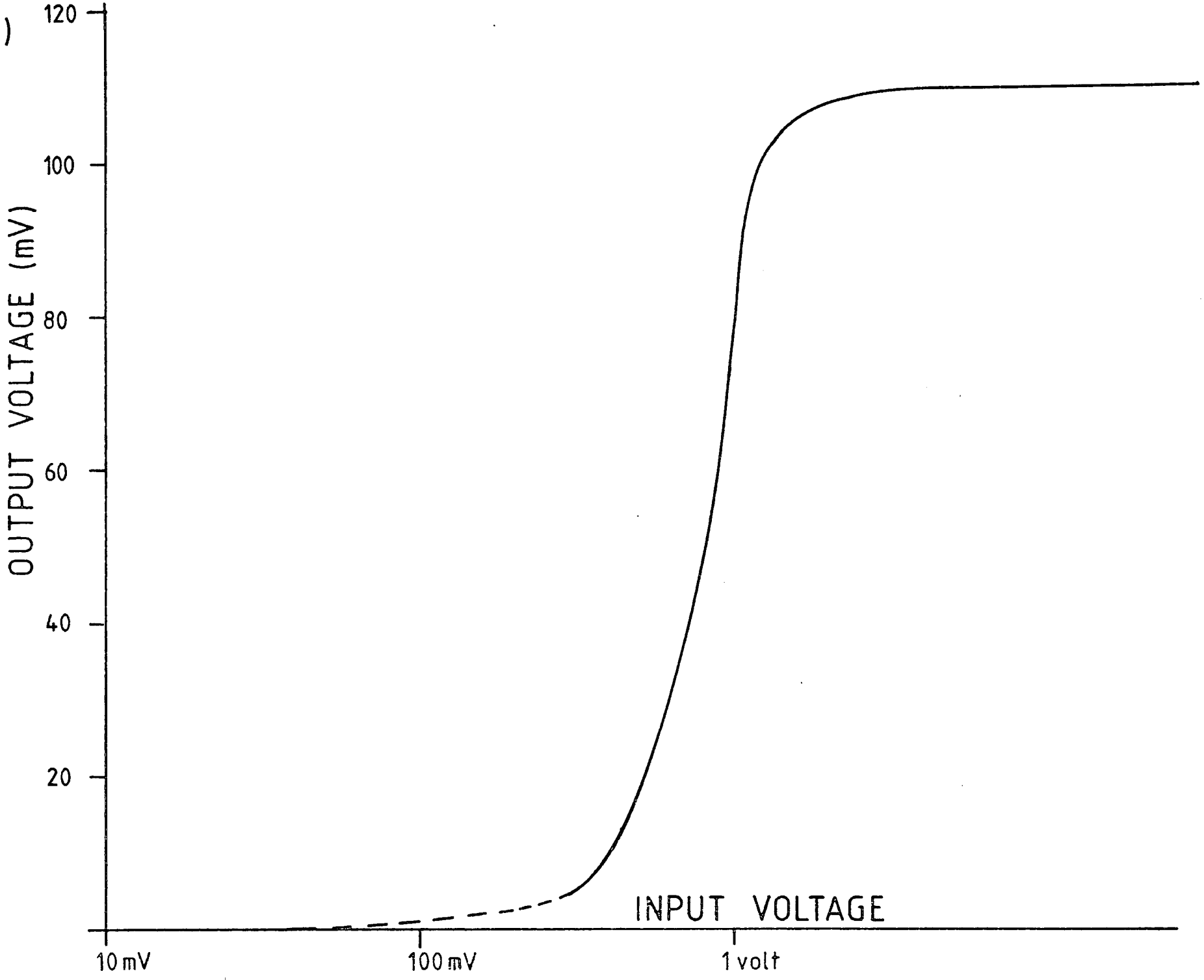
120
100
80
60
40
20
OUTPUT VOLTAGE (mV)
INPUT VOLTAGE
10 mV
100 mV
1 volt

FIG. 9·3 b)

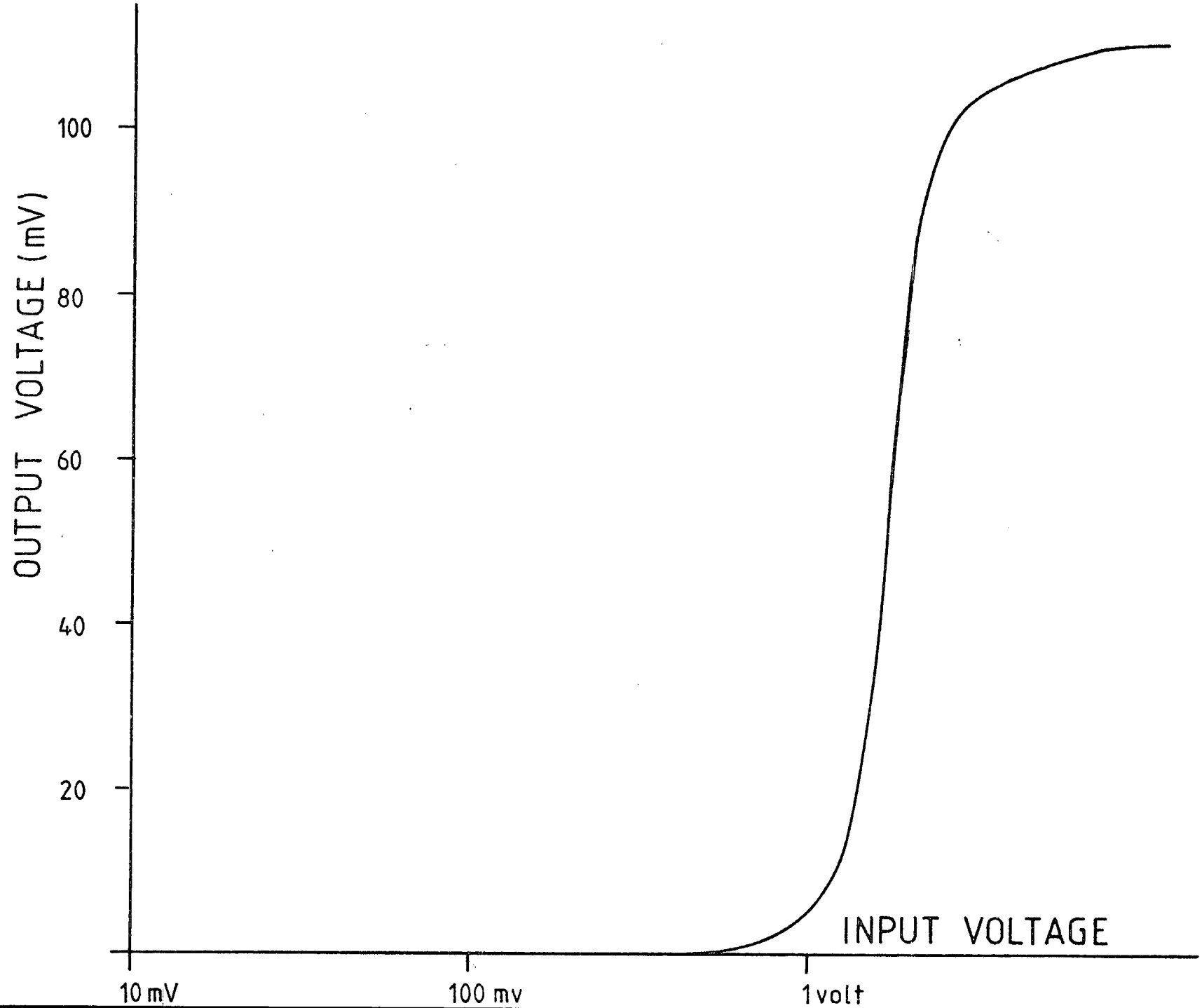
OUTPUT VOLTAGE (mV)
100
80
60
40
20
INPUT VOLTAGE
10 mV
100 mv
1 volt

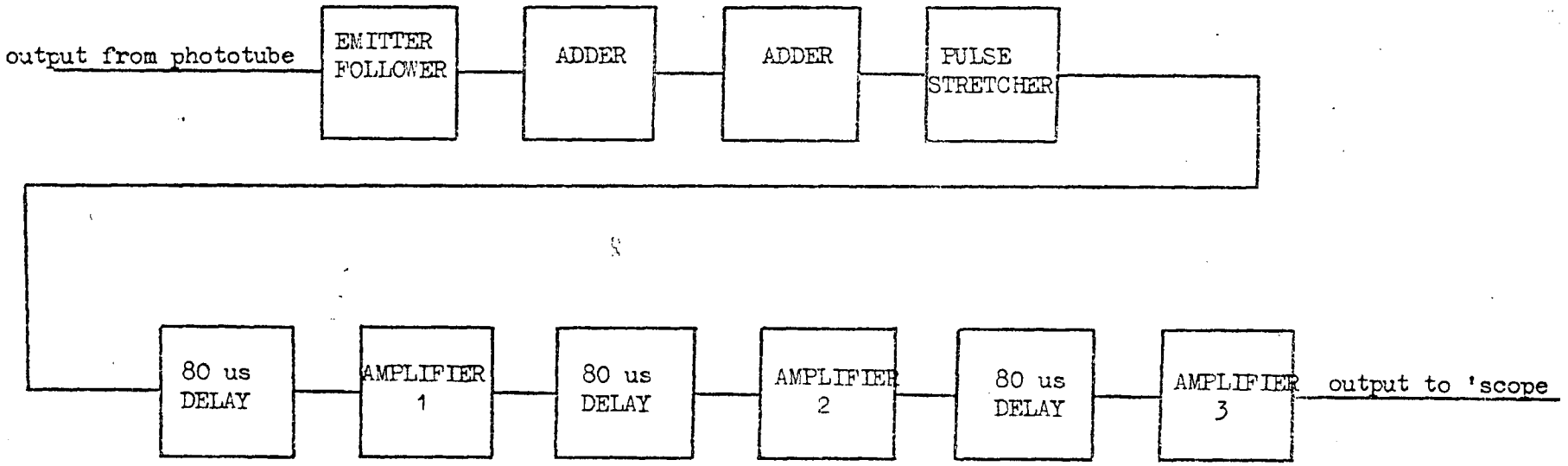

BLOCK DIAGRAM OF ELECTRONICS USED IN TACHYON EXPERIMENT

FIG. 9.4

pulse was applied to the flash-tubes and the resulting display photographed in permanent darkness with a shutterless camera. After each event a 10 second dead time was imposed automatically to enable the cameras to wind on and the spark-gap to recover (see Chapter 2).

9.3 Triggering procedure

On the arrival of a suitable air-shower, indicated by a 1 particle m^{-2} coincidence in detectors 13, 33, 53 with a 2 particle m^{-2} signal from the central detector (C) of the Durham Air-Shower Array (see Fig. 6.1) a trigger-pulse is sent to both the oscilloscope and the flash-tube chamber. The resulting display on the oscilloscope gives a visual record of the pulses which have been produced in both the top and bottom scintillator stacks in the 240 μs immediately previous to the arrival of the air-shower. The flash-tube chamber photograph indicates the number of muons (mainly) passing through the chamber. The number of particles seen to be passing through each stack can be used to calibrate the scintillators in a more direct manner, and also acts as a check on whether the electronics are still functioning correctly.

In this particular experiment the actual air-shower information was not recorded, however Figs. 9.5 and 9.6 show the range of shower sizes and core distances which can be detected with the Durham Air-Shower Array.

FIG 9.5

Range of shower sizes detectable by air-shower array.
The minimum shower-size detectable = $8.1 0^4$ particles.

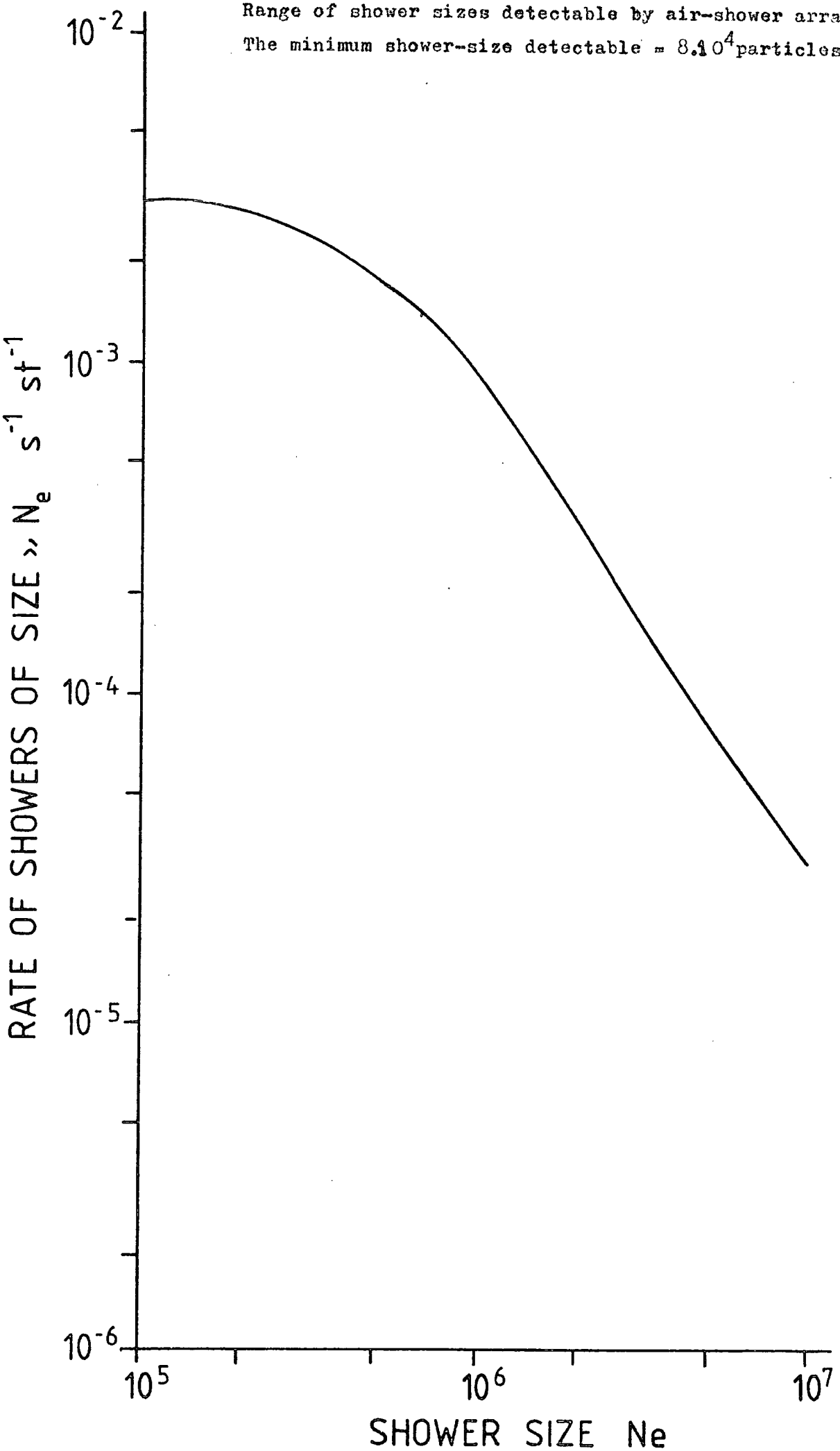

FIG. 9.6 Range of core-distances detectable by air-shower array.

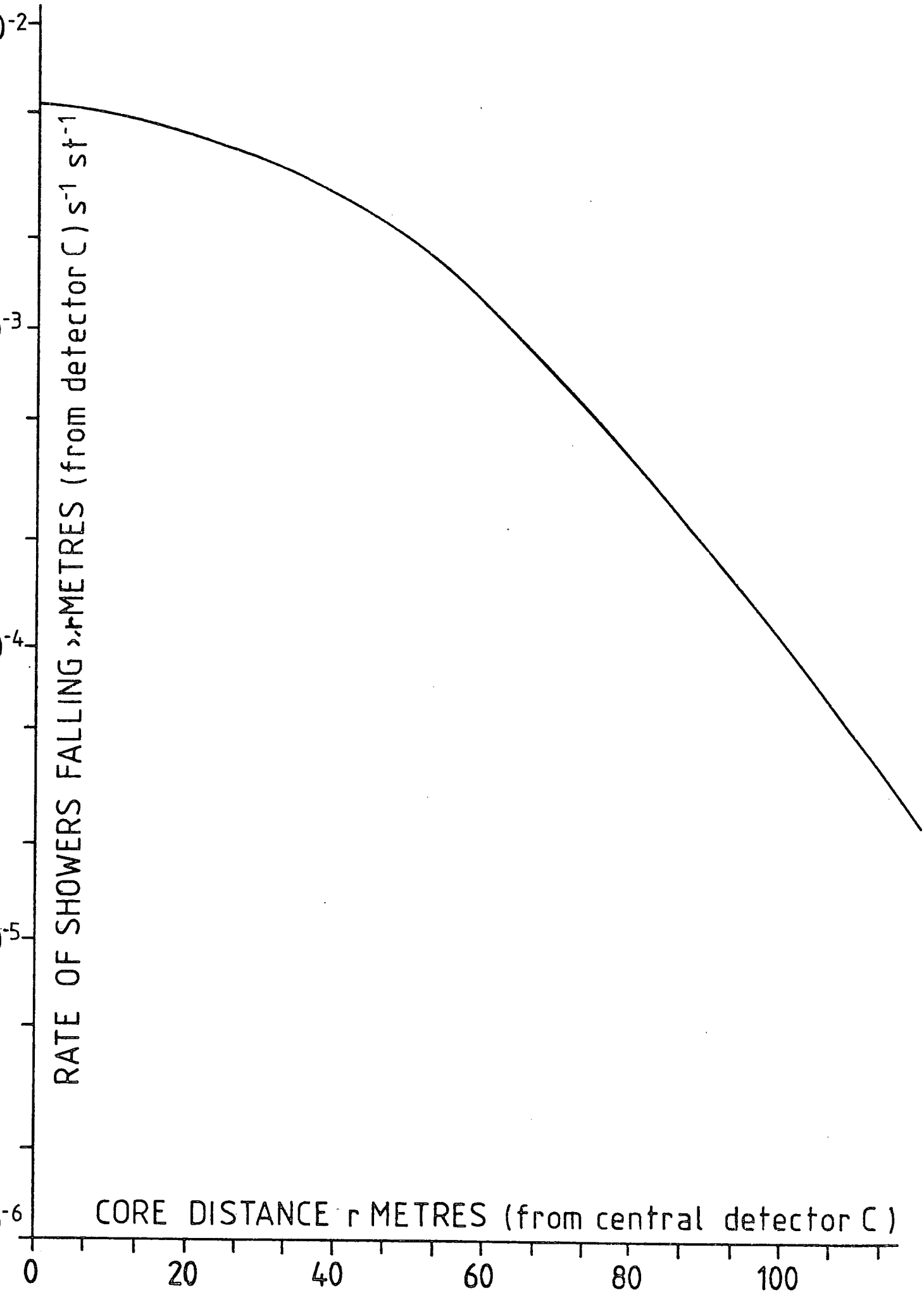

9.4 Data

Between the dates 21st June, 1976 and 30th June, 1976, 7 runs were attempted. However many data collection faults were encountered, out of 120 hours sensitive time, all parameters (i.e. both flash-tube chamber film and scintillator film) were recorded for only 40 hours. Hence the resulting sample of showers has proved small viz 341 (a mean shower detection rate of 12.7 hr^{-1} being characteristic of this triggering mode), however this small sample has provided an intriguing result.

9.5 Data analysis

The data analysis consists of:-

(i) Correlating the flash-tube chamber photographs with the oscilloscope trace photographs. This was achieved by photographing a clock above the chamber, and a watch above the oscilloscope trace, and synchronising the two timers.

(ii) Each flash-tube chamber was scanned to see how many particle tracks appeared to go through either one scintillator or two scintillators in either the upper stack (stack A) or the lower stack (stack B) of scintillators. This number was plotted (as one particle or two particles depending on how many scintillators in a stack were passed) against the recorded pulse height due to the air-shower particles (the 'prompt' pulse). The defining layers F1a, F1b (F2a, F2b) (Fig. 6.7) were used to distinguish particles which actually passed through a

scintillator stack from those that missed the stack but entered the tubes. The resulting scatter-plots for the upper and lower scintillator stacks are shown in Fig. 9.8 and 9.9. Since different gain settings on the amplifiers were used on each of the three successfully recorded runs, the pulse heights have been normalised to the gain settings used in one of the runs (T27) by comparing the heights of the pick-up pulses.

Using the curve of Fig. 9.3, these scatter-plots have been transformed to equivalent output pulse height measurements from the scintillators, Figs. 9.10, 9.11. Finally, since these data were intended to be used in the interpretation of measured pulse heights of particles arriving prior to the shower, a regression fit of the parameter y = number of particles going through a scintillator on x = pulse height produced in scintillator has been performed on each set of data, these are the straight lines on Figs. 9.10, 9.11.

It is immediately clear from Fig. 9.10 that the top scintillator stack will only detect tachyons if they produce a pulse in one scintillator equivalent to 4 or more relativistic particles, well above the height of a noise produced pulse (see Fig. 9.7). However, if the only information we have on the tachyon candidate is the pulse height it produces, then interpretation is difficult because it could have passed through either one or two scintillators in a stack. This point is discussed further below in the actual interpretation of the tachyon candidates' pulse heights.

(iii) Finally the oscilloscope traces were scanned for previous particle pulses and their event numbers, t_{prev} (time before shower arrival)

Figure 9.7: The single particle pulse height distribution for whole of scintillator - stack A.
(The origin of the humped structure is explained in the text.)

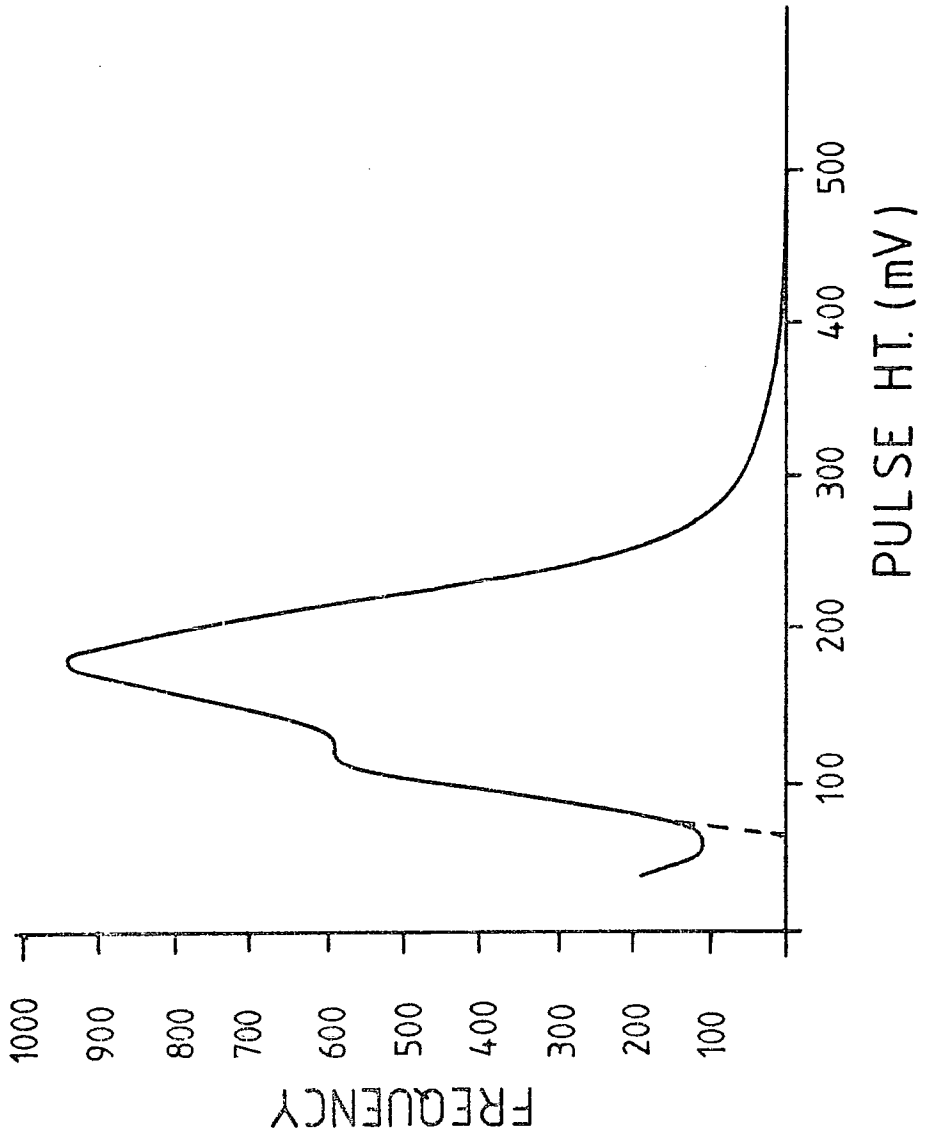

FIG. 9.7

FIG 9.8 Correlation between the number of air-shower particles traversing the upper scintillator - stack (A), determined from the flash-tube chamber, and the magnitude of the air - shower front pulse.

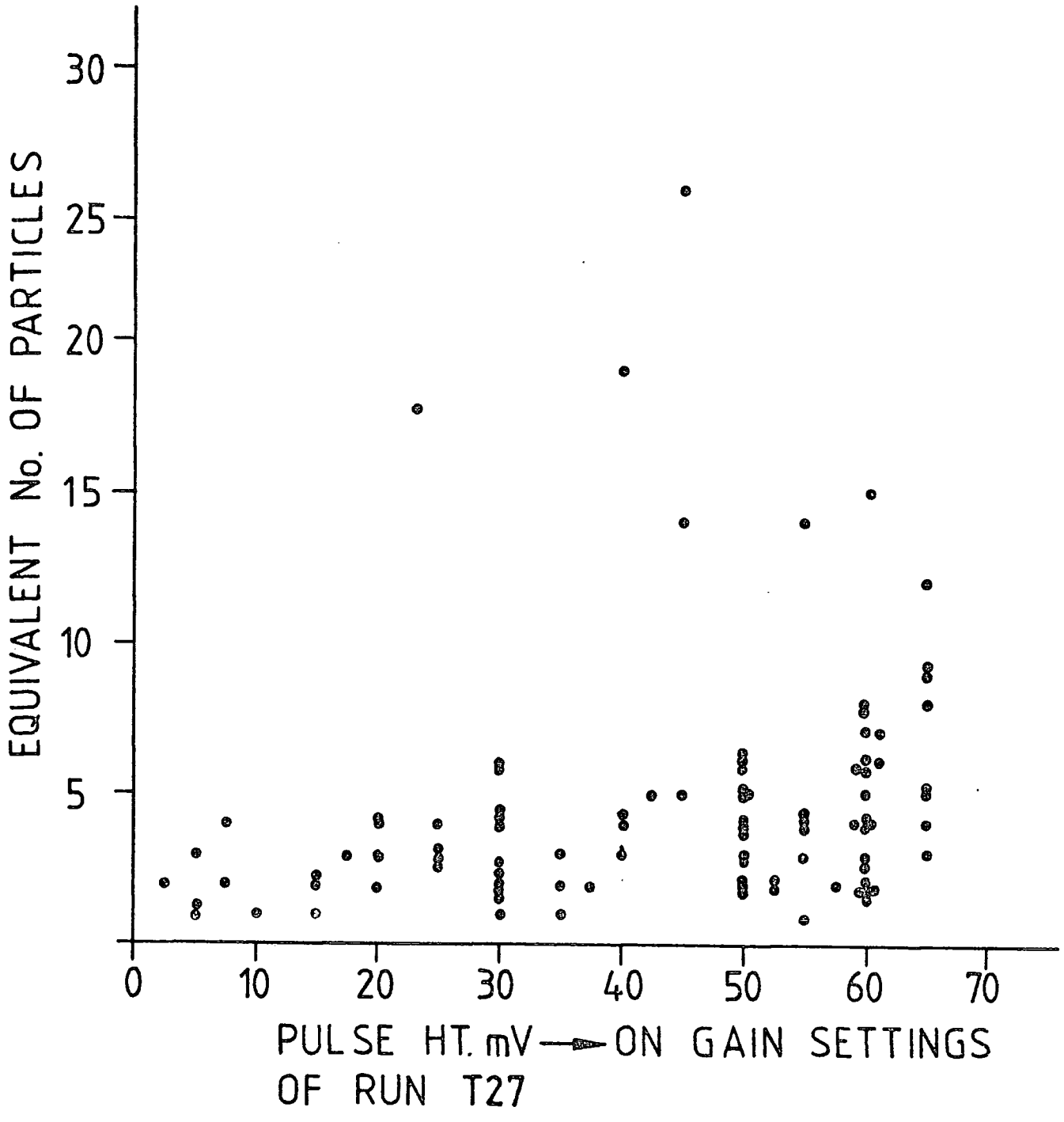

Figure 9.9: Correlation between the number of air-shower particles traversing the lower scintillator-stack (B), determined from the flash-tube chamber, and the magnitude of the air-shower front pulse.

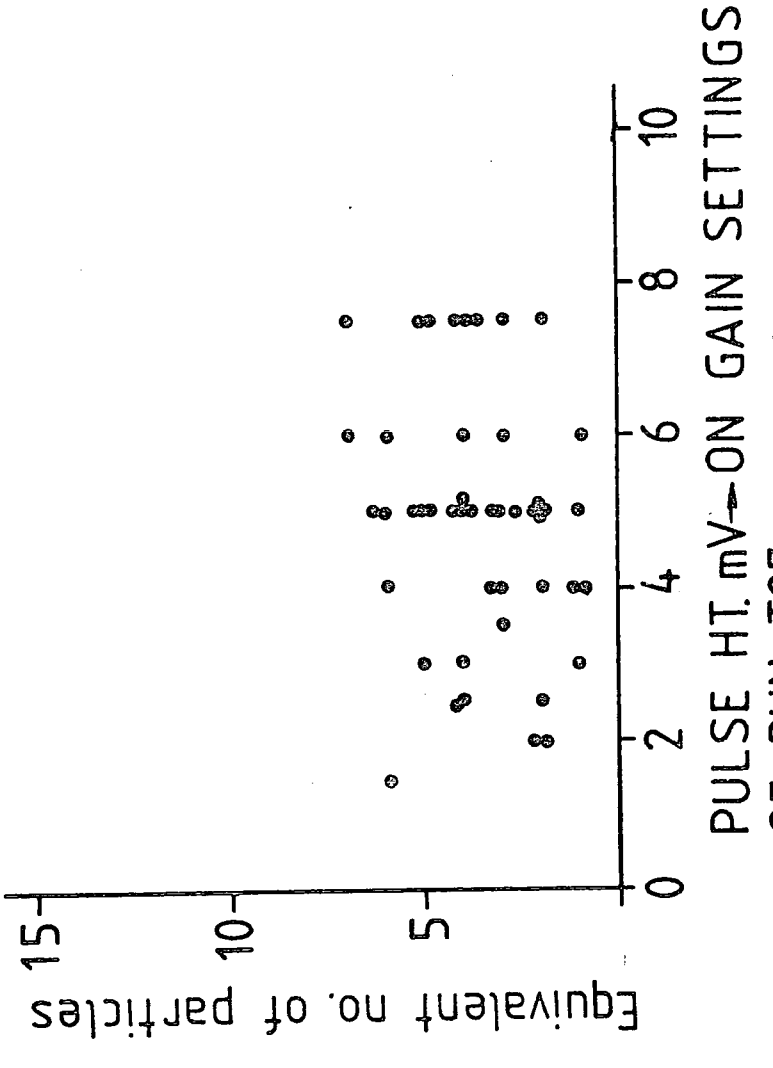

FIG. 9.9

Figure 9.10: The data of Fig. 9.8 converted to equivalent output pulse height from the scintillator stack (A) showing the least squares fitted line of regression of y (no. of particles through stack A) on x (pulse height).

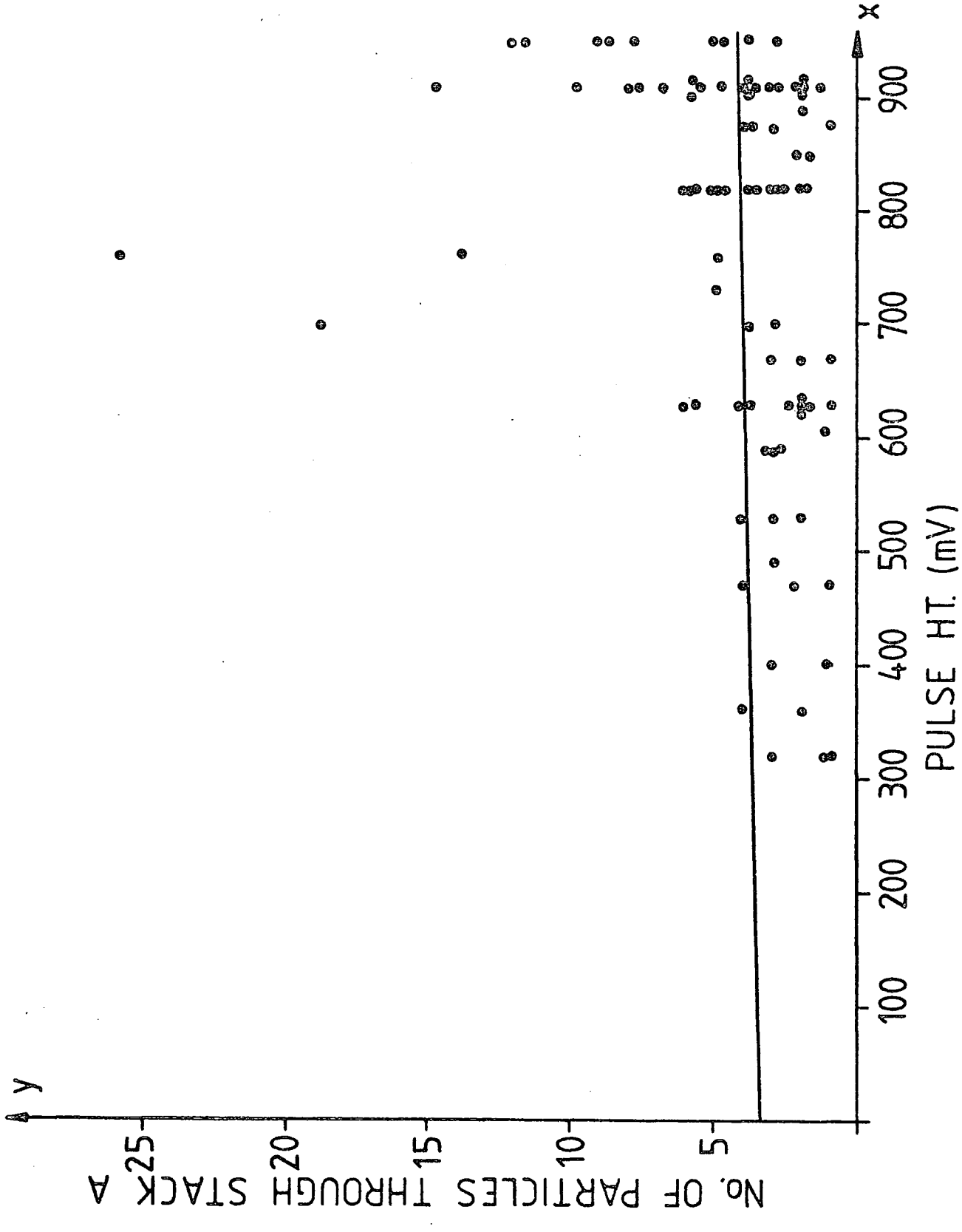

FIG 9.10

Figure 9.11 : As for Figure 9.10 but for data of Fig. 9.9 (stack B).

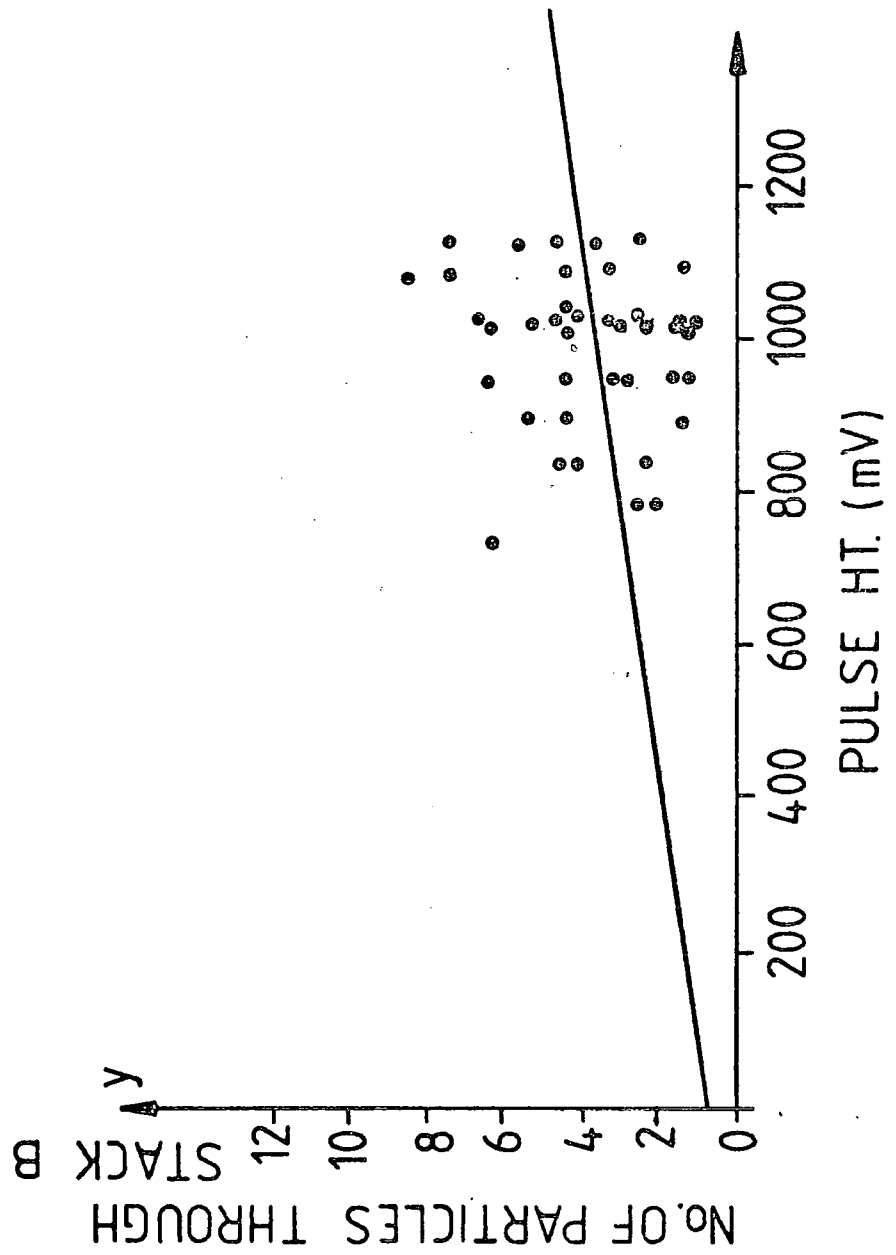

FIG. 9.11

and pulse heights were recorded. A sketch was also made of the corresponding flash-tube chamber photograph to try and identify any unusual particle tracks. On each film, to avoid confusion between real particle pulses and pick-up pulses, a trace was made of an event on which there were only pick-up pulses and a prompt pulse, hence previous particle pulses on other events could easily be identified by projecting the oscilloscope photograph on top of the trace and co-ordinating the pick-up pulse positions. (This also acts as a check that the time-base setting of the oscilloscope is not wandering.)

9.6 Results

In a total of 341 showers, previous particle pulses were observed in 6 instances in stack A, and 2 instances in stack B. The time distributions of these events are shown in Fig. 9.12, 9.13 and a table of the events with the various measured parameters is presented as table 9.1. No coincident events were observed.

The bottom scintillator stack was found to give a consistently lower frequency of pulses for a given number of shower particles (compare the number of points in Fig. 9.9 with the number of points in Fig. 9.8). In the third (and final) successfully recorded run the oscilloscope trace corresponding to the lower stack showed only pulses corresponding to pick-up from the spark gap.

The fault was traced to an amplifier in the delay line/amplifier configuration. Since this fault could have been a gradual deterioration effect all data from

the lower stack should be regarded with some suspicion. Consequently in the analysis that follows, only the information from the upper stack (A) will be considered.

9.7 Discussion of results

9.7.1 Pulse heights

The method of calibrating from the pulse heights corresponding to shower particles involves counting a particle which is deemed to have passed through 2 scintillators, one on top of the other, as equivalent to the sum of 2 single particle pulse heights. Fig. 9.7 indicates that these sort of events outnumber those events which pass through a single scintillator (the kink in the single particle pulse height distribution - Fig. 6.10 - at ~120 mV) in the ratio 3 : 2. This reflects the available solid angles for collection of each type of event.

Hence, from the 6 tachyon candidates roughly half of these will have passed through 2 scintillators, and half through one. From table 9.1 it can be seen (considering stack A only) that roughly 3 tachyon candidates gave pulses between 300 and 400 mV (corresponding to three times the s.p.p.h. from a particle passing through a single scintillator) whereas 3 gave pulses >500 mV (corresponding to three times the single particle pulse height from a particle passing through two scintillators). Hence, despite the apparent 4 particle result from the calibration curve (Fig. 9.10), it would appear reasonable to suggest (conservatively) that the pulses are due to particles ionising at 3 times the rate of a single (sub-luminal) relativistic

FIG. 9·12

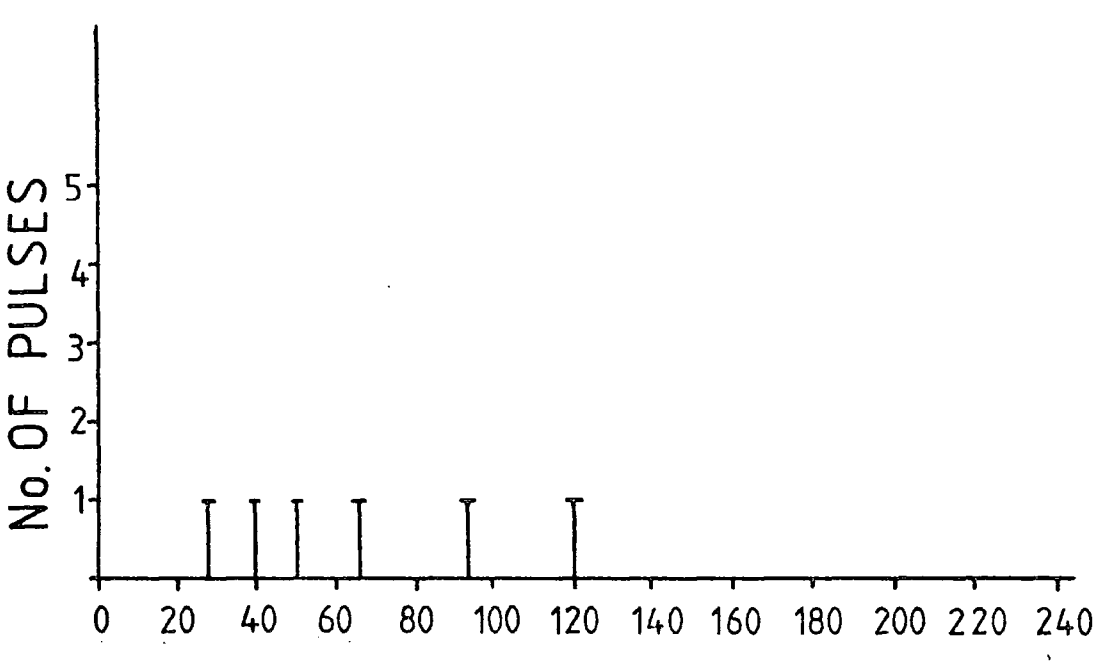

Figure 9.12: The frequency distribution of the time of arrival of pulses - equivalent to three or more singly charged relativistic particles (muons) - previous (t_{prev}) to the arrival of an air-shower ($t_{prev} = 0$).
Results are for scintillator-stack A.

FIG. 9.13

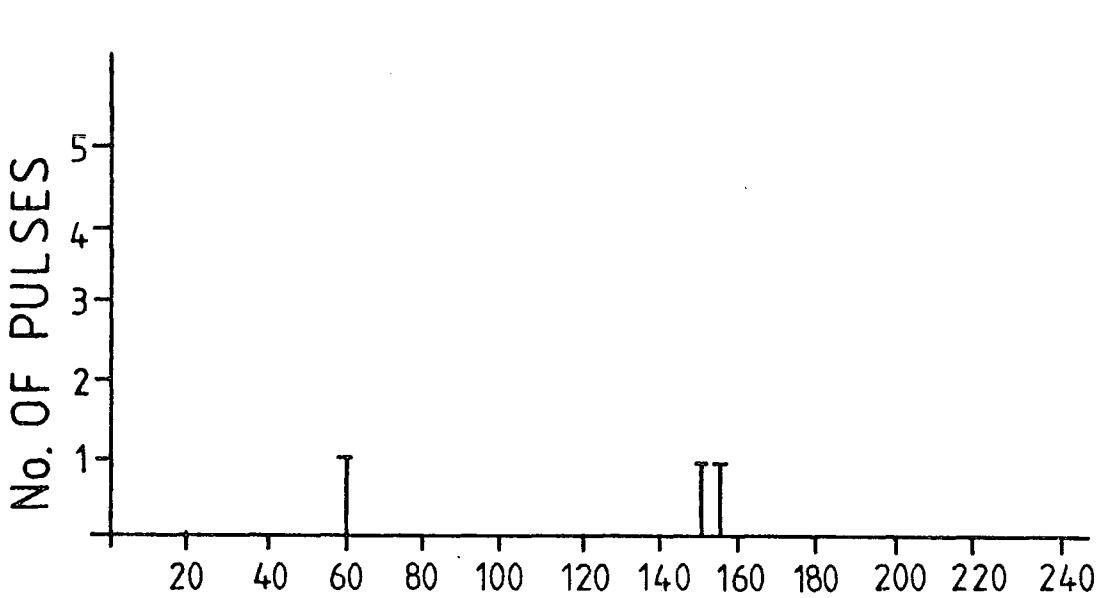

Figure 9.3: The frequency distribution of t_{prev} for lower scintillator-stack (B).
These results are, however, suspect due to a fault in one of the amplifiers in the delay-line/amplification circuit (see text).

TABLE 9.1

PREVIOUS PARTICLES' MEASURED PARAMETERS

Film No.	Event No.	Scint. stack in which previous pt. detected	Is F/T info. available?	Pulse Ht. (mV)	Equiv. No. of Particles	θ proj. from F/T info.	t prev. (us) from Scint. info.
T26	90	A	Yes	400	3	15°	66
T27	29	A	Yes	300	3	?	93
T27	78	A	Yes	320	3	0°	120
T27	79	A	Yes	900	5	11.5°	27
T34	23	A	Yes	530	3	3.5°	50
T34	88	A	No.	530	3	?	40
T27	6	B	Yes	840?	3?	16.5°	153
T27	55	B	Yes	1000?	3?	20.5°	156
T27	64	B	Yes	1000?	3?	0°	60

particle. This reduces the statistical significance of the result, but increases the reliability of the significance estimate.

9.7.2 Flash-tube chamber photographs

Figs. 9. 14, 15, 16, 17, 18 show some of the photographs corresponding to the events listed in table 9.1.

It is immediately clear that not every previous particle pulse has a corresponding particle track candidate. In fact, observation Fig 9.19 shows the actually recorded oscilloscope traces for each event of table 9.1 has indicated that there is not always a discernible particle track(s) responsible for the prompt air-shower pulse.

The occurrence of a prompt air-shower pulse from the scintillator under the iron with no visible particle tracks indicates that the electrons responsible for this pulse must be of low energy and widely scattered. Hence they produce no coherent particle tracks in the flash-tubes. The absence of any track in F1a indicates that the interaction in the iron responsible for producing such electrons must be due to a neutron in the shower. Similarly the pulse due to a particle arriving previous to the shower could be due to the production of low energy, widely scattered electrons by a low energy transfer nuclear interaction of a tachyon in the iron. It is interesting to note that as the velocity of a tachyon increases, so its energy decreases, hence we should only expect low energy transfer interactions from fast tachyons.

Figure 9.14: Event no. 90 on film T26; t_{prev} = 66 μs from oscilloscope trace from stack A, there was no coincident pulse from scintallator stack B. The low efficiency track present corresponds to a t_{prev} of 160 ±20 μs for a charge e particle.

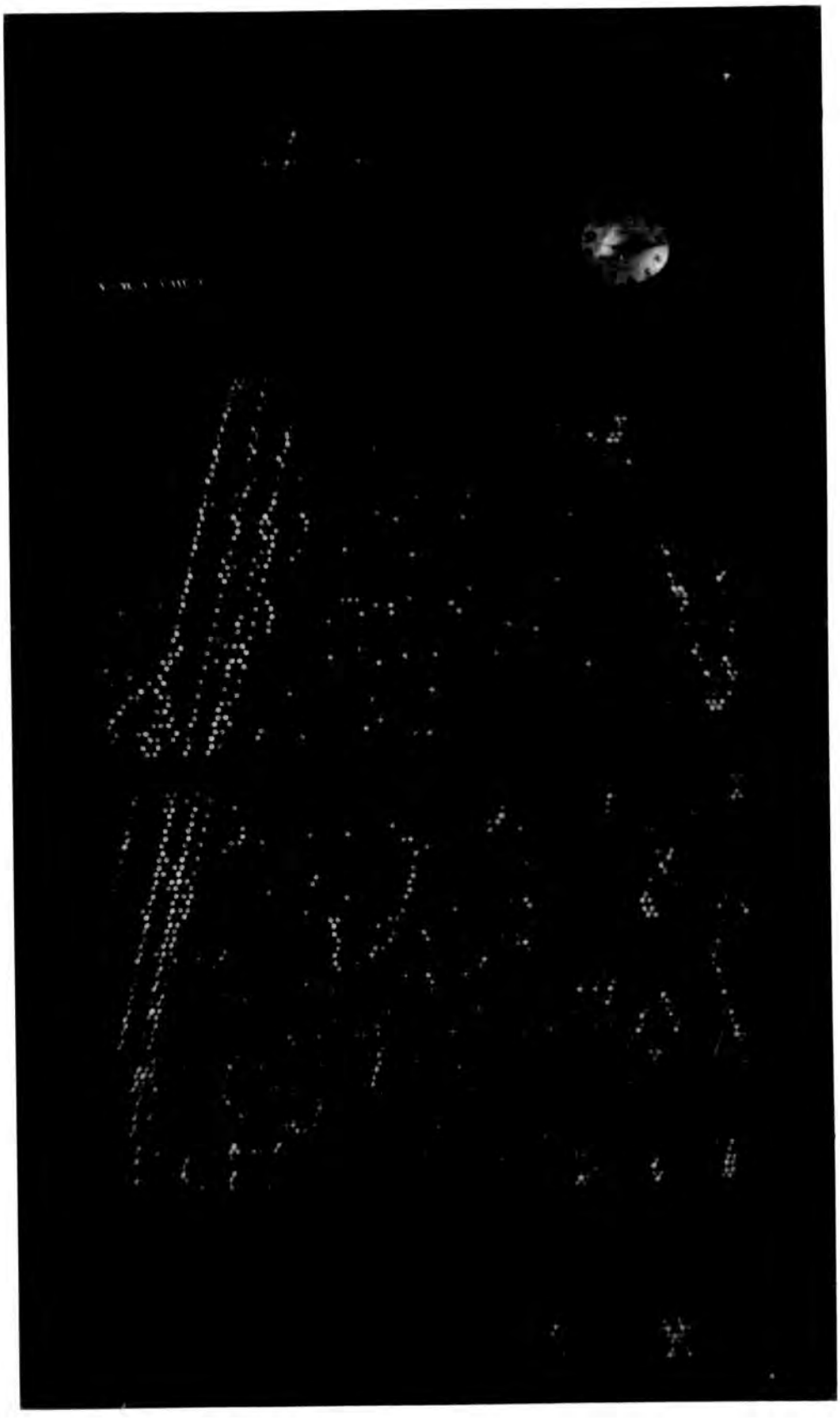

Figure 9.15: Oscilloscope trace corresponding to figure 9.14.

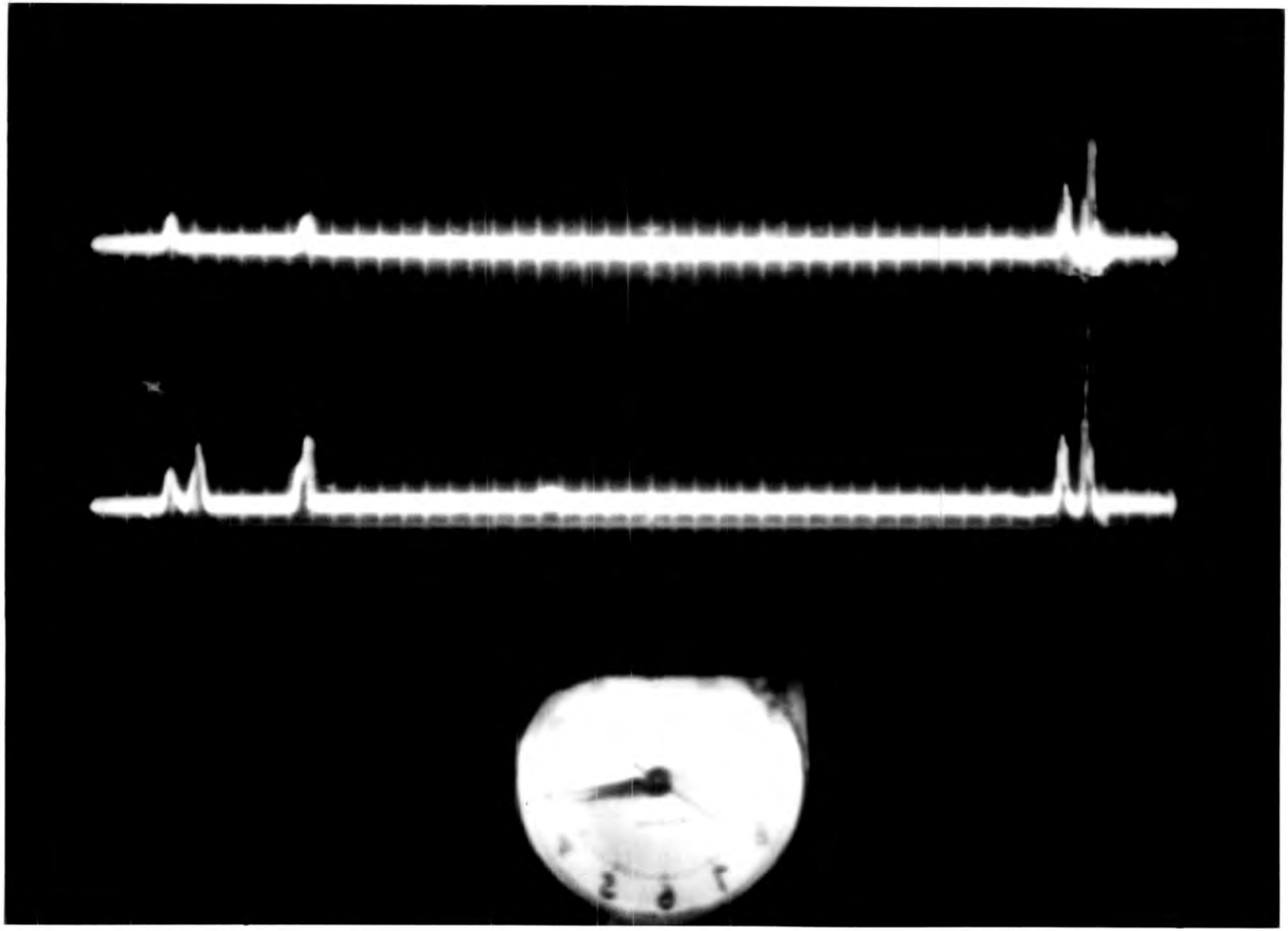

Figure 9.18: Event no. 29 on film T27; t_{prev} = 93 μs from oscilloscope trace from stack A, there was no coincident pulse from scintillator stack B. The low efficiency track present corresponds to a t_{prev} of 188 ± 12 μs for a charge e particle.

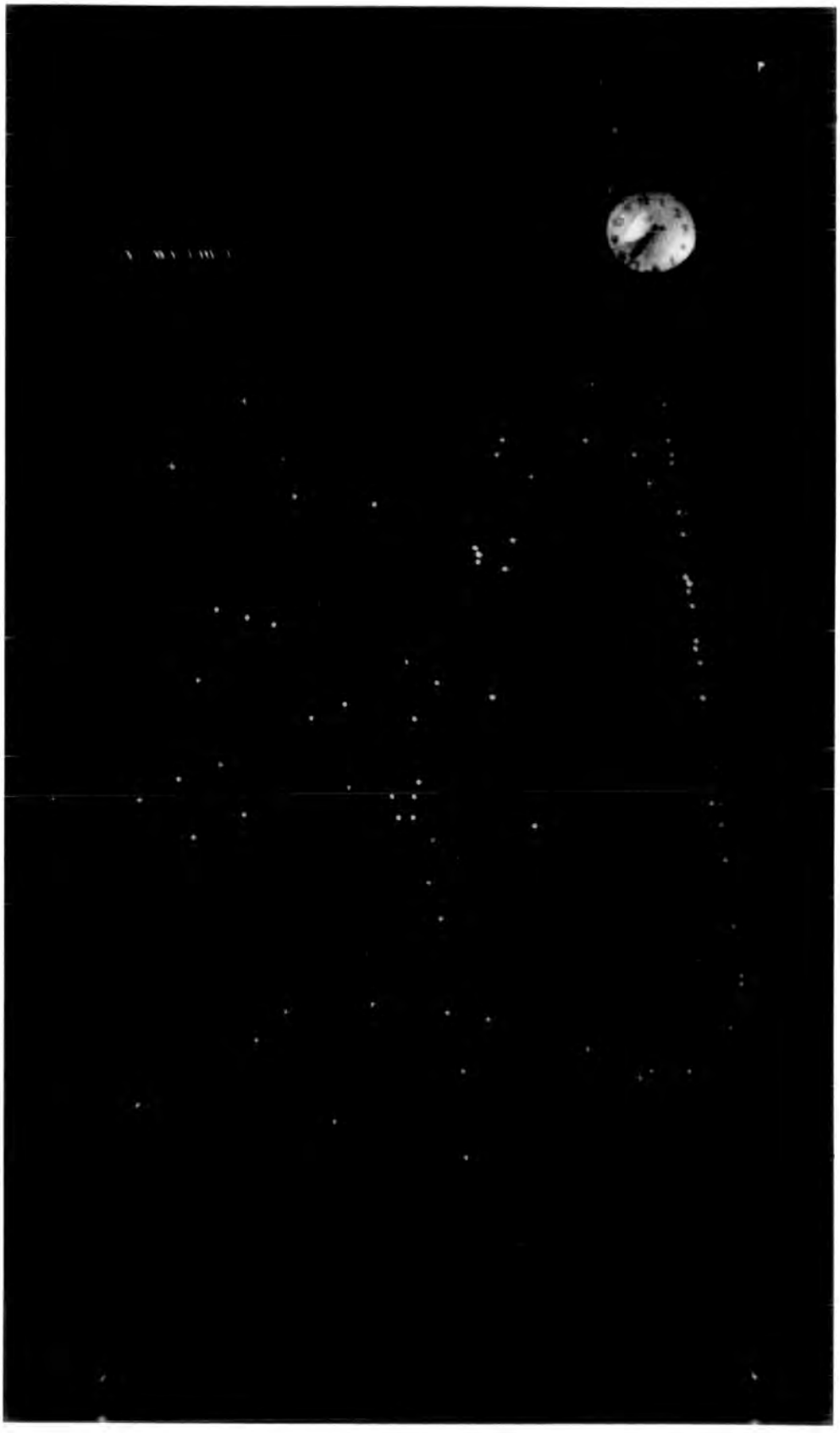

Figure 9.17: Oscilloscope trace corresponding to event no. 78 on film T27, t_{prev} = 120 μs.

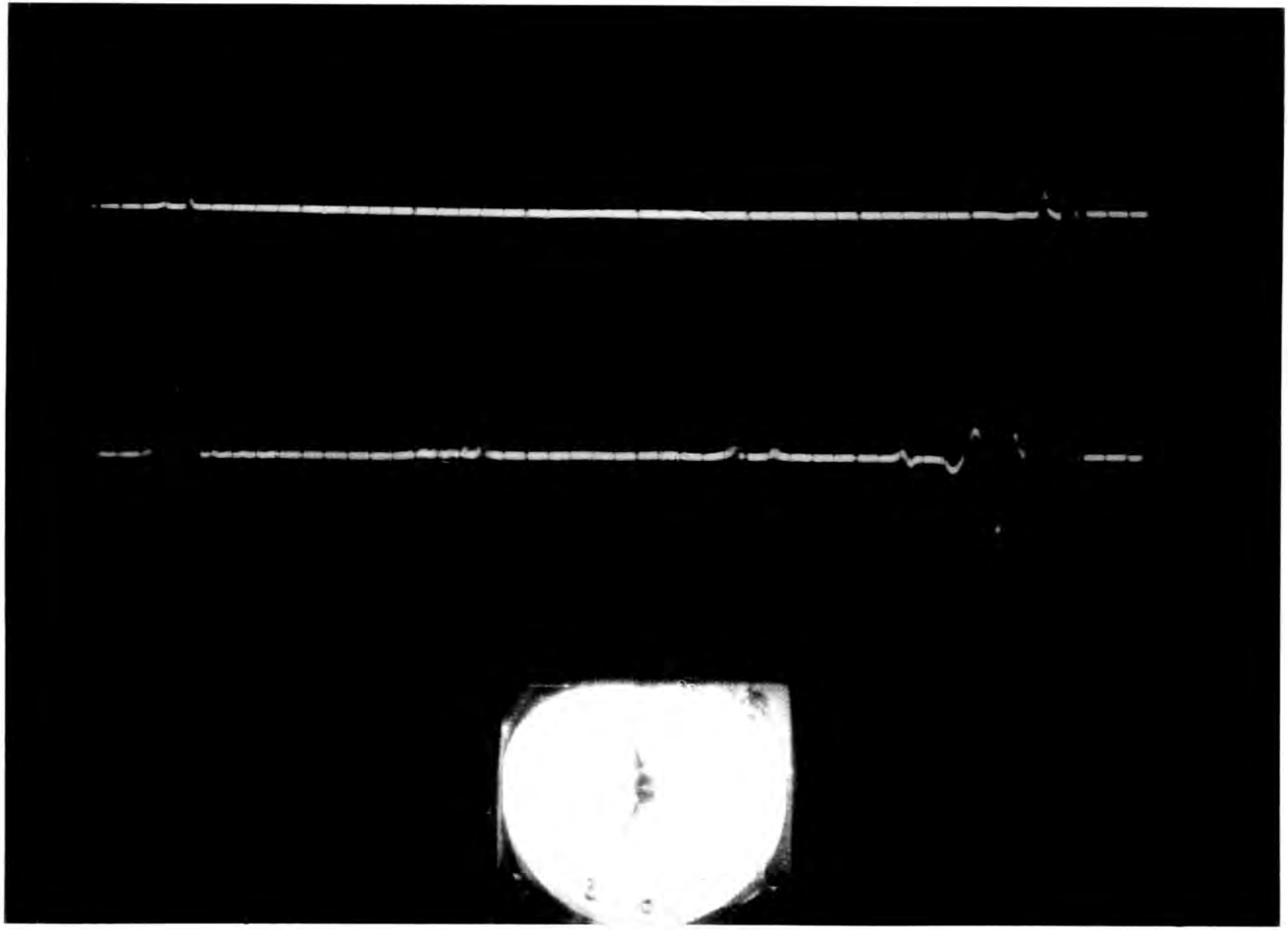

Figure 9.18: Oscilloscope trace corresponding to event no. 79 on film T27, t_{prev} = 27μs.

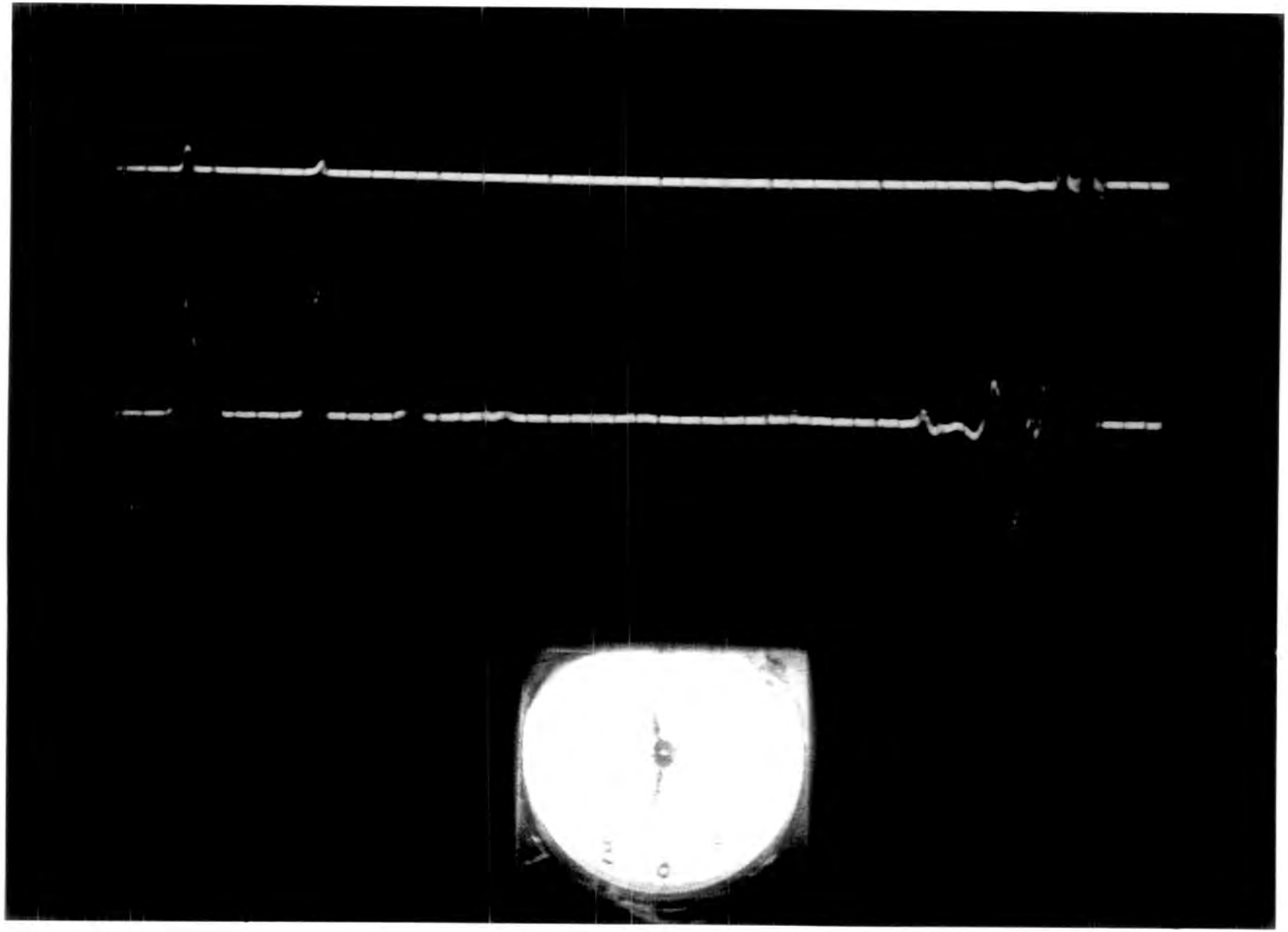

Figure 9.19:
The oscilloscope traces for the six previous particle candidates. Films T26, T27 are from the single screen oscilloscope, T34 from the 4-beam oscilloscope.
Different gains have been used in each film hence the different pick-up pulse sizes.
The previous particle pulses are marked ↓, the prompt pulse's expected position is marked |. All other pulses that appear, appeared identically on every frame of the corresponding film.
The two large pulses separated by 240 μs correspond to direct pick-up by the oscilloscope and amplifier 3, and pick-up by the scintillator /adder/stretcher electronics; the latter pulse thus travels down the delay-line. The time-difference between each pick-up pulse in run T27 is 80 μs, these pulses must be due to pick-up by amplifiers 1 and 2.

The time-difference between the prompt air shower pulse and the scintillator/adder/stretcher pick-up pulse corresponds to the time-delay between the arrival of an air-shower and the application of the high-voltage pulse (- 8 kv.) to the electrodes of the flash-tube chamber.

All pick-up is from this pulse via the mains and power-supplies of the electronics.

p.u. = pick-up pulse
T = previous particle pulse.

FIG. 9·19

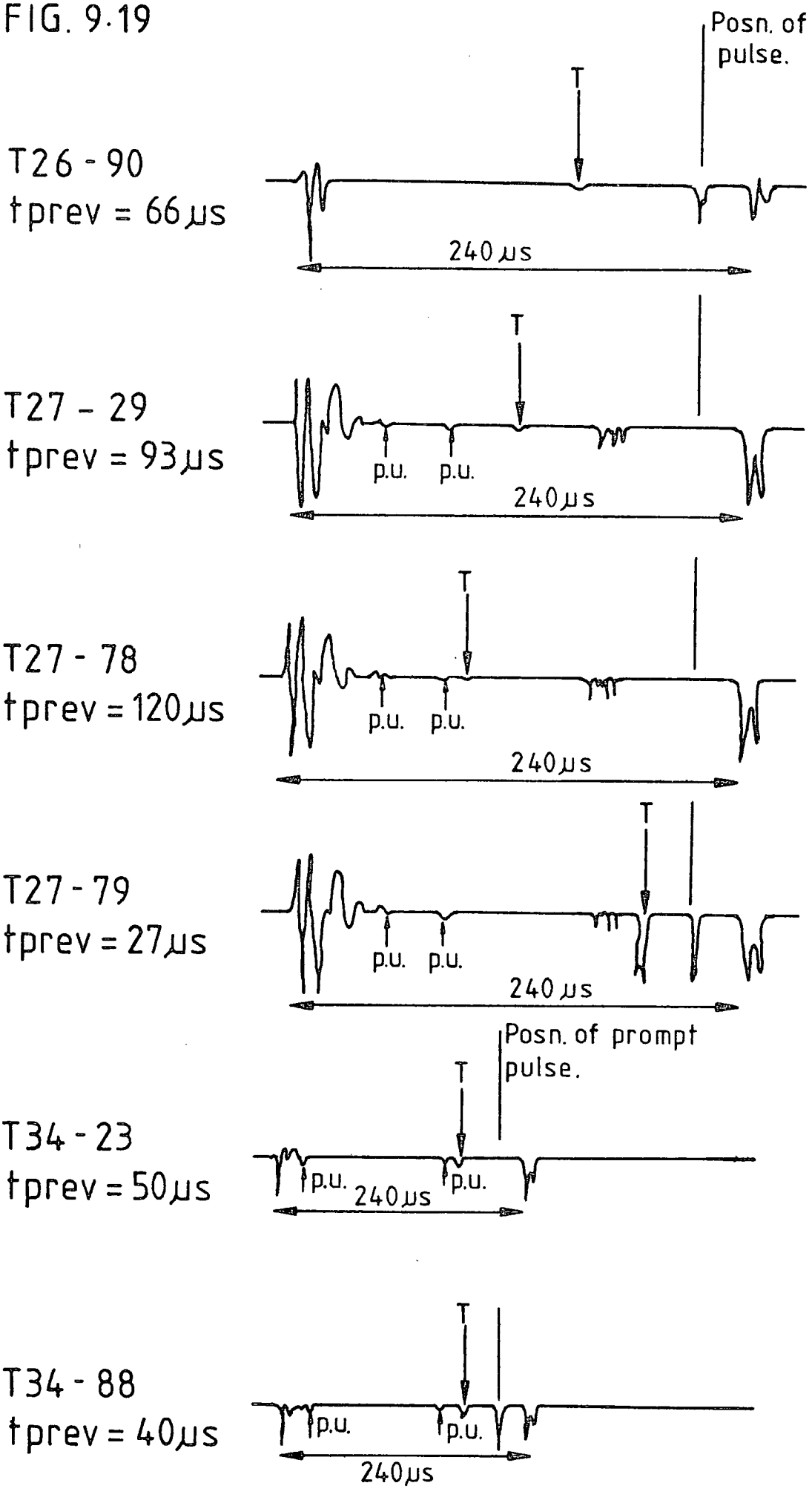
Posn. of prompt pulse.
T
T26 - 90
tprev = 66μs
240μs
T
T27 - 29
tprev = 93μs
p.u.
p.u.
240μs
T
T27 - 78
tprev = 120μs
p.u.
p.u.
240μs
T
T27 - 79
tprev = 27μs
p.u.
p.u.
240μs
Posn. of prompt pulse.
T
T34 - 23
tprev = 50μs
p.u.
240μs
p.u.
T
T34 - 88
tprev = 40μs
p.u.
p.u.
240μs

In two of the Figs. 9.14, 9.15 low efficiency tracks can be seen in the main body of the chamber. In neither case do these tracks appear to be parallel to the shower arrival direction. However, both tracks appear to be due to low momentum stable particles, both showing strong scattering towards the lower end. Their measured efficiencies are $\lesssim 3$ standard deviations away from the expected efficiency of a singly charged particle passing through the chamber at a time previous to the application of the high voltage pulse equal to the time measured for the previous particles.

However, they cannot be responsible for the previous particle pulses, since if they are ionising at 3 times the level of a singly charged particle then their measured efficiencies indicate that they must have passed through the chamber (30 ± 15) μs before the time registered by the pulse from the scintillator stack. Alternatively if these particles were ionising at a rate equivalent to that of a singly charged particle, the calibration data indicate that they would not have produced a measurable pulse (through the delay lines) in the scintillator stack.

From a scan of all the events (irrespective of scintillator response) the rate of such low efficiency tracks (defined as a track with ≤ 0.5 the efficiency of the shower particles in F2a) was found to be 0.04 per shower. The probability that out of the five selected events (one tachyon candidate had no corresponding flash-tube photograph), 2 would have such "background tracks" is just under 2%, which is not inconceivable.

A measurement of the efficiency of response of the chamber to prompt air-shower particles has been made by counting the number of flashes in F2a + F2b for each track which passed through all the defining layers (see Chapter 6). The results are shown in Fig. 9.20, and the mean internal efficiency (see

Chapter 2) found to be 91.8% with a standard error of 5.5%. This figure should be compared with Lloyds (1960) theoretical prediction of 88.5% for a f q = 9 at a time delay of 20 μs (see Chapter 2 for definition of a f q).

Hence if the previous particles are ionising at three times the level of a singly charged relativistic particle, then for time delays 50 μs to 140 μs between the passage of the particle and the application of the high voltage, they should produce tracks with efficiencies in the range 80% to 90%, indistinguishable from the prompt air-shower particles.

Below, a comparison is made between the direction of the shower and the time of arrival of the previous particle. In order to support the assumption that the direction of the shower particles in the chamber represents the arrival direction (in projection) of the shower a comparison has been made between the predicted and observed projected angle distribution (see Fig. 9.21 and Appendix V).

9.7.3 The significance of the results

In order to penetrate the lead - iron barytes brick shielding a relativistic muon needs >0.8 GeV. The rate of arrival from all directions of muons at sea-level with energies greater than 0.8 GeV is $7.81.10^{-3}$ cm^{-2} st^{-1} s^{-1} (Allkoffer et al [1971]). Since the tachyon detector (scintillator stack A) covers 25,190 cm^2, and the time available for observing muons is 81,840 μs (number of showers x length of delay line), the solid angle of acceptance being $\frac{2\pi}{n+2}$ st (where $I(\theta) = I_o \cos^n\theta$ represents the dependence of the intensity of muons on zenith angle θ) and n = 2, the expected number of

Figure 9.20 Distribution in frequency of the number of tubes flashed in F2a + F2b (94 tubes) for all tracks that passed through F1a,b F2a,b F3a,b.
Mean internal efficiency = 91.8%
Standard error = 5.5%
(Predicted efficiency from Lloyd (1960) for afq = 9, t_d = 20 us is 88.8%)

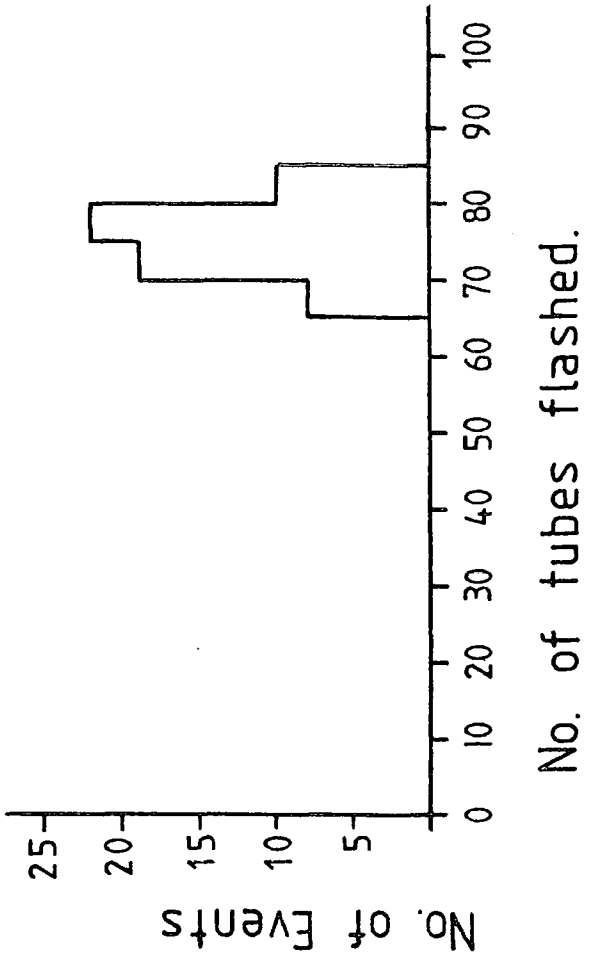

FIG. 9.20

precursors passing through the stack in the total observation time is 25 ± 5 (assuming random fluctuations).

According to Fig. 9.7 however, because of the high lower limit on observable pulses (300mV corresponding to 3mV at output of the electronics) we should only observe 3% of these i.e. $1\ ^{+2.4}_{-0.83}$. Since 6 such pulses were observed, the result significantly differs from the result we should expect due to random background particles. (The probability of observing 6 when the mean number expected is 1 and the distribution in Poissonion is $5.11.10^{-4}$). If we now compare the number of previous particles which arrived in the 120 μs interval immediately previous to the arrival of an air-shower (tachyon candidates) with the number that were observed in the time interval 120 μs before that 120 μs time interval (random background) we find that all the pulses were observed in the tachyon candidates time interval. The probability that this is due to chance is $(\frac{1}{2})^6 = 0.016$. Hence the total probability that the results are due to fluctuations in the random background radiation = 8.10^{-6}.

The time distribution of Fig. 9.12 is suggestive (tachyons from vertical showers travelling at infinite velocity would be expected to arrive between 40 and 80 μs. before the arrival of the shower, depending on the height of production).

If we assume that the direction of arrival of the muon group travelling through the chamber is representative of the air-shower arrival direction, then we can predict the arrival time of a tachyon associated with this shower for various heights of production. Assuming that, if produced, a tachyon is produced in the first collision of a primary cosmic ray proton (for example), then the shape of the t_{prev} - cosθ curve can be predicted from the probability

Figure 9.21 : The distribution in θ for the muons observed in the flash - tube chamber in a sample of 34 showers of size greater than 10^5 particles at sea-level. The continuous curves show the predicted distributions in projected zenith angle acording to the method of Lovati for a distribution of the form

$$I(\theta) = I(0).\cos^n(\theta) \text{ for } n=4,8,12.$$

n = 8 gave the best fit from a minimum χ^2 plot.

FIG. 9·21

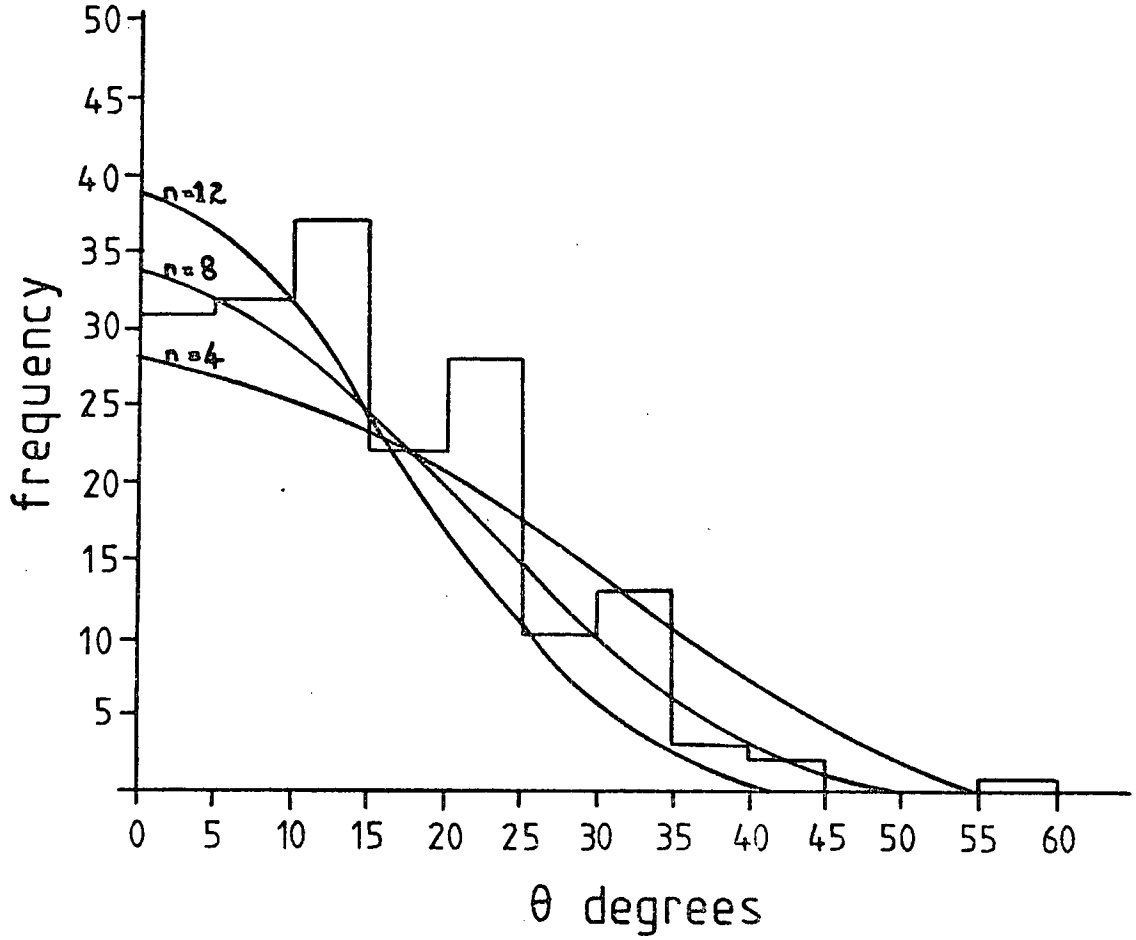

of a proton interacting at various heights in the atmosphere. (The curve would be the same if a tachyon (astrophysical) initiated the shower provided that the mean interaction length in air is the same for tachyons as it is for relativistic protons.)

These predictions are shown in Fig. 9.22 assuming $\beta = \infty$ for the tachyon. The experimental points are also plotted, it is clear that most of the detected signals could have been produced by this simple model, however the point at 120 μs is an unlikely candidate, because the air-shower would have had to originate beyond the limits of the atmosphere (at a height of 40 km).

9.8 Comparison with previous searches

A review of previous searches has been presented in Chapter 8, table 9.2 lists the sea-level searches in cosmic rays which are directly comparable with the above reported search. All the experimenters (see Column 8) searched for small signals, presumably for comparison with Clay and Crouch's - later discredited - results. The object of table 9.2 is to show that using unshielded detectors and small signal response, all but one (Emery et al, see below) were counting mainly noise. Column 6 of table 9.2 shows the expected number of muons with momentum $p > m_\mu c^2$ (i.e. relativistic) which each experiment should have detected taking into consideration the area of tachyon detector, the total sensitive time for detecting tachyons (typically, number of showers x 120 μs) and the solid angle for acceptance of a previous particle ($\frac{2\pi}{n+2}$ st. where n = 2, see above). Hazen et al

FIG 9.22

The tachyon candidates' t_{prev} - cos θ distribution, the dashed curves are the predicted distributions for various heights y of production above sea-level.

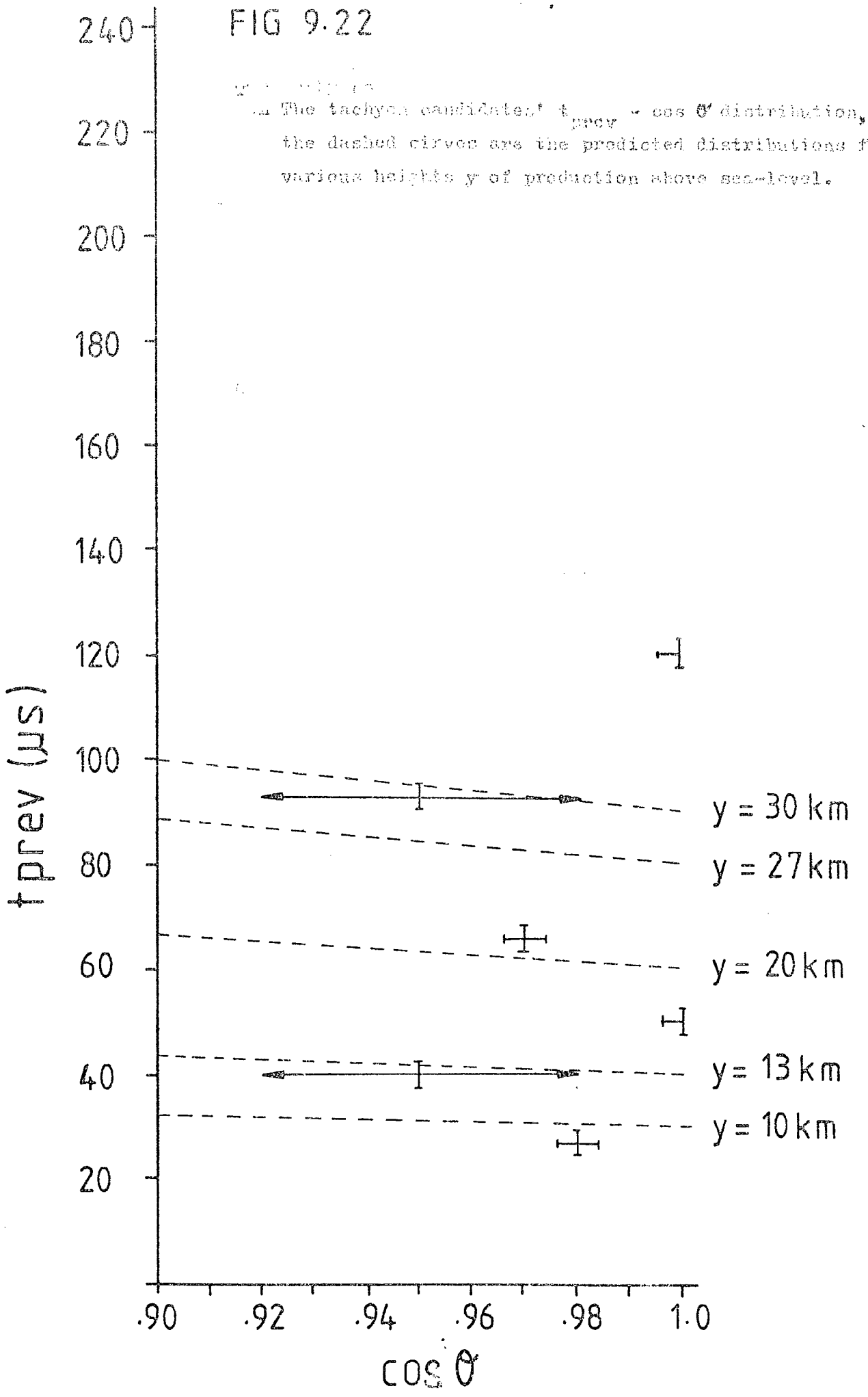

(1976) have pointed out similar remarks in a report on their own experiment.

The search by Emery et al (1975) using geiger tubes should have detected the same significant bunching as the present experiment, since columns 5 and 6 indicate that they were detecting signals above those due to background (noise) effects for about 67% of the time.

However, it is difficult to estimate the sensitive area and solid angle of acceptance of their apparatus (crossed geiger tubes), and perhaps the response of a geiger tube to faster than light particles should not be compared with the response of a plastic scintillator. They themselves admitted this latter possibility and ran a second experiment (Emery et al op cit) using a scintillator, but there they too seem to have been counting noise (see table 9.2, row 3).

One major difference between the present search and previous searches is the fact that the scintillators in stack A are shielded by 15 cms of lead and 15 cms of iron. It is possible that the signals detected as previous particles were in fact due to the secondaries from nuclear interactions of a tachyon in the iron. This could provide an alternative explanation for the apparently highly ionising properties of these previous particles i.e. that they produce several singly charged subluminal particles such as pions which are then detected by the scintillator. If these are spread over a large angle they would leave no trace in the flash-tubes.

No such nuclear interactions would be likely in the case of an unshielded tachyon detector, since the probability for a nuclear interaction in air is very small compared with that for lead or iron. This could be the reason for the negative result of the geiger tube experiment of Emery et al, since

TABLE 9.2

A summary of the tachyon searches reported at the 18th International Cosmic Ray Conference in March, 1975. The experiment of Clay and Crouch is not included since the results are now discredited as they have not been able to be reproduced in a number of similar experiments.

Columns 1-4 are self explanatory.

Column 5 is a standardisation of the reported results to a time-span of 120 μs immediately previous to the shower arrival.

Column 6 is a prediction of the number of pulses calculated to be due to the background muon component, taking the muon rate at sea-level to be 10^{-2} cm^{-2} st.$^{-1}$ s^{-1} and assuming a solid angle of acceptance of $2\pi/(n + 2)$ - where $I(\theta) = I(0)\cos^{n}\theta \equiv$ the intensity of muons (cm^{-2} s^{-1}) at angle θ to the vertical. Clearly the majority of the pulses detected were due to background effects other than the cosmic radiation, e.g. background radioactivity, photomultiplier/scintillator noise, etc.

Column 7 is the minimum detectable pulse claimed by the authors ($\overline{\text{s.p.p.h.}} \equiv$ mean single particle pulse height).

Column 8 is the predicted level of excess that these experiments would have recorded - according to our data - for the 120 μs immediately prior to the shower arrival compared with the 120 μs previous to that.

TABLE 9.2

Authors	Run Time	No. of Showers	Area of Tachy. Det.	No. of Pulses in Prev. 120 us	Expected No. from Background	Min. Detectable Signal	Predicted Level of Excess	Ref.
Prescott et. al.	62 days	4,315	1 sq. m.	~1715	82	5.10^{-4} $\overline{\text{s.p.p.h.}}$	2.5%	New Expt.
Fegan et. al.	426 days	2,649	0.25 sq. m.	~220	13	$\ll \overline{\text{s.p.p.h.}}$	2%	Mode A
Fegan et. al.	426 days	1,514	0.25 sq. m.	~840	8	$\ll \overline{\text{s.p.p.h.}}$	0.4%	Mode B
Emery et. al.	77 days	27,449	"4 sq. m."	~3900	2,020	Not Quoted	25.5%	Geiger Tubes
Emery et. al.	26 days	9,521	0.44 sq. m.	~4185	80	0.1 $\overline{\text{s.p.p.h.}}$	2%	Liquid Scint.
Hazen et. al.	104 hrs.	1,031	1.6 sq. m.	~1640	31	0.05 $\overline{\text{s.p.p.h.}}$	1%	Run I
Hazen et. al.	190 hrs.	2,366	1.6 sq. m.	~4320	75	0.02 $\overline{\text{s.p.p.h.}}$	0.4%	Run II
PRESENT WORK	40 hrs.	241	2.1 sq. m.	9	0.5	3 $\overline{\text{s.p.p.h.}}$	——	

they should - assuming all factors to be comparable between a scintillator and a geiger tube for detecting charged tachyons - have observed a 25% excess of signals in the 120 μs previous to the air-shower arrival (see Column 8 of table 9.2).

Referring back to the point first brought up by Emery et al that perhaps gaseous (gieger tubes, flash-tubes) detectors are not comparable with solid (scintillators) detectors in detecting charged tachyons, this might be because the detected signal is not an ionisation pulse but a Cerenkov pulse. Both energy loss processes are discussed in Chapter 8, however it is clear that for a narrow electric field streaming out behind the tachyon, the probability of producing a Cerenkov pulse in a solid detector would be much higher than in a gaseous detector.

9.9 Conclusion

In a search for highly ionising (three times the ionisation of a charge e subluminal relativistic particle) particles in the 240 μs previous to the arrival of an extensive air shower in the size range 10^5 to 10^7 particles at sea-level 6 events have been observed. This result is in itself significant, since only one event was expected (on average), however, all 6 events were found to occur in the first 120 μs immediately prior to the shower's arrival. The probability of these still being due to the background (unrelated) muon component of the cosmic radiation is reduced to 8.10^{-6}.

A simple model for tachyon production and propagation seems to describe the results fairly well indicating that most of these pulses could be due to tachyons travelling at very high velocities ($\beta \gg c$) produced high in the atmosphere.

None of the events gave rise to unusual tracks in the flash-tube chamber, however if they behave like ordinary relativistic particles with high (~3 times as much) ionising power, then their tracks would be indistinguishable from those due to particles in the shower.

Previous searches have failed because they were looking for low ionising rather than highly ionising particles. However further considerations on the lack of response of the flash-tubes and the negative results of a search with geiger tubes (Emery et al). suggest that either tachyons can only be observed to ionise in dense media i.e. solid detectors, or by the products of their interactions in dense targets.

Note added in proof:

A search for tachyons associated with air-showers at mountain altitude has recently been reported by S. K. Gupta (Bhat et al 1979) as detecting no flux ($< 2.3 \times 10^{-10}$ cm^{-2}s^{-1}st^{-1} at the 95% confidence level) of tachyons ionising at >3 times the ionisation rate of arelativistic muon under 167 g.cm^{-2} of lead and iron absorber in a total running time of 1872 hrs. (mode 2). The apparent contradiction between these two results could be due to the difference in thickness of the scintillating material used (1 cm. as opposed to 5 cms.) or target (167 g.cm^{-2} as opposed to 288 g.cm^{-2}), but can only be resolved by a rerun of the above described experiment without the possibility of any high voltage pick-up pulses.

CHAPTER 10

MEASUREMENTS ON MUONS IN AIR-SHOWERS

10.1 Introduction

Because they are leptons, muons only interact weakly with matter. Hence the muon component of an air-shower grows and maximises, but decays only slowly. Studies of the muon component at sea-level thus gives information on the early stages of air-shower development.

The lateral distribution of muons at sea-level depends on the mean transverse momentum $\bar{p}$ of the pions produced in the later interactions of the hadronic core of the air-shower. However, since the muons only interact weakly with matter, their lateral distribution also gives information on the height of production of muons. This in turn reflects the multiplicity of pions produced in the early interactions of the hadronic core of the shower. Studies on low energy ($\lesssim$10 GeV) muons are useful since they come from pion interactions at around 10^3GeV where the p_T distributions are well known from accelerator studies. Hence information can be gained on the multiplicity of pions produced at energies around 10^6GeV.

Interpretation of such data in isolation is ambiguous, however, in combination with measurements on the hadronic and electromagnetic components light can be shed on the composition of the primary radiation producing air-showers of 10^5 - 10^7 particles.

10.2 Principle of the method of determining the lateral distribution of muons

The flash-tube chamber can be used as a visual detector of muon densities. The lead and iron absorbers above the main body of flash-tubes provide an energy threshold below which muons would not reach the flash-tubes. The lateral distribution and shower size dependence of muons can be determined using the methods described in Chapter 7.

In particular, besides determining the overall lateral distribution of muons above a certain energy $E\mu$, the dependence of the number of muons $N\mu$ on shower size Ne can be investigated at varying distances from the core of the shower.

10.3 Review of previous measurements

The majority of measurements on the lateral distribution of low energy muons are slightly broader than expected from the standard (C K P) model indicating (see Section 10.1) a multiplicity of secondary particles in the early interactions greater than that assumed (see Fig. 10.2).

Above 20m from the core, the data are well described by the empirical formula devised by Greisen and co-workers (Bennet et al [1962]). A collection of previous measurements are presented in Fig. 10.1 (W dowczyk [1973]) and compared with the Greisen curve. All the data refer to $E\mu > 1$ GeV, and the Greisen curve has the form.

$$(10.1) \qquad \rho_\mu (Ne, r) = \frac{14.4 r^{-0.75}}{(1 + r/320)^{2.5}} \left(\frac{Ne}{10^6} \right)^{0.75} \left(\frac{51}{E_\mu + 50} \right) \left(\frac{3}{E_\mu + 2} \right)^{0.14 r^{0.37}}$$

where r is expressed in metres and E_μ in GeV. This formula is valid for $E_\mu = 1 - 10$ GeV.

FIG.10·1 A summary of previous measurements of the lateral distribution of muons of energy $\geqslant 1$ GeV (after Wdowczyk 1973). The continuous curve is Greisen's function (1960) for $E_\mu > 1$ GeV.

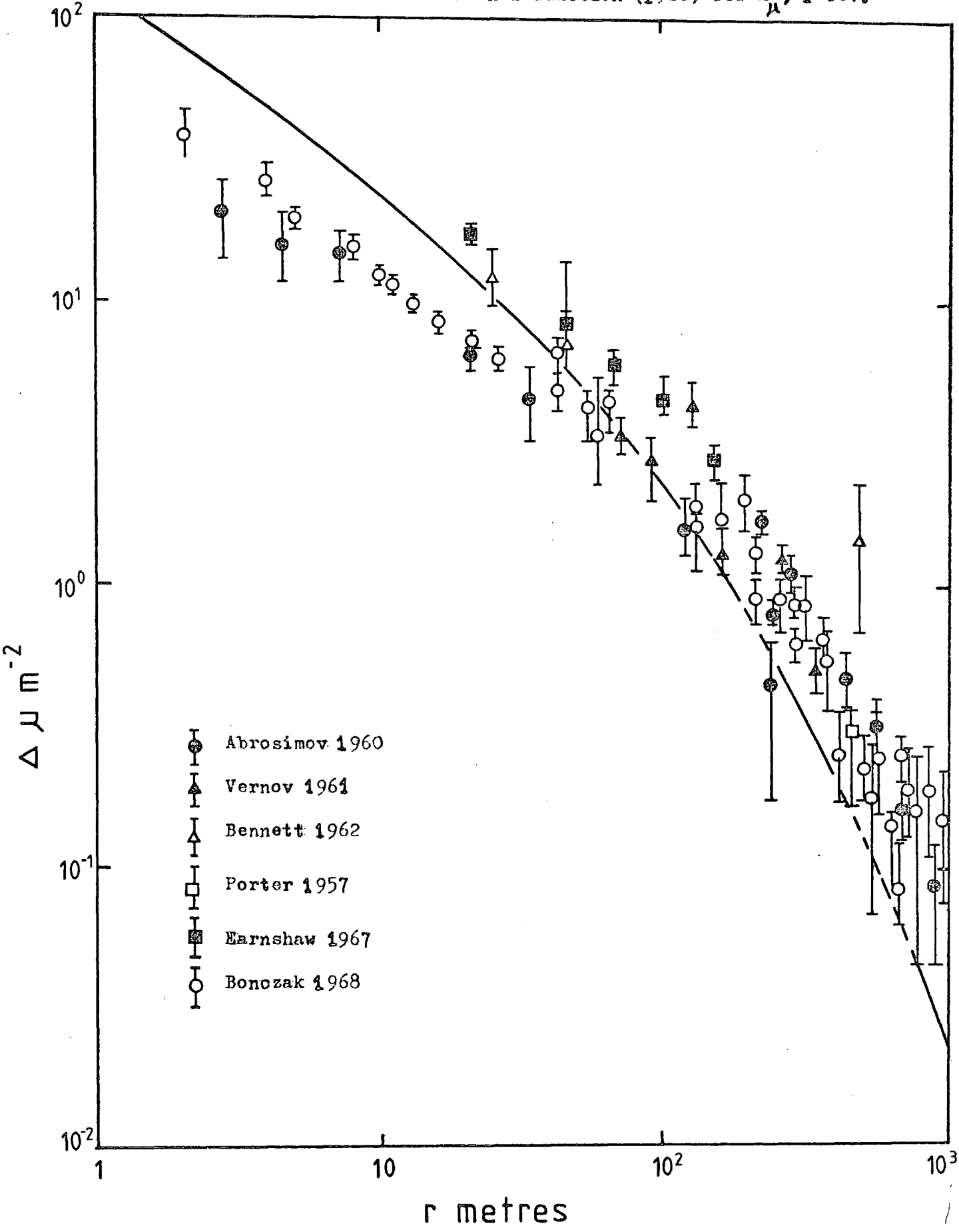

More recently attempts have been made to predict the lateral distribution of low energy muons by assuming various primary compositions and interaction models and calculating the sea-level lateral distributions by Monte Carlo techniques (Greider [1970, 1977], Gaisser et al [1978]).

Fig. 10.2 presents a comparison of low energy data with such theoretical predictions (Greider [1977]). Curves 1 - 3 are based on proton primaries whereas curve 4 is based on iron primaries. Curve 1 represents a model (S M F B) based on the production of several intermediate fire balls moving slowly in the centre of mass frame in the nuclear interactions; curve 2 represents a model based on 2 intermediate fire balls moving apart in the centre of mass frame; curve 3 is the same as curve 2 but with rising cross sections assumed; curve 4 is also a S M F B model. More detailed descriptions of the models can be found in Greider (1970).

If we consider only proton initiated showers then the data are more compatible with a mean multiplicity dependence of secondaries $\langle n_s \rangle$ of $s^{0.375}$ to $s^{0.5}$ rather than $s^{0.25}$ (the dependence of the standard (C K P) model). (See Fig. 10.2.)

All discussions of the dependence of the number of muons N_u on shower size Ne (e.g. W dowczyk (op cit), Gaisser et al (op cit)) conclude that $\alpha \approx 0.75$ (where $N_\mu \propto N_e^{\alpha}$). There have been no attempts to distinguish any dependence of α on core distance, since any systematic dependence would be difficult to justify according to current models of shower development.

FIG. 10·2

A summary of previous measurements of the lateral distribution of low energy muons (after Greider 1977). The curves are the results of simulations according to different models (see text) and primary masses for $E_\mu > 1$ GeV.

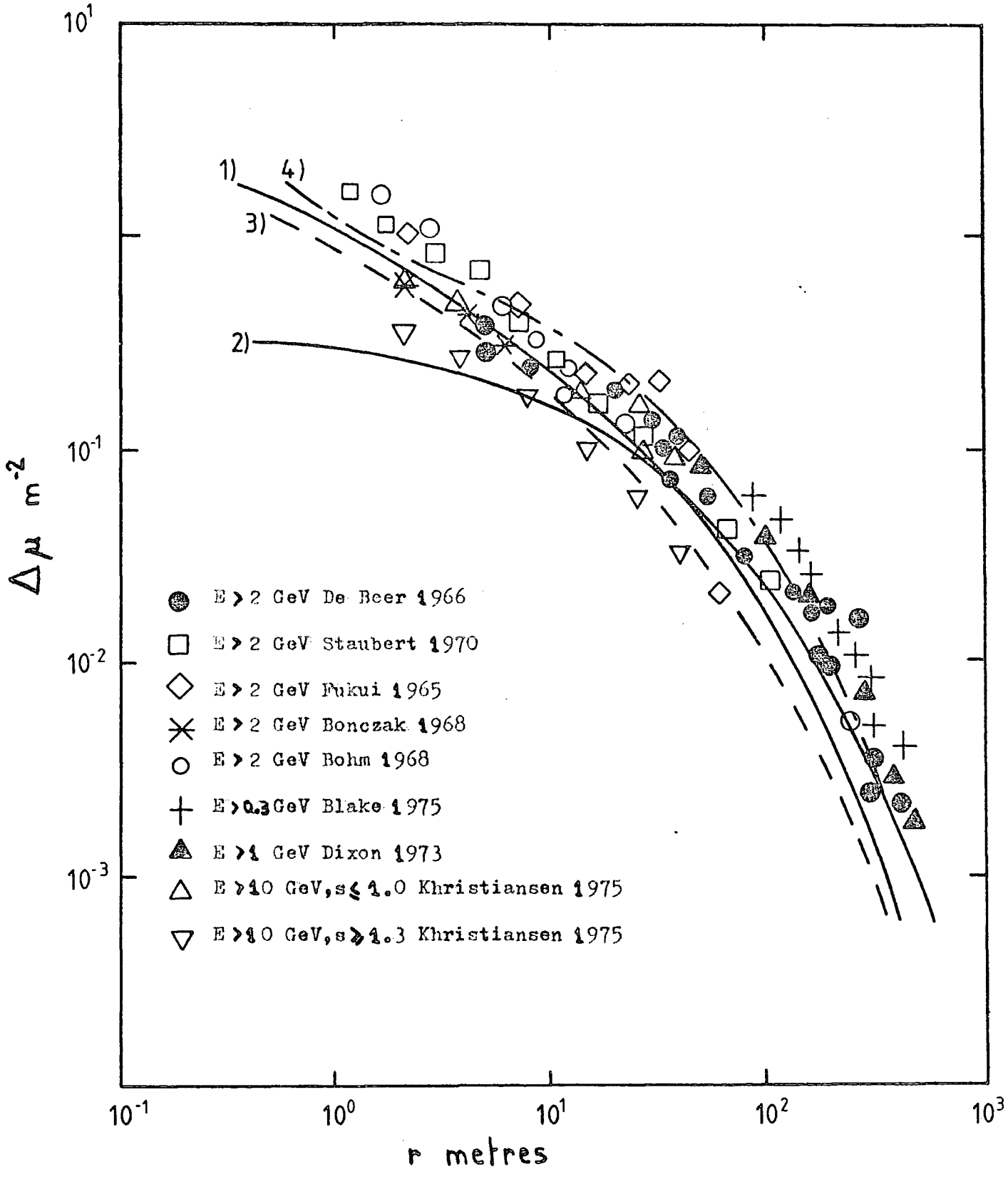

10.4 The method of measuring the lateral distribution of muons

10.4.1 The muon density measurements

The flash-tube chamber was triggered by a "standard" air-shower trigger (see Chapter 6, Section 6.3), the chamber being photographed as described in Chapter 2. The time delay between the occurrence of a trigger pulse and the application of the H.T. pulse was 20 μs. A summary of the basic data collection details is presented in Table 10.1.

The photographs were scanned by projecting onto a 1:20 scale drawing of the front view of the chamber (Fig. 10.3). The number of muons passing through the central space between F2 and F3 were counted. A muon track was defined by at least two co-linear flashes in both F2 and F3, in the cases where more than one track were observed, only tracks parallel to within $\pm 2^{o}$ were counted, non-parallel tracks were attributed to background tracks (i.e. muons unassociated with the air-shower but arriving in the 140 μs prior to the application of the H.T. pulse - this being the time delay during which a muon track could still be visible).

The energy of the muons was determined by the fact that they had to pass through 15 cm of lead, 15 cm of iron, and at least 60 layers of flash-tubes and accompanying aluminium electrodes. The total amount of matter that had to be travelled through was thus 250 $g.cm^{-2}$. Assuming an energy loss of 2 MeV $g.cm^{2}$, the minimum energy required by muons to reach this level is 0.5 GeV.

Since the flash-tube chamber was only viewed in projection, some tracks could be caused by muons which only passed through the barytes brick walls before entering the flash-tubes. Since by far the largest amount of absorption of

FIG. 10·3

Front view of the flash-tube chamber.

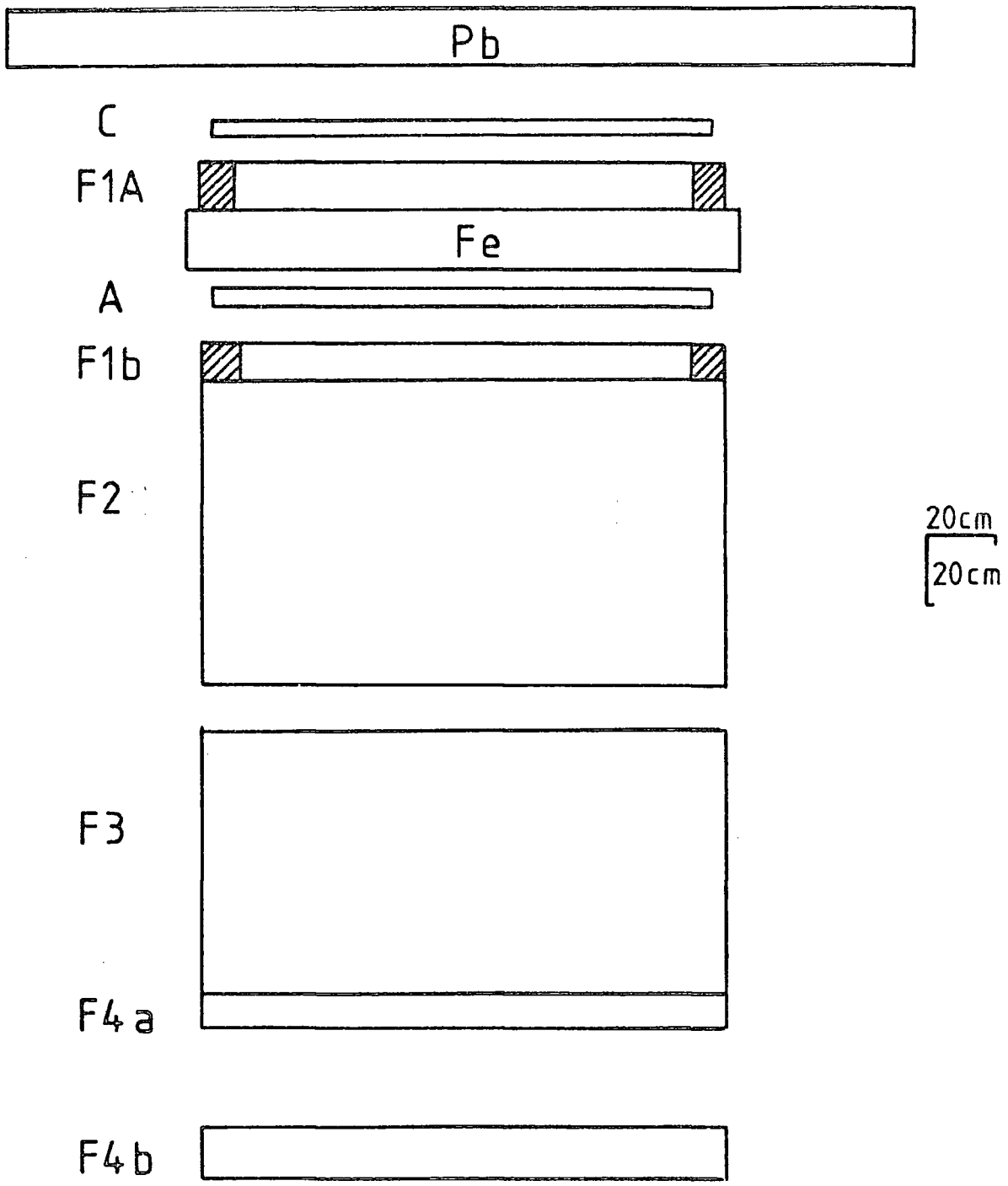

TABLE 10.1

SUMMARY OF DATA USED FOR MUON LATERAL DISTRIBUTION

Total number of events	920
Number of bursts in lead or iron	39
Number of bursts in glass	14
Number of events used	867
Number of Minuit analysed events	630
Number of I.L. analysed events	237

low energy muons takes place in the lead and iron, a simultaneous count was taken of those tracks which appeared in both F1a and F2a, to check whether any such contamination could affect the results. These latter data are referred to below as data from the upper plane, whereas the former are referred to below as data from the central plane. Figs. 10.4a, b, etc. are some typical events.

Those events in which a hadron or muon interacted in the lead or iron or the glass and produced a burst were not included since the muon tracks were generally difficult to distinguish. Figs. 14.5 show such events, but Table 10.1 clearly indicates that these represent only a small fraction of the data and their omission should not affect the results unduly.

10.4.2 The core distance and shower size measurements

Both the intersecting loci and the "Minuit" methods of analysing the data were used.

The "Minuit" method (i.e. computerised least squares fitting of core distance and shower size simultaneously) was chosen as the primary method because of the large amount of data that needed to be analysed. However, the method was found unsatisfactory in those cases in which a detector was saturated. In such cases, the programme ignored the information from the saturated detector(s) and proceeded to fit parameters to the measurements from the remaining detectors. Visual inspection of such events made it evident that the determined core location (and consequent shower size) was incorrect, and method 2 (see Chapter 7) of the intersecting loci methods was used to ascertain the parameters in these cases.

Figure 10.4 a): A low muom density event, although there are 5 muon tracks visible this event was classified as a 2 muon event through the upper plane and a 3 muon event through the central plane.

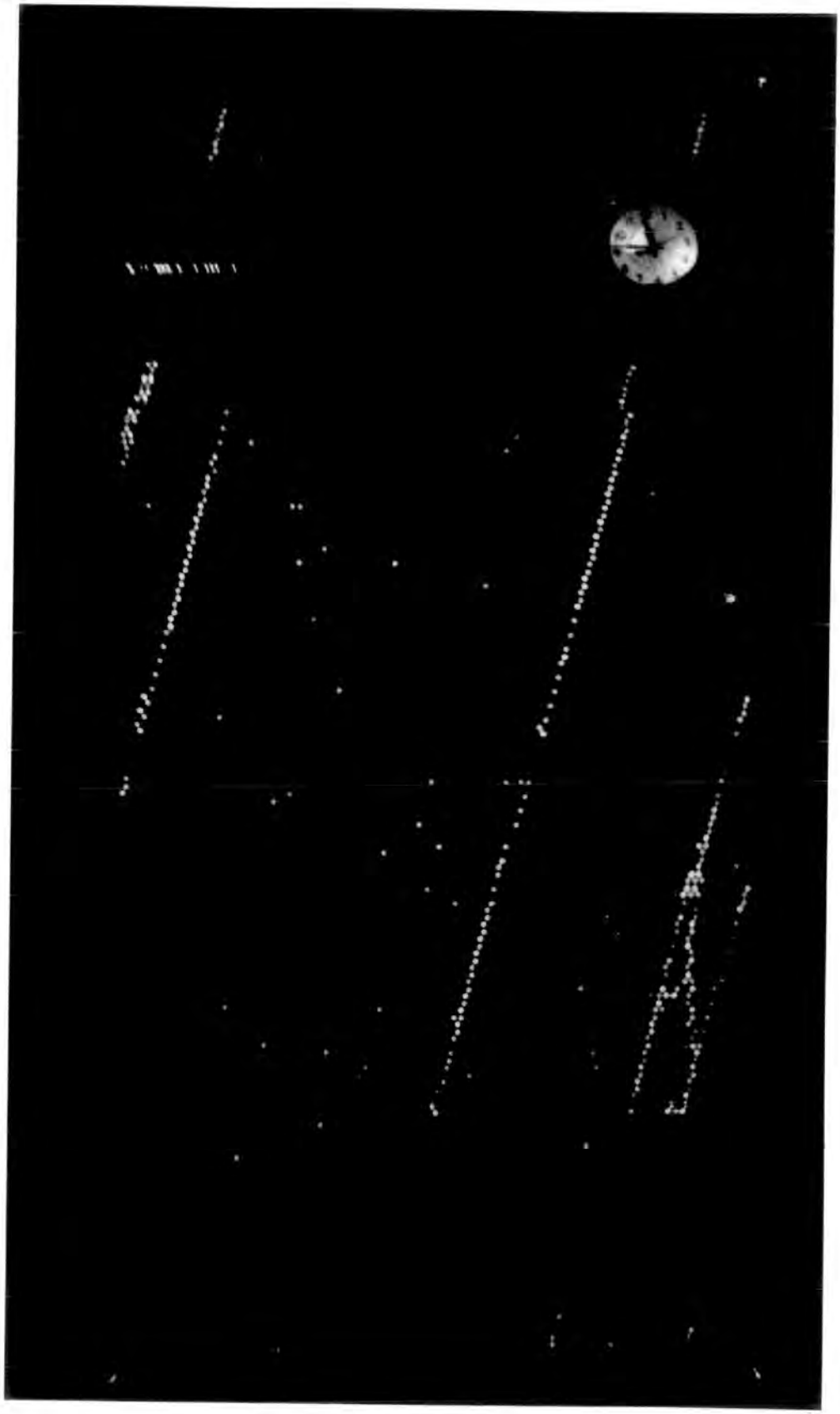

Figure 10.4 b):A high muon density event, with 8 muons through the upper plane, and 11 muons through the central plane.

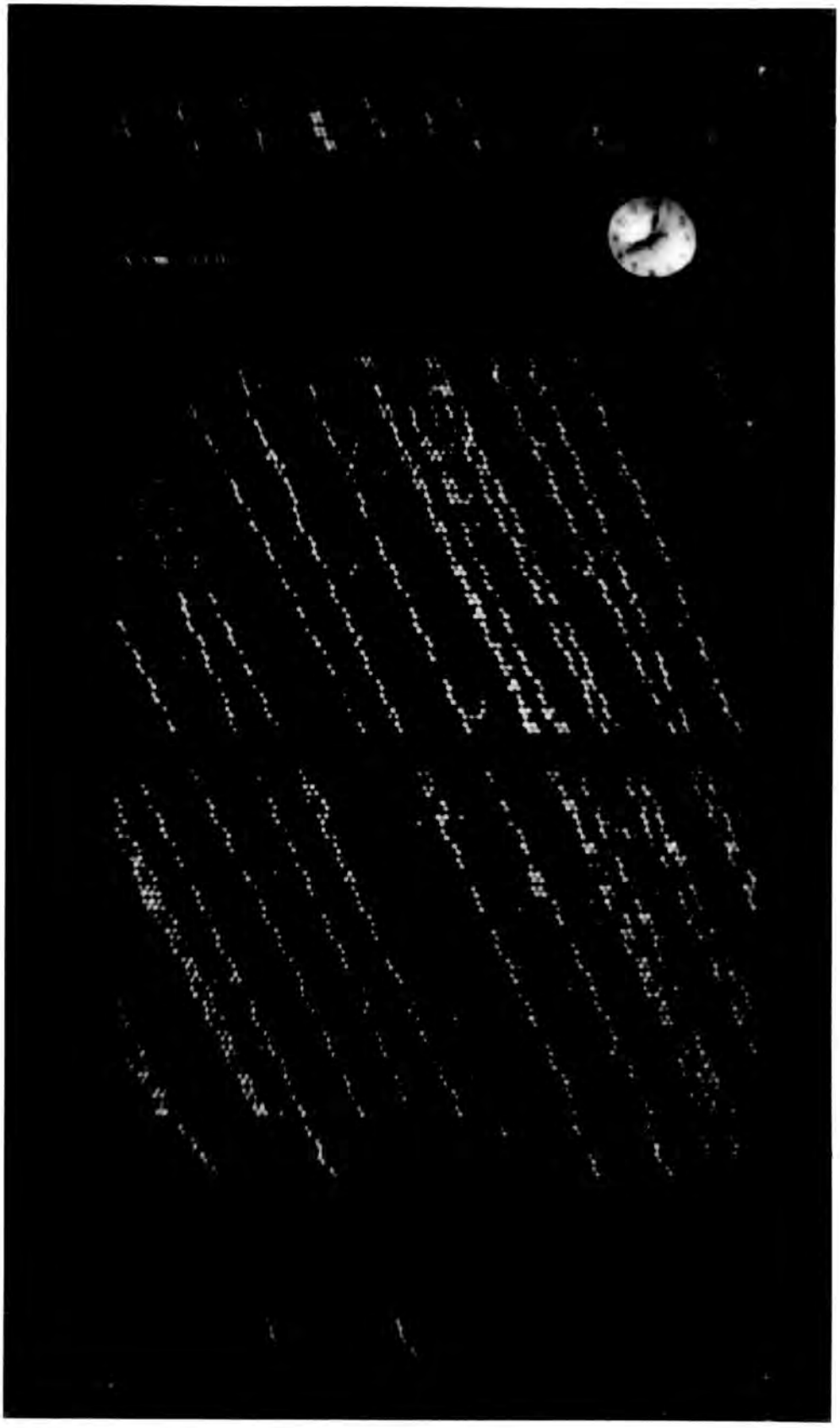

Figure 10.4 c): A comparatively rare type of event ~~...~~ an interaction has taken place in the main body of the chamber, and a cascade has developed in the glass and aluminium below. Such events are excluded from the data analysis.

The lower photograph shows the corresponding pulses from the scintillator stacks, A and B. Note the large prompt pulse from scintillator stack A, but the relatively weak response of stack B despite the large particle flux through it. (re. the discussion of the unreliability of stack B data in chapter 9.)

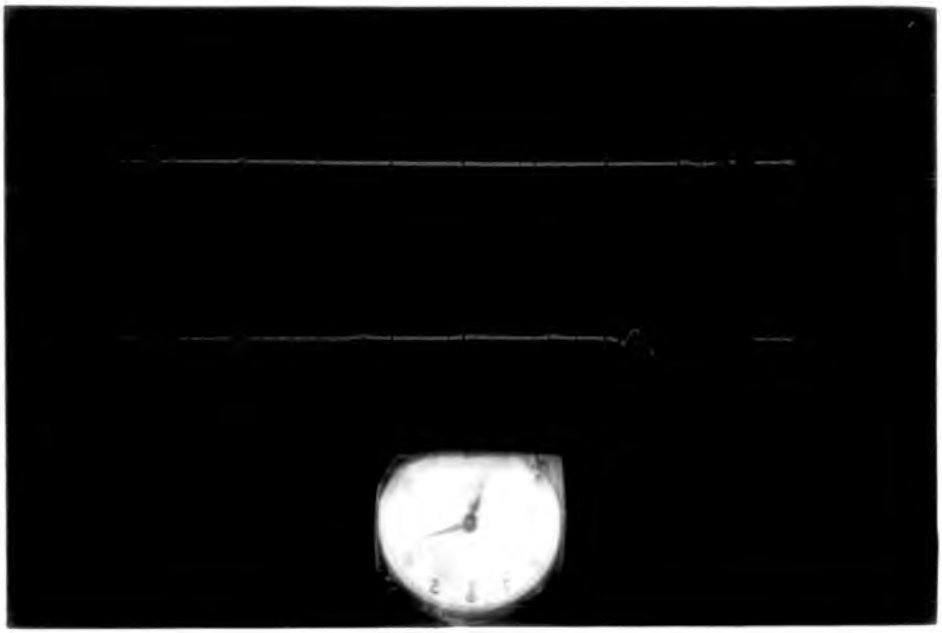

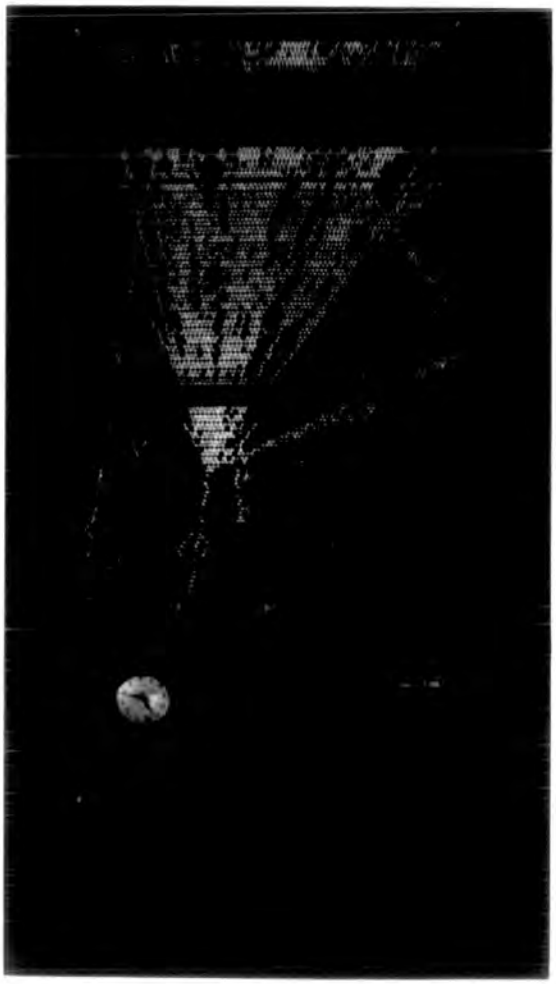

10.5 Results

10.5.1 Introduction

Ideally, the lateral distribution of muons in a single shower should be measured, and repeated for a large number of showers of the same size and the results averaged. However, this is impractical since it requires a large number of muon detectors sampling the shower simultaneously. In the present experiment there is a single muon detector sampling the muon density over a range of core distances and shower sizes. Clearly all the muon densities have to be normalised to a single shower size before proceeding to a determination of the core distance dependence of the muon densities. The first step is thus to determine the shower size dependence of the muon densities, and then to normalise the measurements to the median shower size measured before finally deducing the core distance dependence of the muon density.

10.5.2 The results on the N_μ - N_e dependence

Since two methods of determining shower size and two methods of measuring muon density have been used, there are basically 4 sets of data, these are called a), b), c), d). The meaning of the notation is summarised in Table 10.2.

Table 10.2

N_e \ N_μ	Central Plane	Upper Plane
Minuit Method	a)	c)
Intersecting Loci (I.L.) Method	b)	d)

For example Fig. 10.5a) represents the shower size dependence of the number of muons measured passing through the central plane, the shower sizes being determined by the "Minuit" method of computerised least squares fitting of the shower size and core position of each event. It is worth noting when the data are finally combined together that a) and b) represent different samples (as do c) and d)), whereas a) and c) represent different measurements of the same sample (as do d) and b)) of the universal population of air showers. Figs. 10.5, 10.6, 10.7, 10.8 are thus subdivided into a), b), c), d) according to Table 10.2.

The four (sixteen in all) figures represent a division of the data into different ranges of distance of the chamber from the core of the shower.

The data are presented as scatter plots of the observed number of muons passing through the flash-tube chamber against the size of the air-shower (as determined by either the Intersecting Loci (I.L.) method or the Minuit method) associated with each event. The crosses with error bars represent averages of the scatter plots, the data is binned by the vertical lines so as to give approximately equal statistical accuracy to each of these points, which are then plotted at the average shower size associated with each point. The straight line is a result of a least squares fit of the function

$$y = a\ x^b$$

where y = number of muons passing through chamber N_μ

x = associated shower size N_e in units of 10^5 particles, to the averaged data. The quantity r^2 represents the goodness of fit of the quoted function to the data and can be interpreted as $r^2 = 1$ = perfect linearity, $r^2 = 0$ = non-linearity. The horizontal arrows represent the lower limit of data used to determine the function. Since the data are divided into regions of core

Figure 10.5 a)

Number of muons N_μ through central plane as a function of shower-size N_e (as determined by Minuit method) for core-distance range 0 to 20m.

$$N_\mu = 0.73 N_e^{0.66} \qquad (r^2 = 0.86)$$

Figure 10.5 b)

Number of muons N_μ through central plane as a function of shower-size N_e (as determined by I.L. method) for core-distance range 0 to 20m.

$$N_\mu = 1.82 N_e^{0.48} \qquad (r^2 = 1.0)$$

FIG 10.5 a)

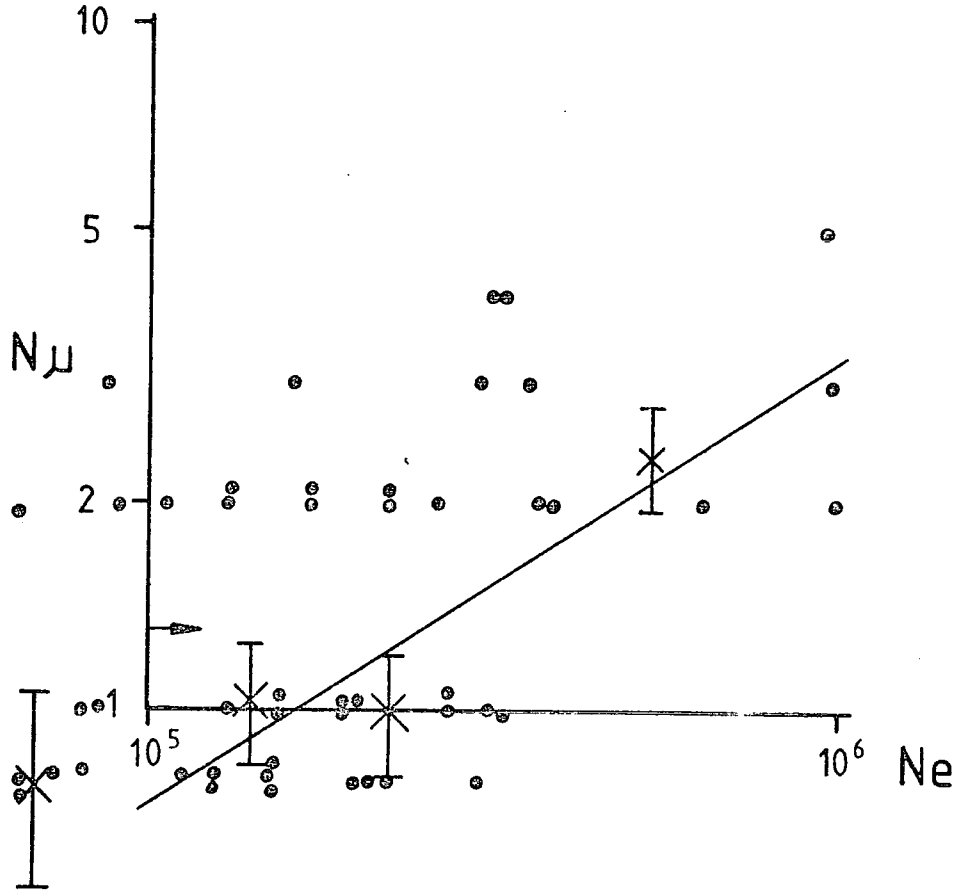

b)

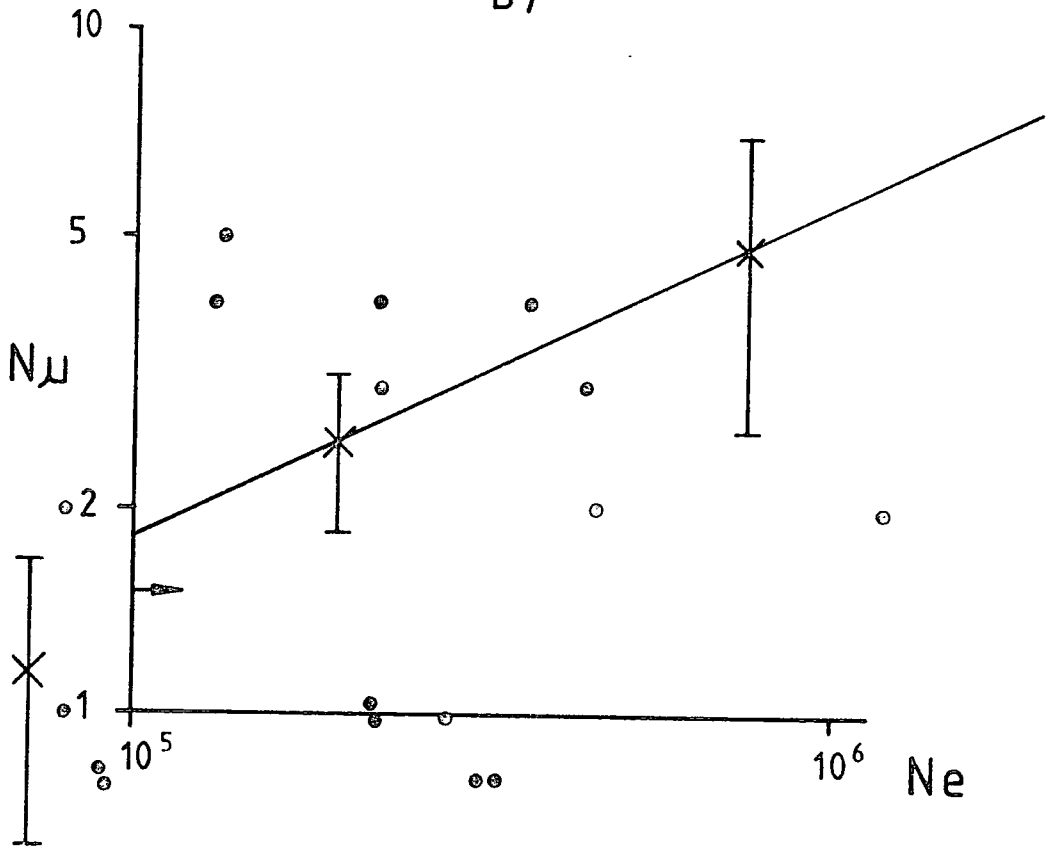

Figure 10.5 c)

Number of muons N_μ through upper plane as a function of shower-size N_e (as determined by Minuit method) for core-distance range 0 to 20m.

$$N_\mu = 0.905 N_e^{0.30} \qquad (r^2 = 0.92)$$

Figure 10.5 d)

Number of muons N_μ through upper plane as a function of shower-size N_e (as determined by I.L. method) for core-distance range 0 to 20m.

$$N_\mu = 0.94 N_e^{0.73} \qquad (r^2 = 1.0)$$

FIG 10.5 c)

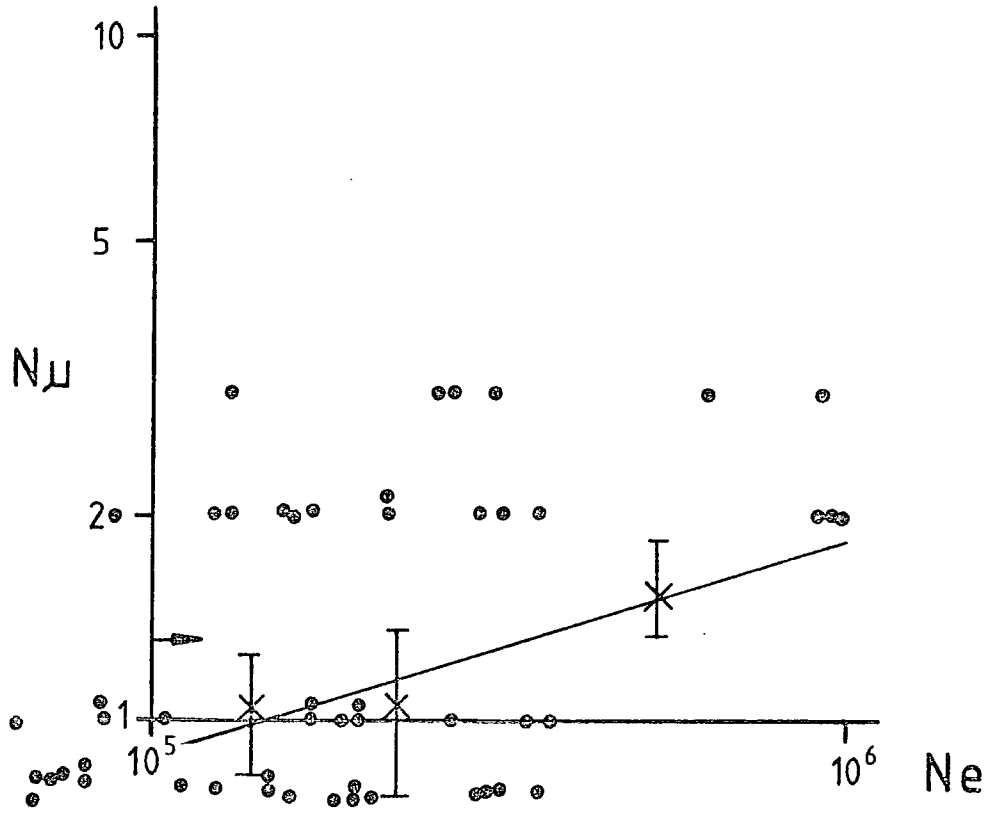

d)

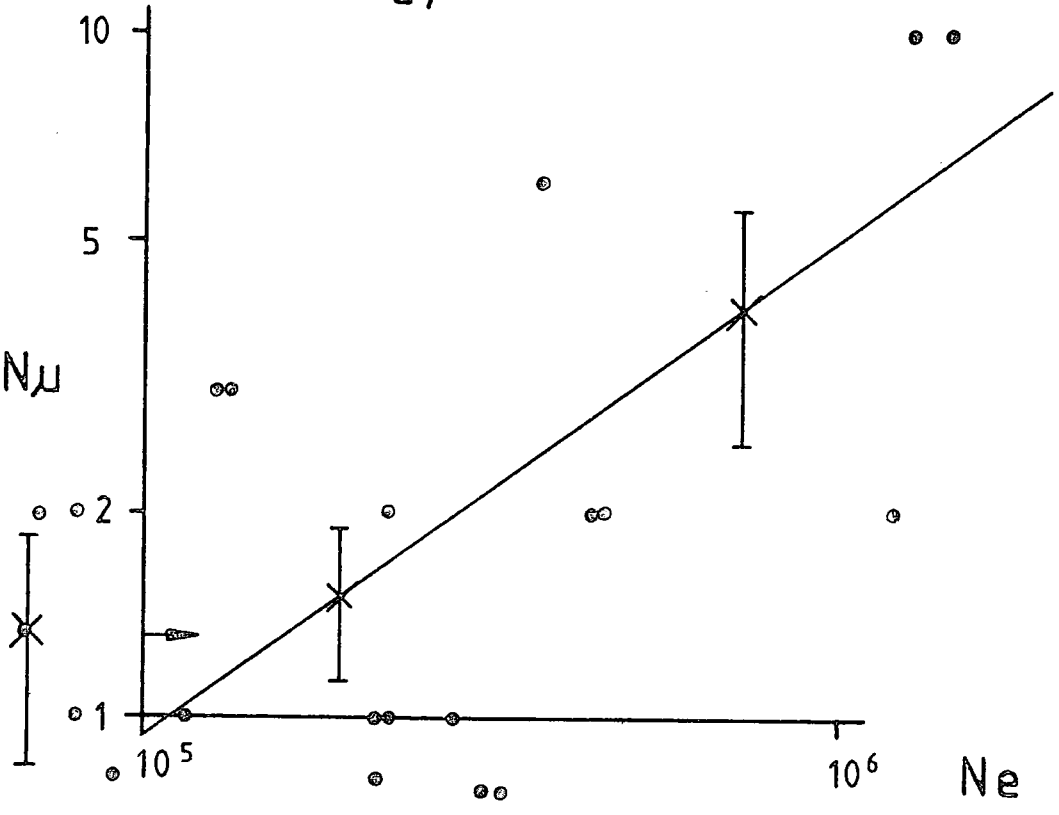

Figure 10.6 a)

Number of muons N'_{μ} through central plane as a function of shower-size N_e (as determined by Minuit method) for core-distance range 20 to 40m.

$$N_{\mu} = 0.72 N_e^{0.59} \qquad (r^2 = 0.95)$$

Figure 10.6 b)

Number of muons N_{μ} through central plane as a function of shower-size (as determined by I.L. method) for core-distance range 20 to 40m.

$$N_{\mu} = 0.90 N_e^{0.62} \qquad (r^2 = 1.0)$$

FIG. 10·6 a)

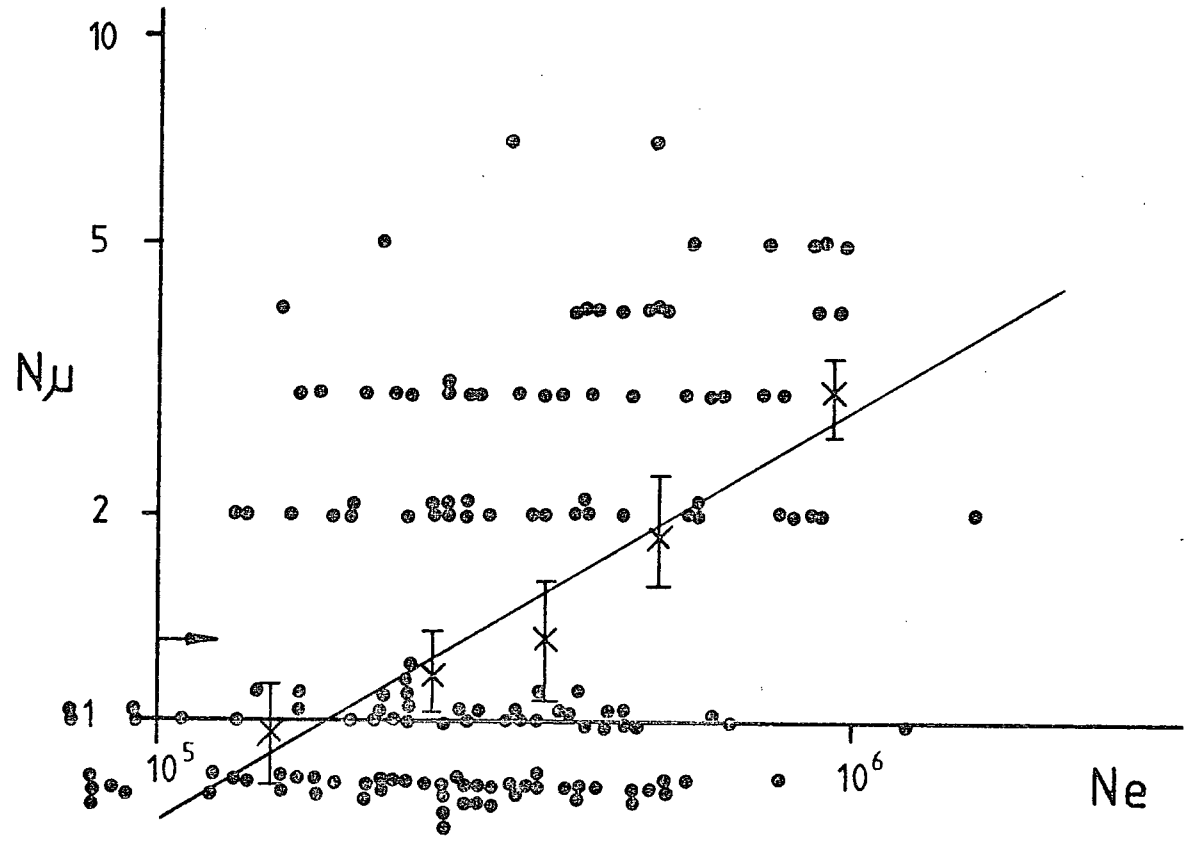

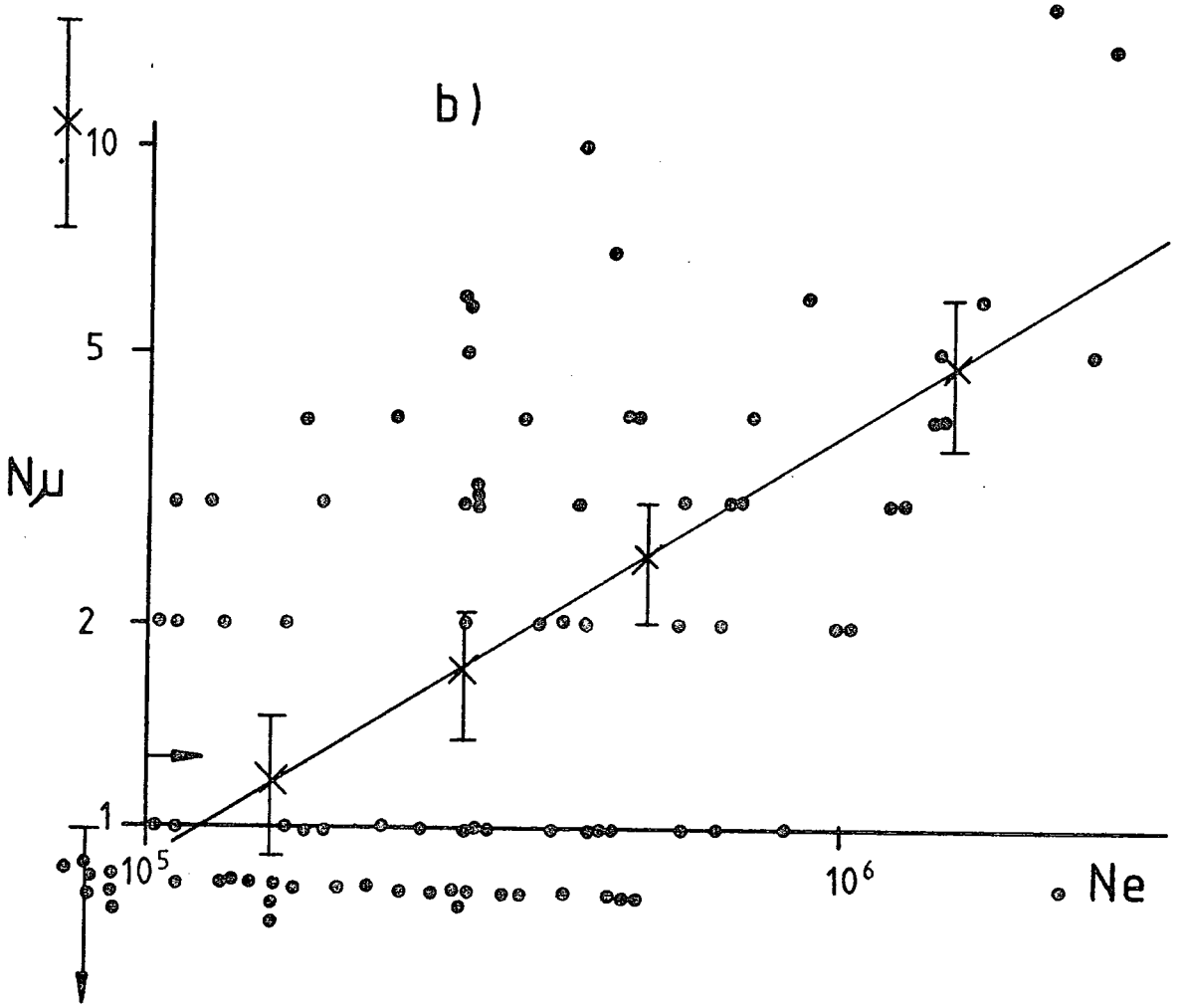

Figure 10.6 c)

Number of muons N_μ through upper plane as a function of shower-size (as determined by Minuit method) for core-distance range 20 to 40m.

$$N_\mu = 0.49 N_e^{0.69} \qquad (r^2 = 0.95)$$

Figure 10.6 d)

Number of muons N_μ through upper plane as a function of shower-size N_e (as determined by I.L. method) for core-distance range 20 to 40m.

$$N_\mu = 0.63 N_e^{0.71} \qquad (r^2 = 0.97)$$

FIG. 10·6 c)

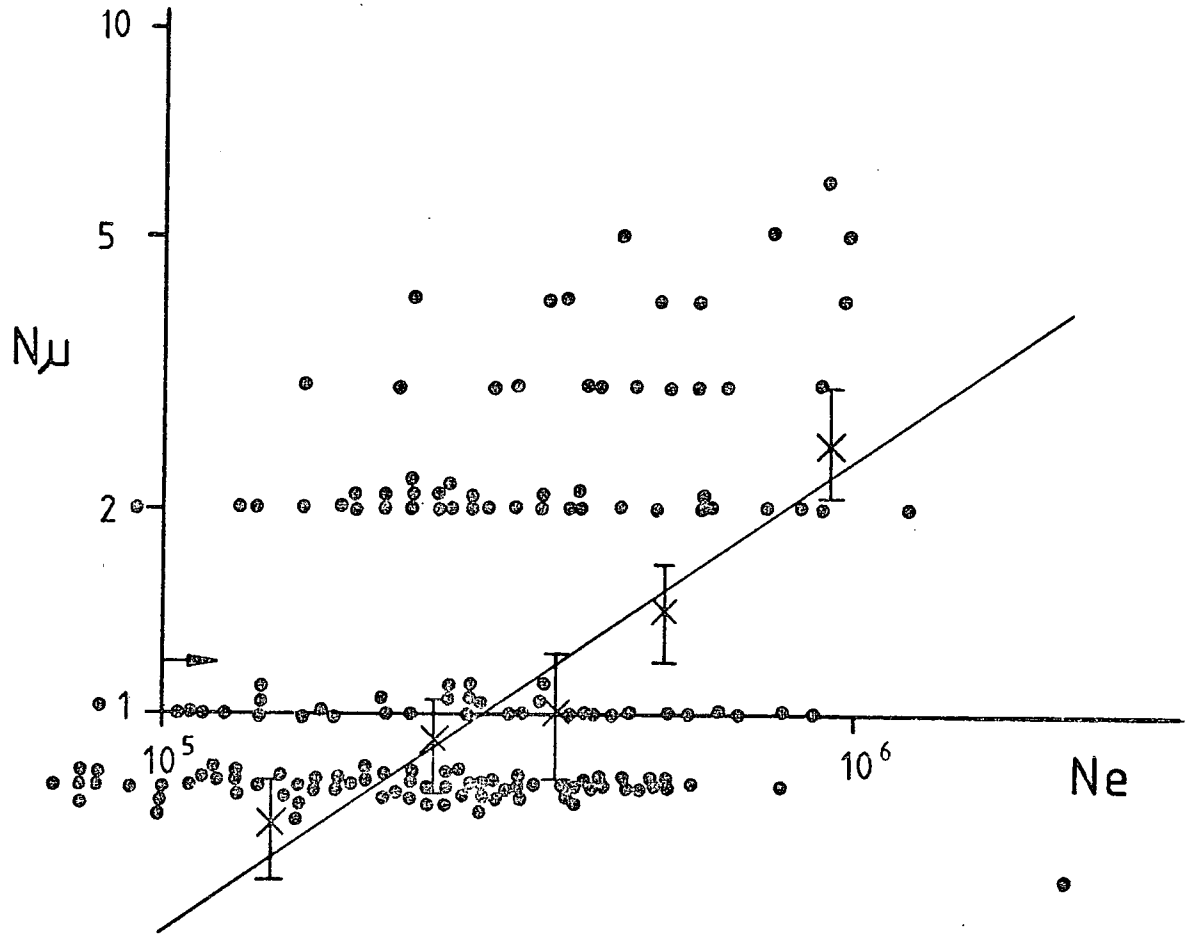

d)

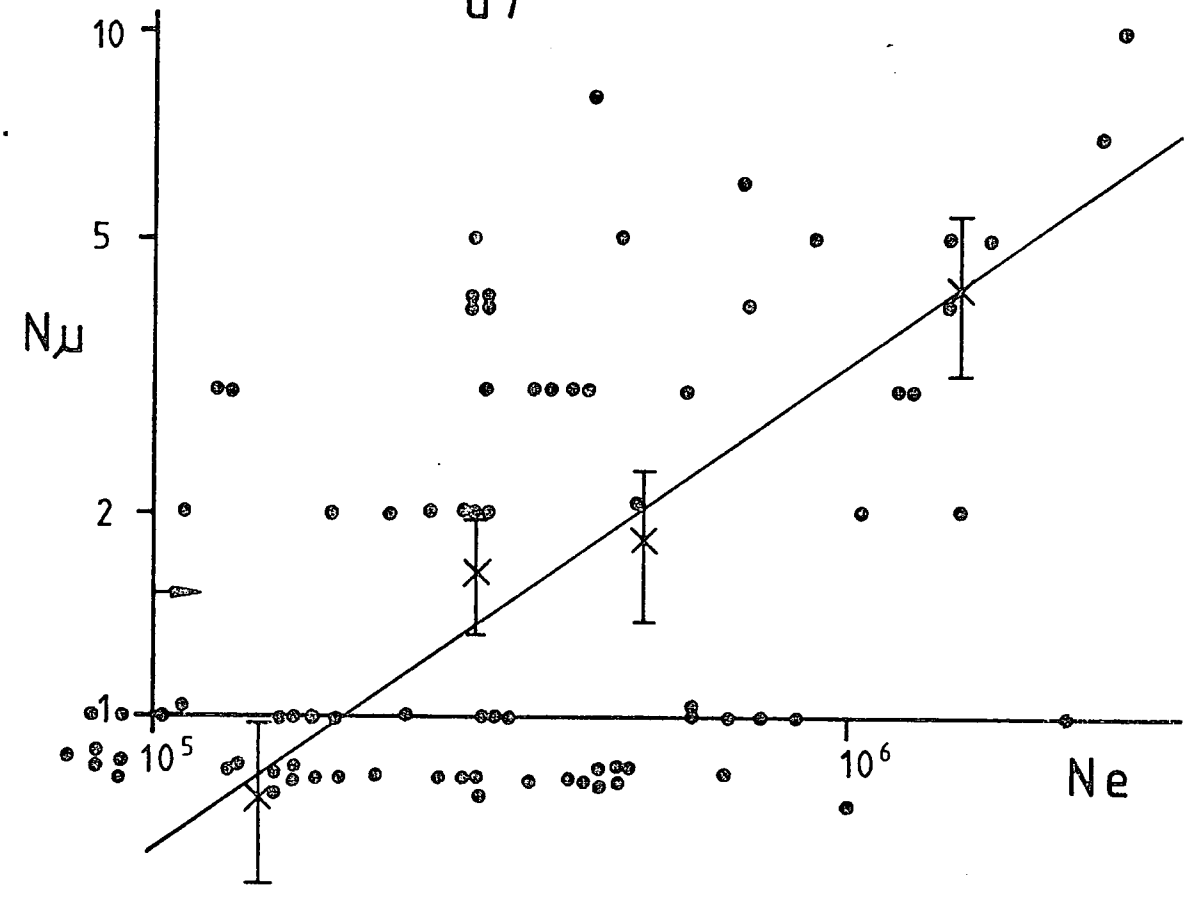

Figure 10.7a)
Number of muons N_μ through central plane as a function of shower-size N_e (as determined by Minuit method) for core-distance range 40 to 60m.

$$N_\mu = 0.81 N_e^{0.30} \qquad (r^2 = 0.51)$$

Figure 10.7 b)
Number of muons N_μ through central plane as a function of shower-size N_e (as determined by I.L. method) for core-distance range 40 to 60m.

$$N_\mu = .07 N_e^{0.33} \qquad (r^2 = 0.46)$$

FIG. 10·7 a)

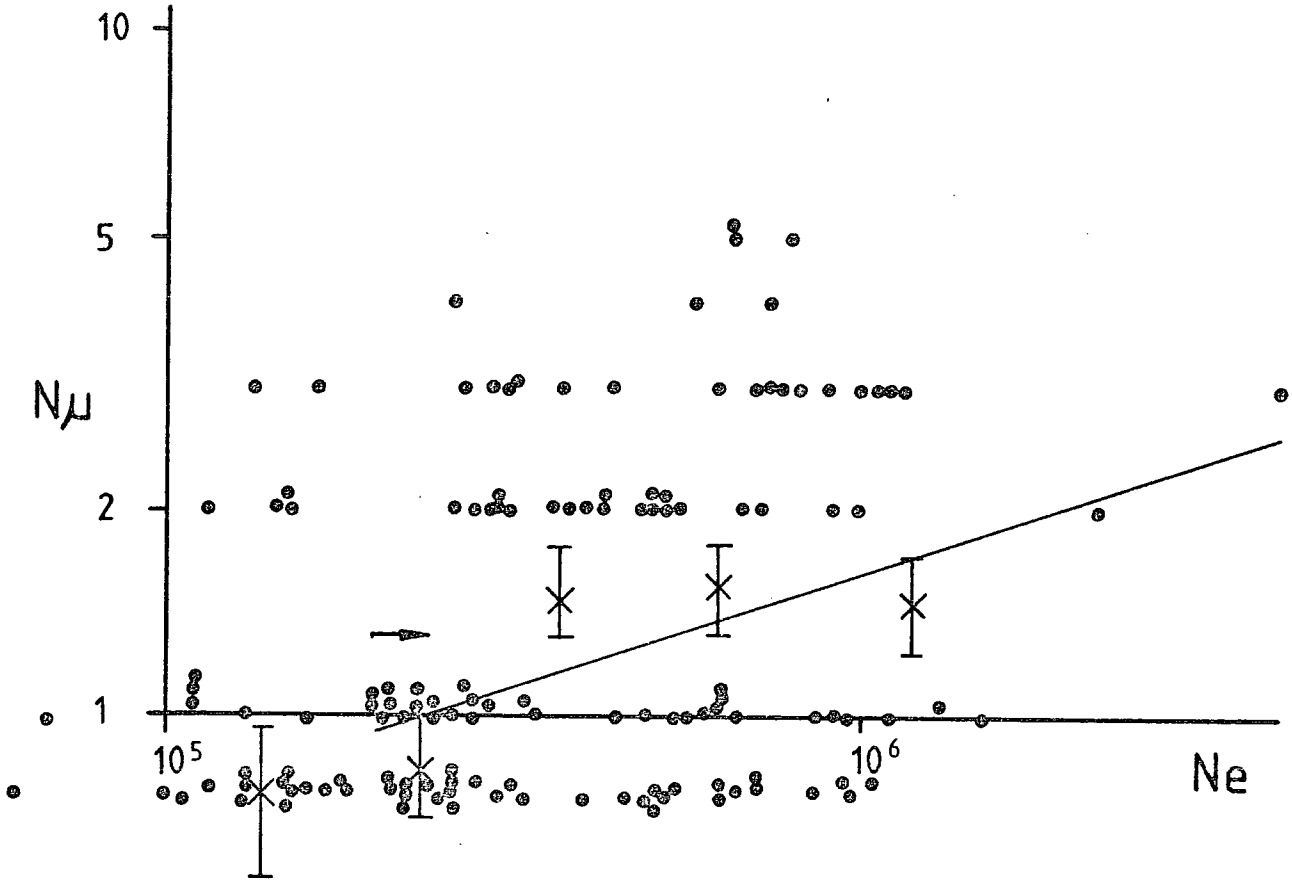

b)

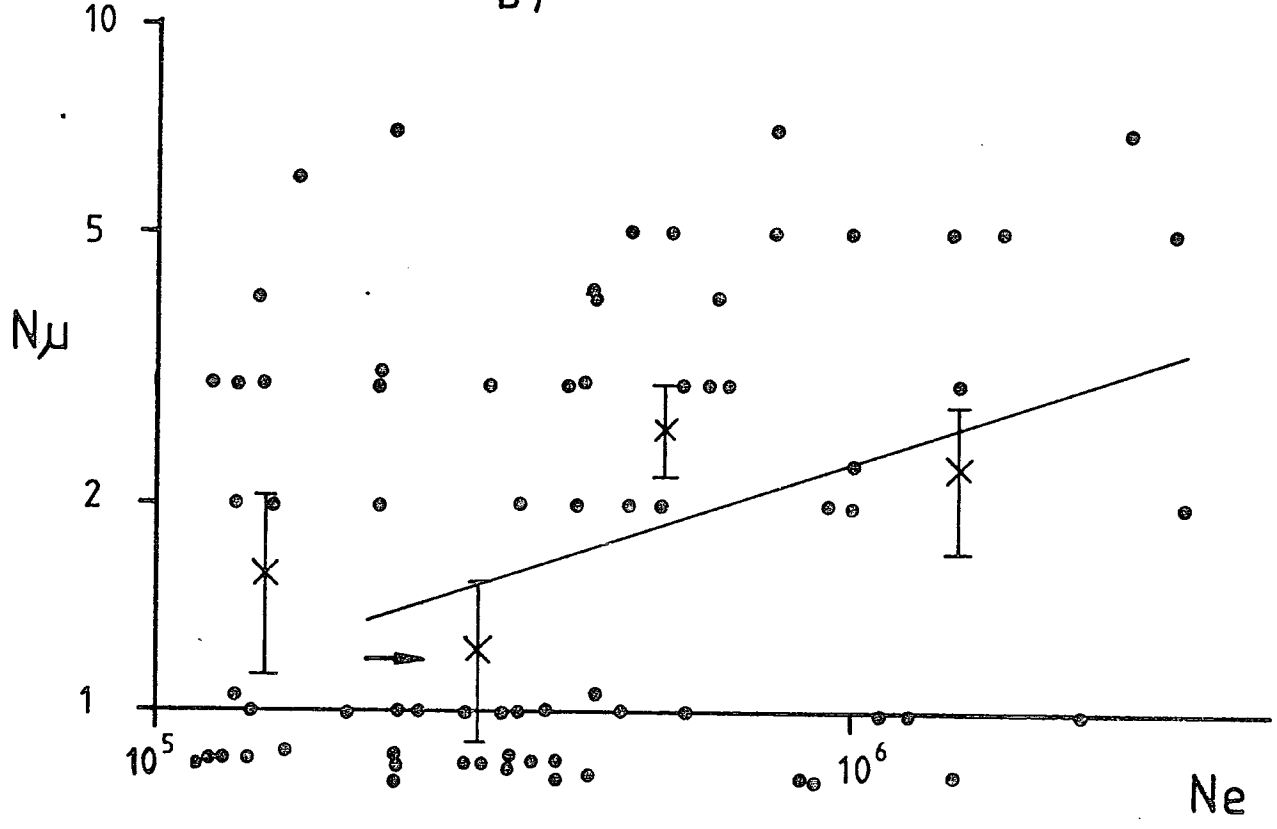

Figure 10.7 c)

Number of muons N_μ through upper plane as a function of shower-size N_e (as determined by Minuit method) for core-distance range 40 to 60m.

$$N_\mu = 0.515 N_e^{0.35} \qquad (r^2 = 0.41)$$

Figure 10.7 d)

Number of muons N_μ through upper plane as a function of shower-size N_e (as determined by I.L. method) for core-distance range 40 to 60m.

$$N_\mu = 1.15 N_e^{0.28} \qquad (r^2 = 0.43)$$

FIG. 10·7 c)

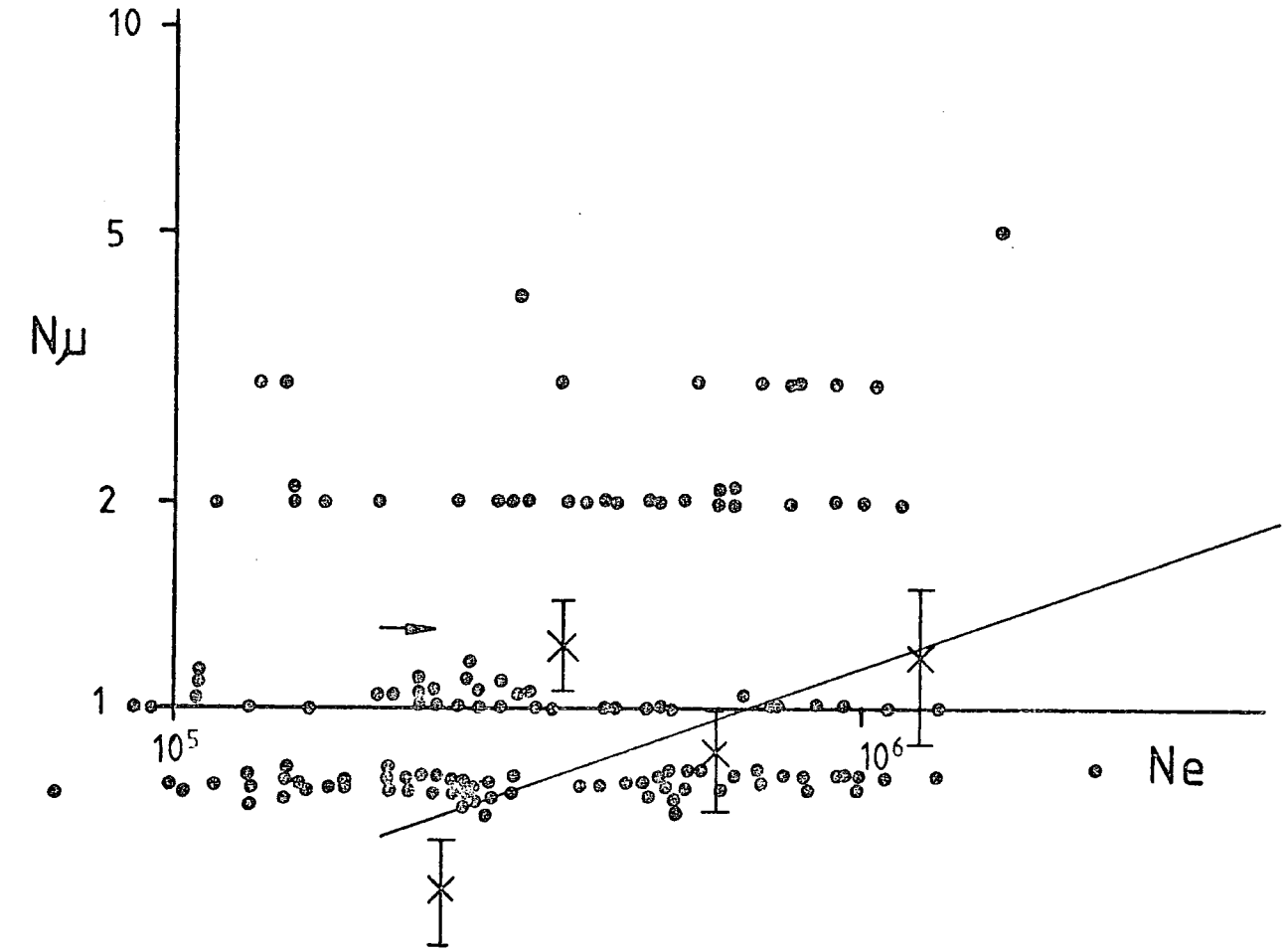

d)

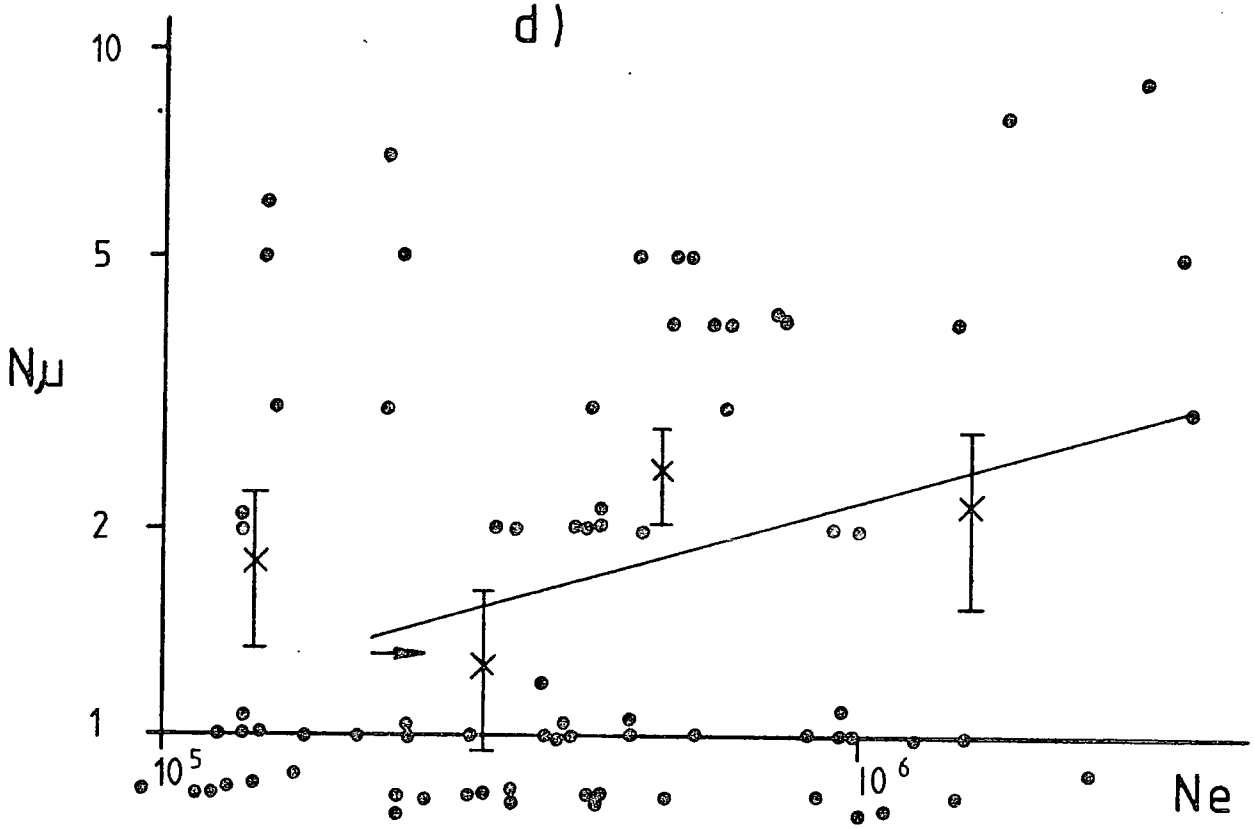

Figure 10.8 a)

Number of muons N_μ through central plane as a function of shower-size N_e (as determined by Minuit method) for core-distances greater than 60m.

$$N_\mu = 0.45 N_e^{0.49} \qquad (r^2 = 0.94)$$

Figure 10.8 b)

Number of muons N_μ through central plane as a function of shower-size N_e (as determined by I.L. method) for core-distances greater than 60m.

$$N_\mu = 2.32 N_e^{-0.01} \qquad (r^2 = 0.009)$$

FIG. 10·8 a)

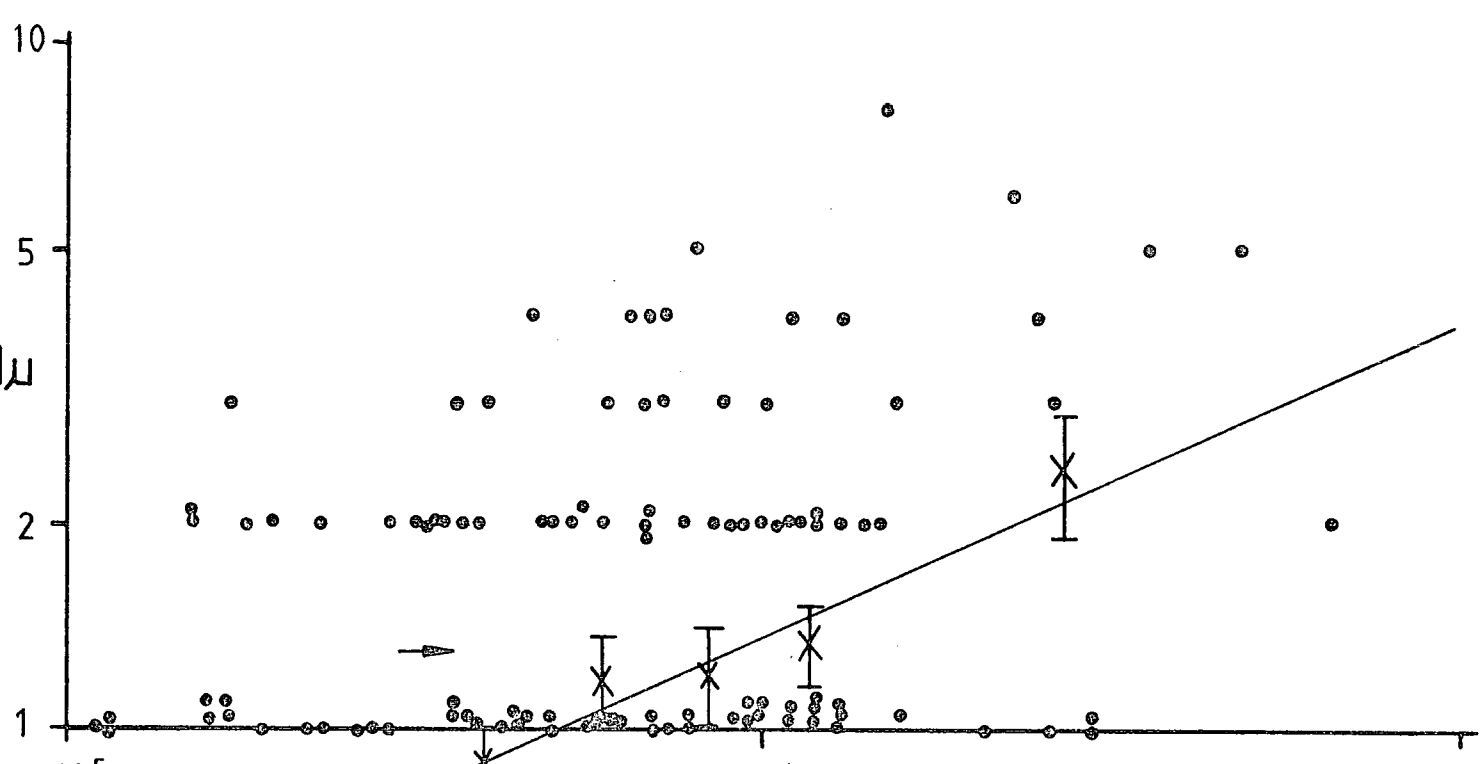

b)

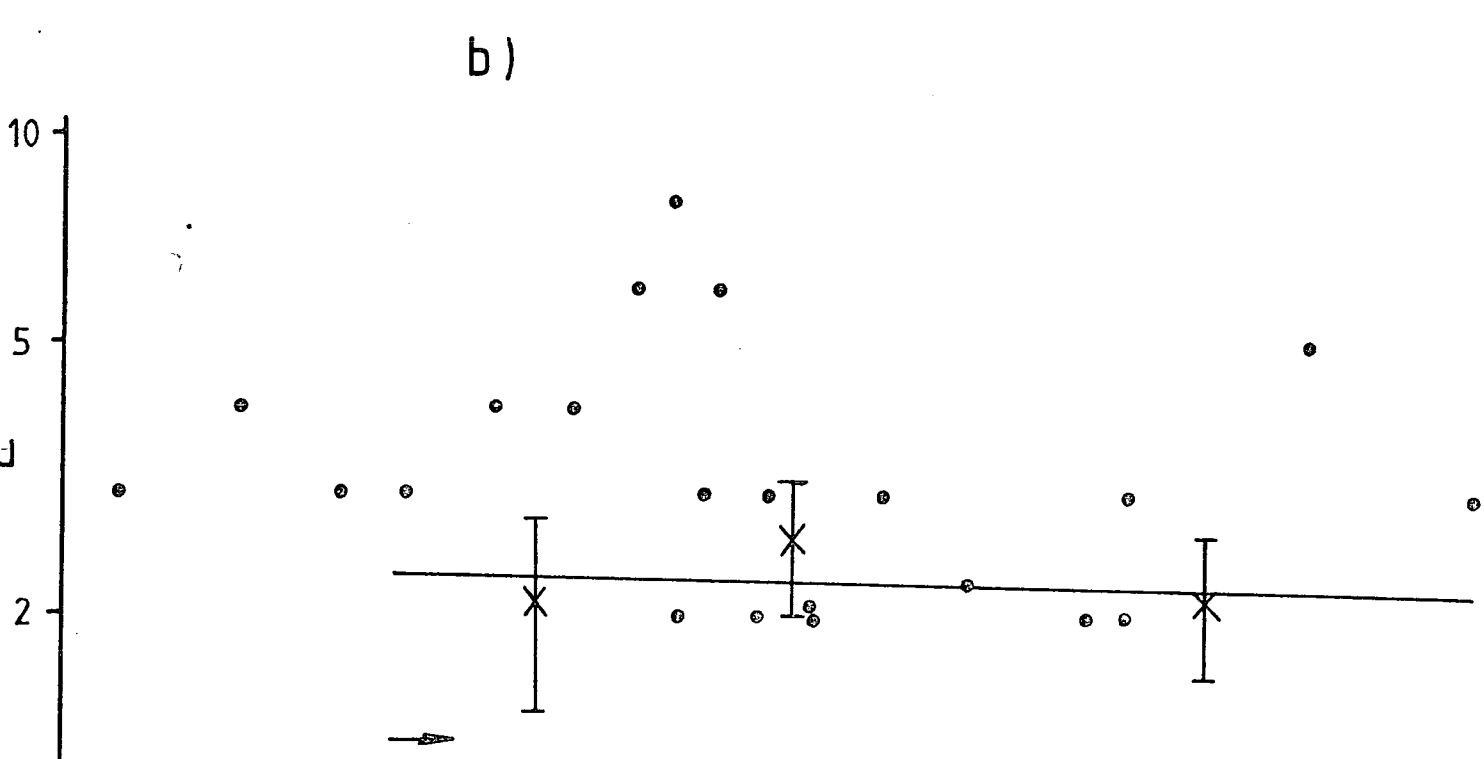

Figure 10.8 c)

Number of muons N_μ through upper plane as a function of shower-size N_e (as determined by Minuit method) for core-distances greater than 60m.

$$N_\mu = 0.33 N_e^{0.56} \qquad (r^2 = 0.84)$$

Figure 10.8 d)

Number of muons N_μ through upper plane as a function of shower-size N_e (as determined by I.L. method) for core-distances greater than 60m.

$$N_\mu = 0.99 N_e^{0.21} \qquad (r^2 = 0.89)$$

FIG. 10·8 c)

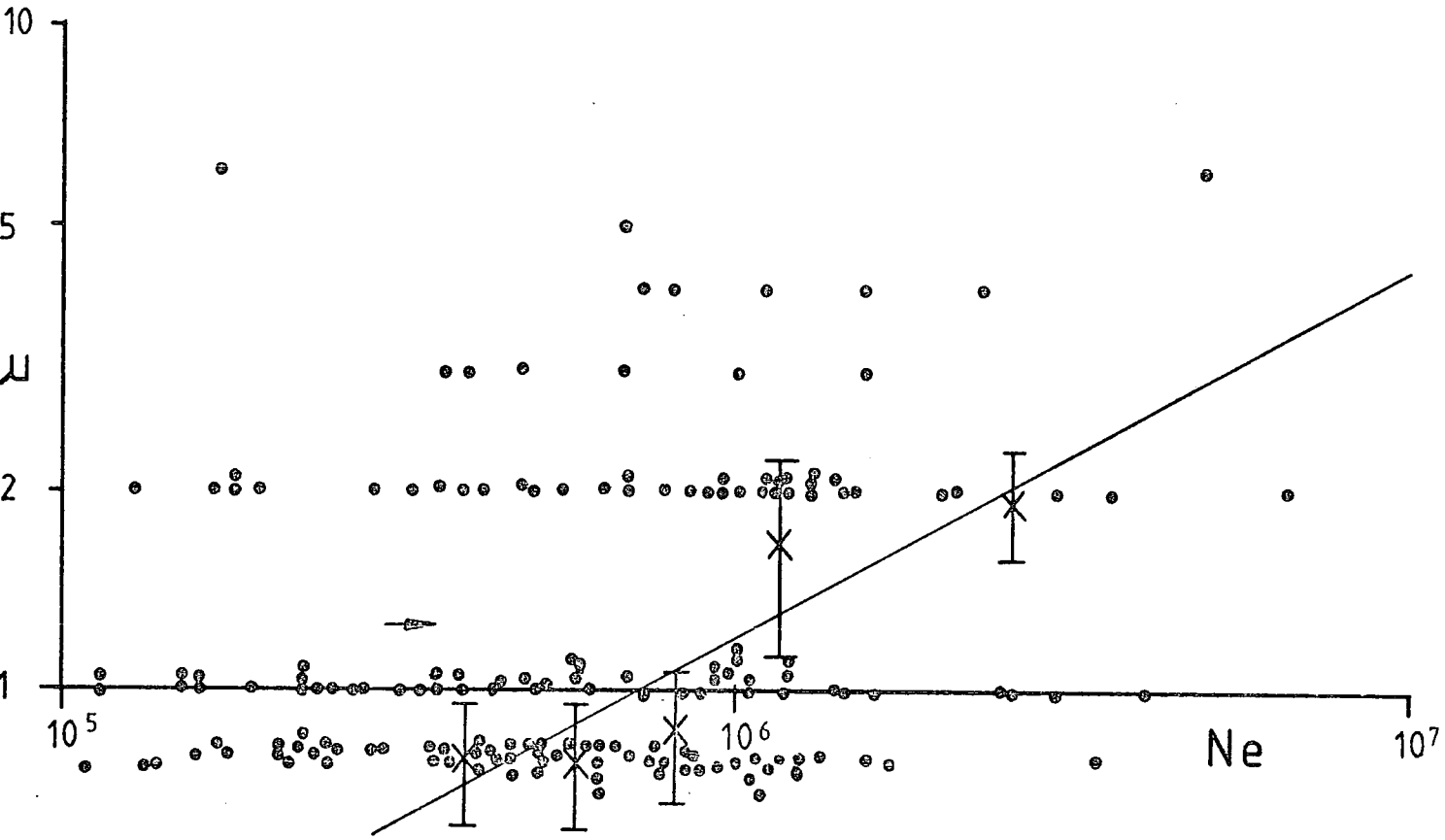

d)

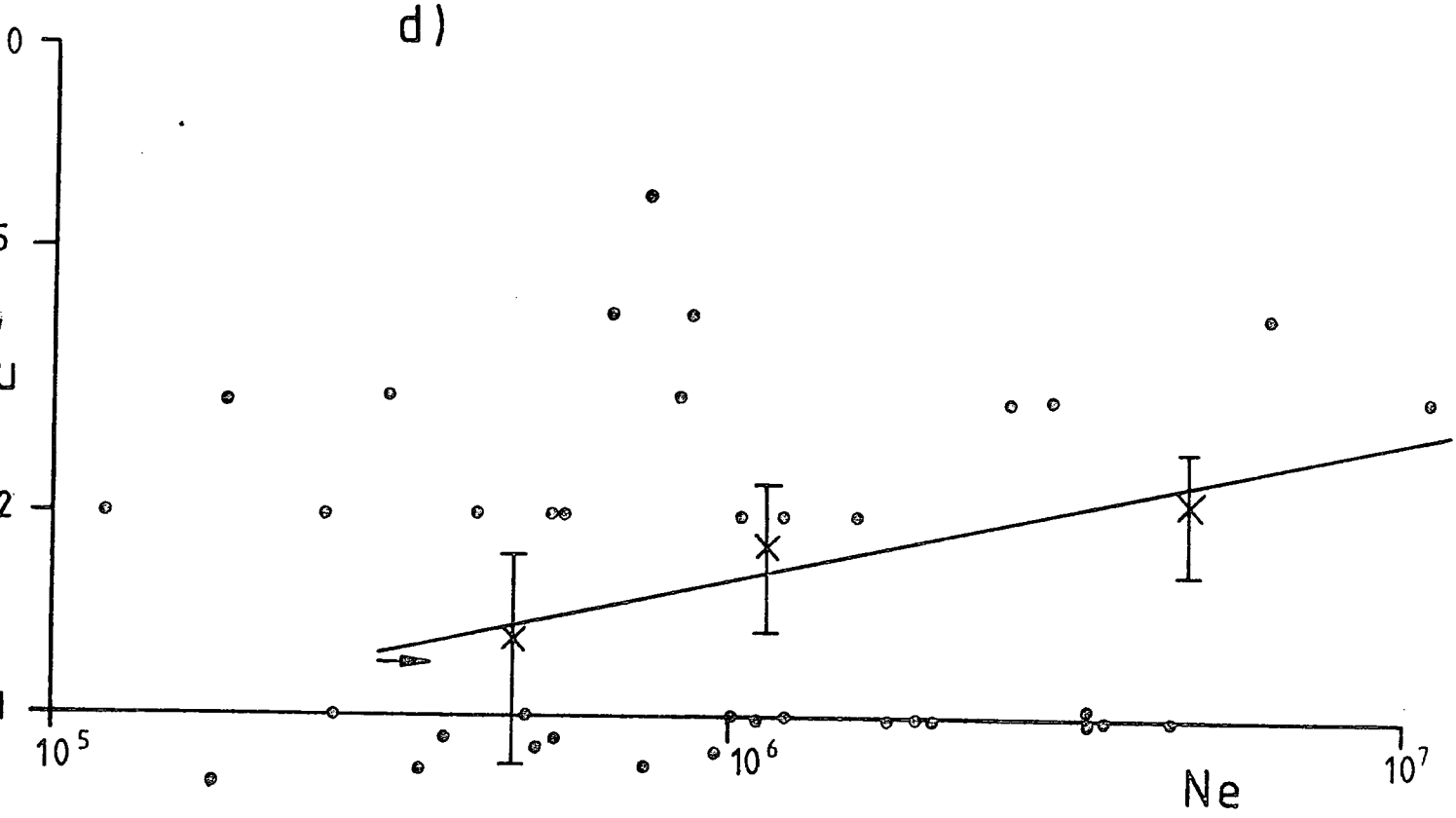

TABLE 10.3

WEIGHTED AVERAGE VALUES OF THE PARAMETERS a, b IN THE EQUATION

$$y = ax^b$$

where y = Number of muons N_μ

x = Shower size Ne in units of 10^5 particles

Core Distance range r_m	$\bar{a}$	$\bar{b}$	No. of measurements used
0 - 20	0.92	0.51	124
20 - 40	0.78	0.65	540
40 - 60	0.77	0.32	382
>60	0.48	0.45	400
0 - 40	0.80	0.62	664
>40	0.60	0.39	782
whole range	0.69	0.49	1,346

distance, these points were determined from Fig. 10.9 which represents the collecting area for different shower sizes on a triggering requirement of ≥ 2 pcles m^{-2} in detectors 13, 33, 53 and >4 pcles m^{-2} in detector C (the "standard" trigger - see Chapter 6, Section 6.3).

Table 10.3 represents mean values of the parameters a and b corresponding to each of the figures 10.5, 10.6, 10.7, 10.8. Also quoted are average values of these parameters over the ranges $r \lesssim 40$ m and over the whole range of r. The mean values were calculated by first taking a weighted mean of the I.L. and Minuit data (e.g. Figs. 10.5a) and 10.5c)), this gives a larger sample from the parent population, then taking an average of the resulting upper plane and central plane measurements, this gives the mean of two samples of the same sample from the parent population of air-showers.

10.5.3 Testing for significance of difference between the 4 samples

Figs. 10.10 and 10.11 show respectively the distribution in core distances and shower sizes used in the measurement of the lateral distribution of muons. The core distances have been binned in 20 m bins since the accuracy of the I.L. method of core location is approximately ± 9 metres (see Chapter 7).

The median shower size, from Fig. 10.11, is 3.10^5 particles. To test whether there is any significant difference between either the measurements from the central and the upper plane, or the measurements using the Minuit and the I.L. methods of core location, all the data is first normalised to this median shower size. This has been done using the results quoted in

Figure 10.9

The collecting area for different shower-sizes based on coincidence between C (>4 pcls./m^2),13 (>2 pcls./m^2),33 (>2 pcls./m^2),53 (>2 pcls./m^2). The numbers on each curve represent the shower-size in units of 10^5 particles.

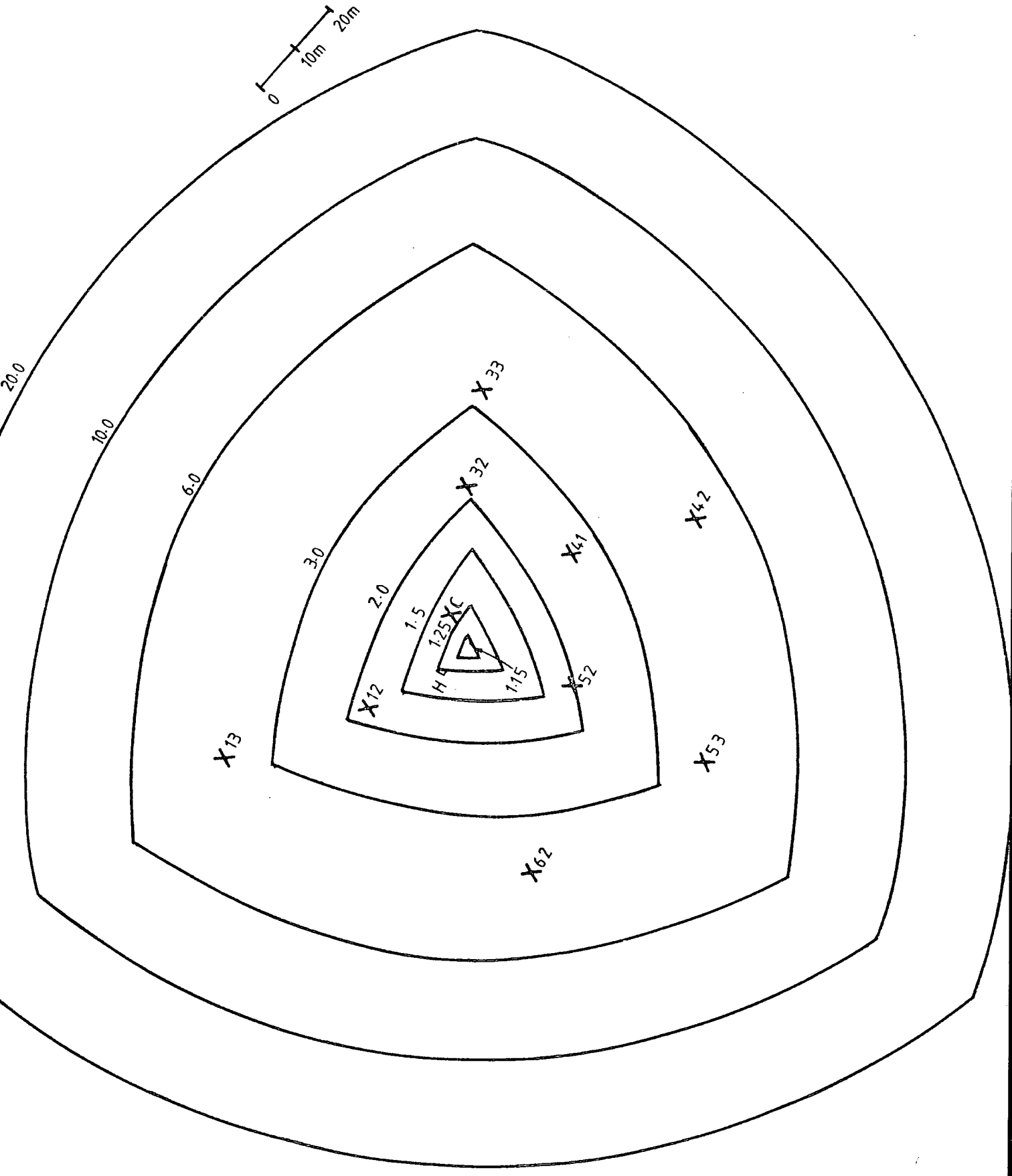
0
10m
20m
20.0
10.0
6.0
3.0
2.0
1.5
1.25
XC
1.15
H
X33
X32
X41
X42
X52
X12
X13
X53
X62

FIG. 10.9

FIG. 10·10

Distribution in core distance for all showers $\geq 10^5$ particles detected.

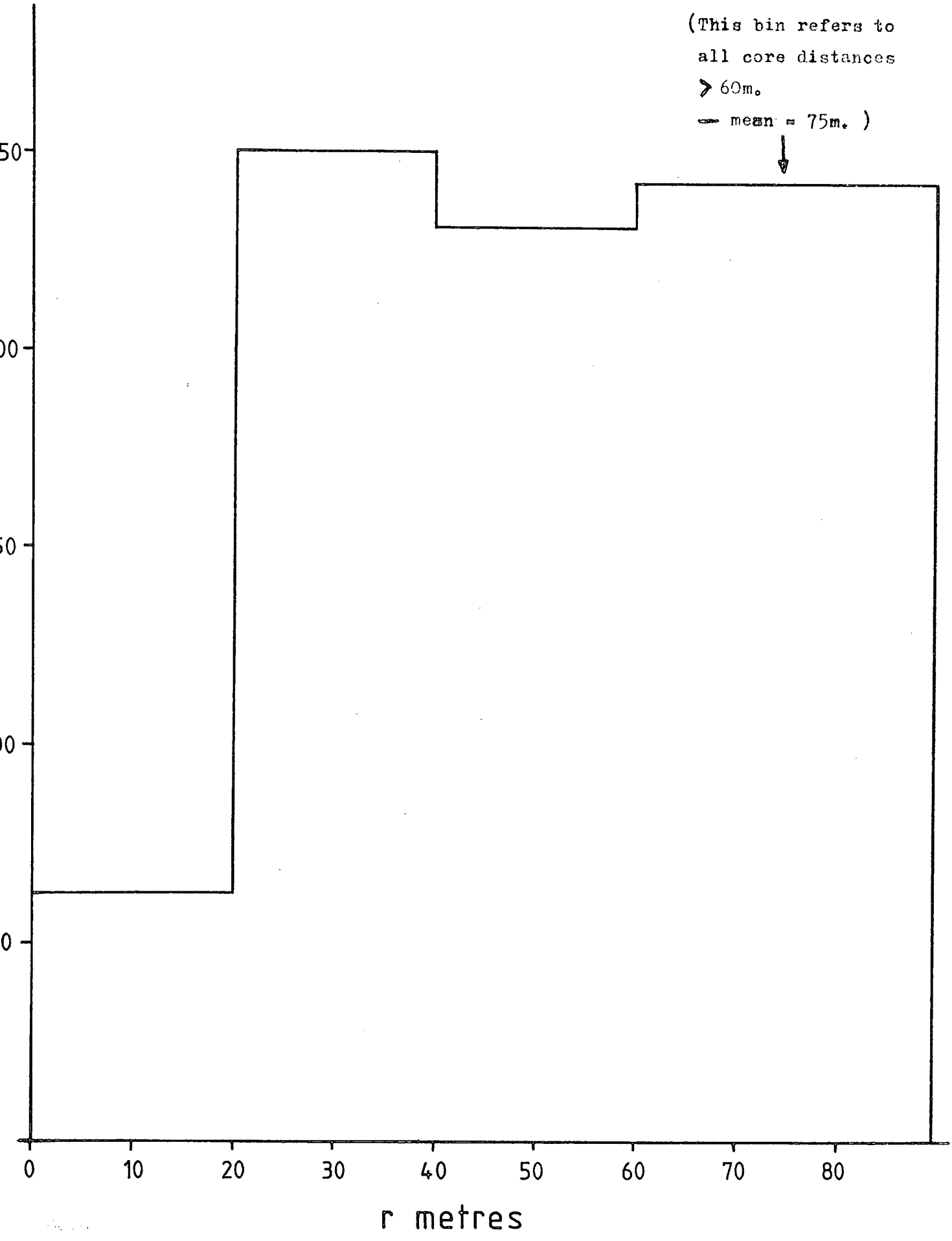

Figure 10.11
The observed distribution in shower-sizes used in the measurement of the lateral distribution of muons. It also summarises the number of showers of size N_e in which no burst was observed in the flash-tube chamber on films T16 to T25.

FIG. 10.11

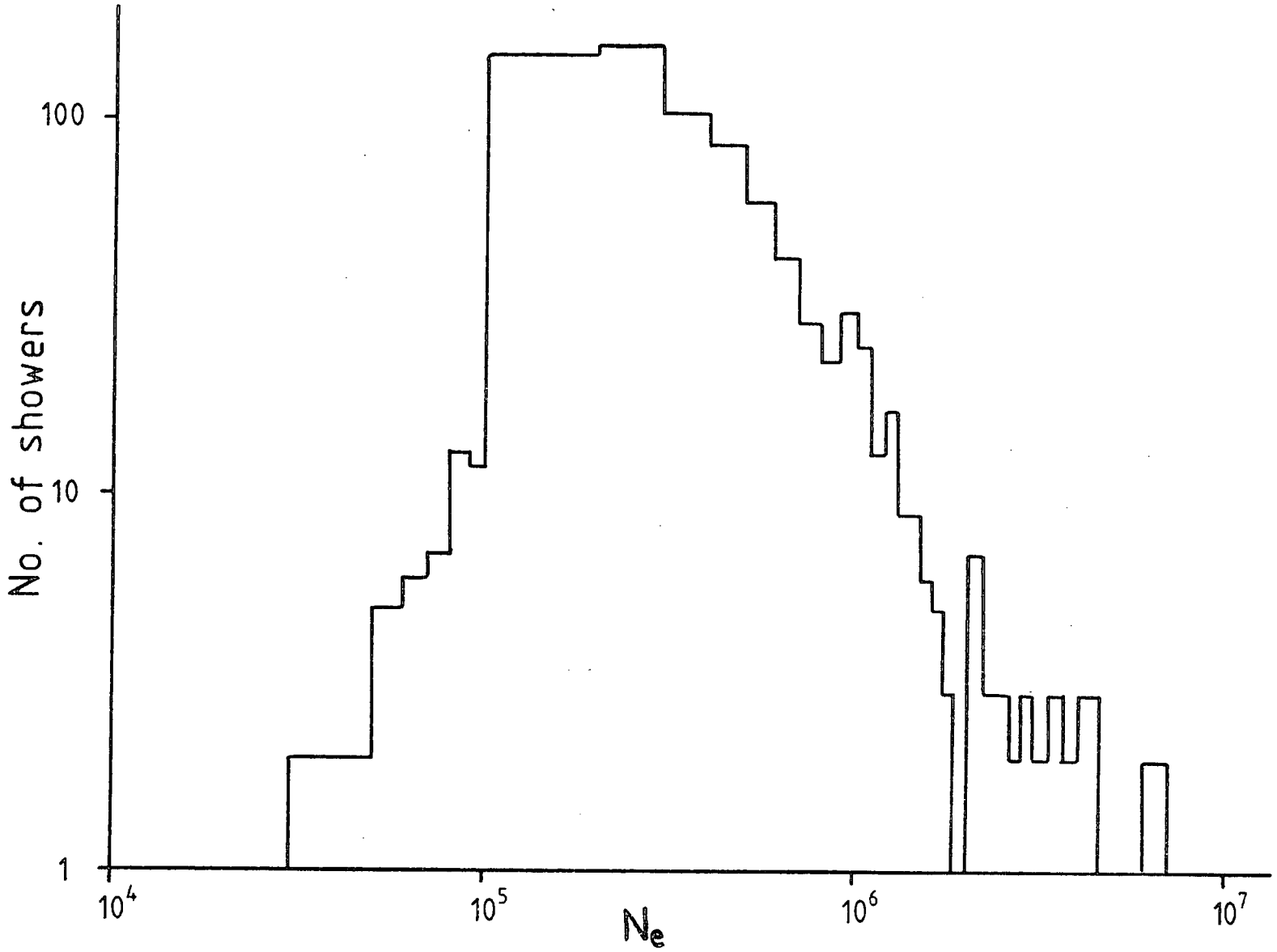

Figs. 10.5, 10.6, 10.7 and 10.8 (not the average values of Table 10.3). The resulting histograms representing the frequency of observing n muons passing through the chamber at different distances from the axis of the shower are presented in Figs. 10.12, 10.13, 10.14 and 10.15. The suffixes a), b), c), d) represent the same subdivision of data as in Table 10.2, e.g. Fig. 10.12c) represents the results for r = 0 - 20 m, of measurements taken at the upper plane using the Minuit method of determining core distance and shower size.

To determine any significant difference between the upper and central plane a student t-test has been conducted on the pairs of data a) and c), the results and their significance are tabulated in Table 10.4.

To determine any systematic difference between the results using the I.L. and the Minuit methods of core location student t-tests have been conducted on the central plane data a) and b) and the upper plane data c) and d), the results and their significance are tabulated in Table 10.5.

The only significant differences (Table 10.5 central plane data $r > 60$ m) can be attributed to a paucity of data using the I.L. method (see also the poor linear fit of Fig. 10.8b)).

10.5.4 The lateral distributions of muons

Since no significant differences between the upper and central plane data were detected, no significant contamination from low energy muons passing through the sides of the chamber is present in the measurements made at the

TABLE 10.4

RESULTS OF STUDENT t-TESTS BETWEEN MEASUREMENTS MADE IN THE CENTRAL PLANE AND IN THE UPPER PLANE

MINUIT MEASUREMENTS		
rm	t	Significance
0 - 20	-1.02	17.5%
20 - 40	3.07	0.5%
40 - 60	2.91	1%
>60	2.15	4%

The numbers in the "Significance" column indicate the probability that the two samples have the same mean.

FIG. 10·12

Frequency of observing N_μ muons at core-distance range 0 to 20m. after normalisation to $N_e = 3.10^5$ particles , for all showers of size greater than 10^5 particles.

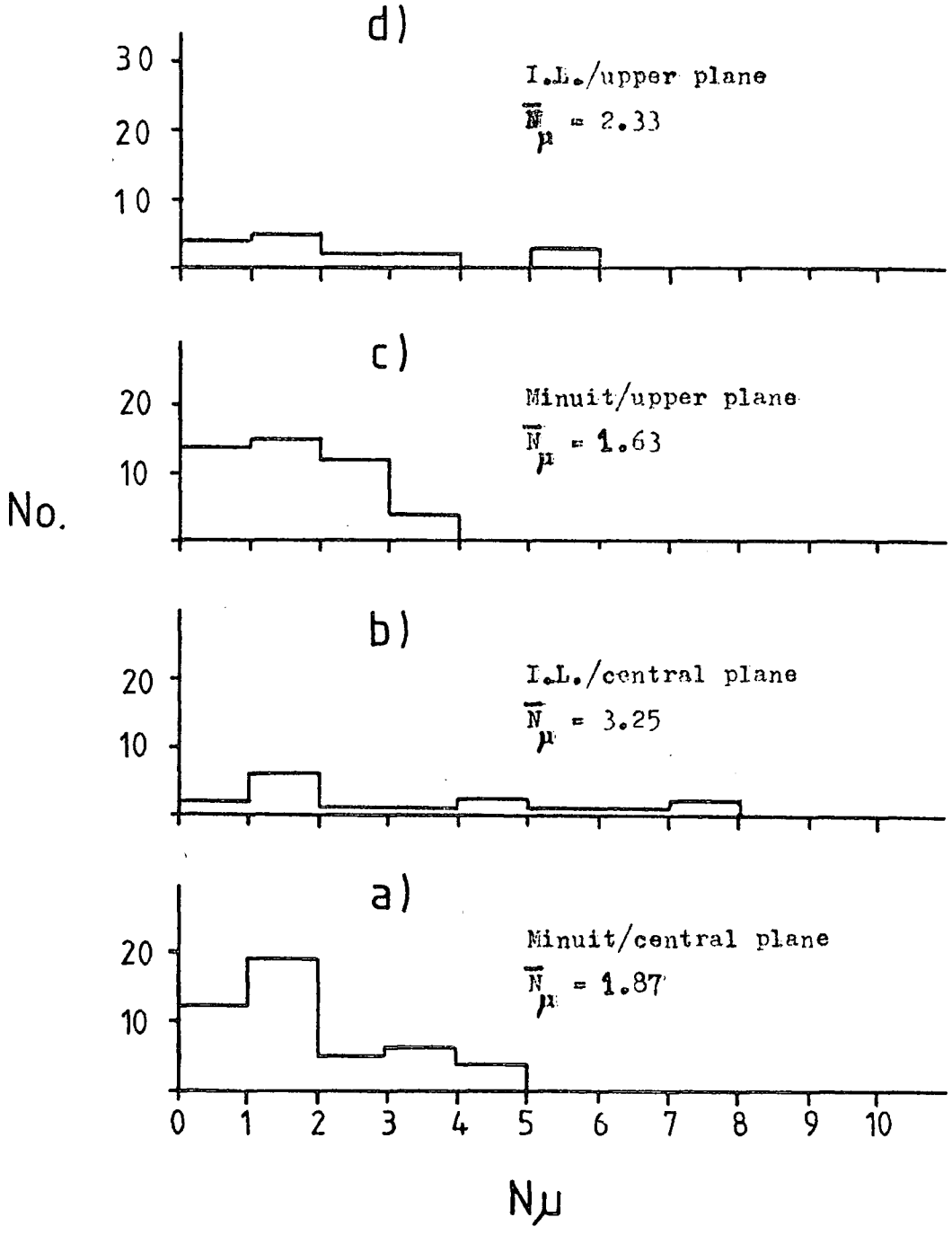

Figure 10.13

Frequency of observing N_μ muons at core-distance range 20 to 40m. after normalisation to $N_e = 3.10^5$ particles , for all showers of size greater than 10^5 particles.

Figure 10.14

Frequency of observing N_μ muons at core-distance range 40 to 60m. after normalisation to $N_e = 3.10^5$ particles , for all showers of size greater than 2.10^5 particles.

FIG. 10·13

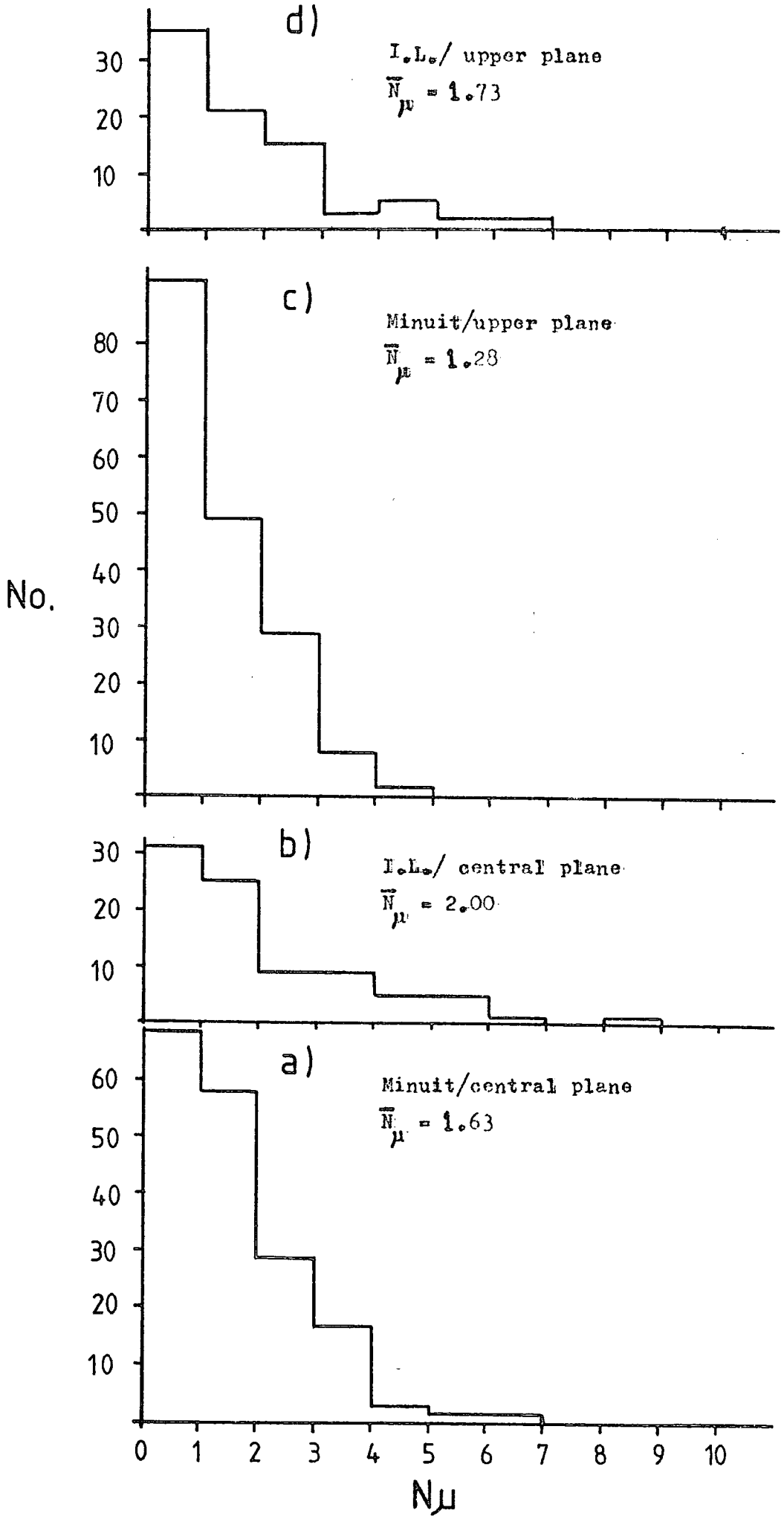
d)
I.L./ upper plane
$\bar{N}_\mu$ = 1.73
c)
Minuit/upper plane
$\bar{N}_\mu$ = 1.28
b)
I.L./ central plane
$\bar{N}_\mu$ = 2.00
a)
Minuit/central plane
$\bar{N}_\mu$ = 1.63
No.
Nμ
0 1 2 3 4 5 6 7 8 9 10
10 20 30 40 50 60 70 80

FIG. 10·14

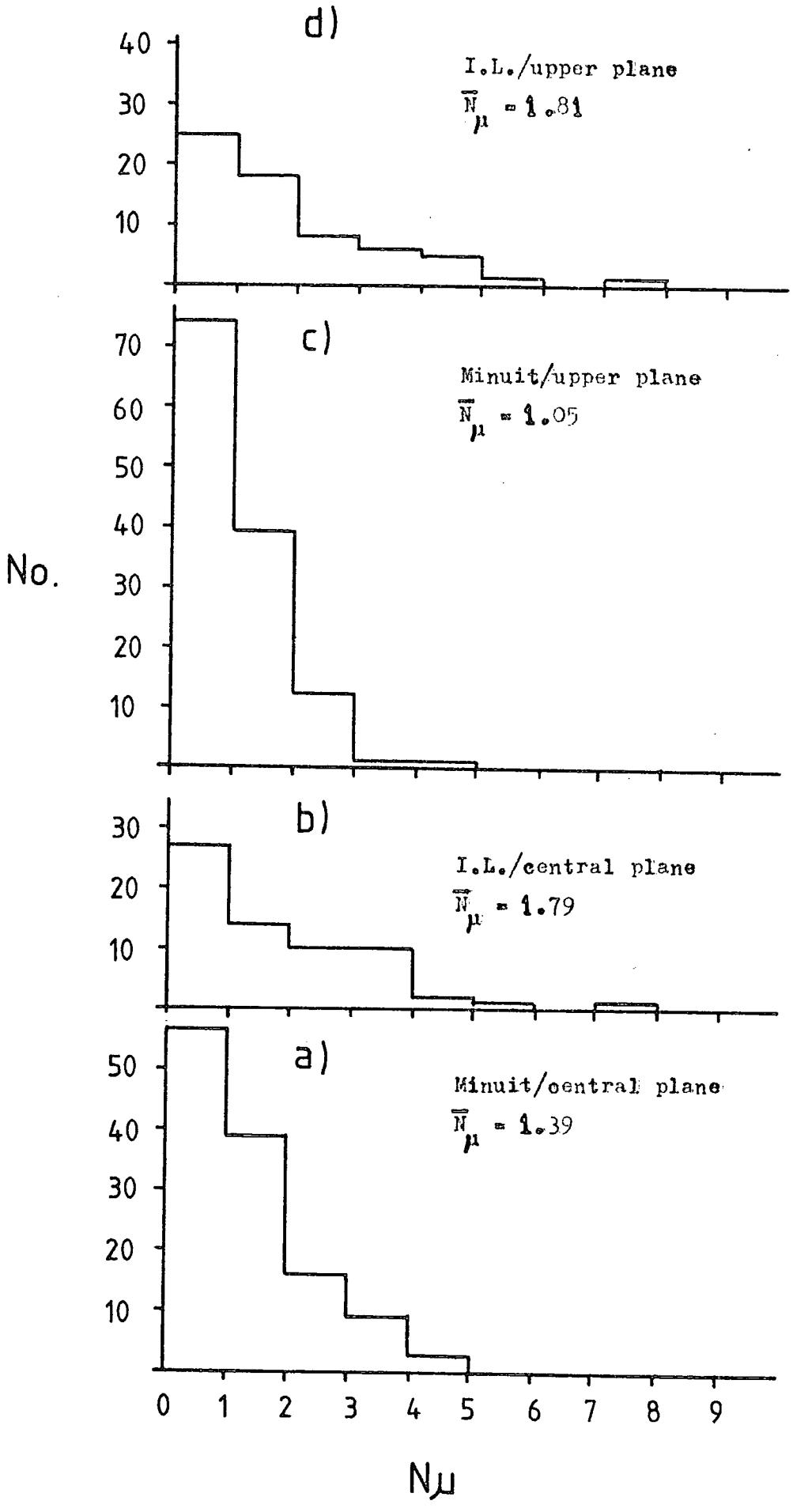
d)
I.L./upper plane
$\overline{N}_\mu$ = 1.81
c)
Minuit/upper plane
$\overline{N}_\mu$ = 1.05
b)
I.L./central plane
$\overline{N}_\mu$ = 1.79
a)
Minuit/central plane
$\overline{N}_\mu$ = 1.39
No.
Nμ
0 1 2 3 4 5 6 7 8 9
10 20 30 40 50
10 20 30 40 50 60 70
10 20 30
10 20 30 40

FIG. 10·15

Frequency of observing N_μ muons at core-distances greater than 60m. after normalisation to $N_e = 3.10^5$ particles , for all showers of size greater than 3.10^5 particles.

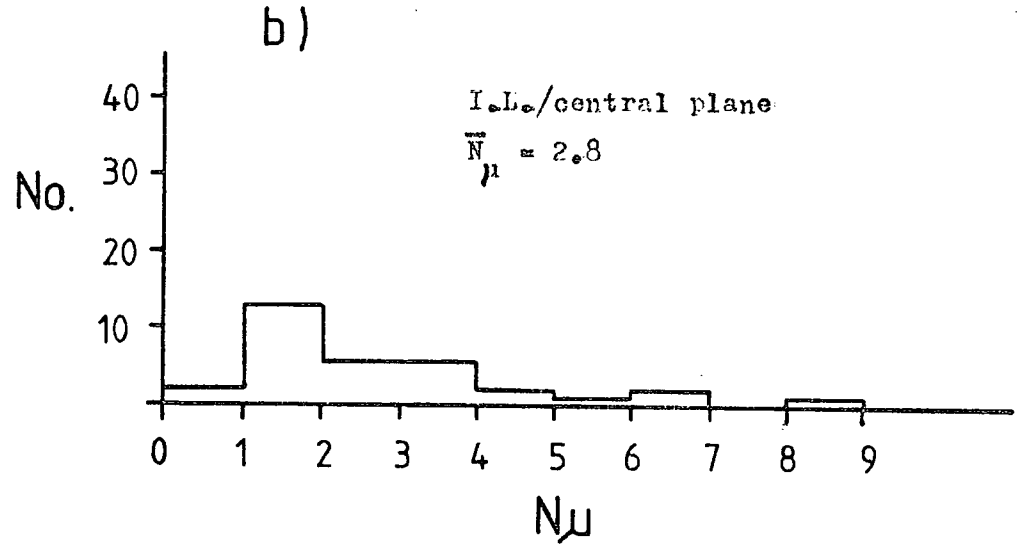

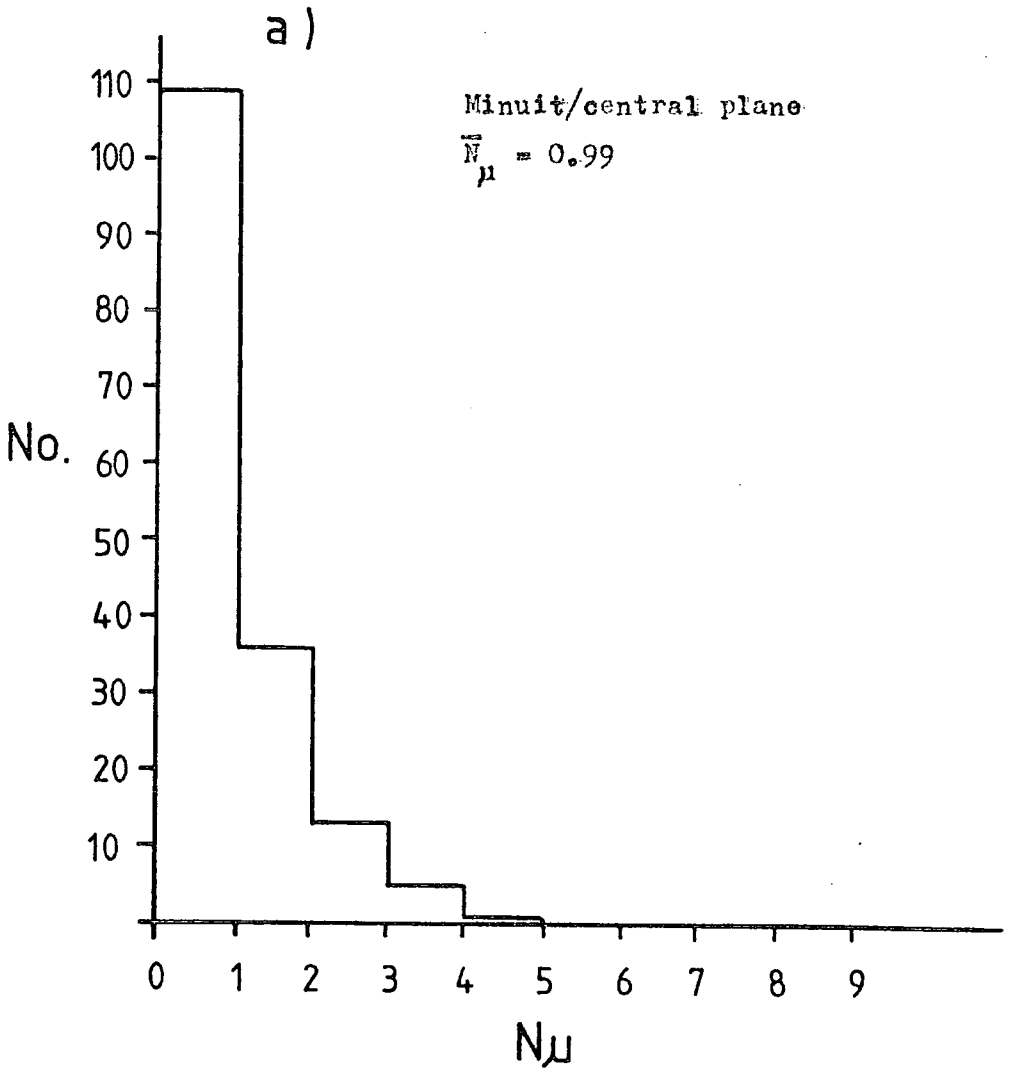

FIG. 10.15 (contd.)

Frequency of observing N_μ muons at core-distances greater than 60m. after normalisation to $N_e = 3.10^5$ particles, for all showers of size greater than 3.10^5 particles.

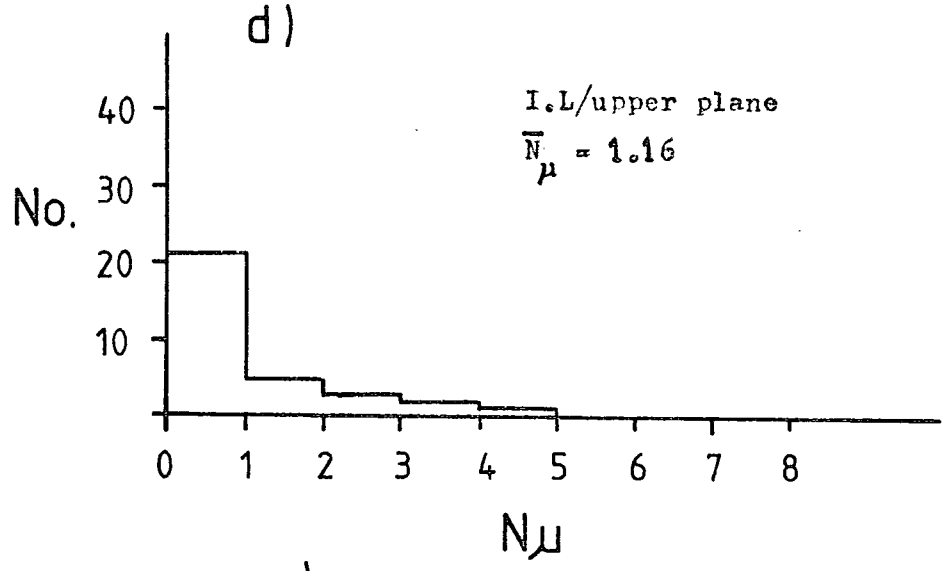

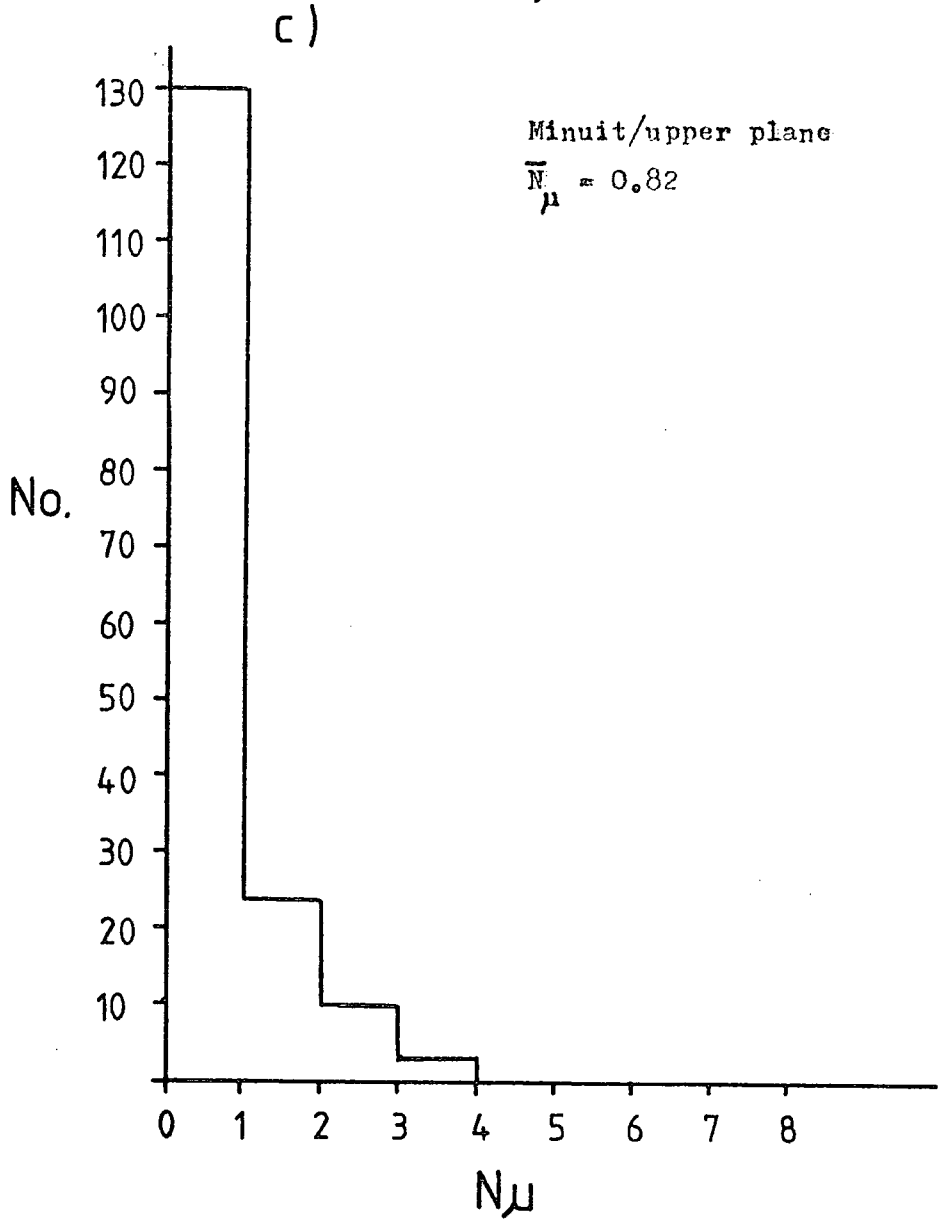

central plane. These data have thus been used in the lateral distribution of muons.

Since no systematic differences between the data using the Minuit method of core location and the I.L. method, these have been pooled to improve the statistics.

Histograms of the pooled data for the different core distance 0 - 20 m, 20 - 40 m, 40 - 60 m and >60 m are presented in two forms, Figs. 10.16 and 10.17. Fig. 10.16 represents the data normalised to a shower size of 3.10^5 particles using the relation $N_\mu \propto (N_e)^{0.75}$; whereas Fig. 10.17 represents the data normalised to a shower size of 3.10^5 particles using the relation $N_\mu \propto (N_e)^b$ where the values of b are given by Table 10.3, column 3, rows 1 - 4.

Fig. 10.18 shows the measured lateral distribution of muons corrected for averaging over bin size and error in core location (σ = 9.2 m). The data are compared with two curves produced by Greisen. Curve 1 is based on analogy to the electron lateral distribution and has the form of equation 10.1. Curve 2 is based on a summary of other data (Greisen [1966]) and has the form:

(10.2)

$$\Delta_\mu (N, r) = 18\left(\frac{N}{10^6}\right)^{0.75} r^{-0.75} \left(1 + \frac{r}{320}\right)^{-2.5}$$

Both the results normalised according to $N_\mu \propto (N_e)^{0.75}$ and $N_\mu \propto (N_e)^b$ (where $b = f(r)$ and is given by Table 10.3) give higher muon densities than predicted by Greisen.

The data normalised according to $N_\mu \propto N_e{}^b$ show better agreement, with the results diverging to roughly a 50% excess for $r \geq 30$ m.

TABLE 10.5

RESULTS OF STUDENT t-TESTS BETWEEN MEASUREMENTS MADE USING THE INTERSECTING LOCI METHOD AND THE "MINUIT" METHOD OF DETERMINING AIR-SHOWER PARAMETERS

CENTRAL PLANE MEASUREMENTS		
rm	t	Significance
0 - 20	-2.06	4%
20 - 40	-2.01	4%
40 - 60	-2.18	4%
>60	-8.97	<0.0001%
UPPER PLANE MEASUREMENTS		
rm	t	Significance
0 - 20	-2.92	1%
20 - 40	-2.95	0.8%
40 - 60	-4.5	0.1%
>60	-2.34	3%

The numbers in the "Significance" column indicate the probability that the two samples have the same mean.

Figures 10.16

Frequency of observing N_μ muons at different core-distance ranges after combining I.L. and Minuit data and normalising to $N_e = 3.10^5$ particles according to $N_\mu \propto (N_e)^{0.75}$.

(i) Core-distance range 0 to 20m.

$$\overline{N}_\mu = 2.42 \pm 0.24$$

(ii) Core-distance range 20 to 40m.

$$\overline{N}_\mu = 1.69 \pm 0.09$$

(iii) Core-distance range 40 to 60m.

$$\overline{N}_\mu = 1.29 \pm 0.09$$

(iv) Core-distances greater than 60m.

$$\overline{N}_\mu = 0.81 \pm 0.08$$

FIG. 10.16 (i)

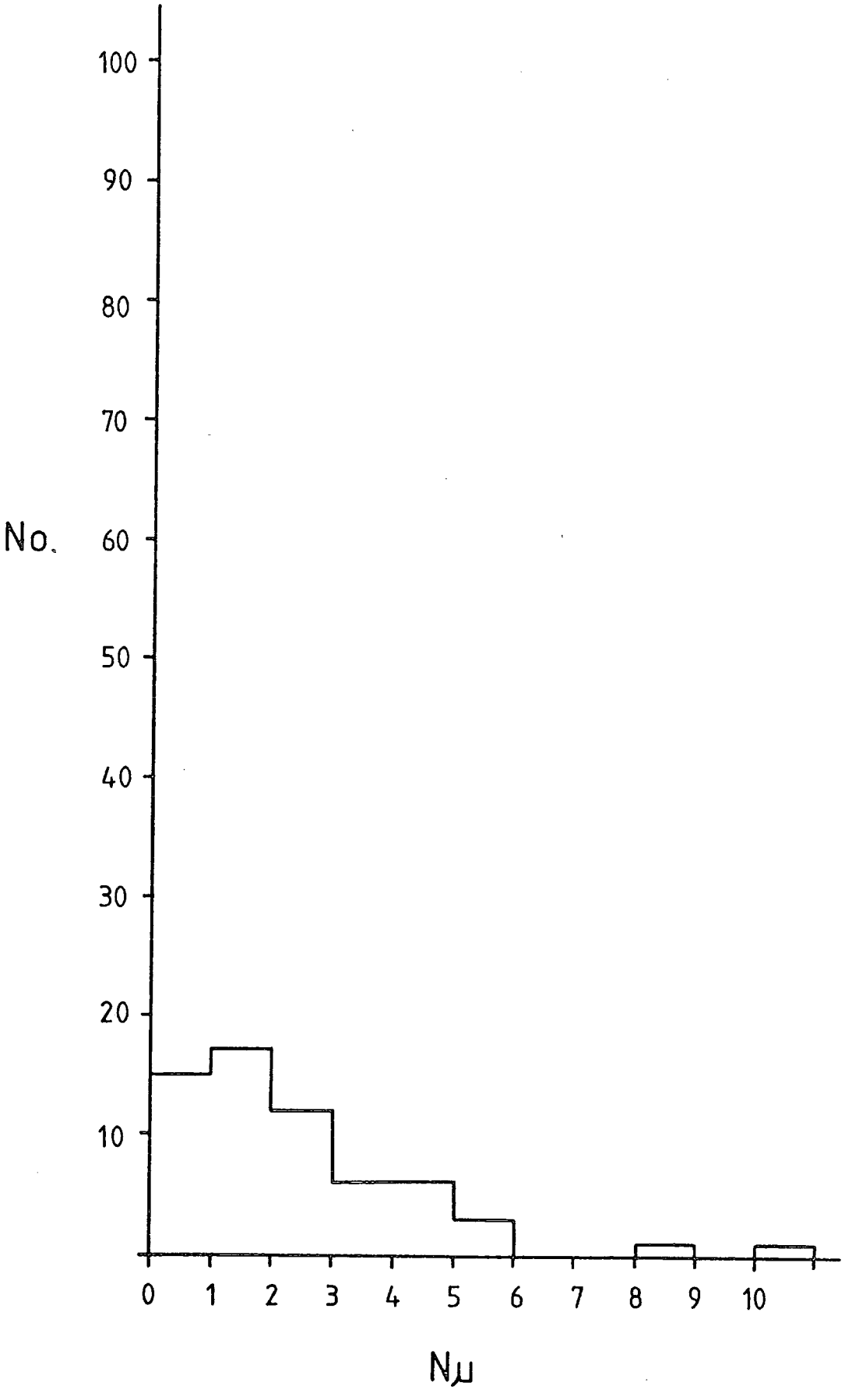

FIG. 10·16 (ii)

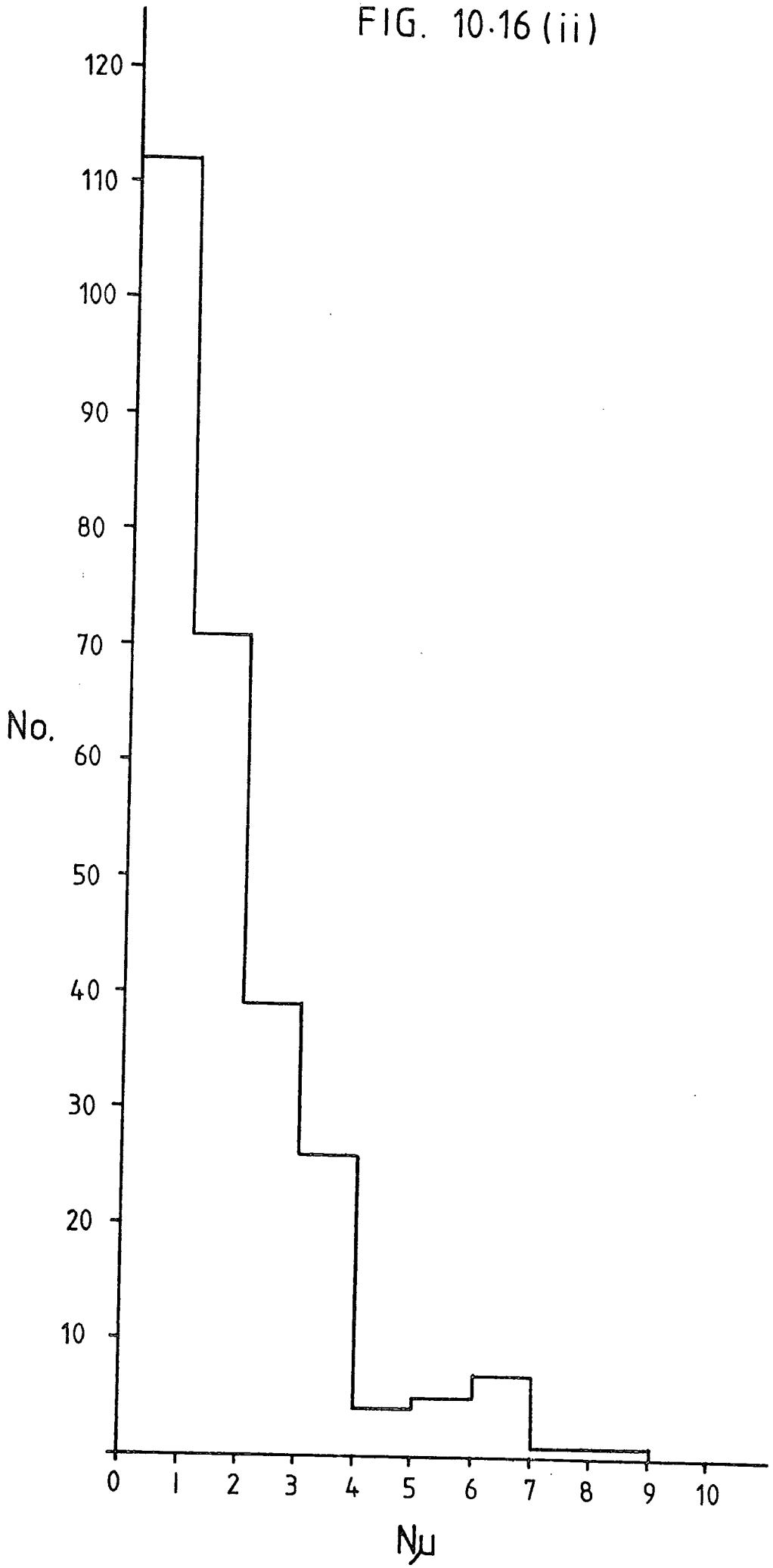

FIG. 10·16 (iii)

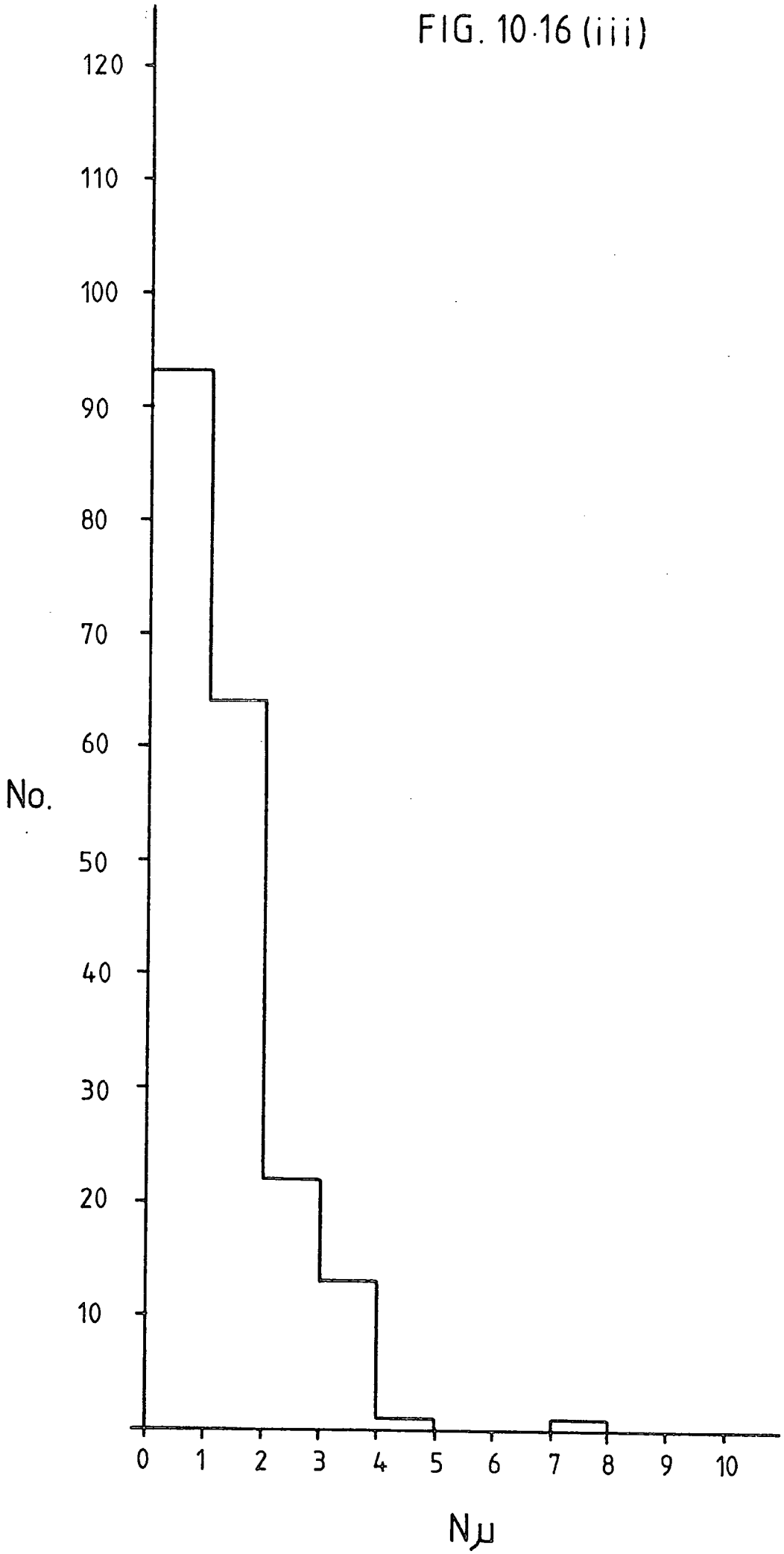

FIG. 10·16 (iv)

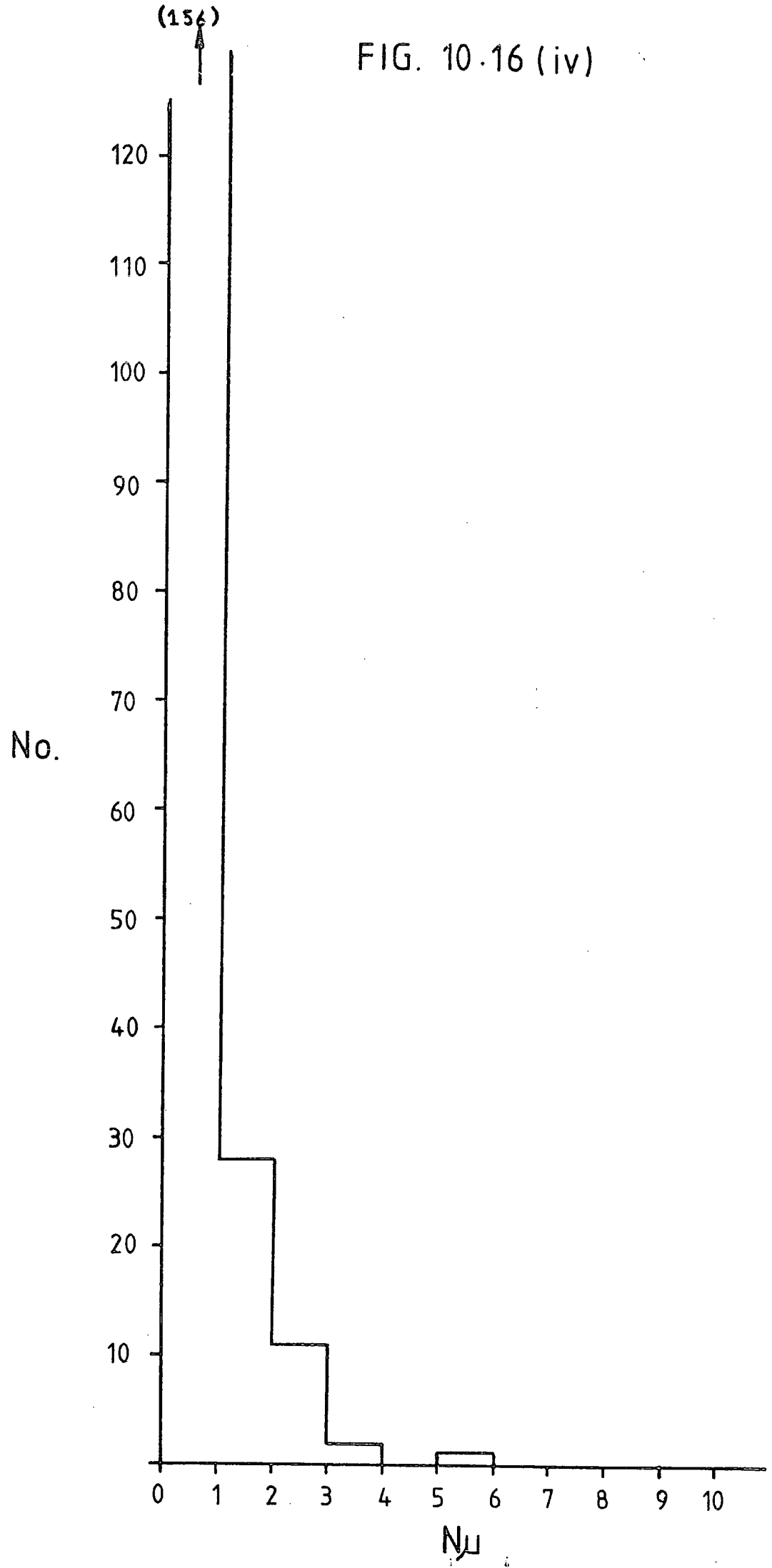

Figures 10.17

Frequency of observing N_μ muons at different core-distance ranges after combining I.L. and Minuit data and normalising to $N_e = 3.10^5$ particles according to $N_\mu \propto (N_e)^b$.

(i) Core-distance range 0 to 20m. $b = 0.51$

$$\overline{N}_\mu = 2.17 \pm 0.21$$

(ii) Core-distance range 20 to 40m. $b = 0.65$

$$\overline{N}_\mu = 1.86 \pm 0.10$$

(iii) Core-distance range 40 to 60m. $b = 0.32$

$$\overline{N}_\mu = 1.57 \pm 0.09$$

(iv) Core-distances greater than 60m. $b = 0.45$

$$\overline{N}_\mu = 1.08 \pm 0.07$$

FIG. 10·17 (i)

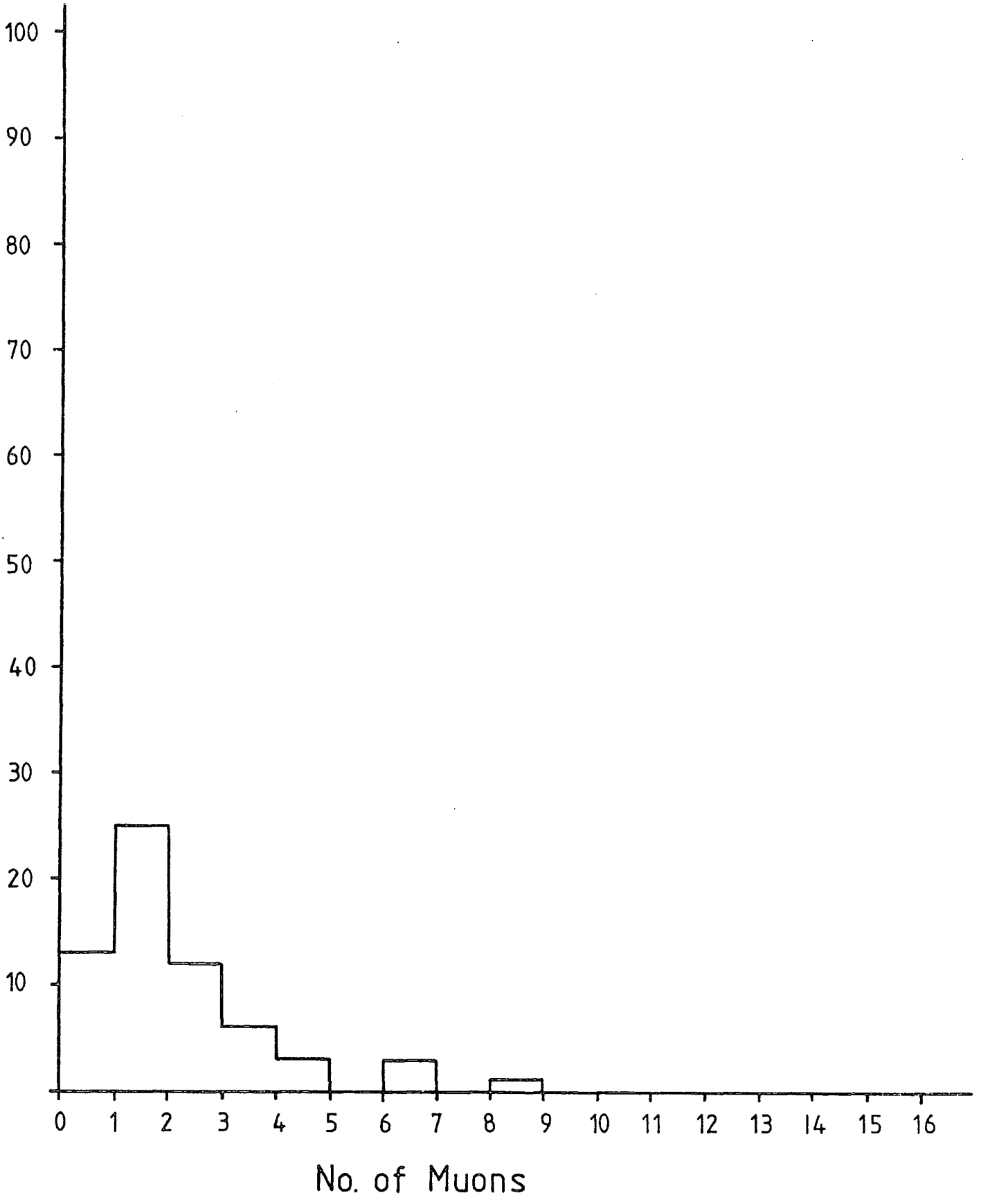
100
90
80
70
60
50
40
30
20
10
0
1
2
3
4
5
6
7
8
9
10
11
12
13
14
15
16
No. of Muons

FIG. 10·17 (ii)

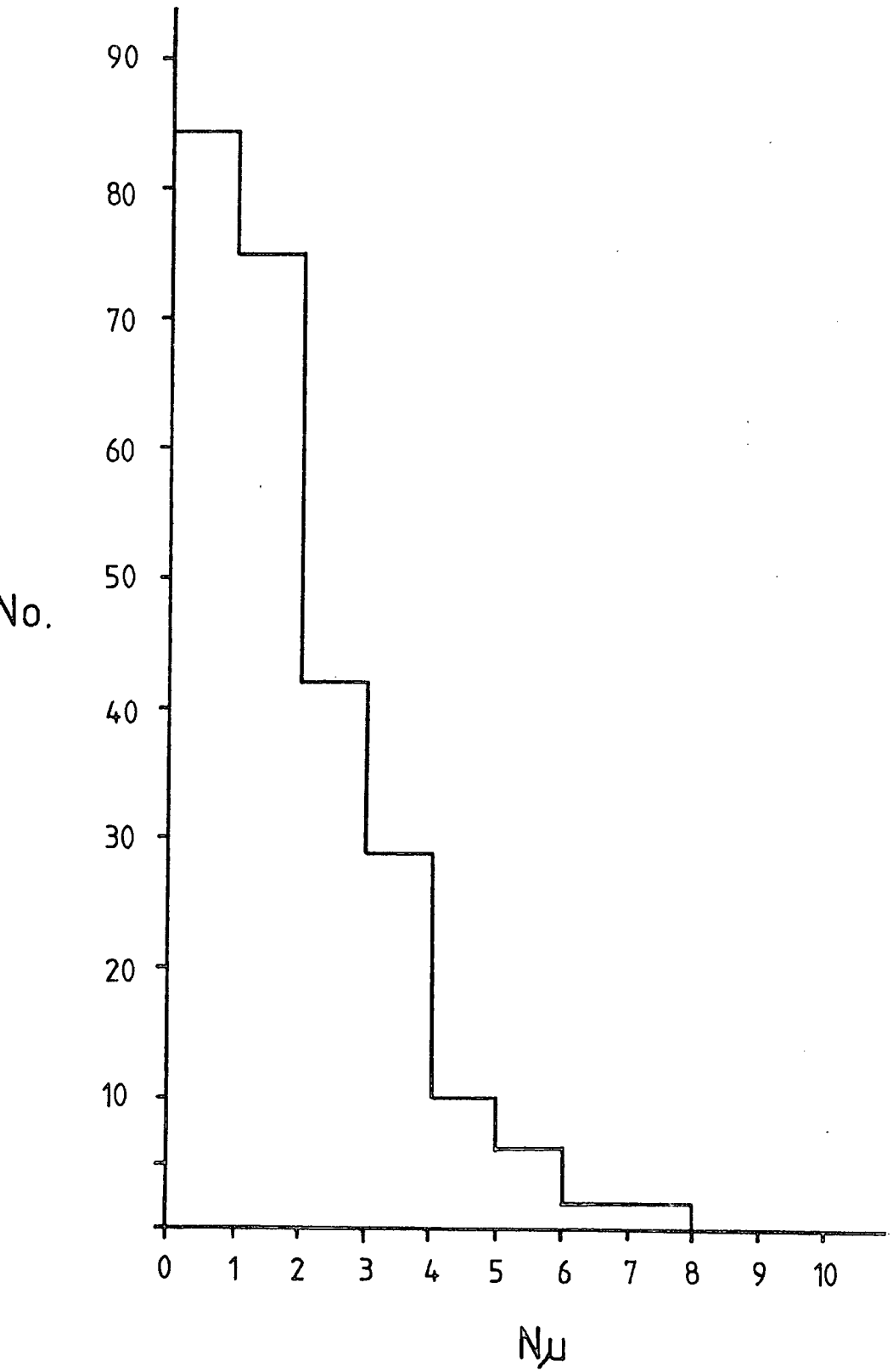

FIG. 10·17 (iii)

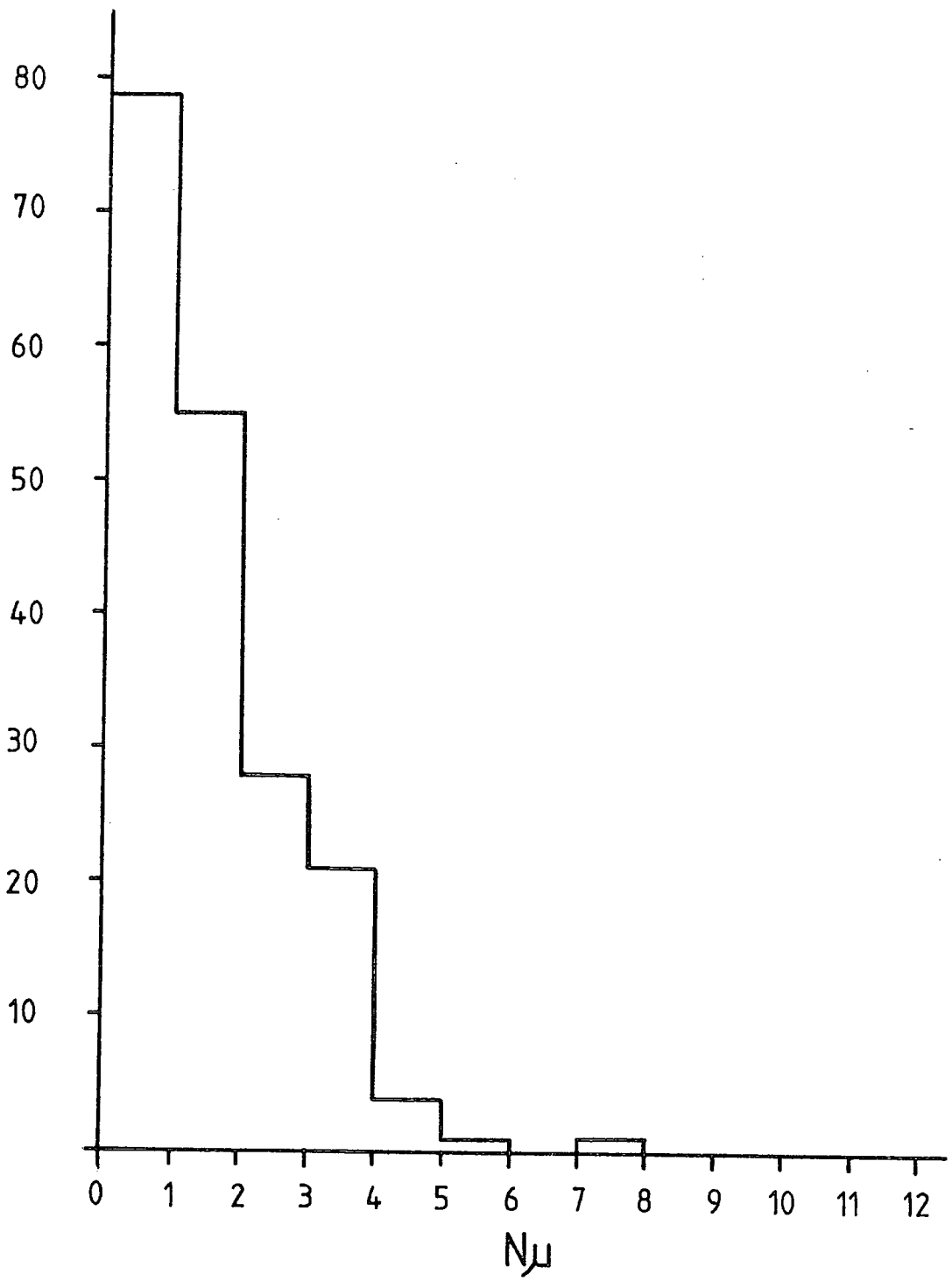

FIG 10·17 (iv)

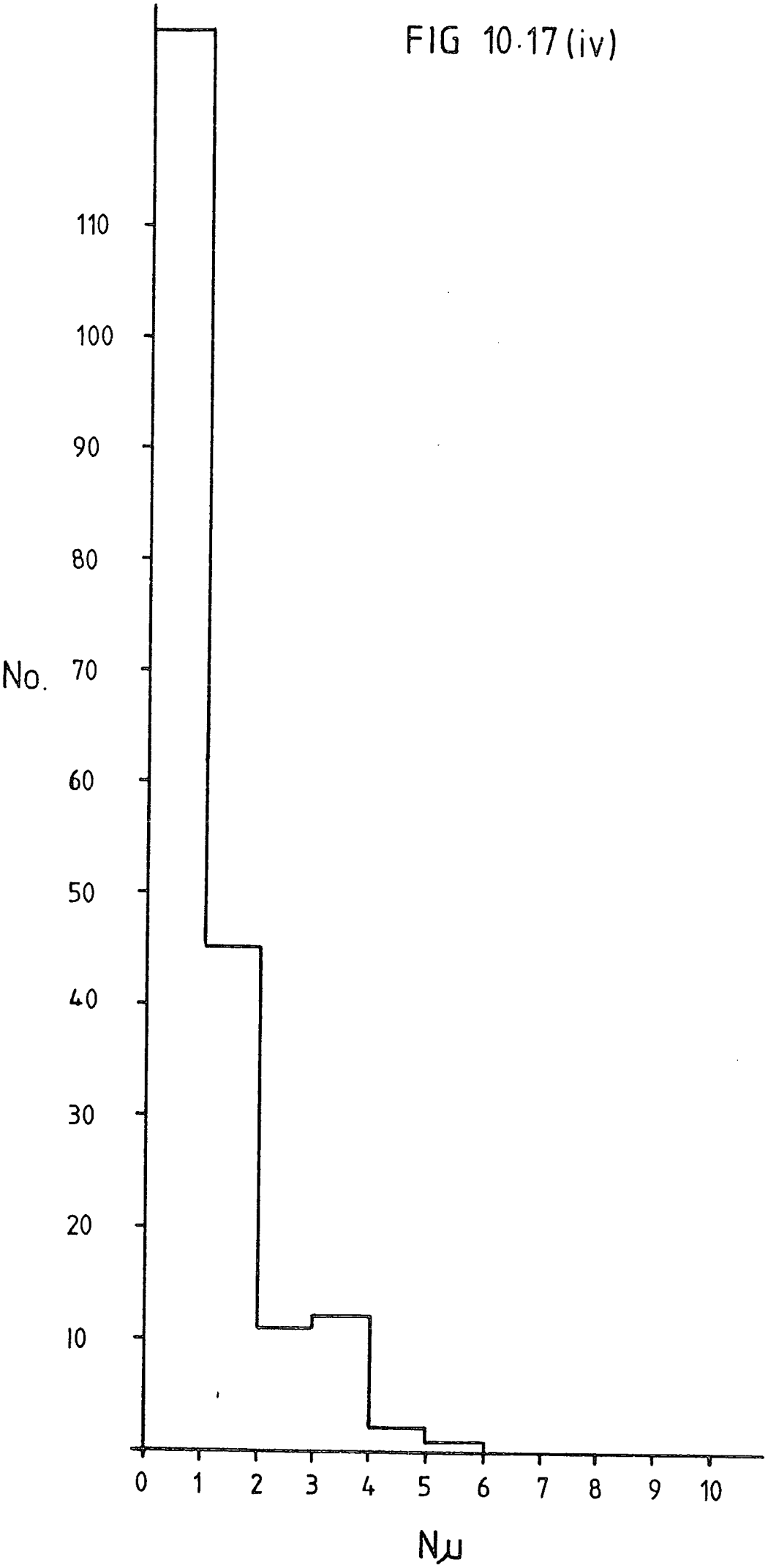

Figure 10.18

Experimentally determined lateral distribution of muons of energy E_μ in a sample of air-showers of size greater than 10^5 particles (867 showers with median shower-size 3.10^5 particles). The results have been corrected for averaging over bin-size and error in core-location.

The results are compared with Greisen's curves (1962,1966) based on :-

i) analogy to the electron lateral distribution function for E_μ greater than 1 GeV. equn. 10.1 (Bennett et al (1962))— Curve 1.

ii) summary of results previous to 1966 (Greisen (1966)) on muons with energy E_μ greater than 0.5GeV— Curve 2a —and greater than 1GeV— Curve 2b—. (See equn. 10.2).

FIG. 10·18

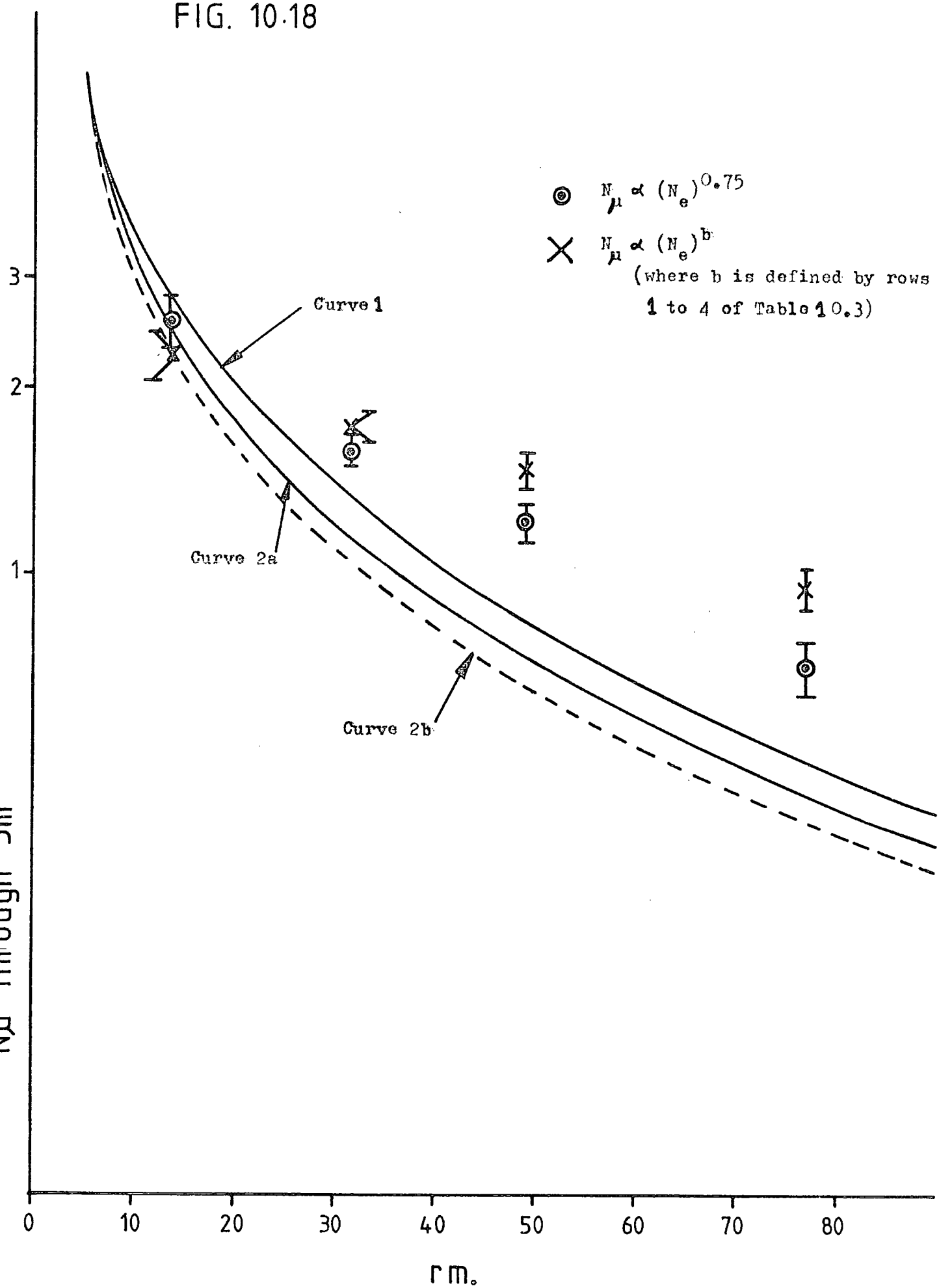
$N_\mu \propto (N_e)^{0.75}$
$N_\mu \propto (N_e)^{b}$
(where b is defined by rows 1 to 4 of Table 10.3)
Curve 1
Curve 2a
Curve 2b
3
2
1
0
10
20
30
40
50
60
70
80
r m.

10.6 Muon groups in air-showers

It has been pointed out (W dowczyk [1971]) that possible coherent production of pions in high energy nuclear interactions could be detected by analysing the spatial distribution of muons in air-showers. If the parent pions are incoherent then their decay muons should be distributed randomly in space.

By comparing the spatial distributions of groups of 2, 3, 4 etc. muons in the flash-tube chamber with random distributions, a search for evidence of such coherence has been carried out. By dividing the data into groups of 2, 3, 4 etc. according to how many muons are detected in the chamber different regions of the air-shower can be investigated i.e. the larger the number of muons detected by the chamber, the nearer to the core of the shower is it on average.

Fig. 10.19 summarises the number of each type of event used in the muon group analysis. The groups were then analysed by measuring the horizontal separation of adjacent muons in the central plane and plotting a histogram of the frequency of each muon separation, the data being divided according to how many muons were detected passing through the chamber.

Using random number tables events with 2, 3, 4 etc. muons were generated by randomly selecting a position for each muon in the event and thus a simulated event was generated.

Comparisons between the observed distributions and the simulated distributions are presented in Figs. 10.20a), b), c), d), e).

Table 10.6 summarises the results of comparing the two sets of data on a chi-square test.

FIG. 10·19

Summary of the numbers of events where n muons (μ's) are observed in flash-tube chamber that are candidates for muon-group analysis.

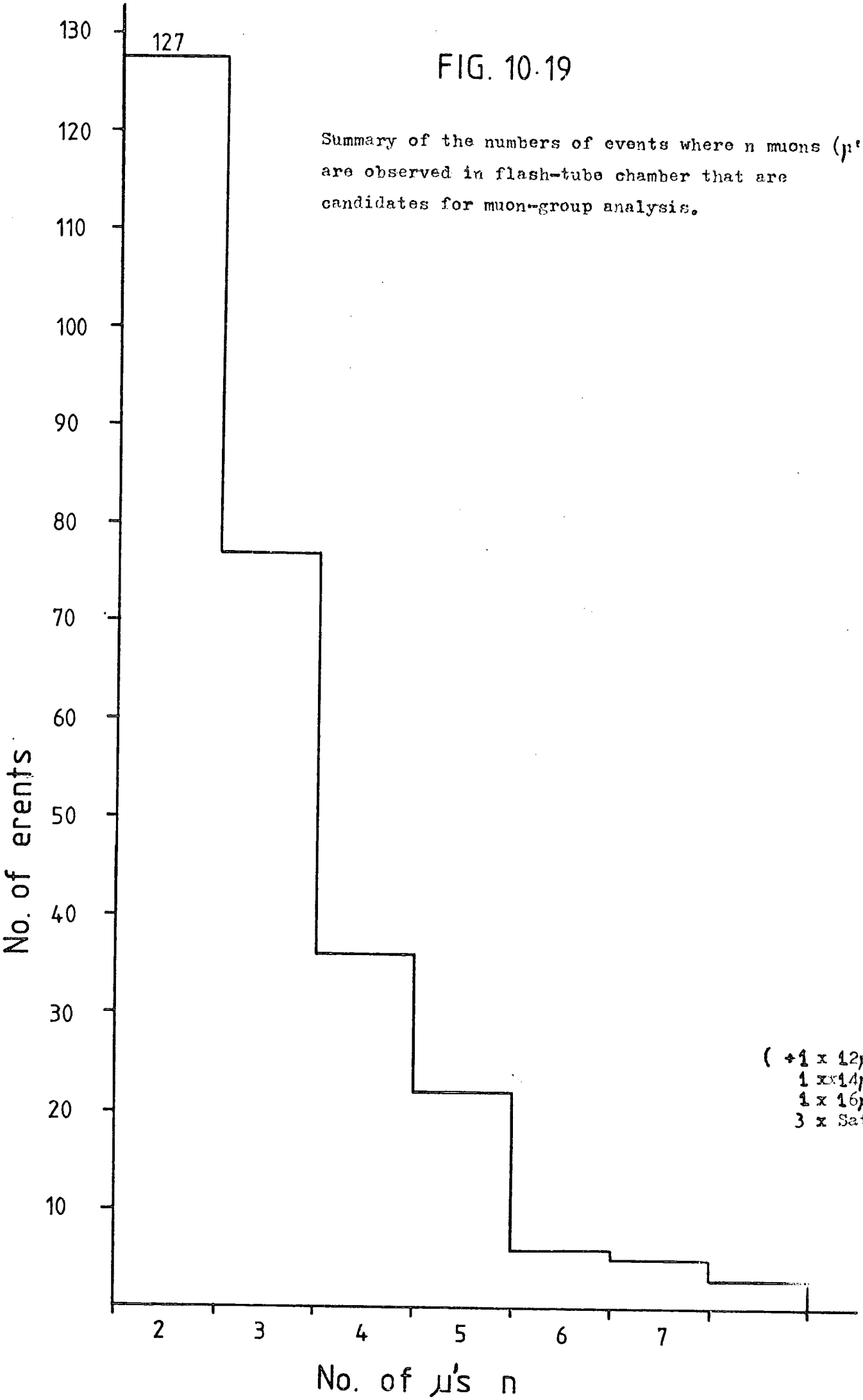

Figures 10.20

Comparison of measured distribution of separations $r_{\mu\mu}$ of adjacent muons with predicted distribution if separations are random. The latter distributions have been generated by simulating randomly spaced groups of n muons.

a) groups of 2 muons, n=2;

b) groups of 3 muons, n=3;

c) groups of 4 muons, n=4;

d) groups of 5 muons, n=5;

e) groups of 6 or more muons, $n \geqslant 6$ where the values of n are chosen to coincide with observation.

FIG. 10·20 a)

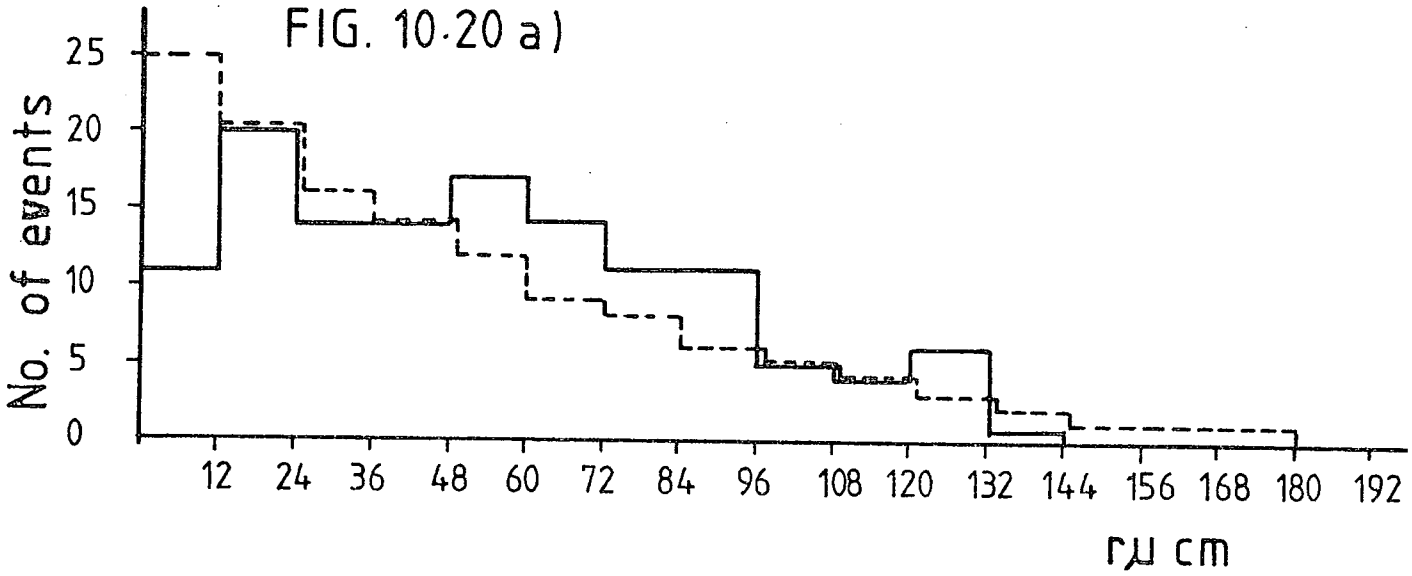

FIG. 10·20 b)

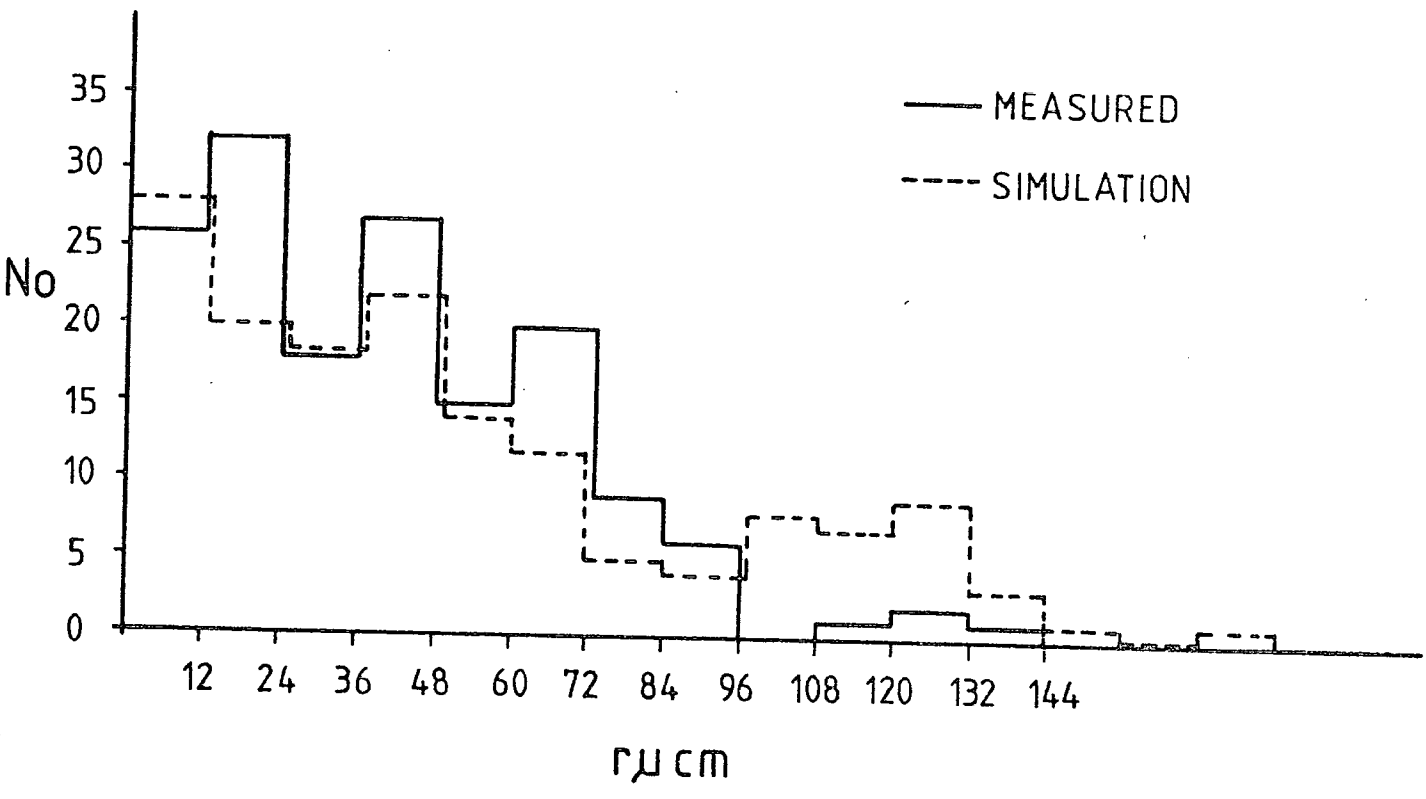

FIG. 10·20 c)

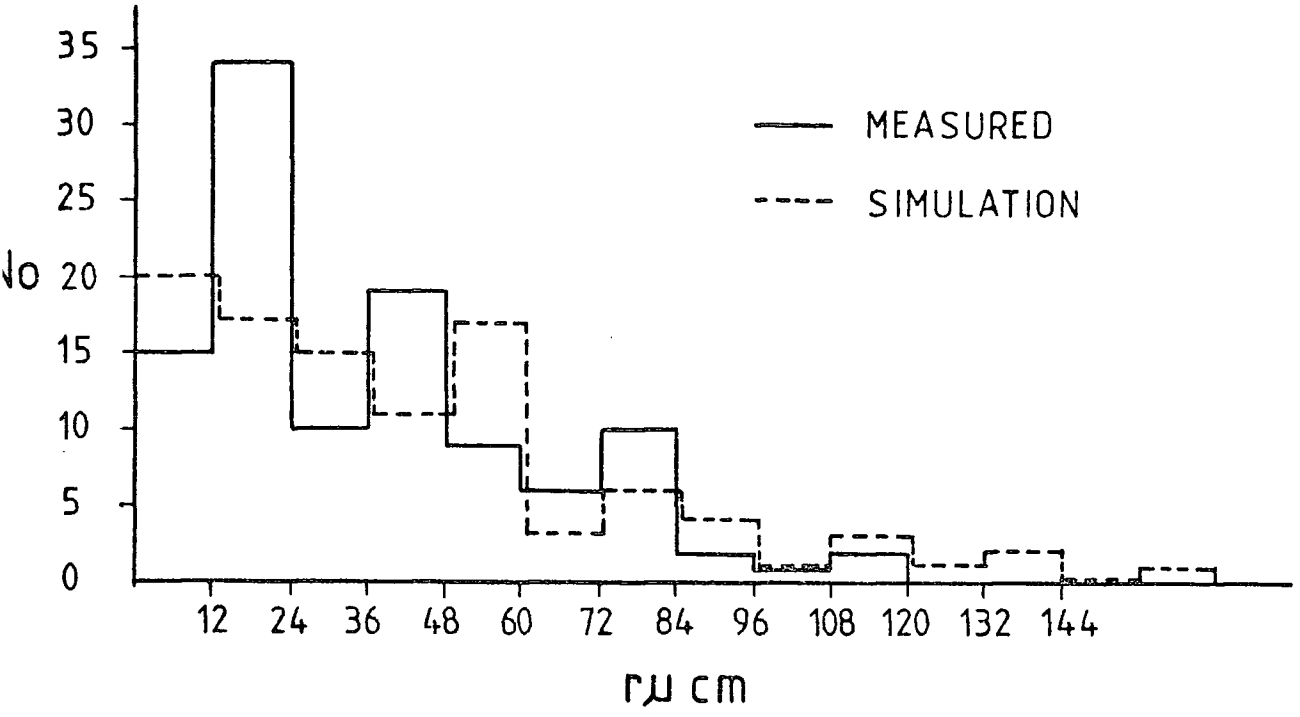

FIG. 10·20 d)

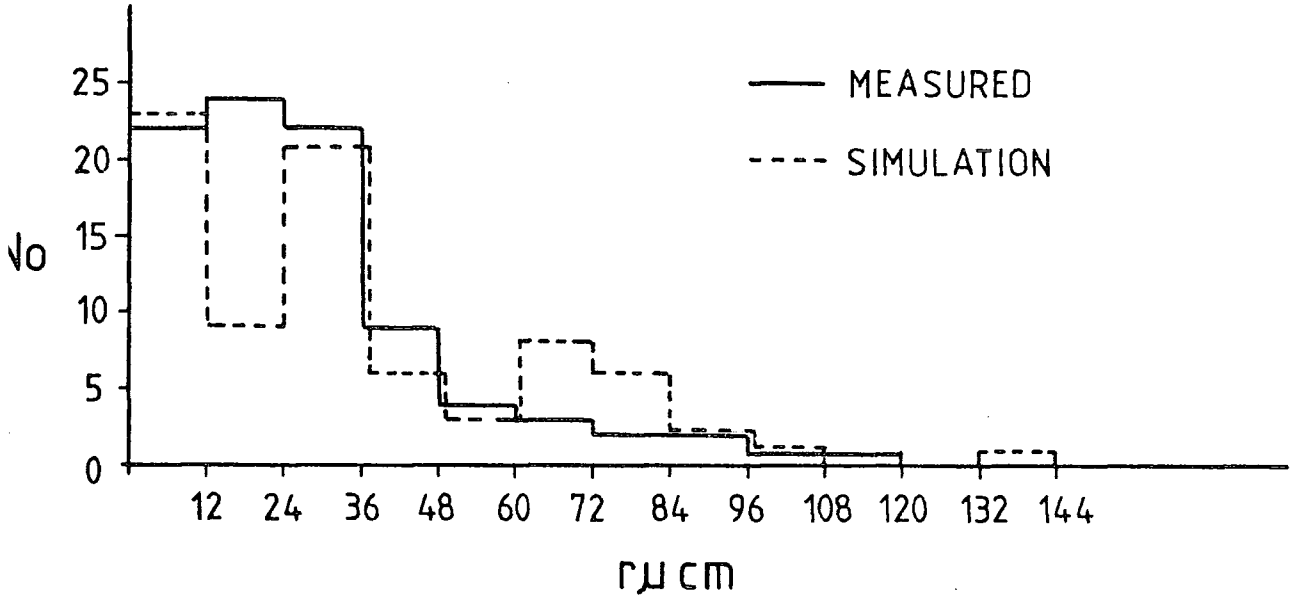

FIG 10·20e)

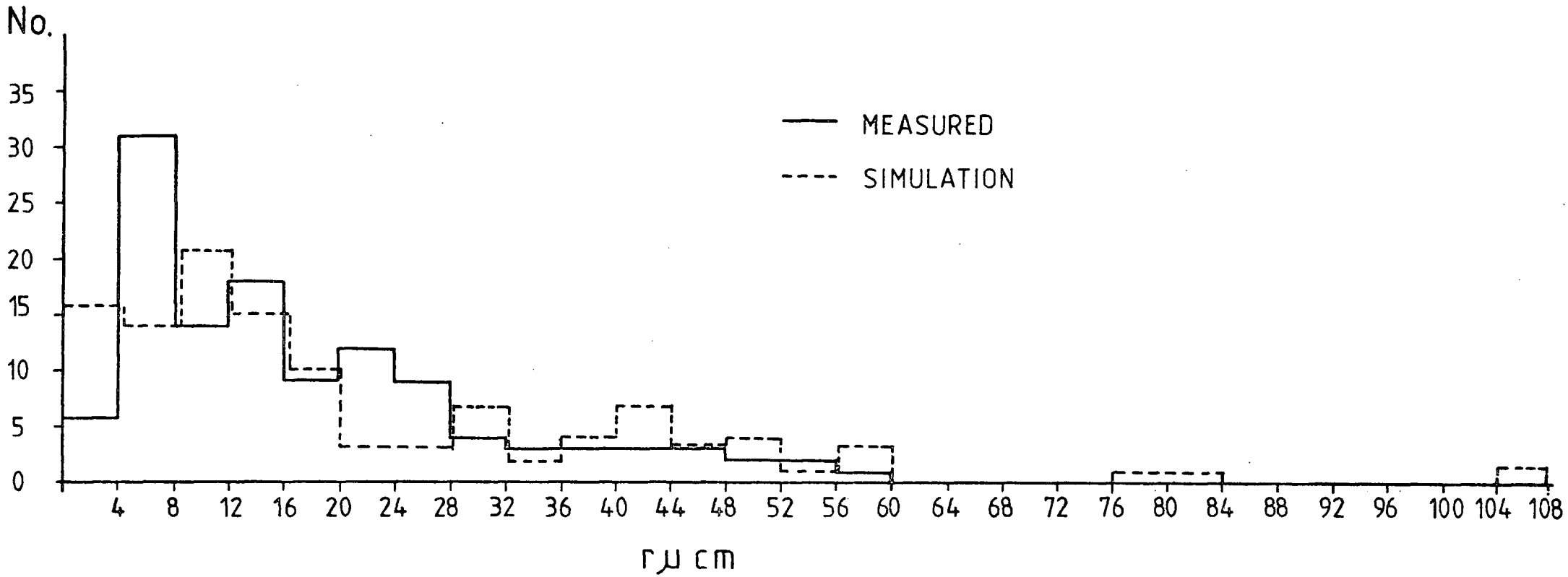
No.
35
30
25
20
15
10
5
0
MEASURED
SIMULATION
4 8 12 16 20 24 28 32 36 40 44 48 52 56 60 64 68 72 76 80 84 88 92 96 100 104 108
cm

TABLE 10.6

RESULTS OF χ^2-FITS OF DISTRIBUTION OF SEPARATIONS r_μ OF n MUONS TO RANDOM DISTRIBUTIONS OF r_μ

n	χ^2	Significance
2	18.4	2.5%
3	34.4	<0.5%
4	29.5	<0.5%
5	29.6	<0.5%
≥6	72.2	<0.5%

The numbers in the "Significance" column indicate the probability that the observed distribution is a random distribution.

An analytical treatment of the problem has been designed (see Appendix II) and a comparison between the data and the results of the analytical treatment of groups of 2 muons is presented in Fig. 10.21.

10.7 Conclusions of the analysis of muon groups

For all muon groups >2 there is a very small probability that the observed distribution is random (< 0.5%) however visual inspection of Figs. 10.20 indicates that only for groups of muons ⩾6 does there seem to be a marked preference for a particular separation distance.

Thus, in the shower size range 10^5 to 7.10^6 within 80 m of the core there is some evidence for coherent grouping of muons at densities >1 m^{-2} (area of detector = 2.95 m^2), but only in regions of densities ⩾2 m^{-2} does this coherence show itself as a marked preference for a particular separation distance between adjacent muons.

FIG. 10·21

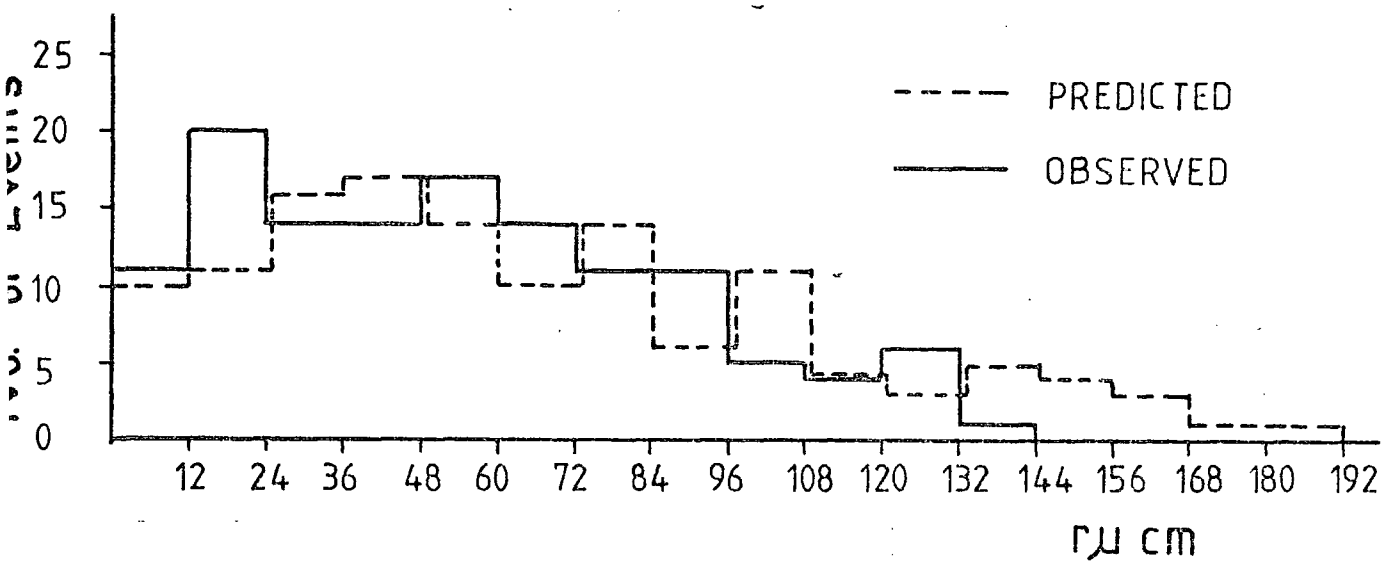

Figure 10.21
Comparison of measured distribution of separations r_u of 2 muons in 2 muon events with predicted distribution from theory (Appendix II).

CHAPTER 11

MEASUREMENTS ON HADRONS IN AIR-SHOWERS

11.1 Introduction

The nuclear cascade forms the backbone for the development of an air-shower, and hence the hadrons are a very important component. Although the least numerous of all the particles, hadrons can easily be distinguished by the large energy per particle carried by them.

As well as providing information on the nature of the primary cosmic-rays, measurements on hadrons in air-showers make accessible energy regions beyond the scope of present accelerators. This last fact has stimulated many theorists to interpret cosmic ray hadron measurements as indicating new behaviour of the fundamental particles at energies just above 2 TeV (the limit of hadron interaction energies available at accelerators - I.S.R.). In particular there is much cosmic ray evidence (see for example McCusker [1975], and Nasri [1977]) for the onset of high transverse momentum interactions at around 10^3 TeV, this effect should be reflected in the lateral distribution of hadrons.

One further measurement of interest is the ratio of charged to neutral hadrons at sea-level. At present theory cannot cope with the measurements (e.g. Gaisser [1976]), and new physics has to be invoked to explain the results (e.g. Tonwar et al 1971a, b).

As with the muon measurements, the lateral distribution and energy spectrum of hadrons in air-showers can be compared with the results of Monte Carlo calculations using different models. Previous results and their compatability with the results of such calculations will be discussed in the next section.

11.2 Summary of previous measurements

In order to obtain an energy spectrum for hadrons, three parameters need to be determined. These are the hadron energy, its distance from the core of the shower, and the size of the shower. Since different groups use different techniques, and there is always a large margin of uncertainty in the hadron energy measurements - especially at higher energies - differences in the burst spectra obtained are not surprising.

Fig. 11.1 shows a comparison of the data of five authors with the predictions of calculations according to different models made by Grieder (1978). Curves 1) to 4) are as described in Chapter 10 (Section 10.2) but briefly curves 1) to 3) represent proton initiated showers and curve 4) represents iron initiated showers. Clearly this latter model fails to give sufficient high energy hadrons to agree with the data, which seem to favour curves 1) and 3) - the latter curve involves the use of rising cross-sections.

A comparison of the lateral distribution of high energy (>100 GeV at least) hadrons, as measured by several authors, with the calculations of Grieder

Figure 11.2
Lateral density distributions for hadrons of different energy. The simulated distributions are for proton-initiated showers, calculated with the SMFB model and a standard transverse-momentum distribution with a cut-off at 5 GeV/c. $E_o = 10^5$ GeV, sea level. Experimental data normalised to $N_o = 10^5$. (After Grieder (1977)).

▫ Matano et al (1970) $>$1700 GeV

○ Baruch et al (1975) $>$1000 GeV

△ Fritze et al (1970) $>$ 800 GeV

◇ ● Kameda et al (1965) $>$ 100 GeV

Figure 11.1
Integral energy spectra of hadrons in air showers at sea level. The theoretical spectra 2) and 3) are for the IDFB model with fixed and rising cross-sections, respectively. Spectra 1) and 4) are for the SMFB model. (After Grieder (1977)).

◆ Tanahashi (1965)

○ Kameda et al (1965)

△ Bohm et al (1968)

✱ Matano et al (1970)

▫ Baruch et al (1975)

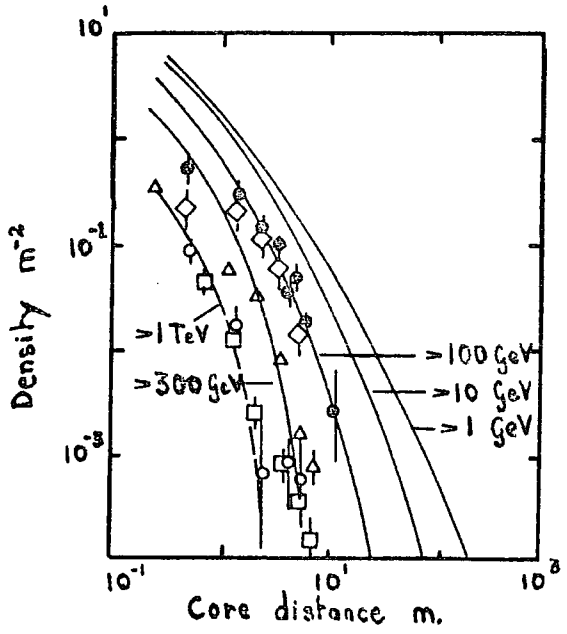

Fig. 11.2 Lateral distribution of hadrons.

Fig. 11.1 Integral energy spectra of hadrons.

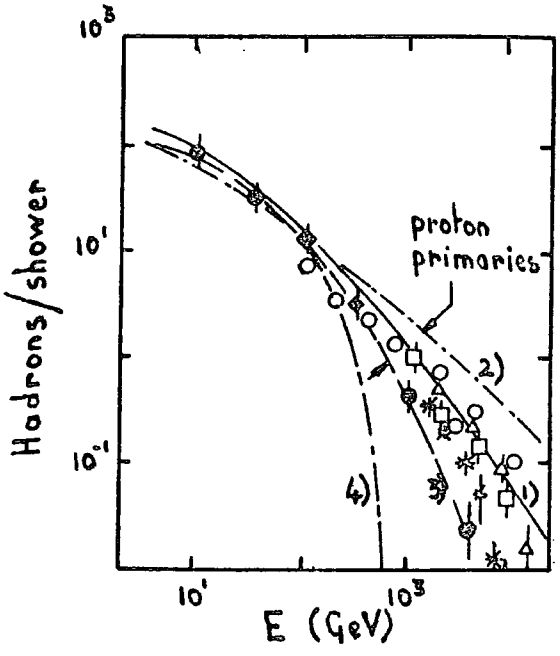

(1978) is presented in Fig. 11.2. The curves are as for curve 1) in Fig. 11.1 i.e. a slow multi fireball model with constant cross-sections. Grieder (1978) points out that to account for the measured numbers of high energy hadrons detected beyond 3 metres from the core, a significant increase in the average transverse momentum would have to be invoked (the calculations assume standard transverse momentum distributions with a cut-off at 5 GeV/c).

This large transverse momentum effect is more strikingly demonstrated in Fig. 11.3 where are plotted the results of various authors' determination of the dependence of the parameter E.r on shower size. Here E represents the energy of a hadron and r the average distance of hadrons of that energy from the core. For high energy events (>100 GeV), this product approximates very closely the average transverse momentum of hadrons of energy E, hence the data clearly demonstrate an increase of the average transverse momentum with shower size - which in turn reflects an increase in transverse momentum with primary energy.

One further parameter of interest is the charged to neutral ratio of sea-level hadrons. Fig. 11.4 shows the results of two measurements (Ashton et al [1975] and Vatcha and Sreekanton [1973]). The full curve is the result of calculations according to Gaisser (1976) including full production of strange particles and nucleon-antinucleon pairs. The data clearly diverge from the results of calculations for $E \geqslant 3.10^5$ and, as Gaisser points out, this is one parameter of sea-level cosmic radiation that cannot be accounted for by suitable admixtures of heavy and light elements in the primary composition. The effect, if real, must therefore reflect a change in the nuclear physics of interactions beyond 3.10^5 GeV.

Figure 11.3

The E.r versus shower size relation as determined by previous authors.

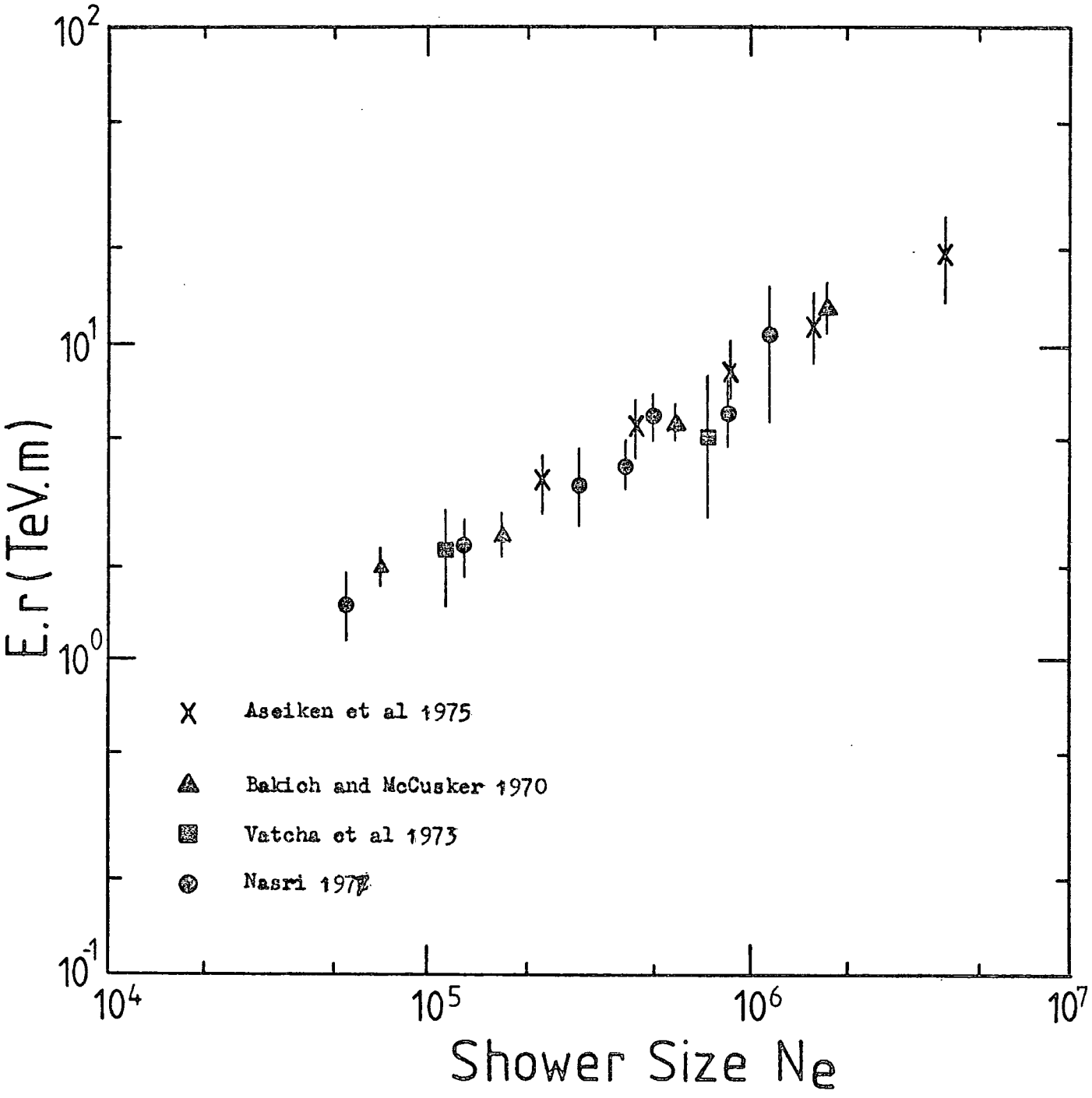

FIG. 11.3

FIG. 11.4 The ratio of charged to neutral hadrons as a function of primary energy E.
(After Gaisser 1976)

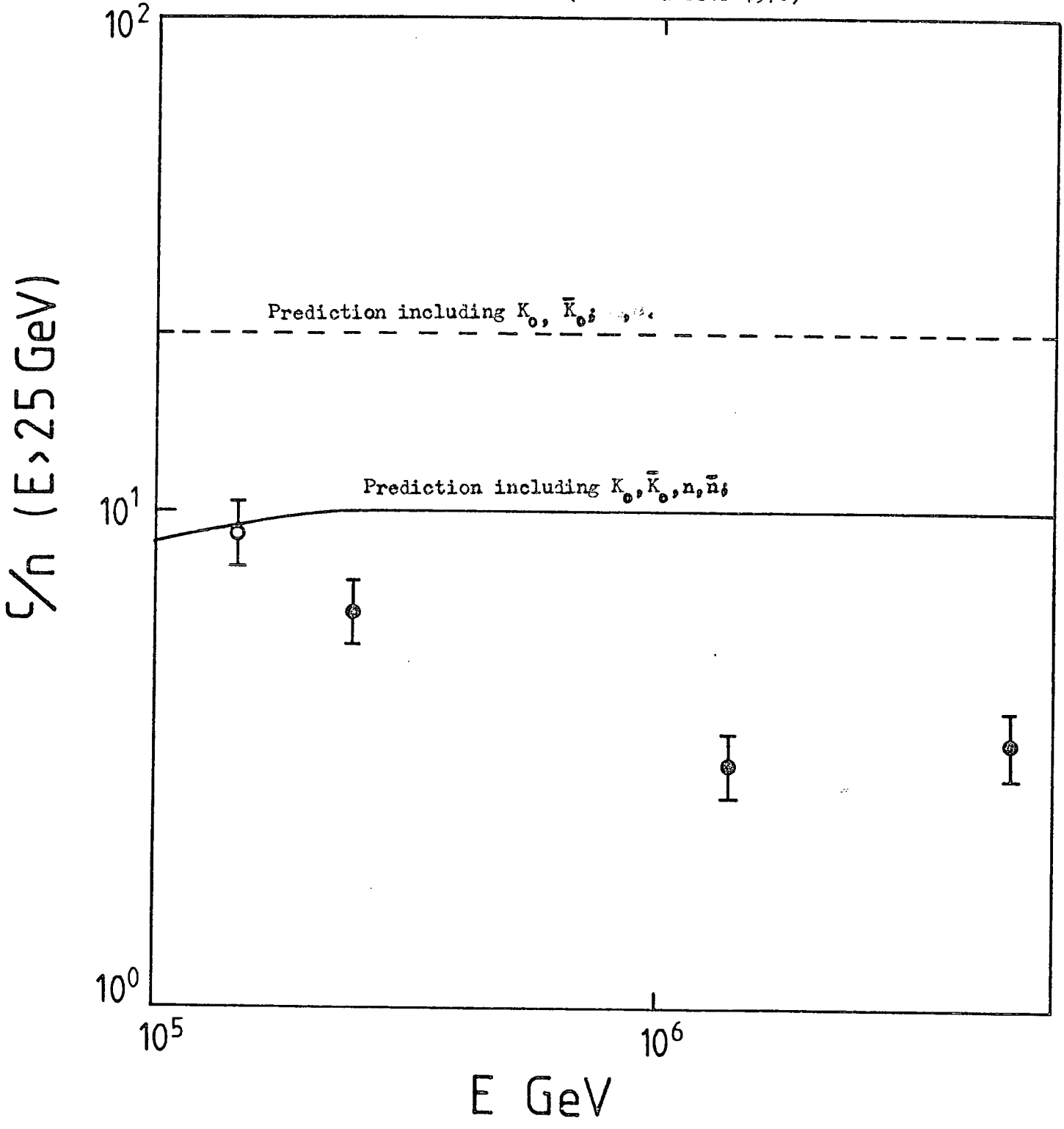

o Ashton et al 1975.

● Vatcha and Sreekantan 1973.

11.3 The present experiment

The measurements on hadrons in air-showers were made simultaneously with the measurements on muons in air-showers (Chapter 10). Bursts which were observed either immediately below the lead (in F1a) or the iron (F1b) and whose width in these defining layers did not extend beyond the edge of the flash-tubes were considered to be bursts produced by hadrons. Any contamination from muon-bremsstrahlung produced bursts would be only small - see Chapter 4 - but since the yield was only small (see Table 11.1) all bursts were used in the analysis.

The energy of the hadron was measured by projecting the photograph onto a 1:20 scale drawing of the front view of the chamber and measuring the width in cms. This measurement was then converted to an equivalent energy using the curves of figures 2.15 and 2.16.

The assignment of nucleon or pion to each event was not possible, however, an overall assessment could be made using the observations of neutral particles - this will be discussed in more detail below.

The charge of the particle producing a burst in the lead could not be ascertained, however, the charge of the particle producing a burst in the iron could be ascertained from the presence or absence of a single particle track in F1a above the centre of the burst. Some typical events are shown in Figs. 11.5a), b).

Table 11.1 gives a summary of the basic data involved in the following analysis. All shower parameters for the "hadron events" were determined using the intersecting loci method, and the distributions in shower size

TABLE 11.1

SUMMARY OF YIELD OF HADRON EVENTS

Total number of air-showers	1648
Total number of hadron bursts	69
Number of bursts in lead	30
Number of charged bursts in iron	21
Number of neutral bursts in iron	6
Number of bursts in iron of unidentifiable charge	12
(The unidentifiable bursts in iron are not used in the charge/neutral ratio analysis.)	

Figure 11.5 a): Two hadrons interacting simultaneously in the lead (app. energy of each is $\sim$80 GeV), one cascade is absorbed in the iron whereas the other continues to develop therein.

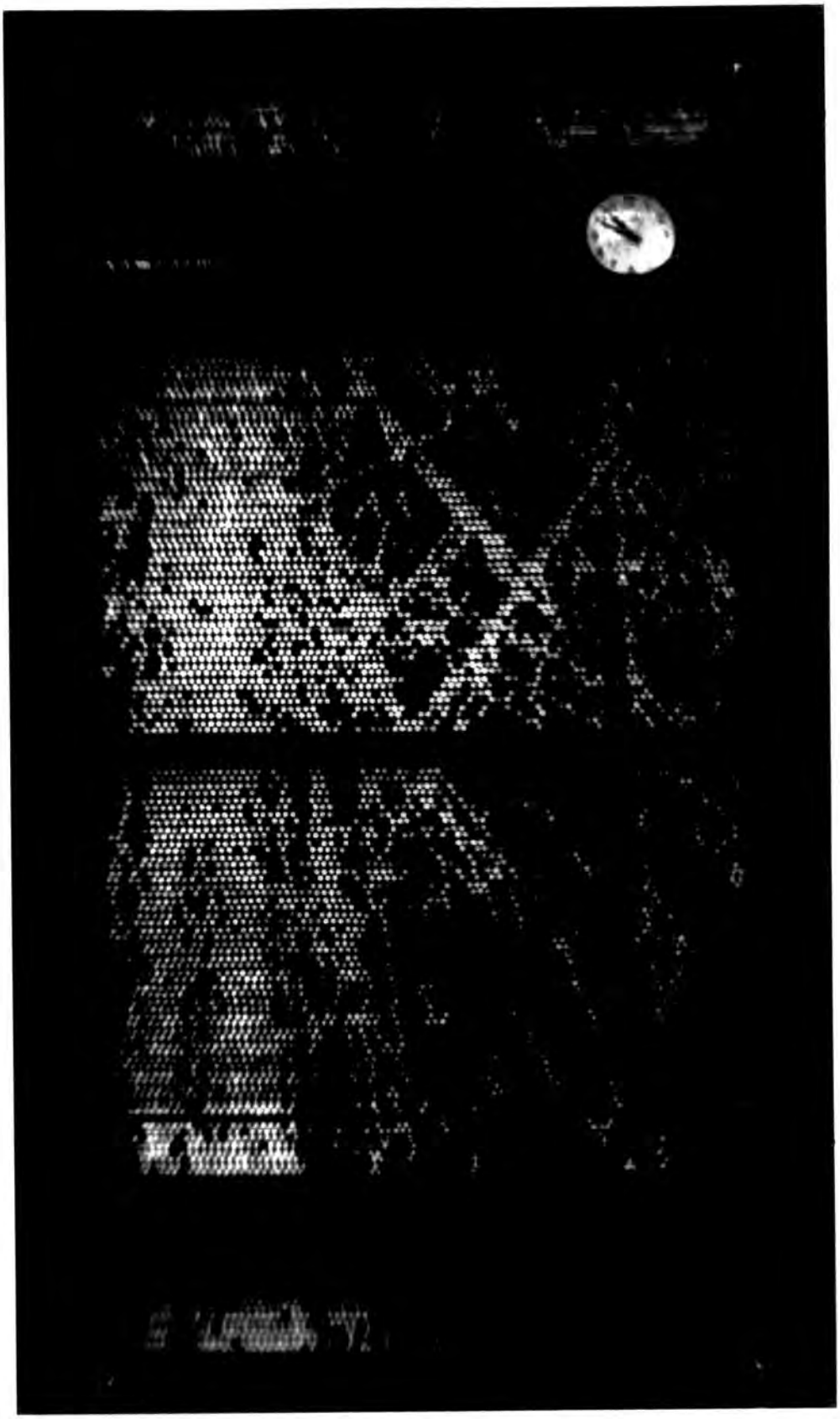

Figure 11.5 b): A charged hadron interacting in the iron target, (energy 40 GeV). A neutral hadron would be recognised by the absence of a single particle track in F_1a directly above the burst. The lower panel is the oscilloscope trace corresponding to this event, the prompt pulse is saturating from scintillator stack A.

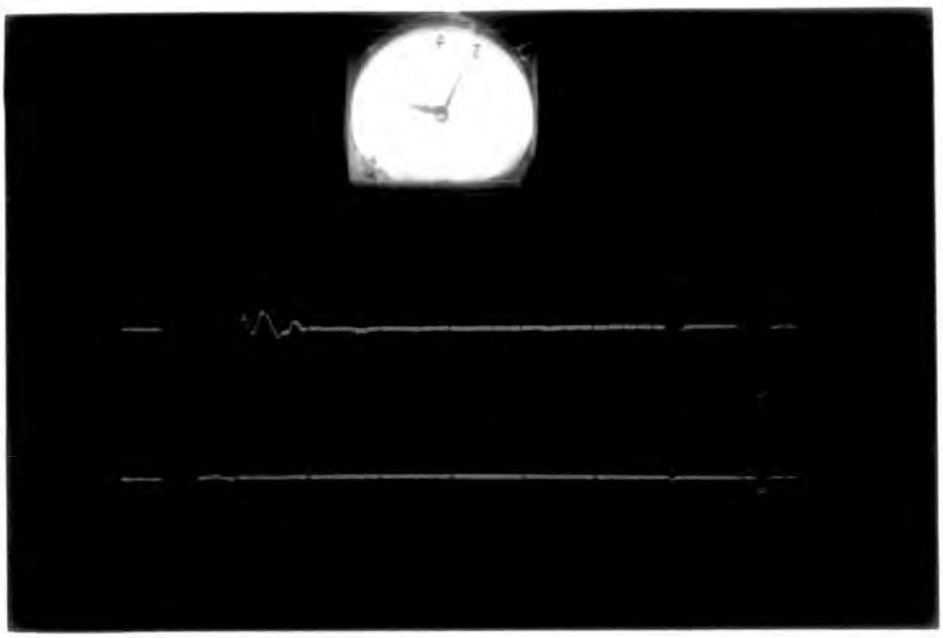

and core positions for these events are presented in Fig. 11.6a) and b) respectively.

In order to increase the statistical accuracy of the data, the runs for the hadron events cover twice the running time for the muon data. The distributions in shower-size and core positions for all events detected in this running time are compared with the same distributions for the set of data used in the muon measurements in Figs. 11.7a), b). It is clear that there is no systematic difference between the two distributions.

11.4 The lateral distribution of hadrons

In order to construct a lateral distribution of hadrons which represents an average over all showers the shower size dependence of the number of hadrons in a shower has to be determined. However, the method used in detecting a hadron (i.e. by triggering on the occurrence of an air-shower whether or not a hadron is detected) and the dominance of events in which no hadron is detected means that the determination of the relationship between the number of hadrons in a shower and the shower size must include a weighting according to the probability of detecting a hadron at a particular shower size. This probability depends upon the mean core distance of showers of a particular size, and on the lateral distribution of hadrons in showers of that size.

Hence, to obtain an accurate lateral distribution of hadrons a method of successive approximations has to be used. Fig. 11.8 represents the first

FIG. 11·6 a)

Distribution in shower size of those events in which a hadron interacted in the flash-tube chamber.

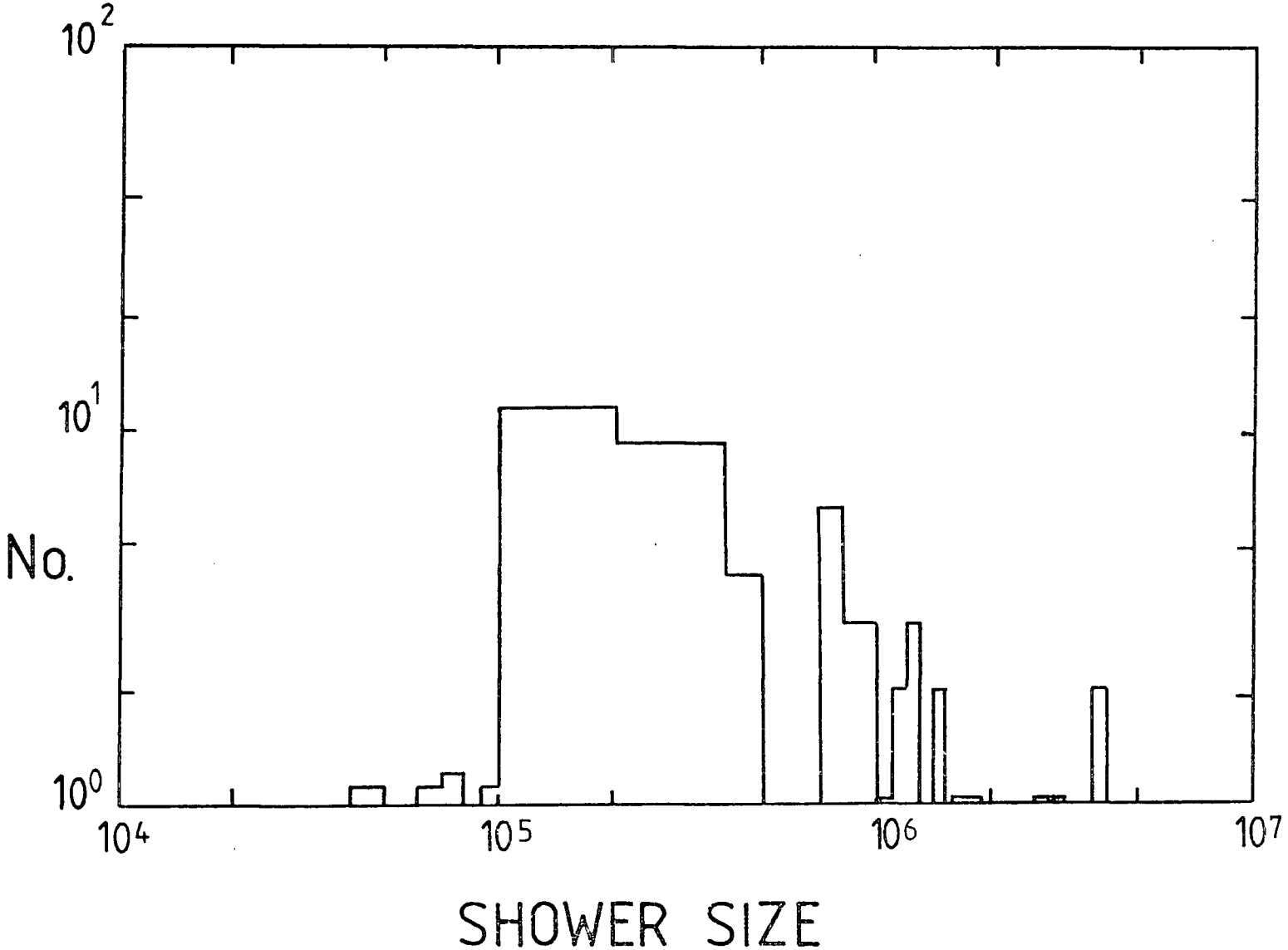

FIG.11·6b)

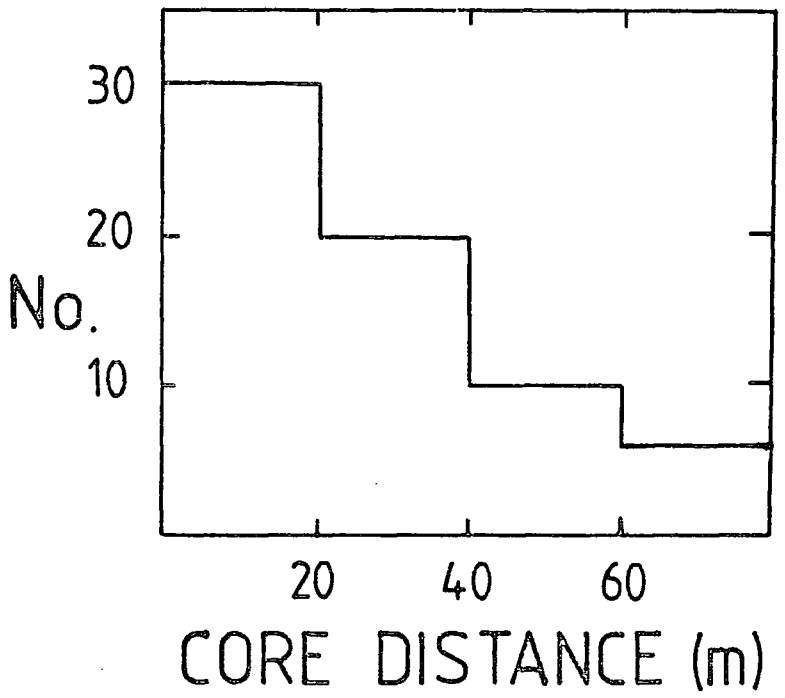

Distribution in core distance from the chamber of those events in which a hadron interacted in the flash-tube chamber.

FIG. 11·7a)

Comparison between distribution in shower size N_e of showers used in muon analysis(- - - -) and showers used in hadron analysis(———).

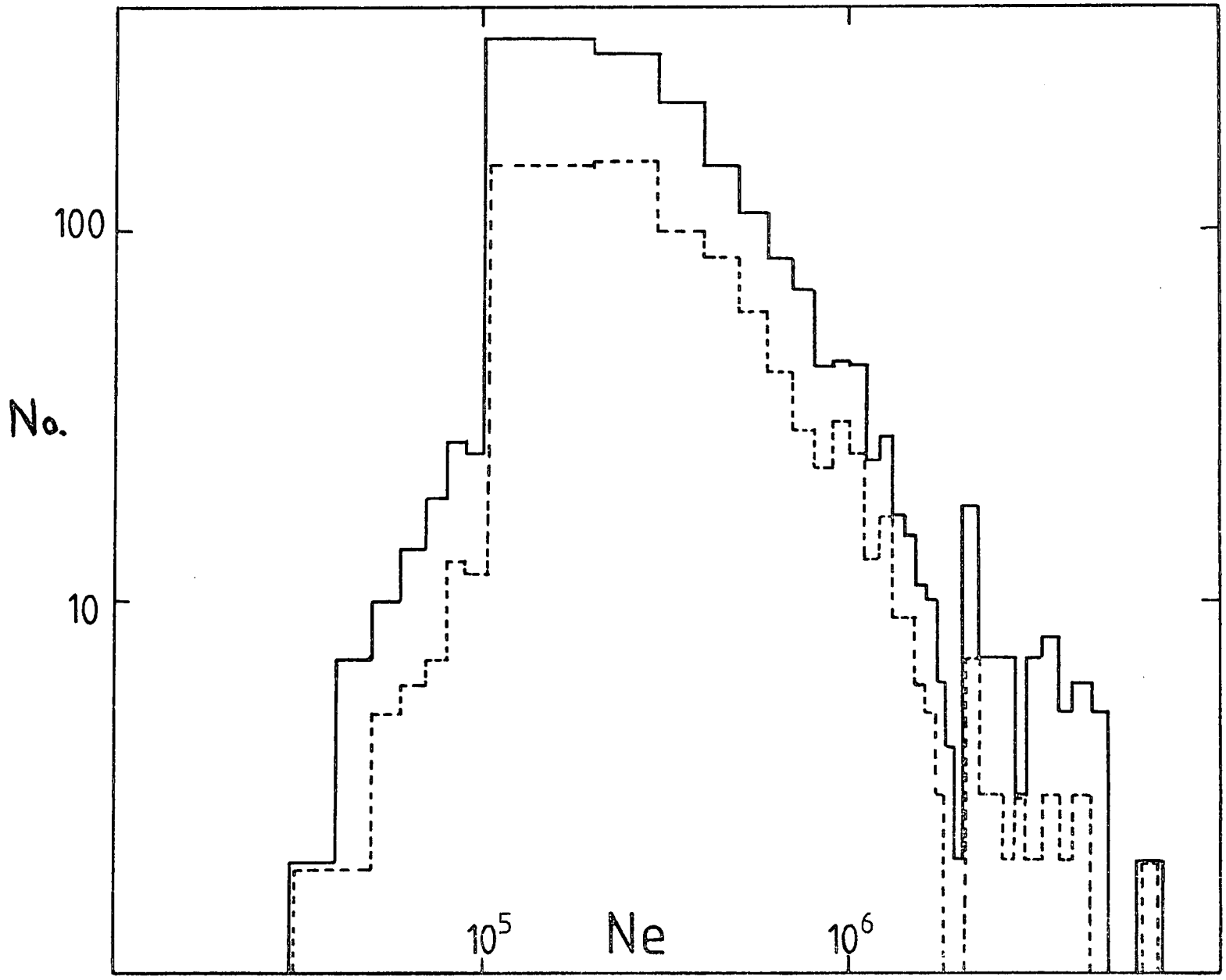

FIG. 11·7 b)

Comparison between core distance r distribution of showers used in muon analysis(- - -) and showers used in hadron analysis(———).

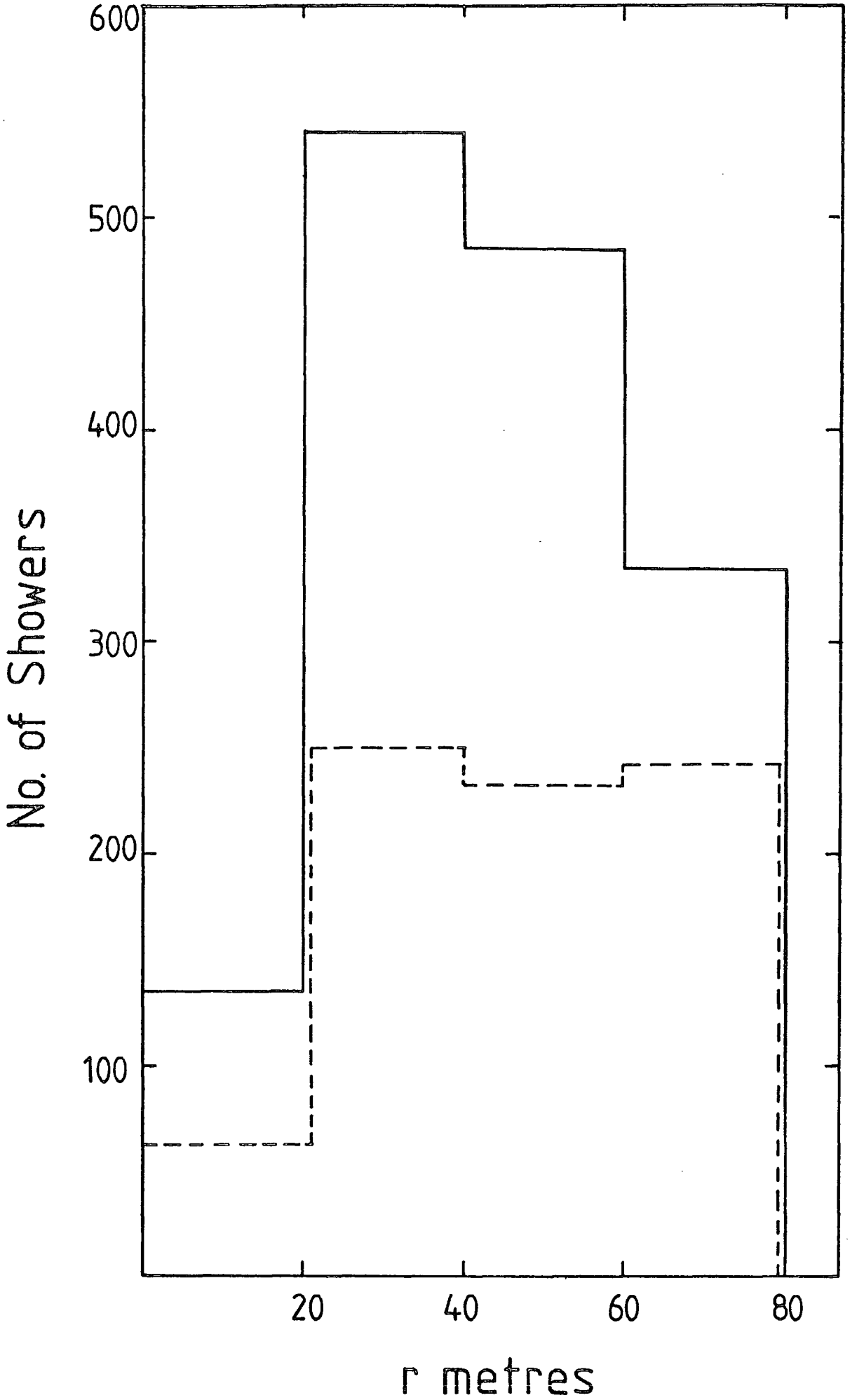

approximation to the dependence of the number of hadrons of energy greater than 10 GeV ($\eta_H(E>10GeV)$) on shower size (Ne). It is the dependence of the average number of hadrons detected by the flash-tube chamber on shower-size. A linear regression fit of the data yields

$$(11.1) \qquad \bar{N}_H\ (E>10\ GeV) = 0.03\left(\frac{Ne}{10^5}\right)^{0.19}$$

Fig. 11.9 is the lateral distribution of hadrons obtained by normalising to a shower size of 3.10^5 particles using equation 11.1.

The former normalisation method yields an exponential lateral distribution of the form

$$(11.2) \qquad \bar{N}_H = 0.14\ \exp(-0.04r)$$

where r is the distance from the core expressed in metres.

A better assessment of the N_H v Ne relation can now be made by weighting the average number of hadrons according to the probability of detecting a hadron in a shower of a certain size. This weighting factor is $1/\exp(-0.4\bar{r}(Ne))$ where $\bar{r}(Ne)$ is the mean distance of the core of a shower of size Ne from the centre of the flash-tube chamber. The dependence of $\bar{r}$ upon Ne depends upon the collecting areas for showers of different size and is depicted in Fig. 11.10.

The second approximation to the relationship between $\bar{\eta}_H$ and ηe is depected in Fig. 11.11. A linear regression analysis yields the relation:

$$(11.3) \qquad \bar{\eta}_H\ (E>10\ GeV) = 0.03\left(\frac{Ne}{10_5}\right)^{0.98}$$

FIG.11.8 Average number of hadrons $\bar{n}_H$ in chamber as a function of shower size n_e. For all hadrons with energies greater than 10 GeV (assuming them all to be pions) -"First approximation"

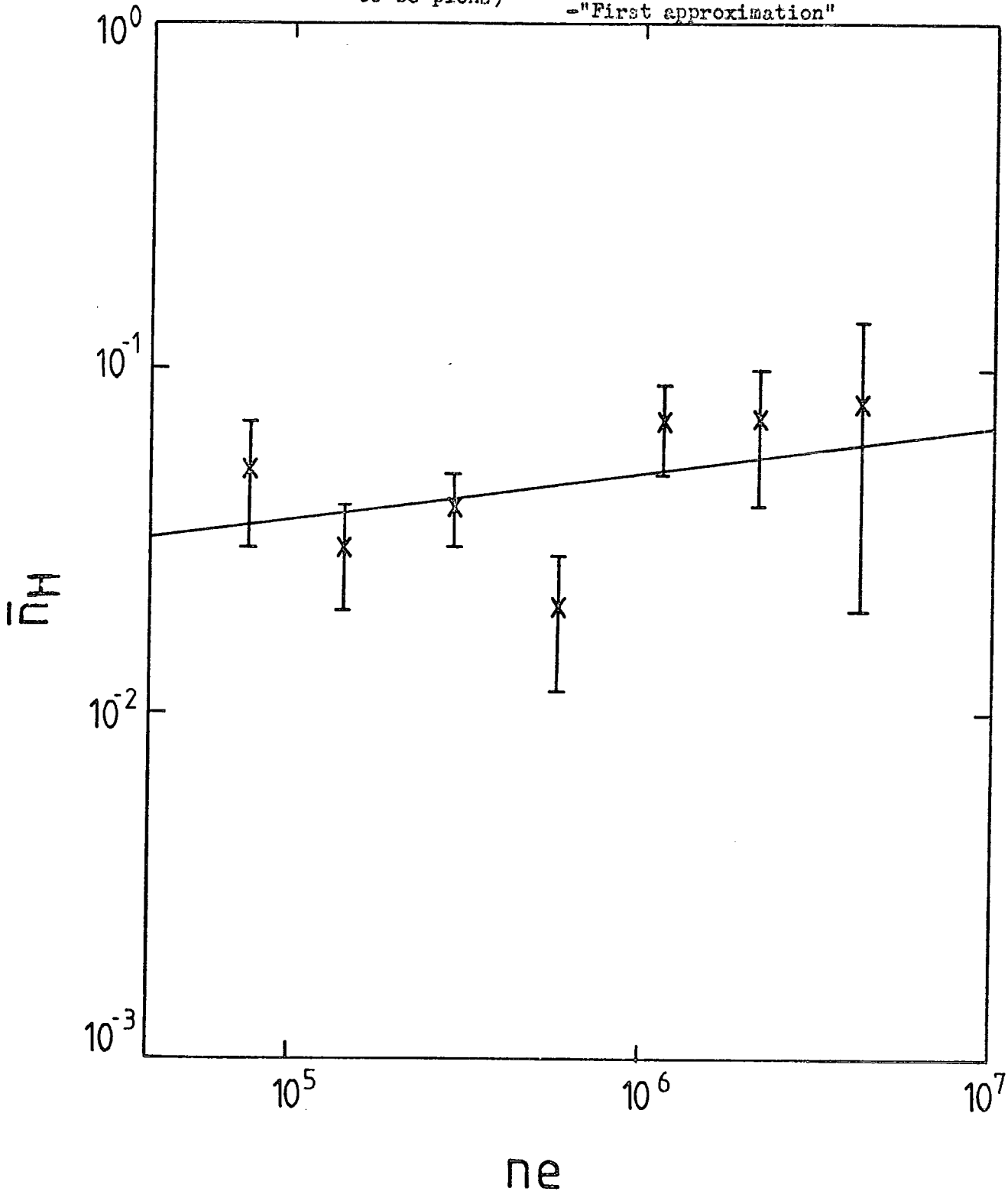

FIG.11.9

Lateral distribution of hadrons with energies greater than 10 GeV normalised to $n_e = 3.10^5$.

-"First approximation" assuming $\bar{n}_h \propto n_e^{0.19}$.

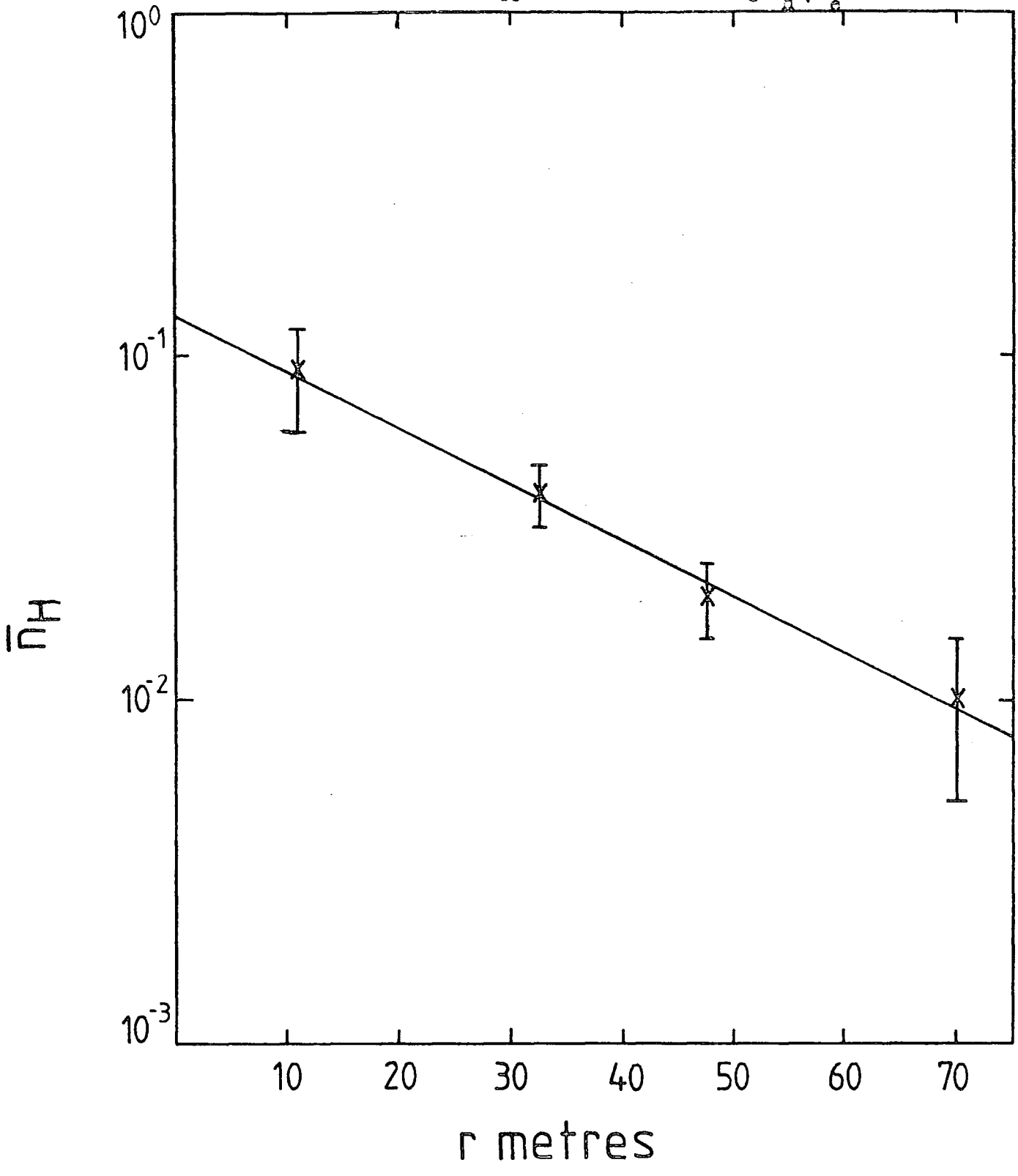

Mean core distance as a function of shower size range. Based on triggering at 2 pcls./m^2 and taking a mean to represent the range.
- Used for weighting in successive approximation fits for hadron distribution.

FIG.11·10

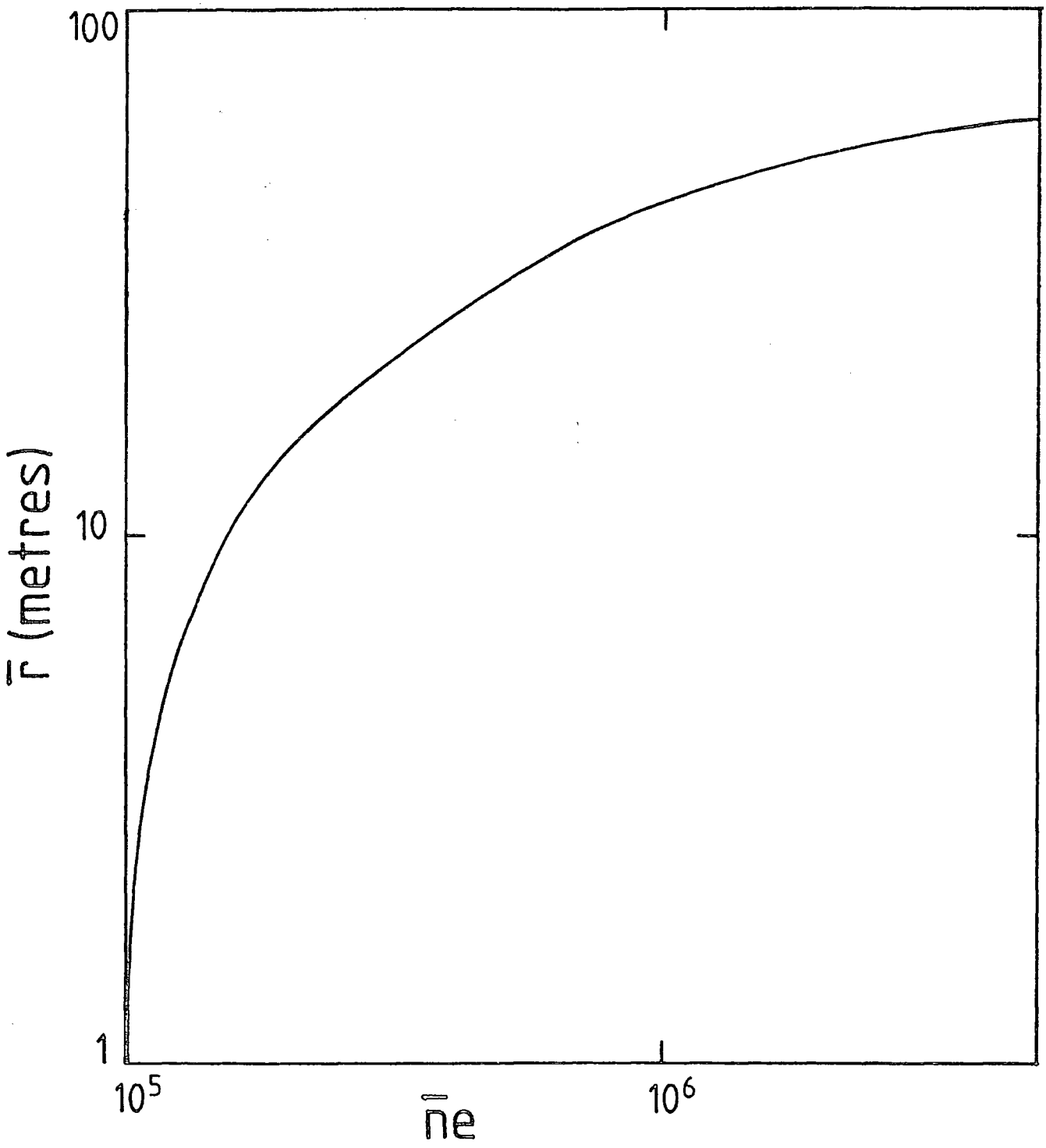

which is in close agreement with the accepted relation:

$\bar{N}_H \propto Ne$

Fig. 11.12 shows the final lateral distribution, normalising to a shower size of 3.10^5 particles using equation 11.3.

This yields the relation:-

(11.4) $\bar{N}_H$ (E>10 GeV) = 0.5 exp(-0.07r)

Also shown in Fig. 11.12 is the lateral distribution of hadrons with energy greater than 50 GeV, normalised to a shower size of 3.10^5 particles using $\bar{N}_H$ (E>50 GeV)$\propto$ Ne. This data has a slightly steeper slope and regressional analysis yields the relation:-

(11.5) $\bar{N}_H$ (E>50 GeV) = 0.42 exp(-0.08r)

11.5 The energy spectrum of hadrons in showers

Table 11.2 summarises the number of hadrons observed in different energy intervals. All the data are presented assuming either all nucleons (column 'p' in Table 11.2) or all pions (column 'π' in Table 11.2). This latter assumption is, however, clearly untenable since none of the bursts in iron observed to be due to neutral particles can be due to pions.

In order to make a better estimate of the relative contributions of pions and nucleons to the energy spectrum - and hence a better estimate of the hadron energy spectrum - the number of bursts in iron due to charged and

FIG. 11·11

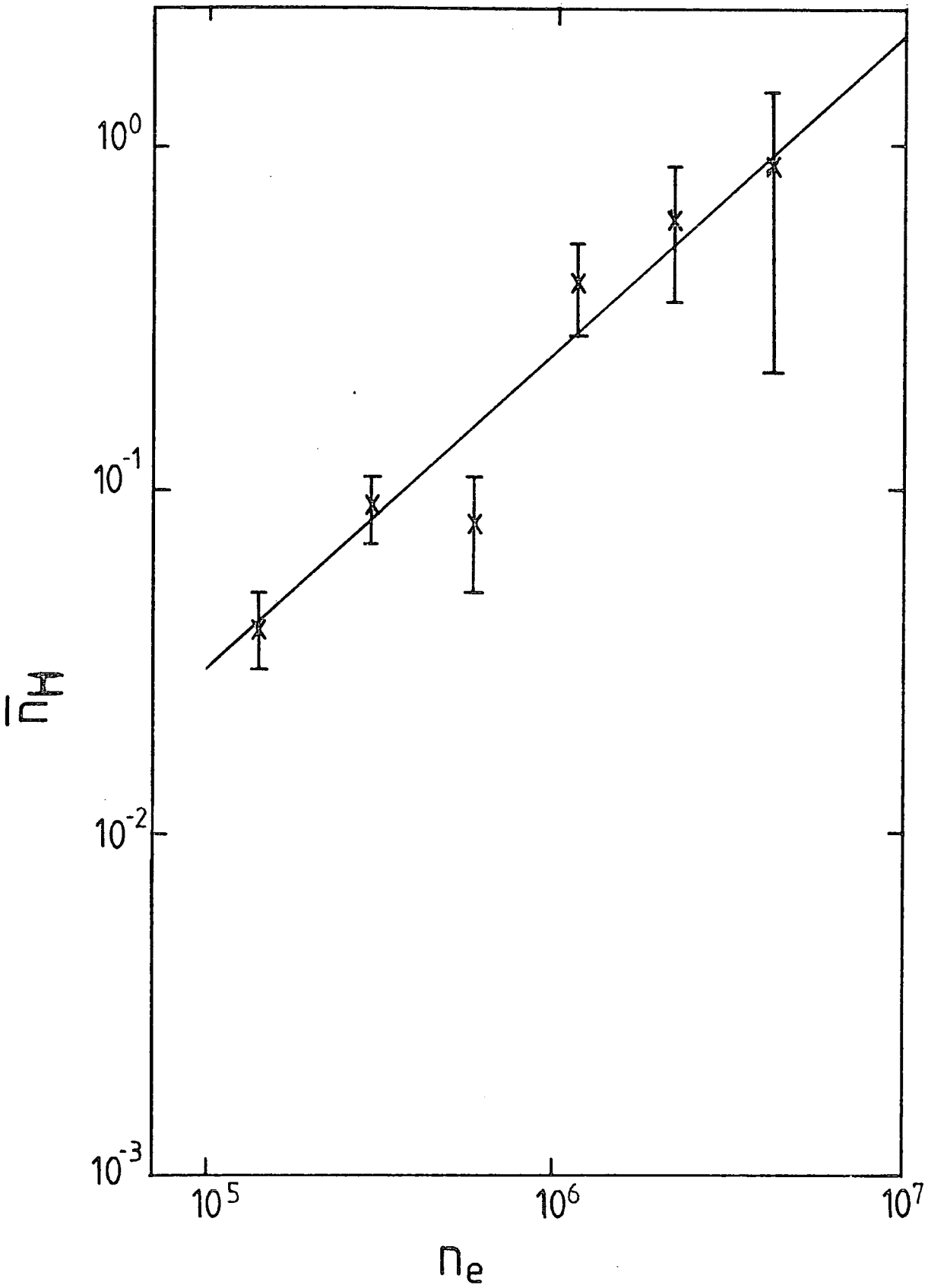

n_H versus n_e, where now the n_H values have been corrected by multiplying by the factor $1/\exp(-0.04\bar{r})$ where $\bar{r}$ is the mean core distance for each shower size range.

FIG.11·12 Lateral distribution of hadrons of energy greater than E GeV.

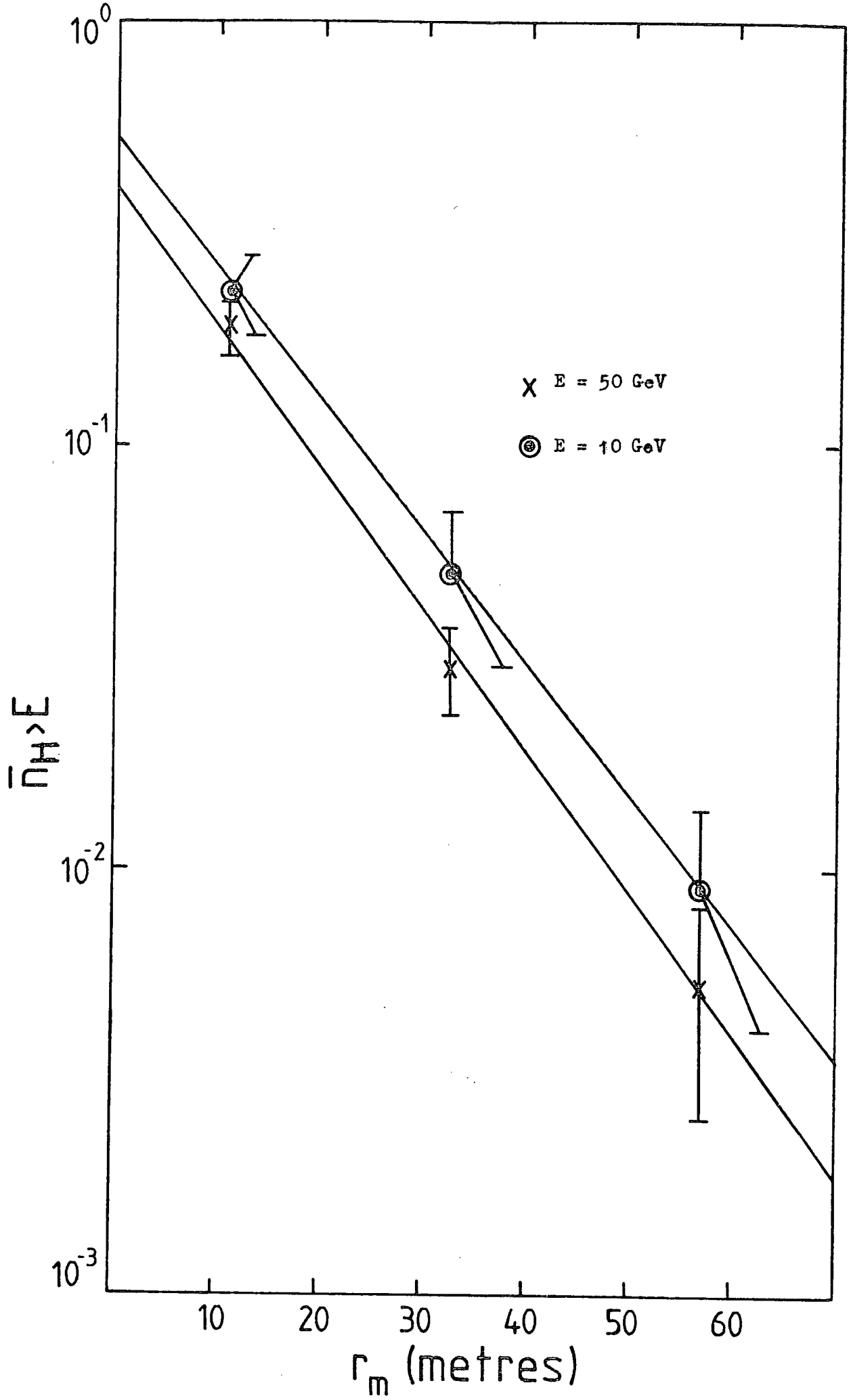

due to neutral particles can be utilised.

If we assume that the number of protons equals the number of neutrons in the sea-level cosmic radiation, then by measuring (from Table 11.2) the ratio of the number of bursts due to charged hadrons in iron to the number of bursts due to neutral hadrons in iron, we can say (ignoring kaons)

$$(11.6) \quad \frac{\Omega p + \Omega \pi}{\Omega n} = 3.5$$

where this ratio is 3.5 and Ωp is the number of protons, $\Omega \pi$ the number of pions, Ωn the number of neutrons responsible for all the bursts produced in the iron.

Assuming $\Omega p = \Omega n$ we can deduce

$$(11.7) \quad \frac{\Omega \pi}{\Omega p} = 2.5$$

$$(11.8) \quad \text{and} \quad \frac{\Omega \pi}{\Omega p + \Omega n} = 1.25$$

Figs. 11.13a), b) and 11.14a), b) show the observed integral energy spectrum of hadrons which interact in the lead or the iron respectively. The subscripts a), b) refer to the assumptions all nucleons or all pions respectively.

Figs. 11.15 and 11.16 are the integral energy spectra of hadrons interacting in the iron or lead respectively assuming that the ratio of the number of pions interacting to the number of nucleons is 1.25.

The scarcity of data makes a quantitative estimate of the slope of the spectrum difficult (due to the large error bars) however one useful

TABLE 11.2

SUMMARY OF ENERGY AND CHARGE OF ALL HADRON EVENTS

Energy GeV.	p					π				
	N_{pb}	N_{Fe}	C	N	U	N_{pb}	N_{Fe}	C	N	U
0 - 10	0	0	0	0	0	0	0	0	0	0
10 - 20	4	6	3	1	2	4	6	3	1	2
20 - 30	1	7	4	0	3	1	9	5	1	3
30 - 40	3	5	2	2	1	3	3	1	1	1
40 - 50	0	2	1	0	1	3	6	4	0	2
50 - 60	4	4	3	0	1	2	1	1	0	0
60 - 70	2	2	1	0	1	1	4	0	1	3
70 - 80	0	3	0	1	2	1	0	0	0	0
80 - 90	1	0	0	0	0	2	4	3	1	0
90 - 100	2	4	3	1	0	0	0	0	0	0
100 - 150	4	1	1	0	0	6	1	1	0	0
150 - 200	3	1	1	0	0	2	1	1	0	0
200 - 300	2	1	0	0	1	2	1	0	0	1
300 - 500	2	1	1	0	0	2	1	1	0	0
500 - 800	1	0	0	0	0	0	0	0	0	0
800 - 1500	0	0	0	0	0	0	0	0	0	0
>1500	1	2	1	1	0	1	2	1	1	0

KEY:

p = Energy assuming nucleon-induced burst
π = Energy assuming pion-induced burst
N_{pb} = Number of bursts in pb; N_{Fe} = Number of bursts in F_e
C = Charged hadron; N = Neutral hadron
U = Unknown charge on hadron

FIG. 11·13 Integral energy spectrum of hadrons which interact in the lead, a) assuming all are nucleons, b) pions.

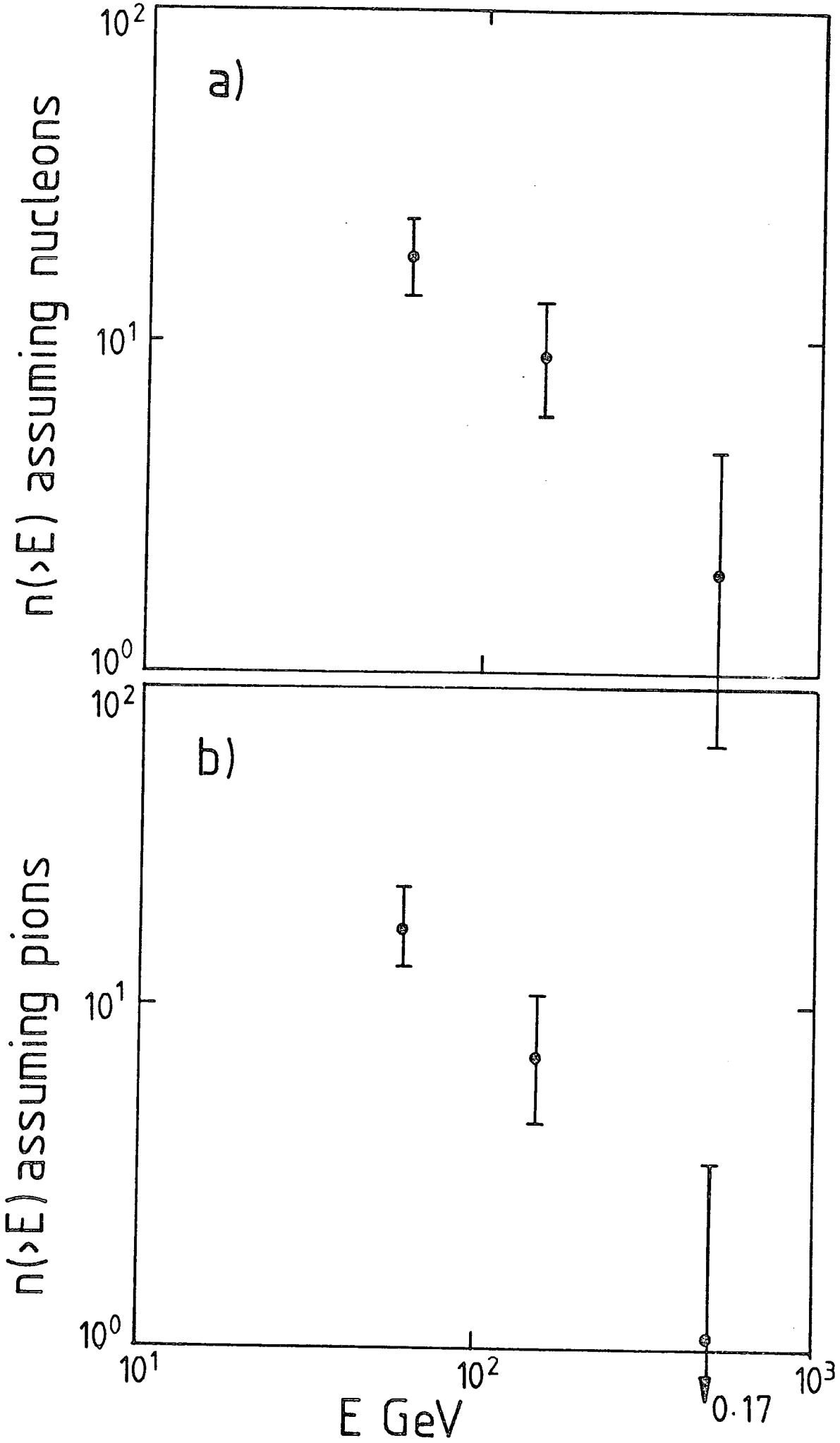

FIG. 11·14 Integral energy spectrum of hadrons which interact in the iron, a)assuming all are nucleons, b) pions.

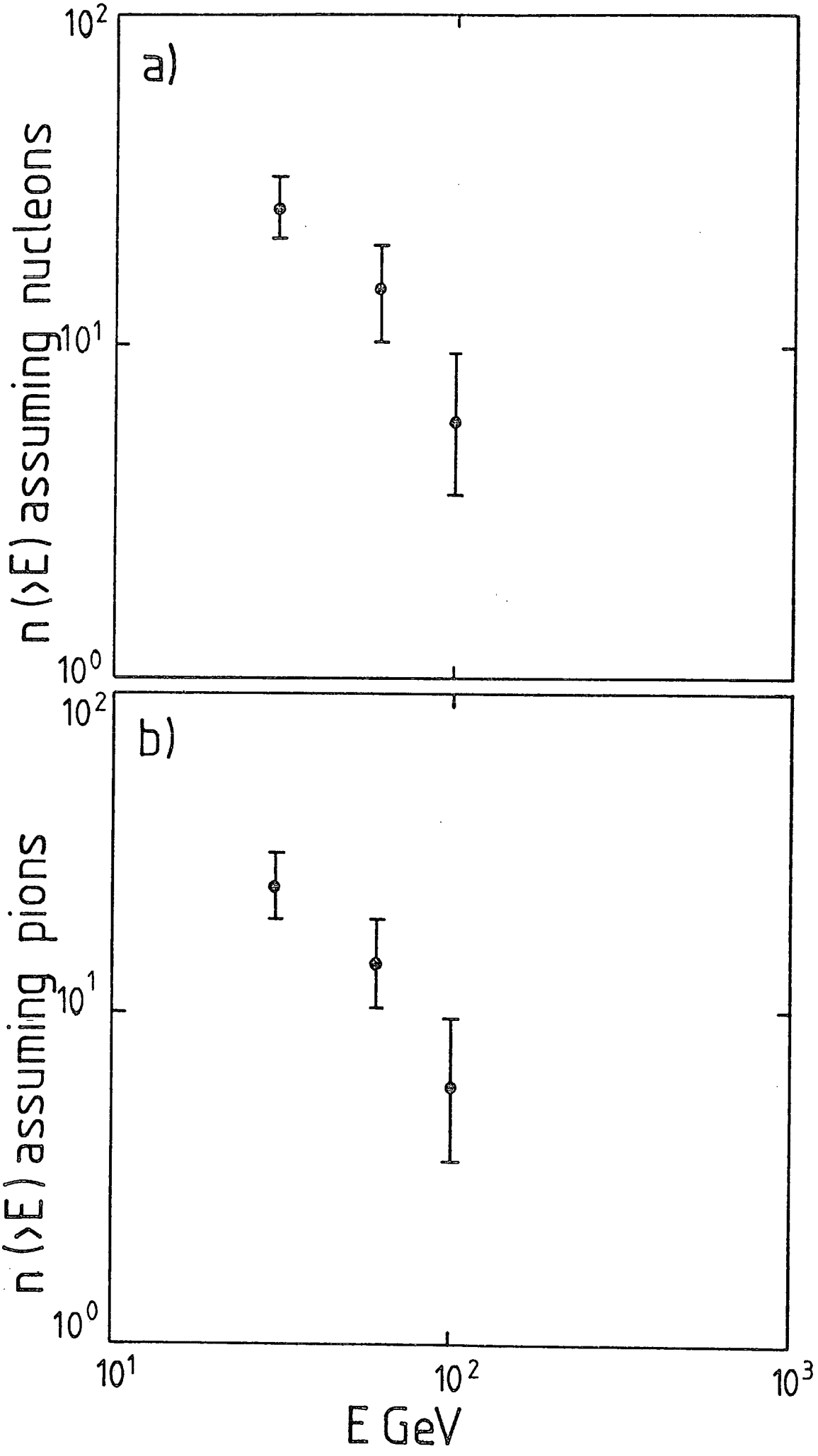

FIG. 11·15 Integral energy spectrum of hadrons that interact in iron, assuming $\frac{n_\pi}{n_{nuc.}}=1.25$

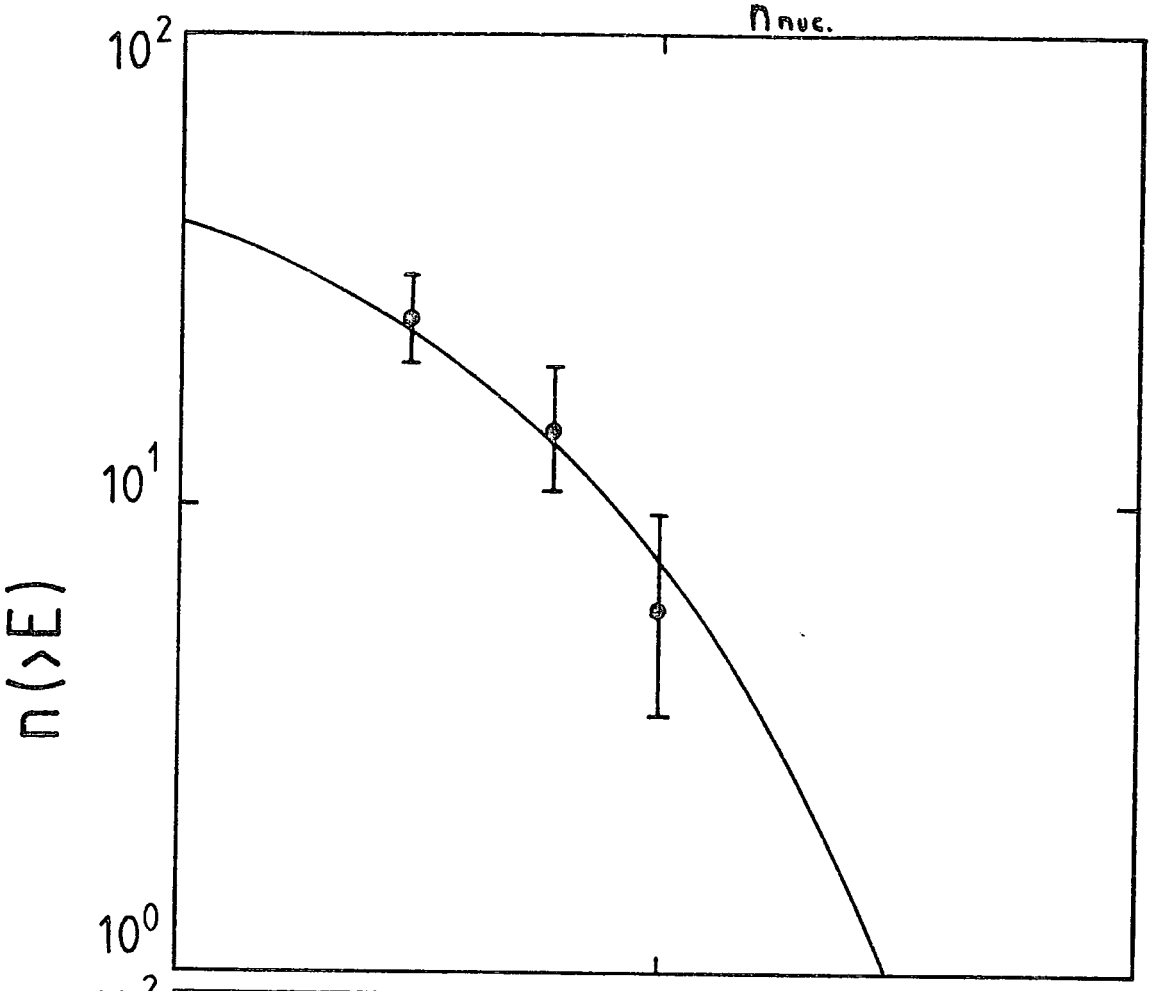

FIG. 11·16 Integral energy spectrum of hadrons that interact in lead, assuming $\frac{n_\pi}{n_{nuc}}=1.25$

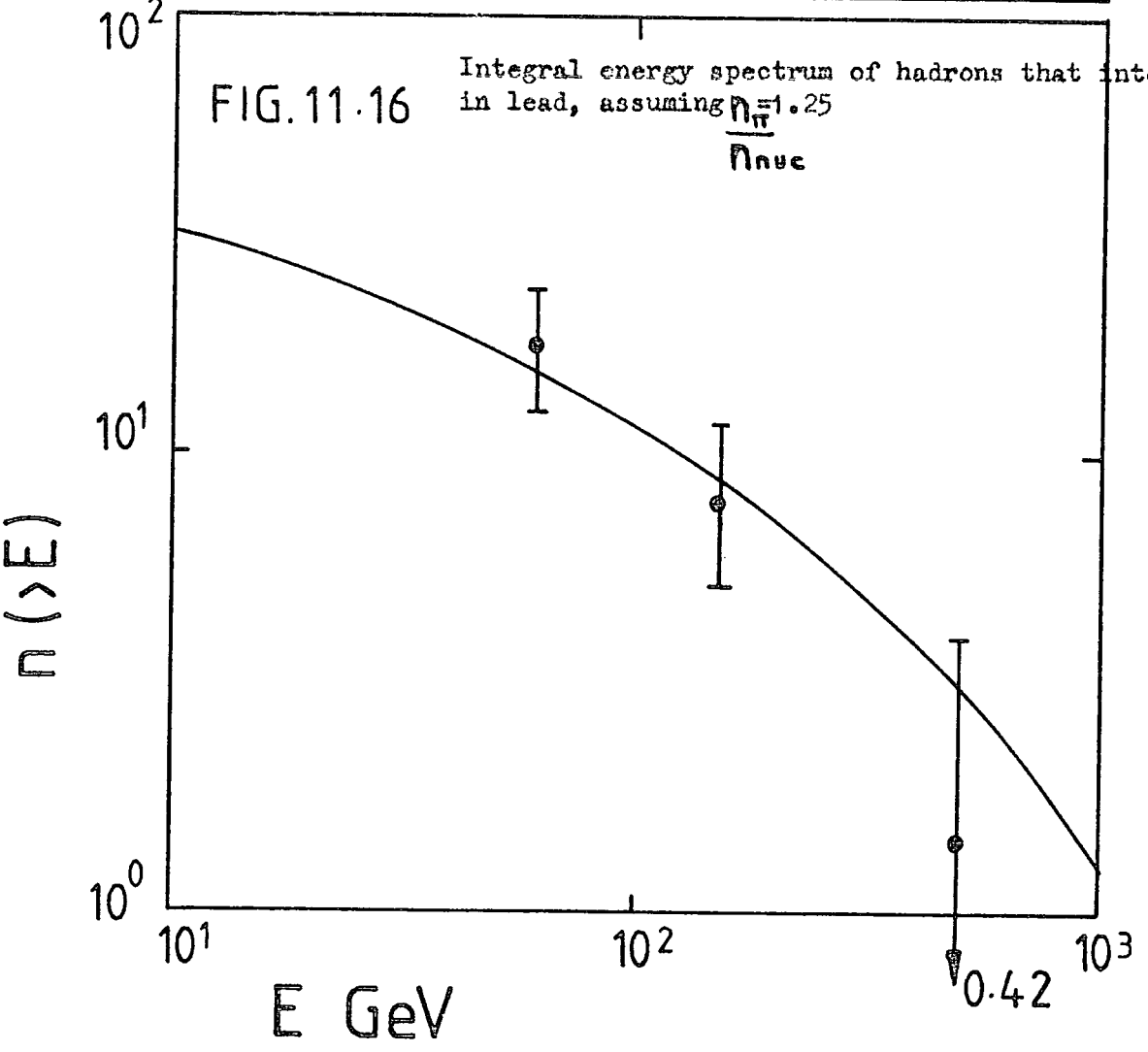

parameter that can be obtained is the median energy of the hadrons which interact in the iron and the lead, E^{Pb}_{med} or E^{Fe}_{med}.

$E^{Fe}_{med} = 40$ GeV, $E^{Pb}_{med} = 60$ GeV.

Since there were 39 interactions in the iron and 30 in the lead, the median energy of all the hadrons which interacted is the weighted mean 48.7 GeV.

11.6 The mean transverse momentum of the hadrons

The form (equn. 11.5) in which the observed lateral distribution of hadrons in air-showers is expressed can be derived from the assumption that the distribution in transverse momentum of the pions produced in the last nuclear interaction in the laboratory frame is:-

(11.9) $$N(p_\perp)dp_\perp = Ap_\perp e^{-p_\perp/p_o}dp_\perp$$

where $\langle p_\perp \rangle = 2p_o$ and A is a constant.

This last interaction is represented in Fig. 11.17 as being - on average - λ^{air}_{π} above sea-level.

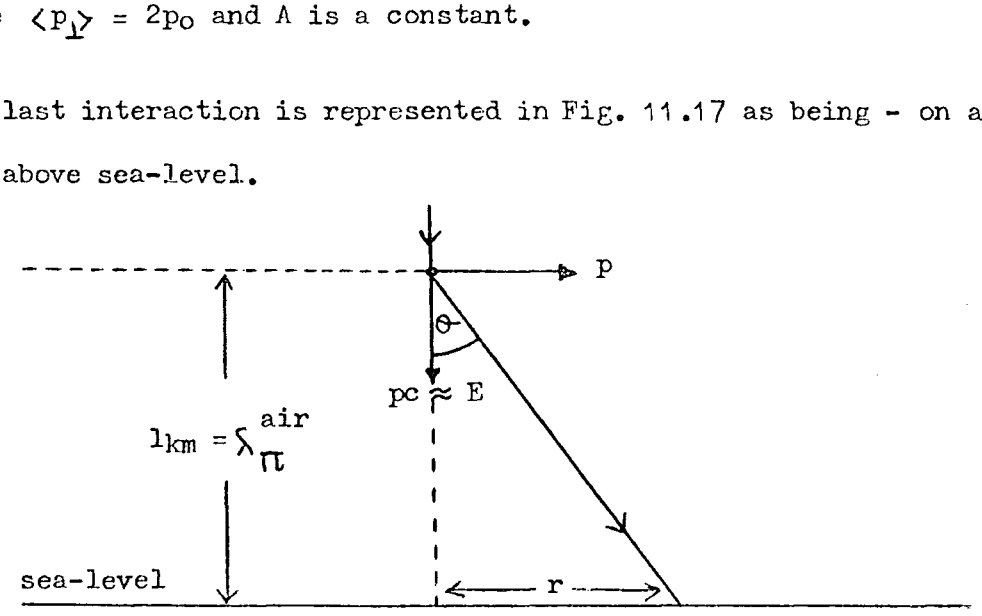

Fig. 11.17

Because of its transverse momentum, the detected pion arrives at some angle θ to the initial direction of travel of the interacting hadron. However typical values for $\langle p_\perp \rangle$ are ~0.3 - 0.5 GeV at interaction energies ~10^5 GeV and so θ is very small. We can also approximate the longitudinal momentum p to be equal to the energy of the pion i.e. pc = E (since $E = c(p^2 + p_\perp^2)^{\frac{1}{2}}$ and $p \gg p_\perp$).

Hence $\theta = \frac{p_\perp c}{E} = \frac{r}{l}$ where r is the distance from the core of the shower at which the pion is detected. Hence $\frac{dp_\perp c}{E} = \frac{dr}{l}$ and $N(p_\perp)dp \propto N(r)dr$.

So $N(p_\perp)dp_\perp = Ap_\perp e^{-p_\perp/p_0} dp_\perp$

$$= A \frac{Er}{lc} e^{-Er/p_0 lc} dr \frac{E}{lc}$$

So the density distribution $\Delta(r)dr$ of hadrons of energy E observed at one point at sea-level is

$$(11.10) \qquad \Delta(r)dr = \frac{N(r)dr}{2\pi r} = Ke^{-r/r_0}$$

where $K = A\left(\frac{E}{lc}\right)^2$ = constant

(11.11)

and $r_0 = \frac{p_0 lc}{E}$

Since we have a mixture of hadrons at sea-level we can substitute a weighted mean interaction length λ_{mix}^{air} for λ_{π}, which is 110 g.cm^{-2} (for λ_p^{air} = 97 g.cm^{-2} and λ_{π}^{air} = 120 g.cm^{-2}). We can also use E_{med} = 48.7 GeV for the median energy of the observed hadrons.

From Fig. 11.12 (and equn. (11.4))

$$r_0 = (14.3 \pm 3.6)\text{m}$$

$$\therefore \quad E.r = 0.70 \pm 0.36 \text{ TeV.m}$$

and $\langle p_\perp \rangle = 0.64 \pm 0.33$ GeV.

Figure 11.18

Figure 11.3 with present data included.

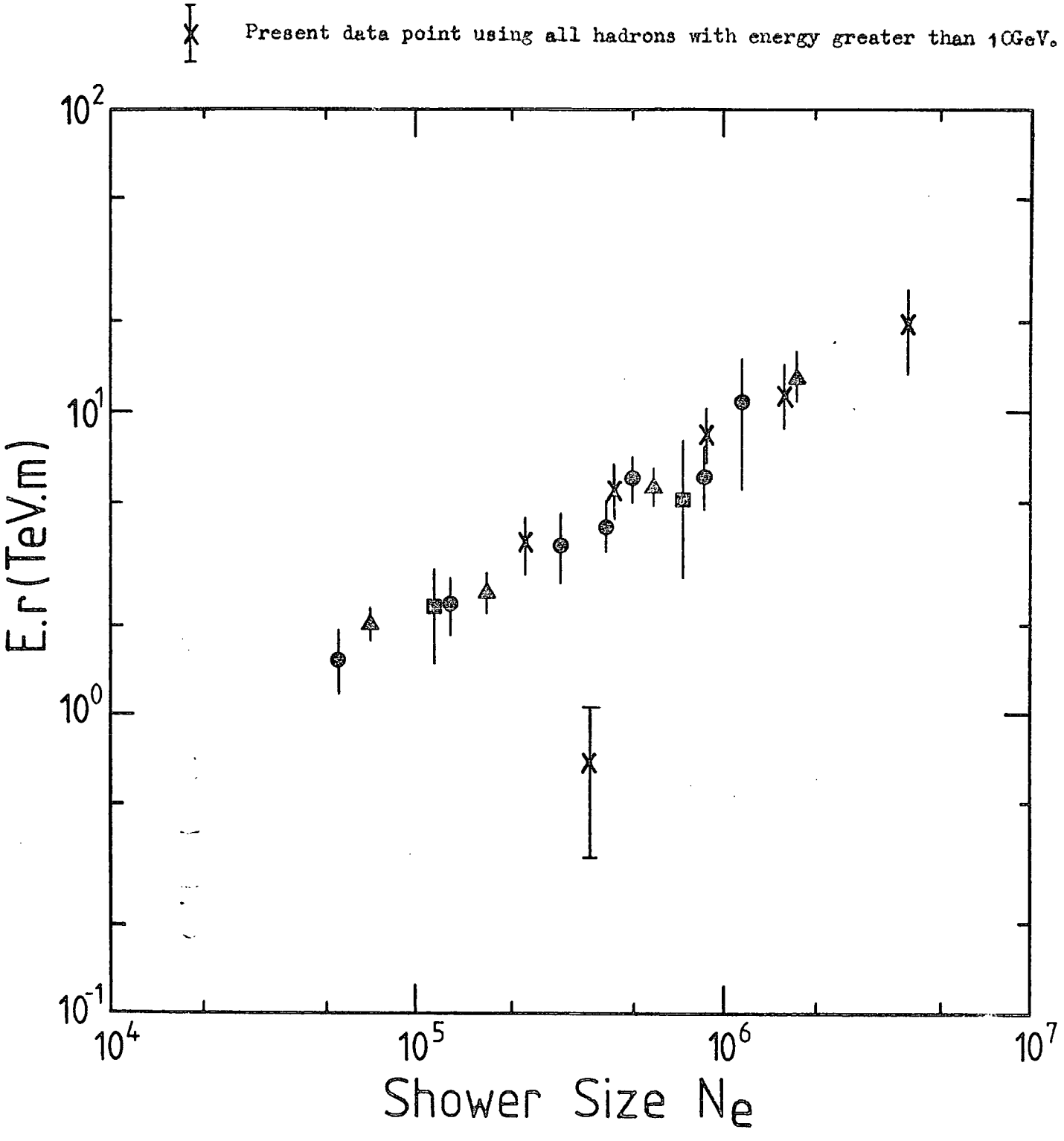

FIG. 11·18

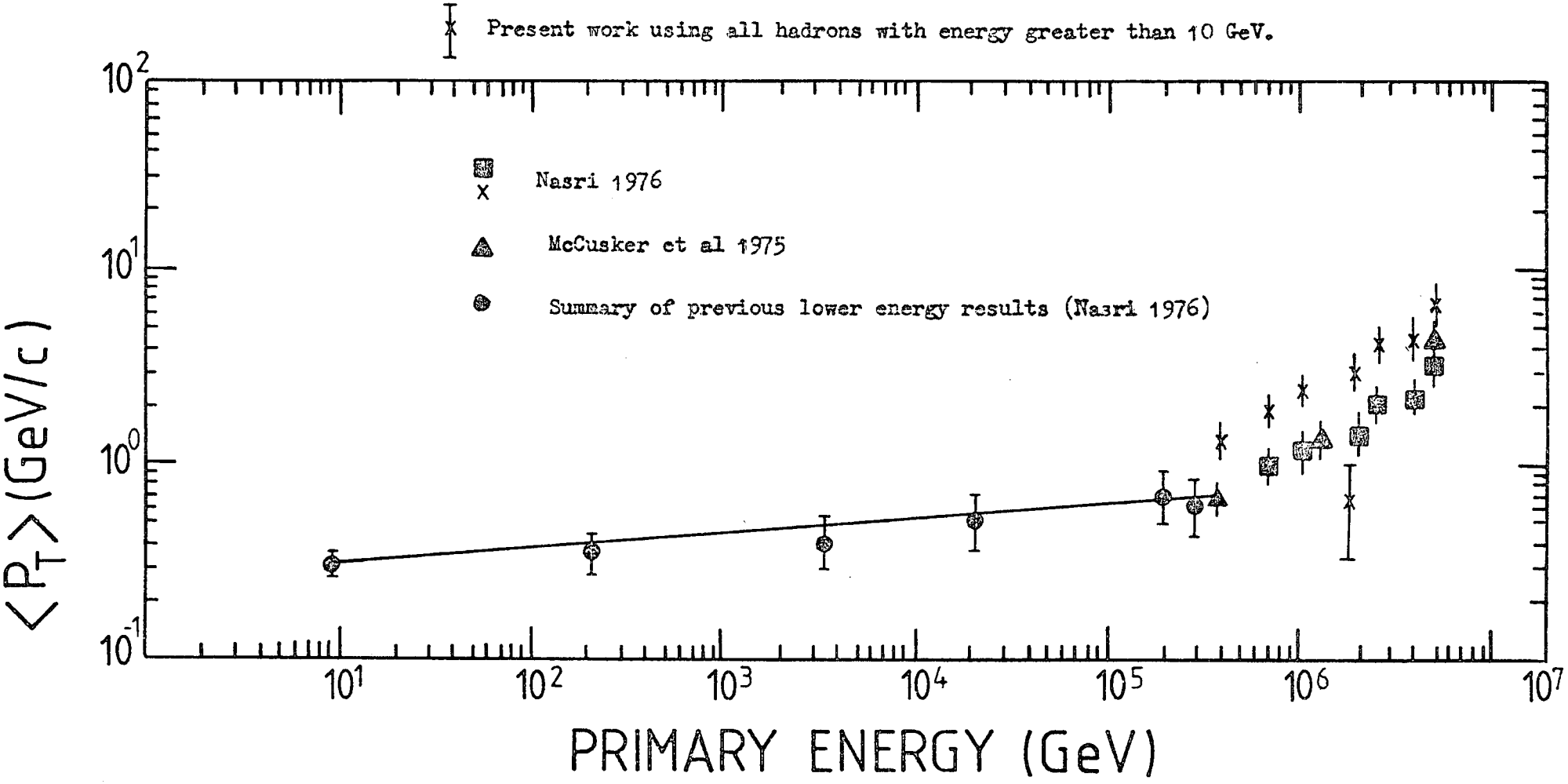

FIG. 11-19 Variation of mean transverse momentum p_T with primary energy. A comparison with previous work.

The error in r_o has been estimated from best and worst slope fits to Fig. 11.12.

These quantities have been measured by various techniques in both the laboratory and cosmic rays. Figs. 11.18 and 11.19 show comparisons of the present data with previous measurements.

The present measurement is an average over a range of shower sizes and hadron energies. This latter case being the probable cause of the disagreement between the present measurement and previous measurements.

11.7 The charge to neutral ratio of sea-level hadrons

The significance of this measurement has been discussed in Section 11.2. Fig. 11.20 is the same figure as Fig. 11.4 but with the present measurement (equation 11.6) added. The measurement agrees well with those of Vatcha and Sreekantan (1973) indicating further support to Gaisser's conclusion that accepted models of nuclear interactions cannot account for the observed ratio of charged to neutral hadrons in air-showers initiated by protons at energies greater than 10^6 GeV.

11.8 Summary and conclusions

The lateral distribution of hadrons in air-showers of median size 3.10^5 particles is slightly steeper for hadrons greater than 50 GeV than for

FIG. 11.20 Figure 11.4 with present data included.

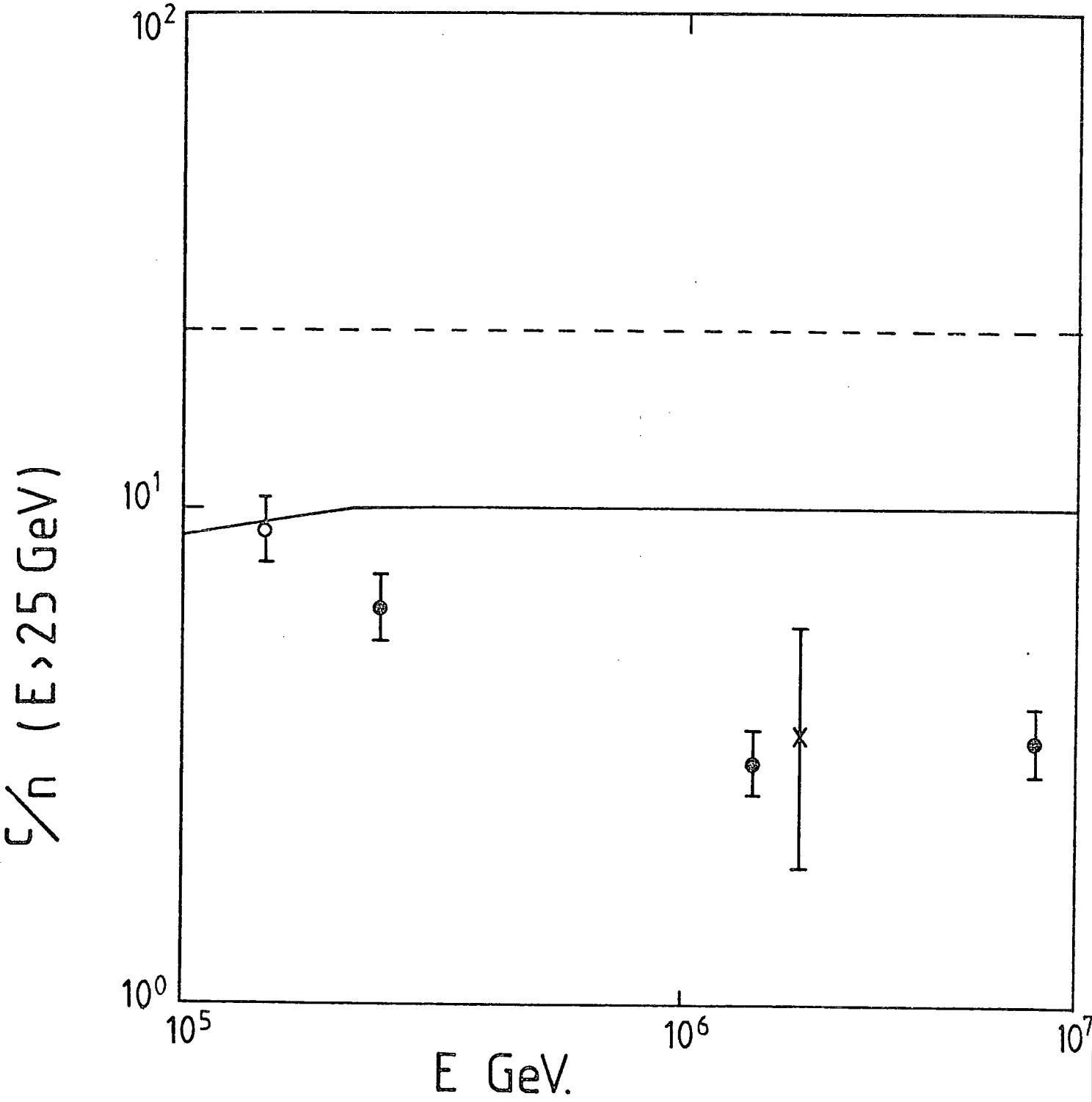

X Present work plotted at median shower size, which has been converted to primary energy according to Kempa (1976).

hadrons greater than 10 GeV. The number of hadrons was found to be proportional to the shower-size.

The median energy of the hadrons detected was 48.7 GeV, however, no evidence was found for these hadrons to have large mean transverse momentum. This is probably due to the fact that the measurement was an average of a large range of shower sizes and hadron energies.

The ratio of charged to neutral hadrons was found to be well below that predicted by normal production models indicating a change in the nuclear physics of interactions above 10^6 GeV.

CHAPTER 12

SUMMARY AND CONCLUSIONS

The flash-tube chamber has been shown to be an adequate instrument for investigating high energy phenomena associated with sea-level cosmic radiation. However, its limitations can be easily superceded by operating it in conjunction with an extensive air-shower array.

The early work found no evidence for a sudden decrease in ionising power of very fast particles, as predicted by Garibyan from transition radiation theory (see Chapter 3). A study of the incoherent component of the cosmic radiation found no evidence for other than a smoothly falling energy spectrum between 7.10^2 GeV and 5.10^3 GeV of slope 2.7 (Chapter 4).

A phenomenon partly due to the poor resolution of the instrument has been intensively investigated (Chapter 5) as possible evidence for the existence of highly charged particles in the sea-level cosmic radiation. An alternative explanation for these events has been proposed, based on the narrowing effects of the nuclear cascade on young nuclear-electromagnetic showers in dense targets.

Experiments concerned with the use of the flash-tube chamber in conjunction with an air-shower array are described in later chapters.

Of particular interest are the results of Chapter 9 which indicate, from a small sample of air-showers however, the existence of precursors to air-showers with arrival times in the range 20 to 100 μs before the arrival of the air-shower. These could be interpreted as faster than light particles created in the first few interactions of the primary cosmic ray particles,

however, more extensive observations are necessary to confirm such a contentious conclusion.

Chapter 10 is concerned with those measurements on muons in air-showers that can be undertaken with a flash-tube chamber used in conjunction with an air shower array.

The measurement of the lateral distribution of muons in air-showers indicates a strong divergence from previous work on low energy muons with a 50% excess of muons at distances from the core greater than 30 m. The possibility that this is purely an instrumental effect, due to the large error in core location (σ = 9.2 m) cannot be discounted. However, this would imply that the present arrangement is only useful for investigating air-shower structure upto 30 m. from the core.

The study of muon grouping indicated very strongly that the muons at densities > 1 m^{-2} were coherently grouped, however not until we reached densities > 2 m^{-2} does this show itself as a marked preference for a particular separation.

The final study on hadrons in air-showers showed that the number of hadrons is proportional to shower size. The lateral distribution of hadrons > 50 GeV was found to be slightly steeper than for hadrons > 10 GeV, however no evidence was found for hadrons of median energy 48.7 GeV having large transverse momentum.

The ratio of charged to neutral hadrons was found to be well below that predicted by normal production models.

To summarise the measurements on muons and hadrons in showers it might be said that the present arrangement provides convincing results only in regions of high particle densities, i.e. < 30 m. from the core. However despite

these limitations three investigated results have emerged, the possibility of the existence of precursors to air-showers, the non-random spacing of muons in air-showers at densities $>1\ m^{-2}$, and the very low ratio of neutral to charged hadrons in air-showers. All these indicate the probability of a change in the nuclear physics of interactions above 10^6 GeV.

APPENDIX I

The question of Cerenkov radiation from a charged tachyon

Let us first summarise the tachyon parameters relevant to a discussion of Cerenkov radiation:-

Velocity = $v > c$;

Mass parameter = μ;

Energy $E = \dfrac{\mu c^2}{(v^2/c^2 - 1)^{\frac{1}{2}}}$;

Momentum $p = \dfrac{\mu v}{(v^2/c^2 - 1)^{\frac{1}{2}}}$;

The Frank - Tamm equation for the rate of energy loss via Cerenkov radiation for a particle of velocity v moving through a medium of refractive index $n(\nu)$ is:-

$$\frac{dE}{ds} = \frac{-z^2e^2}{c^2} \int \left(1 - \frac{c^2}{v^2 n^2(\nu)}\right) \nu d\nu \quad \text{for } n(\nu) > \frac{c}{v}$$

$$\frac{dE}{ds} = 0 \text{ for } n(\nu) < \frac{c}{v} \text{ .}$$

where Ze is the charge on the particle.

For subluminal particles ($v < c$), $n(\nu)$ becomes less than or equal to unity for frequencies much greater than the visible, hence avoiding an "ultraviolet catastrophe".

For a tachyon in a vacuum, $n(\nu) = 1$ and $v > c$; hence the above scheme will not work, and an assertion that no photon can carry enough energy away so that the tachyon's energy becomes negative has to be made.

This is a reasonable assertion since R.I.P. (the Re-Interpretation Principle) maintains that a negative energy tachyon would be interpreted as a positive energy antitachyon moving in the opposite direction. Hence if we did not maintain the above assertion, a tachyon once created would quickly develop into a state of oscillation between tachyon and antitachyon emitting an endless supply of energy in the form of high frequency radiation. Thus it would rapidly increase in velocity as its energy decreased to being an oscillator of infinite velocity emitting infinite amounts of high frequency radiation.

Hence, to avoid such an ultraviolet catastrophe in the case of a tachyon of energy E, the limits of integration in a vacuum must be 0 and E/h

$$\therefore \quad \frac{dE_{TACH}}{ds_{vac}} = \frac{-Z^2e^2}{c^2} \int_0^{E/\hbar} \left(1 - \frac{c^2}{v^2}\right) \nu \, d\nu$$

$$= \frac{-Z^2e^2\mu^2E^2}{2\hbar^2p^2} .$$

However, the upper limit of integration is not Lorentz-invariant. The energy of a photon transforms differently to the energy of a tachyon under a Lorentz transformation, the tachyon would preferentially move towards those frames of reference in which it lost most energy, resulting again in an ultraviolet catastrophe.

Ignoring this we are left with:-

$$\frac{dE}{ds} = -Z^2e^2u^2E^2/2\hbar^2p^2$$

which, for Z = 1, gives the distance s moved through by a tachyon as:-

$$s = \frac{2\hbar^2}{e^2\mu^2c^2}\left[E_i - E_F + \mu^2c^4\left(\frac{1}{E_F} - \frac{1}{E_i}\right)\right]$$

where E_i and E_F are the initial and final energy states.

Take, as an example, $E_i = \mu c^2$, $E_F = 1\,eV$ and assume $\mu c^2 \gg 1\,eV$

$$\therefore \quad s \simeq \frac{2\hbar^2c^2}{e^2E_F} \simeq 5.10^{-3}\ cm.$$

and $\frac{dE}{ds}$ at this energy $\simeq$ 200 eV/cm.

Some general points are worth making in conclusion:-

a.) Cerenkov radiation is emitted by relaxation of the polarised medium, polarised by the transverse component of the particle's electric field thus producing a cone in which the conditions for Cerenkov emission are satisfied. The effect is produced by the strong, nearly planar field of the particle normal to its direction of motion.

b.) The electric field of a tachyon is strongest along the direction of motion producing only a very narrow "Cerenkov cone" which could only polarise atoms in a very dense medium. The high density necessary to provide candidates for polarisation would also provide strong absorption of the radiation, and thus the Cerenkov effect should be negligible.

c.) Besides this narrow cone angle difficulty, if the medium under consideration is a vacuum, the effect must be caused by "polarisation of the vacuum" (into, presumably, virtual $e^+ - e^-$ dipoles).

However, the term "polarisation of the vacuum" is a technical term of quantum mechanics. It is used when the "vacuum", defined as a "sea" out

of which creation and annihilation operators create or destroy particles when considering a particular set of states, does not actually correspond to a real physical vacuum, but contains particles and fields whose effects can be felt by the considered system. For example, when considering the electron states in an atom, the vacuum as defined contains the nucleus which can be polarised because there is a net charge on the nucleus.

These physical considerations of a general nature as well as the difficulties of formulating a finite scheme for Cerenkov radiation mathematically suggests that the Cerenkov effect is not applicable to any tachyon in any medium.

APPENDIX II

Expected separation distribution for two muons through a one-dimensional detector

Let there be α muons per unit length, l being the length of the detector.

$\therefore$ Probability of a muon falling in the interval x, x + dx is

$$P(x, dx) = \alpha dx$$

Similarly the probability of a muon falling in the interval x + t, x + t + dt is

$$P(x + t, dt) = \alpha dt$$

Now assume that a muon falls at x, the probability that the second muon falls at distance t away (i.e. at x + t) is given by the probability of it not falling in between x and x + t multiplied by the probability of it falling in the interval x + t, x + t + dt.

Divide the interval t into a large number n of intervals δt, i.e. $n\delta t = t$

$\therefore$ $P_x(t)\delta t$ = Probability of there being a separation t, assuming one muon falls at x.

$$= (1 - \alpha\delta t)^n \alpha\delta t, \text{ but } \delta t = \frac{t}{n}$$

So, letting $n \to \infty$, i.e. $\delta t \to 0$

$$\left\lfloor_{t}^{\delta t \to 0} Px(t)\delta t = \left\lfloor_{t}^{\substack{n\to\infty \\ \delta t \to 0}} \left(1 - \frac{\alpha t}{n}\right)^n \alpha\delta t \right.\right.$$

i.e. $Px(t)\, dt = \alpha e^{-\alpha t}\, dt$

But x can have any value from 0 to 1; however, if we require a second muon to fall at distance t away then x can only have any value from 0 to 1 - t.

$\therefore$ P(t) dt = Probability of there being a separation t

$$= \int_0^{1-t} P_x(t)\, dt.\, P(x)\, dx$$

$$= \int_0^{1-t} \alpha\, e^{-\alpha t}\, dt\, \alpha dx$$

$$= \alpha^2\, e^{-\alpha t}\, dt \int_0^{1-t} dx$$

$$\therefore\ P(t)\, dt = \alpha^2 (1 - t)\, e^{-\alpha t}\, dt$$

To determine α it is sufficient to consider the normalisation

$$\int_0^1 P(t)\, dt = 1$$

which gives the equation

$$\alpha l = \ln \frac{1}{2 - y}$$

which, solved numerically, yields

$$\alpha l = 1.8415$$

$$\therefore\ P(t)\, dt = \frac{3.39}{l^2}\ (1 - t)\, e^{-\alpha t}\, dt.$$

APPENDIX III

To show that R represents the ratio of the number of "slow" pions emitted in the backward cone to the number of pions emitted in the forward cone.

FIG III.I

Before collision.

In the centre of mass frame:

p or Π ⟶ ⟵ p

(incident hadron) (target nucleon)

After collision.

a.) In the centre of mass frame.

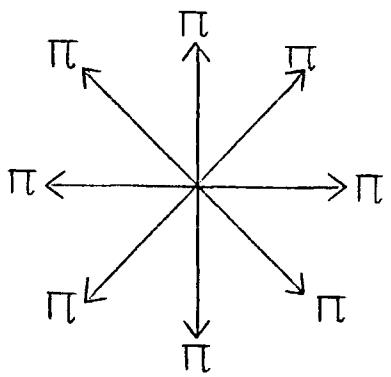

isotropic emission

backward cone forward cone

b.) In the laboratory frame.

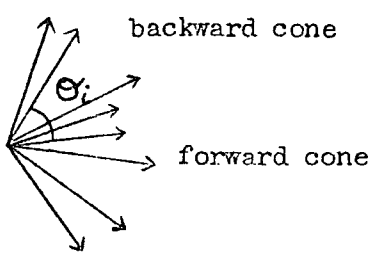

If θ_i is the angle the i^{th} particle makes with the direction of travel of the incident hadron, p_T^i and p_L^i the transverse and longitudinal momentum of the i^{th} particle in the centre of mass frame then

$$\tan \theta_i = \frac{p_T^i}{p_L^i}$$

The distribution in $\tan \theta$ can thus be calculated from the distributions in p_T and p_L viz.

$$\frac{1}{\sigma_{in}} \frac{d\sigma}{dp_T} = \frac{1}{\langle p_T \rangle} a \left(\frac{p_T}{\langle p_T \rangle} \right)^c \exp \left(\frac{-bp_T}{\langle p_T \rangle} \right)$$

$$\frac{1}{\sigma_{in}} \frac{d\sigma}{dp_L} = \frac{1}{\langle p_L \rangle} k \exp \left[-r \left(\frac{p_L}{\langle p_L \rangle} \right) - q \left(\frac{p_L}{\langle p_L \rangle} \right)^2 \right]$$

(Dao et al [1974])

where $a = 6.23$; $b = 2.37$; $c = 1.37$;

$k = 0.91$; $r = 0.83$; $q = 0.03$.

Let $\frac{p_T}{p_L} = z$

then the probability distribution of z, P(z) can be calculated from

$$P(z) = \int_0^\infty P_T(\nu z)\, P_L(\nu) |\nu| d\nu$$

where $P_T = P(p_T) \equiv c_1 \frac{d\sigma}{dp_T}$

$$P_L = P(p_L) \equiv c_2 \frac{d\sigma}{dp_L}$$

and c_1, c_2 are constants.

$$\therefore P(z) = Kz^{1.37} \int_0^\infty \nu^{2.37} e^{-(\alpha + \beta)\nu} e^{-\gamma\nu^2} d\nu$$

where $K = \dfrac{c_1\ c_2\ \sigma^2 \text{in a k}}{\langle p_T \rangle^{2.37} \langle p_L \rangle}$

$$\alpha = \frac{r}{\langle p_L \rangle} \; ; \; \beta = \frac{bz}{\langle p_T \rangle} \; ; \; \gamma = \frac{q}{\langle p_L \rangle^2}$$

This expression can be solved analytically if we assume that fluctuations to large values of p_L are rare (i.e. $>4\langle p_L \rangle$) in which case:-

$$P(z) \simeq K z^{1.37} \int_0^\infty \nu^{2.37}\ e^{-(\alpha + \beta)\nu}\ d\nu$$

$$= K.\ 2.37.\ 1.37.\ \Gamma(0.37)\ \frac{z^{1.37}}{(0.83/\langle p_L \rangle + 2.37z/\langle p_T \rangle)^{3.37}}$$

which for high energy interactions (>500 GeV, $\langle p_L \rangle > 10$ GeV/c

$\langle p_T \rangle \simeq 0.4$ GeV/c)

and $\tan\theta \gg 0.0125$

simplifies to

$$P(z) \simeq \frac{K'}{z^2}$$

where $K' = \dfrac{c_1\ c_2\ \sigma^2 \text{in. } 18.76\ \Gamma(0.37)}{(2.37)^{3.37}} \cdot \dfrac{\langle p_T \rangle}{\langle p_L \rangle}$

Hence $\underline{\underline{P(\tan\theta) \propto \cot^2\theta}}$

For isotropic emission in the centre of mass frame, half of the pions will lie in the forward cone, and half in the backward cone. The boundary of the two cones in the laboratory frame is given by

$$\tan\theta_b = \frac{1}{\gamma\ \text{c.m.}}$$

where γ c.m. = Lorentz factor of the centre of mass frame in the laboratory frame

$$= \sqrt{\frac{\gamma_L + 1}{2}}$$

where γ_L = Lorentz factor of the incident hadron in the laboratory frame

Since we have a range of values for γ_L it is simplest to use a value for γ c.m. typical of the energies of the majority of the events.

Taking γ c.m. = 25 gives $\tan \theta_b = 0.04$. Hence 50% of the pions will lie within $\tan^{-1}(0.04)$ of the core of the burst. This corresponds to less than one tube width in a stack of 8 layers of flash-tubes of average diameter 1.8 cms. and average vertical distance between centres of 1.9 cms. (i.e. F1a).

The method of calculating R was to count

a.) the number of flashes within the central 3 tube widths (corresponding to the forward core);

b.) the number of flashes within 5 tube widths on each side of these 3 (corresponding to the backward core).

Hence, the backward cone region was defined by the range of θ $\tan^{-1}(0.07)$ to $\tan^{-1}(0.3)$.

(The angles are calculated from the vertical distance from the bottom of the lead target to the bottom of F1a, and the defined number of tube widths from the core.)

Hence the fraction of events $F_{0.07}^{0.3}$ which lie in this region is given by

$$F_{0.07}^{0.3} = K' \int_{0.07}^{0.3} \cot^2 \theta \, d\theta$$

where $K' \int_{0.04}^{\infty} \cot^2 \theta \, d\theta = 0.5$

i.e. $K' \simeq \frac{1}{45}$

So $F_{0.07}^{0.3} = 0.25$

and $F_{0.04}^{0.07}$ 0.25

(See Fig III. II)

This latter fraction corresponds to the region of overlap between the inner and outer cone regions in the scanning process, and hence the fraction of pions falling here may be equally divided between the two regions.

Fig. III. II

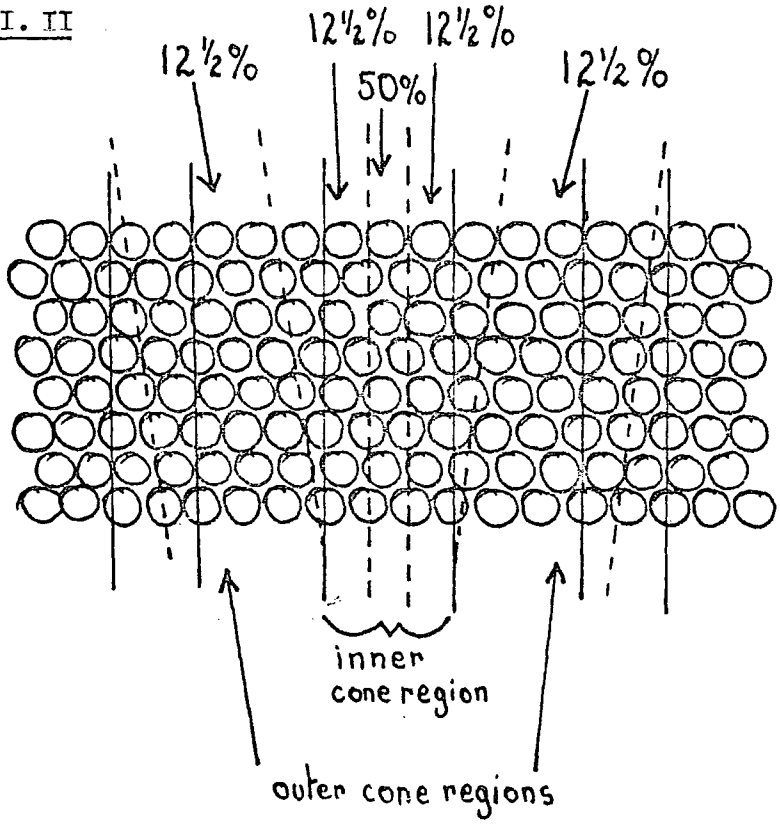

Hence:-

$$\frac{\text{Number of pions in outer cone region as defined by scanning}}{\text{Number of pions in inner cone region as defined by scanning}} = \frac{3}{5}$$

$$\frac{\text{Number of flash-tubes in outer cone region}}{\text{Number of flash-tubes in inner cone region}} = \frac{10}{3}$$

But considering the angular spread of the backward cone, the number of flash-tubes in the outer cone region available for flashing is only ~ 0.6 the number of flash-tubes present.

If we now consider the age parameter s of the subsequent e $-\gamma$ shower produced to be ~ 1, and that the number of electrons in each region thus corresponds to the number of pions in each region.

Then:-

$$\frac{\text{Number of electrons detected in backward core region}}{\text{Number of electrons detected in forward core region}} = 0.6 \times \frac{10}{3} \times \frac{3}{5} = 1.2$$

(i.e. a constant)

We thus expect any distribution in the ratio of the number of pions in the backward core to the number of pions in the forward core to be reflected in the distribution of $R = \frac{\text{Number of tubes flashed in the back. cone region}}{\text{Number of tubes flashed in the for. core region}}$ with a shift slightly to the right (i.e. to a higher value for the mean).

APPENDIX IV

Calculation of the Lorentz factor of a "fireball" which produces a highly collimated electron - photon shower.

In the centre of mass frame:-

Before collision:-

p or π ⟶ ⟵ p

(incident hadron) (one target nucleon)

After collision:-

a.)

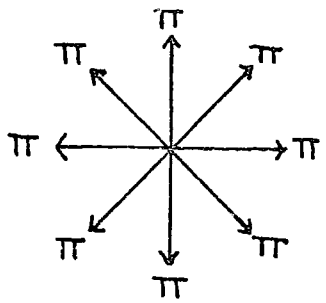

no fireball

b.)

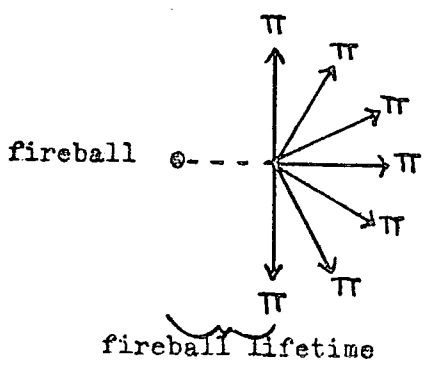

c.)

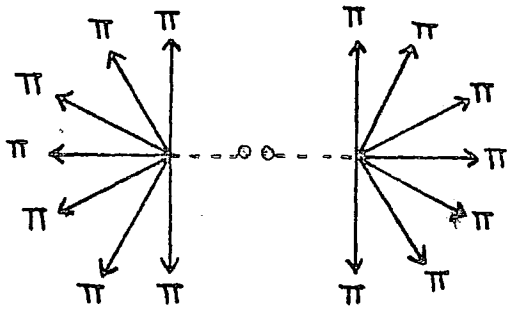

two fireballs

let γ_i = the Lorentz factor of the incident hadron in the laboratory frame

γ_c = the Lorentz factor of the centre of mass frame in the laboratory frame

γ_F = the Lorentz factor of the fireball in the laboratory frame

The case of one fireball:-

By definition the fireball must emit pions isotropically in its own rest frame. However in order to produce a highly collimated beam we shall assume that the backward cone in the fireball rest frame must transform into the forward cone region of the centre of mass frame (see diagram (b)).

Hence the slowest moving pions (emitted normal to the direction of travel of the incident hadron) must be travelling forward in the laboratory frame with a Lorentz factor equal to γ_c.

Since the subsequent electron - photon shower is due to the decay of the neutral pions produced in the nuclear interaction we shall only consider the dynamics of the π_o's. (The contribution from charged pions is small

since it relies on the products from their subsequent nuclear interactions which can be ignored in the case of a young shower.)

If the multiplicity of π_o's produced is n_o, the mean energy of each π_o is $\frac{Eo}{3n_o}$, where Eo is the energy transfer to the fireball from the incident hadron. This is the mean energy of each π_o in the laboratory frame, the corresponding energy in the centre of mass frame is

$$\gamma_c\left(\frac{Eo}{3n_o} - \beta_c p_o\right)$$

and $\gamma_F\left(\frac{Eo}{3n_o} - \beta_F p_o\right)$ in the fireball rest frame.

Considering again those pions emitted normally to the direction of travel of the incident hadron, they have only transverse momentum in the centre of mass frame, hence their total energy in this frame is

$$\left(p_T^2 + m_{\pi_o}^2\right)^{\frac{1}{2}}$$

where p_T = transverse momentum of π_o

m_{π_o} = mass of π_o

Now if we call the Lorentz factor of the fireball in the centre of mass frame γ_{Fc}, we have two expressions for the energy of one of these π_o's in the fireball rest frame, which can be equated

$$\text{i.e. } \gamma_F\left(\frac{Eo}{3n_o} - \beta_F p_o\right) = \gamma_{Fc}\left(\left(p_T^2 + m_{\pi_o}^2\right)^{\frac{1}{2}} - \beta_{Fc} p_T\right)$$

The problem of finding γ_F is now solved by using the kiremetical relationship:-

$$\gamma_{Fc} = \gamma_F \gamma_c (1 - \beta_F \beta_c)$$

substituting for β:-

$$\gamma_{Fc} = \gamma_F \gamma_c - (\gamma_F^2 - 1)^{\frac{1}{2}} (\gamma_c^2 - 1)^{\frac{1}{2}}$$

and putting in some numbers viz:-

$\beta_{Fc} \simeq 1$

$m_{\pi o} = 0.14$ GeV/c

$p_T = 0.4$ GeV/c (Feinberg [1972])

$n_o = (2.9 \log Eo + 0.03 Eo^{\frac{1}{2}}) A^{0.14}$ (Feinberg [1972],

$= 13$ Hayakawa [1969])

Eo = 500 GeV (an average value for burst size 500 particles)

$$p_o = \left\{ \left(\frac{Eo}{3n_o} \right) - m_{\pi o}^2 \right\}^{\frac{1}{2}}$$

Gives $\gamma_F = 147$

and $\gamma_{Fc} = 3$

A P P E N D I X V

An explicit derivation of the "Lovati formulae" for the projected angular distribution in a telescope of cosmic rays incident with an angular distribution $I(\phi) = I(0)\cos^{n}\phi$ where n is an integer greater than or equal to zero, showing the necessary modifications to the derivation and subsequent formulae necessary for the particular geometry used in the measurement of the incoherent hadron spectrum at sea-level with the Flash-Tube Chamber.

Figure V (i.) The symmetrical case

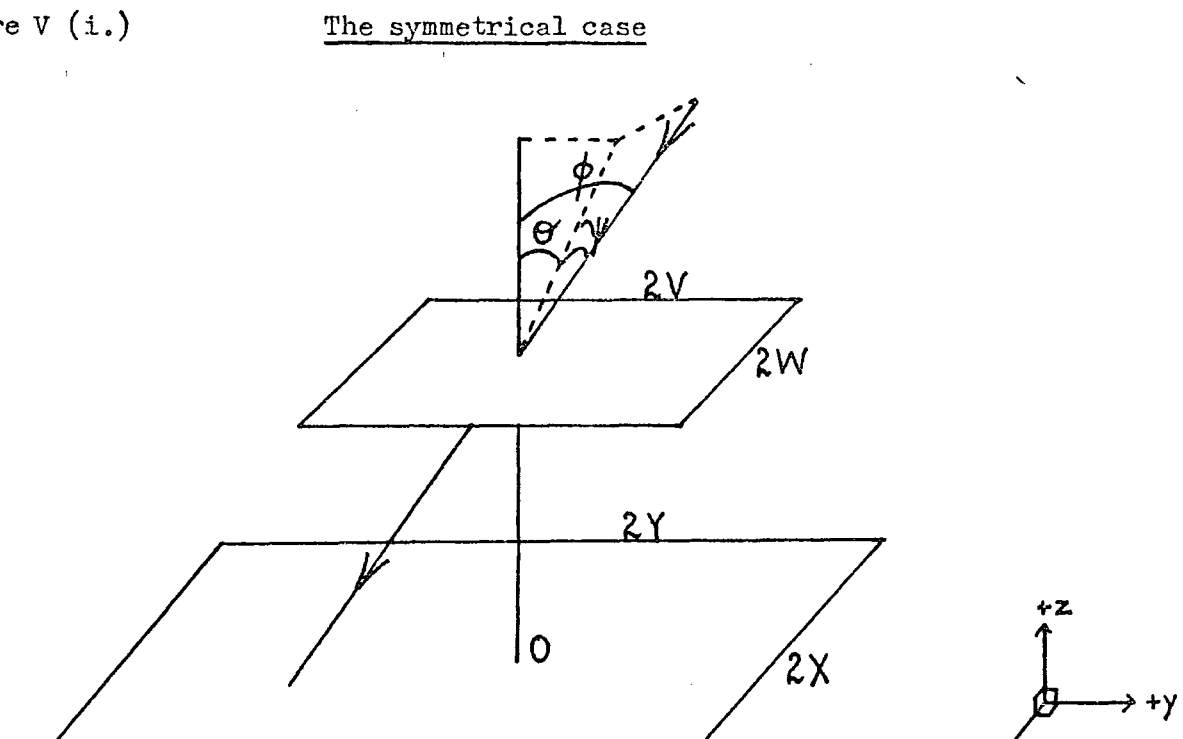

Total flux through both planes = $\iiint dxdy\ \cos\phi\ I(\phi)\ dw = F_n$

where w, w + dw is the total solid angle in which a particle arriving at zenith angle ϕ, $\phi + d\phi$ could travel.

Thus $dw = d\theta d\psi \cos\psi$.

If we assume $I(\phi) = I(0)\cos^n\phi$

then $F_n = I_o \iiint dx dy d\theta d\psi \cos^{n+1}\phi \cos^{n+2}\psi$

Figure V (iia.) Side view of planes when asymmetrically arranged with respect to the yz-plane through O

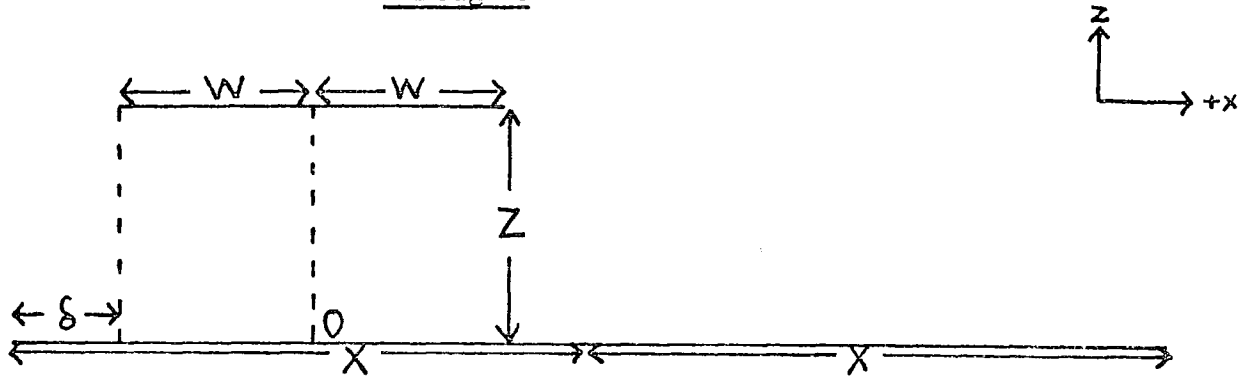

Figure V (iib.) Side view of planes when symmetrically arranged with respect to the yz-plane through O

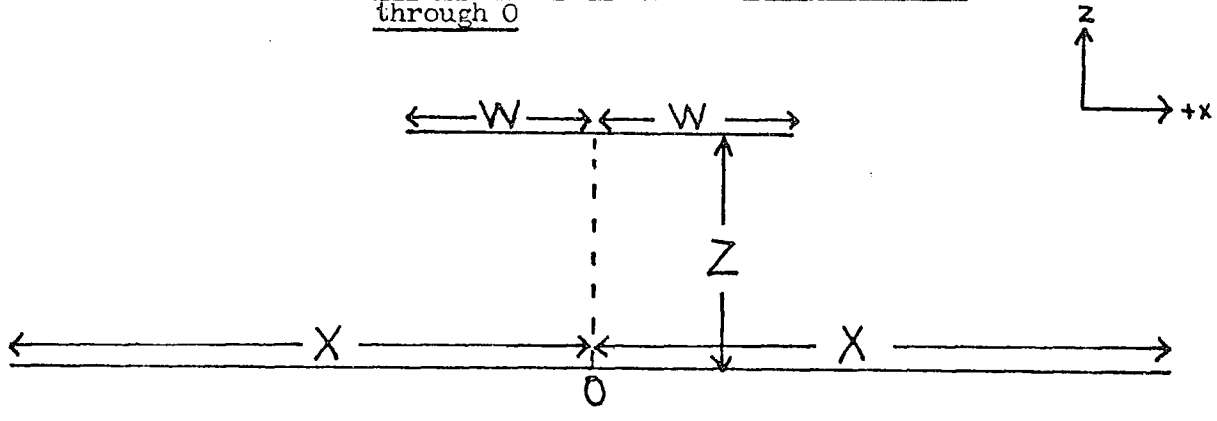

In both cases there is symmetry with respect to the xz-plane through O.

Hence we can limit ourselves to considering only the region

$$0 \leqslant \theta \leqslant \tan^{-1} \frac{Y + V}{Z}$$

i.e. $-V \leqslant y \leqslant Y - Z\tan\Theta$

But in order to take account of the situation (Fig. V (iia.)) of asymmetry with respect to the yz-plane through O we should consider the full 180° of the xz-plane through O.

i.e. $-\tan^{-1}\left(\frac{(W + x)\cos\Theta}{Z}\right) \leqslant \psi \leqslant \tan^{-1}\left(\frac{(W - x)\cos\Theta}{Z}\right)$

and for the symmetrical case (Fig. V (iib.))

$$-X \leqslant x \leqslant +X$$

whereas for the asymmetrical case (Fig. V (iia.))

$$-(W + \delta) \leqslant x \leqslant 2X - W - \delta$$

If we call the angular distribution observed in a yz-plane $N_n(\Theta)$

then $F_n = \int N_n(\Theta)d\Theta$

Now for the symmetrical case, with $\tan\Theta \leqslant \frac{Y + V}{Z}$

$$N_n(\Theta) = 2I_o \cos^{n+1}\Theta(Y + V - Z\tan\Theta)\int_{-X}^{+X} dx \int_{\psi 1}^{\psi 2} \cos^{n+2}\psi\, d\psi$$

where $\psi_1 = \tan^{-1}\left[\frac{(W - x)\cos\Theta}{Z}\right]$

$$\psi_2 = \tan^{-1}\left[\frac{(W + x)\cos\Theta}{Z}\right]$$

and for $n > 2$ we find

$$N^{symm.}_{n>2}(\Theta) = \frac{K\cos^n\Theta\, Z^{n+1}}{n(n+2)}\left(A_-^{-n/2} - A_+^{-n/2}\right) + \frac{n+1}{n+2} N_{n-2}(\Theta)\cos^2\Theta$$

where $K = 4I_o\ (Y + V - Z\tan\theta)$

$A^{\pm} = Z^2 + (W \pm X)^2 \cos^2\theta$

However for theasymmetrical case we have different limits for x, and we find for $n > 2$.

$$N^{\text{asymm.}}_{n>2}(\theta) = K \cos^n\theta\, Z^{n+1} \left(A_1^{-n/2} - A_2^{-n/2} - A_3^{-n/2} + A_4^{-n/2}\right) + \frac{n+1}{n+2} N_{n-2}(\theta) \cos^2\theta$$

where $K = 4I_o\ (Y + V - Z\ \tan\theta)$

$A_1 = Z^2 + (2W + \delta - 2X)^2 \cos^2\theta$

$A_2 = Z^2 + (2W + \delta)^2 \cos^2\theta$

$A_3 = Z^2 + (2X - \delta)^2 \cos^2\theta$

$A_4 = Z^2 + \delta^2 \cos^2\theta$

For $n \leqslant 2$ the calculations for $n > 2$ are inapplicable, the various calculations required for the cases $n = 0$, $n = 1$, $n = 2$ yield the following results.

$$N_0^{\text{symm}}(\theta) = \frac{1}{2} K \cos\theta \left[(X - W)\ \tan^{-1}\left(\frac{(W - X)\cos\theta}{Z}\right) + (X + W)\ \tan^{-1}\left(\frac{(W + X)\cos\theta}{Z}\right)\right]$$

$$N_1^{\text{symm}}(\theta) = \frac{1}{3} K \cos\theta \left[\frac{Z^2 + 2(W + X)^2 \cos^2\theta}{A_+^{\frac{1}{2}}} - \frac{Z^2 + 2(W - X)^2 \cos^2\theta}{A_-^{\frac{1}{2}}}\right]$$

$$N_2^{\text{symm}}(\theta) = \frac{1K}{16} \cos^2\theta\, Z^3\ (\ln A_- - \ln A_+) + \frac{3}{4} N_o(\theta) \cos^2\theta$$

The different limits for x for the asymmetrical case yield the following results:

$$N_0^{asymm}(\theta) = \frac{1}{4} K \cos\theta \left[(2W + \delta) \tan^{-1} \left(\frac{(2W + \delta)\cos\theta}{Z} \right) - \delta \tan^{-1} \left(\frac{\delta \cos\theta}{Z} \right) \right.$$
$$- (2W + \delta - 2X) \tan^{-1} \left(\frac{(2W + \delta - 2X)\cos\theta}{Z} \right)$$
$$\left. + (2X - \delta) \tan^{-1} \left(\frac{(2X - \delta)\cos\theta}{Z} \right) \right]$$

$$N_1^{asymm}(\theta) = \frac{\sqrt{2}}{6} K \cos\theta \left[\frac{2A_1 - Z^2}{A_1^{\frac{1}{2}}} + \frac{2A_4 - Z^2}{A_4^{\frac{1}{2}}} - \frac{2A_2 - Z^2}{A_2^{\frac{1}{2}}} - \frac{2A_3 - Z^2}{A_3^{\frac{1}{2}}} \right]$$

$$N_2^{asymm}(\theta) = \frac{1K}{32} \cos^2\theta Z^3 \left[\ln A_1 + \ln A_4 - \ln A_2 - \ln A_3 \right] + \frac{3}{4} N_o(\theta) \cos^2\theta$$

The above results are summarised in Table 4.3.

APPENDIX VI

Expected ratio of the number of nuclear interactions in lead to the number of nuclear interactions in iron

1. The case of normal incidence

If λ_H^T is the interaction length of a hadron H is a target T then the probability of finding the hadron at depth y is

$$e^{-y/\lambda_H^T}$$

Hence the probability of the hadron interacting in the interval

$$y,\ y + dy \text{ is } e^{-y/\lambda_H^T}\ \frac{dy}{\lambda_H^T}$$

Thus the probability P_H^T of a hadron interacting in a target thickness y^T is given by:-

$$P_H^T = \int_0^{y^T} \frac{1}{\lambda_H^T}\ e^{-y/\lambda_H^T}\ dy$$

$$= 1 - e^{-y^T/\lambda_H^T}$$

and $(1 - P_H^T)$ gives the probability of the hadron travelling through the target without interacting.

So if we have y^{Fe} cms of Fe situated below y^{Pb} cms of Pb.

$$\frac{\text{Number of nuclear interactions in Pb}}{\text{Number of nuclear interactions in Fe}} = \frac{P_H^{Pb}}{P_H^{Fe}(1 - P_H^{Pb})}$$

$$= \frac{1 - e^{-y^{Pb}/\lambda_H^{Pb}}}{e^{-y^{Pb}/\lambda_H^{Pb}}\ (1 - e^{-y^{Fe}/\lambda_H^{Fe}})}$$

2. The case of all angles of incidence between 0 and $\pi/2$

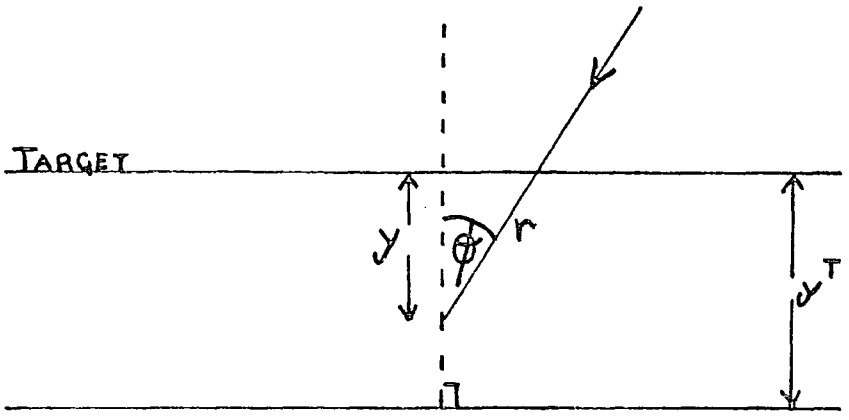

Assume that the intensity of hadrons at zenith angle ϕ is

$$I(\phi) = I(0)\cos^n\phi$$

Then the number $N(\phi, r)\,d\phi$ of hadrons which arrive at angle $(\phi, \phi = d\phi)$ to the vertical at distance r from their point of entry is:-

$$N(\phi, r)\,d\phi = I_o \cos^n\phi\, 2\pi \sin\phi\, d\phi\, e^{-r/\lambda_H^T}$$

The probability of interacting in the next dr is

$$N(\phi, r)\frac{dr}{\lambda_H^T} = N(\phi, y)\frac{dy}{\cos\phi\,\lambda_H^T}$$

Hence the probability of P_H^T of their being an interaction in the whole thickness y^T of the target is:-

$$P_H^T = \frac{\int_0^{\pi/2}\int_0^{y^T} e^{-y/\lambda_H^T\cos\phi}\frac{dy}{\lambda_H^T\cos\phi}\, I_o\cos^n\phi\, 2\pi\sin\phi.\cos\phi\, d\phi}{\int_0^{\pi/2} 2\pi\sin\phi.\cos\phi.\, I_o\cos^n\phi.\, d\phi}$$

Let $t = \cos\phi$

and noting that $\int_0^{\pi/2} \sin\theta . \cos^{n+1}\theta \, d\theta = \frac{1}{n+2}$

Then $P_H^T = \frac{1}{n+2} \int_0^1 \int_0^{yT} e^{-y/t\lambda_H^T} \frac{t^n}{\lambda_H^T} \, dy \, dt$

If we now make the substitution $a = \frac{y}{\lambda_H^T}$, $A = \frac{y^T}{\lambda_H^T}$

then $P_H^T = \frac{1}{n+2} \int_0^1 \int_0^A e^{-a/t} \, t^n \, dt \, da$

this is simply solved by an iterative procedure

i.e. if $I_n = \int_0^1 e^{-a/t} \, t^n \, dt$

then $I_n = \frac{e^{-a}}{n+1} - \frac{a}{n+1} I_{n-1}$

For protons we substitute n = 8 and for pions n = 5.5 which leads to the results

$P_p^{Pb} = 0.57$; $P_\pi^{Pb} = 0.46$;

and following the same argument as in Section 1

$P_p^{Fe} = 0.25$; $P_\pi^{Fe} = 0.25$.

APPENDIX VII

A discription of the calculations of the burst size-energy relationship for nuclear-electromagnetic cascades in the iron and lead.

VII i.) The nuclear interaction model

a.) The hadron is assumed to be incident vertically on the absorber.

b.) Hadron energy losses by ionization processes are neglected.

c.) The hadron is assumed to interact at successive depths t(measured in radiation lengths) according to the probability distribution:-

$$p(t)\,dt = \frac{1}{\lambda} e^{-t/\lambda}$$

where λ is the interaction length of the primary particle in radiation lengths.

d.) The inelasticity, K, for the pions is assumed to be unity. The inelasticity for protons is assumed to be 0.80 for interactions in the lead, and 0.63 for interactions in the iron (Jones et al [1969]).

e.) The mean multiplicity of secondary particles is assumed to be of the form:- $\bar{n}_s = 3.0\, A^{0.19}\, (KE)^{\frac{1}{4}}$

where A is the atomic mass of the absorber and E the energy of the incident particle. This equation is based on a number of surveys (e.g. Greider [1970],

Wdowczyk [1973]). All the secondary particles are assumed to be pions with the number of charged pions ($\pi^{\pm}$) being twice the number of neutral pions (π^{o}).

f.) It is assumed that half the secondary pions created moved in the forward cone in the C.M.S. system. In the laboratory system pions moving in the backward cone in the C.M.S. are assumed to have negligible energy. Each pion in the laboratory system has an average equal energy and the probability of a secondary pion having an energy in the region E, E + dE is $p(E)\,dE = e^{-E/E^1}\,\frac{dE}{E^1}$ where E^1 is the mean energy of the pions in the forward cone in the laboratory system.

ii.) The method of calculation

Each absorber is divided into four equal layers, and the incident primary particle is allowed to interact in each layer according to c.) above. The total number of charged pions with energy >1 GeV and the total number of neutral pions with energy $\geq$ 0.2 GeV is then calculated from f.) above. The mean energy for pions with cut off energy E_{cut} GeV can be calculated from:

$$\int_{E_{cut}}^{\infty} E\, e^{-E/E^1}\,\frac{dE}{E^1} \Bigg/ \int_{E_{cut}}^{\infty} e^{-E/E^1}\,\frac{dE}{E^1}$$ to be $(E_{cut} + E^1)$ GeV.

The neutral pions are then assumed to decay immediately into two photons with equal energy which then initiate an electron photon

cascade. The charged pions either interact again deeper in the absorber or emerge with no further interaction. The average depth $\overline{X}$ of the successive interactions is given by

$$\overline{X} = - \frac{x}{\exp(X/\lambda_{\pi} - 1)}$$

where X is the distance from the bottom of the absorber for the first interaction. (The first interaction is assumed to take place in the middle of the four equal layers.)

The nuclear cascade is terminated when all of the hadrons (primary and secondary) have either passed out of the bottom of the absorber or their energy has fallen below the cut off.

The energy cut off for $\pi^{\pm}$ of 1 GeV is based on the fact that the inelastic cross section for strong interactions of pions drops very sharply at this value (Hayakawa [1969]).

The energy cut off for π^{o} of 0.2 GeV is based on the assumption that photons created almost at rest do not contribute significantly to the electromagnetic cascade.

The photons arising from the decay of the neutral pions are assumed to give electron burst sizes below the absorber according to the transition curves of figure VII (i.) (Ivanenko and Samasudov, [1967a, 1967b]).

The results of these calculations (Saleh [1975], Parvaresh [1975], Nasri [1977]) are presented in Chapter 4 (figures 4.9a) and 4.9b)).

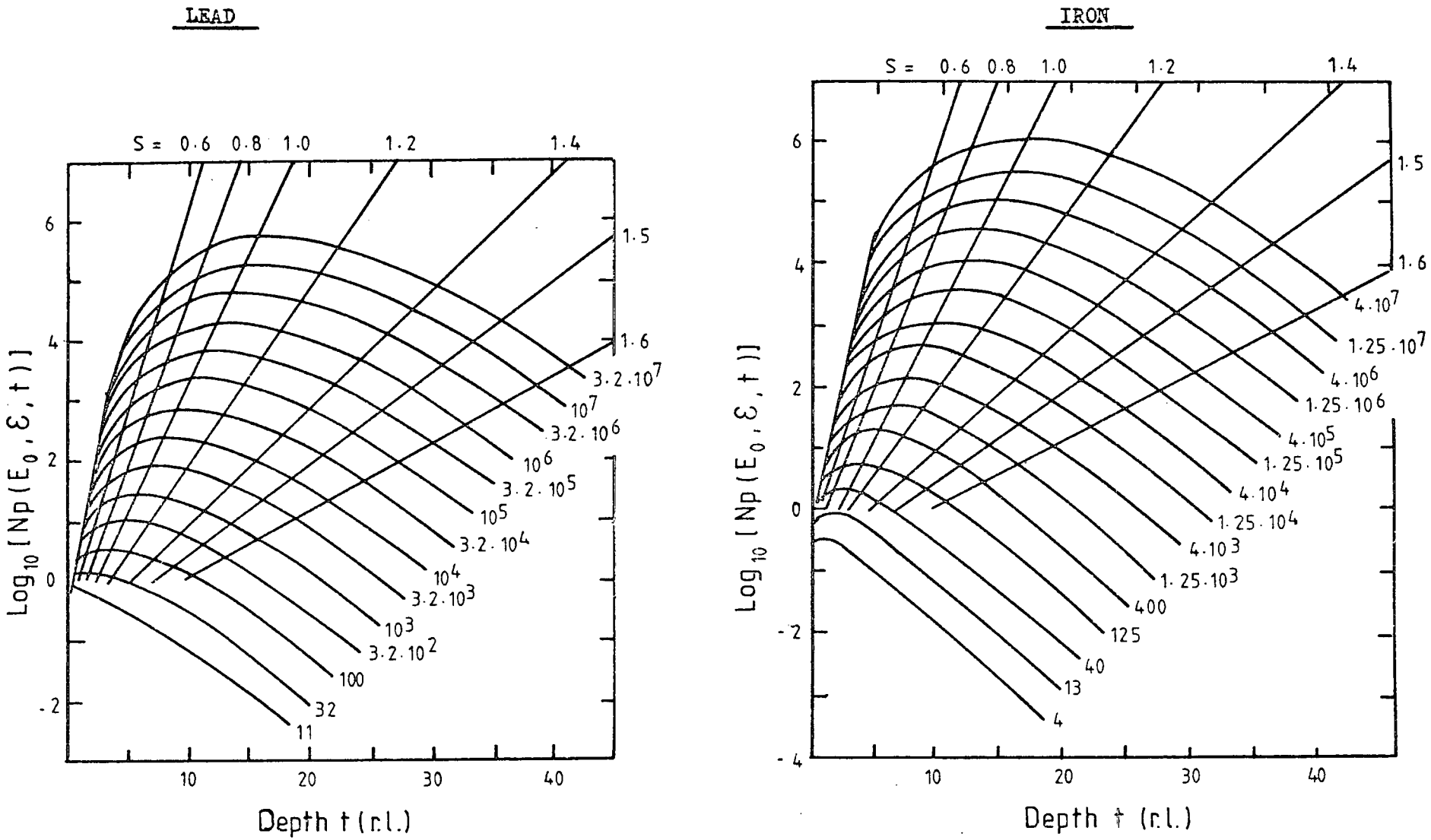

Figure vii(i) Transition curves for photon induced cascades in lead and iron according to Ivanenkov and Samusodov(1967a,1967b). The energies of the primary photon are in units of critical energy.

A more elegant treatment of the problem using a Monte Carlo rather than an average treatment has been performed by Cooper (Cooper [1974]). The same interaction model and photon transition curves were used by Cooper and an example of a comparison of the two methods is shown in figure VII (ii.). Clearly both techniques give similar results.

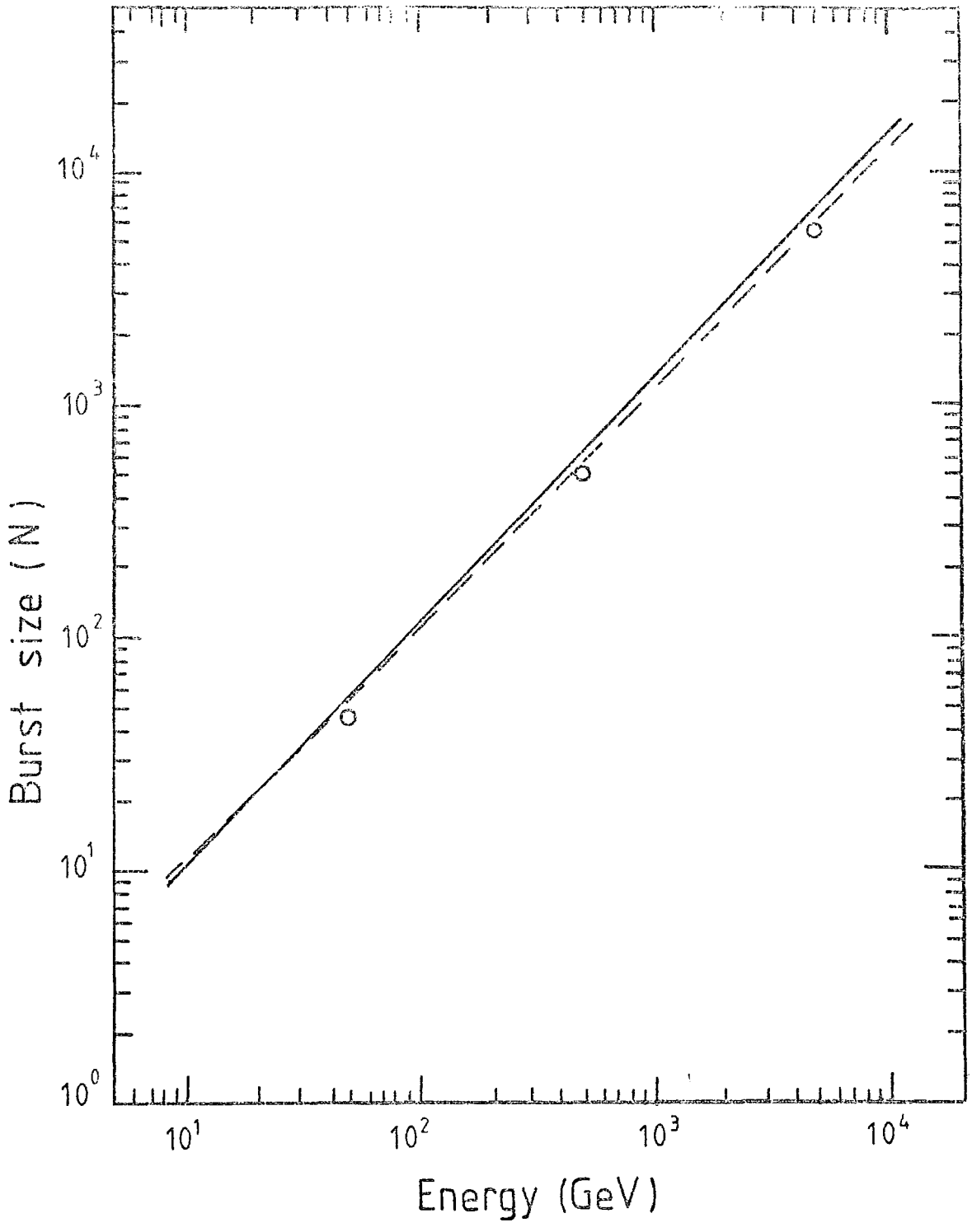

Figure vii(ii) A comparison between the average treatment method (solid line) and Monte Carlo method (broken line) in calculating the average burst size (N) produced by primary pions incident on 15 cms. of lead as a function of energy. The open circles represent Monte Carlo calculations for pions incident at a zenith angle of 30°. (After Cooper (1974)).

ACKNOWLEDGEMENTS

The author wishes to thank Professor A.W. Wolfendale F.R.S. for the provision of the facilities for this work, and for his constant interest and encouragement.

Dr. F. Ashton, who supervised the work described herein, is thanked for his invaluable guidance and advice both during and since the period in which this work was carried out.

Many members of the cosmic ray research groups at Durham have provided assistance in carrying out the work. In particular Drs. M.G. Thompson and A.C. Smith are thanked for the provision of the facilities of the Durham Air Shower Array. Messrs. M.W. Treasure and T.R. Stewart are especially thanked for their co-operation and guidance in the operation of the air-shower array. The members of the Flash-Tube Chamber group have provided helpful and stimulating discussions of all aspects of this work, in particular Drs. A. Parvaresh, A.J. Saleh, A.Nasri, H. Nejebat and Mr. J. Fatemi.

The technical staff of the Physics department are particularly thanked for their assistance in the reconstruction of the flash-tube chamber, especially Messrs. W. Leslie, K. Tindle and the staff of the engineering workshop . Mr. M. Lee is thanked for the production of all the photographs, Mrs. D. Hallam for her careful drawing of the figures and Mrs. S. Bloor for her painstaking work in typing out this thesis.

I should also like to thank my wife for her constant support and patience throughout the preparation of the thesis, and my parents for their encouragement.

Finally the Science Research Council is thanked for the provision of a Research Studentship.

REFERENCES

n.b. Publications by authors are chronologically listed where the author has been referred to on several occasions.

P.I.C.C.R. = Proceedings Of Internatiol Conference on Cosmic Rays

Aarons, M.E. and Sudarshan, E.C.G., (1968), Phys. Rev., 173, 1622.

Abrosimov, T., et al, (1960), Sov. Phys., JETP, 38, 100.

Aderholz, M., et al, (1974), Nucl. Inst. and Meth., 118, 419.

Allkoffer, et al, (1971), PICCR, (Hobart), 1314.

Alvager, T. and Kreisler, M.N., (1968), Phys. Rev., 171, 1357.

Amaldi, E. et al, (1963), Il Nuov. Cim., 28, 773.

Antippa, A.F., (1972), Il Nuov. Cim., 10A, 389.

Antippa, A.F. and Everett, A.E., (1971), Phys. Rev., D4, 2198.

Antippa, A.F. and Everett, A.E., (1973), Phys. Rev., D8, 2352.

Aseiken, V.S. et al, (1975), PICCR, (Munich), 8, 2960.

Ashton, F. et al, (1969), Izvest. Akad. Nauk., 33, 1817.

Ashton, F. et al, (1970), Acta. Phys. Hung., 29, Suppl.3, 29.

Ashton, F. et al, (1971), J. Phys. A, 4, 895.

Ashton, F. et al, (1971), Nucl. Inst. and Meth., 93, 349.

Ashton, F., "Cosmic Rays at Ground-Level", (1973), ed. A.W. Wolfendale, (Inst. of Phys., London).

Ashton, F., et al, (1973), PICCR, (Denver), 3000.

Ashton, F. and Parvaresh, A., (1975), PICCR, (Munich), 2016.

Ashton, F. et al, (1975a), PICCR, (Munich), 3311.

Ashton, F. and Saleh, A., (1975), PICCR, (Munich), 2507.

Ashton, F. et al, (1977*), PICCR, (Plovdiv), 7, 364.

Ashton, F. et al, (1977*), PICCR, (Plovdiv), 11, 503.

Ashton, F. et al, (1977*), PICCR, (Plovdiv), 11, 400.

Ashton, F. et al, (1977*), PICCR, (Plovdiv), 12, 1.

Ashton, F. et al, (1977*), PICCR, (Plovdiv), 12, 11.

Ashton, F. et al, (1977*), PICCR, (Plovdiv), 12, 14.

Ashton, F. et al, (1977*), PICCR, (Plovdiv), 12, 370.

Ashton, F. et al, (1977*), PICCR, (Plovdiv), 12, 458.

Babecki, J. et al, (1961), Sov. Phys., JETP, 13, 1089.

Bakich, A.M. et al, (1970), Acta Phys. Acad. Sci. Hung., 29, Suppl.3, 501.

Baltay, C. et al, (1970), Phys. Rev. D1, 759.

Bartlett, D.F. and Lahana, M.D., Phys. Rev. D6, 1817.

Baruch, J.E.F. et al, (1973), Nature, 242, 6.

Baruch, J.E.F. et al, (1975), PICCR, (Munich), 2949.

Baruch, J.E.F. et al, (1975), PICCR, (Munich), 4303.

Bennett, S. et al, (1962), J. Phys. Soc. Japan, 17, 196.

Bethe, H.A., (1930), Ann. Phys., 5, 325.

Bethe, H.A. and Heitler, W., (1934), Proc. Roy. Soc., A146, 83.

Bhat, P.N., et al, (1979), J. Phys. G, 5, L13.

Blake, P.R., et al, (1975), PICCR, (Munich), 8, 2768.

Blandford, R.D., et al, (1977), Nature, 267, 211.

Bloch, F., (1933), Ann. Phys., 16, 285.

Bohm, E. et al, (1968), Can. Journ. Phys., 46, 550.

Bohr, N., (1913), Phil. Mag., 25, 10.

Bohr, N., (1915), Phil. Mag., 30, 581.

Bohr, N., (1948), Kgl. Danske. Videnskab Selskab, 18, 8.

Bonczak, B. et al, (1968), Can. Journ. Phys., 46, S102.

Brooke, G. et al, (1964), Proc. Phys. Soc., 83, 843.

Brooke, G. and Wolfendale, A.W., (1964), ibid, (Brooke et al)

Carrithers, W.C. et al, (1966), Phys. Rev., 142, 1070.

Clay, R.W., and Crouch, P.C., (1974), Nature, 248, 28.

Coats, R.B., (1967), Ph.D. Thesis, (University of Durham).

Cobb, J.H., et al, (1976), Nucl. Inst. and Meth., 133, 315.

Cohen, M.H. et al, (1977), Nature, 268, 405.

Cooper, D., (1974), Ph.D. Thesis, (University of Durham).

Cowan, E.W. and Matthews, K., (1971), Phys. Rev., D4, 37.

Crispin, A. and Fowler, G.N., (1970), Rev. Mod. Phys., 42, 290.

Crouch, P.C. and Tanahashi, G., (1974), unpublished report.

Danburg, J.S. et al, (1971), Phys.Rev., D4, 53.

Danburg, J.S. and Kalbfleisch, G.R., (1972), Phys. Rev., D5, 1575.

Dao, F.T. et al, (1974), Phys. Rev. Lett., 33, 389.

Davies, M.B. et al, (1969), Phys. Rev., 183, 1132.

De Beer, J.F. et al, (1966), Proc. Phys. Soc., 89, 567.

Diggory, I.S. et al, (1974), J. Phys. A, 7, 641.

Dimcovski, Z. et al, (1971), Nucl. Inst. and Meth., 94, 151.

Dirac, P.A.M., (1931), Proc. Roy. Soc., A133, 60.

Dixon, H.E. et al, (1973), PICCR, (Denver), 4, 2556.

Dmitriev, V.A. et al, (1960), Sov. Phys., JETP, 37, 637.

Earnshaw, J.C. et al, (1967), Proc. Phys. Soc., 90, 91.

Einstein, A., (1905), Ann. der. Phys., 17, 891.

Emery, M.W. et al, (1975), PICCR, (Munich), 2486.

Eyeions, D.A. et al, (1955), Proc. Phys. Soc., (London), A68, 793.

Fegan, D.J. et al, (1975), PICCR, (Munich), 2480.

Feinberg, G., (1967), Phys. Rev., 159, 1089.

Feinberg, E.L., (1972), Phys. Rep., 5, 237.

Fermi, E., (1940), Phys. Rev., 57, 485.

Fleischer, R.L. et al, (1971), Phys. Rev., D4, 24.

Fowler, P., (1975), PICCR, (Munich), 4049.

Fritze, R. et al, (1970), Acta Phys. Acad. Sci. Hung., 29, Suppl.3, 439.

Fukui, S. et al, (1965), PICCR, (London), 2, 642.

Gaisser, T. and Rudolf, P., (1976), J. Phys. G, 2, 781.

Gaisser, T. et al, (1978), Rev. Mod. Phys., 50, 859.

Garibyan, G.M., (1958), Sov. Phys., JETP, 6, 1079.

Garibyan, G.M., and Ispiryan, K.A., (1972), JETP Lett., 11, 585.

Gell-Mann, M., (1964), Phys. Lett., 8, 214.

Giacomelli, et al, (1975), Il Nuov. Cim., 28A, 21.

Goldoni, R., (1972), Lett. Nuov. Cim., 5, 495.

Goldoni, R., (1973a), Il Nuov. Cim., 14A, 501.

Goldoni, R., (1973b), Il Nuov. Cim., 14A, 527.

Greisen, K., (1956), "Progress in Cosmic Ray Physics", III, Ch. 3.

Greisen, K., (1960), Ann. Rev. Nucl. Phys., 10, 63.

Grieder, P.K.F., (1970), Inst. for Nucl. Stud., University of Tokyo, Report No. INS-J-125.

Grieder, P.K.F., (1977), Rev. de. Nuov. Cim., Ser. 2, 7, 1.

Grigorov, N.L. et al, (1965), PICCR, (London), 2, 860.

Gurevich, I.I. et al, (1972), Phys. Lett., 38B, 549.

Harris, F. et al, (1973), Nucl. Inst. and Meth., 63, 77.

Hayakawa, S., (1969), "Cosmic Rays", (Wiley International).

Hazen, W.E. et al, (1975a), PICCR, (Munich), 2485.

Hazen, W.E. et al, (1976), Nucl. Phys., B96, 401.

Holroyd, F.W., (1971), Ph.D. Thesis, University of Durham.

Ivanenkov, I.P. and Samusodov, B.E., (1967a), Bull. Acad. Sci., U.S.S.R., (Phys. Ser.), 30, 1722.

Ivanenkov, I.P. and Samusodov, B.E., (1967b), Sov. Jour. Nucl. Phys., 5, 442.

Jabs, A. (1975), Il Nuov. Cim., 26A, 133.

Jackson, C.D., (1970), "Classical Electrodynamics", (J. Wiley, New York), Ch. 13.

Jeanne, D. et al, (1974), Nucl. Inst. and Meth., 111, 287.

Jones, D.G.,et al, (1963), Proc. Phys. Soc.,(London), 81, 1237.

Jones, W.V., (1969), Phys. Rev., 187, 1868.

Jones, L.W.,et al, (1970), Phys.Rev. Lett., 25, 1679.

Kamata, K. and Nishimura, J., (1958), Prog. of Theor. Phys., Suppl. 6, 93.

Kameda, T. et al, (1965), PICCR, (London), 2, 681.

Kaneko, T. et al, (1971), PICCR, (Hobart), 7, 2759.

Kempa, J., (1976), Nuov. Cim., 31A, 568.

Khristiansen, G.B. et al, (1975), PICCR, (Munich), 8, 2801.

Landau, L.D., (1944), Jour. Phys., U.S.S.R., 8, 201.

Lemke, H., (1975a),Lat.Nuov. Cim., 12, 342.

Lemke, H., (1975b), Il Nucv. Cim., 27A, 141.

Lemke, H., (1975c), Lett. Nuov. Cim., 12, 619.

Lemke, H., (1976a), Lett. Nuov. Cim., 17, 209.

Lemke, H., (1976b), Il Nuov. Cim., 35A, 181.

Lloyd, J.L., (1960), Proc. Phys. Soc., 75, 387.

Lovati, A. et al, (1954), Il Nuov. Cim., 12, 526.

Maccabee, H.D. et al, (1968), Phys. Rev., 165, 469.

Matano, T.,et al, (1970), Acta Phys. Acad. Sci. Hung., 29, Suppl. 3, 451.

McCusker, C.B.A., (1975), Phys. Rep., 20C, 229.

Messel, H. and Crawford, D., (1970), "Tables", (Oxford, Pergamon).

Millikan, R.A., (1910), Phil. Mag., XIX, 209.

Narlikar, J.V. and Sudarshan, E.C.G., (1976), Month. Not. Roy. Ast. Soc. 175, 105.

Nasri, A., (1977), Ph.D. Thesis, (University of Durham).

O'Dell, F.W.,et al, (1962), J. Phys. Soc. Japan, 17, Suppl.AIII, 23.

Parker. L., (1969), Phys. Rev., 188, 2287.

Parvaresh, A., (1975), Ph.D. Thesis,(University of Durham).

Pattison, J.B.M., (1965), Ph.D. Thesis, University of Durham.

Pavlopoulos, T.G., (1967), Phys. Rev., 159, 1106.

Porter, N.A. et al, (1957), Phil. Mag., 2, 900.

Prescott, J.R., (1975), PICCR, (Munich), 2474.

Prescott, J.R., (1976), Jour. of Phys. G:Nucl. Phys. 2, 261.

Price, P.B. et al, (1975), Phys. Rev. Lett., 35, 487.

Purcell, et al, (1963), Phys. Rev., 129, 2326.

Ramana Murthy, P.V., (1968), Nucl. Instr. and Meth., 63, 77.

Ramana Murthy, P.V., (1971), Lett. Nuov. Cim., 1, 908.

Recami, E. and Mignani, R(1974), Rev. de. Nuov. Cim., 4, 209.

Rutherford, E., (1911), Phil. Mag. XXI, 669.

Saleh, A.J., (1975), Ph.D. Thesis, University of Durham.

Schwinger, J., (1966), Phys. Rev., 144, 1087.

Schwinger, J., (1968), Phys. Rev., 173, 1536.

Siohan, F. et al, (1973), PICCR, (Denver), 3, 2135.

Smith, G.C. and Matthieson, E., (1975), Nucl. Instr. and Meth., 131, 13.

Staubert, R. et al, (1970), Acta. Phys. Acad. Sci. Hung., 29, Suppl.3, 661.

Sternheimer, R.M., (1952), Phys. Rev., 88, 851.

Sternheimer, R.M., (1953), Phys. Rev., 91, 256.

Sternheimer, R.M., (1954), Phys. Rev., 93, 351, 1434.

Sternheimer, R.M., (1956), Phys. Rev., 103, 511.

Sudarshan, E.C.G. et al, (1962), Amer. Jour. of Phys., 30, 718.

Tanahashi, G., (1965), Jour. Phys. Soc. Japan, 20, 883.

Tonwar, S.C. et al, (1971a), Nuov. Cim. Lett., 1, 531.

Tonwar, S.C, et al, (1971b), Nuov. Cim. Lett., 2, 39.

Tsytovich, T.N., (1962), Sov. Phys., JETP, 16, 1260.

Vavilov, P.V., (1957), Sov. Phys., JETP, 5, 749.

Vatcha, R.H. and Sreekantan, S., (1973), Jour. Phys. A, 6, 1067.

Vernov, S.N. et al, (1961), Sov. Phys., JETP, 41, 340.

Wdowczyk, J. and Wolfendale, A.W., (1971), Jour. Phys. A, 4, L36.

Weinberg, S., (1974), Rev. Mod. Phys., 46, 255.

Whalley, M.R. and Thompson, M.G., (1975), PICCR, (Munich), 2568.

Whitmore, J., (1974), Phys. Rep. Phys. Lett. C, 10C, 273.

Williams, E.J., (1929), Proc. Roy. Soc., A125, 420.

Williams, R.W., (1948), Phys. Rev., 74, 1689.

Yock, P.C.M., (1969), Int. Jour. Theor. Phys., 2, 247.

Yock, P.C.M., (1970), Ann. of Phys., 61, 315.

Yock, P.C.M., (1973), Ann. of Phys., 82, 449.

Yock, P.C.M., (1975), Nucl. Phys. B, 86, 216.

Yodh, G.B. et al, (1975), PICCR, (Munich), 2528.

Zweig, C., (1965), "Symmetries in Elementary Particle Physics", (Acad. Press, New York), p.192.